Engineering Materials

Kanchan Upadhyay
Sabu Thomas
Raunak Kumar Tamrakar *Editors*

Hybrid Phosphor Materials

Synthesis, Characterization and Applications

Springer

Engineering Materials

This series provides topical information on innovative, structural and functional materials and composites with applications in optical, electrical, mechanical, civil, aeronautical, medical, bio- and nano-engineering. The individual volumes are complete, comprehensive monographs covering the structure, properties, manufacturing process and applications of these materials. This multidisciplinary series is devoted to professionals, students and all those interested in the latest developments in the Materials Science field, that look for a carefully selected collection of high quality review articles on their respective field of expertise.

Indexed at Compendex (2021)

More information about this series at https://link.springer.com/bookseries/4288

Kanchan Upadhyay · Sabu Thomas ·
Raunak Kumar Tamrakar
Editors

Hybrid Phosphor Materials

Synthesis, Characterization and Applications

Springer

Editors
Kanchan Upadhyay
IIUCNN
Mahatma Gandhi University
Kottayam, Kerala, India

Sabu Thomas
IIUCNN
Mahatma Gandhi University
Kottayam, Kerala, India

Raunak Kumar Tamrakar
Department of Applied Physics
Bhilai Institute of Technology
Durg, Chhattisgarh, India

ISSN 1612-1317 ISSN 1868-1212 (electronic)
Engineering Materials
ISBN 978-3-030-90505-7 ISBN 978-3-030-90506-4 (eBook)
https://doi.org/10.1007/978-3-030-90506-4

© Springer Nature Switzerland AG 2022
This work is subject to copyright. All rights are reserved by the Publisher, whether the whole or part of the material is concerned, specifically the rights of translation, reprinting, reuse of illustrations, recitation, broadcasting, reproduction on microfilms or in any other physical way, and transmission or information storage and retrieval, electronic adaptation, computer software, or by similar or dissimilar methodology now known or hereafter developed.
The use of general descriptive names, registered names, trademarks, service marks, etc. in this publication does not imply, even in the absence of a specific statement, that such names are exempt from the relevant protective laws and regulations and therefore free for general use.
The publisher, the authors and the editors are safe to assume that the advice and information in this book are believed to be true and accurate at the date of publication. Neither the publisher nor the authors or the editors give a warranty, expressed or implied, with respect to the material contained herein or for any errors or omissions that may have been made. The publisher remains neutral with regard to jurisdictional claims in published maps and institutional affiliations.

This Springer imprint is published by the registered company Springer Nature Switzerland AG
The registered company address is: Gewerbestrasse 11, 6330 Cham, Switzerland

Contents

Introduction

Metal Halide Perovskite-Based Phosphors and Their Applications in LEDs 3
Jizhong Song and Leimeng Xu

Mechanoluminescent Phosphors 51
Yuan Deng, Hanlu Zhang, and Lin Dong

Synthesis and Charecterization

Molecular Hybrid Phosphors 73
Saroj Kumar Kushvaha and Kartik Chandra Mondal

Organic–Inorganic Hybrids for White-Light Phosphors 105
Geeta Sharma and Pankaj Poddar

Synthesis of Phosphorus-Based Phosphors 119
Vasile Simulescu, Simona Funar-Timofei, Vlad Chiriac, and Gheorghe Ilia

Progress and Prospects of Graphitic Structure—Based Phosphors 151
Velayudhan Prajitha, Keloth Paduvilan Jibin, K. S. Sisanth, Jesiya Susan George, and Sabu Thomas

Synthesis, Properties and Applications of Polymeric Matrix-Based Phosphor Hybrids 165
Samit Kumar Ray, Amritanshu Banerjee, Bidyut Kumar Bhangi, Barnali Dutta, and Debapriya Pyne

Applications

Upconversion Hybrid Phosphors for Biological Applications 195
Kaushal Kumar, Sachin Kumar Maurya, and Manoj Kumar Mahata

Biological Application of Hybrid Phosphors 223
Sajjad Husain Mir, M. K. Mohammad Ziaul Hyder,
and A. M. Masudul Azad Chowdhury

Hybrid Phosphor Materials for Optoelectronic Application 241
Jemy James, Sharin Maria Thomas, Ajeesh Kumar Somakumar,
Blessy Joseph, Nandakumar Kalarikkal, and Sabu Thomas

Functionalised (ZnO:Dy@AuNP) Nanoassembly for Sensing Nitro Aromatic Compound 255
G. L. Praveen, Kanchan Upadhyay, Sony George, and Sabu Thomas

Hybrid Nanostructures for Biomedical Applications 275
R. Rajakumari, Abhimanyu Tharayil, Sabu Thomas,
and Nandakumar Kalarikkal

Progress on Lanthanide Ion-Activated Inorganic Hybrid Phosphors: Properties and Applications 303
Preeti Padhye Kulkarni, Monika Malik, and Pankaj Poddar

Introduction

Metal Halide Perovskite-Based Phosphors and Their Applications in LEDs

Jizhong Song and Leimeng Xu

Abstract Electric lighting has become a significant part of human daily life, accounting for approximately 15% of global power consumption. Among various illumination, white light-emitting diodes (WLEDs) have become a major research focus of the industry due to their long lifespan and high energy efficiency. Current commercial WLEDs are fabricated mainly through utilizing blue LEDs with phosphor coatings. Under the environment of energy-saving emission reduction, according to the haitz's law of LED industry, LED will follow the development process of aiming high brightness and low cost. Thus, exploring new phosphors for lightings, compatible with the cost reduce, is highly desired. Metal halide perovskite phosphors have attracted wide attention due to their outstanding luminescence feature and low-cost solution-processing. In this chapter, we first introduced perovskite phosphors of different colors, including three primary colors (blue, green, red), and other colors (e.g. white, yellow and orange). Then, we further summarized the stability improvement strategies of through hybrizing perovskite phosphors with inorganic materials, organic molecules and polymer, and the non-luminous perovskites and luminous perovskites. Finally, we presented some strategies of perovskite phosphor applications in WLEDs, such as by combining GaN chip with three-primary-color perovskite phosphors, through energy transfer in one perovskite, and by doping ions in perovskites.

Keywords Metal halide perovskite · Phosphors · Hybrid phosphors · Composite materials · Light-emitting diodes · Backlight · Lighting · Different colors

1 General Aspects

Light is always what human persuade for, especially electric lighting is a vital part of human daily life, according to statistics, illumination consumes 15% of the world's electricity, among which white light-emitting diodes (WLEDs) have superiorities

J. Song (✉) · L. Xu
School of Physics and Microelectronics, Zhengzhou University, Zhengzhou 450052, China
e-mail: songjizhong@njust.edu.cn

© Springer Nature Switzerland AG 2022

K. Upadhyay et al. (eds.), *Hybrid Phosphor Materials*, Engineering Materials,
https://doi.org/10.1007/978-3-030-90506-4_1

of long lifespan and high energy efficiency, leading to a major research focus in photoelectric industry [1–5]. To realize white emitting, different materials have been exploited, the most primary method is to coat the blue chip with phosphors, the efficiency of WLEDs mainly depend on the performance of phosphor coatings. Under the environment of energy-saving emission reduction, according to the haitz's law of LED industry, LED will follow the development process of aiming high brightness and low cost [6, 7].

As technology developing, traditional materials could not satisfy the operating requirements any more. For example, the traditional incandescent lamp emits visible light by heating the filament electrically to incandescent state through thermal radiation, which has a very low energy-utilization rate, and the filament temperature ups to 3000 °C, which is a dangerous degree in some industries. For another example, the most common energy-saving lamps in our daily life are based on plasma conduction and phosphor luminescence, such luminescent materials have lower working temperature (1160 K) and higher energy-conversion efficiency than incandescent lamps, but their efficiency is still low and the pollution is serious. Hence, exploring new luminescent materials is highly important and urgent. In this field, many materials have achieved much progress, but few could reach the commercial grade. High-efficiency luminescence did not get enough recognition until perovskite phosphors were reported. Perovskite phosphors have attracted wide attention due to their outstanding luminescence feature (such as high efficiency and brightness) and low-cost solution-process.

Perovskite materials are particularly attractive and promising materials in optical field, high photoluminescence quantum yield (PLQY), easily tunable spectra and simple synthesis make them ideal luminous materials. Compared with the synthesis methods of other lighting materials, perovskite phosphors are fabricated by solution process, which allow low-cost and large-scale manufacture [8–21]. Speaking of highly luminescent and efficient phosphors, many progresses have been achieved, a lot of comparative mature technologies have been exploited to synthesize perovskite materials, which have been widely applied in light-emitting diodes (LEDs).

The earliest perovskite phosphor materials are organic–inorganic hybrid perovskites [22–24]. In 2007, Parashkov and his coworkers found $(RNH_3)_2PbX_4$ with perovskite structure could act as luminous materials, and Pierre synthesized $(RNH_3)_2PbX_4$ nanoparticles through nebulization/lyophilization method in 2009 [22]. However, this kind of structure was unstable, which limits the practical applications. Until the end of 2014, researchers sostenuto developed stable organic–inorganic perovskite (e.g. $FAPbX_3$, $MAPbX_3$) [25, 26] and all-inorganic perovskite (e.g. $CsPbX_3$) [27, 28] system. The crystal structures of perovskites are shown in Fig. 1. Figure 1a demonstrated the chemical formula of three-dimensional (3D) ABX_3 perovskite (purple A = cesium (Cs), formamidine (FA), methylamine (MA); black B = Pb, Sn; green X = Cl, Br, I, the black B atoms and the green X atoms form the B-octahedrons ($[BX_6]^{4-}$), A-site cations are filled between B-octahedrons) [29]. Figure 1c demonstrated the chemical formula of two-dimensional (2D) perovskite, $(A')_mA_{n-1}B_nX_{3n-1}$ (A′ represents large organic cation; A represents small organic or inorganic cation such as Cs^+, MA^+, FA^+, Rb^+; B and X represent metal anions and

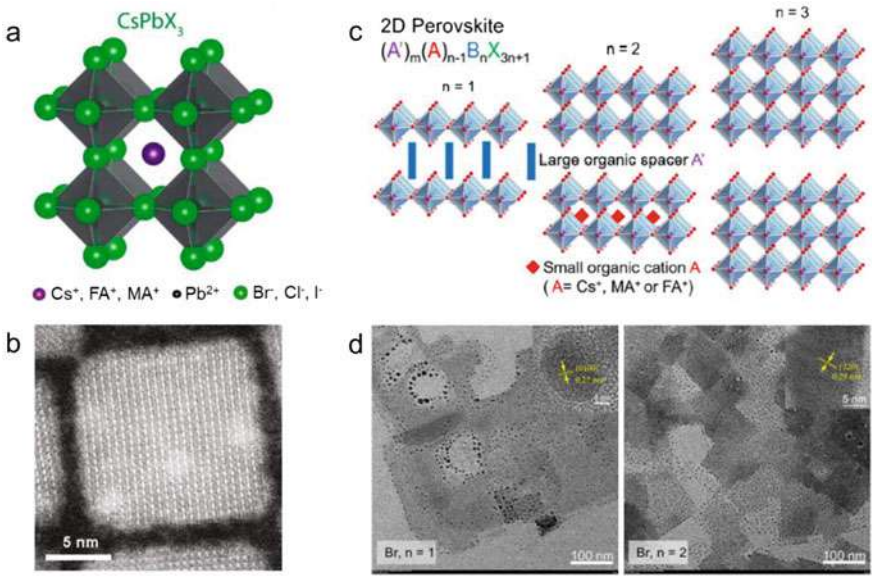

Fig. 1 **a** The crystal structure of 3D perovskites. **b** The high-angle annular dark-field scanning transmission electron micrograph (HAADF-STEM) [29]. **c** The structure of 2D perovskites [31]. **d** TEM images of 2D Ruddlesden–Popper (RP) perovskite with Br series; herein the expression for 2D perovskite is $(BA)_2(MA)_{n-1}Pb_nBr_{3n+1}$ [32]

halogen elements, respectively.). Figure 1b, d exhibited the TEM images of typical 3D and 2D perovskite structures [29, 30]. Besides 3D and 2D structures, perovskite structures of 1D and 0D were also successively prepared, as well as other derived structures such as double-perovskite structures.

In 2015, Kovalenko et al. firstly designed highly luminescent perovskite-based colloidal quantum dots (QDs) by hot-injection method, which pushed the research of perovskites into a hot trend [33]. The as synthesized all-inorganic perovskite exhibited uniformly dispersed grains, high PLQY, narrow full width at half maximum (FWHM) and tunable spectra. Especially, the tunable spectra, covering the whole visible range, could be realized by different methods, such as composition adjustment [33], shape transformation [34] and size control [35, 36]. For instance, by adjusting ingredient proportion of Cl, Br, and I during synthesis, entire-visible spectra of 410–700 nm could be easily realized. The as synthesized $CsPbX_3$ colloidal solutions and their PL spectra are shown in Fig. 2a. For another instance, Tisdale et al. found that nanoplatelets with only few unit cells in thickness exhibited narrow and blue-shifted absorption/emission, and hence allowed lead-bromide-based and lead-iodide-based nanoplatelets to cover the whole visible range. Figure 2b showed the bandgaps of perovskite nanoplatelets with different thickness. Furthermore, Yang and Sargent et al. reported that size effect of QDs could also effectively affect light emission, $CsPbBr_3$ QDs emitted a sky-blue light by decreasing the size of nanocrystals (NCs).

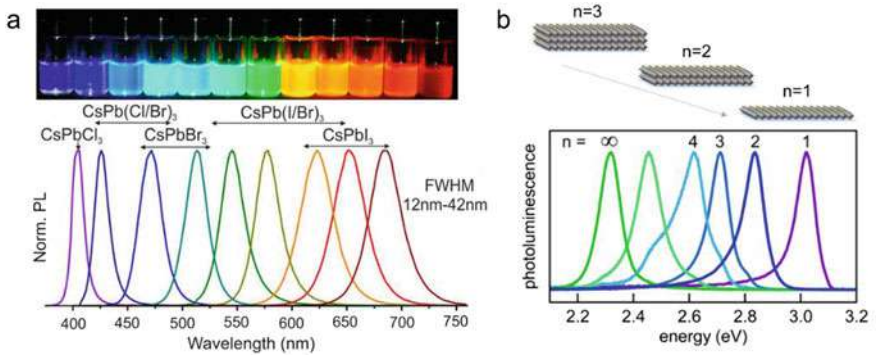

Fig. 2 **a** Spectra adjusted by composition engineering for $CsPbX_3$ NCs [33]. **b** Spectra adjusted by dimension [34]

However, despite these attractive advantages of lead halide perovskites (LHPs) in photoluminescent (PL) applications, one of the key challenges is the toxicity of Pb. Pb exposure during the fabrication process of optoelectronic devices is huge, which threats the human and the environment. Thus, to further extend the family of perovskite phosphors without the presence of toxic Pb, various lead-free perovskites have been developed, including tin- (Sn), bismuth- (Bi), copper- (Cu) and indium-based (In) perovskite system. Sn-based perovskites are suitable for fabricating broad-emission LEDs (e.g. yellow LEDs), but Sn-based perovskites face a problem of self-oxidation of Sn^{2+} to Sn^{4+}, which severely damages its metallic behaver. Bi-based perovskites have high bandgap, usually are applied in blue emitters (e.g. $MA_3Bi_2Br_9$ blue LEDs). In addition, using the energy transition between Bi and other ions (such as Tb^{3+}, Eu^{3+}, Er^{3+}), we can fabricate other perovskites (e.g. orange and red). Cu-based perovskites are new-type perovskites with many interesting PL properties (e.g. Cs_2CuI_3 and $Cs_3Cu_2I_5$) [37–43]. Furthermore, two perovskite structures could nest together to form a metal halide double perovskite (MHDP) structure (usually Bi- and In-based double perovskite) [44–46], which exhibited promising prospect in luminescence and LEDs for its good water-oxygen and thermal stability.

In this chapter, we introduce the basic structures and optical properties of perovskite phosphors according to color classification, such as blue phosphors, green phosphors, red phosphors, and other color system. Meanwhile, different strategies to enhance the optical properties and stabilities of perovskite phosphors were also presented, for example, ion doping, ligands passivation, ion exchange, alloying and so on. Finally, LED backlight applications based on perovskite phosphors are exhibited, which tremendously show the development of perovskites and illuminations. All these perovskite phosphors and applications motivated the development of new lightings in the future.

2 Different Color Perovskite Phosphors

Light is one of the foundations of our life. For more than thousands of years, human attend to control light instead of depending on the sun, until the creation of electric lamp. However, more efficient light sources are what human always persuades for, perovskite, as a more energy-efficient luminescent material, attracts increasing attentions, many synthetic methods of high-quality perovskite phosphors have been reported. After several years of development, perovskite phosphors can show a variety of different light emission colors, including primary blue, green, red (RGB), and other colors, such as white, orange, and yellow light. In all the colors, the three-primary colors are the most attentional, white is the basic color for illumination applications.

The perovskite phosphors with different colors and their synthesis and improvement methods are described in detail below.

2.1 Blue Perovskite Phosphors

As one of the three-primary color, blue is the key, not only for its application in industry and biology, but also because there are more difficulties and bottlenecks in blue perovskite phosphors. The general problems of blue perovskite phosphors are low brightness, low luminous efficiency, and poor stability. So far, many breakthroughs have been achieved, but the efficient and stable blue perovskite phosphors are still scarce.

2.1.1 Lead Halide Perovskite

Structure of blue perovskites can be described as $APbBr_{3-x}Cl_x$, where Cl^- plays a vital role in tuning spectrum from green to blue. Because of smaller ionic radius and stronger bonding of Cl^-, blue perovskites have smaller NCs. However, compared with green and red perovskite phosphors, mixed halogen perovskites of Cl and Br exhibit lower efficiency. So, research on blue perovskite is lagging behind and still has a long way to go.

Synthetic methods of blue LHPs are similar to those of green and red, which can be classified into hot-injection, room-temperature synthesis and anion exchange. The emission wavelength of perovskite can be tuned from 400 nm to ~520 nm by controlling the proportion of Cl and Br [47]. Besides altering the spectra by adjusting the component during synthesis process, post-processing can also achieve the same effect. For instance, the anion exchange after synthesis can effectively modulate the spectrum without changing the crystal structure [48], and the final QDs exhibit a higher efficiency and stability. The schematic diagram of anion exchange shown in Fig. 3a, b exhibited the TEM and PL spectra of NCs after anion exchange. We can

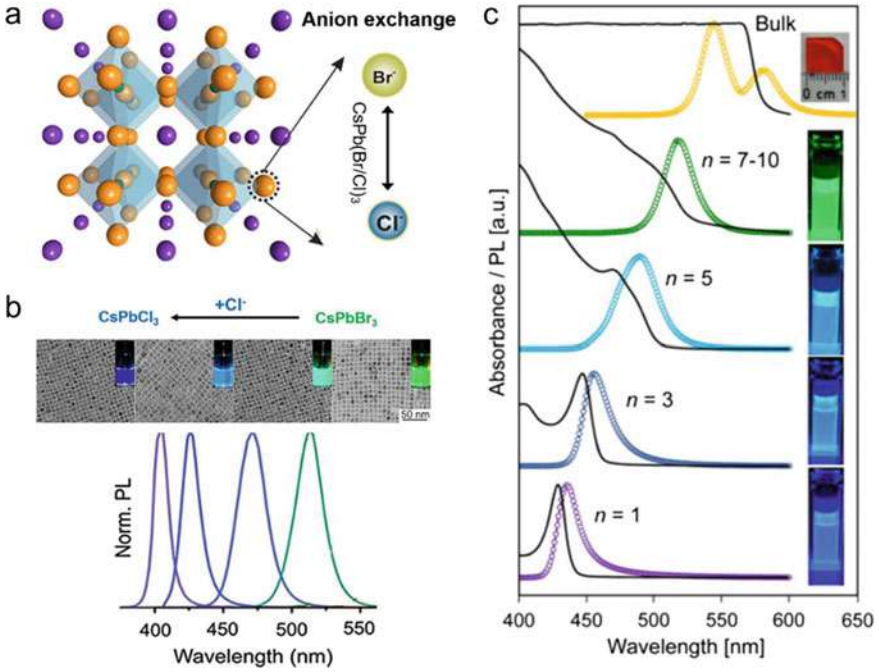

Fig. 3 Schematic diagrams of methods and spectra of blue LHP. **a** Anion exchange in $CsPbBr_{3-x}Cl_x$ perovskites [48]. **b** The corresponding TEM and PL spectra of anion-exchange NCs [33, 47, 48]. **c** PL spectra and samples of perovskite structures (usually 2D perovskites) [62]

clearly see that $CsPbBr_{3-x}Cl_x$ NCs have smaller grain size and still maintain the same morphology with $CsPbBr_3$.

Anion-exchange can easily adjust anion species of perovskites, thereby control the spectrum [49]. For the anion-exchange of LHPs, inorganic salts are generally used as halide source, such as LiX, ZnX_2, PbX_2 and CuX_2. Parthiban et al. [50] used lithium salts (LiX, X = I, Cl, and Br) as halide source at room temperature to carry out the anion exchange, this method could tune the green emission ($CsPbBr_3$) at 508 nm over the entire visible spectral region (425–655 nm). In addition, Wang et al. [51–54] reported that metal halide or halide acid could effectively regulate the spectra by anion exchange post-treatment, leading to enhanced stability and PLQY of LHP.

In addition, organic molecules can also affect the anion-exchange process [48, 50, 52, 55–60]. In 2015, Georgian et al. testified the feasibility of anion exchange in $CsPbX_3$ NCs, they realized blue emission at 468 nm and even violet light at 404 nm by inorganic and organic halide, including PbX_2 and organometallic Grignard reagents (MeMgX) and oleylammonium halides (OAmX) [48]. Yang et al. further exploited the anion exchange mechanism, which could occurr easily due to three reasons: firstly, halide anions have high diffuse/migrate ability in perovskite lattice, secondly,

the perovskite structure and cation framework are rigid and highly defect-tolerant, and finally, the effective vacancy-assisted diffusion mechanism [55–57, 60].

Apart from NCs, adjusting the number of layers (n values) of low-dimensional low-dimensional perovskite structures could effectively tune the spectra from green to deep blue arrange. The quantum confinement effect and blue shift of spectra resulting from low-dimensional perovskite structure, make it a worthy method to fabricate blue-emission perovskites. As is shown in Fig. 3c, with the n values varying from ∞ (bulk) to 1 (2D), the PL spectra of $CsPbX_3$ blue shift to ~420 nm. These 2D and quasi-two-dimensional (quasi-2D) structure can be realized by introducing large organic cations. For example, William et al. synthesized $L_2[FAPbBr_3]PbBr_4$ (where L is an organic ligand (octylammonium, butylammonium)) nanoplatelets, which exhibited continuous emission over a 1.5 eV spectral range, from 2.2 to 3.7 eV. The dimension control provided an approach to adjust the spectra of low-dimensional perovskites [61].

As a matter of fact, in 2016, Sudhir Kumar and his coworkers had elaborated the possibility and validity of this strategy [62], they found that with reducing the stacking number to $n \leq 5$, there would be an obvious blue shift, and sharper excitonic absorption feature. They further illustrated that the two main methods were beneficial to obtaining efficient blue emission, (i) precisely controlling the stacking layer through separating ligand co-surfactant colloidal chemistry to yield a high degree of blue shift by the quantum confinement effect [63]; (ii) using the fluorescent, wide-band-gap, and low-dielectric-constant organic hosts as the barrier materials to form perovskite dielectric quantum wells and then generate efficient radiative recombination by the dielectric confinement effect and the near-field Förster resonance energy transfer (FRET).

In order to make the blue QDs meet the application requirements, it is not enough to rely on composition engineering, anion exchange, and morphology engineering merely. More methods are needed to improve the performance of blue perovskite in terms of brightness and efficiency, strategies such as ligand engineering and ion doping have been proved effective and promising.

Edward and his coworkers reported a strategy of surface ligand engineering in 2016, which achieved high efficiency at 490 nm [64]. In their work, they firstly find an extremely effective ammonium salt, didodecyl (dimethyl) azanium bromide (DDAB). They demonstrated that the deprotonated acidic oleic acid (OA) protons facilitated the removal of the oleylamine (OAm) ligand by protonation, and promoted the coordination of the Br^- with the positively charged surface metal centers (Cs^+ or Pb^{2+}), and the existence of DDA^+ on the crystal surface helped to maintain their solubility in solvent (toluene, octane, hexane and so on). Other halide molecules can also act as ligands [65], such as PEABr [66], IPABr [66], BABr [67], Octylammonium bromide (OCTABr) [61], etc.

Despite of ligand engineering [68], efficient blue emission also can be realized by ion doping. Ion doping can be divided into three types according to the different positions of the doping/substitution ions in the crystal: X-site doping, A-site doping and B-site doping [61, 69, 70]. The role of halogens in adjusting the spectra and bandgap

is the most obvious. However, it is not enough for highly efficient perovskite materials, especially mixed halogens are unfavorable to stable spectra and high efficiency. Here we would not introduce X-site doping in detail. Candidates of A-site cations are mainly FA^+ and MA^+, which lead to a better stability [71, 72] and slight red-shift (due to bigger ion radius [73]) in blue perovskite.

A-site ions mildly influence the absorption and emission, so the spectra of A-site doped perovskites exhibit blue shift or red shift slightly. FA^+ and MA^+ are often used to finely tune the spectra, or to improve the brightness. However, all-inorganic lead halide perovskite (LHP) is more stable compared to organic–inorganic hybrid ones [33, 74, 75]. Weidman et al. [73] varied A-site cation between Cs, MA, and FA (cation size: Cs < MA < FA, whose corresponding effective ionic radii are 1.67, 2.17, and 2.77 Å, respectively) to enhance the stability and PLQY of nanoplatelets. Relatively, the FA-doped perovskite exhibited higher PLQY than MA-doped perovskite. In addition, Sang-Wook et al. synthesized Rb^+ doped $Cs_xRb_{1-x}PbX_3$ blue perovskite QDs with a high PLQY of 86%, extended the range of A-site doping ions [76].

Relatively, B-site doping is a promising method in enhancing properties of lead halide perovskites, which can be used to regulate the spectra, and the currently promising ions are Mn^{2+}, Ni^{2+}, Zn^{2+}, Al^{3+}, Bi^{3+}, Cd^{3+}, Co^{2+} and rare earth elements [77–91]. In 2017, Liu et al. synthesized $CsPb_xMn_{1-x}Cl_3$ NCs by improved hot-injection method which enhanced the PLQY of $CsPbCl_3$ from 5 to 54% [92]. Al and Ni doping were also effective ways to improve the performance of blue perovskites. Meng et al. proposed Al^{3+}-doped blue-emitting $CsPbBr_3$ perovskite NCs, where a small amount of Pb^{2+} were substituted by Al^{3+}, this method generated a blue shift in the spectrum from 515 to 456 nm. The possible reason of spectral shifts in such quantum-confined particles may be associated with electronic doping by aluminum ions or size changes upon doping [80]. Furthermore, many other cations such as Cd^{3+}, Co^{2+}, Yb^{3+} also have important effect on the blue emission of $CsPbX_3$ (X = Cl, Br or mixture) [77, 78, 81, 93–96].

In conclusion, blue Pb-based perovskites still face the problems of instability and low efficiency, methods in enhancing the properties of blue 3D perovskites are significantly needed to be explored. For example, optimal surface engineering and doping are highly desired.

2.1.2 Lead-Free Halide Perovskite

Toxicity of lead is the main concern of LHP materials, the lead exposure in fabrication process and devices may lead to many healthy problems. Therefore, replacing lead with other atoms and without destroying the outstanding properties of perovskite becomes a hot research direction. Lead-free perovskites can be ideal alternatives for perovskite-based lightings. The lead-free halide perovskites (LFHPs) are mainly classified into several systems: Sn-based, Bi-based [46, 97–101], In-based [102–106], Cu-based [107–111], and antimony-based (Sb) [112, 113] perovskites. Sn-based perovskites are barely applied in blue perovskite phosphors. But doping other element could make Sn-based perovskite emit blue light. For example, Tang et al. synthesized

Cs_2SnCl_6:xBi perovskite [114], with a deep blue light under UV light, and acquired a high PLQY of 78.9% with 2.75% Bi-doping, as shown in Fig. 4a. Relatively, Bi, In, Cu and Sb-based system are usually used as blue lead-free perovskite phosphors [10, 114]. The main structure of lead-free perovskites are given as follows, $A_3B'_2X_9$, $A_2BB'X_6$, $A_3B_2X_5$ (A = MA, FA, Cs, B is univalent cation such as Ag^+, Na^+, Cu^+, B′ is trivalent cation such as Bi^{3+}, In^{3+}, Sb^{3+}).

In 2016, Tang and his coworkers used Bi in organic–inorganic perovskite, and synthesized $MA_3Bi_2Br_9$ blue perovskite, which solved the problem of low PLQY in blue light perovskite (≈12%). Figure 4b presented the structure of $MA_3Bi_2Br_9$, where blue globule is anion of Cs, FA or MA, green and purple globule constitute gradient octahedron, which represent the Sb, Bi, Sb and Cl, Br respectively. Figure 4c demonstrated the absorption and PL spectra of $MA_3Bi_2Br_9$ [101, 115]. And then, in 2018, they applied Cl-passivation strategy and further boosted the PLQY up to 54.1% at 422 nm. By kinetic controlling during the synthesis, Cl^- locating on the surface of QDs act as passivating ligand to effectively suppress surface defects and enhance the PLQY [98, 100]. Afterwards, Zeng et al. synthesized $FA_3Bi_2Br_9$ QDs with a blue emission at 437 nm, a high PLQY of 52% and good air stability [46]. Zhang's

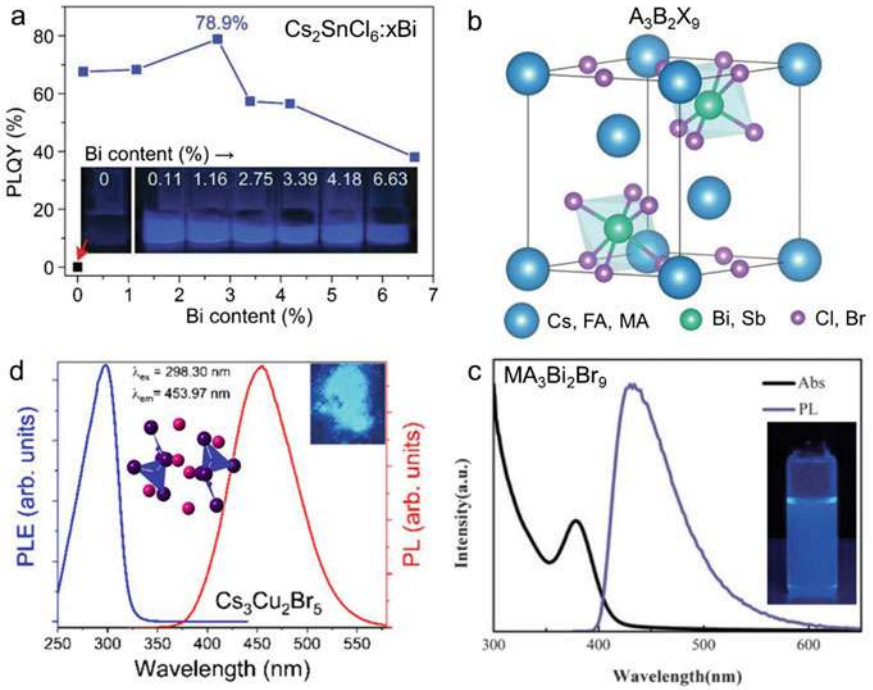

Fig. 4 **a** The PL images of and PL Cs_2SnCl_6:xBi [114]. **b** Crystalline structure of $A_3B_2X_9$ [101]. **c** The absorption, PL spectra of $MA_3Bi_2Br_9$, the illustration showed the solution photograph [101]. **d** PL and PL excitation (PLE) spectra of $Cs_3Cu_2Br_5$, illustrations are schematic diagrams of crystal structure and sample photograph [111]

group further used weak-polar solvent at room temperature method to synthesize blue $Cs_3Bi_2Br_9$ QDs with a PLQY of 29.6% [97].

Except $A_3B_2X_9$, recent investigators found that Cu can also be used to prepare lead-free blue perovskite phosphors. The all inorganic Cu-based perovskite Cs_2CuX_4 (X = Cl, Br, I) QDs were first facilely synthesized in 2018 [108], and then, blue-emitting $Cs_3Cu_2I_5$ films were fabricated. Cu-based perovskites have much higher PLQY than Bi-based perovskite [101], up to 92.1% for single crystals and 62.1% for thin film at 445 nm [110]. Especially, the PLQY of $Cs_3Cu_2Br_5$ can achieve near-unity PLQY [111]. The crystal structure and PL spectra of $Cs_3Cu_2X_5$ is demonstrated in Fig. 4d, the 0D $Cs_3Cu_2X_5$ crystal structures contained unique $[Cu_2X_5]^{3-}$ dimers made of a trigonal planar CuX_3 sharing an edge with a tetrahedral CuX_4 unit, surrounded by Cs^+. This Cu-based perovskite phosphor presented a very high PLQY accompanied by a large Stokes shift and has a high conversion efficiency and a low self-absorption. Relatively, Cu-based perovskites had much more superiority than Bi-based ones, which may originate from the unique 0D electronic structure (each Cu-I photoactive site is separated by Cs ions, combined with the embedded core/shell structure).

Not only Bi-based and Cu-based perovskites, but also metal halide double perovskites (MHDPs) perform well in blue emission. Theoretical calculations demonstrated that a lead-free halide double perovskite structure could be formed through replacing two toxic Pb^{2+} in the crystal lattice with a pair of nontoxic elements. The expression is $A_2B^+B^{3+}X_6$ (e.g. $Cs_2InSbCl_6$, $Cs_2AgInBr_6$, $Rb_2AgInBr_6$, and $Rb_2CuInCl_6$) [116–119]. The double perovskite is mainly prepared through hot injection. Zhou et al. used this method to synthesize $Cs_2AgBiBr_6$ NCs with pure cubic shape and high crystallinity [120]. Through deliberately controlling the ligand ratio and reaction temperature, the quality of $Cs_2AgBiBr_6$ NCs could be improved tremendously. Furthermore, Liu and Tang et al. reported the preparation of $Cs_2AgInCl_6$ by using HCl as the solvent [103, 105]. Considering ion-exchange reactions have well-established advantages, Creutz et al. explored the colloidal heterometallic Cs_2AgBiX_6 NCs(X = Cl or Br) [121–123] through ion-exchange.

In addition, Bi^{3+}, Sb^{3+}, Eu^{2+}, Ce^{3+} are also commonly used as doping ions in double perovskite for blue-emitting phosphors [109, 124, 125]. Zou et al. designed a Sb^{3+}-doped $Cs_2NaInCl_6$ double perovskite with a bright blue emission, the PLQY is up to 75.89%. The Sb^{3+} in $Cs_2NaInCl_6$ led to a narrow and relatively unusual blue emission of self-trapped excitons (STEs). According to density functional theory (DFT), the doped Sb^{3+} ions broke the parity-forbidden transition rule and effectively modulated the density of state (DOS), hence boosted the PLQY [109, 118]. The improved PLQY is attributed to the fact that the optimized Sb^{3+}-doping concentration could effectively modulate the relaxation of parity-forbidden transition. Furthermore, Kovalenko et al. investigated the role of Sb^{3+}, and the impact of Na^+ and K^+ in Cs_2MInCl_6:xSb(M = Na, K). The Cs_2KInCl_6 crystalline is tetragonal double perovskite phase, while $Cs_2NaInCl_6$ is cubic structure, which results in distinct emission colors of broad blue and green emission in $Cs_2NaInCl_6$:xSb, and Cs_2KInCl_6:xSb compounds, respectively [106, 126].

Blue perovskite phosphors are mainly LFHPs based on Bi, Cu and Sn, and MHDPs based on monovalent cations (Ag, Na, K) and trivalent cations (In, Bi, Sb). Different from LHPs, the spectra of LFHPs could be adjusted by ion doping and alloying. Interestingly, from the optical properties of the above perovskite materials, we can find that no matter Bi-based or Cu-based perovskite, halide element seems unimportant in adjusting the spectrum. This is because both the valence and the conduction bands are dominated by the Cu or Bi states [107, 110], which lead to small differences in PL emission peaks.

3 Green Perovskite Phosphors

Different from blue perovskites, green perovskites made more achievements, especially LHPs. The efficiency of perovskite-based LED devices has reached nearly to their theoretical limits. Green LHP phosphors exhibit the best-performance, and many works have reported near 100% of PLQY and highest luminance of up to 3.8×10^5 cd/cm^2 [127]. However, the toxicity and instability of LHP are always inevitable shortcoming. Therefore, the development of green lead-free perovskites is still extremely important.

3.1 Lead Halide Perovskite

Lead halide perovskites have many advantages, such as tunable spectra, narrow FWHM, and high luminescent efficiency [27, 33]. Figure 5 showed the PL properties

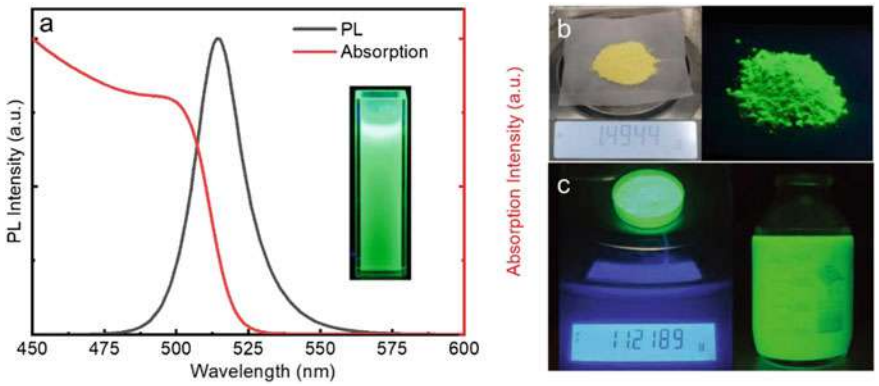

Fig. 5 **a** Absorption (red line) and PL spectra of $CsPbBr_3$ NCs. (Inset) Photograph of $CsPbBr_3$ solution under UV lamp [128, 129]. **b** and **c** Photographs of mass prepared green LHP powders and dispersions [131, 132]

of typical green LHPs. Figure 5a demonstrated the absorption and PL spectra of lead halide perovskite, whose PL peak is usually at 516–520 nm with a narrow FWHM of 19–29 nm [128–130]. The illustration is the photograph of $CsPbBr_3$ QD solution [128, 129]. Fig. 5b, c displayed large-quantity synthesized perovskite powders [131] and dispersions [132]. For the synthesis of $APbBr_3$ (where A = Cs, MA, FA), the two most common methods are hot-injection method [27, 33, 129, 130, 133] and room temperature synthesis method [74, 75, 134–136]. In addition, some other methods are also explored, such as solvothermal synthesis [21, 137, 138], solvent-free mechanosynthesis [139], microwave-assisted synthesis [140], vapor-phase growth method [133], ball grinding method and so on. Generally, perovskites synthesized by hot-injection exhibited more outstanding optical properties and more uniform grain distribution. For hot-injection, long chain organic molecules are necessary, the common used molecules are octadecene (ODE), OAm and OA, which guaranteed the integrity of ionic crystal structure of $APbX_3$. As for room-temperature synthesis, it has many advantages, such as simple operating conditions, low reaction temperature. Profiting from flexible modifying strategies on the surface or component of the perovskite crystals, the performance of the perovskites synthesized at room temperature has been comparable to that of the hot injection method [48, 52, 53, 65, 70, 75, 135].

Since the first report in 2015, green perovskites, $CsPbBr_3$ NCs, have achieved a very high PLQY more than 60%. Then, ligand engineering was introduced to improve the optical properties [17, 75, 141–148]. Ligands are indeed essential in the preparation of perovskite emitters. OA and OAm are the most traditional ligands, and they can control the morphology of NCs [35, 149–152]. OA and OAm chelated with the NCs surface, which protected the nanostructure from polar solvent. However, ligand loss resulting from proton transfer between OA and OAm lead to deteriorative emitting properties. To further enhance the PLQY and brightness of perovskite quantum dots (QDs), various ligands were introduced. For example, Bakr et al. introduced DDAB by ligand-exchange strategy, because of the excellent passivation of DDAB on NCs, the PLQY was increased by near 50% and higher brightness were reported [64]. Other ligands such as tetraoctylammonium bromide (TOAB) [134], octylphosphonic acid (OPA) [153], 3,3-diphenylpropylamine bromide (DPPA-Br) [154] etc. were also reported to be efficient ligands.

In addition, cation doping is another effective method for controlling photoluminescence [65]. The ions used in $APbBr_3$ are Sn^{4+} (Sn^{2+}), Na^+, Rb^+, Ag^{2+}, Mg^{2+}, Fe^{3+}, Zn^{2+}, Cd^{2+} and so on [155–159]. Yu et al. reported that Sn partially substituted Pb in $CsPbBr_3$, which showed a significantly improved PLQY [159]. However, Sn ion is an easily oxidized ion, it is sensitive to the operation requirement and the proportion of replacement. On this basis, Dong et al. investigated the ion exchange by metal halides [155]. Halogens guaranteed the halogen-rich environment to exchange cations between metal halide and perovskite NCs. Other transition metal halides (FeX_3, CoX_2, NiX_2, CuX_2) could be used as halides sources efficiently as well, which not only efficiently controlled the PL spectra, but also significantly improved the stability of NCs [155–157]. Up to now, green lead halide perovskites have achieved a high efficiency with PLQY up to near 100%.

3.2 *Lead-Free Perovskite*

In terms of green emission, replacing Pb is also an urgent task in perovskite phosphors. According to previous reports, Sn, Mn and Cu were successfully applied to fabricate green perovskite phosphors. Different from LHPs, LFHPs achieved green emission via quantum limiting effect through reducing the dimension of NCs. For example, Xia et al. reported a lead-free 0D hybrid metal halide $(C_8H_{14}N_2)_2SnBr_6$ to replace toxic Pb-based perovskite, whose emission peak located at 507 nm with a PLQY of 36 4% under the excitation of 365 nm UV light [160]. Figure 6a demonstrated the structure of $(C_8H_{14}N_2)_2SnBr_6$, and the green emission came from excited-state structural distortion of $[SnBr_6]^{4-}$ octahedral units. The PL spectra and crystal graph are shown in Fig. 6b [160]. Organic cations protected Sn^{2+} in $[SnBr_6]^{4-}$ octahedrons from being oxidized to Sn^{4+}, and intermolecular interactions such as hydrogen bonding and π–π stacking further stabilized the oxidation resistance of Sn^{2+}.

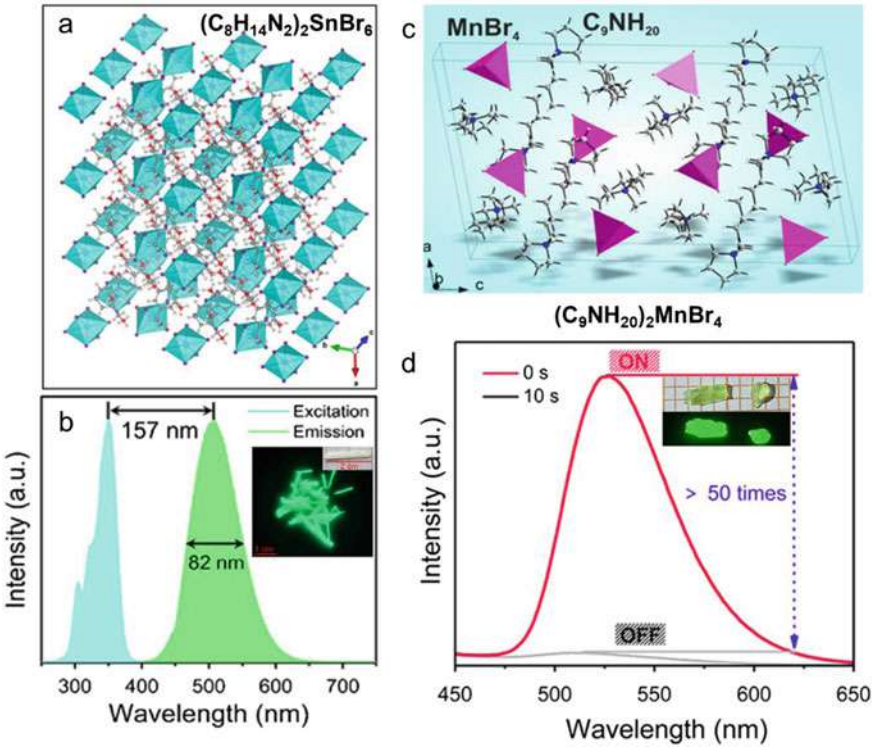

Fig. 6 **a** Crystal structure diagrams of $(C_8H_{14}N_2)_2SnBr_6$, **b** The excitation and emission spectra of $(C_8H_{14}N_2)_2SnBr_6$. Inset: sample photograph of $(C_8H_{14}N_2)_2SnBr_6$ crystals under 365 nm UV irradiation [160]. **c** Unit cell structure model of $(C_9NH_{20})_2MnBr_4$. **d** PL spectra of as-synthesized $(C_9NH_{20})_2MnBr_4$ crystals in the daylight and upon 365 nm UV excitation [162]

Mn-based perovskites are promising to be green emitters. Lin et al. further explored $(C_7H_{13}N_2)_2MnCl_4$ metal halide compound, which emitted a broad PL emission at 536 nm with a high PLQY up to 70.8% (upon 365 nm light excitation) [161]. Xia et al. also synthesized 0D $(C_9NH_{20})_2MnBr_4$ lead-free perovskite with a PL peak at 528 nm and a higher PLQY of 81.08% [162]. The crystal structure and optical spectra of $(C_9NH_{20})_2MnBr_4$ are demonstrated in Fig. 6c, d. A general perspective is that the emission peak springs from the Mn, whose emission peak is about 580 nm, due to the quantum confinement effect, the spectrum blue shift to green-light range. Interestingly, the chemical structure and optical properties of these 0D compounds are very stable, the phase structures remained nearly invariable after exposing to air and moisture conditions for 90 days and the PLQY still maintained 68.66%. Moreover, on the basis of $(C_9NH_{20})_2MnBr_4$, Xia's group designed the Zn/Mn alloying to inhibit the concentration quenching caused by the energy transfer of Mn^{2+}, this novel method successfully acquired a near-unity PLQY at 518 nm [163]. In addition, Cu also has some attractive properties in lead-free perovskite. Han's group fabricated β-$Cs_3Cu_2Cl_5$ with excellent optical and thermal stability by hot-injection method, which exhibited a near-unity PLQY at room-temperature, which is one of highest record in green all-inorganic LFHPs [164].

4 Red Perovskite Phosphors

4.1 Lead Halide Perovskite

Red is the last color of three-primary color we introduce here. The structure of red perovskite is the same as that of blue and green perovskite except for different halogen ions, where the X in $APbX_3$ is I, or mixture of I and Br. Through adjusting the composition of halogen ions, the spectra of red perovskite can be adjusted in the range of 630–700 nm. Illustrations of Fig. 7a and b demonstrated the typical fluorescent photographs of red perovskites [165, 166].

Generally, red $APbX_3$ perovskites are synthesized by hot injection, the α-$APbI_3$ phase are obtained by rapid cooling to room temperature. In 2014, Kovalenko et al. reported all-inorganic LHP nanocrystals, which have considerable application prospects in light-emitting and photoelectric devices [33].

Though red LHPs have many outstanding properties and application prospects, there still a severe problem: it is hard to acquire stable phase. Both theoretical calculations and experiments exhibited that luminous phase $APbI_3$, e.g., α-$APbI_3$ only exist with the temperature above 300 °C, which can easily transform into nonluminous δ-$APbX_3$ phase at operative environment [95, 167, 168]. So $APbX_3$ is at metastable state, which means that obtaining the phase stability $APbI_3$ is highly difficult. Based on this situation, ligand engineering and ion doping are used to enhance the phase stability of red perovskite phosphors.

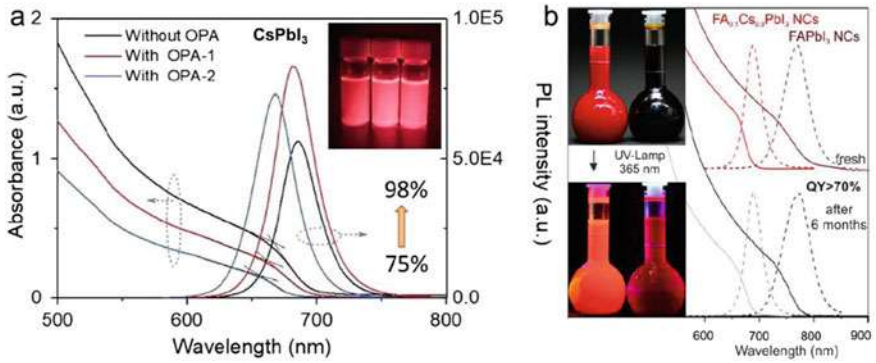

Fig. 7 **a** Absorption and PL spectra of $CsPbI_3$ and OPA-passivated $CsPbI_3$ colloidal solutions. Illustration demonstrated solutions under UV-light excitation [165]. **b** Optical absorption and PL spectra of $FAPbI_3$ NCs and $FA_{0.1}Cs_{0.9}PbI_3$ NCs before and after 6 months of storage. The insets contain photographs of the $FAPbI_3$ NCs and $FA_{0.1}Cs_{0.9}PbI_3$ NCs colloidal solutions in toluene under daylight (upper image) and under a UV lamp ($\lambda = 365$ nm; lower image) [166]

Passivation engineering is a feasible approach [95, 167, 169, 170], as mentioned before. Organic molecules, long-chain cations and amine played vital roles in passivating the surface of nanocrystals or films [35, 149–151]. During the process of fabricating perovskites, solvent, ligands such as acid and amine have great influence on QDs. Luther used methyl acetate (MeOAc) as purification solvent to remove excess unreacted precursors without inducing agglomeration and keep cubic phase for months [95].

Acidic ligand, such as octylphosphonic acid (OPA) and bis-(2,2,4trimethylpentyl) phosphinic acid (TMPPA), have been proven to be effective ligands to stabilize the phase [171, 172]. For example, OPA formed a strong interaction with undercoordinated Pb atoms on the surface and resulted in a nearly uniform PLQY and better solution stability [165]. As demonstrated in Fig. 7a, as the increase of OPA, the PL peaks blue shift from 685 to 667 nm, and the PLQY increase from 75 to 98%. Meanwhile, OPA passivated LHP colloidal QDs demonstrated higher luminance [165]. Likewise, Gao and coworkers found that, by weakening the hydrogen bonding between the functional moieties of passivators and the organic cations/molecules and molecules in the perovskite, the defect sites were significantly passivated and the non-radiative recombination losses was minimized [169]. Except for acid, amine ligand also exert influence on stability of α-$CsPbI_3$ [168, 170, 173].

Researches have proved inorganic cations can also passivate LHPs. Stranks et al. firstly found that KI passivated the triple-cation perovskite thin films ($(Cs_{0.06}FA_{0.79}MA_{0.15})Pb(I_{0.85}Br_{0.15})_3$), the experimental results exhibited that K^+ did not incorporated into the perovskite lattice, but formed passivation layers with halogen on the surfaces [174]. After being passivated, LHPs demonstrated a near-100% PLQY with extremely stable PL spectra. This phenomenon could be explained by the interaction between potassium bromide and LHP films [175]. The potassium halide passivated surface halide vacancies in mixed halide perovskites, improved the

optical properties and suppress the ion migration in perovskite film, which lead to high PLQY and improved stability. However, as a matter of fact, only a few cations, such as K [174, 175] and Ag [93], were found to have passivating effect on surface of perovskite, most cations usually be thought of a good dopant rather than passivators.

When it comes to ion doping, doping smaller cations to stabilize the lattice and phase structure is a general strategy in blue and green perovskites, but for red lead iodide perovskites, too small doping cations would lead to severe lattice distortion and deteriorated optical performance. According to defect tolerance theory, small organic cations like MA^+ and FA^+ are conductive to stabilize the crystalline structure of perovskite, and also help to decrease lattice defects and increase the PLQY of red perovskite. Kovalenko led the way of synthesizing stable $FA_xCs_{1-x}PbI_3$ NCs, as demonstrated in Fig. 7b. The $FA_{0.1}Cs_{0.9}PbI_3$ QDs solution had a PLQY of 70% at 685 nm, even after 6 months of storage. Both $FAPbI_3$ and $FA_{0.1}Cs_{0.9}PbI_3$ NCs retained their high QY in solution (with less than 5% relative decrease) [166]. Moreover, Ag^+, Ni^{2+}, Cu^{2+}, Sr^{2+} and Ti^{2+}as dopant are used to enhance the phase stability of $CsPbI_3$ NCs [93, 176–179].

In brief, phase instability is the main problem of red LHPs. Although solvent engineering, ligand passivation, inorganic doping are valid methods to stabilize radiative α-$CsPbX_3$ phase, there still need more researches to lucubrate the mechanism of phase decomposition and enhance stability of red lead halide perovskites.

4.2 Lead-Free Halide Perovskite

Similarly, there have been many reports about lead-free red perovskite, Sn-based LFHPs and MHDPs (which can be further classified into 3D, 2D and 0D according to crystal morphology) still play important roles in red LFHP system.

Sn has a suitable ionic radius and similar electron structure with Pb, which makes it an ideal choice for red perovskite [180]. Inspired by hot-injection method of lead halide perovskite, Deng et al. used tetravalent tin (Sn^{4+}) instead of divalent lead (Pb^{2+}) to synthesize stable Cs_2SnI_6 perovskite NCs. Simultaneously, by controlling reaction time, the shapes of Cs_2SnI_6 NCs were easily tuned from spherical QDs, nanorods, nanowires, and nanobelts to nanoplatelets, and the light emission could be tuned from bright red to dark red [10].

2D LFHPs have better photoelectric properties comparable to 3D ones. Researchers synthesized superior-photoluminescence 2D $(PEA)_2SnI_4$ perovskite with tunable visible emission properties (from ~635 to ~468 nm) via different I/Br ratio. Figure 8a showed crystalline structure of $(PEA)_2SnI_xBr_{4-x}$, the organic–inorganic layers are arranged alternately (light gray balls represent $-NH^{3+}$ groups, red polyhedral represent corner-sharing $[SnX_6]^{4-}$ octahedra and X represents halide). Figure 8b demonstrated the spectra and LED device photograph of $(PEA)_2SnI_xBr_{4-x}$ [181]. Interestingly, PEA cations provided a physical barrier to slow down oxygen diffusion and subsequent degradation, which lead to superior stability.

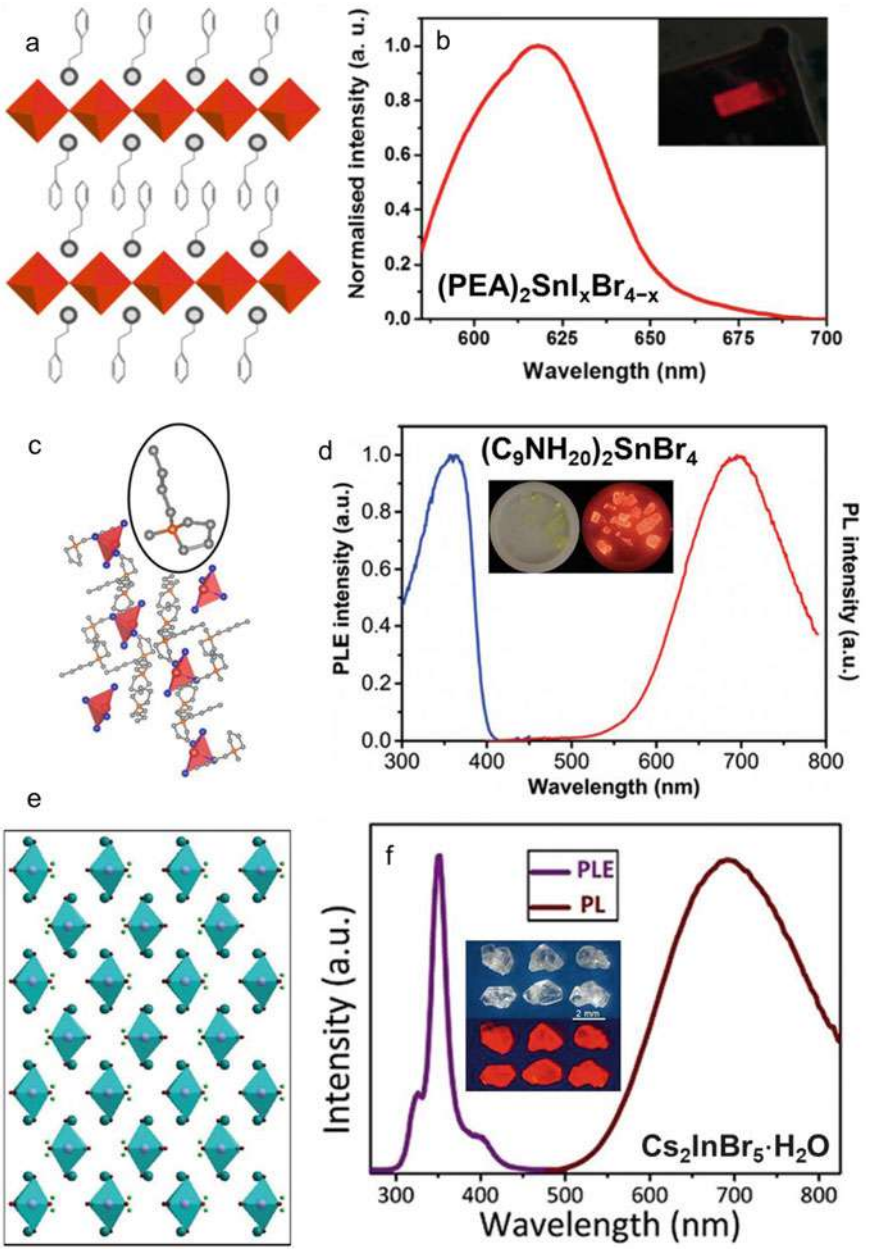

Fig. 8 **a** Crystal schematic of $(PEA)_2SnI_xBr_{4-x}$ perovskite. **b** PL spectrum of $(PEA)_2SnI_xBr_{4-x}$. (Inset) Image of the $(PEA)_2SnI_xBr_{4-x}$ based LED under operation [181]. **c** Crystal structure of $(C_9NH_{20})_2SnBr_4$. **d** Excitation and emission spectra of $(C_9NH_{20})_2SnBr_4$ bulk crystals. Illustration is the image of $(PEA)_2SnI_xBr_{4-x}$ bulk crystals under ambient light (left) and UV irradiation (right) [182]. **e** Crystal structure of $Cs_2InBr_5{\cdot}H_2O$ viewed along the (001) axis. **f** Excitation (monitored at 695 nm) and emission (excited at 355 nm) spectra of a $Cs_2InBr_5{\cdot}H_2O$ single crystal. Illustration is the image of $Cs_2InBr_5{\cdot}H_2O$ single crystals under ambient light (top) and UV light (bottom) [183]

However, in both 3D and 2D Sn-based perovskites, the oxidation of Sn^{2+} to Sn^{4+} was still an insurmountable problem, and researchers made huge efforts in this aspect. Ma and coworkers synthesized 0D $(C_9NH_{20})_2SnBr_4$ LFHPs as shown in Fig. 8c. The structure of $(C_9NH_{20})_2SnBr_4$ is similar to green $(C_9NH_{20})_2MnBr_4$ (Sn is red, Br is blue, N is orange, C is gray, red polyhedral represents $[SnBr_4]^{2-}$; hydrogen atoms are omitted for clarity). As shown in Fig. 8d, through photoexcitation, the NCs exhibited a highly strong broadband deep-red emission peaked at 695 nm, with a high PLQY of around 46% and large Stokes shift of 332 nm [182]. Due to the barrier effect of large organic cations, $[SnBr_4]^{2-}$ anions were surrounded by $C_9NH_{20}^+$, such a 0D structure protected Sn(II) from oxidation, and hence improved the stability of Sn-based perovskites.

Although Sn based LFHPs reduced the toxicity of lead-base ones, they still face the questions of instability. In recent years, MHDPs attract more and more attention, and much progress has been achieved. For example, MHDPs serving as red phosphors have received considerable attention.

As the typical structure of double perovskite, $A_2BB'X_6$ (respectively, B and B′ are monovalent cations like Ag^+, Na^+, Rb^+ et al. and trivalent cations like In^{3+}, Bi^{3+} et al.) is easy to adjust the component. For example, Cs_2AgInX_6 (X = Cl, Br, and I) got much attention because of excellent stability and high PLQY, which opened the way to the development of MHDPs [103–105]. The as synthesized single crystals could maintain 90% of the initial PL intensity for a long-time storage, exhibited an excellent stability. Bi^{3+} is another attractive cation in $A_2BB'X_6$, direct bandgap transition resulting from Bi^{3+} is responsible for the efficient broadband red PL. Zhao et al. innovatively developed the broad-band Na-Bi Cs_2NaBiX_6 (X = Cl, Br) double perovskite NCs. Meanwhile, the PL spectra could be easily tuned from violet to red by adjusting the halogen elements [184].

Not only halogen could tune the spectra, some cations could also realize tunable emission by adjusting band gap. Sapra et al. reported tunable emission via alloying of $Cs_2AgBiCl_6$ NCs with Na, the ration of Ag and Na could easily tune the band gap from 3.39 eV ($Cs_2NaBiCl_6$) to 3.82 eV ($Cs_2AgBiCl_6$), these series of alloyed double perovskite exhibited a broad PL ranging from 440 to 850 nm [185]. Zhang et al. also successfully tuned the emission of $A_2BAlF_6:Mn^{4+}$ (A = Rb, Cs; B = K, Rb) double perovskite from blue to red [186].

In addition, A_2BX_6 perovskite could be viewed as a special double perovskite, except that B cation and B′ cation are the same ones. Many researchers believed that A_2BX_6 has superior luminescent properties result of quantum confinement. $A_2B'X_5$ is similar to A_2BX_6 in structure, so it should have similar properties. Su et al. reported a luminous indium-based $Cs_2InBr_5{\cdot}H_2O$ perovskite with a broad emission peak of ≈695 nm and a high PLQY of 33% [183]. Figure 8e demonstrated the crystal structure of $Cs_2InBr_5{\cdot}H_2O$ viewed along the (001) axis (cyan: Cs, brown: Br, pink: In, red: O, green: H), and Fig. 8f exhibited the optical properties and images of $Cs_2InBr_5{\cdot}H_2O$ single crystals under ambient light and UV light.

5 Other Color Perovskite Phosphors

Although blue, green and red are the most important colors in light emission, some other colors of light play vital roles in lighting and dispaly field. For example, white is a better light source for lighting rather than blue, green or red. Orange or yellow are also suitable for fabricating white LEDs, integrating blue and orange or yellow can effectively realize warm white emission. Even a single yellow or orange light can be used as an LED in industry.

5.1 White Perovskite Phosphors

White light is the most widely used color in lighting, so a high-efficiency white emission is urgent pursuit in both industrial and academic areas [5, 75, 187–189]. Generally, broadband is an essential condition for white emission, which typically originates from STEs that exist in semiconductors with localized carriers and a soft lattice [188]. Mn^{2+}-doped LHPs and MHDPs containing Bi^{3+}, Sb^{3+}, as well as Cu-based LFHPs are the main white emitters.

For LHPs, achieving white emission by integrating the mixture of blue, green and red emitting NCs is a more comprehensive strategy. The energy transfer of Mn^{2+} can effectively tune the spectra of $APbCl_3$ from blue to orange, which exhibited enticing prospect in white-emission. Im et al. [190] obtained a obtained Mn-doped $(CH_3NH_3)PbBr_{3-(2x+1)}Cl_{2x+1}$:$Mn^{2+}$ QDs with a Mn-dissolution limit of 90%, as shown in Fig. 9a. The synthesized collodial LHPs QDs emitted blue from orange as doping ratio changed. By subtly adjusting the doping concentration, a white emission could be acquired. Furthermore, Wang and Zhang et al. [191] successfully synthesized white-emission Zn/Mn-codoped $CsPb_2Cl_xBr_{5-x}$ perovskites, which demonstrated a white spectra consisting of bimodal emission at 474 and 598 nm [85, 191].

In the respect of broad emission, LFHPs are suitable for fabricating white-light emitters. As mentioned before, STEs and energy transfer can give rise to white emission, which could be achieved by ion doping or alloying, and cations like Na^+, Bi^{3+}, Sb^{3+} are suitable choices. Tang and Yella et al. found that MHDPs could exhibit efficient and stable white-light emission by exciting STEs originating from the Jahn Teller distortion of the $[AgCl_6]^-$ octahedron, and the Na-alloyed $Cs_2AgInCl_6$:Bi exhibited a high PLQY of 86 ± 5% [5, 192, 193]. Due to effective energy transfer of Mn^{2+}, Xu et al. reported Sb/Mn-codoped $Cs_2NaInCl_6$ MHDPs with tunable dual-emission, whose emission covered the white-light spectrum with PLQY up to 84% [126].

Cu-based LFHPs also could realize white light by mixing two phases of $Cs_3Cu_2I_5$ and $CsCu_2I_3$. For instance, White et al. produced blue-emitting $Cs_3Cu_2I_5$ nanoplates and yellow-emitting $CsCu_2I_3$ nanorods by a hot-injection route [194], the mixed phases obtained an excellent white emission.

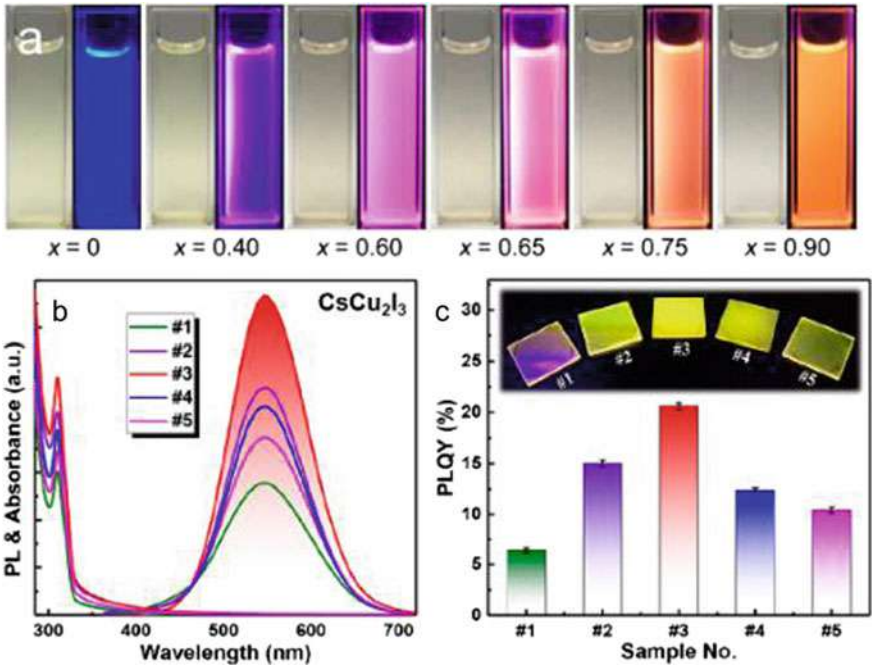

Fig. 9 **a** Image of 3D-$MAPb_{1-x}Mn_xBr_{3-(2x+1)}Cl_{2x+1}$ QDs in the visible (top) and 365 nm UV light (bottom), respectively [190, 191]. **b** Absorption and PL spectra of five samples (samples obtained by dripping toluene at different times). **c** Statistical PLQYs of the $CsCu_2I_3$ thin films prepared with different conditions. The insets present the photographs of the $CsCu_2I_3$ thin films under UV lamp (254 nm) excitation [195]

5.2 Yellow Perovskite Phosphors

Yellow-emitting perovskite can be used to fabricate WLEDs by combining a blue-light excitation source. Although it is possible to adjust the Mn^{2+} concentration in the LHP to achieve yellow light emission, we prefer to synthesize LFHP materials with yellow intrinsic luminescence. Sn-based, Cu-based, and In-based perovskites with broad-band emission are all ideal yellow-emitting perovskite materials. In addition, 1D and 0D Pb-based LHP single crystals have also been found to exhibit yellow emission recently [196–199].

Self-trapped-exciton emission is an effective method to achieve bright and high-efficiency emission, which can be realized through rational ion doping. For example, $(PMA)_3InBr_6$ (PMA^+: $(C_6H_5CH_2NH_3)^+$) has been reported, which possesses the characteristic of wide direct band gap (3.78 eV) and strong yellow-light with a PLQY of ~35% [200]. In addition, Xia and Han's group reported Sb^{3+}-doped $Cs_2InCl_5 \cdot H_2O$ single crystals and Ag^+-doped $Cs_2NaInCl_6$ NCs. The PLQYs of these materials could be up to 95.5% at yellow range [125, 201].

According to the previously reported research, the PL spectrum of Sn is the closest to the yellow range. Hence Sn-based perovskites are the most suitable materials for yellow emission. In addition, 2D perovskite significantly improved the oxidation resistance of Sn, the Sn-based lead-free 2D perovskite $(OCTAm)_2SnX_4$ (OCTAm = octylammonium cation) with high stability has been synthesized. Furthermore, the PL intensity did not decay after 6 months of storage in environmental conditions [202], which was almost one of the best performances in Sn-based perovskite.

Furthermore, many studies have reported that Cu-based perovskites exhibited yellow emission. Shan et al. fabricated stable $CsCu_2I_3$-based yellow LEDs. Experimental results and theoretical characterizations indicated that the yellow electroluminescence originated from the broadband emission of STEs centered at 550 nm [195]. As seen in Fig. 9b, c, the PL spectra exhibited an excellent stability, a relative PLQY varied as experimental conditions change, and the maximum PLQY reached 20.6%.

5.3 Orange Perovskite Phosphors

Orange is also suitable for fabricating WLEDs, and it is more comprehensive than yellow, especially in warm white LEDs. Almost all orange perovskite luminescence comes from the energy transfer of doped ions. Except for Mn^{2+}-doped LHPs we have mentioned before [82, 86, 87, 89, 92, 203–206], energy transfer from Bi^{3+} to other cations (e.g. Sb^{3+}, In^{3+} and Tb^{3+}) is also important for orange emission [200, 201, 207]. According to energy transfer between Bi^{3+} and Sb^{3+}, we can find that emissive light of Sb^{3+} is close to orange [208]. In addition, some Sn-based LFHPs are reported to emit orange light as well [209–211].

Although PL performance of Bi-based double perovskite is poor (the high energy level (3.4 eV) of Bi^{3+} lead to a weak emission), effective energy transfer between Bi^{3+} and other cations provide a new way to study light emission of perovskites [200, 201, 207, 208]. For example, Xia et al. established relationship between doped ions and MFDP NCs, which provided a guide in tuning optical performances of double perovskites in the visible light region. They found that Bi^{3+} and Tb^{3+} doping demonstrated some special properties. Although Bi^{3+} is harmful to PL of double perovskite, its interaction with Tb^{3+} actually improves perovskite performance, and the STEs resulting from Bi^{3+} led to an efficient energy-transfer channel from Bi^{3+} to Tb^{3+} ions. Thus, the emission of Cs_2Ag-$(In_{1-x}Tb_x)Cl_6$ could be continuously tuned from green to orange by adjusting Tb^{3+} concentration [207].

Sb-based double perovskites have good prospects in orange emission. Xie et al. reported two kinds of Sb-based 0D LFHPs, $(TTA)_2SbCl_5$ (TTA = tetraethylammonium) and $(TEBA)_2SbCl_5$ (TEBA = benzyltriethylammonium). These phosphors have a broad orange emission and an additional dual-band blue emission with near-unity PLQY up to 68% even in the single-component compound's dual-emission WLEDs, which made them candidates for single-component WLEDs [208]. As shown in Fig. 10a, b, $(TTA)_2SbCl_5$ and $(TEBA)_2SbCl_5$ have the same structure,

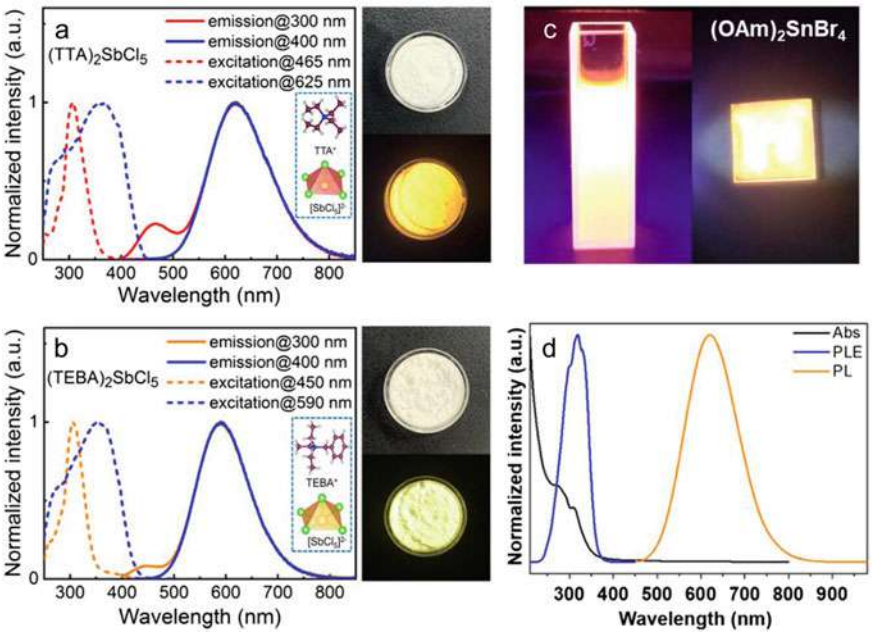

Fig. 10 **a** and **b** PL, PLE spectra and optical sample pictures of $(TTA)_2SbCl_5$ and $(TEBA)_2SbCl_5$ [208]. **c** Photograph of the colloidal suspension and film of $(OAm)_2SnBr_4$ perovskites under UV light. **d** Normalized absorption, PL (excited by 365 nm) and PLE spectra of the $(OAm)_2SnBr_4$ perovskite [211]

the nuances of spectra originate from large organic cations. In Fig. 10a, b, the excitation and emission spectra of $(TTA)_2SbCl_5$ and $(TEBA)_2SbCl_5$ are demonstrated at left, and the PL images of powders (under ambient light and 365 nm UV light) are showed at right, in addition, the illustrations exhibited the corresponding crystal structures.

Inherent broadband emission of Sn-based perovskite makes it a candidate for orange PL [209, 210]. For example, Rogach et al. demonstrated a lead-free 2D Ruddlesden Poppertype $(C1_8H_{35}NH_3)_2SnBr_4$ perovskite. The orange emission originated from the insulating character of the organic OAm cations, which prevented electronic band formation between the $[SnBr_6]^{4-}$ octahedron layers. Meanwhile, because of the strong self-trapped effect, PLQYs of the perovskite in colloidal suspensions and in films were 88%, and 68%, respectively [211]. The photographs of the colloidal $(OAm)_2SnBr_4$ QDs and film are demonstrated in Fig. 10c, and the optical spectra of $(OAm)_2SnBr_4$ are shown in Fig. 10d. The excellent Sn-based perovskites further extended the application prospect in WLEDs.

In conclusion, different color-emission perovskites have a great potential in fabricating WLEDs. Here we summarized the luminescent properties of perovskite with different color-emission, such as PL spectra, PLQY and FWHM etc. of different-color-emission perovskites in Table 1.

Table 1 Different color perovskite phosphors

	Samples	Emission peak (nm)	FWHM (nm)	PLQY (%)	References
Blue	$CsPb(BrCl)_3$	452	23	>60	[27]
	$CsPbBr_3$ NPLs	460	12	Near to 100	[212]
	$MAPbBr_3$:EA	473	20	/	[213]
	$CsPbCl_{0.9}Br_{2.1}$:PEA	480	21	27	[214]
	Quasi 2D $CsPbBr_3$ in $Cs4PbBr_6$	475–512	21–37	>20	[215]
	Cs_2SnCl_6:Bi (2.75%)	455	66	78.9	[114]
	$Cs_3Cu_2I_5$	445	~63	87	[216]
	$(CH_3NH_3)_3Bi_2Br_9$	423	62	12	[101]
	$Cs_3Sb_2Br_9$	410	41	46	[113]
	quasi-2D PEA_2PbBr_4	477	28	88	[66]
	$L_2[APbBr_3]PbBr_4$	405	70–90	22	[61]
	$CsPbCl_3$:Co	400	12–40	30	[77]
	$MA_3Bi_2Br_9$	430	12–25	12	[101]
	$Cs_3Cu_2Br_5$	455	75	50.1	[111]
Green	$CsPbBr_3$	514	29	>85	[27]
	$MAPbBr_3$	510	18	~80	[217]
	$FAPbBr_3$	520	19	>90	[218]
	$CsPbBr_3$:NaI(NaBr)	509	~25	85	[219]
	$CsPbBr_3$:AgI(Ag_2CO_3)	519	~20	/	[220]
	$CsPbBr_3$:Sn(IV)I($SnBr_2$)	510	~40	83	[159]
	$CsPbBr_3$I(solution treating)	512	19	90	[221]

(continued)

Table 1 (continued)

	Samples	Emission peak (nm)	FWHM (nm)	PLQY (%)	References
	$CsPbBr_3$|(triple-ligand surface engineering)	515	20	>90	[134]
	$MAPbBr_3$:POEA	~520/506	/	/	[222]
	$CsPbBr_3$@glass (TeO_2-H_3BO_3-Al_2O_3-ZnO-Na_2CO_3)	522	~20	~70	[223]
	$CsPbBr_3$ in $CsPb_2Br_5$	526	21	83	[224]
	$CsPbBr_3$ in $CsPb_2Br_5$ film	526	/	16.5	[225]
	$CsPbBr_3$ in Cs_4PbBr_6	517	/	55	[226]
	$(C_8H_{14}N_2)_2SnBr_6$	507	82	36 ± 4	[160]
	$(C_9NH_{20})_2MnBr_4$	528	64	81.08	[162]
Red	$CsPbI_3$	~680	33	95 ± 2	[227]
	$CsPbI_{2.25}Br_{0.75}$	619	19	≈85%	[228]
	$CsPbI_3$:Zn|(ZnI_2)	682	/	98.5	[229]
	$CsPbI_3$:Mn|(MnI_2)	680–696	20–40	82–89.6	[230]
	Cs_2SnI_6	620	449	<1	[231]
	$(OCTAm)_2SnBr_4$	620	140	88	[232]
	$(PEA)_2SnI_xBr_{4-x}$	630	/	0.04–0.24	[181]
	$(C_9NH_{20})_2SnBr_4$	695	146	46	[182]
	$Cs_2InBr_5{\cdot}H_2O$	695	~130	33	[183]
Others	$CsPbCl_3$:Fe(III)|($FeCl_3$)	410/584	18/75	4.32	[233]
	$CsPbCl_3$:Mn(II)|($MnCl_2$;$Mn(OAc)_2$)	390–425/580–625	/	12.7–75	[86, 204, 230, 234–238]
	$Cs_2AgInCl_6$	560	~200	1.6	[102]
	$(C_4N_2H_{14}Br)_4SnBr_6$	570	105	95 ± 5	[239]

(continued)

Table 1 (continued)

	Samples	Emission peak (nm)	FWHM (nm)	PLQY (%)	References
	$CsCu_2I_3$	568	~75	15.7	[240]
	$MA_3Bi_2X_9$	360–540	50–91	0.03–15	[101]
	$Cs_3Bi_2X_9$	393–545	48–70	0.018–26.4	[46]
	Cs_2AgBiX_6	395–575	68–82	0.1–6.7	[241]
	$CsSnX_3$	490–945	36–80	<1	[242]
	$CsPbX_3$@glass (GeO_2-B_2O_3-ZnO-CaO-K_2O)	478–698	~23	80	[243]
	$CsPb(BrI)_3$@glass (P_2O_5-SiO_2-ZnO)	523–693	22–37	40.5	[244]
	$CsPb_2Cl_xBr_{5-x}$:Mn	450/580	/	49	[191]
	$CsCu_2I_3$	550	~100	20.6	[195]
	$(TTA)_2SbCl_5$	625	140	86	[208]
	$(TEBA)_2SbCl_5$	590	135	98	[208]
	$(C_{18}H_{35}NH_3)_2SnBr_4$	620	140	88/68	[211]

6 Hybrid Perovskite Phosphors

In fact, at present, perovskite-based phosphors are highly promising for practical application, but some problems still need to be overcome, such as optical and thermal stability. Therefore, in addition to finding a solution from the perspective of the materials themselves, combining perovskite with other materials to make hybrid perovskite phosphors is also a feasible strategy [245, 246]. We can divide these strategies into three types: hybrid perovskites by combining inorganic materials [179, 223, 247–256], hybrid perovskite by combining small organic molecules and polymers, and hybrid perovskite phosphors by combining non-luminous and luminous perovskite.

6.1 Hybrid Perovskite by Combining Inorganic Materials

With the widespread application of perovskites in the field of lightings and displays, stability problem has increasingly become an urgent issue, which limits its further application. Inorganic materials (especially inorganic oxides) have excellent stability in air, wrapping highly stable inorganic substances on the perovskite is a feasible strategy to improve the stability [247].

We first introduce the perovskite@glass hybrid phosphors. Many works synthesized PQDs in glass to further protect QDs from environmental damage [179, 254]. However, researchers found that the PLQY of hybrid $CsPbX_3$@glass is only 20–30%, which was much lower than the pure perovskite phosphors. This phenomenon may be due to the unmatched structure between glass and perovskite phosphors. Meanwhile, surface modification or silica encapsulation can also form a non-dense protective layer, which does not adequately avoid the influence of the external environment. To solve this problem, Xu et al. grew $CsPbBr_3$ QDs among a specially designed TeO_2-based glass matrix, which could maintain a PLQY of ~70% [223, 255].

In addition, SiO_2 and Al_2O_3 are the main composition to protect perovskite phosphors in glass [257]. Xia et al. synthesized stable $CsPbX_3$@SiO_2 hybrid perovskite phosphors to enhance the stability and PLQY [250]. Further, Liang et al. significantly enhanced the stability of PQDs by hybridizing SiO_2/Al_2O_3 monolith (SAM), through a simple sol–gel process in nonpolar solvent hexane [248]. As seen in Fig. 11a–c, the PL spectra of perovskite colloidal solutions and phosphors did not drift and the PL intensity did not decrease.

Some researchers also proposed that surface passivation of the NCs by inorganic ligands could maintain a high PLQY [250]. Young et al. demonstrated the surface-passivated QDs, whose barrier layer were formed of dual-silicon nitride and silicon oxide ligands of the polysilazane (PSZ). Finally, these compound-structure QDs maintained a high PLQY and greatly improved the environmental stability of $CsPbBr_3$ [249]. The reaction process is demonstrated in Fig. 11d, and the reaction

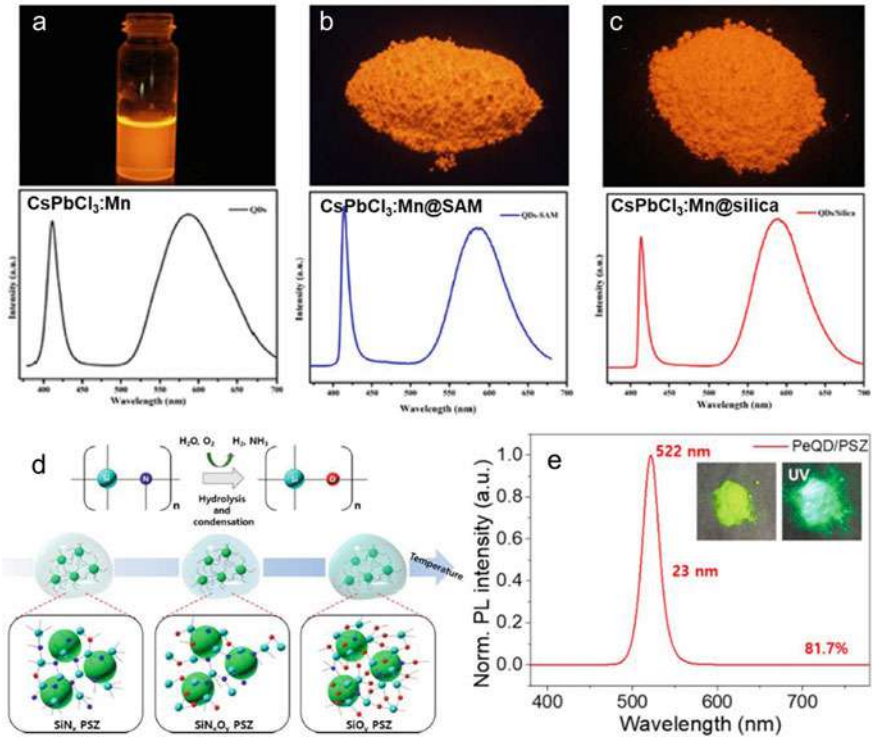

Fig. 11 Hybrid perovskites compositing with inorganic materials. **a** Mn-doped $CsPbCl_3$ PQDs and corresponding PL spectra, **b** Orange PQDs@SAM composite and corresponding PL spectra, **c** Orange PQDs@SiO_2 composite and corresponding PL spectra under the UV light [248]. **d** Schematic diagram of the sol–gel process (moisture-induced hydrolysis) to obtain the $CsPbBr_3$ QDs/PSZ composites. **e** Normalized PL intensity of $CsPbBr_3$ PeQD/PSZ composite. Inset: actual images of the PeQD/PSZ powder in the sun and with UV light [249]

occurred with the exist of SiN_X PSZ and QDs, and the product of the hydrolysis polymerization reaction protected the perovskite phosphors. What's more, Fig. 11e shows that the hybrid perovskite phosphors exhibited a stable and bright emission.

Other strategies such as spontaneous encapsulation, epitaxial growth, etc. have been reported, all of which have beneficial effect on improving the stability of perovskite phosphors [251–253, 256]. In conclusion, inorganic materials can effectively improve the stability of perovskite phosphors.

6.2 Hybrid Perovskite by Combining Organic Molecules or/and Polymers

Organic polymers in enhancing the stability of perovskites are getting more and more attention because of their excellent isolation from water, and almost all organic polymers are water-insulated. Especially many polymers are suitable for encapsulating perovskites and optoelectronic applications due to their transparency. Colella et al. found that polymers can enhance the stability of perovskites, and they further explored the feasibility of the interaction between the two materials [258]. The prospect of using polymers to stabilize perovskite structure has received wide attention. According to the different combination process, hybrid perovskites with polymer can be divided into two categories: polymer-perovskite hybrid phosphors, and perovskite phosphors coated by polymer.

The polymer-perovskite hybrid phosphors can be synthesized by adding polymers to the reaction precursor to interact with perovskite precursors. For instance, Zhang et al. explored a one-pot method synthesized perovskite/polymers composites ($CsPbBr_3$ composite with poly (methyl methacrylate) (PMMA), polystyrene (PS), and poly(butyl methacrylate) (PBMA)) [259]. According to Fig. 12a, PMMA, PBMA and PS are separately used to synthesized polymer-$CsPbBr_3$ hybrid perovskites. The good resistance of polymers to moisture, air and light greatly improve the environmental stability of hybrid perovskites. For another instance, Liu et al. adopted an in-situ-synthesis hot injection method to synthesize composite perovskite nanorods by replacing OA with polyacrylic acid-grafted graphene oxide (GO-g-PAA) [260].

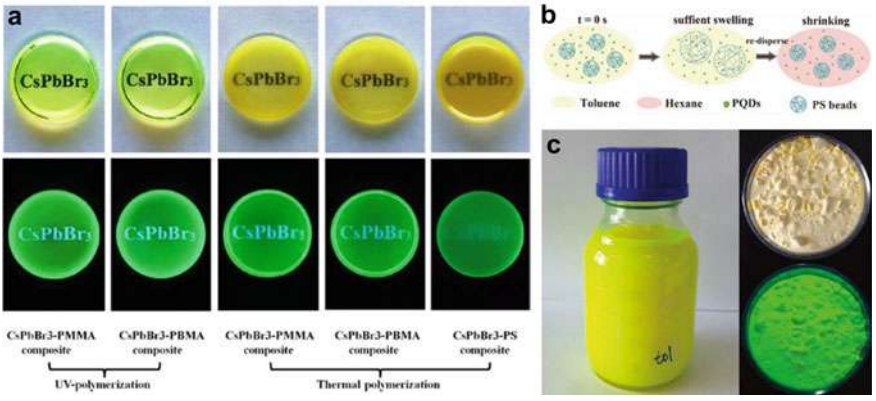

Fig. 12 Hybrid perovskites combining with polymer. **a** Photographs of transparent disks from the perovskite–polymer composite under ambient room light (up) and UV illumination (down) [259]. **b** Schematic illustration of the preparation process of PQDs@PS composite spheres via swelling–shrinking strategy. **c** $CsPbBr_3$@PS composites in large scale. The photographs of large-scale production and hybrid phosphor powders under normal indoor light (up) and UV light (down) illumination [261]

Compared to previous works, the perovskite compounds have much higher PLQY and thermal stability.

Another strategy is coating perovskite with polymers to form core–shell structure. This strategy would not change the structure of perovskite phosphors. Alivisatos et al. dropped the synthesized polymers (e.g. PS and its derivative (poly (styrene-ethylene-butylenestyrene) (SEBS), and hydrophobic silicone resin) on perovskites to enhance the stability [257, 262, 263]. Xie et al. further used PMMA, which is well matched with perovskite, to enhance the combination between perovskites and polymers for the better stability of perovskites [264]. In fact, in-situ polymerized strategy could effectively improve the weak bonding between polymers and perovskites. For example, Lin et al. reported an in-situ synthesis method for forming perovskite-polymer hybrid materials. They prepared a highly luminous perovskite PS composite beads with uniform morphology by a simple swelling shrinking strategy [261]. The schematic diagram is demonstrated in Fig. 12b. When PS swells in toluene, QDs enter the inside of PS, and then PQDs@PS shrinks in hexane. Hybrid perovskites with perfect stability and high PLQY can be obtained without inert gas or baking/heating operations. Figure 12c showed the massive powders of PQDs@PS.

In addition, small organic molecules also could be considered as a candidate for enhancing luminescent properties of perovskite phosphors. However, we usually do not consider these small molecules as the substrates of composite materials, but as ligands for analysis [149–151, 165, 173, 265]. A classic example is bilateral interfacial passivation strategy in PQDs film. Song et al. proposed a bilateral passivation strategy, drastically enhanced the efficiency and stability of QD-based light-emitting diodes (QLEDs) [266]. Besides TSPO1, DPEPO, TPPO and DMAC-SPS have been revealed to have passivation effect, which further demonstrates the feasibility of perovskite composite organic small molecules.

6.3 *Hybrid Perovskite by Combining Non-luminous and Luminous Perovskites*

Coating perovskites with stable perovskites is also an effective way to prevent them from water, light and heat. Currently, only cesium lead halide perovskite has been found to have this capacities so far [246], mainly in $CsPb_2Br_5$ [224, 225, 267] and $CsPb_4Br_6$ [215, 226, 268–272].

$CsPb_4Br_6$ as a perovskite material has better stability than the luminous perovskites $CsPbBr_3$. The passivation of $CsPbBr_3$ was achieved in robust and air-stable rhombic prism hexabromide (Cs_4PbBr_6) microcrystals was achieved, which led to a PLQY up to 90% [270, 271]. The dominant perspective is that Cs_4PbBr_6 limited excitons in $CsPbBr_3$ and hence enhanced the radiative recombination [226, 269, 272].

In 2019, Song et al. reported a new anion cation reaction method to synthesize $CsPbBr_3$@Cs_4PbBr_6 composite. They found that the phase transformation between

$CsPbBr_3$ and Cs_4PbBr_6 is temperature-dependent. Lower temperature was suitable for preparing Cs_4PbBr_6 NCs, while increasing the temperature was favorable to form $CsPbBr_3$ NCs [268, 271]. The composite displayed a much higher luminescence, narrow FWHM (19 nm), and better stability. The nanostructure and optical properties of $CsPbBr_3$@Cs_4PbBr_6 are shown in Fig. 13a–d.

In addition, hybrid perovskite can be formed by combining $CsPbBr_3$ and $CsPb_2Br_5$ [224]. The interaction between $CsPbBr_3$ and $CsPb_2Br_5$ is shown in Fig. 13e. Yao et al. synthesized a $CsPb_2Br_5$ coated $CsPbBr_3$ hybrid perovskite by ligand-assisted precipitation. The high-quality dual-phase perovskite NCs were synthesized in the bromide-rich circumstance with a PLQY as high as 92% and a narrow FWHM of 19 nm (showed in Fig. 13f) [267]. In addition, the as-synthesized dual-phase perovskite NCs exhibited extremely high thermal stability [225].

In summary, Cs_4PbBr_6 and $CsPb_2Br_5$ exhibit higher stability than $CsPbBr_3$ NCs, simultaneously, excellent lattice matching makes them ideal materials to encapsulate $CsPbBr_3$ NCs and then improve the stability.

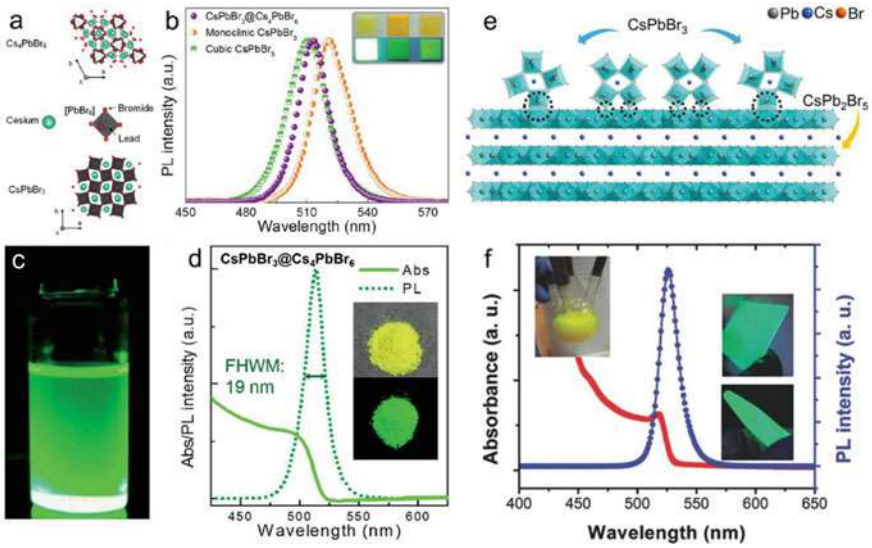

Fig. 13 **a** Crystal structure of $CsPbBr_3$ and Cs_4PbBr_6. **b** The PL spectra and inset photographs of $CsPbBr_3$@Cs_4PbBr_6, monoclinic $CsPbBr_3$ and cubic $CsPbBr_3$ films (from left to right). **c** Typical $CsPbBr_3$@Cs_4PbBr_6 solution dispersed in toluene under UV light. **d** PL and absorption spectra of $CsPbBr_3$@Cs_4PbBr_6 powders, inset: photographs of powder sample under day light and UV light, respectively [268, 271]. **e** Schematic illustration of the interfacial stability of dual phase $CsPbBr_3$/$CsPb_2Br_5$ [224]. **f** Absorption and PL spectra of $CsPbBr_3$/$CsPb_2Br_5$ hybrid perovskite. Inset: the as-obtained products and light emission of $CsPbBr_3$/$CsPb_2Br_5$ deposited on the glass and tube excited with UV light [225]

7 Applications of Perovskite Phosphors in LEDs

Perovskite has exhibited promising prospect in the new generation of lighting devices. Perovskite-based WLEDs continually serve as alternative to traditional incandescent lights and energy-saving lamps because of their excellent characteristics and low cost solution process [187]. Here we only focus on the WLEDs based on perovskite phosphors. According to the different white-emission generation mechanism of the perovskite LEDs, WLEDs can be divided into three types: LEDs prepared by combining perovskite with GaN chips, LEDs prepared by self-capture (energy transfer) of perovskites, LEDs prepared by doped perovskites.

7.1 WLED by Combining GaN Chip with Perovskite Phosphors

WLEDs can be constructed by integrating perovskite phosphors on GaN chips [187, 273–275]. The device structure and WLED are shown in Fig. 14a, b. Chen et al. synthesized high-quality $FAPbX_3$ and mixed-organic-cation $FA_xMA_{1-x}PbBr_3$ perovskite QDs with blue, green and red emission and successfully fabricated WLEDs based on GaN chips [274]. The single-emitting GaN-based LEDs of blue, green, pink and red are shown in Fig. 14c–f [276]. Furthermore, integrating blue and yellow or orange perovskites on the GaN chips can also produce white LEDs.

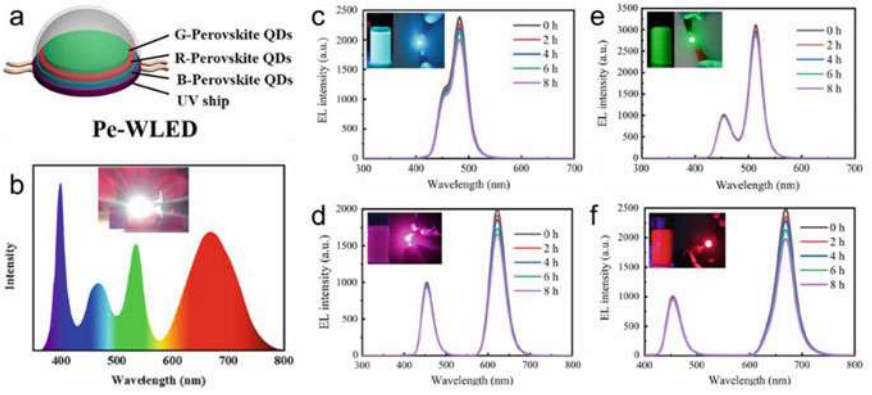

Fig. 14 Pe-LEDs composite GaN chip. **a** Device structure of WLED Based on the three-primary color QDs. **b** The as-fabricated Pe-WLED device and the corresponding electroluminescent spectra [274]. **c–f** $MAPbX_3$ PQDs serve as fluorescent material for multicolored LED. A spectrum of cyan (**c**), pink (**d**), green (**e**) and red (**f**) $MAPbX_3$ perovskite QDs was excited by a blue GaN LED [276]

7.2 WLED Through Energy Transfer in One Perovskite

Energy transfer has been discovered in Mn^{2+}-doped LHPs and some Bi^{3+}-doped LFHPs. As previously mentioned, a self-trapping level from Mn is provided, which emits orange light at wavelengths of 570–610 nm, through coupling with the perovskite's own luminescence of 410–450 nm, the white light emission can be obtained when excited by UV light. Wang et al. reported a new type of Mn-doped 2D $CsPb_2Cl_xBr_{5-x}$ perovskite nanoplatelets with a high energy-transfer efficiency from perovskite to Mn impurities at the required emission wavelengths (about 450 nm for perovskite emission and 580 nm for Mn emission). The as synthesized perovskite exhibited a high PLQY of 49%. Furthermore, the perovskite could be blended with PS to improve the stability without changing the white light emission [191]. The principle and broad photoluminescence of Mn-doped WLED are showed in Fig. 15 [87, 191, 277].

7.3 WLED by Doping Ions in Perovskites

Ion-doping perovskites could also be used to synthesize white-emission perovskites, especially Bi^{3+}-doping. However, unlike Mn^{2+}, Bi^{3+} provides a high new energy level (3.4 eV) in the bandgap, where excitons transit from energy level of Bi^{3+} to a lower energy state (energy levels of Tb^{3+}, Eu^{3+}, etc. or ground state) for emission. By adjusting doping concentration of Bi^{3+}, white-emission perovskites could be fabricated, which are ideal luminous materials for WLEDs. The emissive principle and optical properties of Bi^{3+}-doped LFHPs are showed in Fig. 16. Figure 16a exhibited the emitting principle of Bi^{3+}-doped LFHPs, 30% of Bi doping provides an appropriate bandgap and emits a white light. Figure 16b, c demonstrated the PL spectra of $Cs_2AgIn_{1-x}Bi_xCl_6$ and white-light perovskite phosphors [192, 278].

8 Conclusion

Electric lighting assumed approximately 15% of global power consumption. Among various illumination, white LEDs (WLEDs) have become one of the focus research in the lighting and display industry due to their long lifespan and high energy efficiency. Under the environment of energy-saving emission reduction, according to the haitz'law of LED industry, LED will follow the development process of aiming high brightness and low cost. Thus, exploring new phosphors for lightings, compatible with the cost reduce, is highly desired. Metal halide perovskite phosphors have attracted wide attention due to their outstanding luminescence feature and low-cost solution-processing. According to whether containing lead element, metal halide

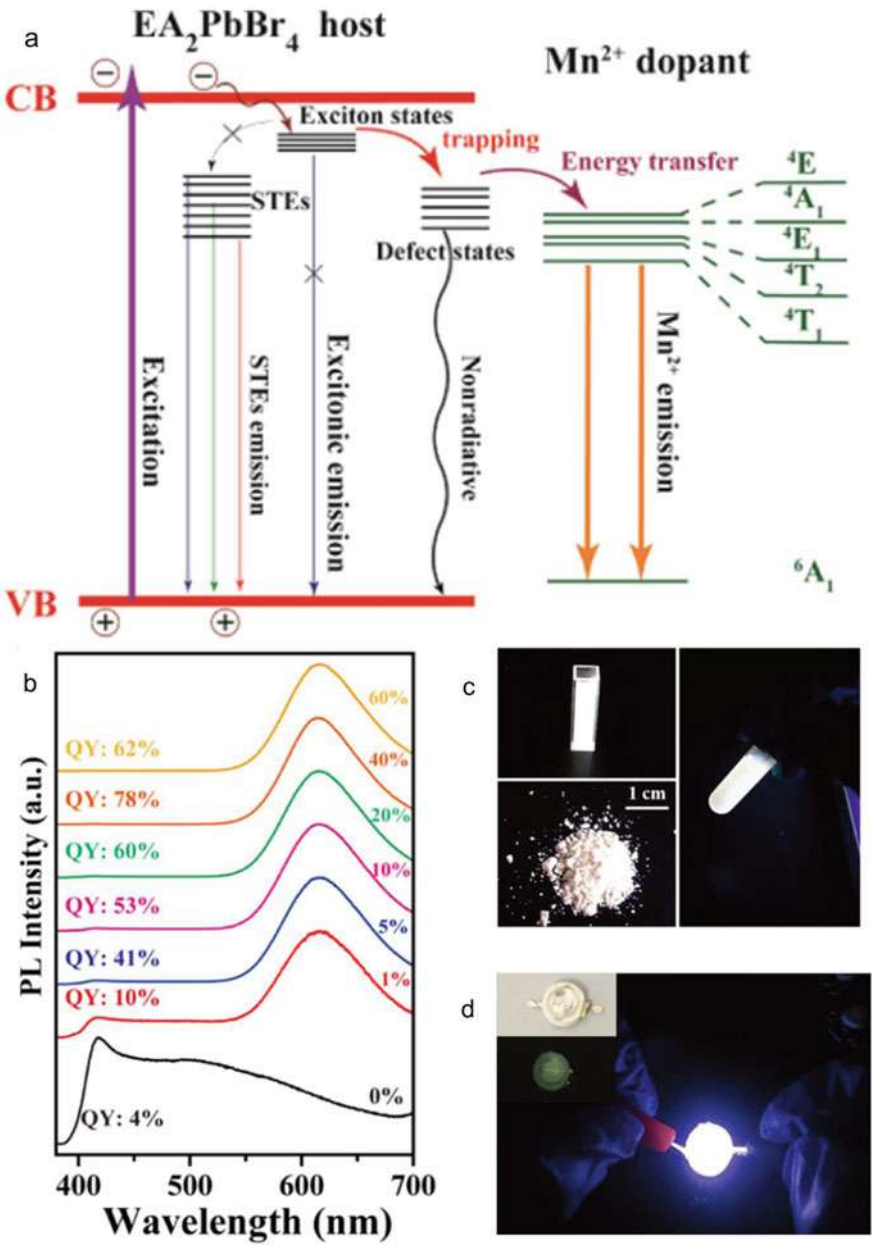

Fig. 15 Self-capture and energy transfer in Mn-doped WLEDs. **a** Schematic diagram of self-capture and energy transfer in Mn-doped perovskite. **b** Normalized PL spectra ($\lambda_{ex} = 360$ nm) of self-capture perovskites with different Mn^{2+} concentrations [277]. **c** Images of the samples (perovskite solutions, powders and mixture of perovskites and PS-toluene solution) under the irradiation of a 365 nm UV lamp. **d** WLEDs fabricated by coating self-capture perovskites nanoplatelets-PS composites on the hemispheric lamp-chimney, inset: optical image of the WLED and lamp-chimney [191]

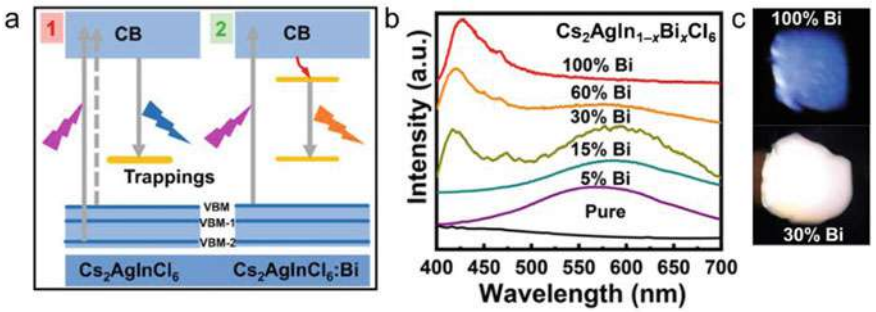

Fig. 16 Emissive principle and optical properties of Bi^{3+}-doped $Cs_2AgIn_{1-x}Bi_xCl_6$. **a** Principle of Bi^{3+}-doped LFHPs emits light [278]. **b** PL spectra of $Cs_2AgIn_{1-x}Bi_xCl_6$ perovskites doped with different concentrations of Bi^{3+}. **c** PL photos of $Cs_2AgIn_{1-x}Bi_xCl_6$ perovskite under UV light [192]

perovskite can be classified into two categories lead halide perovskite and lead-free halide perovskite.

Metal halide perovskites can be identified as a highly promising luminescent materials so far due to high PLQY. In this chapter, we introduced different color perovskite phosphors, including three primary colors of blue, green, red, and other color (e.g., white, yellow and orange). Among which green and red perovskite have much progress in PL and PLQY. While deep blue-light perovskite still cannot solve obstacle of instability and low PLQY. Then, we further summarized different-color hybrid perovskite phosphors through combining perovskite with inorganic materials, organic molecules and polymers, and the non-luminous and luminous perovskites. These hybrid strategies make perovskite phosphors with high stability. Finally, we presented some strategies of perovskite phosphors applications in WLEDs, such as combining three-primary-color perovskite phosphors with GaN chips, preparing by energy transfer in one perovskite and doping ions in perovskites.

Progress in perovskite phosphors have greatly promoted the development of LED devices. We believe perovskite phosphors can be the ideal materials for future lightings and displays, and would further motivate researches in chemistry and physic field.

References

1. Chen, D.Q., Xiang, W.D., Liang, X.J., et al.: Advances in transparent glass-ceramic phosphors for white light-emitting diodes-a review. J. Eur. Ceram. Soc. **35**, 859–869 (2015)
2. Zhou, Q., Dolgov, L., Srivastava, A.M., et al.: Mn^{2+} and Mn^{4+} red phosphors: synthesis, luminescence and applications in WLEDs. A review. J. Mater. Chem. C **6**, 2652–2671 (2018)
3. Chen, D., Zhou, Y., Zhong, J.: A review on Mn^{4+} activators in solids for warm white light-emitting diodes. RSC Adv. **6**, 86285–86296 (2016)
4. Cho, J., Park, J.H., Kim, J.K., et al.: White light-emitting diodes: history, progress, and future. Laser Photonics Rev. **11**, 1600147 (2017)

5. Luo, J., Wang, X., Li, S., et al.: Efficient and stable emission of warm-white light from lead-free halide double perovskites. Nature **563**, 541–545 (2018)
6. Anonymous: Haitz's law. Nat. Photonics **1**, 23–23 (2007)
7. Mroziewicz, B.: Revolution in technology of LEDs, are the Craford's and Haitz's laws still in power? Elektronika **47**, 380–382 (2006)
8. Perumal, A., Shendre, S., Li, M., et al.: High brightness formamidinium lead bromide perovskite nanocrystal light emitting devices. Sci. Rep. **6**, 36733 (2016)
9. Rosales, B.A., Men, L., Cady, S.D., et al.: Persistent dopants and phase segregation in organolead mixed-halide perovskites. Chem. Mater. **28**, 6848–6859 (2016)
10. Wang, A.F., Yan, X.X., Zhang, M., et al.: Controlled synthesis of lead-free and stable perovskite derivative Cs_2SnI_6 nanocrystals via a facile hot-injection process. Chem. Mater. **28**, 8132–8140 (2016)
11. Amendola, V., Fortunati, I., Marega, C., et al.: High-purity hybrid organolead halide perovskite nanoparticles obtained by pulsed-laser irradiation in liquid. ChemPhysChem **18**, 1047–1054 (2017)
12. Li, X.L., Li, L.H., Ma, Z.H., et al.: Low-cost synthesis, fluorescent properties, growth mechanism and structure of $CH_3NH_3PbI_3$ with millimeter grains. Optik **142**, 293–300 (2017)
13. Ruan, L., Shen, W., Wang, A., et al.: Alkyl-thiol ligand-induced shape- and crystalline phase-controlled synthesis of stable perovskite-related $CsPb_2Br_5$ nanocrystals at room temperature. J. Phys. Chem. Lett. **8**, 3853–3860 (2017)
14. Protesescu, L., Yakunin, S., Nazarenko, O., et al.: Low-cost synthesis of highly luminescent colloidal lead halide perovskite nanocrystals by wet ball milling. ACS Appl. Nano Mater. **1**, 1300–1308 (2018)
15. Dong, L., Chen, Z., Ye, L., et al.: Gram-scale synthesis of all-inorganic perovskite quantum dots with high Mn substitution ratio and enhanced dual-color emission. Nano Res. **12**, 1733–1738 (2019)
16. Zhang, T.T., Li, H.Y., Yang, P.Z., et al.: Room-temperature synthesized formamidinium lead halide perovskite quantum dots with bright luminescence and color-tunability for efficient light emitting. Org. Electron. **68**, 76–84 (2019)
17. Brown, A.A.M., Damodaran, B., Jiang, L.D., et al.: Lead halide perovskite nanocrystals: room temperature syntheses toward commercial viability. Adv Energy Mater. **10**, 2001349 (2020)
18. Cui, J., Xu, F.F., Dong, Q., et al.: Facile, low-cost, and large-scale synthesis of $CsPbBr_3$ nanorods at room-temperature with 86 % photoluminescence quantum yield. Mater. Res. Bull. **124**, 110731 (2020)
19. Liu, Q., Liu, K.K., Liang, Y.C., et al.: Gram-scale and solvent-free synthesis of Mn-doped lead halide perovskite nanocrystals. J. Alloys Compd. **815**, 152393 (2020)
20. Akkerman, Q.A., Gandini, M., Di Stasio, F., et al.: Strongly emissive perovskite nanocrystal inks for high-voltage solar cells. Nat. Energy. **2**, 16194 (2016)
21. Chen, X., Peng, L., Huang, K., et al.: Non-injection gram-scale synthesis of cesium lead halide perovskite quantum dots with controllable size and composition. Nano Res. **9**, 1994–2006 (2016)
22. Audebert, P., Clavier, G., Alain-Rizzo, V., et al.: Synthesis of new perovskite luminescent nanoparticles in the visible range. Chem. Mater. **21**, 210–214 (2009)
23. Schmidt, L.C., Pertegas, A., Gonzalez-Carrero, S., et al.: Nontemplate synthesis of $CH_3NH_3PbBr_3$ perovskite nanoparticles. J. Am. Chem. Soc. **136**, 850–853 (2014)
24. Zhang, F., Huang, S., Wang, P., et al.: Colloidal synthesis of air-stable $CH_3NH_3PbI_3$ quantum dots by gaining chemical insight into the solvent effects. Chem. Mater. **29**, 3793–3799 (2017)
25. Zhang, F., Zhong, H., Chen, C., et al.: Brightly luminescent and color-tunable colloidal $CH_3NH_3PbX_3$ (X = Br, I, Cl) quantum dots: potential alternatives for display technology. ACS Nano **9**, 4533–4542 (2015)
26. Zheng, X., Deng, Y., Chen, B., et al.: Dual functions of crystallization control and defect passivation enabled by sulfonic zwitterions for stable and efficient perovskite solar cells. Adv. Mater. **30**, 1803428 (2018)

27. Song, J., Li, J., Li, X., et al.: Quantum dot light-emitting diodes based on inorganic perovskite cesium lead halides ($CsPbX_3$). Adv. Mater. **27**, 7162–7167 (2015)
28. Wang, Y., Li, X., Song, J., et al.: All-inorganic colloidal perovskite quantum dots: a new class of lasing materials with favorable characteristics. Adv. Mater. **27**, 7101–7108 (2015)
29. Akkerman, Q.A., Raino, G., Kovalenko, M.V., et al.: Genesis, challenges and opportunities for colloidal lead halide perovskite nanocrystals. Nat. Mater. **17**, 394–405 (2018)
30. Akkerman, Q.A., Abdelhady, A.L., Manna, L.: Zero-dimensional cesium lead halides: history, properties, and challenges. J. Phys. Chem. Lett. **9**, 2326–2337 (2018)
31. Mao, L., Stoumpos, C.C., Kanatzidis, M.G.: Two-dimensional hybrid halide perovskites: principles and promises. J. Am. Chem. Soc. **141**, 1171–1190 (2019)
32. Chang, Y.H., Lin, J.C., Chen, Y.C., et al.: Facile synthesis of two-dimensional Ruddlesden-Popper perovskite quantum dots with fine-tunable optical properties. Nanoscale Res. Lett. **13**, 247 (2018)
33. Protesescu, L., Yakunin, S., Bodnarchuk, M.I., et al.: Nanocrystals of cesium lead halide perovskites ($CsPbX_3$, X = Cl, Br, and I): novel optoelectronic materials showing bright emission with wide color gamut. Nano Lett. **15**, 3692–3696 (2015)
34. Weidman, M.C., Goodman, A.J., Tisdale, W.A.: Colloidal halide perovskite nanoplatelets: an exciting new class of semiconductor nanomaterials. Chem. Mater. **29**, 5019–5030 (2017)
35. Liu, W., Zheng, J., Cao, S., et al.: General strategy for rapid production of low-dimensional all-inorganic $CsPbBr_3$ perovskite nanocrystals with controlled dimensionalities and sizes. Inorg. Chem. **57**, 1598–1603 (2018)
36. Dong, Y., Wang, Y.K., Yuan, F., et al.: Bipolar-shell resurfacing for blue LEDs based on strongly confined perovskite quantum dots. Nat. Nanotechnol. **15**, 668–674 (2020)
37. Hao, F., Stoumpos, C.C., Cao, D.H., et al.: Lead-free solid-state organic-inorganic halide perovskite solar cells. Nat. Photonics **8**, 489–494 (2014)
38. Kumar, M.H., Dharani, S., Leong, W.L., et al.: Lead-free halide perovskite solar cells with high photocurrents realized through vacancy modulation. Adv. Mater. **26**, 7122–7127 (2014)
39. Liao, W., Zhao, D., Yu, Y., et al.: Lead-free inverted planar formamidinium tin triiodide perovskite solar cells achieving power conversion efficiencies up to 6.22. Adv. Mater. **28**, 9333–9340 (2016)
40. Zhao, Z., Gu, F., Li, Y., et al.: Mixed-organic-cation tin iodide for lead-free perovskite solar cells with an efficiency of 8.12. Adv. Sci. **4**, 1700204 (2017)
41. Liao, Y.Q., Liu, H.F., Zhou, W.J., et al.: Highly oriented low-dimensional tin halide perovskites with enhanced stability and photovoltaic performance. J. Am. Chem. Soc. **139**, 6693–6699 (2017)
42. Wu, C., Zhang, Q., Liu, Y., et al.: The dawn of lead-free perovskite solar cell: highly stable double perovskite $Cs_2AgBiBr_6$ film. Adv. Sci. **5**, 1700759 (2018)
43. Wei, F.X., Deng, Z.Y., Sun, S.J., et al.: Synthesis and properties of a lead-free hybrid double perovskite: $(CH_3NH_3)_2AgBiBr_6$. Chem. Mater. **29**, 1089–1094 (2017)
44. Jin, Z.X., Zhang, Z., Xiu, J.W., et al.: A critical review on bismuth and antimony halide based perovskites and their derivatives for photovoltaic applications: recent advances and challenges. J. Mater. Chem. A **8**, 16166–16188 (2020)
45. Wei, Y., Yang, H., Gao, Z., et al.: Bismuth activated full spectral double perovskite luminescence materials by excitation and valence control for future intelligent LED lighting. Chem. Comm. **56**, 9170–9173 (2020)
46. Leng, M.Y., Yang, Y., Zeng, K., et al.: All-inorganic bismuth-based perovskite quantum dots with bright blue photoluminescence and excellent stability. Adv. Funct. Mater. **28**, 1704446 (2018)
47. Kumawat, N.K., Liu, X.K., Kabra, D., et al.: Blue perovskite light-emitting diodes: progress, challenges and future directions. Nanoscale **11**, 2109–2120 (2019)
48. Nedelcu, G., Protesescu, L., Yakunin, S., et al.: Fast anion-exchange in highly luminescent nanocrystals of cesium lead halide perovskites ($CsPbX_3$, X = Cl, Br, I). Nano Lett. **15**, 5635–5640 (2015)

49. Rao, L., Tang, Y., Yan, C., et al.: Tuning the emission spectrum of highly stable cesium lead halide perovskite nanocrystals through poly(lactic acid)-assisted anion-exchange reactions. J. Mater. Chem. C **6**, 5375–5383 (2018)
50. Ramasamy, P., Lim, D.H., Kim, B., et al.: All-inorganic cesium lead halide perovskite nanocrystals for photodetector applications. Chem. Comm. **52**, 2067–2070 (2016)
51. Chen, Y.C., Chou, H.L., Lin, J.C., et al.: Enhanced luminescence and stability of cesium lead halide perovskite $CsPbX_3$ nanocrystals by Cu^{2+}-assisted anion exchange reactions. J. Phys. Chem. C **123**, 2353–2360 (2019)
52. Dutt, V.G.V., Akhil, S., Mishra, N.: Fast, tunable and reversible anion-exchange in $CsPbBr_3$ perovskite nanocrystals with hydrohalic acids. CrystEngComm **22**, 5022–5030 (2020)
53. Fang, S., Li, G., Lu, Y., et al.: Highly luminescent $CsPbX_3$ (X = Cl, Br, I) nanocrystals achieved by a rapid anion exchange at room temperature. Chem. Eur. J. **24**, 1898–1904 (2018)
54. Li, F., Liu, Y., Wang, H., et al.: Postsynthetic surface trap removal of $CsPbX_3$ (X = Cl, Br, or I) quantum dots via a ZnX_2/hexane solution toward an enhanced luminescence quantum yield. Chem. Mater. **30**, 8546–8554 (2018)
55. Akkerman, Q.A., D'Innocenzo, V., Accornero, S., et al.: Tuning the optical properties of cesium lead halide perovskite nanocrystals by anion exchange reactions. J. Am. Chem. Soc. **137**, 10276–10281 (2015)
56. Jang, D.M., Park, K., Kim, D.H., et al.: Reversible halide exchange reaction of organometal trihalide perovskite colloidal nanocrystals for full-range band gap tuning. Nano Lett. **15**, 5191–5199 (2015)
57. Karimata, I., Kobori, Y., Tachikawa, T.: Direct observation of charge collection at nanometer-scale iodide-rich perovskites during halide exchange reaction on $CH_3NH_3PbBr_3$. J. Phys. Chem. Lett. **8**, 1724–1728 (2017)
58. Li, M., Zhang, X., Lu, S., et al.: Phase transformation, morphology control, and luminescence evolution of cesium lead halide nanocrystals in the anion exchange process. RSC Adv. **6**, 103382–103389 (2016)
59. Parobek, D., Dong, Y., Qiao, T., et al.: Photoinduced anion exchange in cesium lead halide perovskite nanocrystals. J. Am. Chem. Soc. **139**, 4358–4361 (2017)
60. Li, G.J., Ho, J.Y.L., Wong, M., et al.: Reversible anion exchange reaction in solid halide perovskites and its implication in photovoltaics. J. Phys. Chem. C **119**, 26883–26888 (2015)
61. Weidman, M.C., Seitz, M., Stranks, S.D., et al.: Highly tunable colloidal perovskite nanoplatelets through variable cation, metal, and halide composition. ACS Nano **10**, 7830–7839 (2016)
62. Kumar, S., Jagielski, J., Yakunin, S., et al.: Efficient blue electroluminescence using quantum-confined two-dimensional perovskites. ACS Nano **10**, 9720–9729 (2016)
63. Akkerman, Q.A., Motti, S.G., Srimath Kandada, A.R., et al.: Solution synthesis approach to colloidal cesium lead halide perovskite nanoplatelets with monolayer-level thickness control. J. Am. Chem. Soc. **138**, 1010–1016 (2016)
64. Pan, J., Quan, L.N., Zhao, Y., et al.: Highly efficient perovskite-quantum-dot light-emitting diodes by surface engineering. Adv. Mater. **28**, 8718–8725 (2016)
65. Shen, Z., Zhao, S., Song, D., et al.: Improving the quality and luminescence performance of all-inorganic perovskite nanomaterials for light-emitting devices by surface engineering. Small **16**, 1907089 (2020)
66. Xing, J., Zhao, Y., Askerka, M., et al.: Color-stable highly luminescent sky-blue perovskite light-emitting diodes. Nat. Commun. **9**, 3541 (2018)
67. Vashishtha, P., Ng, M., Shivarudraiah, S.B., et al.: High efficiency blue and green light-emitting diodes using Ruddlesden-Popper inorganic mixed halide perovskites with butylammonium interlayers. Chem. Mater. **31**, 83–89 (2018)
68. Tsai, H., Nie, W., Blancon, J.C., et al.: High-efficiency two-dimensional Ruddlesden-Popper perovskite solar cells. Nature **536**, 312–316 (2016)
69. Fang, T., Zhang, F., Yuan, S., et al.: Recent advances and prospects toward blue perovskite materials and light-emitting diodes. InfoMat. **1**, 211–233 (2019)

70. Chen, Y., Liu, Y., Hong, M.: Cation-doping matters in caesium lead halide perovskite nanocrystals: from physicochemical fundamentals to optoelectronic applications. Nanoscale **12**, 12228–12248 (2020)
71. Amat, A., Mosconi, E., Ronca, E., et al.: Cation-induced band-gap tuning in organohalide perovskites: interplay of spin-orbit coupling and octahedra tilting. Nano Lett. **14**, 3608–3616 (2014)
72. Pellet, N., Gao, P., Gregori, G., et al.: Mixed-organic-cation perovskite photovoltaics for enhanced solar-light harvesting. Angew. Chem. Int. Ed. **53**, 3151–3157 (2014)
73. Dou, L., Wong, A.B., Yu, Y., et al.: Atomically thin two-dimensional organic-inorganic hybrid perovskites. Science **349**, 1518–1521 (2015)
74. Song, J., Xu, L., Li, J., et al.: Monolayer and few-layer all-inorganic perovskites as a new family of two-dimensional semiconductors for printable optoelectronic devices. Adv. Mater. **28**, 4861–4869 (2016)
75. Li, X., Wu, Y., Zhang, S., et al.: $CsPbX_3$ quantum dots for lighting and displays: room-temperature synthesis, photoluminescence superiorities, underlying origins and white light-emitting diodes. Adv. Funct. Mater. **26**, 2435–2445 (2016)
76. Baek, S., Kim, S., Noh, J.Y., et al.: Development of mixed-cation $Cs_xRb_{1-x}PbX_3$ perovskite quantum dots and their full-color film with high stability and wide color gamut. Adv. Opt. Mater. **6**, 1800295 (2018)
77. Cao, Z., Li, J., Wang, L., et al.: Enhancing luminescence of intrinsic and Mn doped $CsPbCl_3$ perovskite nanocrystals through Co^{2+} doping. Mater. Res. Bull. **121**, 110608 (2020)
78. Cai, T., Yang, H., Hills-Kimball, K., et al.: Synthesis of all-inorganic Cd-doped $CsPbCl_3$ perovskite nanocrystals with dual-wavelength emission. J. Phys. Chem. Lett. **9**, 7079–7084 (2018)
79. Nayak, P.K., Sendner, M., Wenger, B., et al.: Impact of Bi^{3+} heterovalent doping in organic-inorganic metal halide perovskite crystals. J. Am. Chem. Soc. **140**, 574–577 (2018)
80. Liu, M., Zhong, G., Yin, Y., et al.: Aluminum-doped cesium lead bromide perovskite nanocrystals with stable blue photoluminescence used for display backlight. Adv. Sci. **4**, 1700335 (2017)
81. Yong, Z.J., Guo, S.Q., Ma, J.P., et al.: Doping-enhanced short-range order of perovskite nanocrystals for near-unity violet luminescence quantum yield. J. Am. Chem. Soc. **140**, 9942–9951 (2018)
82. De, A., Mondal, N., Samanta, A.: Luminescence tuning and exciton dynamics of Mn-doped $CsPbCl_3$ nanocrystals. Nanoscale **9**, 16722–16727 (2017)
83. Hou, S., Gangishetty, M.K., Quan, Q., et al.: Efficient blue and white perovskite light-emitting diodes via manganese doping. Joule **2**, 2421–2433 (2018)
84. Khan, U., Zhinong, Y., Khan, A.A., et al.: High-performance $CsPbI_2Br$ perovskite solar cells with zinc and manganese doping. Nanoscale Res. Lett. **14**, 116 (2019)
85. Li, F., Xia, Z., Pan, C., et al.: High Br^- content $CsPb(Cl_yBr_{1-y})_3$ perovskite nanocrystals with strong Mn^{2+} emission through diverse cation/anion exchange engineering. ACS Appl. Mater. Interfaces **10**, 11739–11746 (2018)
86. Liu, W., Lin, Q., Li, H., et al.: Mn^{2+}-doped lead halide perovskite nanocrystals with dual-color emission controlled by halide content. J. Am. Chem. Soc. **138**, 14954–14961 (2016)
87. Wei, Q., Li, M., Zhang, Z., et al.: Efficient recycling of trapped energies for dual-emission in Mn-doped perovskite nanocrystals. Nano Energy **51**, 704–710 (2018)
88. Wang, H., Zhao, X., Zhang, B., et al.: Blue perovskite light-emitting diodes based on RbX-doped polycrystalline $CsPbBr_3$ perovskite films. J. Mater. Chem. C **7**, 5596–5603 (2019)
89. Xu, L., Yuan, S., Zeng, H., et al.: A comprehensive review of doping in perovskite nanocrystals/quantum dots: evolution of structure, electronics, optics, and light-emitting diodes. Mater. Today Nano **6**, 100036 (2019)
90. Luo, B., Li, F., Xu, K., et al.: B-site doped lead halide perovskites: synthesis, band engineering, photophysics, and light emission applications. J. Mater. Chem. C **7**, 2781–2808 (2019)
91. Gebhardt, J., Rappe, A.M.: Mix and match: organic and inorganic ions in the perovskite lattice. Adv. Mater. **31**, 1802697 (2019)

92. Liu, H., Wu, Z., Shao, J., et al.: $CsPb_xMn_{1-x}Cl_3$ perovskite quantum dots with high mn substitution ratio. ACS Nano **11**, 2239–2247 (2017)
93. Lu, M., Zhang, X., Bai, X., et al.: Spontaneous silver doping and surface passivation of $CsPbI_3$ perovskite active layer enable light-emitting devices with an external quantum efficiency of 11.2. ACS Energy Lett. **3**, 1571–1577 (2018)
94. Abdi-Jalebi, M., Dar, M.I., Sadhanala, A., et al.: Impact of monovalent cation halide additives on the structural and optoelectronic properties of $CH_3NH_3PbI_3$ perovskite. Adv. Energy Mater. **6**, 1502472 (2016)
95. Swarnkar, A., Marshall, A.R., Sanehira, E.M., et al.: Quantum dot–induced phase stabilization of a-$CsPbI_3$ perovskite for high-efficiency photovoltaics. Science **354**, 92–95 (2016)
96. Ishii, A., Miyasaka, T.: Sensitized Yb^{3+} luminescence in $CsPbCl_3$ film for highly efficient near-infrared light-emitting diodes. Adv. Sci. **7**, 1903142 (2020)
97. Gao, M., Zhang, C., Lian, L., et al.: Controlled synthesis and photostability of blue emitting $Cs_3Bi_2Br_9$ perovskite nanocrystals by employing weak polar solvents at room temperature. J. Mater. Chem. C **7**, 3688–3695 (2019)
98. Leng, M., Yang, Y., Chen, Z., et al.: Surface passivation of bismuth-based perovskite variant quantum dots to achieve efficient blue emission. Nano Lett. **18**, 6076–6083 (2018)
99. Shen, Y., Yin, J., Cai, B., et al.: Lead-free, stable, high-efficiency (52%) blue luminescent $FA_3Bi_2Br_9$ perovskite quantum dots. Nanoscale Horiz. **5**, 580–585 (2020)
100. Xie, J.L., Huang, Z.Q., Wang, B., et al.: New lead-free perovskite $Rb_7Bi_3Cl_{16}$ nanocrystals with blue luminescence and excellent moisture-stability. Nanoscale **11**, 6719–6726 (2019)
101. Leng, M., Chen, Z., Yang, Y., et al.: Lead-free, blue emitting bismuth halide perovskite quantum dots. Angew. Chem. Int. Ed. **55**, 15012–15016 (2016)
102. Locardi, F., Cirignano, M., Baranov, D., et al.: Colloidal synthesis of double perovskite $Cs_2AgInCl_6$ and Mn-doped $Cs_2AgInCl_6$ nanocrystals. J. Am. Chem. Soc. **140**, 12989–12995 (2018)
103. Luo, J., Li, S., Wu, H., et al.: $Cs_2AgInCl_6$ double perovskite single crystals: parity forbidden transitions and their application for sensitive and fast UV photodetectors. ACS Photonics **5**, 398–405 (2017)
104. Volonakis, G., Haghighirad, A.A., Milot, R.L., et al.: $Cs_2InAgCl_6$: a new lead-free halide double perovskite with direct band gap. J. Phys. Chem. Lett. **8**, 772–778 (2017)
105. Zhou, J., Xia, Z., Molokeev, M.S., et al.: Composition design, optical gap and stability investigations of lead-free halide double perovskite $Cs_2AgInCl_6$. J Mater. Chem. A **5**, 15031–15037 (2017)
106. Noculak, A., Morad, V., McCall, K.M., et al.: Bright blue and green luminescence of Sb(III) in double perovskite Cs_2MInCl_6 (M = Na, K) matrices. Chem. Mater. **32**, 5118–5124 (2020)
107. Xie, L.L., Chen, B.K., Zhang, F., et al.: Highly luminescent and stable lead-free cesium copper halide perovskite powders for UV-pumped phosphor-converted light-emitting diodes. Photonics Res. **8**, 768–775 (2020)
108. Yang, P., Liu, G., Liu, B., et al.: All-inorganic Cs_2CuX_4 (X = Cl, Br, and Br/I) perovskite quantum dots with blue-green luminescence. Chem. Comm. **54**, 11638–11641 (2018)
109. Zeng, R., Zhang, L., Xue, Y., et al.: Highly efficient blue emission from self-trapped excitons in stable Sb^{3+}-doped $Cs_2NaInCl_6$ double perovskites. J. Phys. Chem. Lett. **11**, 2053–2061 (2020)
110. Jun, T., Sim, K., Iimura, S., et al.: Lead-free highly efficient blue-emitting $Cs_3Cu_2I_5$ with 0D electronic structure. Adv. Mater. **30**, 1804547 (2018)
111. Roccanova, R., Yangui, A., Nhalil, H., et al.: Near-unity photoluminescence quantum yield in blue-emitting $Cs_3Cu_2Br_{5-x}I_x$ ($0 \leq x \leq 5$). ACS Appl. Electron. Mater. **1**, 269–274 (2019)
112. Ma, Z., Shi, Z., Yang, D., et al.: Electrically-driven violet light-emitting devices based on highly stable lead-free perovskite $Cs_3Sb_2Br_9$ quantum dots. ACS Energy Lett. **5**, 385–394 (2019)
113. Zhang, J., Yang, Y., Deng, H., et al.: High quantum yield blue emission from lead-free inorganic antimony halide perovskite colloidal quantum dots. ACS Nano **11**, 9294–9302 (2017)

114. Tan, Z.F., Li, J.H., Zhang, C., et al.: Highly efficient blue-emitting Bi-doped Cs_2SnCl_6 perovskite variant: photoluminescence induced by impurity doping. Adv. Funct. Mater. **28**, 1801131 (2018)
115. Park, B.-W., Philippe, B., Zhang, X., et al.: Bismuth based hybrid perovskites $A_3Bi_2I_9$ (A: methylammonium or cesium) for solar cell application. Adv. Mater. **27**, 6806–6813 (2015)
116. Zhao, X.G., Yang, J.H., Fu, Y., et al.: Design of lead-free inorganic halide perovskites for solar cells via cation-transmutation. J. Am. Chem. Soc. **139**, 2630–2638 (2017)
117. Zhao, X.G., Yang, D., Sun, Y., et al.: Cu-In halide perovskite solar absorbers. J. Am. Chem. Soc. **139**, 6718–6725 (2017)
118. Igbari, F., Wang, Z.K., Liao, L.S.: Progress of lead-free halide double perovskites. Adv. Energy Mater. **9**, 1803150 (2019)
119. Slavney, A.H., Hu, T., Lindenberg, A.M., et al.: A bismuth-halide double perovskite with long carrier recombination lifetime for photovoltaic applications. J. Am. Chem. Soc. **138**, 2138–2141 (2016)
120. Zhou, L., Xu, Y.F., Chen, B.X., et al.: Synthesis and photocatalytic application of stable lead-free $Cs_2AgBiBr_6$ perovskite nanocrystals. Small **14**, 1703762 (2018)
121. Creutz, S.E., Crites, E.N., De Siena, M.C., et al.: Colloidal nanocrystals of lead-free double-perovskite (elpasolite) semiconductors: synthesis and anion exchange to access new materials. Nano Lett. **18**, 1118–1123 (2018)
122. Cheng, P., Wu, T., Li, Y., et al.: Combining theory and experiment in the design of a lead-free ($(CH_3NH_3)_2AgBiI_6$) double perovskite. New J. Chem. **41**, 9598–9601 (2017)
123. Zhou, J., Rong, X., Molokeev, M.S., et al.: Exploring the transposition effects on the electronic and optical properties of $Cs_2AgSbCl_6$ via a combined computational-experimental approach. J. Mater. Chem. A **6**, 2346–2352 (2018)
124. Li, G., Tian, Y., Zhao, Y., et al.: Recent progress in luminescence tuning of Ce^{3+} and Eu^{2+}-activated phosphors for pc-WLEDs. Chem. Soc. Rev. **44**, 8688–8713 (2015)
125. Jing, Y.Y., Liu, Y., Jiang, X.X., et al.: Sb^{3+} dopant and halogen substitution triggered highly efficient and tunable emission in lead-free metal halide single crystals. Chem. Mater. **32**, 5327–5334 (2020)
126. Liu, X., Xu, X., Li, B., et al.: Tunable dual-emission in monodispersed Sb^{3+}/Mn^{2+} codoped $Cs_2NaInCl_6$ perovskite nanocrystals through an energy transfer process. Small **16**, 2002547 (2020)
127. Jiang, J.T., Wang, D.Y., Wu, M.F., et al.: Ultrasonication-assisted trace amount solvent synthesis of Cs_4PbBr_6 crystal with ultra-bright green light emission. APL Mater. **8**, 071115 (2020)
128. Krieg, F., Ochsenbein, S.T., Yakunin, S., et al.: Colloidal $CsPbX_3$ (X = Cl, Br, I) nanocrystals 2.0: zwitterionic capping ligands for improved durability and stability. ACS Energy Lett. **3**, 641–646 (2018)
129. Li, C., Zang, Z., Chen, W., et al.: Highly pure green light emission of perovskite $CsPbBr_3$ quantum dots and their application for green light-emitting diodes. Opt. Express **24**, 15071–15078 (2016)
130. Kumar, S., Jagielski, J., Kallikounis, N., et al.: Ultrapure green light-emitting diodes using two-dimensional formamidinium perovskites: achieving recommendation 2020 color coordinates. Nano Lett. **17**, 5277–5284 (2017)
131. Liu, Y., Shi, B.F., Liu, Q., et al.: Large-scale synthesis of layered double hydroxide nanosheet-stabilized $CsPbBr_3$ perovskite quantum dots for WLEDs. J. Alloys Compd. **843**, 155819 (2020)
132. Dou, Y., Wang, S., Zhang, C., et al.: Ten-gram-scale synthesis of $FAPbX_3$ perovskite nanocrystals by a high-power room-temperature ultrasonic-assisted strategy and their electroluminescence. Adv. Mater. Technol. **5**, 1901089 (2020)
133. Lan, S., Li, W., Wang, S., et al.: Vapor-phase growth of $CsPbBr_3$ microstructures for highly efficient pure green light emission. Adv. Opt. Mater. **7**, 1801336 (2019)
134. Song, J., Li, J., Xu, L., et al.: Room-temperature triple-ligand surface engineering synergistically boosts ink stability, recombination dynamics, and charge injection toward EQE-11.6% perovskite QLEDs. Adv. Mater. **30**, 1800764 (2018)

135. Song, J., Fang, T., Li, J., et al.: Organic-inorganic hybrid passivation enables perovskite QLEDs with an EQE of 16.48. Adv. Mater. **30**, 1805409 (2018)
136. Shan, Q., Song, J., Zou, Y., et al.: High performance metal halide perovskite light-emitting diode: from material design to device optimization. Small **13**, 1701770 (2017)
137. Chen, M., Zou, Y., Wu, L., et al.: Solvothermal synthesis of high-quality all-inorganic cesium lead halide perovskite nanocrystals: from nanocube to ultrathin nanowire. Adv. Funct. Mater. **27**, 1701121 (2017)
138. Yassitepe, E., Yang, Z., Voznyy, O., et al.: Amine-free synthesis of cesium lead halide perovskite quantum dots for efficient light-emitting diodes. Adv. Funct. Mater. **26**, 8757–8763 (2016)
139. Zhu, Z.Y., Yang, Q.Q., Gao, L.F., et al.: Solvent-free mechanosynthesis of composition-tunable cesium lead halide perovskite quantum dots. J. Phys. Chem. Lett. **8**, 1610–1614 (2017)
140. Pan, Q., Hu, H., Zou, Y., et al.: Microwave-assisted synthesis of high-quality "all-inorganic" $CsPbX_3$ (X = Cl, Br, I) perovskite nanocrystals and their application in light emitting diodes. J. Mater. Chem. C **5**, 10947–10954 (2017)
141. Fu, Y.P., Zhu, H.M., Chen, J., et al.: Metal halide perovskite nanostructures for optoelectronic applications and the study of physical properties. Nat. Rev. Mater. **4**, 169–188 (2019)
142. Wang, K., Xing, G., Song, Q., et al.: Micro- and nanostructured lead halide perovskites: from materials to integrations and devices. Adv. Mater. 2000306 (2020)
143. Wei, Y., Cheng, Z., Lin, J.: An overview on enhancing the stability of lead halide perovskite quantum dots and their applications in phosphor-converted LEDs. Chem. Soc. Rev. **48**, 310–350 (2019)
144. Goetz, K.P., Taylor, A.D., Paulus, F., et al.: Shining light on the photoluminescence properties of metal halide perovskites. Adv. Funct. Mater. **30**, 1910004 (2020)
145. Beal, R.E., Slotcavage, D.J., Leijtens, T., et al.: Cesium lead halide perovskites with improved stability for tandem solar cells. J. Phys. Chem. Lett. **7**, 746–751 (2016)
146. Stoumpos, C.C., Malliakas, C.D., Peters, J.A., et al.: Crystal growth of the perovskite semiconductor $CsPbBr_3$: a new material for high-energy radiation detection. Cryst. Growth Des. **13**, 2722–2727 (2013)
147. Kulbak, M., Cahen, D., Hodes, G.: How important is the organic part of lead halide perovskite photovoltaic cells? Efficient $CsPbBr_3$ cells. J. Phys. Chem. Lett. **6**, 2452–2456 (2015)
148. Ling, Y., Tian, Y., Wang, X., et al.: Enhanced optical and electrical properties of polymer-assisted all-inorganic perovskites for light-emitting diodes. Adv. Mater. **28**, 8983–8989 (2016)
149. De Roo, J., Ibanez, M., Geiregat, P., et al.: Highly dynamic ligand binding and light absorption coefficient of cesium lead bromide perovskite nanocrystals. ACS Nano **10**, 2071–2081 (2016)
150. Pan, A., He, B., Fan, X., et al.: Insight into the ligand-mediated synthesis of colloidal $CsPbBr_3$ perovskite nanocrystals: the role of organic acid, base, and cesium precursors. ACS Nano **10**, 7943–7954 (2016)
151. Sun, S., Yuan, D., Xu, Y., et al.: Ligand-mediated synthesis of shape-controlled cesium lead halide perovskite nanocrystals via reprecipitation process at room temperature. ACS Nano **10**, 3648–3657 (2016)
152. Liang, Z., Zhao, S., Xu, Z., et al.: Shape-controlled synthesis of all-inorganic $CsPbBr_3$ perovskite nanocrystals with bright blue emission. ACS Appl. Mater. Interfaces **8**, 28824–28830 (2016)
153. Tan, Y., Zou, Y., Wu, L., et al.: Highly luminescent and stable perovskite nanocrystals with octylphosphonic acid as a ligand for efficient light-emitting diodes. ACS Appl. Mater. Interfaces **10**, 3784–3792 (2018)
154. Han, D., Imran, M., Zhang, M., et al.: Efficient light-emitting diodes based on in situ fabricated $FAPbBr_3$ nanocrystals: the enhancing role of the ligand-assisted reprecipitation process. ACS Nano **12**, 8808–8816 (2018)
155. van der Stam, W., Geuchies, J.J., Altantzis, T., et al.: Highly emissive divalent-ion-doped colloidal $CsPb_{1-x}M_xBr_3$ perovskite nanocrystals through cation exchange. J. Am. Chem. Soc. **139**, 4087–4097 (2017)

156. Bi, C., Wang, S., Li, Q., et al.: Thermally stable copper(ii)-doped cesium lead halide perovskite quantum dots with strong blue emission. J. Phys. Chem. Lett. **10**, 943–952 (2019)
157. Yao, J.S., Ge, J., Han, B.N., et al.: Ce^{3+}-doping to modulate photoluminescence kinetics for efficient $CsPbBr_3$ nanocrystals based light-emitting diodes. J. Am. Chem. Soc. **140**, 3626–3634 (2018)
158. Ding, H., Liu, W., Zheng, Y., et al.: Transition metal halide-doped, highly stable all-inorganic perovskite nanocrystals for fabrication of white light-emitting diodes. J. Mater. Chem. C **7**, 1690–1695 (2019)
159. Wang, H.C., Wang, W., Tang, A.C., et al.: High-performance $CsPb_{1-x}Sn_xBr_3$ perovskite quantum dots for light-emitting diodes. Angew. Chem. Int. Ed. **56**, 13650–13654 (2017)
160. Su, B., Song, G., Molokeev, M.S., et al.: Synthesis, crystal structure and green luminescence in zero-dimensional tin halide $(C_8H_{14}N_2)_2SnBr_6$. Inorg. Chem. **59**, 9962–9968 (2020)
161. Deng, Y., Dong, X., Yang, M., et al.: Two low-dimensional metal halides: ionothermal synthesis, photoluminescence, and nonlinear optical properties. Dalton Trans. **48**, 17451–17455 (2019)
162. Li, M., Zhou, J., Molokeev, M.S., et al.: Lead-free hybrid metal halides with a green-emissive $[MnBr_4]$ unit as a selective turn-on fluorescent sensor for acetone. Inorg. Chem. **58**, 13464–13470 (2019)
163. Zhou, G., Liu, Z., Huang, J., et al.: Unraveling the near-unity narrow-band green emission in zero-dimensional Mn^{2+}-based metal halides: a case study of $(C_{10}H_{16}N)_2Zn_{1-x}Mn_xBr_4$ solid solutions. J. Phys. Chem. Lett. **11**, 5956–5962 (2020)
164. Zhang, R., Mao, X., Zheng, D., et al.: A lead-free all-inorganic metal halide with near-unity green luminescence. Laser Photonics Rev. **14**, 2000027 (2020)
165. Lu, M., Guo, J., Sun, S., et al.: Surface ligand engineering-assisted $CsPbI_3$ quantum dots enable bright and efficient red light-emitting diodes with a top-emitting structure. Chem. Eng. J. **404**, 126563 (2021)
166. Protesescu, L., Yakunin, S., Kumar, S., et al.: Dismantling the "red wall" of colloidal perovskites: highly luminescent formamidinium and formamidinium-cesium lead iodide nanocrystals. ACS Nano **11**, 3119–3134 (2017)
167. Li, B., Zhang, Y., Fu, L., et al.: Surface passivation engineering strategy to fully-inorganic cubic $CsPbI_3$ perovskites for high-performance solar cells. Nat Commun. **9**, 1076 (2018)
168. Han, B., Cai, B., Shan, Q., et al.: Stable, efficient red perovskite light-emitting diodes by (α, δ)-$CsPbI_3$ phase engineering. Adv. Funct. Mater. **28**, 1804285 (2018)
169. Xu, W.D., Hu, Q., Bai, S., et al.: Rational molecular passivation for high-performance perovskite light-emitting diodes. Nat. Photonics **13**, 418–424 (2019)
170. Zhu, Y., Zhao, J., Yang, G., et al.: Ammonium acetate passivated $CsPbI_3$ perovskite nanocrystals for efficient red light-emitting diodes. Nanoscale **12**, 7712–7719 (2020)
171. Fu, Y., Zhu, H., Schrader, A.W., et al.: Nanowire lasers of formamidinium lead halide perovskites and their stabilized alloys with improved stability. Nano Lett. **16**, 1000–1008 (2016)
172. Wang, C., Chesman, A.S., Jasieniak, J.J.: Stabilizing the cubic perovskite phase of $CsPbI_3$ nanocrystals by using an alkyl phosphinic acid. Chem. Comm. **53**, 232–235 (2016)
173. Li, G.P., Huang, J.S., Zhu, H.W., et al.: Surface ligand engineering for near-unity quantum yield inorganic halide perovskite QDs and high-performance QLEDs. Chem. Mater. **30**, 6099–6107 (2018)
174. Abdi-Jalebi, M., Andaji-Garmaroudi, Z., Cacovich, S., et al.: Maximizing and stabilizing luminescence from halide perovskites with potassium passivation. Nature **555**, 497–501 (2018)
175. Yang, J.N., Song, Y., Yao, J.S., et al.: Potassium bromide surface passivation on $CsPbI_{3-x}Br_x$ nanocrystals for efficient and stable pure red perovskite light-emitting diodes. J. Am. Chem. Soc. **142**, 2956–2967 (2020)
176. Behera, R.K., Dutta, A., Ghosh, D., et al.: Doping the smallest shannon radii transition metal ion Ni(II) for stabilizing alpha-$CsPbI_3$ perovskite nanocrystals. J. Phys. Chem. Lett. **10**, 7916–7921 (2019)

177. Zhang, J., Zhang, L., Cai, P., et al.: Enhancing stability of red perovskite nanocrystals through copper substitution for efficient light-emitting diodes. Nano Energy **62**, 434–441 (2019)
178. Yao, J.S., Ge, J., Wang, K.H., et al.: Few-nanometer-sized alpha-$CsPbI_3$ quantum dots enabled by strontium substitution and iodide passivation for efficient red-light emitting diodes. J. Am. Chem. Soc. **141**, 2069–2079 (2019)
179. Zhang, Z.L., Shen, L.L., Zhang, H.L., et al.: Novel red-emitting $CsPb_{1-x}Ti_xI_3$ perovskite QDs@glasses with ambient stability for high efficiency white LEDs and plant growth LEDs. Chem. Eng. J. **378**, 122125 (2019)
180. Yang, W.F., Igbari, F., Lou, Y.H., et al.: Tin halide perovskites: progress and challenges. Adv. Energy Mater. **10**, 1902584 (2020)
181. Lanzetta, L., Marin-Beloqui, J.M., Sanchez-Molina, I., et al.: Two-dimensional organic tin halide perovskites with tunable visible emission and their use in light-emitting devices. ACS Energy Lett. **2**, 1662–1668 (2017)
182. Zhou, C., Lin, H., Shi, H., et al.: A zero-dimensional organic seesaw-shaped tin bromide with highly efficient strongly stokes-shifted deep-red emission. Angew. Chem. Int. Ed. **57**, 1021–1024 (2018)
183. Zhou, L., Liao, J.F., Huang, Z.G., et al.: A highly red-emissive lead-free indium-based perovskite single crystal for sensitive water detection. Angew. Chem. Int. Ed. **58**, 5277–5281 (2019)
184. Wang, C., Liu, Y., Guo, Y.R., et al.: Lead-free sodium bismuth halide Cs_2NaBiX_6 double perovskite nanocrystals with highly efficient photoluminesence. Chem. Eng. J. **397**, 125367 (2020)
185. Lamba, R.S., Basera, P., Bhattacharya, S., et al.: Band gap engineering in $Cs_2(Na_xAg_{1-x})BiCl_6$ double perovskite nanocrystals. J. Phys. Chem. Lett. **10**, 5173–5181 (2019)
186. Deng, T.T., Song, E.H., Zhou, Y.Y., et al.: Tailoring photoluminescence stability in double perovskite red phosphors $A_2BAlF_6:Mn^{4+}$ (A = Rb, Cs; B = K, Rb) via neighboring-cation modulation. J. Mater. Chem. C **5**, 12422–12429 (2017)
187. Wang, H.C., Bao, Z., Tsai, H.Y., et al.: Perovskite quantum dots and their application in light-emitting diodes. Small **14**, 1702433 (2018)
188. Smith, M.D., Karunadasa, H.I.: White-light emission from layered halide perovskites. Acc. Chem. Res. **51**, 619–627 (2018)
189. Dohner, E.R., Hoke, E.T., Karunadasa, H.I.: Self-assembly of broadband white-light emitters. J. Am. Chem. Soc. **136**, 1718–1721 (2014)
190. Arunkumar, P., Gil, K.H., Won, S., et al.: Colloidal organolead halide perovskite with a high mn solubility limit: a step toward pb-free luminescent quantum dots. J. Phys. Chem. Lett. **8**, 4161–4166 (2017)
191. Wu, H., Xu, S., Shao, H., et al.: Single component Mn-doped perovskite-related $CsPb_2Cl_xBr_{5-x}$ nanoplatelets with a record white light quantum yield of 49%: a new single layer color conversion material for light-emitting diodes. Nanoscale **9**, 16858–16863 (2017)
192. Manna, D., Das, T.K., Yella, A.: Tunable and stable white light emission in Bi^{3+}-alloyed $Cs_2AgInCl_6$ double perovskite nanocrystals. Chem. Mater. **31**, 10063–10070 (2019)
193. Hu, Q., Niu, G., Zheng, Z., et al.: Tunable color temperatures and efficient white emission from $Cs_2Ag_{1-x}Na_xIn_{1-y}$ Bi_yCl_6 double perovskite nanocrystals. Small **15**, 1903496 (2019)
194. Vashishtha, P., Nutan, G.V., Griffith, B.E., et al.: Cesium copper iodide tailored nanoplates and nanorods for blue, yellow, and white emission. Chem. Mater. **31**, 9003–9011 (2019)
195. Ma, Z., Shi, Z., Qin, C., et al.: Stable yellow light-emitting devices based on ternary copper halides with broadband emissive self-trapped excitons. ACS Nano **14**, 4475–4486 (2020)
196. Lin, H.R., Zhou, C.K., Neu, J., et al.: Bulk assembly of corrugated 1D metal halides with broadband yellow emission. Adv. Opt. Mater. **7**, 1801474 (2019)
197. Zhou, J., Li, M.Z., Molokeev, M.S., et al.: Tunable photoluminescence in Sb^{3+}-doped zero-dimensional hybrid metal halides with intrinsic and extrinsic self-trapped excitons. J. Mater. Chem. C **8**, 5058–5063 (2020)

198. Tan, Z.F., Hu, M.C., Niu, G.D., et al.: Inorganic antimony halide hybrids with broad yellow emissions. Sci. Bull. **64**, 904–909 (2019)
199. Lin, F., Wang, H., Liu, W., et al.: Zero-dimensional ionic antimony halide inorganic–organic hybrid with strong greenish yellow emission. J. Mater. Chem. C **8**, 7300–7303 (2020)
200. Chen, D., Hao, S., Zhou, G., et al.: Lead-free broadband orange-emitting zero-dimensional hybrid $(PMA)_3InBr_6$ with direct band gap. Inorg. Chem. **58**, 15602–15609 (2019)
201. Han, P., Mao, X., Yang, S., et al.: Lead-free sodium-indium double perovskite nanocrystals through doping silver cations for bright yellow emission. Angew. Chem. Int. Ed. **58**, 17231–17235 (2019)
202. Wang, A., Guo, Y., Zhou, Z., et al.: Aqueous acid-based synthesis of lead-free tin halide perovskites with near-unity photoluminescence quantum efficiency. Chem. Sci. **10**, 4573–4579 (2019)
203. Zhu, J., Yang, X., Zhu, Y., et al.: Room-temperature synthesis of Mn-doped cesium lead halide quantum dots with high Mn substitution ratio. J. Phys. Chem. Lett. **8**, 4167–4171 (2017)
204. Parobek, D., Roman, B.J., Dong, Y., et al.: Exciton-to-dopant energy transfer in Mn-doped cesium lead halide perovskite nanocrystals. Nano Lett. **16**, 7376–7380 (2016)
205. Li, F., Xia, Z.G., Gong, Y., et al.: Optical properties of Mn^{2+} doped cesium lead halide perovskite nanocrystals via a cation-anion co-substitution exchange reaction. J. Mater. Chem. C **5**, 9281–9287 (2017)
206. Majher, J.D., Gray, M.B., Strom, T.A., et al.: $Cs_2NaBiCl_6$:Mn^{2+}—a new orange-red halide double perovskite phosphor. Chem. Mater. **31**, 1738–1744 (2019)
207. Liu, Y., Rong, X., Li, M., et al.: Incorporating rare-earth terbium(iii) ions into $Cs_2AgInCl_6$: Bi nanocrystals toward tunable photoluminescence. Angew. Chem. Int. Ed. **59**, 11634–11640 (2020)
208. Li, Z.Y., Li, Y., Liang, P., et al.: Dual-band luminescent lead-free antimony chloride halides with near-unity photoluminescence quantum efficiency. Chem. Mater. **31**, 9363–9371 (2019)
209. Li, J., Tan, Z., Hu, M., et al.: Antimony doped Cs_2SnCl_6 with bright and stable emission. Front. Optoelectron. **12**, 352–364 (2019)
210. Yan, A.P., Li, K., Zhou, Y., et al.: Tuning the optical properties of Cs_2SnCl_6:Bi and Cs_2SnCl_6:Sb lead-free perovskites via post-annealing for white LEDs. J. Alloys Compd. **822**, 153528 (2020)
211. Zhang, X., Wang, C., Zhang, Y., et al.: Bright orange electroluminescence from lead-free two-dimensional perovskites. ACS Energy Lett. **4**, 242–248 (2018)
212. Wu, Y., Wei, C.T., Li, X.M., et al.: In situ passivation of $PbBr_6^{4-}$ octahedra toward blue luminescent $CsPbB_r3$ nanoplatelets with near 100% absolute quantum yield. ACS Energy Lett. **3**, 2030–2037 (2018)
213. Wang, Q., Ren, J., Peng, X.F., et al.: Efficient sky-blue perovskite light-emitting devices based on ethylammonium bromide induced layered perovskites. ACS Appl. Mater. Interfaces **9**, 29901–29906 (2017)
214. Li, Z., Chen, Z., Yang, Y., et al.: Modulation of recombination zone position for quasi-two-dimensional blue perovskite light-emitting diodes with efficiency exceeding 5. Nat. Commun. **10**, 1027 (2019)
215. Zou, Y., Xu, H., Li, S., et al.: Spectral-stable blue emission from moisture-treated low-dimensional lead bromide-based perovskite films. ACS Photonics **6**, 1728–1735 (2019)
216. Wang, L., Shi, Z., Ma, Z., et al.: Colloidal synthesis of ternary copper halide nanocrystals for high-efficiency deep-blue light-emitting diodes with a half-lifetime above 100 h. Nano Lett. **20**, 3568–3576 (2020)
217. Huang, H., Zhao, F., Liu, L., et al.: Emulsion synthesis of size-tunable $CH_3NH_3PbBr_3$ quantum dots: an alternative route toward efficient light-emitting diodes. ACS Appl. Mater. Interfaces **7**, 28128–28133 (2015)
218. Zhang, F., Shi, Z., Li, S., et al.: Synergetic effect of the surfactant and silica coating on the enhanced emission and stability of perovskite quantum dots for anticounterfeiting. ACS Appl. Mater. Interfaces **11**, 28013–28022 (2019)

219. Li, S., Shi, Z.F., Zhang, F., et al.: Sodium doping-enhanced emission efficiency and stability of $CsPbBr_3$ nanocrystals for white light-emitting devices. Chem. Mater. **31**, 3917–3928 (2019)
220. Zhou, S., Ma, Y., Zhou, G., et al.: Ag-doped halide perovskite nanocrystals for tunable band structure and efficient charge transport. ACS Energy Lett. **4**, 534–541 (2019)
221. Li, J., Xu, L., Wang, T., et al.: 50-fold EQE improvement up to 6.27% of solution-processed all-inorganic perovskite $CsPbBr_3$ QLEDs via surface ligand density control. Adv. Mater. **29**, 1603885 (2017)
222. Chen, Z., Zhang, C., Jiang, X.F., et al.: High-performance color-tunable perovskite light emitting devices through structural modulation from bulk to layered film. Adv. Mater. **29**, 1603157 (2017)
223. Yuan, S., Chen, D., Li, X., et al.: In situ crystallization synthesis of $CsPbBr_3$ perovskite quantum dot-embedded glasses with improved stability for solid-state lighting and random upconverted lasing. ACS Appl. Mater. Interfaces **10**, 18918–18926 (2018)
224. Zhang, X.L., Xu, B., Zhang, J.B., et al.: All-inorganic perovskite nanocrystals for high-efficiency light emitting diodes: dual-phase $CsPbBr_3$-$CsPb_2Br_5$ composites. Adv. Funct. Mater. **26**, 4595–4600 (2016)
225. Tan, Y., Li, R., Xu, H., et al.: Ultrastable and reversible fluorescent perovskite films used for flexible instantaneous display. Adv. Funct. Mater. **29**, 1900730 (2019)
226. Shin, M., Nam, S.-W., Sadhanala, A., et al.: Understanding the origin of ultrasharp sub-bandgap luminescence from zero-dimensional inorganic perovskite Cs_4PbBr_6. ACS Appl. Energy Mater. **3**, 192–199 (2019)
227. Pan, J., Shang, Y., Yin, J., et al.: Bidentate ligand-passivated $CsPbI_3$ perovskite nanocrystals for stable near-unity photoluminescence quantum yield and efficient red light-emitting diodes. J. Am. Chem. Soc. **140**, 562–565 (2018)
228. Li, G., Rivarola, F.W., Davis, N.J., et al.: Highly efficient perovskite nanocrystal light-emitting diodes enabled by a universal crosslinking method. Adv. Mater. **28**, 3528–3534 (2016)
229. Shen, X., Zhang, Y., Kershaw, S.V., et al.: Zn-alloyed $CsPbI_3$ nanocrystals for highly efficient perovskite light-emitting devices. Nano Lett. **19**, 1552–1559 (2019)
230. Zou, S., Liu, Y., Li, J., et al.: Stabilizing cesium lead halide perovskite lattice through Mn(II) substitution for air-stable light-emitting diodes. J. Am. Chem. Soc. **139**, 11443–11450 (2017)
231. Wang, A.F., Guo, Y.Y., Muhammad, F., et al.: Controlled synthesis of lead-free cesium tin halide perovskite cubic nanocages with high stability. Chem. Mater. **29**, 6493–6501 (2017)
232. Zhou, C., Tian, Y., Yuan, Z., et al.: Highly efficient broadband yellow phosphor based on zero-dimensional tin mixed-halide perovskite. ACS Appl. Mater. Interfaces **9**, 44579–44583 (2017)
233. Rana, P.J.S., Swetha, T., Mandal, H., et al.: Energy transfer dynamics of highly stable Fe^{3+} doped $CsPbCl_3$ perovskite nanocrystals with dual-color emission. J. Phys. Chem. C **123**, 17026–17034 (2019)
234. Das Adhikari, S., Dutta, S.K., Dutta, A., et al.: Chemically tailoring the dopant emission in manganese-doped $CsPbCl_3$ perovskite nanocrystals. Angew. Chem. Int. Ed. **56**, 8746–8750 (2017)
235. Li, C.H., Li, Y., Zhou, T.L., et al.: Ultrasonic synthesis of Mn-doped $CsPbCl_3$ quantum dots (QDs) with enhanced photoluminescence. Opt. Mater. **94**, 41–46 (2019)
236. Das Adhikari, S., Dutta, A., Dutta, S.K., et al.: Layered perovskites $L_2(Pb_{1-x}Mn_x)Cl_4$ to Mn-doped $CsPbCl_3$ perovskite platelets. ACS Energy Lett. **3**, 1247–1253 (2018)
237. He, M.L., Cheng, Y.Z., Yuan, R.R., et al.: Mn-doped cesium lead halide perovskite nanocrystals with dual-color emission for WLED. Dyes Pigm. **152**, 146–154 (2018)
238. De Siena, M.C., Sommer, D.E., Creutz, S.E., et al.: Spinodal decomposition during anion exchange in colloidal Mn^{2+}-doped $CsPbX_3$ (X = Cl, Br) perovskite nanocrystals. Chem. Mater. **31**, 7711–7722 (2019)
239. Zhou, C., Lin, H., Tian, Y., et al.: Luminescent zero-dimensional organic metal halide hybrids with near-unity quantum efficiency. Chem. Sci. **9**, 586–593 (2018)
240. Lin, R., Guo, Q., Zhu, Q., et al.: All-Inorganic $CsCu_2I_3$ single crystal with high-PLQY (approximately 15.7%) intrinsic white-light emission via strongly localized 1D excitonic recombination. Adv. Mater. **31**, 1905079 (2019)

241. Yang, B., Chen, J., Yang, S., et al.: Lead-free silver-bismuth halide double perovskite nanocrystals. Angew. Chem. Int. Ed. **57**, 5359–5363 (2018)
242. Jellicoe, T.C., Richter, J.M., Glass, H.F., et al.: Synthesis and optical properties of lead-free cesium tin halide perovskite nanocrystals. J. Am. Chem. Soc. **138**, 2941–2944 (2016)
243. Guhrenz, C., Benad, A., Ziegler, C., et al.: Solid-state anion exchange reactions for color tuning of $CsPbX_3$ perovskite nanocrystals. Chem. Mater. **28**, 9033–9040 (2016)
244. Jiang, J., Shao, G., Zhang, Z., et al.: Ultrastability and color-tunability of $CsPb(Br/I)_3$ nanocrystals in P-Si-Zn glass for white LEDs. Chem. Comm. **54**, 12302–12305 (2018)
245. Righetto, M., Meggiolaro, D., Rizzo, A., et al.: Coupling halide perovskites with different materials: From doping to nanocomposites, beyond photovoltaics. Prog. Mater. Sci. **110**, 100639 (2020)
246. Cao, M.H., Damji, Y., Zhang, C.Y., et al.: Low-dimensional-networked cesium lead halide perovskites: properties, fabrication, and applications. Small Methods 2000303 (2020)
247. Wang, H.C., Lin, S.Y., Tang, A.C., et al.: Mesoporous silica particles integrated with all-inorganic $CsPbBr_3$ perovskite quantum-dot nanocomposites (MP-PQDs) with high stability and wide color gamut used for backlight display. Angew. Chem. Int. Ed. **55**, 7924–7929 (2016)
248. He, M.L., Cheng, Y.Z., Shen, L.L., et al.: Mn-doped $CsPbCl_3$ perovskite quantum dots (PQDs) incorporated into silica/alumina particles used for WLEDs. Appl. Surf. Sci. **448**, 400–406 (2018)
249. Yoon, H.C., Lee, S., Song, J.K., et al.: Efficient and stable $CsPbBr_3$ quantum-dot powders passivated and encapsulated with a mixed silicon nitride and silicon oxide inorganic polymer matrix. ACS Appl. Mater. Interfaces **10**, 11756–11767 (2018)
250. Liu, Y., Li, F., Liu, Q., et al.: Synergetic effect of postsynthetic water treatment on the enhanced photoluminescence and stability of $CsPbX_3$ (X = Cl, Br, I) perovskite nanocrystals. Chem. Mater. **30**, 6922–6929 (2018)
251. Yu, Y., Hou, J., Zhang, L., et al.: Ultrastable laurionite spontaneously encapsulates reduced-dimensional lead halide perovskites. Nano Lett. **20**, 2316–2325 (2020)
252. Zhang, J.B., Liu, X.F., Jiang, P.F., et al.: Red-emitting $CsPbBrI_2$/PbSe heterojunction nanocrystals with high luminescent efficiency and stability for bright light-emitting diodes. Nano Energy. **66**, 104142 (2019)
253. Juan, F.Y., Xu, F., Wang, M., et al.: Photoluminescence enhancement of perovskite $CsPbBr_3$ quantum dots by plasmonic Au nanorods. Chem. Phys. **530**, 5 (2020)
254. Ye, Y., Zhang, W.C., Zhao, Z.Y., et al.: Highly luminescent cesium lead halide perovskite nanocrystals stabilized in glasses for light-emitting applications. Adv. Opt. Mater. **7**, 1801663 (2019)
255. Chen, D., Yuan, S., Chen, J., et al.: Robust $CsPbX_3$ (X = Cl, Br, and I) perovskite quantum dot embedded glasses: nanocrystallization, improved stability and visible full-spectral tunable emissions. J. Phys. Chem. C **6**, 12864–12870 (2018)
256. Lv, W., Li, L., Li, M., et al.: Self-assembly of completely inorganic perovskite nanocrystals with improved stability by anchoring on kaolinite lamellae. Adv. Opt. Mater. **8**, 1901485 (2020)
257. Yang, W., Gao, F., Qiu, Y., et al.: $CsPbBr_3$-quantum-dots/polystyrene@silica hybrid microsphere structures with significantly improved stability for white leds. Adv. Opt. Mater. (2019)
258. Masi, S., Rizzo, A., Aiello, F., et al.: Multiscale morphology design of hybrid halide perovskites through a polymeric template. Nanoscale **7**, 18956–18963 (2015)
259. Xin, Y., Zhao, H., Zhang, J.: Highly stable and luminescent perovskite-polymer composites from a convenient and universal strategy. ACS Appl. Mater. Interfaces **10**, 4971–4980 (2018)
260. Pan, A., Jurow, M.J., Qiu, F., et al.: Nanorod suprastructures from a ternary graphene oxide-polymer-$CsPbX_3$ perovskite nanocrystal composite that display high environmental stability. Nano Lett. **17**, 6759–6765 (2017)
261. Wei, Y., Deng, X.R., Xie, Z.X., et al.: Enhancing the stability of perovskite quantum dots by encapsulation in crosslinked polystyrene beads via a swelling-shrinking strategy toward superior water resistance. Adv. Funct. Mater. **27**, 1703535 (2017)

262. Raja, S.N., Bekenstein, Y., Koc, M.A., et al.: Encapsulation of perovskite nanocrystals into macroscale polymer matrices: enhanced stability and polarization. ACS Appl. Mater. Interfaces **8**, 35523–35533 (2016)
263. Hai, J., Li, H., Zhao, Y., et al.: Designing of blue, green, and red $CsPbX_3$ perovskite-codoped flexible films with water resistant property and elimination of anion-exchange for tunable white light emission. Chem. Comm. **53**, 5400–5403 (2017)
264. Wang, Y., Varadi, L., Trinchi, A., et al.: Spray-assisted coil-globule transition for scalable preparation of water-resistant $CsPbBr_3$@PMMA perovskite nanospheres with application in live cell imaging. Small **14**, 1803156 (2018)
265. Park, S.M., Abtahi, A., Boehm, A.M., et al.: Surface ligands for methylammonium lead iodide films: surface coverage, energetics, and photovoltaic performance. ACS Energy Lett. **5**, 799–806 (2020)
266. Xu, L., Li, J., Cai, B., et al.: A bilateral interfacial passivation strategy promoting efficiency and stability of perovskite quantum dot light-emitting diodes. Nat. Commun. **11**, 3902 (2020)
267. Zhu, B.S., Li, H.Z., Ge, J., et al.: Room temperature precipitated dual phase $CsPbBr_3$-$CsPb_2Br_5$ nanocrystals for stable perovskite light emitting diodes. Nanoscale **10**, 19262–19271 (2018)
268. Xu, L., Li, J., Fang, T., et al.: Synthesis of stable and phase-adjustable $CsPbBr_3$@Cs_4PbBr_6 nanocrystals via novel anion–cation reactions. Nanoscale Adv. **1**, 980–988 (2019)
269. Su, Y., Zeng, Q.H., Chen, X.J., et al.: Highly efficient $CsPbBr_3$ perovskite nanocrystals induced by structure transformation between $CsPbBr_3$ and Cs_4PbBr_6 phases. J. Mater. Chem. C **7**, 7548–7553 (2019)
270. Quan, L.N., Quintero-Bermudez, R., Voznyy, O., et al.: Highly emissive green perovskite nanocrystals in a solid state crystalline matrix. Adv. Mater. **29**, 1605945 (2017)
271. Xu, J., Huang, W., Li, P., et al.: Imbedded nanocrystals of $CsPbBr_3$ in Cs_4PbBr_6: kinetics, enhanced oscillator strength, and application in light-emitting diodes. Adv. Mater. **29**, 1703703 (2017)
272. Shang, Y., Li, G., Liu, W., et al.: Quasi-2D inorganic $CsPbBr_3$ perovskite for efficient and stable light-emitting diodes. Adv. Funct. Mater. **28**, 1801193 (2018)
273. Li, G., Wang, H., Zhang, T., et al.: Solvent-polarity-engineered controllable synthesis of highly fluorescent cesium lead halide perovskite quantum dots and their use in white light-emitting diodes. Adv. Funct. Mater. **26**, 8478–8486 (2016)
274. Zhang, Y.-W., Wu, G., Dang, H., et al.: Multicolored mixed-organic-cation perovskite quantum dots ($FA_xMA_{1-x}PbX_3$, X = Br and I) for white light-emitting diodes. Ind. Eng. Chem. Res. **56**, 10053–10059 (2017)
275. Coe-Sullivan, S., Liu, W.H., Allen, P., et al.: Quantum dots for LED downconversion in display applications. ECS J. Solid State Sci. Technol. **2**, 3026–3030 (2013)
276. Zhenfu, Z., Liang, J., Zhihai, W., et al.: Perovskite quantum dots as fluorescent materials for multi-colored lighting. J. Mater. Sci. **53**, 15430–15441 (2018)
277. Luo, B., Guo, Y., Li, X., et al.: Efficient trap-mediated Mn^{2+} dopant emission in two dimensional single-layered perovskite $(CH_3CH_2NH_3)_2PbBr_4$. J. Phys. Chem. C **123**, 14239–14245 (2019)
278. Liu, Y., Jing, Y.Y., Zhao, J., et al.: Design optimization of lead-free perovskite $Cs_2AgInCl_6$: Bi nanocrystals with 11.4% photoluminescence quantum yield. Chem. Mater. **31**, 3333–3339 (2019)

Mechanoluminescent Phosphors

Yuan Deng, Hanlu Zhang, and Lin Dong

1 Introduction

Mechanoluminescence (ML) is a well-known phenomenon of light emission induced by the deformation when certain solids suffer external mechanical stress. Mechanoluminescent materials which could convert mechanical energy directly into photons have attracted increasing attention in recent years for their wide potential applications in stress sensing and imaging, structural damage monitoring, wearable illuminating devices, self-powered display, mechanical energy collection and conversion, bioimaging and photodynamic therapy [1–7]. Great progress has been made in developing novel materials with strong mechanoluminescence emission and their applications. This chapter introduces mechanoluminescent phosphors from six aspects, i.e., a brief history, the major material categories, the synthesis methods, the fundamental mechanism, the applications and the outlook of mechanoluminescence.

2 A Brief History of Mechanoluminescence

Mechanoluminescence is a phenomenon of light emission upon external mechanical stimuli. The major excitation of mechanical energy includes friction, stretching, compression, shearing, shanking, bending, impact and other forms of deformation [8–10]. Hence, mechanoluminescence can be generally classified into fracto-ML, plastic-ML, elastic-ML, and tribo-ML [11].

Y. Deng · H. Zhang · L. Dong (✉)
Henan Key Laboratory of Diamond Optoelectronic Materials and Devices, Key Laboratory of Material Physics, Ministry of Education, School of Physics and Microelectronics, Zhengzhou University, Zhengzhou 450052, People's Republic of China
e-mail: ldong@zzu.edu.cn

© Springer Nature Switzerland AG 2022

K. Upadhyay et al. (eds.), *Hybrid Phosphor Materials*, Engineering Materials,
https://doi.org/10.1007/978-3-030-90506-4_2

Some fracture-correlated luminescence phenomena such as earthquake luminescence have been recorded since ancient times. China is the earliest country to record earthlights in the world. In the Book of *Songs, Xiao Ya, Suburbs of October*, the strange acousto-optic phenomenon occurred in Qishan earthquake in Shaanxi 2800 years ago was recorded. Similar foreign records first appeared in *The Annals* by a Roman historian Tacitus, which recorded the strong seismic light in Asia Minor in AD 17. *The True History of Three Reigns of Japan* also recorded the luminescence phenomenon during the earthquake and tsunami in the Mutsu area in AD 869 [12]. The clear ML phenomenon was first recorded in the book *The Advancement of Learning* by British scientist Francis Bacon published in 1605, "When a sharp knife quickly runs across the sugar cube surface, a flash of light can be seen." [13–15]. As those luminescence phenomena are caused by mechanical force, B. P. Chandra put forward the uniform name of "Mechanoluminscence" in 1978 [16].

Although ML has been a very long historical period since the first observed ML phenomena, quite limited attention has been attracted. The absence of non-destructive ML materials with strong and repeatable light emission greatly hinders the practical application. It was not until 1999 that Xu's group successfully prepared two kinds of high-brightness ML materials that could be observed by the naked eye, which attracted the interest of researchers once again [17].

3 Categories of Mechanoluminescent Materials

Generally, over half of all inorganic solids and 30% of the organic polymer solids exhibit ML, including crystalline solids, non-crystalline solids, insulators, semiconductors, and certain conductors [18]. According to their chemical composition, most ML materials can be categorized into three types: Metal-organic compound ML material, organic ML materials and inorganic ML materials.

3.1 Metal Organic Compound Mechanoluminescent Materials

The two representative metal organic compound ML materials are rare earth metal organic complexes and transition metal organic complexes [19].

Rare earth complexes are widely studied in the ML field because of their strong light absorption capacity, high conversion efficiency and luminescence in the visible region. Europium dibenzoylmethide triethylammonium (EuD_4TEA) [20] and Eu(HFNH)Phen (HFNH:4,4,5,5,6,6,6-heptafluoro-l-(2-naphthy1) hexane-1,3-dione; phen:1,10-phenanthroline) [21] are relatively common rare-earth complex materials. This kind of material is generally a complex with an annular structure, which is obtained by chelating cooperation between two or more ligands and the

same metal ion (Eu) to form chelating rings. EuD_4TEA was discovered by Hurt in 1966, which is one of the brightest triboluminescent materials. It has potential application prospect in damage sensor [22]. Eu(HFNH)Phen is a new europium complex and a kind of triboluminescent material with a central symmetric structure. Transition metal organic complexes have been widely studied for their emission in different molecular configurations. There are mainly Mn, Cu and Pt complexes. Figure 1 shows the chemical structures of several rare earth metals and transition metal complexes, respectively.

3.2 Organic Mechanoluminescent Materials

According to the length of the molecular chain, organic ML materials are composed of organic small molecular materials and organic polymer materials. Organic small molecule ML materials mainly include carbazole derivatives, phenothiazine derivatives, N-phenylimide derivatives, tetraphenryl derivatives and so on. Carbazole and its derivatives are very popular in the field of organic optoelectronics because of their advantages such as high trilinear energy level, luminous quantum efficiency and long phosphorescence life. In 1981, Inoue and Tazuke [25] found that carbazole derivatives had ML properties and studied their luminescence mechanism by comparing the materials before and after doping. Not long ago, Yang et al. [26] group synthesized compounds with phenothiazine structure as the luminescent group, and realized the dual emission of ML and phosphorescence. Nishida's group successfully synthesized blue-emitting ML materials using N-phenylimide derivatives based on the dipole structure and non-central symmetric molecular arrangement. In view of the strong electron-absorbing properties of carbonyl groups, which are conducive to the formation of large molecular dipole moments and strong intermolecular hydrogen bonds, Nakayama's [27] group took tetraphenyl as the core and introduced aldehyde groups containing carbonyl structures to obtain a series of ML materials. In 2012, Chen's [28] group introduced 1, 2-dioxy cyclobutane into the polymer and used it as the backbone chain of the polymer. When it was stretched by an external force, 1, 2-dioxy cyclobutane polymer broke, emitting weak blue light and achieving ML of the polymer material.

Organic ML materials can be divided into aromatic hydrocarbon and non-aromatic hydrocarbon organic crystals, according to whether the molecular structure of organic materials contains aromatic rings. Non-aromatic hydrocarbon organic ML materials mainly contain sugar cubes [29], tartaric acid (dipotassium tartaric acid, etc.), cis-4-octene, esters (cholesteryl salicylate [30, 31], organic salt (lithium acetate, potassium hydrogen malonate, etc. [32]), organic acid (L-ascorbic acid). Aromatic hydrocarbon organic ML materials mainly contain hexaphenylcarbodiphosphorane [33], coumarin [34], phenol derivatives (resorcinol, m-aminophenol, etc. [35]), N-isopropylcarbazole, N-ethyl-3-vinylcarbazole, N-isopropyl-3-vinylcarbazole and 3,6-dibromocarbazole, etc. [36] (Fig. 2).

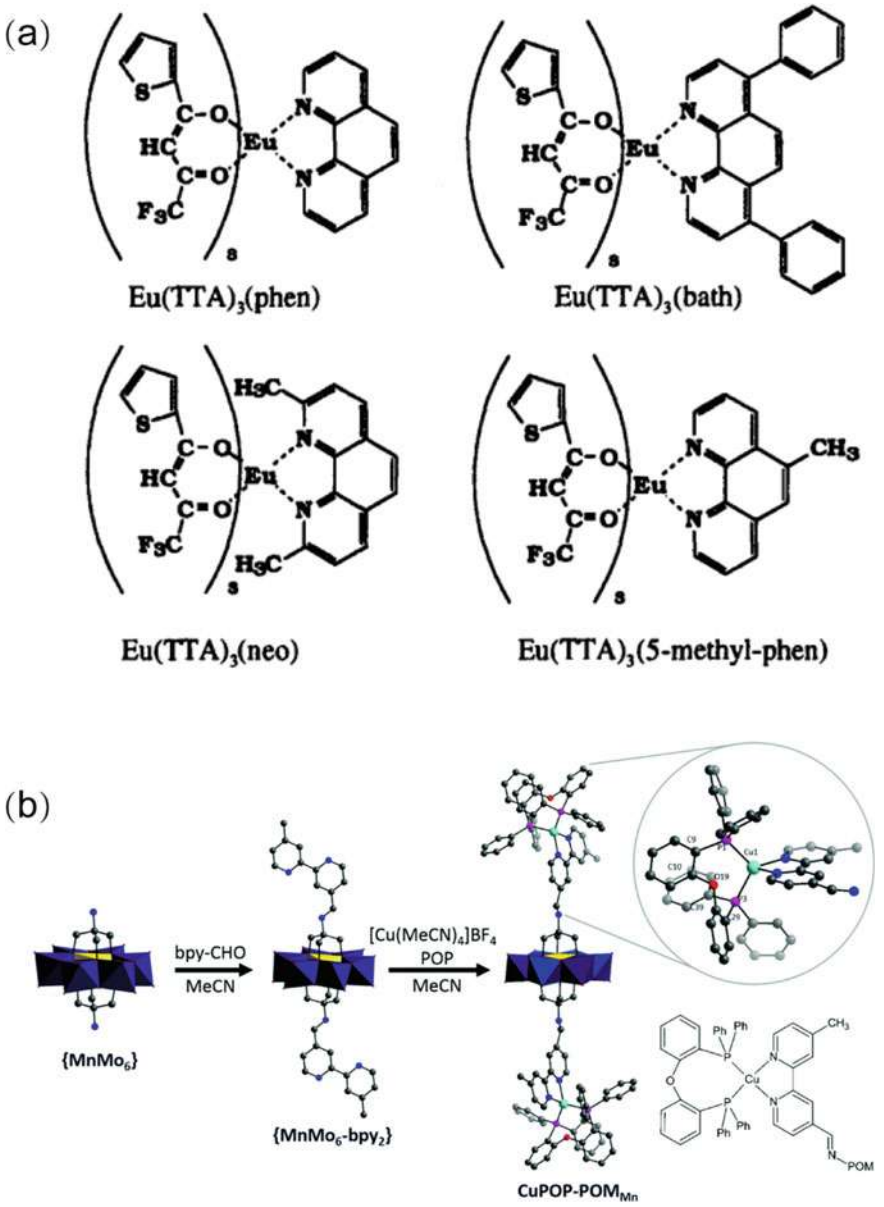

Fig. 1 Chemical structures of Eu and Mn complexes [23, 24]

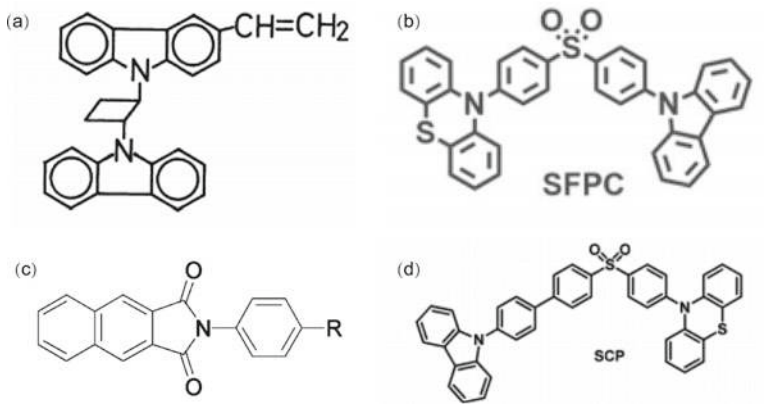

Fig. 2 Chemical structures of some organic mechanoluminescent materials [26, 27, 37, 38]

3.3 Inorganic Mechanoluminescent Materials

Since Xu's group discovered three kinds of elastic-ML materials $Ca_2Al_2SiO_7:Ce^{3+}$ [39], $ZnS:Mn^{2+}$ [17] and $SrAl_2O_4:Eu^{2+}$ [40] in 1999, inorganic ML materials have attracted the attention of researchers and been continuously developed. Existing inorganic ML materials can be classified into aluminate, silicate, phosphate, sulfide and so on. These materials are doped with transition metals (Mn^{2+}/Cu^{2+}/Cu^{+}) or lanthanide ions (Tb^{3+}/Eu^{3+}/Pr^{3+}/Sm^{3+}/Er^{3+}/Dy^{3+}/Ho^{3+}/Nd^{3+}/Tm^{3+}/Yb^{3+}) to achieve their ML properties. Its ML color almost covers the entire visible range, as highlighted in the following list (in accordance with the reported order): $SrAl_2O_4:Ce^{3+}$ (375 nm) [41], $Ca_2Al_2SiO_7:Ce^{3+}$ (402 nm) [39, 42], $(Ca,Sr)Al_2Si_2O_8$ (403–428 nm) [43], $SrMg_2(PO_4)_2:Eu^{2+}$ (412 nm) [44], $CaYAl_3O_7:Ce^{3+}$(421 nm) [45], $CaAl_2Si_2O_8:Eu^{2+}$ (428 nm) [46], $CaYAl_3O_7:Eu^{2+}$/$SrBaMgSi_2O_7:Eu^{2+}$ (440 nm) [47, 48], $ZnS:Cu^{+/2+}$ (456, 505, 520, 586 nm) [49], $Sr_2MgSi_2O_7:Eu^{2+}$ (464 nm) [49], $CaZr(PO_4)_2:Eu^{2+}$ (474 nm) [50], $ZrO_2:Ti^{4+}$ (478 nm) [51], $CaZnOS:Tb^{3+}$ (485, 545, 580, 619 nm) [6], $BaSi_2O_2N_2:Eu^{2+}$ (493 nm) [52, 53], $CaZnOS:Cu^{+/2+}$ (498 nm) [54], $SrCaMgSi_2O_7:Eu^{2+}$ (499 nm) [55], $ZnGa_2O_4:Mn^{2+}$ (505 nm) [56], $MgGa_2O_4:Mn^{2+}$ (506 nm) [56], $ZnAl_2O_4:Mn^{2+}$ (512 nm) [57], $ZnS:Al^{3+}$, $Cu^{+/2+}$ (512 nm) [49], $SrAl_2O_4:Eu^{2+}$ (520 nm) [40], $Ca_2MgSi_2O_7:Eu^{2+}$ (530 nm) [58], $CaZnOS:Er^{3+}$ (530, 560 nm) [6], $Zn_2(Ge_{0.9}Si_{0.1})O_4:Mn^{2+}$ (535 nm) [59], $CaZnOS:Sm^{3+}$ (566, 602, 610, 620, 649, 670 nm) [6, 60], $Sr_3Sn_2O_7:Sm^{3+}$ (570, 582, 610, 624, 665 nm) [61], $BaZnOS:Mn^{2+}$ (584, 610 nm) [62], ZnS:Mn (585 nm) [17], CaZnOS:Mn (610 nm) [63], $(Ba,Ca)TiO_3:Pr^{3+}$/$CaNb_2O_6:Pr^{3+}$/$Ca_2Nb_2O_7:Pr^{3+}$/$Sr_2Nb_2O_7:Pr^{3+}$/$Ca_3Nb_2O_8:Pr^{3+}$/$NaNbO_3:Pr^{3+}$ (613 nm) [64–68], $Ca_3Ti_2O_7:Pr^{3+}$ (615 nm) [69], $LiNbO_3:Pr^{3+}$ (619 nm) [70], $ZnS:Mn^{2+}$, Te^{2+} (648 nm) [71], $SrAl_2O_4:Eu^{2+}$, Nd^{3+} (883 nm) [49], $CaZnOS:Nd^{3+}$ (908 nm, 1094 nm, 1390 nm) [6], $SrAl_2O_4:Eu^{2+}$, Er^{3+} (1530 nm) [72] (Fig. 3).

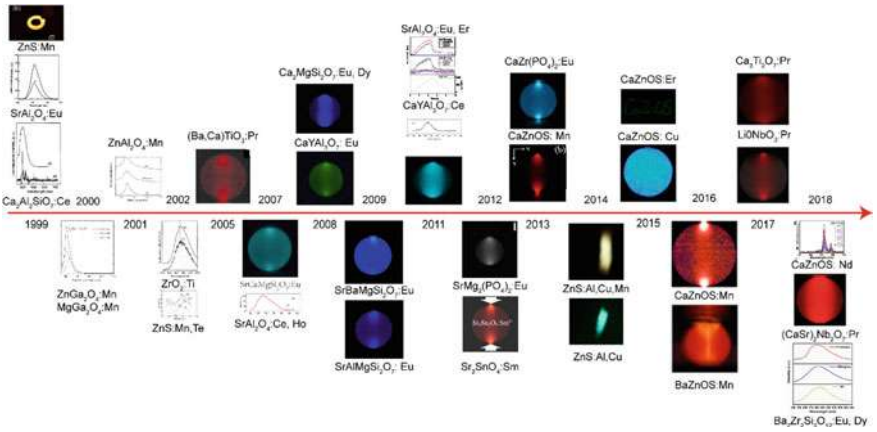

Fig. 3 Development of mechanoluminescent materials

4 Methods of Materials Synthesis

The most commonly used synthesis methods of inorganic ML materials mainly include the high-temperature solid-phase reaction method and the sol–gel method. The size of the materials prepared by these two synthesis methods is in the micron range (10–100 μm). To further expand the application of ML materials in the biological direction, it is very important to realize the sub-micrometer-sized ML materials. In 2006, Xu's group reported the synthesis of nano-sized (10–30 nm) $SrAl_2O_4:Eu^{2+}$ via ultrasonic spray pyrolysis technology [73]. However, this synthesis method has not been speculated in the preparation of ML, so we will not give a detailed example of this method in the following content. In the following sections, we describe the solid reaction method and the sol–gel method by synthesizing ZnS:Mn and $SrAl_2O_4:Eu^{2+}$. This is the first and best studied of all ML materials.

4.1 Solid-State Reactions

A solid-phase high-temperature reaction, the most common method to prepare ML materials, is a process in which the mixed powder or sample material diffuses with each other at high temperature so that the microscopic discrete particles gradually form a continuous solid structure.

Most inorganic ML materials have been prepared using this method. Take ZnS:Mn, which is widely studied, as an example. Firstly, an appropriate amount of $MnCO_3$ (99.95%, AR) and ZnS (99.99%, AR) powders were thoroughly mixed by wet grinding in ethanol. Then, the mixed powders were loaded into an alumina boat compactly and sintered at a series of temperatures for 3 h in nitrogen/argon

atmospheres. The particle size of ZnS:Mn powder prepared by this method is about micron level (10–30 μm) [1, 74].

Although this method is simple to operate, the particle size of the resulting material is large, and there will be segregation of components. In this way, the luminous efficiency will be reduced. If the burning temperature is too high, it will be sintered seriously. In the final grinding, the lattice position where the activator is located will be destroyed, resulting in the reduction of luminous efficiency.

4.2 Sol–Gel Method

The sol–gel method, suitable for preparing small size (<10 m) ML materials, is an important method for the synthesis of inorganic compounds or materials under low temperature or mild conditions. It plays an important role in soft chemical synthesis and is widely used in the preparation of nanoparticles. The chemical process of the sol–gel method is firstly to disperse the raw materials in the solvent, and then to generate the active monomer through a hydrolysis reaction. The active monomer is then polymerized to become the sol, and then to generate the gel with a certain spatial structure. After drying and heat treatment, nanoparticles and the required materials are prepared.

After dissolving $Al(O\text{-}i\text{-}C_3H_7)_3$, $Sr(NO_3)_3$, $Eu(NO_3)_3{\cdot}2.9H_2O$ in ammonia water according to mass weighing, Xu's research group dispersed the obtained nanoparticles in N, N-dimethylformamide (DMF). The sol particles were dried at 200 °C, and then the dried particles were calcined under 700 °C in the air atmosphere. Finally, it was placed in a hydrogen atmosphere (5% H_2–N_2) and sintered at 750–1400 °C for 2 h. The particle size of $SrAl_2O_4{:}Eu^{2+}$ prepared by this method is about 1–2 μm [75].

This method is simple and easy to master. The prepared products are uniform and of small particle size, but it takes a long time, produces samples and requires high cost.

5 Fundamental Mechanisms of Mechanoluminescence

According to the different modes of mechanical force acting on the excitation ML phenomenon, ML can be divided into two types: Deformation ML and tribo-ML [76]. According to the degree of recovery of the deformation of the material during the stress process, the deformation ML can be divided into elastic-ML, plastic-ML and fracto-ML. Tribo-ML may be caused by triboelectricity, tribochemical reactions, frictional heat generation, etc., and can be divided into electrically induced tribo-ML, chemically induced tribo-ML and thermally induced tribo-ML. There are different opinions on the luminescence mechanism of tribo-ML, and this phenomenon is

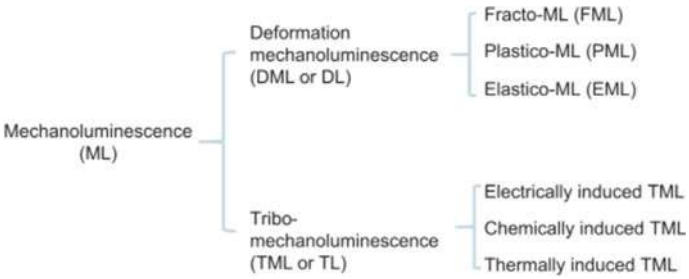

Fig. 4 Classification of mechanoluminescence [77]

more only considered as a phenomenon to be discussed and not too much systematic research has been done, so the deformation ML is mainly introduced below (Fig. 4).

5.1 Mechanism of Fracto-ML

Fracto-ML refers to the phenomenon that light is emitted when the material is fractured or damaged under the action of external mechanical force. The main reason for its luminescence is that when the material is damaged, its internal chemical bonds are broken, making its cracks in an excited state with high energy, and this excited state may excite the gas in the environment or the luminescent center of the material in different ways. According to different excitation modes, fracture stress luminescence can be divided into eleven different types: (i) Piezoelectrification-induced fracto ML; (ii) Defective phase piezoelectrification-induced fracto ML; (iii) Charged dislocation electrification-induced fracto ML; (iv) Baro-diffusion electrification-induced fracto ML; (v) Chemically-induced fracto ML; (vi) Thermally stimulated fracto ML; (vii) Incandescent fracto ML; (viii) Stress perturbation-induced fracto ML; (ix) Thermal excitation-induced fracto ML; (x) Mechanically excited fracto ML (True ML); (xi) Deep trap-induced fracto ML. Most of these mechanisms are theoretical speculations, some of which can correspond to some experimental phenomena; Some are just theoretical assumptions [76].

5.2 Luminescence Mechanism of Plastic-ML

Plastic-ML refers to the phenomenon that the material emits light in the process of plastic deformation when subjected to external forces. The process of plastic-ML of a material can also contain many different luminescence mechanisms. The luminescent mechanism of plastic-ML materials can be divided into four types: (1) mechanism of mechanical interaction between dislocation and defect center;

(2) Thermodynamic excitation induction mechanism; (3) The crystal surface electrification induction mechanism caused by the movement of charged dislocation; (4) Induction mechanism of electrostatic interaction between dislocation and defect center, etc. [76].

The plastic-ML spectrum can be divided into impulse type and continuous type, in which the impulse type luminescence is caused by the crystal surface acting on electricity caused by the movement of a charged dislocation. The whole process of action can be explained as follows: During plastic deformation, dislocations with different electric charges move in opposite directions to the surface of the crystal, thus making the surface of the crystal charged and creating an electric field inside the crystal. With the increase of the shape variable, the internal electric field gradually increases until it reaches the breakdown threshold, which makes the surface emit an electroluminescent pulse. On the other hand, continuous luminescence is caused by dissociation of electron trap through tunneling effect under the action of a strong electric field of moving dislocation line charge. Related scholars have carried out a series of experimental studies and theoretical derivation on this phenomenon.

5.3 Luminescence Mechanism of Elastic-ML

Elastic-ML refers to the phenomenon of emitting light during the elastic deformation of materials under external forces. The research of elastic-ML started relatively late, and several typical materials that have been widely studied are ZnS:Mn, ZnS:Cu, $SrAl_2O_4:Eu^{2+}$, etc. The luminescence mechanisms of elastic-ML materials are summarized in B. P. Chandra, and are almost identical to those of plastic-ML. In recent decades, more and more people have paid attention to elastic-ML materials and conducted some in-depth studies on them. Some new luminescence mechanism of elastic-ML has been proposed, among which the piezoelectric induction mechanism is the one most recognized by researchers [78–80]. Piezoelectric induction mechanism refers to when a stressed luminescent material with piezoelectric properties is strained, the valence band is tilted due to the potential generated by the piezoelectric charge, so that the bound carriers become free carriers. When these free electrons and holes recombine, they release energy in a non-radiative manner, and the released energy excites the luminescent center to produce light (Fig. 5).

6 Applications of Mechanoluminescence

ML materials can emit light under one or more types of mechanical stimuli (compression, twisting, bending, impact, touch, friction, vibration, etc.). Over the past two decades, researchers have demonstrated ML materials in many applications, such as stress sensors [82, 83], stress imaging distributions [1], visualization of crack propagation [84], structural health diagnosis [85], excitation sources [86], light sources

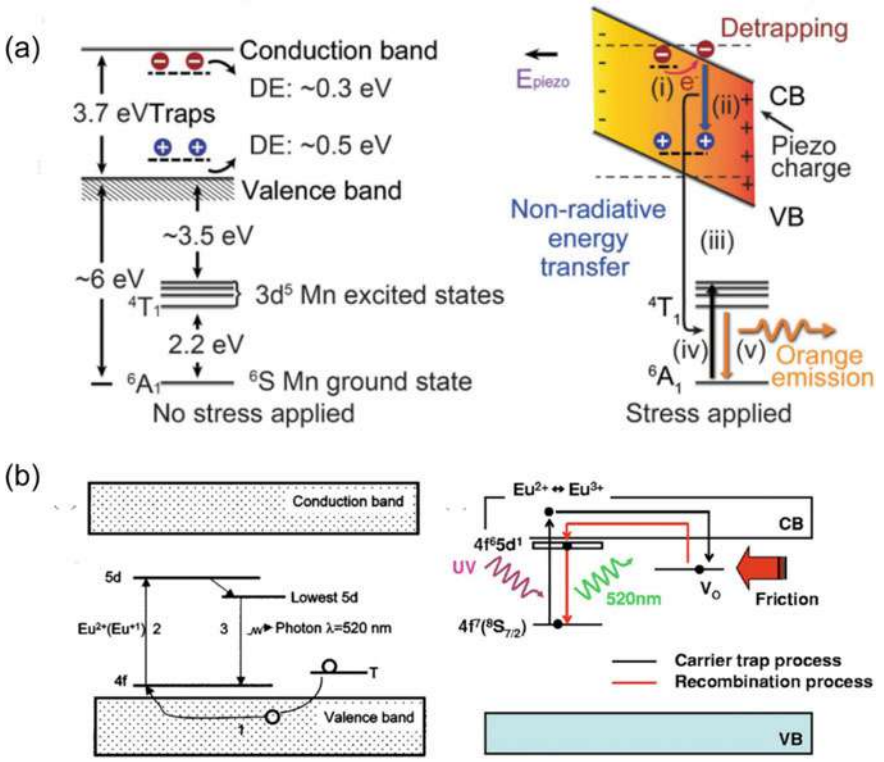

Fig. 5 Schematic diagrams of ML mechanism of ZnS:Mn [1] and $SrAl_2O_4:Eu^{2+}$ [40, 81]

and displays [4, 87], anti-counterfeiting [88] and NIR-ML imaging [89]. Most of these applications are based on ZnS-based and $SrAl_2O_4$-based ML materials. Here, we take a brief introduction to the high-impact applications of the last two decades.

6.1 Stress Sensor/Imaging Stress Distributions

Based on the linear relationship between instantaneous ML intensity of the ML material and stress, ML composite materials formed by ML materials and polymers can replace the strain gauge based on electric or optical fiber. ML composite materials can be coated on the surface of the target, which is more flexible and easy to adjust.

In 2009, Xu's group coated $SrAl_2O_4:Eu^{2+}$ composite material on the surface of the bolt. During the bolt tightening process, the instantaneous axial force of the bolt was detected by the different light intensities emitted by the composite film. This study proved that ML imaging can be used to analyze real-time stress distribution.

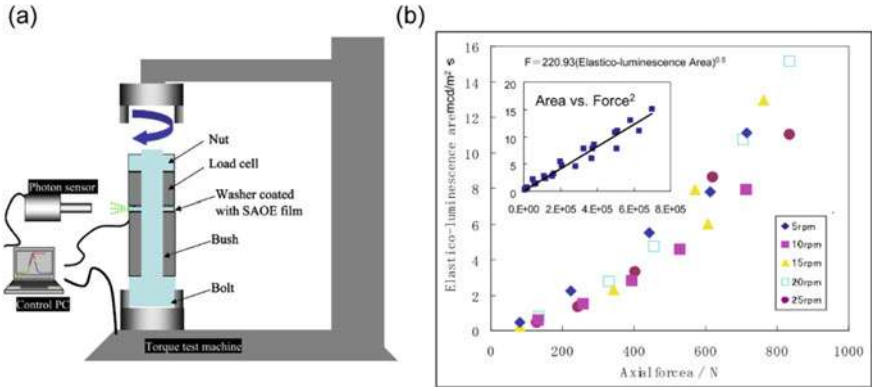

Fig. 6 Axial force sensor based on $SrAl_2O_4:Eu^{2+}$ ML. **a** Schematic diagram of an experimental system to measure ML, torque and axial force simultaneously. **b** Relationship of ML area on the axial force at different tightening speeds (inset: linear relationship of ML area on the square of axial force) Reproduced with permission from Ref. [90], Copyright 2010, SPIE

This novel system can also monitor the health of load-bearing structures in real-time, such as buildings and bridges [90].

In 2015, Wang et al. designed a signature recording system based on ZnS:Mn ML materials [1]. This system emits different intensities of light when humans are writing to analyze the difference in force during the writing process, and it can also quantify the difference in the pressure rate of the written letters. Thereby improving the security of electronic signatures (Figs. 6 and 7).

6.2 Structural Health Diagnosis

The failure of social infrastructure (buildings, bridges, etc.) is related to its aging structure. Xu group used ML-imaging technologies to realize monitoring and diagnosis of the structural health of the macroscopic social infrastructure. This monitoring and diagnosis system is realized by encapsulating the ML sensor and camera in a black box. The ML sensor uses $SrAl_2O_4:Eu^{2+}$ ML material, so an ultraviolet excitation source is also installed in the black box to restore the ML of $SrAl_2O_4:Eu^{2+2}$ (Fig. 8).

6.3 Light Sources and Displays

The colors of the ML of these materials cover the entire visible range, which is ideal for the multi-color display. When several ML materials of different colors are combined, the emission of white light can be realized.

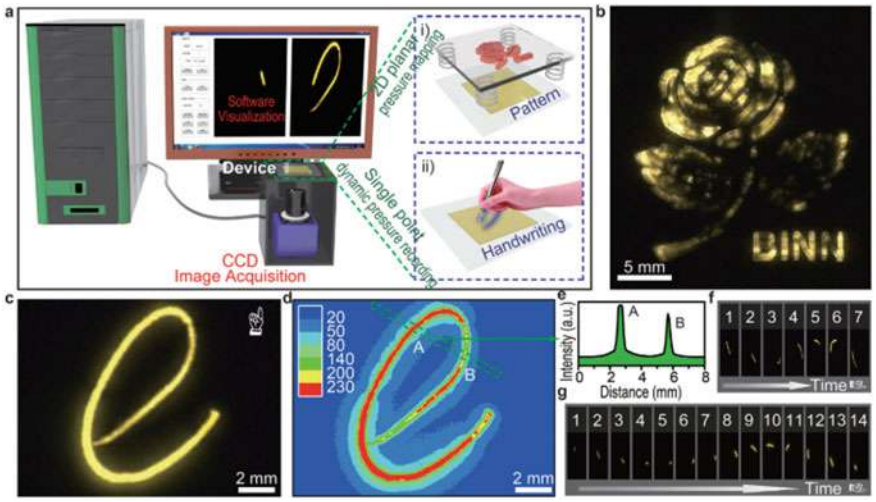

Fig. 7 ML mapping of handwriting. **a** Test system diagram. **b** ML mapping of 2D planar pressure distributions. **c** ML distributions generated from a handwritten "e". **d** The corresponding 2D distribution of relative ML intensity from **c**. **e** The line profile of relative ML intensity from the marked area in **d**. **f** and **g** Dynamic ML frames under different speeds, respectively. Reproduced with permission from Ref. [1], Copyright 2015, WILEY–VCH Verlag GmbH & Co. KGaA, Weinheim

In 2014, Jeong et al. combined ZnS-based ML materials of different colors with PDMS, and used gas-flow excited composite film to realize wind-driven stress display of different colors, and realized gas-flow driven white light emission by mixing ratio of powder of different colors [4]. The research suggests that the use of wind-powered mechanical luminaries in actual displays or lighting systems could pave the way for new types of environmentally friendly lights, reducing energy waste and promoting sustainable development (Fig. 9).

6.4 Photodynamic Therapy

Xu group proposed that ML generated from ML materials can be used to drive photochemical reactions related to prodrug activation. A hybrid material composed of ML nanoparticles and photosensitizer is proposed. When using ultrasonic excitation, the hybrid material emits activator photons. $SrAl_2O_4:Eu^{2+}$, $CaYAl_3O_7:Eu^{2+}$ and $CaZnOS:Mn^{2+}$ [63, 91, 92] can produce ML under the stimulation of ultrasound, which is a more suitable material for this hybrid material. In 2019, Guosong Hong et al. synthesized ZnS:Ag,Co nanoparticles with ML using a combination of hydrothermal method and high-temperature heating, and coated the surface of the nanoparticles with a ZnS shell to improve ML intensity of ZnS:Ag,Co. Using

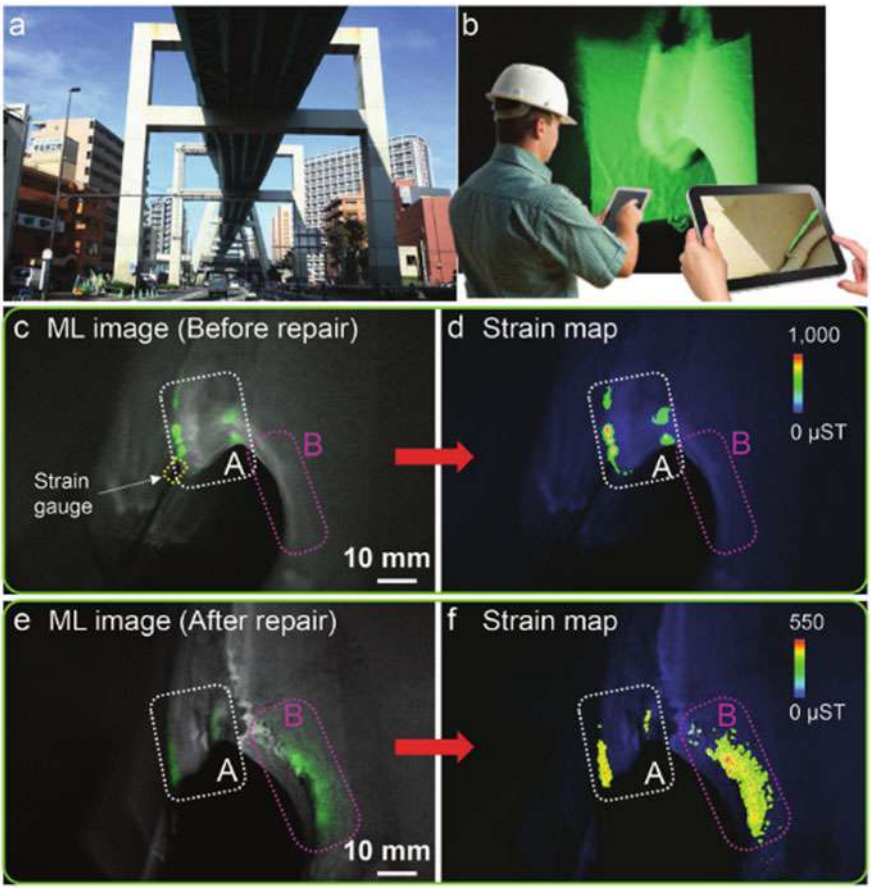

Fig. 8 ML sensor field quantitative strain imaging and effective diagnosis of highway joint sections. **a** Outside view of the diagnosed highway. **b** Future status of on-site inspections of infrastructure. Before and after repair of ML device and its corresponding stress distribution. Reproduced with permission from Ref. [2], Copyright 2018, WILEY–VCH Verlag GmbH & Co. KGaA, Weinheim

ZnS:Ag,Co@ZnS nanoparticles achieve motor activities of acousto-optic stimulation in mice. This research not only promoted the application of ML materials in the biological field, but also promoted the development of acousto-optic genetics [7] (Fig. 10).

ML materials have application prospects in wearable light-emitting devices, anti-counterfeiting, NIR-ML imaging and other fields, so we won't describe them one by one here.

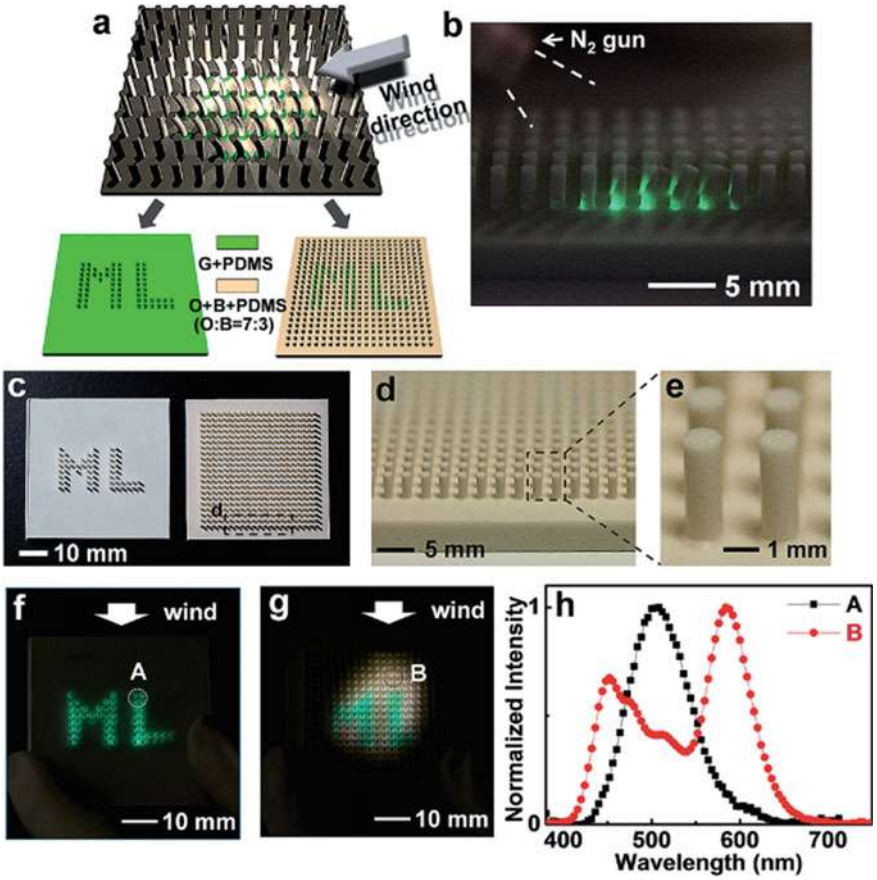

Fig. 9 Wind-driven ML display. **a** Schematic diagram of a wind-driven display device. **b** Display of ML under nitrogen flow. **c–e** Photographs and **f**, **g** ML images of two patterned display devices. **h** ML spectra captured from spots A and B in frames **f** and **g**. Reproduced with permission from Ref. [4], Copyright 2014, The Royal Society of Chemistry

7 Outlook

Based on the special luminescence properties of ML materials, they have broad application prospects in many fields, and they have gradually attracted the attention of researchers. In the past two decades of research, certain research progress has been made in the field of ML. Among them, more than 40 kinds of high-performance ML materials have been developed, and a new ML mechanism in piezoelectric ML materials, a piezoelectric induced de-trapping model, has been proposed. Its application has also been continuously developed, which not only realizes ML-driven by pressure and wind, but also realizes ML-driven by ultrasound, and realizes the application of ML materials in the biological field. Although the development of ML materials

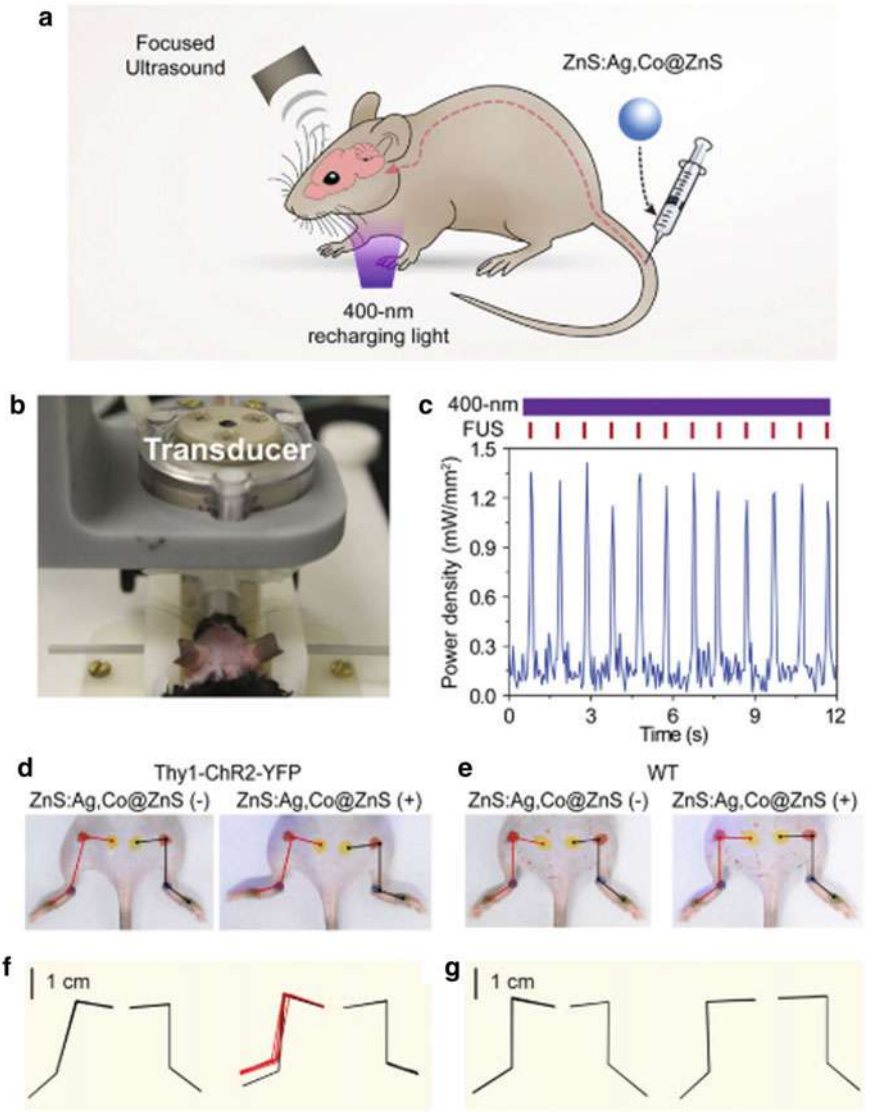

Fig. 10 Sono-optogenetic stimulation of the motor activity in rats. **a** A schematic diagram of acousto-optic stimulation in a rat. **b** Photograph of in vivo sono-optogenetic stimulation setup. **c** The equivalent power density of the 470 nm emission of ZnS:Ag,Co@ZnS nanoparticles under FUS repeated excitation under 400 nm continuous activation. **d** and **e** were the photos of sono-optogenetic stimulation of Thy1-ChR2-YFP mouse (**d**) and a wild-type (WT) mouse (**e**) before and after injected by ZnS:Ag,Co@ZnS nanoparticles. **f** and **g** Hindlimb kinematics of Thy1-ChR2-YFP mouse (**f**) and a wild-type (WT) mouse (**g**) under sono-optogenetic stimulation. Reproduced with permission from Ref. [7], Copyright 2019

has made preliminary achievements, the size of most ML materials is at the micron level, which hinders the application of ML materials in the field of fine devices and biology to a certain extent. Therefore, in future research, the universal realization of the nanometerization of ML materials will help promote the development of ML materials.

References

1. Wang, X., Zhang, H., Yu, R., Dong, L., Peng, D., Zhang, A., Zhang, Y., Liu, H., Pan, C., Wang, Z.L.: Dynamic pressure mapping of personalized handwriting by a flexible sensor matrix based on the mechanoluminescence process. Adv. Mater. **27**(14), 2324–2331 (2015)
2. Liu, L., Xu, C.-N., Yoshida, A., Tu, D., Ueno, N., Kainuma, S.: Scalable elasticoluminescent strain sensor for precise dynamic stress imaging and onsite infrastructure diagnosis. Adv. Mater. Techno. **4**(1), 1800336 (2019)
3. Zhang, J., Bao, L., Lou, H., Deng, J., Chen, A., Hu, Y., Zhang, Z., Sun, X., Peng, H.: Flexible and stretchable mechanoluminescent fiber and fabric. J. Mater. Chem. C **5**(32), 8027–8032 (2017)
4. Jeong, S.M., Song, S., Joo, K.-I., Kim, J., Hwang, S.-H., Jeong, J., Kim, H.: Bright, wind-driven white mechanoluminescence from zinc sulphide microparticles embedded in a polydimethylsiloxane elastomer. Energy Environ. Sci. **7**(10), 3338–3346 (2014)
5. Patel, D.K., Cohen, B.-E., Etgar, L., Magdassi, S.: Fully 2D and 3D printed anisotropic mechanoluminescent objects and their application for energy harvesting in the dark. Mater. Horizons **5**(4), 708–714 (2018)
6. Du, Y., Jiang, Y., Sun, T., Zhao, J., Huang, B., Peng, D., Wang, F.: Mechanically excited multicolor luminescence in lanthanide ions. Adv. Mater. **31**(7), e1807062 (2019)
7. Wu, X., Zhu, X., Chong, P., Liu, J., Andre, L.N., Ong, K.S., Brinson, K., Jr.; Mahdi, A.I., Li, J., Fenno, L.E., Wang, H., Hong, G.: Sono-optogenetics facilitated by a circulation-delivered rechargeable light source for minimally invasive optogenetics. Proc. Natl. Acad. Sci. **116**(52), 26332–26342 (2019)
8. Wu, J., Wu, Z., Han, S., Yang, B.-R., Gui, X., Tao, K., Liu, C., Miao, J., Norford, L.K.: Extremely deformable, transparent, and high-performance gas sensor based on ionic conductive hydrogel. ACS Appl. Mater. Interfaces **11**(2), 2364–2373 (2019)
9. Amoateng, D.O., Totaro, M., Crepaldi, M., Falotico, E., Beccai, L.: Intelligent position, pressure and depth sensing in a soft optical waveguide skin. In: IEEE international conference on soft robotics, pp. 349–354 (2019)
10. Walton, A.J.: Triboluminescence. Adv. Phys. **26**(6), 887–948 (2006)
11. Bünzli, J.-C.G., Wong, K.-L.: Lanthanide mechanoluminescence. J. Rare Earths **36**(1), 1–41 (2018)
12. Zhao, X.: On the phenomenon of earthquake luminescence (in Chinese). Encyclopedic Knowl. **22**, 8–9 (2006)
13. Pu, J.-H., Zha, X.-J., Tang, L.-S., Bai, L., Bao, R.-Y., Liu, Z.-Y., Yang, M.-B., Yang, W.: Human skin-inspired electronic sensor skin with electromagnetic interference shielding for the sensation and protection of wearable electronics. ACS Appl. Mater. Interfaces **10**(47), 40880–40889 (2018)
14. Eddingsaas, N.C., Suslick, K.S.: Mechanoluminescence: light from sonication of crystal slurries. Nature **444**(7116), 163 (2006)
15. Jha, P., Chandra, B.P.: Survey of the literature on mechanoluminescence from 1605 to 2013. Luminescence **29**(8), 977–993 (2014)
16. Chandra, B.P., Shrivastava, K.K.: Dependence of mechano-luminescence in Rochelle-salt crystals on the charge produced during their fracture. J. Phys. Chem. Solids **26**(4), iv (1978)

17. Xu, C.N., Watanabe, T., Akiyama, M., Zheng, X.G.: Artificial skin to sense mechanical stress by visible light emission. Appl. Phys. Lett. **74**(9), 1236–1238 (1999)
18. Peng, S., Blanloeuil, P., Wu, S., Wang, C.H.: Rational design of ultrasensitive pressure sensors by tailoring microscopic features. Adv. Mater. Interfaces **5**(18), 201800403 (2018)
19. Liu, M., Wu, Q., Shi, H., An, Z., Huang, W.: Progress of research on organic/organometallic mechanoluminescent materials. Acta Chimica Sinica Chin. Ed. **76**(4), 246 (2018)
20. Fontenot, R.S., Bhat, K.N., Hollerman, W.A., Alapati, T.R., Aggarwal, M.D.: Triboluminescent properties of dysprosium doped europium dibenzoylmethide triethylammonium. Ecs J. Solid State Sci. Technol. **2**(9), P384–P388 (2013)
21. Yu, J.B., Zhang, H.J., Deng, R.P., Zhou, L., Peng, Z.P., Fu, L.S.: Triboluminescence of a new europate complex. J. Rare Earths **22**(1), 126–128 (2004)
22. Fontenot, R.S., Bhat, K.N., Hollerman, W.A., Aggarwal, M.D.: Triboluminescent materials for smart sensors. Mater. Today **14**(6), 292–293 (2011)
23. Takada, N., Sugiyama, J.I., Minami, N., Hieda, S.: Intense mechanoluminescence from europium tris(2-thenoyltrifluoroacetone) phenanthroline. Mol. Cryst. **295**(1), 71–74 (1997)
24. Schoenweiz, S., Sorsche, D., Schwarz, B., Rau, S., Streb, C.: Structural and reactivity insights into covalently linked Cu(I) complex-Anderson polyoxometalates. Dalton Trans. **46**(30), 9760–9764 (2017)
25. Inoue, T., Tazuke, S.: Poly[trans-1-(3-vinyl-9-carbazolyl)-2-(9-carbazolyl)cyclobutane]. Synthesis and comparison with poly(9-ethyl-3-vinylcarbazole). J. Polymer Sci. Polymer Chem. Ed. (1981)
26. Yang, J., Gao, X., Xie, Z., Gong, Y., Fang, M., Peng, Q., Chi, Z., Zhen, L.: Elucidating the excited state of mechanoluminescence in organic luminogens with room-temperature phosphorescence. Angewandte Chemie (2017)
27. Nakayama, H., Nishida, J.I., Takada, N., Sato, H., Yamashita, Y.: Crystal structures and triboluminescence based on trifluoromethyl and pentafluorosulfanyl substituted asymmetric N-phenyl imide compounds. Chem. Mater. **24**(4), 671 (2012)
28. Chen, Y., Spiering, A.J.H., Karthikeyan, S., Peters, G.W.M., Sijbesma, R.P.: Mechanically induced chemiluminescence from polymers incorporating a 1,2-dioxetane unit in the main chain. Nat. Chem. **4**(7), 559–562 (2012)
29. Zink, J.I., Hardy, G.E., Sutton, J.E.: Triboluminescence of sugars. J. Phys. Chem. **80**(3), 248–249 (1976)
30. Chandra, B., Tiwari, S., Ramrakhiani, M., Ansari, M.: Mechanoluminescence in centrosymmetric crystals. Cryst. Res. Technol. **26**(6), 767–781 (1991)
31. Chandra, B., Elyas, M., Shrivastava, K., Verma, R.: Mechanoluminescence and piezoelectric behaviour of monoclinic crystals. Solid State Commun. **36**(11), 931–933 (1980)
32. Chandra, B., Zink, J.I.: Triboluminescence of triclinic crystals. J. Lumin. **23**(3–4), 363–372 (1981)
33. Zink, J.I., Kaska, W.C.: Triboluminescence of hexaphenylcarbodiphosphorane. Emission from a molecular excited state populated by mechanical stress. J. Am. Chem. Soc. **95**(22), 7510–7512 (1973)
34. Zink, J.I., Klimt, W.: Triboluminescence of coumarin. Fluorescence and dynamic spectral features excited by mechanical stress. J. Am. Chem. Soc. **96**(14), 4690–4692 (1974)
35. Hardy, G.E., Baldwin, J.C., Zink, J.I., Kaska, W.C., Liu, P.-H., Dubois, L.: Triboluminescence spectroscopy of aromatic compounds. J. Am. Chem. Soc. **99**(11), 3552–3558 (1977)
36. Sweeting, L.M., Rheingold, A.L.: Crystal structure and triboluminescence. 1. 9-anthryl carbinols. J. Phys. Chem. **92**(20), 5648–5655
37. Inoue, T., Tazuke, S.: Triboluminescence and tribopolymerization of 9-ethyl-3-vinylcarbazole. Chem. Lett. **1981**(5), 589–592 (2006)
38. Xu, B., Mu, Y., Mao, Z., Xie, Z., Wu, H., Zhang, Y., Jin, C., Chi, Z., Liu, S., Xu, J.: Achieving remarkable mechanochromism and white-light emission with thermally activated delayed fluorescence through the molecular heredity principle. Chem. Sci. **7** (2016)
39. Tiwari, G., Brahme, N., Sharma, R., Bisen, D.P., Sao, S.K., Kurrey, U.K.: Enhanced long-persistence of Ca2Al2SiO7:Ce3+ phosphors for mechanoluminescence and thermoluminescence dosimetry. J. Mater. Sci. Mater. Electron. **27**(6), 6399–6407 (2016)

40. Xu, C.-N., Watanabe, T., Akiyama, M., Zheng, X.-G.: Direct view of stress distribution in solid by mechanoluminescence. Appl. Phys. Lett. **74**(17), 2414–2416 (1999)
41. Zhang, H., Yamada, H., Terasaki, N., Xu, C.-N.: Ultraviolet mechanoluminescence from SrAl2O4:Ce and SrAl2O4:Ce,Ho. Appl. Phys. Lett. **91**(8), 081905 (2007)
42. Akiyama, M., Xu, C.-N., Matsui, H., Nonaka, K., Watanabe, T.: Recovery phenomenon of mechanoluminescence from Ca2Al2SiO7: Ce by irradiation with ultraviolet light. Appl. Phys. Lett. **75**(17), 2548–2550 (1999)
43. Zhang, L., Xu, C.-N., Yamada, H., Bu, N.: Enhancement of mechanoluminescence in CaAl2Si2O8: Eu2+ by partial Sr2+ substitution for Ca2+. J. Electrochem. Soc. **157**(3), J50 (2010)
44. Kamimura, S., Yamada, H., Xu, C.-N.: Development of new elasticoluminescent material SrMg2(PO4)2:Eu. J. Lumin. **132**(2), 526–530 (2012)
45. Zhang, H., Xu, C.-N., Terasaki, N., Yamada, H.: Electro-mechano-optical luminescence from CaYAl3O7: Ce. Electrochem. Solid State Lett. **14**(11), J76 (2011)
46. Zhang, L., Yamada, H., Imai, Y., Xu, C.-N.: Observation of elasticoluminescence from CaAl2Si2O8: Eu2+ and its water resistance behavior. J. Electrochem. Soc. **155**(3), J63 (2007)
47. Zhang, H., Yamada, H., Terasaki, N., Xu, C.-N.: Blue light emission from stress-activated CaYAl3O7: Eu. J. Electrochem. Soc. **155**(5), J128 (2008)
48. Zhang, H., Yamada, H., Terasaki, N., Xu, C.-N.: Stress-induced mechanoluminescence in SrCaMgSi2O7: Eu. Electrochem. Solid State Lett. **10**(10), J129 (2007)
49. Zhang, J.-C., Wang, X., Marriott, G., Xu, C.-N.: Trap-controlled mechanoluminescent materials. Prog. Mater Sci. **103**, 678–742 (2019)
50. Zhang, J.C., Xu, C.N., Long, Y.Z.: Elastico-mechanoluminescence in CaZr(PO4)2:Eu2+ with multiple trap levels. Opt. Express **21**(11), 13699–13709 (2013)
51. Akiyama, M., Xu, C.-N., Nonaka, K.: Intense visible light emission from stress-activated ZrO2:Ti. Appl. Phys. Lett. **81**(3), 457–459 (2002)
52. Botterman, J., Eeckhout, K.V.d., Baere, I.D., Poelman, D., Smet, P.F.: Mechanoluminescence in BaSi2O2N2:Eu. Acta Materialia **60**(15), 5494–5500 (2012)
53. Zhang, L., Xu, C.-N., Yamada, H.: In strong mechanoluminescence from oxynitridosilicate phosphors. In: IOP Conference Series: Materials Science and Engineering, p. 212001 (2011)
54. Tu, D., Xu, C.-N., Fujio, Y., Yoshida, A.: Mechanism of mechanical quenching and mechanoluminescence in phosphorescent CaZnOS:Cu. Light: Sci. Appl. **4**(11), e356 (2015)
55. Zhang, H., Terasaki, N., Yamada, H., Xu, C.-N.: Mechanoluminescence of europium-doped SrAMgSi2O7(A=Ca, Sr, Ba). Jpn. J. Appl. Phys. **48**(4), 04C109 (2009)
56. Matsui, H., Xu, C.-N., Akiyama, M., Watanabe, T.: Strong mechanoluminescence from UV-irradiated spinels of ZnGa2O4: Mn and MgGa2O4: Mn. Jpn. J. Appl. Phys. **39**(12R), 6582 (2000)
57. Matsui, H., Xu, C.-N., Tateyama, H.: Stress-stimulated luminescence from ZnAl2O4:Mn. Appl. Phys. Lett. **78**(8), 1068–1070 (2001)
58. Zhang, H., Yamada, H., Terasaki, N., Xu, C.-N.: Green mechanoluminescence of Ca2MgSi2O7: Eu and Ca2MgSi2O7: Eu, Dy. J. Electrochem. Soc. **155**(2), J55 (2007)
59. Zhao, H., Wang, X., Li, J., Li, Y., Yao, X.: Strong mechanoluminescence of Zn2(Ge0.9Si0.1)O4:Mn with weak persistent luminescence. Appl. Phys. Express **9**(1), 012104 (2016)
60. Wang, W., Peng, D., Zhang, H., Yang, X., Pan, C.: Mechanically induced strong red emission in samarium ions doped piezoelectric semiconductor CaZnOS for dynamic pressure sensing and imaging. Opt. Commun. **395**, 24–28 (2017)
61. Kamimura, S., Yamada, H., Xu, C.-N.: Strong reddish-orange light emission from stress-activated Srn+1SnnO3n+1:Sm3+ ($n = 1, 2, \infty$) with perovskite-related structures. Appl. Phys. Lett. **101**(9), 091113 (2012)
62. Li, L., Wong, K.-L., Li, P., Peng, M.: Mechanoluminescence properties of Mn2+-doped BaZnOS phosphor. J. Mater. Chem. C **4**(35), 8166–8170 (2016)
63. Zhang, J.C., Xu, C.N., Kamimura, S., Terasawa, Y., Yamada, H., Wang, X.: An intense elastico-mechanoluminescence material CaZnOS:Mn2+ for sensing and imaging multiple mechanical stresses. Opt. Express **21**(11), 12976–12986 (2013)

64. Zhang, J.-C., Fan, X.-H., Yan, X., Xia, F., Kong, W., Long, Y.-Z., Wang, X.: Sacrificing trap density to achieve short-delay and high-contrast mechanoluminescence for stress imaging. Acta Mater. **152**, 148–154 (2018)
65. Luo, Z., Hu, X., Tian, X., Luo, C., Xu, H., Li, Q., Li, Q., Zhang, J., Qiao, F., Wu, X., Borisenko, V.E., Chu, J.: Structure-property relationships in graphene-based strain and pressure sensors for potential artificial intelligence applications. Sensors **19**(5), 1250 (2019)
66. Zhang, J.-C., Long, Y.-Z., Wang, X., Xu, C.-N.: Controlling elastico-mechanoluminescence in diphase (Ba, Ca)TiO3:Pr3+ by co-doping different rare earth ions. RSC Adv. **4**(77), 40665–40675 (2014)
67. Pan, C., Zhang, J.-C., Zhang, M., Yan, X., Zhang, H.-D., Long, Y.-Z., Sun, X.-Y., Jiang, H.-T.: Trap-controlled mechanoluminescence in Pr3+-activated M2Nb2O7 (M = Sr, Ca) isomorphic perovskites. Opt. Mater. Express **8**(6), 1425 (2018)
68. Li, Y., Gecevicius, M., Qiu, J.: Long persistent phosphors–from fundamentals to applications. Chem. Soc. Rev. **45**(8), 2090–2136 (2016)
69. Fan, X.H., Zhang, J.C., Zhang, M., Pan, C., Yan, X., Han, W.P., Zhang, H.D., Long, Y.Z., Wang, X.: Piezoluminescence from ferroelectric Ca3Ti2O7:Pr(3+) long-persistent phosphor. Opt. Express **25**(13), 14238–14246 (2017)
70. Tu, D., Xu, C.N., Yoshida, A., Fujihala, M., Hirotsu, J., Zheng, X.G.: LiNbO3:Pr(3+): a multipiezo material with simultaneous piezoelectricity and sensitive piezoluminescence. Adv. Mater. **29**(22) (2017)
71. Rao, N.M., Reddy, D.R., Reddy, B.K., Xu, C.N.: Intense red mechanoluminescence from (ZnS)1–x(MnTe)x. Phys. Lett. A **372**(22), 4122–4126 (2008)
72. Terasawa, Y., Xu, C.N., Yamada, H., Kubo, M.: Near infra-red mechanoluminescence from strontium aluminate doped with rare-earth ions. IOP Conf. Ser. Mater. Sci. Eng. **18**(21), 212013 (2011)
73. Xu, C.N., Li, C., Imai, Y., Yamada, H., Adachi, Y., Nishikubo, K.: Development of elastico-luminescent nanoparticles and their applications. Adv. Sci. Technol. **45**, 939–944 (2006)
74. Qian, X., Cai, Z., Su, M., Li, F., Fang, W., Li, Y., Zhou, X., Li, Q., Feng, X., Li, W., Hu, X., Wang, X., Pan, C., Song, Y.: Printable skin-driven mechanoluminescence devices via nanodoped matrix modification. Adv. Mater. **30**(25), e1800291 (2018)
75. Liu, Y., Xu, C.-N.: Influence of calcining temperature on photoluminescence and triboluminescence of europium-doped strontium aluminate particles prepared by sol−gel process. J. Phys. Chem. B **107**(17), 3991–3995 (2003)
76. Chandra, B., Rathore, A.: Classification of mechanoluminescence. Cryst. Res. Technol. **30**(7), 885–896 (1995)
77. Zhang, H., Wei, Y., Huang, X., Huang, W.: Recent development of elastico-mechanoluminescent phosphors. J. Lumin. **207**, 137–148 (2019)
78. Chandra, V. K., Chandra, B.P., Jha, P.: Strong luminescence induced by elastic deformation of piezoelectric crystals. Appl. Phys. Lett. **102**(24), 241105 (2013)
79. Chandra, B.P., Chandra, V.K., Jha, P.: Piezoelectrically-induced trap-depth reduction model of elastico-mechanoluminescent materials. Physica. B **461**, 38–48 (2015)
80. Zhang, Y., Gao, G., Chan, H.L., Dai, J., Wang, Y., Hao, J.: Piezo-phototronic effect-induced dual-mode light and ultrasound emissions from ZnS:Mn/PMN-PT thin-film structures. Adv. Mater. **24**(13), 1729–1735 (2012)
81. Dong, W., Huang, Y., Yin, Z., Zhou, Y., Chen, J.: Stretchable tactile and bio-potential sensors for human-machine interaction: a review. In: Chen, Z., Mendes, A., Yan, Y., Chen, S. (eds.) Intelligent Robotics and Applications, vol. 10984, pp. 155–163
82. Kim, J.S., Kim, G.-W.: New non-contacting torque sensor based on the mechanoluminescence of ZnS: Cu microparticles. Sens. Actuat. A **218**, 125–131 (2014)
83. Kim, G.-W., Kim, J.-S.: Dynamic torsional response analysis of mechanoluminescent paint and its application to non-contacting automotive torque transducers. Measure. Sci. Technol. **25**(1), 015009
84. Kim, J.S., Kwon, Y.-N., Shin, N., Sohn, K.-S.: Mechanoluminescent SrAl2O4:Eu,Dy phosphor for use in visualization of quasidynamic crack propagation. Appl. Phys. Lett. **90**(24), 241916 (2007)

85. Fujio, Y., Xu, C.-N., Terasawa, Y., Sakata, Y., Yamabe, J., Ueno, N., Terasaki, N., Yoshida, A., Watanabe, S., Murakami, Y.: Sheet sensor using SrAl2O4: Eu mechanoluminescent material for visualizing inner crack of high-pressure hydrogen vessel. Int. J. Hydrogen Energy **41**(2), 1333–1340 (2016)
86. Terasaki, N., Zhang, H., Yamada, H., Xu, C.N.: Mechanoluminescent light source for a fluorescent probe molecule. Chem. Commun. (Camb.) **47**(28), 8034–8036 (2011)
87. Jeong, S.M., Song, S., Kim, H.: Simultaneous dual-channel blue/green emission from electromechanically powered elastomeric zinc sulphide composite. Nano Energy **21**, 154–161 (2016)
88. Zhang, J.C., Pan, C., Zhu, Y.F., Zhao, L.Z., He, H.W., Liu, X., Qiu, J.: Achieving thermo-mechano-opto-responsive bitemporal colorful luminescence via multiplexing of dual lanthanides in piezoelectric particles and its multidimensional anticounterfeiting. Adv. Mater. **30**(49), e1804644 (2018)
89. Li, L., Wondraczek, L., Li, L., Zhang, Y., Zhu, Y., Peng, M., Mao, C.: CaZnOS:Nd(3+) emits tissue-penetrating near-infrared light upon force loading. ACS Appl. Mater. Interfaces **10**(17), 14509–14516 (2018)
90. Quan, C., Li, C., Qian, K., Xu, C.-N., Adachi, Y., Asundi, A.K., Chau, F.S., Ueno, N.: Real-time detection of axial force for reliable tightening control. **7522**, 75223G (2009)
91. Terasaki, N., Yamada, H., Xu, C.-N.: Ultrasonic wave induced mechanoluminescence and its application for photocatalysis as ubiquitous light source. Catal. Today **201**, 203–208 (2013)
92. Zhan, T., Xu, C.N., Fukuda, O., Yamada, H., Li, C.: Direct visualization of ultrasonic power distribution using mechanoluminescent film. Ultrason. Sonochem. **18**(1), 436–439 (2011)

Synthesis and Charecterization

Molecular Hybrid Phosphors

Saroj Kumar Kushvaha and Kartik Chandra Mondal

Abstract Phosphors constitute the most important component of organic light emitting diodes (OLEDs), therefore, there has been continuous development in this field. Molecular hybrid phosphors are basically transition metal complexes that are formed by complexation of heavy metal ion with suitable ligand system. The cyclometalated transition metal complexes constitute the major chunk of molecular hybrid phosphors. This chapter covers molecular hybrid phosphors based on complexes of heavy metals such as gold, iridium, platinum, rhodium and ruthenium.

1 Introduction

Phosphors are the materials that show the phenomenon of luminescence on exposure to radiant energy. When these materials exhibit luminescence phenomena immediately on exposure to the radiation, they are called fluorescent materials. Fluorescent materials stop glowing immediately after the supply of the exciting radiation is switched off. However, when they show continuous emission even after being exposed to the photon radiation, they are called phosphorescent material. The phosphorescent materials keep glowing for milliseconds to days even after stopping the supply of external radiation. Five hundred years ago (1603) luminescence was first documented by V. Cascariolo while he was burning baryte with coal. The ZnS and CaS were identified as phosphors in 1866 and 1870, respectively. In 1880s bioluminescence was documented in fire flies.

In this context it is necessary to mention that instead of supply of the photon energy for excitation of electron in a material, a high energy electron beam can be utilized to obtain the emission of visible light. This phenomenon is well known as cathodoluminescence. The beam of high energy electron acts similar to photon. The electron is excited from valence band to the conductance band and is recombined with hole in the conductance band. The energy difference of this process can be emitted

S. K. Kushvaha · K. C. Mondal (✉)
Department of Chemistry, Indian Institute of Technology Madras, Chennai 600036, India
e-mail: csdkartik@iitm.ac.in

© Springer Nature Switzerland AG 2022

K. Upadhyay et al. (eds.), *Hybrid Phosphor Materials*, Engineering Materials,
https://doi.org/10.1007/978-3-030-90506-4_3

as visible light. This was implemented in cathode ray tube of computer (aperture grille) to give rise to monochrome display in 1980s.

The processes of fluorescence and phosphorescence in the phosphor materials have been utilized in making solid-state lighting devices such as light-emitting devices (LEDs) and solar cells. Fluorescence is the fundamental phenomenon that occurs in white LEDs, fluorescent lights, Cathode-ray tubes (CRTs), scintillation sensors. The phosphorescence is the fundamental phenomenon of the devices where continuous luminescence is required, such as radar screens, aircraft instruments, glow-in-dark watches. Since white LEDs are in greatest demand due to their high luminous efficiency with low power consumption, environmental friendliness, and longevity, scientists have been working tirelessly to improve over the quality of LEDs by suitable modifications in phosphor materials. The most important part of a solid-state lighting device is the emitting layer, which is made by blending with a conducting material. The quality of phosphor used in the emitting layer controls the light produced. Therefore, the preparation of phosphors requires a great deal of control and care. The phosphor materials are of pure organic nature as well as hybrid. The phosphor materials which are made by blending or coordination of two standalone chemical moieties to form a periodically ordered material are called hybrid phosphors [1]. The complexation of suitable organic molecule with the heavy metal ion to prepare hybrid phosphors is very common strategy. The hybrid phosphors prepared by introduction of a heavy metal into the organic material are advantageous than pure organic phosphors due to enhanced emission properties. The literature survey reveals that the majority of hybrid phosphors have been prepared by adding a suitable guest activator to the host material. The controlled blending of dopant/activator to the host on nanoscale level enables tuning of electronic and optical properties; hence, hybrid phosphors are the most versatile class of luminescent materials. The host–guest combinations can be made by utilizing organic–inorganic or inorganic–inorganic components. Recently, so much of the research has been directed towards the syntheses of hybrid phosphors in which rare-earth ions (REIs) have been used as dopant. In this chapter, we will focus on metal complex-based hybrid phosphors, which are generally prepared by the complexation of metal ions with the organic ligand systems. This type of organic–inorganic framework has promising applications in solid-state lighting devices, for example, in white LEDs. With the continuous improvement in absorption/emission and charge transport properties by controlled molecular design, this field is becoming more and more promising for solid-state lighting purposes.

1.1 Fundamental Phenomena Involved in Luminescence

Before going to the detailed discussion about hybrid phosphors, it is imperative to discuss the fundamental phenomena involved in the working of phosphors. The absorption of electromagnetic radiation by a material is governed by Beer-Lambert law, which is given by the equation, $A = \log 10(I0/I) = \in Cl$, where A is the

absorbance of light through the material of path length ⌊ and concentration C and ∈ is the molar absorptivity or extinction coefficient of absorbing material (I_0 and I are the intensities of incident and final radiation, respectively). On absorption of electromagnetic radiation, the luminescent materials exhibit two major phenomena: fluorescence and phosphorescence. When a material is irradiated with the radiant energy, electron gets excited to the higher energy level. Once, irradiation of material is switched off, electron comes back to the original energy level by emission of extra energy in the form of light or heat. When electron comes back to the ground state without changing spin state throughout this journey via a radiative pathway, the phenomenon is known as fluorescence. Fluorescence is a spin allowed process that happens in a short span of time (10^{-9}–10^{-7} s). Alternatively, the excited electron can return to the ground state by following another pathway which involves a change in the spin state. It can go to the triplet state by non-radiative process which ultimately decays ground state by radiative emission. This process is known as phosphorescence and takes longer time than the fluorescence. The phosphorescence lifetime (10^{-5}–10^{3} s) is longer because electron has to flip its spin orientation while decaying to the singlet ground state from an excited triplet state. Though, singlet–triplet spin relaxations are quantum mechanically spin forbidden, but due to the spin–orbit or vibronic coupling, they become allowed [2]. Such spectra appear at higher wavelengths when compared to fluorescence. Often in luminescent materials, a long-lived emission band is obtained, which has frequency similar to fluorescence but lifetime similar to phosphorescence, this type of emission is called delayed fluorescence which is usually observed when emission takes place in a rigid and viscous media. In addition to the radiative processes, excited electron can also lose energy through non-radiative pathways such as internal conversion and inter-system crossing. Basically, each electronic energy state is consisting of several vibrational levels (υ) and energy dissipates from higher vibrational level to lower vibrational level within the electronic level; this process is called internal conversion. The lifetime of internal conversion is shorter than the fluorescence lifetime. After absorbing a photon of suitable energy an electron undergoes transition to the excited triplet (T_1) state from an initial excited singlet state (S_1) by losing energy in the form of heat. This change in nature of the spin state is known as inter-system crossing (ISC). The geometrical parameters of an excited singlet state are significantly different than those of excited triplet state. All the photophysical processes which occur in luminescent materials are shown in the Jablonski diagram (Fig. 1) and the time scale for these photophysical processes has been given in Table 1. An important generalization about emission has been given in Kasha's rule, which states that electrons can get excited to any of the excited electronic states (like S_1, S_2, S_3 etc.) depending on wavelengths of absorbed radiation, however, most of the photons will emit from lowest excited electronic state (i.e. S_1 or T_1). This happens due to rapid internal conversions from higher excited states to lower excited spin states. In other words, emission wavelength is independent of absorption wavelength. The fluorescence material does not glow after switching of the source of radiation.

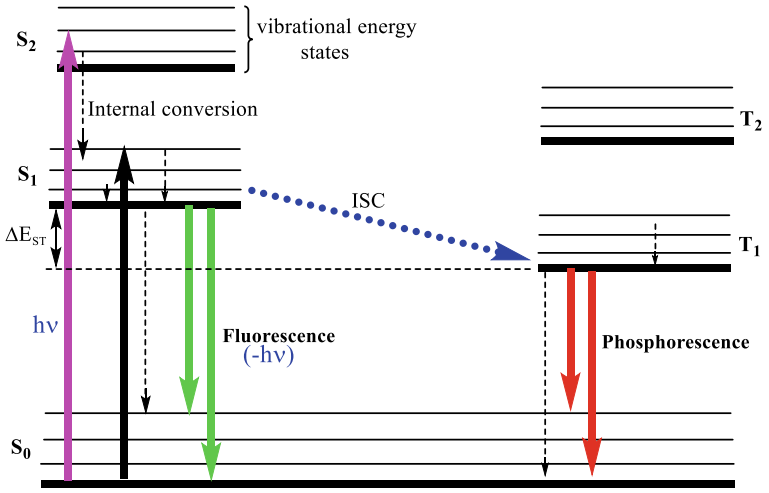

Fig. 1 Jablonski diagram depicting different photophysical phenomena (solid arrows represent radiative decay and dotted arrows represent non-radiative decay)

Table 1 The time scale of various photophysical processes (adopted from Ref. [2], copyright: Elsevier B.V., 2009)

Transition	Process	Time scale (s)
$S_0 \rightarrow S_1$ or S_n	Absorption (Excitation)	10^{-15}
$S_1 \rightarrow S_0$	Fluorescence	10^{-9}–10^{-7}
$T_1 \rightarrow S_0$	Phosphorescence	10^{-3}–10^{0}
$S_n \rightarrow S_1$	Internal conversion	10^{-14}–10^{-10}
$S_1 \rightarrow T_1$	Inter-system crossing	10^{-10}–10^{-8}
$S_1 \rightarrow S_1$	Vibrational relaxation	10^{-12}–10^{-10}
$S_1 \rightarrow S_0$	Non-radiative relaxation Quenching	10^{-7}–10^{-5}
$T_1 \rightarrow S_0$	Non-radiative relaxation Quenching	10^{-3}–10^{0}

In contrast, the phosphorescent materials keep glowing even after irradiation source is switched off, this is why phosphorescent materials are used where continuous luminescence is required. The efficient phosphors are characterized by high fluorescence lifetime and high fluorescence quantum yield. The lifetime is defined by the amount of time an electron spends in the excited states before it comes back to the ground state. The fluorescence lifetime (τ) of such materials can be calculated by the equation, $\tau = (kr + knr)^{-1}$, where k_r and k_{nr} are decay constants for radiative (fluorescence) and non-radiative emissions. Fluorescence quantum yield is one of the parameters that describes the quality of fluorophore, higher quantum yield is associated with the better fluorophore. The fluorescence quantum yield is defined as the ratio of the number of photons emitted to the photons absorbed. The fluorescence

lifetime (τ) and quantum yield (ϕ) are related to each other that can be expressed by the Eq. (1).

$$\phi = \frac{Kr}{Kr + Knr} = \frac{\tau}{\tau_0} \tag{1}$$

The quantum yield of any fluorophore can never be ≥ 1. The quantum yield equal to unity means 100% quantum yield which implies that all the photons absorbed are emitted back. In other words, the total number of molecules excited are equal to the number of photons absorbed. However, this is practically impossible since some of the photons are used up in thermal motions. This is why excellent fluorophores have near 100% quantum yield but not exactly 100%. Frank–Condon Principle governs the electronic and vibrational transitions which produce absorption and emission spectra. According to the Frank–Condon principle "the absorption of light is an instantaneous process that allows only rearrangement of electrons but not heavy nuclei, therefore, internuclear distance do not change. Thus, electronic transitions between two levels have more probability to occur when vibrational wave functions of both electronic levels significantly overlap with each other." For example, if $\upsilon = 0$ vibrational level of one electronic level and $\upsilon = 2$ vibrational level of another electronic level fall in same vertical line, then their vibrational wave functions will have maximum overlap, hence $\upsilon = 0$ to $\upsilon = 2$ will be most favored electronic transition. Such transitions are called vertical transitions (Fig. 2, top). It is also important to note that the transitions which are most likely during absorbance are also most likely transitions during emission/fluorescence. For instance, if $\upsilon = 0$ (S_0) to $\upsilon = 2$ (S_1) transition is most likely during absorbance, then $\upsilon = 2$ (S_1) to $\upsilon = 0$ (S_0) will be most likely transition during fluorescence. Therefore, fluorescence and absorption spectra are usually a mirror image of each other (Fig. 2, bottom). This condition is known as the mirror image rule.

1.2 Singlet and Triplet Excitons

In OLEDs, voltage is applied across organic semiconductor layer that generates positive holes and electrons. These holes and electron come across each other while traveling through the semiconductor layer and form strongly coupled electron-hole pairs called excitons. The hole and electron have half spin and called fermions. Depending upon the orientation of spin, hole and electron can couple to have either spin state zero ($S = 0$, singlet) or one ($S = 1$, triplet), resulting in formation of singlet or triplet excitons [3]. There are three spin combinations possible which give spin state $S = 1$ and there is only one combination that gives spin state $S = 0$, therefore theoretically 75% triplet excitons and 25% singlet excitons are formed in OLEDs (Fig. 3) [4]. Since, decay of triplet excited states to singlet ground state is forbidden, so only singlet excitons can decay to singlet ground state. Hence, maximum 25% internal quantum yield is obtained and 75% of triplet excitons are wasted. The mechanism

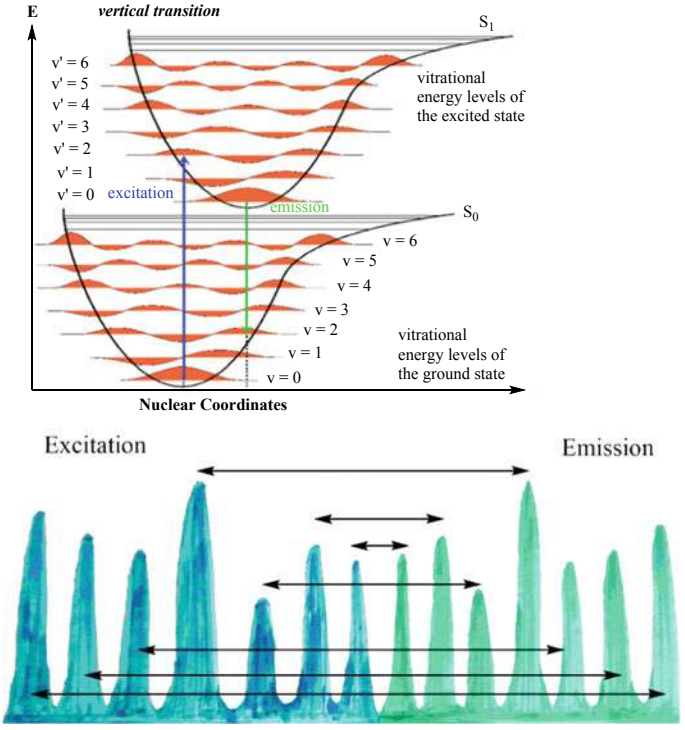

Fig. 2 (Top) Morse diagram explaining Frank–Condon principle/Vertical transitions. (bottom) Mirror imaging of absorption and emission spectra. Source: Visser, A.J.W.G., and Rolinski, O.J. (2010) Photobiological Sciences Online (KC Smith, ed.), American Society for Photobiology. http://www.photobiology.info/Visser-Rolinski.html

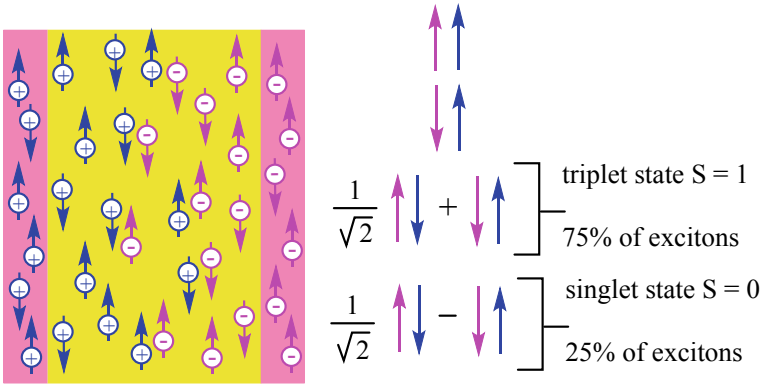

Fig. 3 Possible combinations of singlet (25%) and triplet exciton (75%) formation [3] (adopted from ref [3])

of thermally activated delayed fluorescence (TADF) has been utilized to minimize the wastage of triplet excitons.

1.3 Thermally Activated Delayed Fluorescence (TADF)

Due to limited quantum yield from singlet excitons, it is necessary to harvest triplet exciton emission so that the internal quantum yield can be increased. To accomplish triplet state harvest, different strategies have been used such as introduction of heavy metal ions to the pure organic emitter that increases spin-orbit coupling resulting to the emission from triplet states. Such triplet state emitters have high quantum yield and are called phosphorescent materials. And another strategy is to design such an organic emitter that has less singlet-triplet gap so that reverse inter-system crossing (RISC) can be possible, leading to the TADF [3, 5]. Pure organic compounds capable of showing TADF have become highly demanding since they can achieve nearly 100% quantum yield. The phenomena of TADF was first introduced by Perrin et al. in 1929 [6]. In the TADF, thermal activation prompts the triplet excitons to convert into singlet excitons and then decay to the ground singlet state. Since, the process of RISC is a slow process, therefore, conversion of once excited triplet (T1) to excited singlet (S1) then decay to the singlet ground state takes time (Fig. 4). This is why this type of emission is called delayed fluorescence. This pathway enables all the excitons (singlet and triplet) to undergo radiative decay, giving almost 100% of quantum yield.

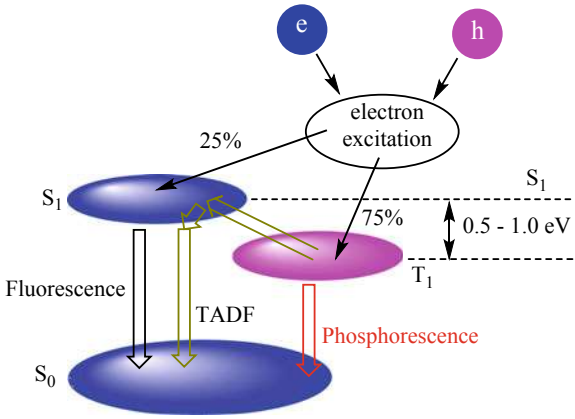

Fig. 4 Thermally activated delayed fluorescence [7] (adopted from Ref [5], copyright: Nature Publishing Group, a division of Macmillan Publishers Limited, 2012)

1.4 Triplet–Triplet Annihilation

Fluorescent OLEDs fabricated from fluorescent transition metal complexes are not viable since the small portion of excited states are singlet in nature, the rest being triplet states. Theoretically, in luminescent emitters 25% of excitons are singlet, and 75% are triplet excitons. Thus, theoretically, quantum yield should not exceed 25%, however, there are reports with higher singlet quantum yields. The reason for exceeding of theoretical quantum yield is the process of triplet–triplet annihilation (TTA) [8]. The concept of TTA was first introduced while explaining delayed fluorescence in anthracene derivatives in the 1960s [9]. TTA is an energy transfer process between two molecules in triplet excited states, in which one molecule transfers its excited state energy to the other molecule. This energy transfer process results in one molecule going to the higher excited states (singlet, triplet or even quintet) and the other molecule going to its ground state. The molecule in the singlet excited state decays to the singlet ground state that increases the quantum yield in fluorescent OLEDs. In this way, singlet emission supported by TTA increases experimental quantum yield of fluorescent materials. The mechanism of TTA can be induced by adding a suitable sensitizer to the emitter (annihilator). Basically, sensitizer absorbs the low energy photon to populate first excited triplet state through inter-system crossing which subsequently facilitates TTA. The sensitizer chosen for the purpose should be able to absorb light in the visible-to-near-IR region affording low energy excitations and the lifetime of excited triplet states should be high, typically in microseconds. The mechanism of TTA has been utilized to convert two photons into one photon with higher energy, which is known as photon upconversion.

2 Luminescent Transition Metal Complexes

Luminescent metal complexes can emit light from singlet as well as triplet excited states while coming back to the ground state. Most of the excited states formed after exciton formation are triplet in nature. Only about 25% excited states are singlet in nature. Therefore, maximum external quantum yield that can be obtained from singlet state is about 25% [10]. Hence, singlet state light harvesting for lighting purpose does not fulfill the purpose of quality and commercial viability of lighting devices. Although, Earlier the phosphors used in the fabrication of electro-optic devices were based on singlet emitters [11]. Now a days, excited triplet state harvesting for light emission applications is being done due to its obvious advantages including high quantum efficiency. In principle, harvesting of both singlet and triplet excited states will give nearly 100% quantum efficiency and therefore, it is being investigated intensively. In the year 1998, Ma and co-workers fabricated a phosphorescent light-emitting device which was made by using osmium complex doped with PVK [12]. Subsequently, Thompson and Forrest showed that platinum porphyrin doped in tris(8-hydroxyquinoline)aluminum (Alq_3) can be used as triplet emitters in light emitting

devices [13]. Since then, a vast number of phosphorescent metal complexes have been reported which have been used as triplet excited state emitters in solid state lighting devices. The observations revealed that if we use a heavy metal in preparation of luminescent complexes, the metal induced spin-orbit coupling will enable singlet-triplet mixing, the singlet triplet mixing will enable radiative transition from triplet to singlet [14]. In this way triplet state decay can be harvested and quantum yield can be increased. The majority of the phosphorescent complexes which have been used in OLEDs fabrication belong to the class of cyclometalated complexes. The cyclometalated complexes based on iridium, platinum and coinage metals constitute the majority of phosphorescent complexes. Therefore, in this chapter we will discuss cyclometalated metal complexes and their applications in OLEDs in detail.

2.1 Cyclometalated Complexes

The term cyclometalation is used for the intramolecular (or rarely intermolecular) ligand metalation in the transition metal complexes that results into formation of a new metal—carbon sigma bond and chelate rings [15]. The cyclometalated complexes of heavy metals such as iridium and platinum are the potential candidates for the chemo-sensors [16], sensitizers [17] and photocatalyst [18]. This class of complexes are most widely employed molecular hybrid phosphors for OLEDs fabrication, therefore, it is imperative to discuss the strategies applied in the synthesis of these complexes. The most crucial factor for any material to be used in fabrication of OLEDs is its quantum efficiency and emission color. Therefore, chemists always focus on improving quantum yield and tuning of emission color. Although, the factors which determine these properties are complicated and difficult to control; However, molecular rigidity is the primary factor which determines these factors. As a result, suitable ligand design for synthesis of rigid complexes becomes an essential step during preparation of cyclometalated complexes. Basically, rigid molecules have lesser geometric distortion, hence, they do not accelerate non-radiative relaxation by vibrational coupling between excited and ground state. The degree of non-emissive d-d transitions is also affected by ligand field; therefore, it should be taken care of. The energy gap between HOMO and LUMO of cyclometalating and ancillary ligand should be managed in such a way that it allows participation of heavy metal in the emissive transition state [19]. The involvement of metal is very essential to ensure phosphorescent emission. It is necessary to understand the energy gap law, which states that the quantum yield is expected to decrease with decrease in emission energy. This implies that the preparation of Near infra-red emitters with high quantum yield is challenging to accomplish. The specific modifications in the ligand are done, for example, introduction of a functional group for increasing solubility of the complexes, so that solution processability is improved. The introduction of hydrophilic group increases its water solubility, hence, enhances usability in biological applications (Fig. 5 and Table 2).

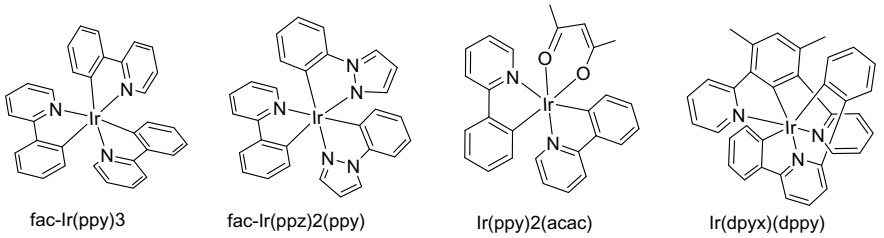

Fig. 5 High performance phosphors

Table 2 Selected cyclometalated Ir(III) complexes with high quantum efficiencies [18–20]

Name	$\tau(\mu s)$	λ_{max} (nm)	∅	References
fac-Ir(ppy)$_3$	1.6	518	0.97	Ref. [18]
fac-Ir(ppz)$_2$(ppy)	1.7	500	0.95	Ref. [18]
fac-Ir(ppy)$_2$(acac)	1.6	516	0.85	Ref. [19]
Ir(dpyx)(dppy)	3.9	585	0.21	Ref. [20]

2.1.1 Cyclometalated Iridium (III) Complexes

The vast variety of transition metal complexes have been investigated for their emissive properties and their applications in solid-state emitting devices; among them Ir(III) complexes have shown most promising emissive properties, due to their most efficient triplet excited states which induce the phenomena of phosphorescence [21–24]. In fact, Ir(III) based cyclometalated complexes have achieved commercial applications in the LEDs. The observations reveal that the spin-orbit coupling in heavy atoms can induce high triplet emission, hence improved phosphorescence quantum yield (PLQY). In fact, 100% internal quantum efficiency has been achieved by using Ir(III) complexes in converting electric energy into photons [14, 25]. The harvesting of highly emissive triplet along with singlet is the key to achieve 100% quantum yield. The PLQY in Ir(III) complexes is lowered due to vibronic-coupled non-radiative decay and crossing from emissive state to upper non-emissive excited state. Hence, the vibronic coupled non-radiative decay can be reduced by utilizing rigid ligand system that will restrict intramolecular motion and strong sigma donor ligand molecules can be used which will destabilize upper excited state, thus crossing will be avoided. The literature survey says that most of the cyclometalated Ir(III) complexes have C^N type donor system. Some of the illustrative examples are shown in Fig. 6 [10, 26, 27]. Generally, the highest occupied molecular orbital (HOMO) of these complexes is located at the π-orbital of phenyl moiety of ligand system and d orbital of iridium metal. However, the lowest unoccupied molecular orbital (LUMO) is located at electron-deficient pyridyl moiety. The electronic transitions which occur on the absorption of light are ligand-to-metal charge transfer (MLCT) and intra-ligand/ligand centered (CT) π–π* transitions in the range of

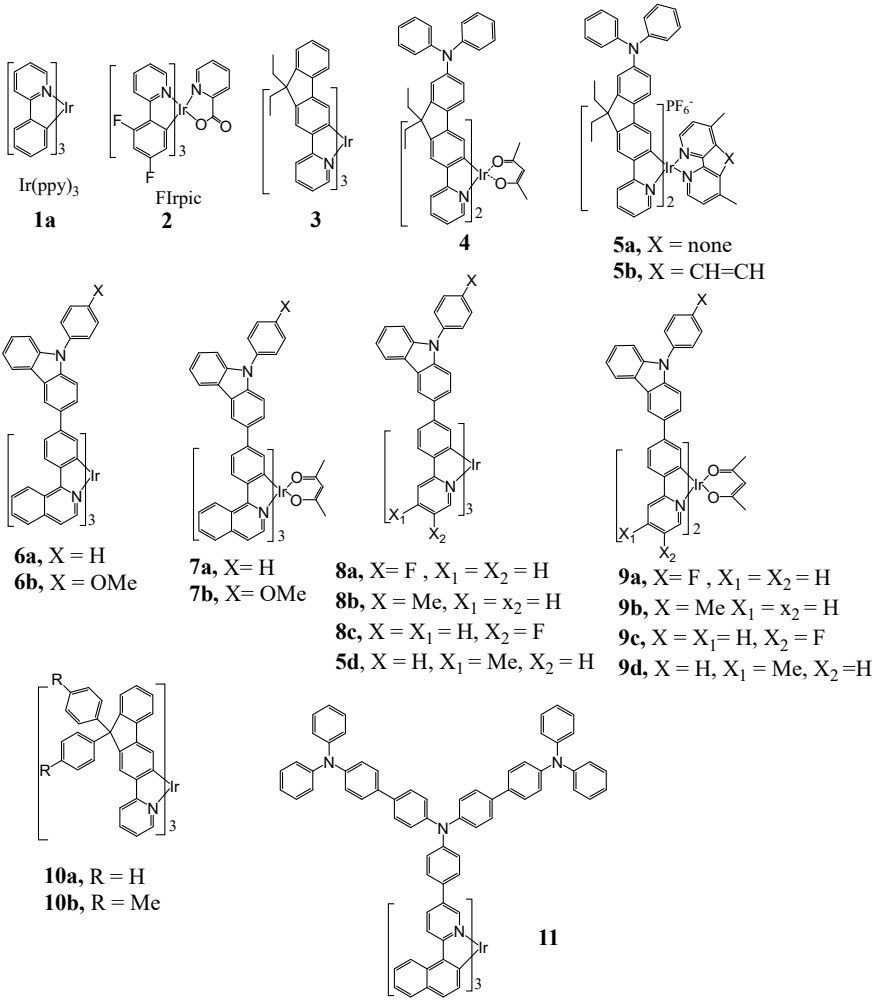

Fig. 6 Structures of cyclometalated octahedral Ir(III) complexes with various emission colors (adopted from Ref [8], copyright: Wiley-VCH Verlag GmbG & Co. KGaA, Weinheim, 2014)

250–350 nm [28]. The lowest triplet excited state is the source of phosphorescence, which may originate either from ^{3}MLCT or $^3\pi$-π^* transition.

The cyclometalated Ir(III) complexes of type **1** and **2** represent the basic Skelton present in most complexes. Complexes **3** and **4** belong to the category of $Ir(L)_3$ and $Ir(L)_2L'$ type complexes with substituted ligands [29]. The complexes **3** and **4** were synthesized from diphenylaminoflourenylpyridine, and the complex **3** is amorphous in nature that gives improved compatibility with different phosphorescent hosts and organic dopants. The OLED devices fabricated from **3** shows strong orange color emission with power efficiency (PE) = 21 lm W^{-1}, current

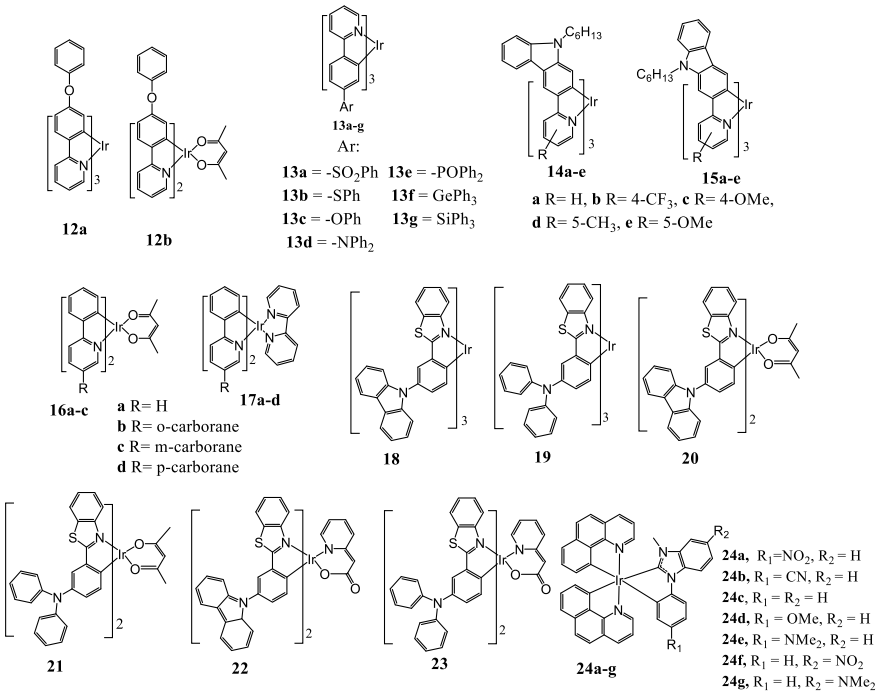

Fig. 7 Structures of cyclometalated octahedral Ir(III) complexes with various emission colors

efficiency (*CE*) = 30 cd A $^{-1}$, and external quantum efficiency (EQE) = 10%. The device based on **1** performs better than the one fabricated from **2**. A white OLED device was also fabricated from **1**. In a subsequent report, charged complexes **5a**–**b** were synthesized using C^N type of ligands. The fabricated OLED device from **5a** exhibited an improved current and power efficiency of 20 cd A^{-1} and 19 lm W^{-1}. The development of blue emitters is essential for both multicolor display and white-OLEDs. This is a bit challenging task in OLEDs area since operational lifetime for blue light emitting materials are usually shorter than the yellow or red-light emitting materials. The reason behind shorter lifetime is that the high energy excited states for charge transport/host/light emitting materials have to be generated. The complex FIrpic (**2**) is one of most representative Ir(III) complex that emits in the blue region. The complex **2** was designed by introducing a fluoro group on the phenyl ring and replacing acetylacetonate ancillary ligand by picolinate. This substitution resulted into increase in HOMO–LUMO gap. The different strategies for improving blue emitters have been adopted over the time. The most frequently applied strategy is to introduce electron withdrawing groups on the phenyl ring or electron donating groups on the pyridine ring of the C^N ligand.

The seminal report of heteroleptic $(C^N)_2Ir(NHC)$ type of complex by Bielawski et al. is an interesting example of NHC based Ir(III) complex where they have used one NHC ligand and two cyclometalating 2-phenylpyridyl (C^N) ligands [30]. This

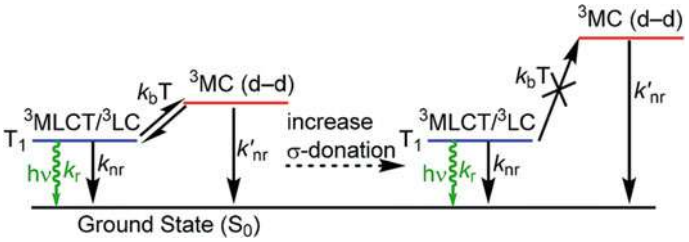

Fig. 8 Partial excited-state diagram for cyclometalated Ir(III) complexes, showing partially occupied ^{3}MC states and destabilization of these states when stronger s-donor ligands are incorporated (Reproduced from Ref. [30]). Copyright (2019) The Royal Society of Chemistry

complex emits at 497 nm in THF with the emission yield approximately 19%. Moreover, Zuo et al. have reported a series of heteroleptic $(C^N)_2Ir(NHC)$ complexes [31]. The major blue organic light emitting diodes (OLEDs) reported recently are NHC based homoleptic tris-cyclometalated Ir(III) complexes. It has been observed in several complexes of iridium that phosphorescence energy decreases when an electron donating group is present a phenyl moiety or an electron withdrawing group is present on N-heterocyclic carbene (NHC) ligand. Hence, substitution of ligand molecules greatly affects the emissive region of these luminophores and gives a pathway for color tuning. The incorporation of stronger σ-donor ligands such as NHCs destabilizes metal centered triplet (^{3}MC) that allows efficient photophosphorescence and higher photostability (Fig. 8). Ideally, where σ-donor only perturbs the unoccupied antibonding d-orbitals and does not affect frontier molecular orbitals (FMO) involved in the luminescent T_1 excited state, the ^{3}MC perturbation does not affect luminescence spectra but should enhance quantum yield. The absorption spectra of complexes **24a**–**24 g** has been studied in different solvents such as toluene, THF, DCM and acetonitrile. The toluene solutions of these complexes exhibit absorption maxima in the range of 540–555 nm. The concentration dependent absorption spectra recorded in the range of 5×10^{-6}–1×10^{-4} mol L^{-1} in toluene show that the absorption follows Beer-Lambert law without undergoing ground state aggregation [27]. The absorption spectra in all solvents show intense bands in the range of 290–420 nm and weaker bands in the range of 420–500. The molar absorption coefficient ($\varepsilon \approx 10^4$ L mol^{-1} cm^{-1}) values suggest that these intense bands appear due to ligand centered and spin allowed $^1\pi$–π^* transitions. However, weaker bands observed in the range of 420–500 nm are due to charge transfer spectra (^{3}MLCT/^{3}LLCT).

2.1.2 Platinum (II) Based Cyclometalated Complexes

The solid-state lighting technology has continuously emerged with the understanding of simultaneous harvesting of singlet and triplet state. In recent times, triplet state

harvesting has enabled us to in-cash the phenomena of phosphorescence to synthesize high yielding phosphors. The triplet state harvesting along with singlet state harvesting has made possible to achieve 100% internal quantum efficiency. In this regard, platinum like other heavy metal ions has proved to be instrumental in synthesizing highly emissive metal complexes. The spin–orbit coupling in Pt(II) triggers triplet state emission and hence high quantum yield is obtained. The Pt(II) based phosphors have highest potential in electroluminescence (EL) applications due to their higher quantum yields, relatively low triplet state lifetime and color tunability. Although, the first phosphorescent emitter reported was based on Pt(II)-porphyrin [13], however, there are fewer reports of cyclometalated Pt(II) complexes compared to the Ir(II) analogues. Despite of excellent developments in Ir(III) based emitters, there are still pressing challenges which remain to be addressed for example; (i) preparation of efficient and stable deep-blue emitters, (ii) efficient and high color-quality white OLEDs, and (iii) achieve sufficiently long operational lifetime of OLED devices. These issues could not be completely resolved. However, cyclometalated Pt(II) complexes have potential to be address these issues due to their square planar geometry. The properties of Pt(II) cyclometalated complexes can be tuned due to their unique square planar geometry and hence there is high scope of OLEDs applications. The most common examples of cyclometalated Pt(II) complexes are prepared by utilizing C^N, C^N^N, C^N^C and N^C^N type of ligand systems. It is important to note that the tridentate ligands of type C^N^N, C^N^C and N^C^N form more rigid square planar Pt(II) complexes than C^N type bidentate ligands, therefore, tridentate ligands are more emissive. The controlled modification of ligand structures enables us to fine tune excited state in the complexes. To make study systematic, the Pt(II) complexes have been classified in different ways. The Pt(II) complexes have been grouped based on chelating atoms of ligand molecules as well as emission region. The most common classification that is used for Pt(II) phosphors is based on chelation/denticity of ligands.

2.1.3 Bidentate Pt (II) Complexes

C^N Type Bidentate Pt (II) Complexes

The strong ligand field of C^N chelation makes dual C^N chelated Pt(II) complexes highly robust and they strongly emit in the solution state. This kind of ligand chelation increases energy gap between metal centered d–d states. The energy gap between high lying d–d states and emitting states (π–π* and MLCT) should be as high as possible because low energy gap can lead to the thermal equilibrium that eventually leads to the quenching through non-radiative decay along the metal centered d-d states [33]. It is noteworthy that C^N chelated complexes are mostly in square planar geometry where metal can interact with solvent and can also undergo reversible coordination that enables other deactivation pathways. One of the representative complex of such kind, cis-[$Pt(ppy)_2$(**26**), was synthesized in comparatively low yield by the reaction of *trans*-[$PtCl_2(SEt_2)_2$] with 2-(o-phenylpyridine)lithium [34]. In this complex. the

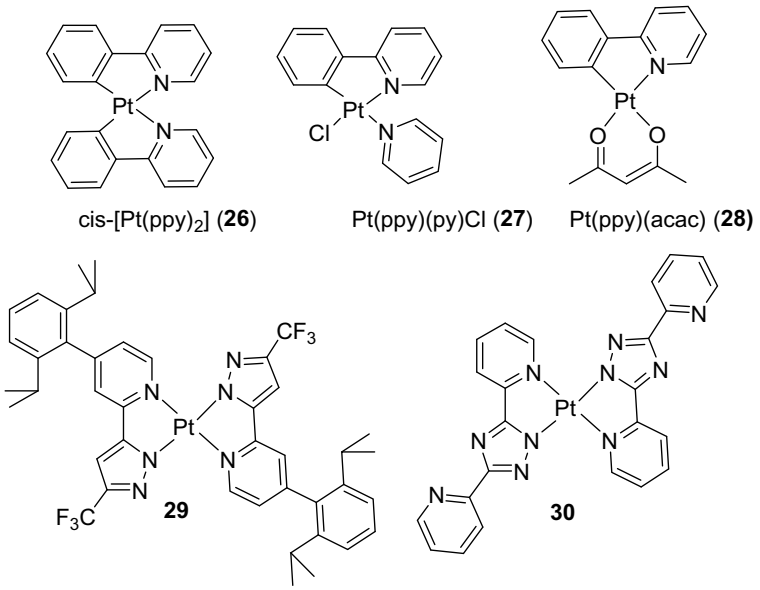

Fig. 9 Selected C^N and N^N homoleptic and heteroleptic square planar Pt(II) complexes (where ppy is phenyl-pyridine, ppz is phenyl-pyrazole, acac is acetyl-acetonate

phenyl rings in ppy chelate are in a cis-manner in the complex which can be attributed to strong trans effect induced by phenyl ring. The studies revealed that the C^N homoleptic complexes exhibit low emission efficiency, therefore, chemists turned their attention to prepared analogous heteroleptic complexes with improved emission properties [35]. Some of the representative homoleptic and heteroleptic C^N ligated platinum complexes are shown in Fig. 9. The desired properties of Pt(II) complexes can be fine-tuned by modification of ligand based frontier orbitals in analogous Ir(II) complexes. The most important strategy is to add electron withdrawing groups on ligand molecule, to lower the position of HOMO. Brooks et al. applied this proven color tuning strategy which is frequently used for Ir complexes to heteroleptic Pt complexes with bidentate cyclometalating ligands [36]. His group prepared blue emitters by adding electron withdrawing groups such as fluoride group to the specific positions of ligand, which lowered position of HOMO and therefore, reducing energy gap (Fig. 10). Another way to reduce HOMO–LUMO energy gap is to substitute the pyridine by azole to raise LUMO, resulting into reduction in HOMO–LUMO gap.

N^N Bidentate Pt(II) Complexes

Pyridyl-azole are interesting molecule which make N^N type of ligand systems for preparation of luminescent metal complexes. These ligands have been used to prepare bidentate homoleptic blue emitting Pt(II) complexes [37]. For example, **29** and **30**

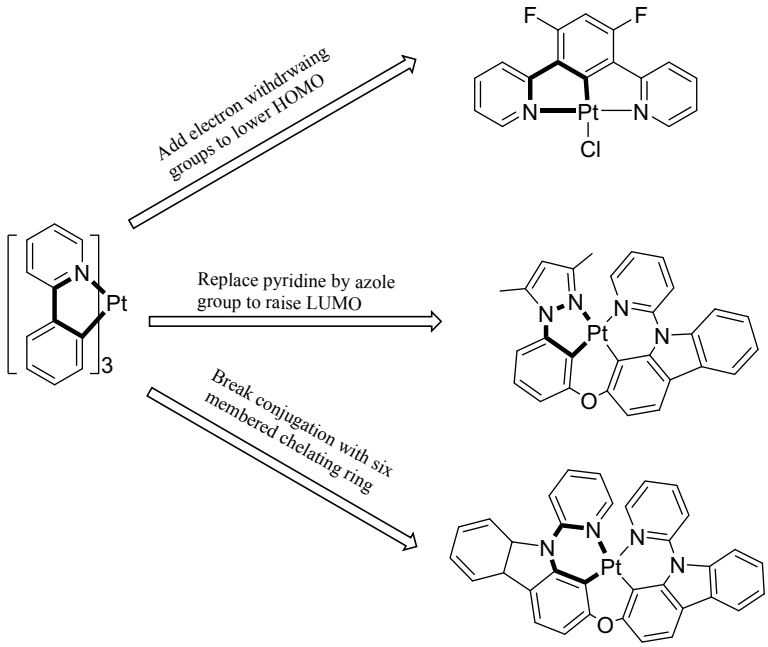

Fig. 10 Color-tuning strategies for the development of new Pt(II) based blue emitters. (adopted from Ref [33], copyright: Wiley-VCH Verlag GmbG & Co. KGaA, Weinheim, 2016)

are two bidentate homoleptic complexes capable of efficient emission. Complex **29** emits at 475 nm with high phosphorescence quantum yield of 0.58 in powder form while it weakly emits in solution phase. The OLEDs prepared from **29** gives a peak EQE of 9.1% with Commission International de L'Eclairge (CIE) coordinates of (0.19, 0.28). Complex **30** is strongly emissive when used in doped thin films. The devices made from **30** with about 1% doping concentration exhibit an emission peak at 482 nm and a peak EQE of 11.5% with CIE coordinates of (0.19, 0.45).

Tridentate Cyclometalated Pt(II) Complexes

Tridentate cyclometalated Platinum have been reported in various coordination patterns and combinations with the coordination environment of C^N^N, C^N^C, N^C^N, N^C^N, and C^C^N. The cyclometalated coordination complexes with C^C^N coordination environment are rarely reported. The tridentate platinum complexes are comparatively more rigid than the bidentate C^N or N^N cyclometalated complexes [38]. The rigidity suppresses non-radiative relaxation hence improves emission efficiency. Therefore, photo-optic devices based on tridentate cyclometalated platinum perform better than the analogous bidentate complexes.

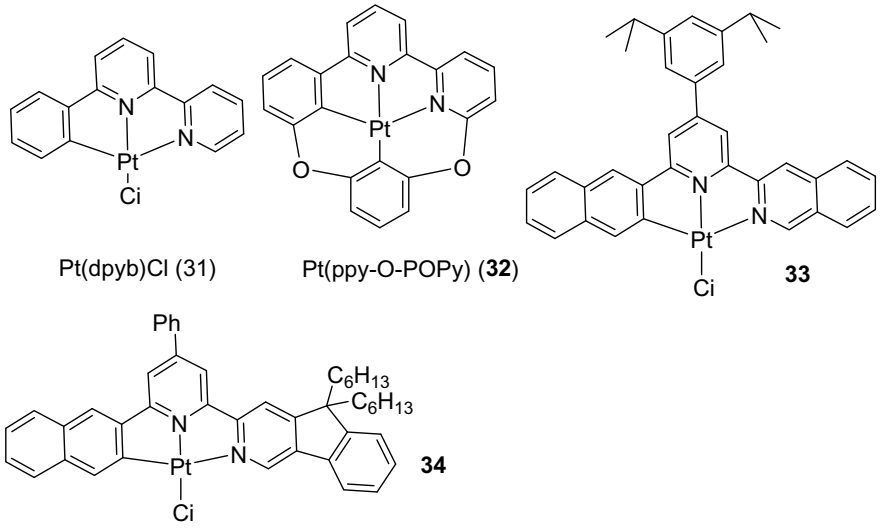

Fig. 11 The cyclometalated Pt(II) complexes with C^N^N coordination environment

C^N^N Cyclometalated Pt(II) Complexes

Several C^N^N based cyclometalated platinum complexes have been reported by Che et al. [38] and their photophysical properties have been studied. These tridentate C^N^N metal complexes have been shown to emit in the range of 550–630 nm depending upon steric and electronic factors of ligand system. Although, the device performance of C^N^N cyclometalated platinum complexes has been less efficient that those of N^C^N cyclometalated complexes but these complexes have been really crucial in understanding color tuning strategies. The performance of these complexes has been markedly improved by increasing conjugation in the ligand system. For instance, **33** had phosphorescence quantum yield ($\varnothing p$) 0.68 [39] and maximum current efficiency (CE) 20.2 cd A^{-1}, that is a better performance than the tetradentate Pt(II) Schiff base phosphors [40]. The emission efficiencies have also been improved by extending π-conjugation in the ligand adding fluorene to it, evident by increased triplet emission and EL efficiency. The $\varnothing p$ for **34** was found to be 0.73 that is a high value for platinum cyclometalated phosphor, therefore, this complex was used to fabricate vacuum processed device that showed EQE 5.5%, CE 14.7 cd A^{-1}, PE 9.2 lm W^{-1} [41] (Fig. 11).

N^C^N Cyclometalated Pt(II) Complexes

N^C^N platinum complexes prepared by 1,3-dipyrid2-ylbenzene and its analogous ligand systems are the class of phosphors that give highest triplet quantum yield, therefore, they have been used in fabrication of highly efficient OLEDs [42]. It is

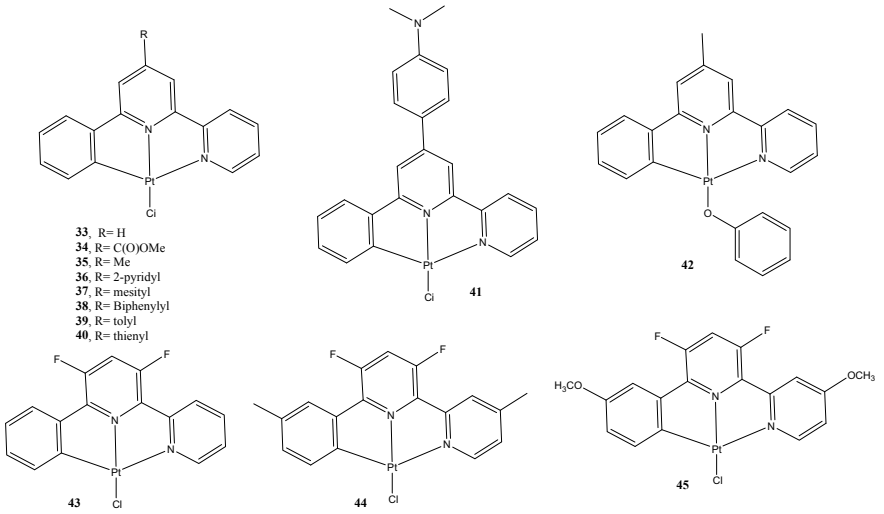

Fig. 12 The structures of high-performance N^C^N platinum phosphors

established fact that the tridentate cyclometalated complexes are comparatively rigid, therefore, they exhibit better luminescence properties with high phosphorescence quantum yield. The observations reveal that the carbon-platinum bond distance also play an important role in the device performance [43]. Williams et al. noted that the carbon-platinum bond distance in N^C^N complexes is about 1.9 Å that is shorter than the typical bond lengths of corresponding bonds in C^C^N complexes [44]. The shorter carbon-platinum bond distance is expected to raise energy of d-d states therefore deactivating them, that result in the better performance of devices fabricated by N^C^N Pt(II) complexes (Fig. 12) [45].

Tetradentate Phosphorescent Pt(II) Complexes

As we discussed that the increased denticity gives higher rigidity to the metal complex hence helping in reducing non-radiative emission. In case of tetradentate ligands, Pt(II) complexes get extra rigidity to maintain square planar shape, without using monodentate/axillary ligands. Although, cyclometalated platinum complexes are considered less efficient than the analogous Iridium complexes, however, tetradentate ligand-platinum complexes of type Pt[ppy-O-POPy] (**46**–**49**, Figs. 13 and 14) have shown quantum efficiencies in the range of 0.39–0.64 and emission lifetime in the range of 2–9 μs, that are comparable to the quantum yields and lifetimes of iridium complexes [46]. Moreover, they have shown superior emission properties than the similar bidentate and tridentate complexes. In fact, **46** has shown emission with nearly 100% quantum yield in device setting. As per our survey, the first blue emitting tetradentate platinum complexes were synthesized from a simple ligand which

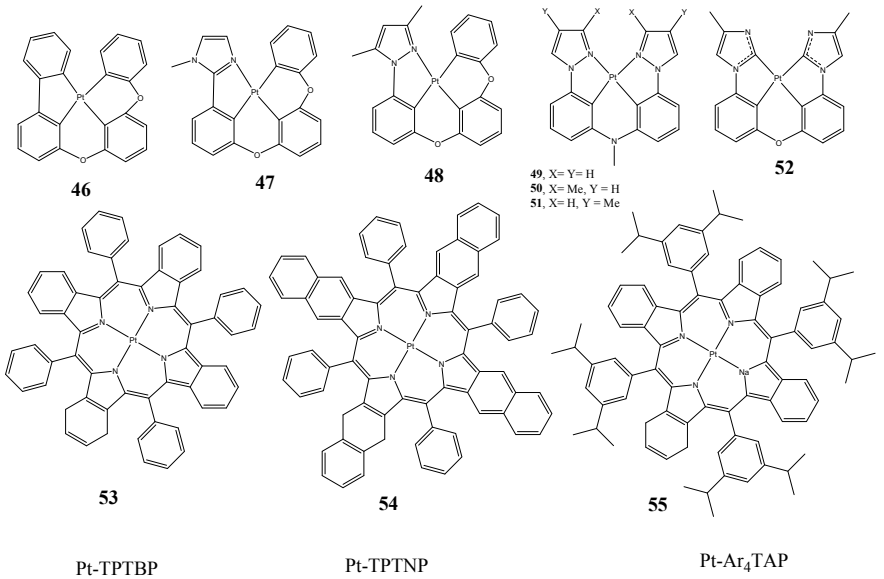

Fig. 13 Tetradentate platinum complexes

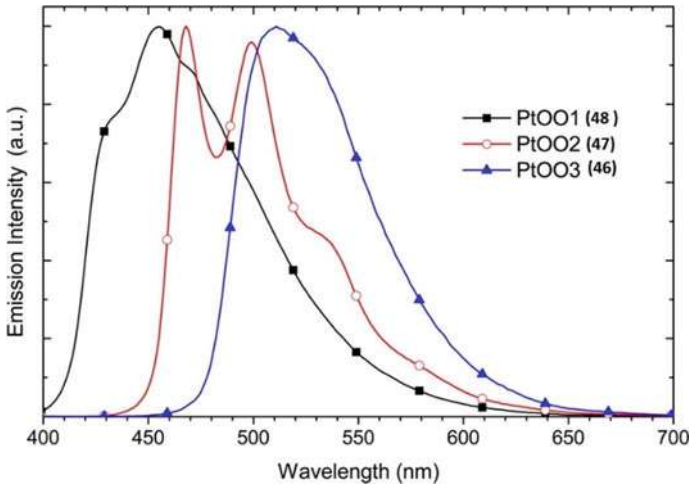

Fig. 14 Emission spectra of **46**–**48** at room temperature in dichloromethane. Reproduced with permission from Ref. [44]. Copyright (2013) American Chemical Society

was formed by bridging of two CˆN bidentate ligands with an aryl-amine linker (**49**–**51**) [47]. These platinum complexes exhibit triplet quantum yield in the range of 0.37–0.63 and much lower emission energies than the analogous blue emitting bidentate platinum complexes. In the **50**, the addition of methyl group 3-position of pyrazolyl ring induces bathochromic shift by 10 nm, giving emission peak at 474 nm and reducing quantum yield to 0.37. This happens due to increase in LUMO energy. In order to achieve deep blue emission, the general strategy is to replace bridging amino group by a linker that reduces degree of conjugation or the replace nitrogen bridge with the oxygen or functionalized carbon. The complex **52**, has been prepared by utilizing phenyl-methyl-imidazole carbene ligands. The emission peaks for measurement at 77 K and room temperature were obtained at 464 nm and 471 nm respectively [48]. The phosphorescence quantum yield was recorded to be 0.77. The triplet energy was calculated to be 6.3 eV which is ideal for obtaining maximum power efficiency. This compound is well qualified candidate for efficient white and blue emitting devices.

π-extended porphyrin platinum complexes are another class of important tetradentate complexes which have been used to fabricate OLEDs. The work by Reynolds et al. that includes the series of π-extended tetrabenzo, tetranaphtho, and tetraanthro Pt-porphyrins (**53**–**55**) shown excellent luminescence properties [43, 49]. They incorporated these complexes into solution processed polymer light emitting diodes (PLEDs) and vapor deposited multilayer organic light emitting diodes (OLEDs). As the π-system is extended across the series Pt-TPTBP, Pt-TPTNP, and Pt-Ar_4TAP the solution emission wavelength maxima shift from 773 to 891 to 1022 nm, respectively. The maximum external quantum efficiency (EQE) for **53**–**55** were obtained in the range of 7.8–9.2%. Other than cyclometalated compounds, there are some reports of Schiff base complexes which have employed in OLEDs fabrication.

2.2 Cyclometalated Au(III) Phosphors

Cyclometalated Ir(III) and Pt(III) complexes have been extensively investigated for their applications in OLEDs and solid state lighting devices and near-unity quantum yields have been realized. However, cyclometalated transition metals complexes of silver, gold and copper are underdeveloped. Gold being a precious metal with chemical inertness and environmentally benign nature shows fascinating organometallic chemistry. Despite the higher abundance of gold than that of iridium and platinum, the phosphorescent gold complexes for OLEDs have rarely been reported. In 2005, the first cyclometalated Au(III) luminescent complexes (**56** and **57**) were reported by Tang et al. [50]. Recently, cyclometalated complexes Au(III) have been reported with bidentate, tridentate and tetradentate ligands, demonstrating color tuning and highly efficient solution processable and vacuum deposited OLEDs. These solution and vacuum processable devices could achieve external quantum efficiencies (EQE) of up to 23.8% (**58**) [51] and 14.7% (**59**) [52] respectively which are comparable to the iridium and platinum analogues. Cheung et al. reported two yellow emitting

cyclometalated Au(III) complexes that have been used as phosphorescent dopant for white OLEDs [53]. The fabricated devices give current efficiencies of 26.0 and 25.7 cd/A corresponding to EQEs up to 11.0 and 10.5%, which can be maintained at 19.8 and 25.3 cd/A at a high brightness level of 10,000 cd/m^2. The computational studies show that the classical Au(III) complexes with C^N^C denticity such as the one mentioned above, undergo non-radiative decay via triplet distorted state, that hampers photophysical properties. Recently, C^C^N type of Au(III)complexes (**60**–**64**) with various ancillary ligands have been reported which show the suppression of non-radiative decay, hence improvement in photophysical properties [54]. These complexes show excellent color tunability from sky blue to red with high PLQY up to 80% in thin films. The solution processable and vacuum-deposited OLEDs fabricated with these complexes have achieved maximum EQEs of 11.9% and 21.6% respectively. The literature reveals that the fabrication of efficient blue emitting OLEDs is difficult than the red and green counterparts. The main reason being deactivation of high lying excited triplet states through different pathways. To overcome this drawback, Tang et al. demonstrated the triplet state harvesting via thermally stimulated delayed phosphorescence (TSDP) mechanism [55]. The TSDP involves up conversion of excitons from lower excited triplet state to higher excited triplet state that generates blue emission. Tang et al. synthesized Au(III) complexes (**65**–**67**) (Fig. 15) and demonstrated that TSDP mechanism enabled blue emission can be achieved by efficient spin allowed reverse interconversion(RIC). The improved color purity and high EQEs up to 7.7% with operational lifetime of 7h at initial brightness of 940 cd m^{-2}. This was first ever case in which chemists showed that the TSDP materials have potential to be efficient phosphorescent dopant for OLEDs. Furthermore, Ertl et al. [56] also synthesized a bipolar alkynylgold(III) complex (**68**) that has been applied as phosphorescent dopant in the fabrication of highly efficient OLEDs with EQE up to 10%. The optimized devices show superior electroluminescence performance with small EQE roll off values.

2.3 Cyclometalated Ru(II) Phosphors

C^N type cyclometalated Ru(II) complexes are less reported than the N^N type diamine complexes. $[Ru(bpy)_2]^{2+}$ (bpy = 2,2′-bipyridine) are the most reported N^N type complexes. Recently, a renewed interest in cyclometalated Ru(II) complexes has been seen among chemists, therefore, cyclometalated complexes analogous to $[Ru(bpy)_2]^{2+}$ have been reported and their applications in n-type dye-sensitized solar cells (DSCs) have been demonstrated [57, 58]. The dye sensitized solar cells have emerged as promising alternative to the conventional photovoltaic technologies. The representative cyclometalated Ru(II) complexes [59] are shown in Fig. 16.

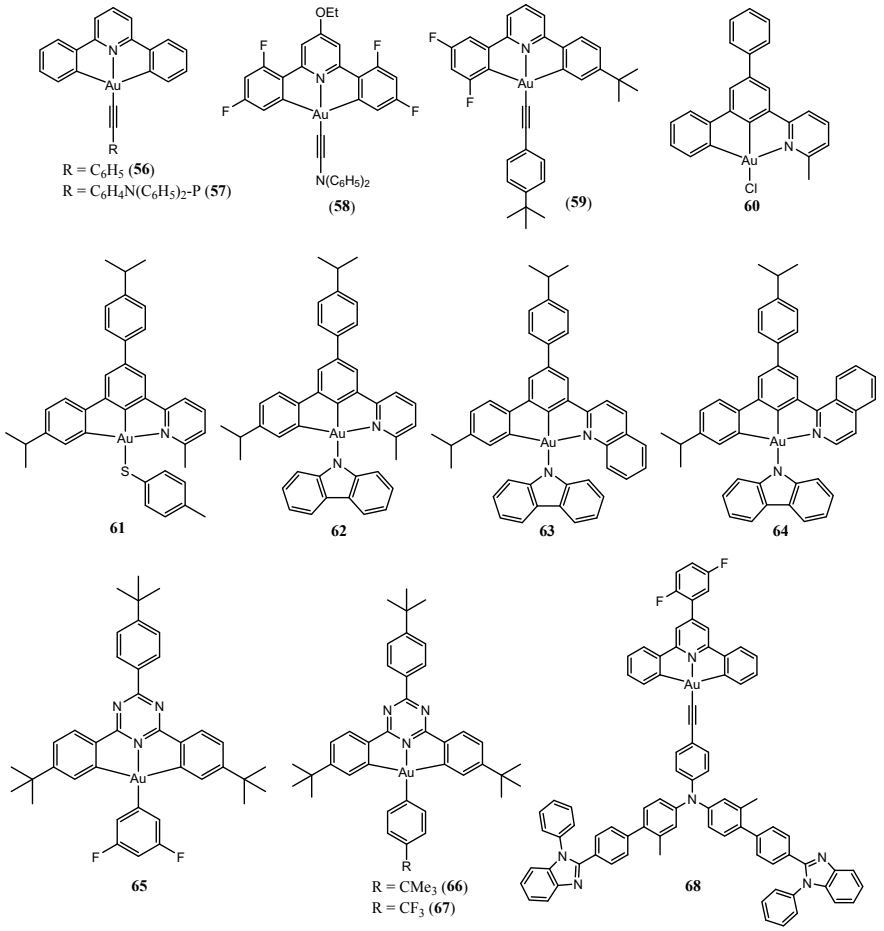

Fig. 15 Selected cyclometalated Au(III) complexes

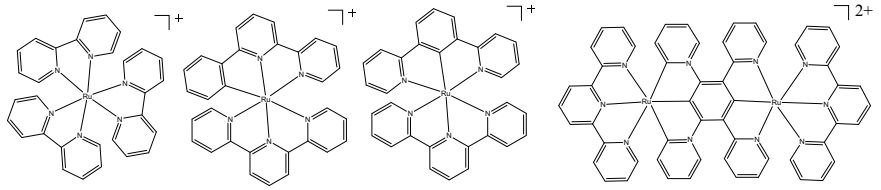

Fig. 16 Representative cyclometalated Ru(II) complexes [59]

2.4 Cyclometalated Rh(III) Complexes

The use of phosphorescent material in the fabrication of OLEDs in today's technological world has given impetus to the research in the field of phosphors. The strong spin-orbit coupling, which enhances phosphorescence quantum efficiency, has enabled rapid development of cyclometalated heavy metal complexes. Now a days, cyclometalated heavy metal complexes are being used in smart phones and other display devices. The cyclometalated Ir(III) complexes have been studied most widely due to high phosphorescent quantum yields that makes them suitable for OLEDs applications. However, cyclometalated Rh(III) complexes have been sparsely studied due to their poor emission properties. The poor emission properties of Rh(III) complexes can be due to several reasons such as: (i) The lower spin–orbit coupling (SOC) constant of Rh compared to Ir, that results in smaller triplet radiative rate constants, k_r (ii) For a given type of complex, the $Rh^{III}|Rh^{IV}$ couple will lie at higher potential than the corresponding $Ir^{III}|Ir^{IV}$ couple, so that the MLCT states will be higher in energy. Therefore, mixing with low lying $^3\pi-\pi^*$ excited states is reduced resulting in to less spin-orbit coupling, decreasing the triplet emission. (iii) The weaker ligand-field splitting of 2nd row rhodium than the corresponding 3rd row iridium metals means that metal-centred d–d excited states—which are strongly distorted relative to the ground state and hence potentially highly deactivating for d^6 complexes—are more likely to be thermally accessible for Rh(III) than for Ir(III) [60]. The brightest cyclometalated rhodium complexes that are reported till now are based on $[Rh\text{-}(pba)2(N\hat{}N)]^+$ type of systems, where pba is 4-(2-pyridyl)benzaldehyde and N^N is a diimine ligand such as a 2,2′-bipyridine or 1,10-phenanthroline. This type of systems have shown quantum yield in the range of 1 to 3% and lifetime in few microseconds at 298 K. The improved emission properties of these systems are rationalized based on aldehyde group leading to pba-localized states [61]. Recently, some reports have appeared in the literature where chemists have shown ligand mediated improvement in emission properties. Williams et al. have achieved high luminescence efficiencies in cyclometalated Rh(III) complexes (**73**) synthesized by utilizing N^C^N type of ligands [60]. Sano et al. [62] have reported improvement of luminescence properties in cyclometalated Rh(III) complexes (**74**, **75** and **76**) by judicious choice of a strong σ-donor cyclometalating ligand with a lower-lying intraligand (IL) state that would raise the d−d excited state and will introduce a lower-lying emissive IL excited state (Fig. 17). The ligand choice gives high thermal stability and quantum efficiency as high as 0.65 in thin films, that offers promising applications in OLEDs. The EQEs up to 12.5 % and operational lifetime over 3000 h at 100 cd m^{-2}. This report presents a breakthrough in the field of rhodium complexes as emitter in OLEDs.

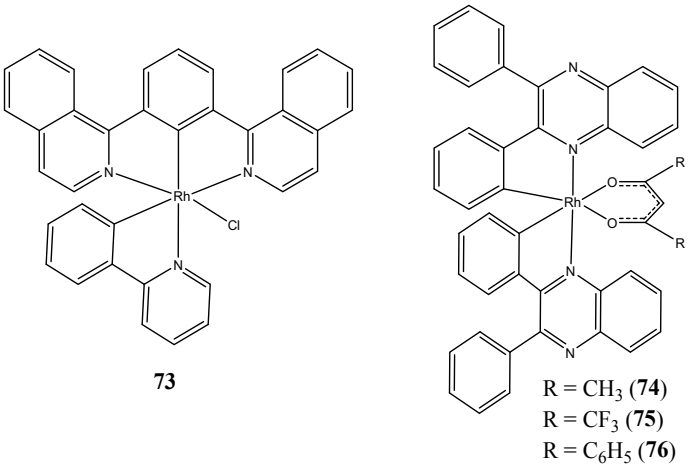

Fig. 17 Cyclometalated rhodium(III) complexes

2.5 Zn(II) Complexes Based Phosphors

Recently, phosphors based on cyclometalated heavy metal complexes have been reported on large scale, most of them are cyclometalated iridium or platinum complexes. The heavy metal salts used in synthesis of these metal complexes are very costly, which make phosphor production a costly affair. Therefore, it is desirable to look for economical alternatives. Zn(II) complexes appear to be cheap alternative to the costly metal complexes of iridium, platinum, gold or osmium. Development of low-cost OLEDs by using cheap emitting layer is one of the highly desirable component of lighting technology. The metal complexes of metals with the atomic number more than 40 are only phosphorescent. The lower metal complexes are fluorescent with the exception of zinc which is phosphorescent. The reaction yields of synthesis of tris-cyclometalated iridium complexes, which are known to be most stable emitter for OLEDs, are only in the range of 10–25%. On the contrary, zinc complexes can be synthesized with the yields up to 50–90% [63]. Therefore, use of zinc complexes in OLEDs as emitting material can be most economical choice. The first report on the use of zinc based emitters in OLEDs was published in 2000, where a series of Zn(II) complexes were used to fabricate white OLEDs [64]. Notably, Znq2 (**77**) with strong yellow fluorescence, **78** and **79** with blue fluorescence and **80** with white greenish fluorescence, were studied as singlet emitters in bilayer structures (ITO/HTL (50 nm)/EML (50 nm)/Al) where two different materials i.e. the hole (N,N-bis(3-methylphenyl)-N,N-diphenyl1,1-biphenyl-4,4-diamine(TPD)) and the emissive layer were sandwiched between the electrodes. The devices fabricated by these complexes showed a maximum brightness of 420 cd/m^2 (at 22 V), 1460 cd/m^2 (at 16 V) and 10,190 cd/m^2 (at 8 V) respectively for 2AZM-Me, 1AZM-Hex and Zn(BZT)$_2$. Among them, Znq$_2$ proved to be most brilliant, showing intense yellow

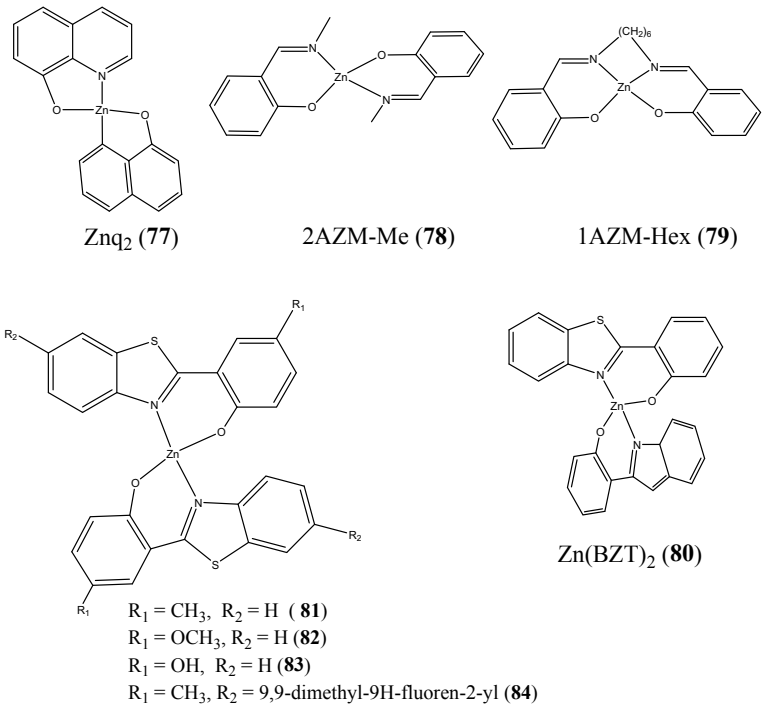

Fig. 18 Selected Zn(II) complexes used for OLEDs applications

emission of 16,200 cd/m^2 at 20 V. Lee et al. achieved a major breakthrough in the device performance Fabrication made up of Zn(II)-chelated complexes based on benzothiazole derivatives [65]. They fabricated a multilayer device utilizing **81**–**84** complexes and tested their performances (Fig. 18). Among these complex **84** showed best emission properties with remarkable brightness of 10,400 cd/m^2 at 14 V. It is evident from literature survey that the Zn(II) complexes were earlier investigated as single emitter or emitter for bilayer devices. However, single emitters suffer from low emission efficiency. Recently, Zn(II) complexes have shown promising applications as dopant in fluorescent and phosphorescent materials. In the recent time, record breaking EQEs of Zn(II) complexes as phosphorescent dopants have proved that these complexes can be low cost alternatives for heavy metal based cyclometalated complexes.

2.6 Carbene Metal-Amide (CMA) Based Phosphors

Carbene metal-amides (CMAs) are coinage metal based linear metal complexes that are synthesized by utilizing a heterocyclic amide and cyclic alkyl amino-carbene(cAAC) ligand. CMAs being linear geometry complexes are represented by a general formula, L-M-X (where L = carbene, M = Cu, Ag or Au and X = anionic ligand). These complexes have emerged as highly photo-emissive phosphors for OLEDs. This class of phosphors are efficient emitters owing to the process of TADF occurring due to charge (electron) transfer from an electron-rich amide ligand (HOMO) to a LUMO of the carbene p-orbital. This transition is favored by coplanar ligands (amide and cAAC) and coupling through the metal d-orbitals. CMAs are being used to fabricate solution and vacuum processed OLEDs [66–72]. The major chunk of such OLEDs is based on copper [70, 73, 74], gold [67, 73, 75–78] and silver [69]. Recent reports by Di et al. and Thompson et al. show that copper based CMA formed by combination of adamantyl [67] and menthyl [70] CAACs afford very emissive materials (Fig. 19). As evident from Fig. 19, the emission properties are tailored to the rigidity of the ligand.

The coinage metal ion in CMA acts as redox innocent center that serves as monoatomic electronic channel communicating between two ligands. Since, metal ion do not play redox active role, emission spectra can be tuned by simple modification of carbazole moiety (Fig. 20) [77]. Romanov et al. have successfully tuned luminescence from blue to deep red by combining metal carbene moiety with sulfone (**89**), dibenzazepine (**91**), phenothiazine (**92**), phenoxazine (**93**), or phenazine (**94**), as conformationally flexible 7-membered carbazole surrogates [77]. The OLEDs devices based on CMA emitters have shown external quantum efficiencies up to 25%.

The CMAs based on carbazole dendrimers have also been synthesized and utilized in fabrication of solution processed OLEDs [73]. The thermal stability and high solubility of carbazole dendrimers provide excellent solution-processability (Fig. 21). The solution processed OLEDs fabricated using carbazole dendrimers have shown EQEs = 10% and practical brightness of 1000 cd/m^2; maximum luminance of

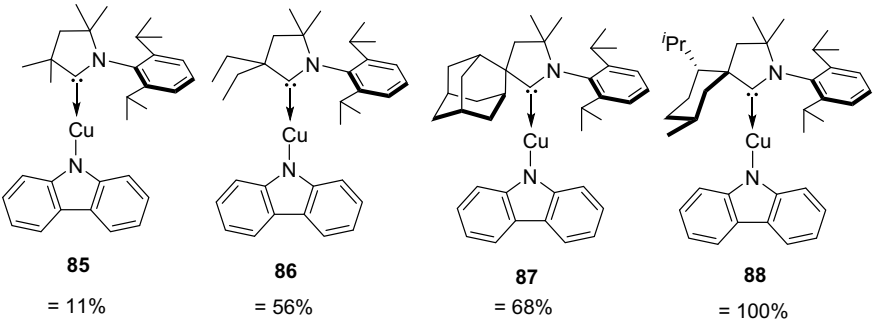

Fig. 19 Copper based CMA showing increased phosphorescence yield on increasing ligand rigidity

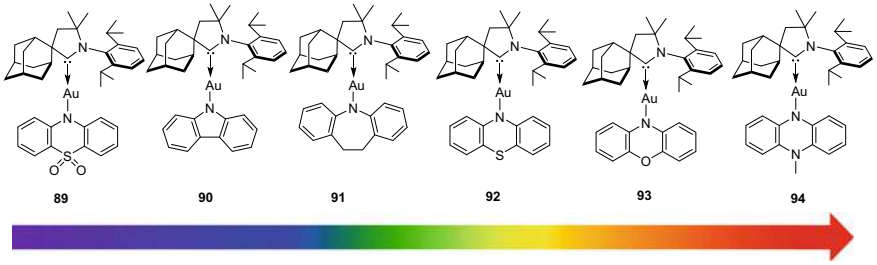

Fig. 20 Tuning of luminescence in CMAs by modification of carbazole moiety (adopted from Ref. [77]). Copyright (2020) American Chemical Society

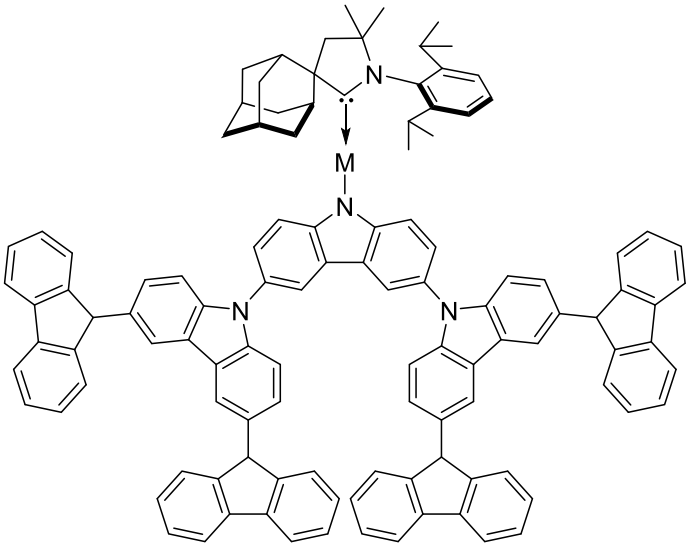

Fig. 21 Dendrimer based emitters

29,000 cd/m^2. The photophysical properties of **95** and **96** indicate that these CMAs can be used for the engineering of flexible OLEDs through inkjet or roll-to-roll printing.

3 Conclusion

Molecular phosphors constitute key component of OLEDs, since emitting layer/phosphors control emission efficiency and color quality of fabricated device. Therefore, improving emitting layer material is one of the most critical component of OLEDs fabrication. Chemists are continuously improving emission properties of phosphors by adopting different strategies such as changing ligand structure. Today, cyclometalated Ir(III) and Pt(II) complexes are being used in smart phones and other display devices. However, heavy metal such as iridium and platinum are very costly, therefore, their use in preparation of cyclometalated complexes is not economical. This factor hinders the development cheap phosphors for OLEDs fabrication. However, CMAs are being recognized as an alternate class of compounds with good emission properties. Additionally, Zn(II) based complexes are also being explored as phosphors for OLEDs application but these complexes suffer from poor emission properties. Therefore, till now heavy metal complexes are only source of molecular phosphors.

References

1. Liu, W., Fang, Y., Li, J.: Copper iodide based hybrid phosphors for energy-efficient general lighting technologies. Adv. Funct. Mater. **28**, 1705593 (2018)
2. Jain, A., Blum, C., Subramaniam, V.: Fluorescence lifetime spectroscopy and imaging of visible fluorescent proteins. In: Advances in Biomedical Engineering. Elsevier (2009). https://doi.org/10.1016/B978-0-444-53075-2.00004-6
3. What is thermally activated delayed fluorescence? https://www.edinst.com/blog/tadf-thermally-activated-delayed-fluorescence/
4. Penfold, T.J., Dias, F.B., Monkman, A.P.: The theory of thermally activated delayed fluorescence for organic light emitting diodes. Chem. Commun. **54**, 3926–3935 (2018)
5. Uoyama, H., Goushi, K., Shizu, K., Nomura, H., Adachi, C.: Highly efficient organic light-emitting diodes from delayed fluorescence. Nature **492**, 234–238 (2012)
6. Kondakov, D.Y.: Triplet-triplet annihilation in highly efficient fluorescent organic light-emitting diodes: current state and future outlook. Phil. Trans. R. Soc. A **373**, 20140321 (2015)
7. Liu, D.K.K., Faulkner, L.R.: Delayed fluorescence efficiencies of anthracene and phenanthrene. J. Am. Chem. Soc. **100**, 2635–2639 (1978)
8. Choy, W.C.H., Chan, W.K., Yuan, Y.: Recent advances in transition metal complexes and light-management engineering in organic optoelectronic devices. Adv. Mater. **26**, 5368–5399 (2014)
9. Zink, D.M., Bergmann, L., Ambrosek, D., Wallesch, M., Volz, D., Mydlak, M.: Singlet harvesting copper-based emitters: a modular approach towards next-generation OLED technology. Transl. Mater. Res. **1**, 015003 (2014)
10. Ma, Y., Houyu, Z., Shen, J., Che, C.: Electroluminescence from triplet metal-ligand charge-transfer excited state of transition metal complexes. Synth. Met. **94**, 245–248 (1998)
11. Baldo, M.A., O'Brien, D.F., You, Y., Shoustikov, A., Sibley, S., Thompson, M.E., Forrest, S.R.: Highly efficient phosphorescent emission from organic electroluminescent devices. Nature **395**, 151 (1998)
12. Baldo, M.A., Thompson, M.E., Forrest, S.R.: Highly efficient fluorescent organic light emitting devices using a phosphorescent sensitizer. Nature **403**, 750–753 (2000)

13. Bruce, M.I.: Cyclometalation reactions. Angew. Chem. Int. Ed. **16**, 73–86 (1977)
14. Thomas, S.W., Venkatesan, K., Muller, P., Swager, T.M.: Dark-field oxidative addition-based chemosensing: new bis-cyclometalated Pt(II) complexes and phosphorescent detection of cyanogen halides. J. Am. Chem. Soc. 16641–16648 (2006). https://doi.org/10.1021/ja065645z
15. Gao, R., Ho, G.D., Hernandez, B., Selke, M., Murphy, D., Djurovich, P.I., Thompson, M.E.: Bis-cyclometalated Ir(III) complexes as efficient singlet oxygen sensitizers. J. Am. Chem. Soc. **124**, 14828–14829 (2002). https://doi.org/10.1021/ja0280729
16. Feng, K., Zhang, R.-Y., Wu, L-Z., Tu, B., Peng, M-L., Zhang, L-P, Zhao, D., Tung, C.-H.: Photooxidation of olefins under oxygen in platinum (II) complex-loaded mesoporous molecular sieves. J. Am. Chem. Soc. **128**, 14685–14690 (2006). https://doi.org/10.1021/ja0648256
17. Huo, S., Carroll, J., Vezzu, D.A.K.: Design, synthesis, and applications of highly phosphorescent cyclometalated platinum complexes. Asian J. Org. Chem. **4**, 1210–1245 (2015)
18. Sajoto, T., Djurovich, P.I., Tamayo, A.B., Oxgaard, J., Goddard, W.A., Thompson, M.E.: Temperature dependence of blue phosphorescent cyclometalated Ir(III) complexes. J. Am. Chem. Soc. **131**, 9813–9822 (2009)
19. Lamansky, S., Djurovich, P., Murphy, D., Abdel-Razzaq, F., Kwong, R., Tsyba, I., Bortz, M., Mui, B., Bau, R., Thompson, M.E.: Synthesis and characterization of phosphorescent cyclometalated iridium complexes. Inorg. Chem. **40**, 1704–1711 (2001)
20. Whittle, V.L., Williams, J.A.G.: A new class of iridium complexes suitable for stepwise incorporation into linear assemblies: Synthesis, electrochemistry, and luminescence. Inorg. Chem. **47**, 6596–6607 (2008)
21. Lee, S., Han, W.-S.: Cyclometalated Ir(III) complexes towards blue-emissive dopant for organic light-emitting diodes: fundamentals of photophysics and designing strategies. Inorg. Chem. Front. **7**, 2396–2422 (2020)
22. You, Y., Nam, W.: Photo-functional triplet excited states of cyclometalated Ir(iii) complexes: beyond electroluminescence. Chem. Soc. Rev. **41**, 7061–7084 (2012)
23. Hutt, J.T., Hutt, J.T., Jo, Olasz, J., Chen, C.-H., Lee, D., Aron, Z.D.: Fluorescence switching of imidazo[1,5-a] pyridinium ions: PH-sensors with dual emission pathways. Org. Lett. **14**, 3162–3165 (2012)
24. Liu, J., Li, M., Lu, Z., Huang, Y., Pu, X., Zhou, L.: Dyes and pigments color tuning of iridium(III) complexes containing 2-phenylbenzothiazole-based cyclometalated ligands for application in highly efficient organic light-emitting diodes. Dye. Pigment. **175**, 108145 (2020)
25. Liu, B., Jabed, M.A., Guo, J., Xu, W., Brown, S.L., Ugrinov, A., Hobbie, E.K., Kilina, S., Qin, A., Sun, W.: Neutral cyclometalated iridium(III) complexes bearing substituted. Inorg. Chem. **58**, 14377–14388 (2019)
26. Dedeian, K., Shi, J., Shepherd, N., Forsythe, E., Morton, D.C.: Photophysical and electrochemical properties of heteroleptic tris-cyclometalated iridium(III) complexes. Inorg. Chem. **44**, 886–887 (2005)
27. Wong, W.Y., Zhou, G.J., Yu, X.M., Kwok, H.S., Tang, B.Z.: Amorphous diphenylaminofluorene-functionalized iridium complexes for high-efficiency electrophosphorescent light-emitting diodes. Adv. Funct. Mater. **16**, 838–846 (2006)
28. Tennyson, A.G., Rosen, E.L., Collins, M.S., Lynch, V.M., Bielawski, C.W.: Bimetallic N-heterocyclic carbine—iridium complexes: investigating metal—metal and metal—ligand communication via electrochemistry and phosphorescence spectroscopy. Inorg. Chem. **48**, 6924–6933 (2009)
29. Li, T.-Y., Liang, X., Zhou, L., Wu, C., Zhang, S., Liu, X., Lu, G.-Z., Xue, L.-S., Zheng, Y.-S., Zuo, J.-L.: N-heterocyclic carbenes: versatile second cyclometalated ligands for neutral iridium(III) heteroleptic complexes. Inorg. Chem. **54**, 161–173 (2015)
30. Thomas, S., Teets, S.: Mixed-carbene cyclometalated iridium complexes with saturated blue luminescence. Chem. Sci. **10**, 6254–6260 (2019)
31. Malinovskii, V.L., Wenger, D., Häner, R.: Transition-metal phosphors with cyclometalating ligands: fundamentals and applications. Chem. Soc. Rev. **39**, 638–655 (2010)
32. Chassot, L., Zelewsky, A. Von: Cyclometalated complexes of platinum (II): homoleptic compounds with aromatic C, N ligands. Inorg. Chem. **26**, 2814–2818 (1987)

33. Fleetham, T., Li, G., Li, J.: Phosphorescent Pt (II) and Pd (II) complexes for efficient, high-color-quality, and stable OLEDs. Adv. Mater. **29**, 1601861 (2017)
34. Brooks, J., Babayan, Y., Lamansky, S., Djurovich, P.I., Tsyba, I., Bau, R., Thompson, M.E.: Synthesis and characterization of phosphorescent cyclometalated platinum complexes. Inorg. Chem. **41**, 4510–4511 (2002)
35. Huang, L.M., Tu, G.-M., Chi, Y., Hung, W.I.: Mechanoluminescent and efficient white OLEDs for Pt(ii) phosphors bearing spatially encumbered pyridinyl pyrazolate chelates. J. Mater. Chem. C **1**, 7582–7592 (2013)
36. Lu, W., Chan, M.C.W., Hui, Z., Che, C.-M., Zhu, N., Lee, S.-T.: Light-emitting tridentate cyclometalated platinum (II) complexes containing σ-alkynyl auxiliaries: tuning of photo- and electrophosphorescence. J. Am. Chem. Soc. **126**, 4958–4971 (2004)
37. Kui, S.C.F., Sham, I.H.T., Cheung, C.C.C., Ma, C.-W., Yan, B., Zhu, N., Che, C.-M., Fu, W.-F.: Platinum (II) complexes with Pi- conjugated Naphthyl substituted cyclometalated ligands. Chem. Eur. J. **13**, 417–435 (2017)
38. Che, C.-M., Kwok, C.-C., Lai, S.-W., Rausch, A.F., Finkenzeller, W.J., Zhu, N.: Photophysical properties and OLED applications of phosphorescent platinum (II) schiff base complexes. Chem. Eur. J. **16**, 233–247 (2010)
39. Yuen, M.-Y., Kui, S.C.F., Low, K.-H., Ma, C.-W., Zhu, N., Che, C.-M.C.: Synthesis, photophysical and electrophosphorescent properties of fluorene based platinum (II) complexes. Chem. Eur. J. **16**, 14131–14141 (2010)
40. Wang, Z., Turner, E., Mahoney, V., Madakuni, S., Groy, T., Li, J.: Facile synthesis and characterization of phosphorescent Pt(N ˆCˆN)X complexes. Inorg. Chem. **49**, 11276–11286 (2010)
41. Yang, X., Yao, C., Zhou, G.: Highly efficient photoluminescent materials based on platinum complexes and their applications in organic light emitting diodes (OLEDs). Platin. Met. Rev. **57**, 2–16 (2013)
42. Williams, J.A.G., Beeby, A., Davies, E.S., Weinstein, J.A., Wilson, C.: An alternative route to highly luminescent platinum (ii) complexes: cyclometalation with N^C^N-coordinating dipyridylbenzene ligands. Inorg. Chem. **42**, 8609–8611 (2003)
43. Farley, S.J., Rochester, D.L., Thompson, A.L., Howard, J.A.K., Williams, J.A.G.: Controlling emission energy, self-quenching, and excimer formation in highly luminescent N^C^N-coordinated platinum (II) complexes. Inorg. Chem. **44**, 8609–8611 (2005)
44. Turner, E., Bakken, N., Li, J.: Cyclometalated platinum complexes with luminescent quantum yields approaching 100%. Inorg. Chem. **52**, 7344–7351 (2013)
45. Vezzu, D.A.K., Deaton, J.C., Jones, J.S., Bartolotti, L., Harris, C.F., Marchetti, A.P., Kondakova, M., Pike, R.D., Huo, S.: Highly luminescent tetradentate bis-cyclometalated platinum complexes: design, synthesis, structure, photophysics, and electroluminescence application. Inorg. Chem. **49**, 5107–5119 (2010)
46. Li, G., Fleetham, T., Li, J.: Efficient and stable white organic light-emitting diodes employing a single emitter. Adv. Mater. **26**, 2931–2936 (2014)
47. Graham, K.R., Sibley, S., Dubovoy, T., Baldo, M., Forrest, S.R., Thompson, M.E.: Extended conjugation platinum (II) porphyrins for use in near-infrared emitting organic light emitting diodes. Chem. Mater. **23**, 5305–7312 (2011)
48. Wong, K.M.C., Wong, K.M.-C., Zhu, X., Hung, L., Zhu, L., Yam, V.W.-W., Kwok, H.-S.: A novel class of phosphorescent gold(III) alkynyl-based organic light-emitting devices with tunable colour. Chem. Commun. **2**, 2906–2908 (2005)
49. To, W.-P., Zhou, D., Tong, G.S.M., Cheng, G., Yang, C., Che, C.M.: Highly luminescent pincer gold(III) aryl emitters: thermally activated delayed fluorescence and solution-processed OLEDs. Angew. Chem. Int. Ed. **56**, 14036–14041 (2017)
50. Tang, M.C., Lee, C.-H., Lai, S.-L., Ng, M., Chan, M.-Y., Yam, V.W.-W.: Versatile design strategy for highly luminescent vacuum-evaporable and solution-processable tridentate gold(III) complexes with monoaryl auxiliary ligands and their applications for phosphorescent organic light emitting devices. J. Am. Chem. Soc. **139**, 9341–9349 (2017)

51. Cheung, W., Lai, S., Kwok, W., Tang, M., Lee, C.: A Materials Solution-processable cyclometalated gold (III) complexes for high-brightness phosphorescent white organic light-emitting devices. J. Mater. Sci. **16**, 838–846 (2020)
52. Li, L., Tang, M.C., Lai, S.-L., Ng, M., Kwok, W.-K., Chan, M.Y., Ya, V.W.-W.: Strategies towards rational design of gold(iii) complexes for high-performance organic light-emitting devices. Nat. Photonics **13**, 185–191 (2019)
53. Yam, V.W.: Realization of thermally stimulated delayed phosphorescence in arylgold(III) complexes and efficient gold(III) based blue-emitting organic light-emitting devices. J. Am. Chem. Soc. **140**, 13115–13124 (2018)
54. Tang, M.-C., Tsang, D.P.-K., Wong, Y.-C., Chan, M.-Y., Wong, K. M.-C., Yam, V.W.-W.: Bipolar gold(III) complexes for solution-processable organic light- emitting devices with a small efficiency roll-off. J. Am. Chem. Soc. **138**, 17861–17868 (2014)
55. McCain, J., Colon, K.L., Barrett, P.C., Monro, S.M.A., Sainuddin, T., Roque, J., Pinto, M., Yin, H., Cameron, C.G., McFarland, S.A.: Photophysical properties and photobiological activities of ruthenium (II) complexes bearing π-expansive cyclometalating ligands with thienyl groups. Inorg. Chem. **58**, 10778–10790 (2019)
56. Ertl, C.D., Ris, D.P., Meier, S.C., Constable, E.C., Housecroft, C.E., Neuburgera, M., Zampese, J.: Sticking and patching: tuning and anchoring cyclometallated ruthenium(ii) complexes. Dalton Trans. **44**, 1557–1570 (2015)
57. Robson, K.C.D., Bomben, P.G., Berlinguette, C.P.: Cycloruthenated sensitizers: improving the dye-sensitized solar cell with classical inorganic chemistry principles. Dalton Trans. **41**, 7814–7829 (2012)
58. Gildea, L.F., Batsanov, A.S., Williams, J.A.G.: Bright orange/red-emitting rhodium(iii) and iridium(iii) complexes: tridentate N^C^N-cyclometallating ligands lead to high luminescence efficiencies. Dalton Trans. **42**, 10388–10393 (2013)
59. Bonnet, S., Collin, J., Gruber, N., Sauvage, J., Scho, E.R.: Photochemical and thermal synthesis and characterization of polypyridine ruthenium (II) complexes containing different monodentate ligands. Dalton Trans. 4654–4662 (2003)
60. Wei, F., Lai, S.-L., Zhao, S., Ng, M., Chan, M.-Y. Yam, V. W.-W.: Ligand mediated luminescence enhancement in cyclometalated rhodium (III) complexes and their applications in efficient organic light-emitting devices.pdf. J. Am. Chem. Soc. **141**, 12863–12871 (2019)
61. Dumur, F.: Zinc complexes in OLEDs: an overview. Synth. Met. **195**, 241–251 (2014)
62. Sano, T., Nishio, T., Hamada, Y., Takahashi, H., Usuki, T., Shibata, K.: Design of conjugated molecular materials for optoelectronics. J. Mater. Chem. **10**, 157–161 (2000)
63. Roh, S.G., Kim, Y.-H., Seo, K.D., Lee, D.-H., Kim, H.K., Park, Y., Park, J.-W., Lee, J.: synthesis, photophysical, and electroluminescent device properties of Zn (II)-chelated complexes based on functionalized benzothiazole derivatives. Adv. Funct. Mater. **19**, 1663–1671 (2009)
64. Conaghan, P.J., Menke, S.M., Romanov, A.S., Jones, S.T.E., Pearson, A.J., Evans, E.W., Bochmann, M., Greenhan, N.C., Credgington, D.: Efficient vacuum-processed light-emitting diodes based on carbene–metal–amides. Adv. Mater. **30**, 1802285 (2018)
65. Di, D., Romanov, A.S., Yang, L., Richter, J.M., Rivett, J.P.H., Jones, S.: High-performance light-emitting diodes based on carbene-metal-amides. Science **356**, 159–163 (2017)
66. Thompson, S., Eng, J., Penfold, T.J.: The intersystem crossing of a cyclic (alkyl)(amino) carbene gold (i) complex. J. Chem. Phys. **149**, 014304–014310 (2018)
67. Romanov, A.S., Jones, S.T.E., Yang, L., Conaghan, P.J., Di, D., Linnolahti, M., Credgington, D.: Mononuclear silver complexes for efficient solution and vacuum-processed OLEDs. Adv. Opt. Mater. **6**, 1801347 (2018)
68. Hamze, R., Peltier, J.L., Sylvinson, Jung, M., Cardenas, J., Haiges, R.: Eliminating nonradiative decay in Cu(I) emitters: >99% quantum efficiency and microsecond lifetime. Science **363**, 601–606 (2019)
69. Romanov, A.S., Chotard, F., Rashid, J., Bochmann, M.: Synthesis of Copper (i) cyclic (alkyl)(amino)carbene complexes with potentially bidentate N^N, N^S and S^S ligands for efficient white photoluminescence. Dalton Trans. **48**, 15445–15454 (2019). https://doi.org/10.1039/c9dt02036e

70. Hamze, R., Shi, S., Kapper, S.C., Ravinson, D.S.M., Estergreen, L., Jung, M.-C., Tadle, A.C., Haiges, R., DJurovich, P.I., Peltier, J. L., Jazzar, R., Bertrand, G., Bradforth, S.E., Thompson, M.E.: 'Quick-silver' from a systematic study of highly luminescent, two-coordinate, d^{10} coinage metal complexes. J. Am. Chem. Soc. **141**, 8616–8626 (2019)
71. Romanov, A.S., Yang, L., Jones, S.T.E., Di, D., Morley, O.J., Drummond, B.H., Reponen, A.P.M., Linnolhti, M., Credgington, D., Bochmann, M.: Dendritic carbene metal carbazole complexes as photoemitters for fully solution-processed OLEDs. Chem. Mater. **31**, 3613–3623 (2019)
72. Taffet, E.J., Olivier, Y., Lam, F., Beljonne, D., Scholes, G.D.: Carbene-metal-amide bond deformation, rather than ligand rotation, drives delayed fluorescence. J. Phys. Chem. Lett. **9**, 1620–1626 (2018)
73. Föller, J., Marian, C.M.: Rotationally assisted spin-state inversion in carbene-metal-amides is an artifact. J. Phys. Chem. Lett. **8**, 5643–5647 (2017)
74. Yang, L., Kim, V., Lian, Y., Zhao, B., Di, D.: High-efficiency dual-dopant polymer light-emitting diodes with ultrafast inter-fluorophore energy transfer high-efficiency dual-dopant polymer light-emitting diodes with ultrafast inter-fluorophore energy transfer. Joule **3**, 2381–2389 (2019)
75. Romanov, A.S., Jones, S.T.E., Gu, Q., Conaghan, P.J., Drummond, B.H., Feng, J., Chotard, F., Buizza, L., Foley, M., Linnolahti, M., Credgington, D., Bochmann, M.: Carbene metal amide photoemitters: tailoring conformationally flexible amides for full color range emissions including white-emitting OLED. Chem. Sci. **11**, 435–446 (2020)
76. Feng, J., Yang, L., Romanov, A.S., Ratanapreechachai, J., Reponen, A.P.M., Linnolahti, M., Hele, T.J.H., Kohler, A., Bassler, H., Bochmann, M., Credgington, D.: Environmental control of triplet emission in donor—bridge—acceptor organometallics. Adv. Funct. Mater. **30**, 1908715 (2020)
77. Jazzar, R., Soleilhavoup, M., Bertrand, G.: Cyclic (Alkyl)- and (Aryl)-(amino)carbene coinage metal complexes and their applications. Chem. Rev. **120**, 4141–4168 (2020)
78. Feng, J., Yang, L., Romanov, A.S., Ratanapreechachai, J., Reponen, A.M., Jones, S.T.E., Linnolahti, M., Hele, T.J.H., Köhler, A., Bässler, H., Bochmann, M., Credgington, D.: Environmental control of triplet emission in donor – bridge—acceptor organometallics. Adv. Funct. Mater. **30**, 1908715 (2020)

Organic–Inorganic Hybrids for White-Light Phosphors

Geeta Sharma and Pankaj Poddar

Abstract The lighting industry is largely revolutionized with the advent of Light-emitting diodes (LEDs) and organic light-emitting diodes (OLEDs). The white light phosphors are being designed with an aim to get better colour stability. The process involved in the synthesis should be easy applicable to large scale as well. This chapter summarizes extensively explored popular classes of organic–inorganic hybrid phosphors. These include: coordination compounds obtained from small organic molecules, organically coated nanoparticles, hybrid-carbon phosphors, organic polymer-based hybrids. The limitations of currently used phosphors for white-light emission and the possible remedies are discussed.

1 Introduction

New energy saving technologies are needed to address the increasing energy demands of the planet. Solid state lightening is a reliable technology for energy demands. Light-emitting diodes (LEDs) and organic light-emitting diodes (OLED) are mostly used for solid-state lighting (SSL) applications. It has revolutionized the lighting and display industries. Because of its far reaching impact it is looked upon as technology of the future [1]. The first attempt to study the principle of SSL was done almost a century ago in 1907, (by H. J. Round) by passing electrical current through silicon carbide crystal [2, 3]. Later in 1920, O. Losevtried to scientifically explain the phenomenon of electroluminescence in a p–n junction. Whereas, the first practical LED was invented by N. Noloyak several years later in 1962 [2, 3]. The popular categories of SSL includes light-emitting diodes (LEDs) and organic light-emitting diodes (OLEDs) [4–9]. These exhibit long life, are robust and highly efficient than the incandescent bulbs and fluorescent lamps. The first white light emission from a

G. Sharma · P. Poddar (✉)
Physical & Materials Chemistry Division, CSIR-National Chemical Laboratory, Dr. Homi Bhabha Road, Pune 411008, India

P. Poddar
Academy of Scientific and Innovative Research, Postal Staff College Area, Sector 19, Kamla Nehru Nagar, Ghaziabad 201002, Uttar Pradesh, India

© Springer Nature Switzerland AG 2022

K. Upadhyay et al. (eds.), *Hybrid Phosphor Materials*, Engineering Materials,
https://doi.org/10.1007/978-3-030-90506-4_4

semiconductor is due to the LED obtained from gallium nitride (GaN) [3]. The white light LEDs (WLEDs) are desirable for lighting applications. Presently the white light emission is obtained from rare earth doped inorganic phosphors. However, there are several potential risks related to supply of these materials. Moreover these are very costly and poses serious environmental issues [10]. Different strategies utilized for designing white-light LEDs include mixing of primary colour LEDs however, it results in expensive and complicated device. Other popular strategy is based on single chip technology, where complementary coloured LEDs are combined with a blue LEDor electrical activation of several phosphors in one OLED. Even after all these efforts, the resulting devices need complicated fabrication technologies, have poor colour stability, and low reproducibility. The quality and colour of the emitted light is defined by two parameters: the colour-rendering index (CRI) and the correlated colour temperature (CCT) of light. CRI measures the ability of a light source to reveal the colours of various objects in comparison a natural light source. CCT describes the dominant colour tone and varies from warm (yellow and red) to cool (blue). It is defined in Kelvin but it is not related to temperature. The white light emission from a phosphor should be according to the human eye sensitivity curve. The white light emission from a phosphor is largely limited due to its incapability to get simultaneously low and high energy emissions.

There are several sources to these emissions: (I) Emissions originating from different excited states of a monomer. These states can be excited by various transitions such as transitions within ligand centres ($\pi \infty \pi^*$ and $n \infty \pi^*$), charge transfer transitions between ligands, charge transfer transitions between ligands and metals, d-d, f-f and d-f transitions in metals, metal to metal charge transfer [12]. Except for f-f transitions, the emissions from these processes depend upon molecular structure. (II) Band-edge emission from the semiconductors: The organically modification of the band-gap can control the dimensions of inorganic skeleton such as remarkable structural tunability is allowed by PbX component [13]. The quantum size effect largely affects the band-edge emission [14]; (III) Emissions originating from defects and impurities: Emissions from solid-state materials is highly influenced by defects. The heat treatment during synthesis of these materials introduces various point defects and substitutional defects [15]. Whereas, in case of nanoparticles the surface sites are common defects. The popular strategies employed to get simultaneous LE (low energy) and HE (high energy) emissions include [11]:

(i) Assembling two or more familiar luminescent species such as organic dyes, metal ions (Mn^{2+}, rare-earth ions), metal-complexes (iridium complex etc.).
(ii) Increasing the decay path of the excited states by introduction of heavy metals (which increases the probability of intersystem crossing), addition of groups such as keto and enol will also initiate the above process. This will result into emission of HE along with LE luminescence from the phosphor.
(iii) The HE emission from the monomer and a LE emission from the excited stacked species can be easily achieved by creation of closely stacked π-conjugated planar groups.

(iv) Creation or elimination of defects via thermal annealing treatment of the host material etc.

Concentration of dopants [16] and extent of aggregation [17, 18] also affects HE and LE emission. Further by using a phosphor having double emissions for a single excitation wavelength also balances the HE and LE emissions [19]. Hence, combining two or more emissions in a single phosphor along with the balance of complementary LE and HE emissions ensures emission of white-light from a phosphor.

Formation of hybrids of organic–inorganic components is a popular approach to design new materials [4, 9, 12, 11, 16] with desired properties. The novel and improved white-light phosphors can be obtained by manipulating the matter at the dimensions of nanometre. Alteration at the molecular level is also a wise strategy to obtain new white-light phosphors. Incorporation of organic–inorganic components in a single matrix makes them structurally versatile and their unique properties makes them fundamentally interesting and technologically viable. The combination of inorganic and organic components brings several excellent features to the new phosphors. The new phosphors have flexibility in their structure, are easily processible and light weight. These materials posses the functionalities of organic components [4, 5, 20]. The photoluminescence and electroluminescence properties of these materials are particularly interesting and important. These materials can easily find applications in lighting phosphors for phosphor-converted WLEDs (pc-WLEDs). The emissive layers in hybrid LEDs (HLEDs) can be designed using these materials. The organic–inorganic hybrid phosphors are classified as follows: (i) coordination compounds obtained from small organic molecules; (ii) organically coated nanoparticles; (iii) hybrid-carbon phosphors; (iv) organic polymer-based hybrids.

(i) **Coordination compounds obtained from small organic molecules**

Molecules which possess metal centres bound to ligands are termed as coordination compounds. Ligands (atoms, ions or molecules) donate electrons to the metals. It is easy to structurally tune these compounds over organic and inorganic compounds hence are used for white-light phosphors [17, 18, 19]. Such as coordination geometry and the ligand metal centres can be deliberately chosen to design the new compound. Depending upon the type of interaction between organic and inorganic components, these materials falls into two categories, Class I and Class II. In Class I, hydrogen bond and Van der Waals forces binds the organic component to the inorganic components. Whereas the organic and inorganic components in Class II hybrids, are bonded by covalent bonds. To get a better luminescence intensity, one needs to select the organic ligands correctly. There should be well organized binding sites so as to ensure complete saturation of the lanthanide ion sphere coordination sites. This arrangement will lead to efficient energy transfer due to minimization of the non-radiative deactivation of the molecule (which can lead to quenching). It also inhibits the back energy transfer which may lead to deactivation. An appropriate energy gap between the triplet state of the ligand and the resonance level of the Ln^{3+} cation will increase the luminescence intensity. Since materials of Class I category suffer numerous problems. There is tendency of cluttering of emitters, dopants may leach out and

organic components may be present in limited concentration in them. Hence the present research pertaining to hybrid materials is mainly focused on Class II materials using lanthanide-organic complexes. Among the synthesis techniques, sol–gel is a powerful and most popular technique for the synthesis of these materials. It is a low temperature synthesis method and forms highly homogeneous samples and maintains high purity. Specific functions such as complexes, organic functions can be easy incorporated using this method. Escribano et al. [20] has systematically explained the various routes for synthesis of hybrid materials. These materials can be designed with and without rare-earth elements, as discussed below:

a. **Rare-earth (RE)-containing compounds**

The transitions in lanthanide ions (*f-f*) are forbidden by Laporte rule. This leads to weak oscillator strength of lanthanides. Their intensity of luminescence can be greatly increased by incorporating them into a complex through antenna effect [21].

First rare-earth ion incorporated coordination compounds were prepared by Coppo et al. [18]. The CIE coordinates of Ir-Eu triad complex in CD_3OD solution are (0.28, 0.30). The quantum yield is found to be 7% at $\varepsilon_{ex} = 400$ nm. The energy transfer is observed from Ir(III) to Eu(III). A single-component white-light-emitting compound is reported by Wang et al. [22]. It has a high CRI of 96. The authors prepared two hybrid crystalline materials: $(H_2DABCO)(Pb_2Cl_6)$ **(1)** and $(H_3O)(Et_2DABCO)_8(Pb_{21}Cl_{59})$ **(2)**, (where, DABCO = 1,4-diazabicyclo[2.2.2]-octane; Et = ethyl). These materials have organic blue light emitting component and the inorganic component possessed yellow/orange emission. Their tunable emission characteristics maintained high CRI white-light emission. The **CRI value for Hybrid 1** and Hybrid 2 are 96 and 88 respectively. Ma et al. [23] used solvothermal method to obtain preparing metal–organic framework based phosphor $\{[Zn_2(L)\cdot H_2O]\cdot 3H_2O\cdot 3DMAc\cdot NH_2(CH_3)_2\}_n$ (Zn(II)–MOF). Trapping of Eu^{3+} and Tb^{3+} ions into the pores of the Zn(II)-MOF is used for obtaining white-light emitting materials.

A bright white-light emitting diode is synthesized by using a europium doped phosphor by Devi et al. [24]. The reported parameters of the phosphor are CRI (95), CCT (5457 K), and CIE ($x = 0.33$, $y = 0.33$). However, red light with CIE value of $x = 0.58$, $y = 0.31$ is displayed by the triangle Eu-phosphor. A single-phase white-light-emitting molecular complex with excellent color quality is displayed by dual emission of a europium complex with a butterfly structure. It is found that there is a energy transfer from ligand to the Eu(III) ion which causes partial lighting up of europium ion due to antenna effect. Enhanced lanthanide emission intensity and lifetime due to fluoride ions in multifunctional hetero pentanuclear Al_3Ln_2 (Ln = Nd, Eu, Yb) clusters is reported by Xu et al. [21]. These complexes show bright white-light emission in both diluted solutions and solid-stat. It is found that there is an incomplete energy transfer from $Al(Mq)_2$-based chromophore to lanthanide centre.

b. **Rare-earth (RE)-free compounds**

High purity RE ions is hard to achieve. Their production process is very tedious. Hence it is highly desired to develop white-light phosphors without RE ions. Studies related to the emission of white-light from RE-free coordination compounds are very scanty. Noble metal [25] coordination compounds and MOF [9] have been explored for non-rare-earth-based white-light emission. White-light emission from a non-rare-earth-based material are recently in focus. These materials have low power consumption and are cheap to manufacture. Moreover, these are safe for the environment. Studies on zinc-based MOF is reported by Mondal et al. [9]. White-light emission from these compounds are obtained at ε ex = 260 nm. The CIE index of the phosphors is (0.31, 0.33) and quantum yield of 32.5% is achieved. The white light emission is obtained due to three emissions at 384, 468 and 570 nm. The first two peaks are due to $\pi - \pi^*$ and $n - \pi^*$ transitions of N_3-ipa whereas emission at 570 The white emission arises due to three peaks in which two peaks at 384 nm and 468 nm come from $\pi - \pi^*$ and $n - \pi^*$ transitions of N_3-ipa, respectively, whereas, charge transfer phenomenon from pyridine moiety to the linker is responsible for the new peak at 570 nm. Composites of carbon dots (CDs) with Zr(IV)-based MOF are synthesized by Wang et al. [17]. The phosphors are RE free and shows white-light-emission at $\varepsilon_{ex} = 365$ nm. The solid-state phosphors show a PL quantum yield of ~37%. These phosphors are further used to construct the WLEDs. The CDs/Zr-MOF nanocomposite are deposited on a commercial UV LED chip. The features of obtained WLEDs are found to be: CIE chromaticity coordinate at (0.31, 0.34), high color rendering index (CRI) of 82 and luminous efficiency of 1.7 lm/W.

(ii) **Organically coated nanoparticles**

The properties of materials at nanoscale are largely different then their bulk counterparts. The properties of these materials depend upon size. Further large surface to volume ratio and availability of large surface sites gives ample opportunity to modify their luminescent properties. This makes them suitable candidates for white-light emission. A new class of hybrid materials formed by organically modified nanoparticles is being reported by several authors [26–31]. The organic component provides passivation and control on the size or acts as luminophores. T. Wang et al. have used electron coupling of defect states in colloidal Ga_2O_3 nanocrystals Rhodamine B (RhB) [26] to obtain white-light-emitting nanophosphors The tuning of chromaticity is achieved by manipulation of size of the nanocrystals and the organic dye molecule used. Forster resonance energy transfer is observed between the two molecules due to which white-light with quantum yield of ~30%, CRI up to 95, and color temperature of 5500 K is obtained. Figure 1 below shows the PL spectra of Ga_2O_3–RhB NCs for different concentrations of RhB; FRET efficiency as a function of the spectral overlap; white light emission is indicated in the CIE coordinates; and a white LED prepared from the same sample.

The luminescence of Ga_2O_3 nanocrystals as the function of size is done by Chirmanov et al. [27]. The authors have studied the Forster resonance energy transfer through variations in the bound dye molecules. The white light emission is achieved due to generation of tunable blue-orange emission. The size of the NC and the molar extinction coefficient of the bound acceptor moiety affects the efficiency of energy

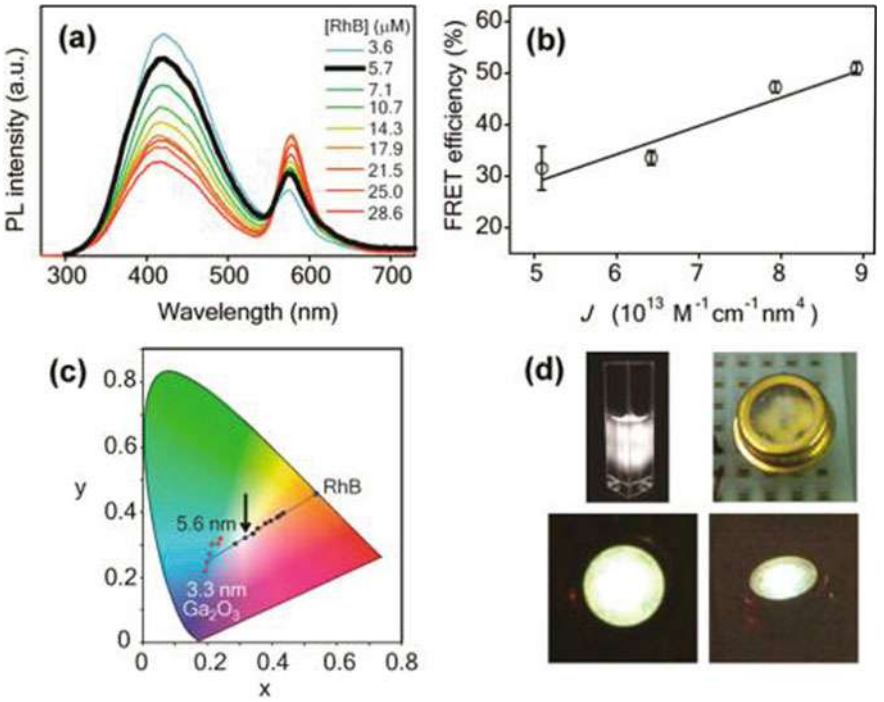

Fig. 1 **a** PL spectra of Ga_2O_3–RhB NCs (3.6 nm) for different concentrations of aqueous RhB, as indicated in the graph (ε exc = 230 nm). The black spectrum corresponds to pure white-light. **b** FRET efficiency as a function of the spectral overlap J. **c** CIE-1931 diagram corresponding to the spectra in (**a**) (black dots) which indicates the pure white-light (0.33, 0.33). The red dots designate Ga_2O_3 NCs emission color for sizes ranging from 3.3 to 5.6 nm, and the blue dot the emission of aqueous RhB solution. **d** Photographs of a colloidal suspension of white-light-emitting Ga_2O_3–RhB NCs (top left) and an LED prepared from the same sample (Ref. [26])

transfer and the spectral properties of nanoconjugate. Layek et al. [28] have obtained white light emission from ZnO-based nanoconjugate. Due to the electronic coupling between ZnO NCs and the organic dye, both acted as a single nanophosphor. FRET is observed due to the spectral overlap between a broad native defect-induced emission band of ZnO NCs and $S_0 \infty S_1$ absorption of conjugated dye molecules. The white-light characteristics were tuned by the NC size modulated blue ZnO emission and the orange-red dye emission by the type and concentration of molecular conjugates. The process of energy transfer from the defect states of NC to the attached dye molecules due to excitation of ZnO NCs is shown in Fig. 2.

Two different approaches of bright white-light emission are reported by Sapra et al. [31]. In the first approach, double colour emission from the CdSe core and shell of an onion-like CdSe/ZnS/CdSe/ZnS NC has been described and ~~in~~ the second one describes broad surface state emission associated with the trap centres of CdS. A high quantum yield of 30% and 17% is obtained for them, respectively. Tuning of white

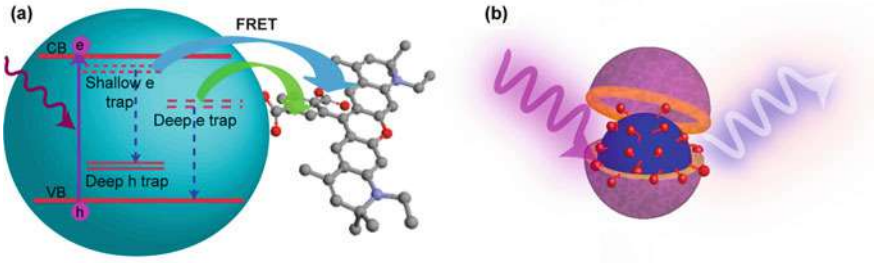

Fig. 2 Schematic representation of **a** ATTO 590-conjugated ZnO NCs, indicating possible energy transfer processes from NC defect-based excited states to the attached dye molecules upon excitation of ZnO NCs into the band-gap (grey balls in the molecular model represent carbon, red balls oxygen, and blue balls nitrogen atoms). **b** Encapsulation of ZnO-ATTO 590 nanoconjugate in a protecting layer of silane to obtain stable single white-light-emitting nanophosphor under UV-excitation (NC is shown in blue, ATTO 590 in red, and silane layer in purple) (Ref. [28])

light is by varying the diameter of the core and the thickness of the shell. This is easily achievable by controlling the synthesis parameters. Due to their intrinsic broadband emissions, low-dimensional lead halides have gained attention as potential candidates for application in photoelectric devices specifically white-light-emitting diodes. Xing-Yu Sun et al. assembled two new hybrid lead halides of $[H_2BPP]Pb_2X_6$ (X = Br, 1, and Cl, 2) containing one-dimensional double $[Pb_2X_6]^{2-}$ chains using optically active 1,3-bis(4-pyridyl)-propane (BPP) as an organic cation. Broadband yellowish-green emissions were exhibited by compounds 1 and 2 under UV-light excitation subsequently verified by photoluminescence quantum efficiencies (PLQEs) of 8.10% and 4.84%, respectively. Combination of both higher-energy (blue) and lower-energy (yellow) light spectra led to broadband light emissions which can be ascribed to individual contributions of the organic and inorganic components, respectively. Growing into magic size is another important approach adopted by many material scientists [30]. Magic Size nanocrystals (MSNCs) of cadmium selenide (CdSe) have size between 1 and 2 nm are semiconducting, thermodynamically stable, and possess unique physical properties. Coordination in the intrinsic energy and surface energy of MSNCs provides them excellent structural and thermodynamical stability. Due to extremely large surface-to-volume ratio in magic sized nanoparticles, interaction between electrons and holes is confined mainly at the surface. Thus, dominance of broadband emission from surface trap states over the band edge emission is observed. Michael J. Bowers et al. have reported white-light emission from magic-sized cadmium selenide nanocrystals [29]. Figure 3 depicts the white-light emission from commercial UV LED (400 nm) illuminating a thin coating of magic-sized CdSe in polyurethane.

(iii) **Hybrid-carbon phosphors**

Graphene quantum dots (GQDs), graphene oxide (GO), carbon dots (C-dots) are most prominent carbon materials. These are extensively used for variety of luminescent applications such as as LEDs, potential biological markers, drug delivery

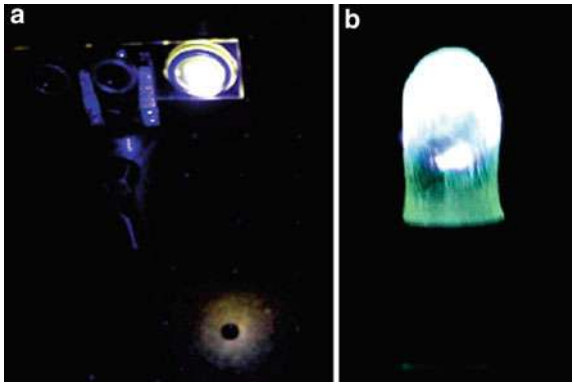

Fig. 3 White-light emission from magic-sized CdSe. **a** The thin film of magic-sized CdSe in polyurethane excited by a frequency-doubled titanium: sapphire laser (400 nm) with white-light clearly seen reflecting off the table surface. **b** A 5 mm commercial UV LED (400 nm) illuminating a thin coating of magic-sized CdSe in polyurethane (Ref. [29])

vehicles, removal of heavy metal ions, etc. [32–42]. Their hybrids with other materials such as polymers [40], rare-earth ions [42], and inorganic materials such as ZnO, $SrBaSi_2O_2N_2:Eu^{2+}$, NaCl [39], etc. have further opened new avenues for these materials. C-dots and GQDs have exciting properties such as tunable luminescence, low cytotoxicity and excellent biocompatibility. These materials belong to a class of environmental friendly materials and are cost effective. These properties make them suitable for white-light emission [43, 44]. Carbon nano particles having size less than 10 nm are called C-dots. The show some exciting properties such as they do not show photobleaching, their photoluminescence is very stable and they can be easily functionalized with various functionalities. The luminescence of C-dots is hampered by self-aggregation [45]. Molecular functionalization causes surface passivation which in-turn enhances the dispersibility of C-dots [43, 44, 46, 47]. Further C-dots show improved photoluminescence performance upon doping with heteroatoms [48]. Zero- and two-dimensional hybrid carbon phosphors are obtained by hydrothermal synthesis by Ding et al. [32]. These hybrid carbon phosphors emit bright white luminescence in the solid-state. The white light emission obtained from the phosphor-coated blue LEDs exhibit high colorimetric purity. The color coordinate for the white light obtained are (0.33, 0.33). The obtained characteristics indicates its suitability for white-light applications. Zhai et al. [36] embedded red emissive C-dots (with PLQYs of 23%) into polyvinyl pyrrolidone (PVP). This arrangement increased the PL quantum yield. These red emissive phosphors are used to obtain the WLEDs. The CRI of the LEDs are found to be 92 and the colour coordinates of (0.33, 0.33). Figure 4 shows the schematic of preparation of C-dots based phosphors for WLEDs.

Orange-emissive C-dots phosphors are synthesized by Chen et al. for WLEDs [41]. The authors used 2,7-dihydroxynaphthalene as the carbon source and for nitrogen source *N*, *N*-dimethylformamide is opted. The features of WLED device designed using orange-emissive C-dots phosphors are: colour coordinate of (0.41, 0.39) and emit warm white-light; the value of CCTis 3330 K. Chen et al. [49] obtained uniform blue-green emissive GQDs with high quantum yield (52.4%) and modified efficient orange-emitting GQDs derived from fullerene (C_{60}). A blend of GQDs

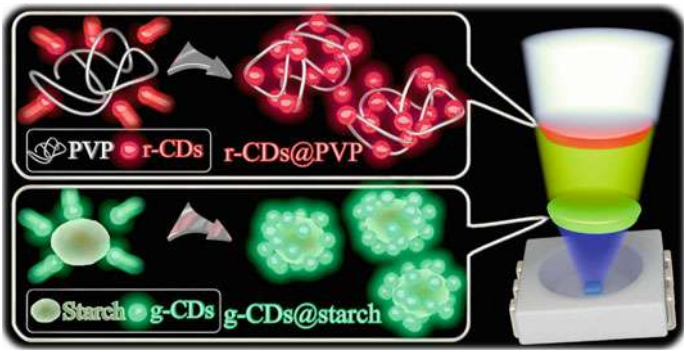

Fig. 4 Preparation of C-dots based phosphors. These are used for WLEDs (Ref. [36])

in polyvinyl alcohol (PVA) is used to obtain transparent photoluminescent films. Highly flexible film exhibit white emission characteristics suitable for commercial standards. Multifunctional N-doped GQDs are synthesized by Yang et al. [50]. The synthesis method opted is one-pot hydrothermal treatment. Benzimidazole is used as the precursor. The GQDs obtained are for high-performance WLEDs. The WLEDs are fabricated by dissolving commercially available yellow phosphors and the as-prepared N-GQDs in the epoxy resin solution. The epoxy resin ispopularly used as a binder and sealant in electronic devices. The obtained WLEDs are having the CIE coordinates at 0.35, 0.31 and CCT of 4427 K. Luo et al. [51] utilized microwave assisted hydrothermal procedure for synthesizing GQDs with white fluorescence. Graphite is used as the precursor. White light emitting diodes are fabricated using 4,4-bis(carbazol-9-yl) biphenyl doped GQDs. The WLED show brilliant performance. The luminance of 200 cdm^{-2} at an applied voltage of 11–14 V is obtained. The parameters obtained make these GQDs a suitable candidate for WLEDs which can be used for solid-state lightening purposes. Most of the C-dot materials exhibit low CRI due to absence of long wavelength emission. This limits C-Dot for white light applications. Moreover, there are not sufficient reports related to light stability and life time of C-dots [34].

(iv) **Organic polymer-based hybrids**

White-light organic polymers have great flexibility. These can be easily coated over large area. These characteristics make them suitable for OLEDs. The hybrids of organic polymers can be formed with metals halides/sulphides and QDs, etc. [52–58]. Chou et al. [55] used luminescent polyfluorene polymer and QDs for obtaining hybrid white-light-emitting-LEDs. A multilayer structure of core–shell CdSe/ZnS QDs is used to fabricate white-light-emitting hybrid organic/inorganic LEDs. The multilayer structure of core–shell CdSe/ZnS QDs acts as a yellow-emitter whereas blue emission is obtained from polyfluorenes. FTO/PEDOT: PSS/PbS/Alq_3/Ni is used to fabricate hybrid white-light-emitting devices (HWLEDs) by Kadim et al. [54]. Excitons in lead sulphide NCs induced an energy transfer in HWLED. A set of

three layers are present in HWLED. Poly (3,4-ethylenedioxythiophene) polystyrene sulfonate (PEDOT: PSS) blended with polymethyl methacrylate (PMMA) organic polymer formed the first layer. PbS NCs formed the second layer. While the third layer of Tris (8-hydroxyquinoline) aluminium (Alq_3) layer is above the PbS layer. Due to confinement effect good efficiency white-light is generated. The values of CIE and CCT are found to be 0.31, 0.33 and 6250 K, respectively. The operation of white-light HWLEDs happen due to the electron injection from the organic molecules (Alq3) while the hole injection is from organic polymer (PEDOT: PSS with PMMA). Tunable bright white-light emission from bulk hybrid semiconductors of Cd and/or Se substituted double-layer [Zn_2S_2(ha)] (ha = n-hexylamine) is reported by Fang et al. [57]. In the ternary hybrid compounds $Zn_{2-2x}Cd_{2x}S_2$(ha) the contribution to PL (inform of two peaks) comes from band-gap emission. Emissions from surface sites and doping of Cd also contribute to the photoluminescence. The optical band-edge (band-gap) is largely affected by dopant (Cd) concentration, which inturn modulates the intensities and position of the emission bands. The emission of bright white-light with significantly enhanced photoluminescence quantum yield is found in ZnS-based hybrid structures (with Cd mole fraction = 0.25) as compared to its CdS-based hybrid analogues. A synergetic effect between doped Cd and Se atoms is observed in quaternary $Zn_{2-2x}Cd_{2x}S_{2-2y}Se_{2y}$(ha) compounds. This provided a better tunability in the band-gap and emission spectra. High quantum yield for the white light is obtained. Hybrid semiconductors show promising results for white light emission. Sun et al. [52] used one-dimensional organic–inorganic hybrid silver halide. The phosphors obtained are suitable for broadband white-light emission. They have synthesized hybrid compounds [H_2DABCO] [Ag_2X_4(DABCO)] (X = Br (1), I (2)). These compounds have one-dimensional $[Ag_2X_4(DABCO)]^{2-}$charged structures. These structures are in turn balanced by balanced by $[H_2DABCO]^{2+}$ cations. Compound 1 show white light emission and the quantum yield is found to be 2.1%. It is having good photochemical stability. Comp ound 2 yields broad band yellow white light emission which is centrered at 556 nm. A third compound $[HDABCO]_3Ag_5Cl_8$ (3) is also synthesized with a high quantum yield of 6.7% and the emission is centred at 585 nm. The organic and inorganic components exhibit good synergy to yield broadband white-light emissions. Encapsulation of dye molecule in the polymer matrix also a popular strategy to obtain white-light emission. Pallavi et al. [56] have prepared reported a new porous organic polymer TPDC-BZ. The surface area is found to be of 610 $m^2\ g^{-1}$. The materials exhibit tunability in the emission colour. The hybrid materials offer high quality and cost-effective strategy for white light generation.

Sarih et al. [58] obtained white light from a mixture of fluorescent organic molecules. Three fluorescent compounds are mixed furocoumarin (FC), dansyl aniline (DA), and 7-hydroxycoumarin-3-carboxylic acid (CC). The results light obtained is pure white light. Low cost WLEDs are fabricated using immobilized mixture in silica aerogel coatings which are put on a UV LED. The obtained value of CIE chromaticity index (0.27, 0.33) indicates white light emission.

2 Summary

In summary, we have described the evolution of SSL and strategies to get white-light LEDs. The parameters used to define white-light (CCT and CRI) are defined. Factors affecting the white-light emissions (LE and HE) are discussed in detail. A brief introduction to different types of organic–inorganic hybrid white-light phosphors is presented (coordination compounds obtained from small organic molecules, organically coated nanoparticles, hybrid-carbon phosphors, polymer-based hybrids). Some recent research related to above categories is briefly presented. The structural tunability obtained from coordination compounds of small organic molecules make them suitable for WLED applications. Good processibility and film forming properties are seen for organic polymers functionalized with metals and organically coated nanoparticles. These makes them suitable for lighting devices. These materials are also explored for large area display applications. Hybrid-carbon phosphors are also extensively explored for WLED applications but these are still far their suitability for commercial exploitation. Details of some popular synthesis methods such as sol–gel is also presented. The qualities for an ideal white light phosphors include high quantum efficiency ($\geq$90%) and high CRI value ($\geq$80). It should also possess high CCT with reasonably long illumination. It should be stable in different atmospheric conditions. The studies pertaining to white light emissions are unstructured. Most of the authors have only studied the properties of phosphors and have not used them for white-light LEDs. QE and of most of the materials are not defined and reports for CCT and CRI are also scanty.

References

1. Bergh, A., Craford, G., Duggal, A., Haitz, R.: The promise and challenge of solid-state lighting. Phys. Today **54**, 42–47 (2001). https://doi.org/10.1063/1.1445547
2. Mondal, M., Mukhopadhyay, L., Rai, V.K.: A concise review on solid state lighting. IEC Int. J. Technol. Manag. 12–15 (2016)
3. Bender, V.C., Marchesan, T.B., Alonso, J.M.: Solid-state lighting: a concise review of the state of the art on LED and OLED modeling. IEEE Ind. Electron. Mag. **9**, 6–16 (2015). https://doi.org/10.1109/MIE.2014.2360324
4. Liu, W., Lustig, W.P., Li, J.: Luminescent inorganic-organic hybrid semiconductor materials for energy-saving lighting applications. EnergyChem **1**, 100008 (2019). https://doi.org/10.1016/j.enchem.2019.100008
5. Carlos, L.D., Ferreira, R.A.S., De Zea Bermudez, V., Julián-López, B., Escribano, P.: Progress on lanthanide-based organic–inorganic hybrid phosphors. Chem. Soc. Rev. **40**, 536–549 (2011). https://doi.org/10.1039/c0cs00069h.
6. Carlos, L.D., Ferreira, R.A.S., De Zea Bermudez, V., Ribeiro, S.J.L.: Lanthanide-containing light-emitting organic-inorganic hybrids: a bet on the future. Adv. Mater. **21**, 509–534 (2009). https://doi.org/10.1002/adma.200801635
7. Binnemans, K.: Lanthanide-based luminescent hybrid materials. Chem. Rev. **109**, 4283–4374 (2009). https://doi.org/10.1021/cr8003983

8. Chen, L.C., Tseng, Z.L., Chang, W.W., Lin, Y.W.: Warm white light-emitting diodes using organic–inorganic halide perovskite materials coated YAG:Ce3+ phosphors. Ceram. Int. **44**, 3868–3872 (2018). https://doi.org/10.1016/j.ceramint.2017.11.176
9. Mondal, T., Mondal, S., Bose, S., Sengupta, D., Ghorai, U.K., Saha, S.K.: Pure white light emission from a rare earth-free intrinsic metal-organic framework and its application in a WLED. J. Mater. Chem. C **6**, 614–621 (2018). https://doi.org/10.1039/c7tc05215d
10. Zhang, X., Liu, W., Wei, G.Z., Banerjee, D., Hu, Z., Li, J.: Systematic approach in designing rare-earth-free hybrid semiconductor phosphors for general lighting applications. J. Am. Chem. Soc. **136**, 14230–14236 (2014). https://doi.org/10.1021/ja507927a
11. Wang, M.S., Guo, G.C.: Inorganic-organic hybrid white light phosphors. Chem. Commun. **52**, 13194–13204 (2016). https://doi.org/10.1039/c6cc03184f
12. Allendorf, M.D., Bauer, C.A., Bhakta, R.K., Houk, R.J.T.: Luminescent metal-organic frameworks. Chem. Soc. Rev. **38**, 1330–1352 (2009). https://doi.org/10.1039/b802352m
13. Saparov, B., Mitzi, D.B.: Organic-inorganic perovskites: structural versatility for functional materials design. Chem. Rev. **116**, 4558–4596 (2016). https://doi.org/10.1021/acs.chemrev.5b00715
14. Nirmal, M., Brus, L.: Luminescence photophysics in semiconductor nanocrystals. Acc. Chem. Res. **32**, 407–414 (1999). https://doi.org/10.1021/ar9700320
15. Hayakawa, T., Hiramitsu, A., Nogami, M.: White light emission from radical carbonyl-terminations in Al_2O_3-SiO_2 porous glasses with high luminescence quantum efficiencies. Appl. Phys. Lett. **82**, 2975–2977 (2003). https://doi.org/10.1063/1.1569038
16. Chen, P., Li, Q., Grindy, S., Holten-Andersen, N.: White-light-emitting lanthanide metallogels with tunable luminescence and reversible stimuli-responsive properties. J. Am. Chem. Soc. **137**, 11590–11593 (2015). https://doi.org/10.1021/jacs.5b07394
17. Pan, M., Liao, W.M., Yin, S.Y., Sun, S.S., Su, C.Y.: Single-phase white-light-emitting and photoluminescent color-tuning coordination assemblies. Chem. Rev. **118**, 8889–8935 (2018). https://doi.org/10.1021/acs.chemrev.8b00222
18. Coppo, P., Duati, M., Kozhevnikov, V.N., Hofstraat, J.W., De Cola, L.: White-light emission from an assembly comprising luminescent iridium and europium complexes. Angew. Chem. Int. Ed. **44**, 1806–1810 (2005). https://doi.org/10.1002/anie.200461953
19. Song, S., Li, X., Zhang, Y.H.: White light emission of an Eu(iii)-doped Gd(iii) complex with 3-sulfobenzoate and 1H-imidazo[4,5-f][1,10]-phenanthroline. Dalton Trans. **42**, 10409–10412 (2013). https://doi.org/10.1039/c3dt50897h
20. Escribano, P., Julián-López, B., Planelles-Aragó, J., Cordoncillo, E., Viana, B., Sanchez, C.: Photonic and nanobiophotonic properties of luminescent lanthanide-doped hybrid organic-inorganic materials. J. Mater. Chem. **18**, 23–40 (2008). https://doi.org/10.1039/b710800a
21. Xu, H.B., Chen, X.M., Zhang, Q.S., Zhang, L.Y., Chen, Z.N.: Fluoride-enhanced lanthanide luminescence and white-light emitting in multifunctional Al_3Ln_2 (Ln = Nd, Eu, Yb) heteropentanuclear complexes. Chem. Commun. **2**, 7318–7320 (2009). https://doi.org/10.1039/b912474h
22. Wang, G.E., Xu, G., Wang, M.S., Cai, L.Z., Li, W.H., Guo, G.C.: Semiconductive 3-D haloplumbate framework hybrids with high color rendering index white-light emission. Chem. Sci. **6**, 7222–7226 (2015). https://doi.org/10.1039/c5sc02501j
23. Ma, M.L., Qin, J.H., Ji, C., Xu, H., Wang, R., Li, B.J., Zang, S.Q., Hou, H.W., Batten, S.R.: Anionic porous metal-organic framework with novel 5-connected vbk topology for rapid adsorption of dyes and tunable white light emission. J. Mater. Chem. C **2**, 1085–1093 (2014). https://doi.org/10.1039/c3tc32001d
24. Devi, R., Boddula, R., Tagare, J., Kajjam, A.B., Singh, K., Vaidyanathan, S.: White emissive europium complex with CRI 95%: butterfly vs. triangle structure. J. Mater. Chem. C **8**, 11715–11726 (2020). https://doi.org/10.1039/d0tc02724c
25. Chao, Y.C., Cheng, K.P., Lin, C.Y., Chang, Y.L., Ko, Y.Y., Hou, T.Y., Huang, C.Y., Chang, W.H., Lin, C.A.J.: Non-toxic gold nanoclusters for solution-processed white light-emitting diodes. Sci. Rep. **8**, 1–9 (2018). https://doi.org/10.1038/s41598-018-27201-x

26. Wang, T., Chirmanov, V., Chiu, W.H.M., Radovanovic, P.V.: Generating tunable white light by resonance energy transfer in transparent dye-conjugated metal oxide nanocrystals. J. Am. Chem. Soc. **135**, 14520–14523 (2013). https://doi.org/10.1021/ja407013z
27. Chirmanov, V., Stanish, P.C., Layek, A., Radovanovic, P.V.: Distance-dependent energy transfer between Ga_2O_3 nanocrystal defect states and conjugated organic fluorophores in hybrid white-light-emitting nanophosphors. J. Phys. Chem. C **119**, 5687–5696 (2015). https://doi.org/10.1021/jp512417h
28. Layek, A., Stanish, P.C., Chirmanov, V., Radovanovic, P.V.: Hybrid ZnO-based nanoconjugate for efficient and sustainable white light generation. Chem. Mater. **27**, 1021–1030 (2015). https://doi.org/10.1021/cm504330k
29. Bowers, M.J., McBride, J.R., Rosenthal, S.J.: White-light emission from magic-sized cadmium selenide nanocrystals. J. Am. Chem. Soc. **127**, 15378–15379 (2005). https://doi.org/10.1021/ja055470d
30. Khanna, P.K., Singh, V., Phalswal, P., More, P.V., Hemmer, E., Mishra, Y.K.: Magic-sized CdSe nanoclusters: a review on synthesis and white light potential. Mater. Adv. (2021). https://doi.org/10.1039/d0ma00921k
31. Sapra, S., Mayilo, S., Klar, T.A., Rogach, A.L., Feldmann, J.: Bright white-light emission from semiconductor nanocrystals: by chance and by design. Adv. Mater. **19**, 569–572 (2007). https://doi.org/10.1002/adma.200602267
32. Ding, Y., Chang, Q., Xiu, F., Chen, Y., Liu, Z., Ban, C., Cheng, S., Liu, J., Huang, W.: Zero- and two-dimensional hybrid carbon phosphors for high colorimetric purity white light-emission. Nanoscale **10**, 4189–4193 (2018). https://doi.org/10.1039/c7nr09631c
33. Xie, Z., Yin, Z., Wu, Y., Liu, C., Hao, X., Du, Q., Xu, X.: White light-emitting diodes based on individual polymerized carbon nanodots. Sci. Rep. **7**, 1–9 (2017). https://doi.org/10.1038/s41598-017-12083-2
34. Cui, B., Feng, X.T., Zhang, F., Wang, Y.L., Liu, X.G., Yang, Y.Z., Jia, H.S.: The use of carbon quantum dots as fluorescent materials in white LEDs. Xinxing Tan Cailiao/New Carbon Mater. **32**, 385–401 (2017). https://doi.org/10.1016/S1872-5805(17)60130-6
35. chao Zhao, Y., jun Huang, L., xin Wang, Y., guo Tang, J., Wang, Y., xian Liu, J., Belfiore, L.A., Kipper, M.J.: Synthesis of graphene oxide/rare-earth complex hybrid luminescent materials via π-π stacking and their pH-dependent luminescence. J. Alloys Compd. **687**, 95–103 (2016). https://doi.org/10.1016/j.jallcom.2016.06.100
36. Zhai, Y., Wang, Y., Li, D., Zhou, D., Jing, P., Shen, D., Qu, S.: Red carbon dots-based phosphors for white light-emitting diodes with color rendering index of 92. J. Colloid Interface Sci. **528**, 281–288 (2018). https://doi.org/10.1016/j.jcis.2018.05.101
37. Jlassi, K., Eid, K., Sliem, M.H., Abdullah, A.M., Chehimi, M.M., Krupa, I.: Rational synthesis, characterization, and application of environmentally friendly (polymer–carbon dot) hybrid composite film for fast and efficient UV-assisted Cd2+ removal from water. Environ. Sci. Eur. **32** (2020). https://doi.org/10.1186/s12302-020-0292-z
38. Rani, J.R., Oh, S.I., Jang, J.H.: Raman spectra of luminescent graphene oxide (GO)-phosphor hybrid nanoscrolls. Materials **8**, 8460–8466 (2015). https://doi.org/10.3390/ma8125470
39. Zhai, Y., Zhou, D., Jing, P., Li, D., Zeng, H., Qu, S.: Preparation and application of carbon-nanodot@NaCl composite phosphors with strong green emission. J. Colloid Interface Sci. **497**, 165–171 (2017). https://doi.org/10.1016/j.jcis.2017.03.007
40. Kausar, A.: Polymer/carbon-based quantum dot nanocomposite: forthcoming materials for technical application. J. Macromol. Sci. Part A: Pure Appl. Chem. **56**, 341–356 (2019). https://doi.org/10.1080/10601325.2019.1578614
41. Chen, L., Zheng, J., Du, Q., Yang, Y., Liu, X., Xu, B.: Orange-emissive carbon dot phosphors for warm white light-emitting diodes with high color rendering index. Opt. Mater. **109**, 110346 (2020). https://doi.org/10.1016/j.optmat.2020.110346
42. Zhang, X., Zhang, W., Li, Y., Li, C.: Hybrid luminescent materials of graphene oxide and rare-earth complexes with stronger luminescence intensity and better thermal stability. Dyes Pigm. **140**, 150–156 (2017). https://doi.org/10.1016/j.dyepig.2017.01.019

43. Madhu, M., Chen, T.H., Tseng, W.L.: White-light emission of single carbon dots prepared by hydrothermal carbonization of poly(diallyldimethylammonium chloride): applications to fabrication of white-light-emitting films. J. Colloid Interface Sci. **556**, 120–127 (2019). https://doi.org/10.1016/j.jcis.2019.08.049
44. Joseph, J., Anappara, A.A.: White light emission of carbon dots by creating different emissive traps. J. Lumin. **178**, 128–133 (2016). https://doi.org/10.1016/j.jlumin.2016.05.051
45. Zhang, Y., Zhuo, P., Yin, H., Fan, Y., Zhang, J., Liu, X., Chen, Z.: Solid-state fluorescent carbon dots with aggregation-induced yellow emission for white light-emitting diodes with high luminous efficiencies. ACS Appl. Mater. Interfaces **11**, 24395–24403 (2019). https://doi.org/10.1021/acsami.9b04600
46. Zhu, J., Shao, H., Bai, X., Zhai, Y., Zhu, Y., Chen, X., Pan, G., Dong, B., Xu, L., Zhang, H., Song, H.: Modulation of the photoluminescence in carbon dots through surface modification: from mechanism to white light-emitting diodes. Nanotechnology **29**, 245702 (9pp) (2018)
47. Yuan, K., Zhang, X., Qin, R., Ji, X., Cheng, Y., Li, L., Yang, X., Lu, Z., Liu, H.: Surface state modulation of red emitting carbon dots for white light-emitting diodes. J. Mater. Chem. C **6**, 12631–12637 (2018). https://doi.org/10.1039/c8tc04468f
48. Kandasamy, G.: Recent advancements in doped/co-doped carbon quantum dots for multi-potential applications C. **5**, 24 (2019). https://doi.org/10.3390/c5020024.
49. Chen, Y.X., Lu, D., Wang, G.G., Huangfu, J., Wu, Q.B., Wang, X.F., Liu, L.F., Ye, D.M., Yan, B., Han, J.: Highly efficient orange emissive graphene quantum dots prepared by acid-free method for white LEDs. ACS Sustain. Chem. Eng. **8**, 6657–6666 (2020). https://doi.org/10.1021/acssuschemeng.0c00106
50. Yang, Y., Liu, Z., Chen, D., Gu, B., Gao, B., Wang, Z., Guo, Q., Wang, G.: Multifunctional N-doped graphene quantum dots towards tetracycline detection, temperature sensing and high-performance WLEDs. J. Photochem. Photobiol. A **405**, 112977 (2021). https://doi.org/10.1016/j.jphotochem.2020.112977
51. Luo, Z., Qi, G., Chen, K., Zou, M., Yuwen, L., Zhang, X., Huang, W., Wang, L.: Microwave-assisted preparation of white fluorescent graphene quantum dots as a novel phosphor for enhanced white-light-emitting diodes. Adv. Func. Mater. **26**, 2739–2744 (2016). https://doi.org/10.1002/adfm.201505044
52. Sun, C., Guo, Y.H., Yuan, Y., Chu, W.X., He, W.L., Che, H.X., Jing, Z.H., Yue, C.Y., Lei, X.W.: Broadband white-light emission in one-dimensional organic-inorganic hybrid silver halide. Inorg. Chem. **59**, 4311–4319 (2020). https://doi.org/10.1021/acs.inorgchem.9b03139
53. Mosca, M., Macaluso, R., Crupi, I.: Hybrid inorganic-organic white light emitting diodes. In: Polymers for Light-Emitting Devices and Displays, pp. 197–262 (2020). https://doi.org/10.1002/9781119654643.ch8.
54. Kadim, A.M.: Hybrid white light emitting devices (HWLEDs) from organic polymer and PbS nanocrystals by multiple excitons (2021). https://doi.org/10.2478/msp-2020-0066
55. Chou, C.H., Yang, C.H., Hsu, C.S., Chen, T.M.: Hybrid white-light emitting-LED based on luminescent polyfluorene polymer and quantum dots. J. Nanosci. Nanotechnol. **7**, 2785–2789 (2007). https://doi.org/10.1166/jnn.2007.622
56. Pallavi, P., Bandyopadhyay, S., Louis, J., Deshmukh, A., Patra, A.: A soluble conjugated porous organic polymer: efficient white light emission in solution, nanoparticles, gel and transparent thin film. Chem. Commun. **53**, 1257–1260 (2017). https://doi.org/10.1039/c6cc08903h
57. Fang, X., Roushan, M., Zhang, R., Peng, J., Zeng, H., Li, J.: Tuning and enhancing white light emission of II–VI based inorganic-organic hybrid semiconductors as single-phased phosphors. Chem. Mater. **24**, 1710–1717 (2012). https://doi.org/10.1021/cm203137r
58. Muhamad Sarih, N., Myers, P., Slater, A., Slater, B., Abdullah, Z., Tajuddin, H.A., Maher, S.: White light emission from a simple mixture of fluorescent organic compounds. Sci. Rep. **9**, 1–8 (2019). https://doi.org/10.1038/s41598-019-47847-5

Synthesis of Phosphorus-Based Phosphors

Vasile Simulescu, Simona Funar-Timofei, Vlad Chiriac, and Gheorghe Ilia

Abstract The present chapter describes phosphorus-based phosphor compounds focused especially, on their synthesis, properties and applications. One of the main properties of phosphor materials is the photoluminescence. The phosphorus-based phosphors have already many applications in medicine (imaging techniques) and also in high power light-emitting diodes (LEDs) as light source for illumination or plant growth, field emission displays (FEDs), cathode ray tubes (CRT), X-ray detectors, projection televisions (PTV), fluorescent lamps, laser technologies, plasma display panels (PDP), ultraviolet-visible photocatalysts or temperature sensing, and so on. The LEDs technology significantly reduced the energy consumption for electric lighting. By using novel phosphor compounds, high emission-efficient fields in displays and UV devices are already produced. On the last two decades the importance and therefore the interest for those compounds increased significantly. While most of them are synthesized via the classic solid-state method, in the last years other synthesis routes developed also, as for instance the combustion method, the sol–gel method, the precipitation method, the hydrothermal method, ultrasonic spray pyrolysis, extraction pyrolytic technique, hydrolysis, and decomposition.

1 Introduction

Phosphors are used daily in our life most commonly as light source for interior illumination or for displays. The interest for phosphorus-based phosphors compounds increased in the last decades, mainly due to their applications in modern medicine

V. Simulescu · S. Funar-Timofei · G. Ilia (✉)
"Coriolan Dragulescu" Institute of Chemistry, 24 M. Viteazu Bvd., 300223 Timisoara, Romania
e-mail: ilia@acad-icht.tm.edu.ro

S. Funar-Timofei
e-mail: timofei@acad-icht.tm.edu.ro

V. Simulescu · V. Chiriac · G. Ilia
Faculty of Chemistry Biology and Geography, West University Timisoara, 16 Pestalozzi Str., 300115 Timisoara, Romania

© Springer Nature Switzerland AG 2022

K. Upadhyay et al. (eds.), *Hybrid Phosphor Materials*, Engineering Materials,
https://doi.org/10.1007/978-3-030-90506-4_5

and in laser or light emitting diodes (LEDs) technologies. Such compounds are usually used for example as red-light sources in displays. In the recent years, liquid crystal displays (LCD) started to be replaced by LEDs. Moreover, the white light emitting diodes (WLEDs) are now used to substitute the traditional incandescent lamps. Usually, W-LED represents the combination of a yellow emitting phosphor compound with a blue LED chip. In this way, the yellow light from the phosphor is mixed with the blue light from the LED chip, resulting in a white light emission.

Phosphorus-based phosphors may contain phosphates and in general rare-earth metal ions. As host, phosphates offer several advantages: low price, easy synthesis, and high thermal, chemical and physical stability. The luminescence properties of phosphors are determined, among others, by the crystal matrix. The phosphate-based phosphors have excellent luminescent, dielectric, semiconducting, catalytic, magnetic, fluorescent and ion-exchange properties. Such luminescent materials are generally obtained by doping rare-earth metals (mostly lanthanide ions) into a crystalline structure as host. The rare-earth elements are considered the 15 lanthanides and also scandium (Sc) and yttrium (Y). Both, scandium and yttrium have different electronic and magnetic properties than lanthanides, but similar chemical properties. Moreover, Sc and Y are metals found in rare-earth minerals, together with lanthanides. On the other hand, lanthanide elements (sometime referred as Ln) are the transitional metals from lanthanum (La) to lutetium (Lu). They are called lanthanides because all the elements in the series are chemically similar to lanthanum (La). In general lanthanides form trivalent cations (europium for instance can form both, divalent and trivalent ions). Usually lanthanides are found in rare-earth minerals together with thorium (Th), an actinide element [1–19].

As we already mentioned, the phosphorus-based phosphors containing phosphates and rare-earth metals, are very interesting materials for many important applications in modern technologies, due to their light emissions. The spectra of their emissions can be modified and controlled by the method of synthesis, host, dopant ions, and ratio of the used reagents, reaction conditions and synthesis environment. The most used method for the synthesis of phosphorus-based phosphors are the solid-state synthesis, the combustion method, the aqueous solutions techniques (sol–gel, co-precipitation and hydrothermal methods), and the molten salts method [1–19]. The sol–gel, co-precipitation and hydrothermal syntheses are so-called wet chemical methods. In comparison with the solid-state syntheses, the advantages of aqueous solution technologies are that they require mild conditions. Moreover, properties as size, morphology, homogeneity and purity of products, could be easily controlled. Very rarely, phosphors were synthesized in melts (alkali metal chlorides and nitrates, boron oxide) [20].

In the preparation of phosphate-based phosphors by using the solid-state synthesis, the initial reagents are salts (in general nitrates or carbonates, but also chlorides or oxides of elements forming the cationic part of the compound), and ammonium hydrogen and dihydrogen phosphates. At high temperature, the salts are decomposed [21–24]. On the other hand, the sol–gel method takes place in mild conditions and consists in mixing certain amounts of aqueous salt solutions of elements forming

the cationic part with a phosphorus-containing reagent, followed by the coagulation of the formed sol [25–29]. In addition, several procedures were developed by replacing or adding steps of the process, as follows: introduction of salting-out agents (for example alcohols), or organic complexants [30–34]. The Pechini method [31] is a version of the sol–gel synthesis, based on the ability of tricarboxylic acids to form chelate complexes with cations, and to enter in polycondensation or esterification reactions [29–31, 34–36]. In general for Pechini sol–gel method, citric acid is commonly used as tricarboxylic acid [29–31]. The hydrothermal method is another synthetic route developed for the synthesis of phosphorus-based phosphors. It allows synthesizing crystal phosphates in an autoclave. The method of synthesis determines the structure, composition, particle size and light emissions of the obtained phosphors. All of these methods commonly used nowadays for the synthesis of phosphors, will be described further in details. Once obtained, the phosphorus-based phosphors compounds could be analyzed by employing several methods, as XRD, SEM, TEM, TG/DTG, photoluminescence excitation (PLE), photoluminescence (PL) spectroscopy, energy dispersive spectroscopy (EDS), fluorescence lifetime measurements and so on [37–41].

2 Solid-State Synthesis

The solid-state synthesis used for obtaining phosphorus-based phosphors compounds became already a classic method in this field [1, 21–24, 34, 42–65]. The solid-state synthesis in almost all cases requires a high temperature. It is still one of the most used in the fields of phosphors. In general, during the solid-state synthesis of phosphors, the mixture of the used reagents is heated at an elevated temperature for several hours, and then the reaction mixture is cooled naturally at room temperature and subsequently heated again at 900–1200 °C. Among the rare-earth (RE) elements, on solid-state synthesis of phosphorus-based phosphors, europium (Eu), terbium (Tb), samarium (Sm), dysprosium (Dy), holmium (Ho), praseodymium (Pr), cerium (Ce) and ytterbium (Yb) are the most used as dopant ions.

The phosphorus-based phosphors synthesized by using the solid-state method in the last decades have applications in LEDs and laser technologies, and also in the field of radiation dosimetry. Currently Al_2O_3:C is still one of the most used phosphor for optically stimulated luminescence (OSL) dosimetry. Due to its advantages (efficiency, possibility of multiple readout, simpler instrumentation, it requires no heating, fast resetting of the dosimeter and so on) OSL became during the recent years one of the most studied techniques for radiation dosimetry. In order to replace Al_2O_3:C, new phosphors $LiMgPO_4$ (LMP) containing different dopants, as terbium (Tb), europium (Eu) and samarium (Sm), were synthesized by using the solid-state method [43–47]. The development of new $LiMgPO_4$:Tb,B based dosimeter systems has been reported in [43, 47]. Lithium magnesium phosphate ($LiMgPO_4$) phosphors, doped with terbium and boron, synthesized by solid-state method, are of great interest for optically stimulated luminescence (OSL) dosimetry, because such compounds

offer linearity over a range of nine orders of magnitude and also an excellent sensitivity. The OSL signal of $LiMgPO_4$:Tb,B phosphors decreased with only 15% from its initial OSL intensity, after a long period of using [43].

The other main applications of phosphorus-based phosphors are for LEDs and laser technologies. A special category of phosphate luminophores synthesized by solid-state method is the class of compounds calcium containing. Many researchers focused on their synthesis on recent years [48–59]. Zhang et al. [48] proved that potassium calcium phosphate ($KCaPO_4$) doped with europium (Eu) emits green light. In another report, this phosphor co-doped with Eu, Tb and Mn showed a white light emission under ultra-violet excitation [49, 50]. Malik et al. [51] prepared by the conventional solid-state method, the phosphor $KCaPO_4$:Dy doped with dysprosium at different concentrations of the dopant element, ranging from 0.1 to 0.4 mol%. The starting reagents K_2CO_3, $CaCO_3$, NH_6PO_4 and dysprosium chloride ($DyCl_3$) were mixed and heated in two steps: first at 650 °C for 6 h, and subsequently at 950 °C for 10 h. The Dy^{3+} concentration influenced both, the thermoluminescence (TL) and the photoluminescence (PL) intensities. Under UV irradiation, the sample synthesized with 0.2 mol% Dy^{3+} concentration showed the maximum TL intensity at 100 °C, a relatively low temperature [51]. Hu et al. [52] also synthesized new phosphors containing phosphorus and calcium, by using the solid-state method. They have used $CaCO_3$, $Ca(H_2PO_4)_2{\cdot}H_2O$ and Eu_2O_3 as reagents. The obtained mixture was placed into an alumina crucible and sintered in a tube furnace for 5 h at different temperatures ranging from 1100 to 1450 °C. After firing, the obtained sample of $Ca_4(PO_4)_2O{:}Eu^{2+}$ were cooled to room temperature and ground into fine powders. The synthesized compound was a multi-color emitting phosphor [52]. By using the solid-state method, also holmium (Ho) and praseodymium (Pr) doped calcium borophosphate (CBP) phosphors were prepared [53]. $CaCO_3$, H_3BO_3, $NH_4H_2PO_4$, Ho_2O_3 and Pr_6O_{11} were mixed together and first heated at 650 °C for 2 h in porcelain crucible. Then, the obtained mixture was cooled to room temperature, and afterwards it was heated again at 950 °C for 4 h, in an electrical furnace. The phosphor material was obtained as powder and further characterized by several techniques (XRD, SEM, IR, NMR and PL emission spectra). The concentrations of holmium (Ho) and praseodymium (Pr) were modified from 0.2 to 1 mol%. The PL measurements showed that CBP phosphors doped with 0.6 mol% of Ho^{3+} and Pr^{3+} could be used as green and red phosphor. From SEM images it was observed that the particle size increased with the Ho^{3+} and Pr^{3+} concentration, from few microns to several tens of microns. Therefore, the luminescence properties of holmium (Ho) and praseodymium (Pr) doped calcium borophosphate (CBP) phosphors was strongly influenced by the particle size, shape, concentration and crystallinity. The obtained doped calcium borophosphate are suitable to be used for WLEDs applications [53].

Raja et al. [54] synthesized by using the solid-state method, novel Cu^{2+}-doped $Li_2CaAl_4(PO_4)_4F_4$ nanophosphor. The reagents Li_2CO_3 and $AlF_3{\cdot}3H_2O$ were grounded in a mortar for 30 min and then $CaCO_3$ and $(NH_4)_2HPO_4$ were added and mixed together for 1 h. Afterwards, CuO was added, and then the obtained mixture was heated in a three-step process: at 650 °C for 8 h, at 700 °C for 4 h and at 750 °C for 2 h. Therefore the Cu^{2+}-doped $Li_2CaAl_4(PO_4)_4F_4$ nanophosphor was obtained

without using lanthanides. It showed four main emission peaks, as follows: violet at 413 nm (very strong), blue at 474 nm, green at 512 nm and orange at 618 nm (relatively weak) [54]. Moreover, a series of Sm^{3+} or Eu^{3+} doped $Ca_3(PO_4)_2$ and Sm^{3+}–Eu^{3+} co-doped $Ca_3(PO_4)_2$ phosphors were prepared in the work published by Wang et al. [55] by using the high temperature solid-state method. They have observed that under excitation at 403 nm, the obtained $Ca_3(PO_4)_2$:Sm^{3+} emits orange-red light. The peak with the highest intensity was found at 602 nm [55]. Also, a novel single-composition white-emitting phosphor $Ca_3(PO_4)_2$:Dy^{3+} has been synthesized by a high temperature solid-state reaction in the work published by Zhang et al. [56]. The luminescent properties were changed by the presence of the charge compensators effect of $Ca_3(PO_4)_2$:Dy^{3+}. Due to the strong excitation bands observed in the wavelength region of 350–410 nm, $Ca_3(PO_4)_2$:Dy^{3+} could be excited by NUV LED-chips [56].

The novel luminescence compounds with apatite structure represent another class of phosphors synthesized by using the high temperature solid-state method [57–59]. Liang et al. [57] obtained $Ca_9La(PO_4)_5(SiO_4)Cl_2$:x$Eu^{2+}$ phosphor materials (abbreviated as CLPSCl:Eu^{2+}). The starting reagents $CaCO_3$, SiO_2, $(NH_4)_2HPO_4$, NH_4Cl, La_2O_3, and Eu_2O_3 were mixed in an agate mortar and further heated at 1250 °C under flowing gas (5% H_2; 95% N_2). After firing, the final products were cooled down to room temperature. The product showed an emission peak in the blue region. Due to their high thermal stability those compounds could be potentially used as blue-emitting phosphor for applications in WLEDs [57]. Another apatite-type $Ba_4Gd_3K_3(PO_4)_6F_2$:Eu^{2+} phosphor (abbreviated as BGKPOF:xEu^{2+}) was developed in the work of Leng et al. [58] via using the solid-state method. The BGKPOF:xEu^{2+} phosphors cover almost the whole visible light spectrum. This makes them very useful for potential applications on WLEDs. Such devices can be fabricated by the deposition of BGKPOF:0.06Eu^{2+} and red $CaAlSiN_3$:Eu^{2+} phosphors, on 395 nm LED chip [58]. Also by using solid-state synthesis, samarium (III) doped fluorapatite phosphors La_6-x$Ba_4(SiO_4)_6F_2$:xSm^{3+} (abbreviated as LBSF:Sm^{3+}) were obtained in the work published in [59]. The solid-state synthesis was performed at 750 °C for 1 h, and the obtained precursor was then heated at 1350 °C for 4 h. The samples were further analyzed by X-ray diffraction, SEM and photoluminescence (PL) spectroscopy. The obtained LBSF:Sm^{3+} phosphor can be excited in the range from 300 to 500 nm, having potential application for the near ultraviolet white light emitting diodes (NUV LEDs). The PL measurements showed that the emission spectrum contained four peaks characteristic for Sm^{3+} ions, at 565, 603, 650 and 711 nm [59].

Malysa et al. [60] found out that Cr^{3+}-doped $Sr_8MgLa(PO_4)_7$ phosphor (abbreviated as SMLP) is a luminescent converter for high power near infrared (NIR) LEDs, with potential applications in NIR spectroscopy. The microcrystalline powders of SMLP doped with different chromium concentration (up to a maximum of 15%) were synthesized for the first time by using solid-state method. A mixture of $SrCO_3$, MgO, La_2O_3, $NH_4H_2PO_4$ and Cr_2O_3 was heated at 1300 °C for 6 h. The novel phosphor material showed a near infrared emission from 700 to 1000 nm (with a maximum at 848 nm), under excitation in the blue/cyan region. The increasing concentration of chromium shifted the emission light to red, and also increased its intensity [60]. Also

by using the conventional solid-state method, Chen et al. [61] successfully synthesized an orange-red emitting phosphor, doped with samarium (Sm). The reagents Na_2CO_3, $SrCO_3$, $(NH_4)_2HPO_4$ and Sm_2O_3 were mixed in a ball mill for 3 h, with zirconia balls and ethanol. The obtained mixture was then heated for 3 h at 1200 °C. After cooling and drying, the crystalline structure of $NaSrPO_4:Sm^{3+}$ phosphor was identified by using XRD (the average particle sizes were in the range of 5–10 μm) [61].

Han et al. [62] developed a solid-state method for the synthesis of a series of novel white-emitting phosphors based on Dy^{3+} doped strontium tetraphosphate ($Sr_3P_4O_{13}:Dy^{3+}$). The starting reagents $SrCO_3$, $NH_4H_2PO_4$ and Dy_2O_3 were mixed for 30 min. Afterwards this mixture was heated for 6 h at 900 °C, and then the obtained sample was cooled at room temperature. It was further characterized by X-ray diffraction, photoluminescence excitation/emission spectra, decay curves and fluorescence measurements. The obtained $Sr_3P_4O_{13}:Dy^3$ phosphors showed a white light emission under NUV light excitation in the region of 300–400 nm. Those results suggested that $Sr_3P_4O_{13}:Dy^{3+}$ phosphors might be a potential candidate for applications on NUV-based white light-emitting diodes (W-LEDs) [62]. In the last decade, also Eu^{3+}-doped phosphate red phosphors were found to be potential candidates for applications in W-LEDs. Gao et al. [63] synthesized co-doped $NaMgPO_4:Eu^{3+},Al^{3+}$ phosphors by using the high temperature solid-state method. In general Eu^{3+}-doped phosphates are characterized by four emission peaks, at 590, 616, 650 and 690 nm.

One of the main issues of the solid-state method could be that a high temperature is required. Zhu et al. [64] and Xia et al. [65] developed solid-state syntheses of phosphor materials, at relatively lower temperatures. In the work published in [64] novel luminescent $Li_2NaBP_2O_8$ phosphor doped with Eu^{3+} was synthesized. The mixture of Eu_2O_3, $NH_4H_2PO_4$, H_3BO_3, Na_2CO_3 and Li_2CO_3 was first heated at 400 °C for 5 h and then sintered at 600 °C for 24 h in air. After that, the reaction mixture was cooled at room temperature. The data indicated that the obtained $Li_2NaBP_2O_8:Eu^{3+}$ is an orange-red emitting phosphor, with potential applications for warm WLEDs [64].

Xia et al. [65] developed a solid-state method for obtaining a precursor of phosphorus-based phosphors, at a temperature as low as 60 °C. They have used lanthanum (La), cerium (Ce), terbium (Tb) and ytterbium (Yb). The $(NH_4)_3PO_4{\cdot}3H_2O$ powder was introduced into a mixture of $La(NO_3)_3{\cdot}6H_2O$:$Ce(NO_3)_3{\cdot}6H_2O$:$Tb(NO_3)_3{\cdot}6H_2O$:$Yb(NO_3)_3{\cdot}6H_2O$, at 17:1:1:1 molar ratio. Polyethylene glycol-400 (PEG-400) was further added as surfactant. Then, the reaction environment became wet and a paste formed very fast. The resulted mixture was kept at 60 °C for 10 h and subsequently washed with water and ethanol. The obtained precursor $La_{0.85}Ce_{0.05}Tb_{0.05}Yb_{0.05}PO_4$ was dried at 90 °C for 5 h and further calcinated at 800 °C for 4 h. The phosphate-based phosphor $LaPO_4:Ce^{3+},Tb^{3+},Yb^{3+}$ was obtained in the last step of the solid-state synthesis, from the thermal decomposition of the precursor. The PL and PLE spectra of the synthesized co-doped phosphor showed several emissions, at 487, 543, 563 and 587 nm. This proved that $LaPO_4:Ce^{3+},Tb^{3+},Yb^{3+}$ is a yellowish-green emitting phosphor [65].

3 Combustion Synthesis

The growing interest from the last decades for phosphor materials was mainly determined by the rapid developments of a variety of displays and other related illumination technologies, based on such compounds. For general lighting applications, such as UV-LEDs or WLEDs, the various hosts of photoluminescent (PL) materials play a vital role. The used hosts include silicates, phosphates, aluminates, aluminosilicates, nitrides, borates and so on [66, 67]. Among all of these, phosphates were proved to be excellent hosts for preparing phosphors, due to the fact that they offer many advantages as good chemical stability, high thermal stability, high luminescent brightness, and easy preparation and incorporation of the dopant ions. While the most of the phosphor materials based on phosphates are synthesized by the solid-state method, as already described here, other synthetic routes were also developed. One of these methods is the combustion synthesis [68–78]. It is commonly called the solution combustion method and represents a promising option for the synthesis of high quality phosphors. This method is relatively fast and particularly useful for the production of ultra-fine powders, because the starting reagents are mixed in liquid phase. In addition, a fuel is required. The fuel is responsible for the ignition, when the solution containing the reagents is heated. In most of the cases urea is used as fuel.

First, the mixture of reagents is heated up to 50 °C, to obtain a homogeneous solution. This solution is then heated more, up to 500–600 °C, or sometime even up to 800 °C. The solution starts to boils and subsequently dehydrates. Afterwards, at a certain time, it spontaneous ignites. After the ignition occurred, the reaction environment is naturally cooled to room temperature and a fine powder is obtained. This is the precursor of the phosphor and it will be subsequently annealed at 900–1200 °C for 3–5 h. In general the phosphates-based phosphors synthesized by using the combustion method, are doped or co-doped with europium (Eu), dysprosium (Dy), yttrium (Y), gadolinium (Gd) and terbium (Tb) [68–78].

A series of different alkaline earth-based sodium-ortho phosphate ($NaMPO_4$, where M is Mg, Ca, Sr and Ba) phosphors, doped with 1 mol% Eu^{3+}, were synthesized by solution combustion method in the work published in [68]. The starting reagents $Mg(NO_3)_2{\cdot}6H_2O$, $Ca(NO_3)_2{\cdot}6H_2O$, $Sr(NO_3)_2$, $Ba(NO_3)_2$, $NH_4H_2(PO_4)$, $NaNO_3{\cdot}9H_2O$ and urea ($NH_2–CO–NH_2$) as fuel, were mixed by using water as solvent. The metal nitrates were used as oxidizers. The obtained aqueous solution was transferred to a furnace and heated up to 600 °C. The resulted fluffy product was afterwards cooled down to room temperature, and the samples were ground again until the fine powders were obtained. The synthesized phosphor materials were further investigated by using XRD, FT-IR, field emission scanning electron microscope (FE-SEM), photoluminescence excitation (PLE) and photoluminescence (PL) spectroscopy. The absorption peaks observed in FT-IR spectra confirmed the presence of water of crystallization. Moreover, it showed the stretching and bending vibration characteristic for phosphate and for metal–oxygen bonds. The PL properties of the obtained phosphors were significantly influenced by the temperature used

for calcination and by the different alkaline metal ions. For example, the PL spectra of $NaCaPO_4:Eu^{3+}$ showed a strong red emission at the wavelength of 611 nm. The PL results of Balakrishna et al. suggested that the $NaCaPO_4:Eu^{3+}$ phosphors can be used for LED applications [68].

Bedyal et al. [69, 70] studied the effects of cationic substitution on the luminescence behavior of Dy^{3+}-doped orthophosphates with general formula $A_3B(PO_4)_2$ (where A = Na,K; B = Y,La) phosphors. The cation substituted dysprosium (Dy^{3+}) doped orthophosphate phosphors were synthesized by using the solution combustion method, as follows: KNO_3, $NaNO_3$, $Y(NO_3)_3{\cdot}6H_2O$, $La(NO_3)_3{\cdot}6H_2O$, $NH_4H_2PO_4$ and $Dy(NO_3)_3{\cdot}xH_2O$ as reagents, and urea as fuel, were mixed in an aqueous solution for 2 h at 50 °C, until the obtained solution became transparent. This solution was transferred to an alumina crucible and heated at 550 °C. Initially the solution boiled and becomes thicker due to its dehydration. At a certain moment the combustion occurred and a foamy product was obtained. This product was then heated at 800 °C for 3 h. Bedyal et al. [70] used the same combustion method described above, for the synthesis of $K_3La(PO_4)_2:Pr^{3+}$ phosphors for WLEDs applications (the optimal concentration of praseodymium was found to be 1.2 mol%). The PL spectra proved that under UV-excitation, the Dy^{3+}-doped orthophosphates exhibited three emissions, at: 481 nm (blue region), 575 nm (yellow region) and 668 nm (red region). Those emissions are due to the 4f–4f transition of the Dy^{3+} ions [69]. The Dy^{3+} ions showed different luminescence behavior, in different host lattices, between blue and yellow regions. Moreover, the co-doped phosphor materials containing both Dy^{3+} and Eu^{3+} combine the effects of these two lanthanides. The combustion synthesis of $K_3Al_2(PO_4)_3:Dy^{3+},Eu^{3+}$ phosphors was described and published by Shinde et al. [71]. First they have observed that the singly doped $K_3Al_2(PO_4)_3:Dy^{3+}$ phosphor exhibited emissions in the blue and yellow regions, and in the same time that the $K_3Al_2(PO_4)_3:Eu^{3+}$ phosphor showed an emission in the red region. Further they proved from PL spectrum, that the phosphor $K_3Al_2(PO_4)_3$ co-doped with Dy^{3+} and Eu^{3+} gives a combination of the blue, yellow and red light emissions. This can be applied to produce white light, so these compounds synthesized by using the combustion method could have potential applications for W-LEDs too [71].

Divalent europium ion (Eu^{2+}) is also an important activator for luminescent materials. Wanjun et al. [72, 73] synthesized by using the combustion method, novel Eu^{2+} doped, Mn^{2+}-doped and Eu^{2+}/Mn^{2+} co-doped $Na_2BaMgP_2O_8$ phosphors. The starting reagents $NaH_2PO_4{\cdot}2H_2O$, $Ba(NO_3)_2$, $Mg(NO_3)_2{\cdot}6H_2O$ and urea as fuel, were mixed together. Further Eu_2O_3 and $MnCO_3$ were dissolved in HNO_3 and added into the reaction mixture. The obtained solution was heated at 600 °C. Its boiling was followed by the decomposition with the evolution of large amounts of gases. Therefore spontaneous ignition occurred and the reaction was finished in only 5 min. The obtained phosphor was then heated slowly at 900 °C for 3 h, under a reducing atmosphere (5% H_2; 95% N_2) [72]. The excitation spectrum showed a very broad band in the NUV region. This is due to the f–d transition of Eu^{2+} ions and also due to the host absorption. $Na_2BaMgP_2O_8:Eu^{2+}$ phosphor showed a blue emission of high intensity, under 350 nm excitation, mainly due to the transition of the Eu^{2+} ion from the 5d excited state to the 4f ground state. No emission peaks characteristic for Eu^{3+} were

observed in the PL spectra. The luminescence intensity increased with increasing the Eu^{2+} concentration. The $Na_2BaMg(PO_4)_2$:Mn^{2+} phosphor, when excited by UV radiation, it showed an emission peak at the wavelength of 614 nm. The co-doped phosphor $Na_2BaMg(PO_4)_2$:Eu^{2+},Mn^{2+} showed a blue emission and a red emission as well, which are mainly determined by the Eu^{2+} occupying the Ba^{2+} sites and by the Mn^{2+} occupying the Mg^{2+} sites respectively. On those phosphors, Eu^{2+} ion can transfer its absorbed energy fully or partly to Mn^{2+}, obtaining a red or an orange light emission. The efficiency of the energy transfer from Eu^{2+} to Mn^{2+} was proved by the excitation and emission spectra, and also by the luminescence decay curves. Therefore, the relative intensities of blue and red emissions could be tuned by modifying the Eu^{2+} and Mn^{2+} contents, making the co-doped $Na_2BaMg(PO_4)_2$:Eu^{2+},Mn^{2+} a promising double color emitting phosphor [72]. Shanshan et al. [74] also used Eu^{2+} and Mn^{2+} to obtain phosphate-based phosphors by the combustion synthesis. The singly doped Eu^{2+} and Mn^{2+}, and the Eu^{2+}/Mn^{2+} co-doped $Mg_{21}Ca_4$-$Na_4(PO_4)_{18}$ phosphors, were synthesized by using this synthetic route. The Eu^{2+} activated sample showed an intense blue emission under UV-light excitation (360 nm), and in the same time the Eu^{2+}/Mn^{2+} co-doped $Mg_{21}Ca_4Na_4(PO_4)_{18}$ sample exhibited a blue emission together with a red emission [74], as showed in the work published in [72]. The Eu^{2+} ion may act as an efficient sensitizer, transferring energy to Mn^{2+} [75]. The aqueous solution of the initial reagents $NaNO_3$, $Ca(NO_3)_2{\cdot}4H_2O$, $Mg(NO_3)_2{\cdot}6H_2O$ and $NH_4H_2PO_4$, was introduced into a muffle furnace at 600 °C for 5 min. The obtained precursors were further annealed at 900 °C for 3 h to form the crystalline phosphates-based phosphors [74].

Min et al. [73] synthesized for the first time Eu^{2+} doped $Ca_4Mg_5(PO_4)_6$ phosphors by using the combustion technique. For the combustion synthesis, Eu_2O_3 was dissolved in HNO_3 to obtain its corresponding nitrate. $NH_4H_2PO_4$, $Ca(NO_3)_2{\cdot}4H_2O$ and $Mg(NO_3)_2{\cdot}6H_2O$ were used as sources for P, Ca and Mg, and urea was used as the fuel. They have observed that for a complete combustion, the oxidizer/fuel ratio should be equal to 1. The aqueous solution of the used reagents was transferred to a porcelain crucible and introduced into a muffle furnace at 600 °C. The boiling solution, after the dehydration, spontaneous ignited. The duration of the reaction was around 5 min, as in the previous described syntheses which used also the combustion technique. Therefore this method offers the advantage of a fast synthesis. Subsequently, the product was slowly cooled to room temperature in the self-generating atmosphere, after the combustion synthesis was finished. The foamy precursor was milled and afterwards annealed at 900 °C for 5 h. $Ca_4Mg_5(PO_4)_6$:Eu^{2+} phosphor was obtained with very good yield, almost quantitatively, as a crystalline and colorless powder. The PL spectrum of the $Ca_4Mg_5(PO_4)_6$:Eu^{2+} phosphor showed an intense blue emission under UV excitation [73].

Even more interesting is to synthesize phosphorus-based phosphors containing yttrium (Y), a rare-earth element which does not belongs to lanthanides. Still, yttrium is a transitional metal with similar chemical properties as lanthanides. It is found on rare-earth minerals, in combination with lanthanides, but never as free element. Park et al. [76] used yttrium (Y) together with europium (Eu) and gadolinium

(Gd), in order to obtain co-doped phosphorus-based phosphors by the combustion synthesis. This time citric acid was used as fuel. The aqueous solutions of $Y(NO_3)_3{\cdot}6H_2O$, $Gd(NO_3)_3{\cdot}5H_2O$, $Eu(NO_3)_3{\cdot}6H_2O$, $Al(NO_3)_3{\cdot}9H_2O$ were used as oxidizers. Gadolinium (Gd) was used for obtaining phosphor materials in other studies [58, 67, 77], but not together with yttrium. NH_4VO_3, $(NH_4)_2HPO_4$ and citric acid were dissolved in water and subsequently used as reducers. This aqueous solution was added to the mixture of the nitrate solution and the molar ratio of the oxidizer to reducer was controlled to be as much as possible close to 1. The reaction environment was dehydrated under heating and a highly viscous gel precursor was formed. At a certain moment, the precursor spontaneously ignited and produced phosphor powders. The synthesized powders were then annealed at 1000 °C for 4 h in air. The obtained phosphor materials synthesized by the combustion method described above showed an intense orange emission [76].

Alkaline earth metal pyrophosphates $M_2P_2O_7$ (M = Ca, Sr, Ba) were proposed for their potential applications as luminescent materials [78–83]. Patel et al. [78] synthesized by the combustion method, rare-earth Tb^{3+}-doped α-$Sr_2(P_2O_7)$ compounds and investigated their thermoluminescence (TL) and photoluminescence (PL) properties. Singly and doubly doped strontium phosphate α-$Sr(PO_3)_2$ was compared with equivalently doped diphosphates α-$Sr_2(P_2O_7)$ and $SrZn(P_2O_7)$. The used reagents $SrCO_3$, $(NH_4)_2HPO_4$ and Tb_4O_7 were mixed with urea, used as fuel. This mixture was annealed at 1200 °C for 3 h, in a muffle furnace in air. After cooling the product at room temperature, the fine powder with crystalline structure was obtained [78]. The PL spectra of the Tb^{3+}-doped α-$Sr_2P_2O_7$ phosphor showed several emissions, at 415, 436, 469, 491, 545 and 584 nm. The highest intensity of the emission was observed at the wavelength of 545 nm. The PL and TL results indicated that the luminescence properties of the Tb^{3+}-doped α-$Sr_2P_2O_7$ phosphor increased with the concentration of Tb^{3+}. The α-$Sr_2P_2O_7$ doped with 5 mol% Tb^{3+} showed an excellent green emission for a given excitation, and therefore it has good potential to be used as a green luminescent material for display systems in solid-state lighting applications [78].

4 Sol–Gel Synthesis

To avoid the high temperatures, many researchers synthesized phosphorus-based phosphors by using the so-called "mild chemistry" methods, as sol–gel and extraction pyrolysis techniques. In comparison with high temperature solid-state synthesis and combustion synthesis, previously described here, the sol–gel technology is a solution-based method by which inorganic or organic–inorganic composite materials are made at relatively low temperature. The sol–gel process was very often used during the last decades for the synthesis of phosphorus hybrid materials [25, 84–87]. The sol–gel method used for the preparation of phosphor materials [26–36, 88–98], includes the version with the introduction of additional organic reagents into the reaction system. By using the sol–gel method, a lot of rare-earth elements were used as dopants for

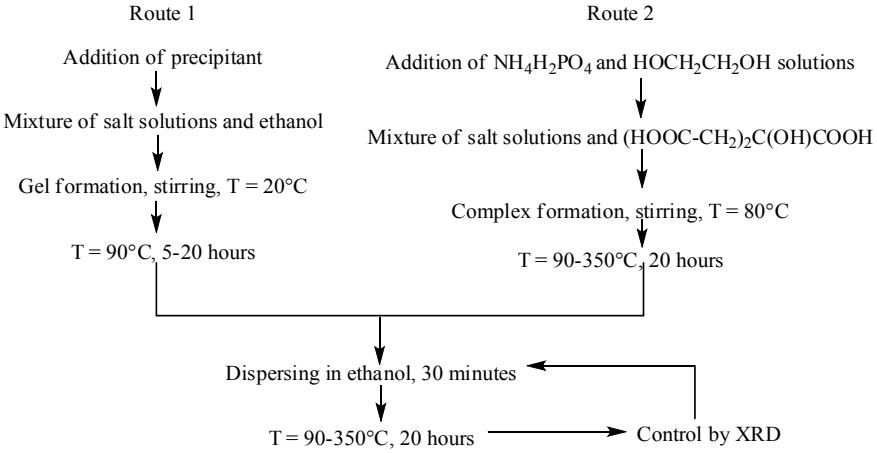

Fig. 1 Scheme of phosphate-based phosphors synthesized by sol–gel method [29]

phosphate-based phosphors synthesis, as europium (Eu), gadolinium (Gd), samarium (Sm), erbium (Er), holmium (Ho), thulium (Tm), lanthanum (La) or cerium (Ce).

In the sol–gel synthesis version with a salting-out agent (Fig. 1, Route 1), stoichiometric ratios were used for the initial solutions of salts, metal salts and precipitants. The obtained gel was further heated at 90 °C for dehydration, and the dry residue was subsequently dispersed in an agate mortar for 30 min. Afterwards the dispersed residue was heated at 600, 800 and 900 °C (sometime up to a maximum temperature of 1100 °C) [29].

The Pechini method [31] is a version of the sol–gel technique, very often used for the synthesis of phosphor compounds. In the Pechini version of the sol–gel method (Fig. 1, Route 2), the initial salt solutions are mixed with an acid. For example, Kanunov et al. [29] used citric acid (CA). First the gel is obtained, and then it is dried by heating at a temperature ranging from 130 to 350 °C. The dry residue is usually dispersed in an agate mortar for around 30 min and subsequently heated at a temperature between 600 and 1100 °C [29]. Phosphors must meet the requirements of microstructure uniformity and optical "purity". Therefore, uniform powder material is needed to synthesize phosphor materials with high quality properties, as required by LEDs applications. The effects of the temperature on the gel formation and on the microstructure of phosphate-based phosphors, were studied and published in the work of Orlova et al. [99].

The modified Pechini method was used to obtain luminescent orthophosphates doped with rare-earth metals, starting from rare-earth nitrates and tripolyphosphate as reagents [89]. The developed Pechini synthesis was based on the ability of the tripolyphosphate anion ($P_3O_{10}^{5-}$) to act both as complexing agent and as orthophosphate precursor. A yellowish polymeric resins was then obtained by heating the aqueous solutions containing RE^{3+} (RE = Y, La, Gd), Eu^{3+}, $P_3O_{10}^{5-}$, citric acid and

ethylene glycol. When heated at different temperatures, the luminescent orthophosphates $YPO_4:Eu^{3+}$, $GdPO_4:Eu^{3+}$ and $LaPO_4:Eu^{3+}$ were obtained by the decomposition of the polymeric resin. Moreover, Filho et al. [89] obtained the deposition of the polymeric precursors on glasses, in order to produce orthophosphate-based thin films, very useful for UV-viz. excitation devices. Such devices could be further used to synthesize phosphorus containing compounds by UV-curing [100–105]. Game et al. [91] also used the Pechini sol–gel method for the synthesis of $LiBaPO_4:Eu^{3+}$ and $LiBaPO_4:Eu^{2+}$ phosphors, both suitable for WLEDs fabrication. The initial reagents $Ba(NO_3)_2$, $LiNO_3$, $(NH_4)H_2PO_4$ and Eu_2O_3 were converted to $Eu(NO_3)_3{\cdot}6H_2O$. The dried precursors were milled and citric acid monohydrated, ethylene glycol and two drops of glacial acetic acid were further added under stirring. The obtained mixture was subsequently heated at 140 °C for 1 h and the gelation started. Afterwards, the mixture was slowly cooled at room temperature and then the obtained gel was again heated up to 350 °C in air. The polymerization took place and the yellowish resin/foam was finally pyrolysed into stunning black foam at 450 °C. The black foam ignited at a temperature of around 600 °C and the pyrolysis was complete after 2 h at 780 °C. The obtained $LiBaPO_4:Eu^{3+}$ phosphor can be reduced to $LiBaPO_4:Eu^{2+}$ by carbo-thermal reduction. The carbo-thermal reduction takes place very slowly, first at 600 °C for 1 h and further at 980 °C for 4 h, in the presence of activated carbon [91]. The Pechini method [31] was proved in this case to be more efficient than the conventional high temperature solid-state synthesis. Under NUV excitation, Eu^{3+} doped orthophosphate showed two intense red emissions at 595 and 615 nm, and in the same time the Eu^{2+} doped orthophosphate showed an intense blue emission at 472 nm [91].

Wu et al. [93] synthesized by using the sol–gel method, Eu^{3+} doped $KCaY(PO_4)_2$ phosphors with crystalline structure. The reagents Eu_2O_3 and Y_2O_3 were dissolved in HNO_3, to obtain their nitrates. $Ca(NO_3)_2{\cdot}4H_2O$, KNO_3 and $(NH_4)_2HPO_4$ were dissolved in water and then mixed under stirring at room temperature with the previously obtained nitrates, by using the molar ratio K:Ca:Y:Eu = 1:1:0.97:0.03. The citric acid and the $(NH_4)_2HPO_4$ were also added to the previously obtained solution. After 30 min, a transparent solution was obtained, which was further dried at 80 °C and the gelation started. The gel was subsequently heated at 400 °C for 3 h and at 800 °C for 4 h in air. Under NUV excitation (392 nm) the synthesized Eu^{3+} doped $KCaY(PO_4)_2$ phosphor showed an intense orange-red emission, at the wavelength of 588 nm. Due to those properties, Eu^{3+}-doped $KCaY(PO_4)_2$ phosphor is suitable to be used for applications in WLEDs [93]. On the other hand, Glorieux et al. [94] used the same sol–gel method to obtain phosphor materials co-doped with Eu^{2+} and Sm^{3+}. They have synthesized singly doped $Ca_{0.5}Zr_2(PO_4)_3:Eu^{2+}$, $Sr_{0.5}Zr_2(PO_4)_3:Eu^{2+}$ and co-doped $Ca_{0.5}Zr_2(PO_4)_3:Eu^{2+},Sm^{3+}$ phosphors by using the sol–gel processes. The luminescence spectra of the doped phosphate-based materials under UV excitation, showed emissions in the range of 425–525 nm. The doped Eu^{2+} and Sm^{3+} phosphates were synthesized by using the sol–gel method, with H_3PO_4 as precipitant. The solution of reagents was heated in steps, at 90, 600 and 800 °C respectively (24 h for each step) [94].

Orlova et al. [95] and Camacho et al. [26] used erbium (Er^{3+}) as dopant for phosphate-based phosphors. In addition to erbium, Camacho et al. [26] added also gadolinium (Gd), ytterbium (Yb), holmium (Ho) and thulium (Tm), by using the Pechini sol–gel method [31]. $(NH_4)_2HPO_4$ and the oxides of the above mentioned rare-earth metals were used as reagents. The oxides Gd_2O_3, Yb_2O_3, Er_2O_3, Ho_2O_3 and Tm_2O_3 were converted into the corresponding nitrates by reacting with HNO_3 at 160 °C. The obtained compounds, after calcination at 1000 °C for 2 h, showed different emission bands function of the used rare-earth metal and function of their concentration, as follows: red emission in the range of 640–690 nm attributed to Er^{3+} and Ho^{3+}, IR emissions at 760 nm due the presence of Ho^{3+} and at 807 nm due to the presence of Tm^{3+}, and green emission attributed to the overlapped bands of Er^{3+} and Ho^{3+}. Camacho et al. also noticed that an increase in the Yb^{3+} concentration enhanced the green emission and in the same time stopped the IR emissions. For example, an increase of Yb^{3+} concentration from 5 to 20 mol% was enough to shift the luminescence from red to green [26].

Kunghatkar et al. [97] synthesized Gd^{3+} activated $CaMgP_2O_7$ phosphor, by using four different synthesis routes: the solid-state reaction method, the sol–gel method, wet chemical and solution combustion method. The PL excitation at 274 nm of the synthesized phosphor materials $CaMgP_2O_7$:Gd^{3+} produced an UV emission at 314 nm. This indicated a good incorporation of the dopant Gd^{3+} into the calcium magnesium pyrophosphate host. Moreover, Kunghatkar et al. [97] proved that the solid-state and sol–gel techniques are more suitable for the synthesis of those phosphate-based phosphors doped with Gd^{3+}, in comparison with the wet chemical route and with the solution combustion method. Palan et al. [98] obtained by solid-state synthesis and by sol–gel method, polycrystalline cerium (Ce^{3+}) doped phosphor materials. The initial reagents $NaNO_3$, $Ca(NO_3)_2{\cdot}6H_2O$, $NH_4H_2PO_4$ and $Ce(NO_3)$ were added to the molten stearic acid, together with acetic acid (2–3 drops). This mixture was heated first at 70 °C, and then at 100 °C. A transparent gel was subsequently formed after cooling at room temperature. The gel was dried by a slowly heating process, and the remaining residue was calcinated at 800 °C for 2 h and at 1000 °C for 1 h, yielding a white powder of $NaCaPO_4$:Ce^{3+} phosphor. The obtained $NaCaPO_4$:Ce^{3+} phosphor showed very good optically stimulated luminescence (OSL) properties under α irradiation. Palan et al. [98] observed that the OSL sensitivity of $NaCaPO_4$:Ce^{3+} phosphor synthesized by using the solid-state method was higher in this case, than the OSL sensitivity of the same compound prepared by using the sol–gel method. When $NaCaPO_4$:Ce^{3+} phosphor was used for radiation dosimetry, the minimum detectable dose was 0.470 mGy if obtained by the solid-state synthesis and 1.118 mGy if synthesized by the sol–gel method. The photoluminescence (PL) excitation and the emission spectra of $NaCaPO_4$:Ce^{3+} phosphors showed two main UV emissions at 383 nm and at 321 nm respectively [98].

5 Co-precipitation Method

Another route, commonly used for the synthesis of phosphors containing phosphate derivatives and rare-earth elements, is the co-precipitation method [106–114]. It can be performed also under microwaves (the so-called microwaves-assisted co-precipitation) [30, 115–118]. It is important to mention that not all the phosphorus-based phosphors synthesized by the classical precipitation method, could be synthesized also by using microwaves. Many rare-earth metals were used in the last decades as dopants of phosphate-based phosphors synthesized by using the co-precipitation method, as for instance europium (Eu) [106–108, 110, 115–117], yttrium (Y), gadolinium (Gd) [109, 110], neodymium (Nd) [111], terbium (Tb) [112–114, 117], cerium (Ce) [112–114], lanthanum (La) [114], dysprosium (Dy) [108, 108, 109], holmium (Ho), thulium (Tm), ytterbium (Yb) [30], and so on.

Van et al. [107, 108] synthesized via co-precipitation method, co-doped tricalcium phosphate (TCP) phosphors, containing Eu^{2+}/Mn^{2+} and Eu^{3+}/Dy^{3+}. The Eu^{2+}/Mn^{2+} co-doped TCP phosphor (abbreviated as Eu/Mn-TCP) was synthesized by co-precipitation method, followed by thermal annealing in argon atmosphere, at a temperature of around 1100 °C. A solution of $(NH_4)_2HPO_4$ was added into an aqueous solution containing $Ca(NO_3)_2$, $Eu(NO_3)_3$, and $Mn(NO_3)_3$ [107] or $Dy(NO_3)_3$ [108]. They previously obtained those nitrates from the reaction of the Eu, Mn and Dy oxydes with nitric acid. The intensity of the emission from TCP at 430 nm increased for the sample with 7.5 mol% Mn^{2+} and 0.3 mol% Eu^{2+} [107]. On the other hand, the co-doped Eu^{3+}/Dy^{3+} hydroxyapatite (HA)/β-tricalcium phosphate (TCP) compounds synthesized by the co-precipitation method, showed the emissions of the dominant Eu^{3+} ion at 590, 616, 650 and 700 nm, with the additional emissions due to the Dy^{3+} ion at 482 and 572 nm. This combination of Eu^{3+} and Dy^{3+} ions is very useful for obtaining red and yellow emitting phosphors. This is of great interest because it has a lot of potential applications in agriculture, such as plant cultivation, where a combination of red and yellow light is required for stimulating the fruit production [108].

The synthesis of the $Ho^{3+}/Tm^{3+}/Yb^{3+}$ co-doped phosphate-based phosphors by using the co-precipitation has been described in the work published in [30]. For the preparation of Ho^{3+}–Tm^{3+}–Yb^{3+}:YPO_4 phosphors, the used reagents were Tm_2O_3, Ho_2O_3, Yb_2O_3, Y_2O_3, $NH_4H_2PO_4$ and NH_4OH. The oxides reacted first with HNO_3 to form their nitrates, as in the previous described syntheses. The host material YPO_4 was prepared by adding an $NH_4H_2PO_4$ to the yttrium nitrate solution. Then, the nitrate solution of the dopant ions ($Ho^{3+}/Tm^{3+}/Yb^{3+}$) was added to the solution of $NH_4H_2PO_4$ and yttrium nitrate. Ammonia solution was further added dropwise and the mixture precipitated within 24 h. The precipitates were filtered and washed, and subsequently calcinated at 700 °C for 3 h. The obtained nanophosphors emitted an intense red color and also showed a good thermal stability [30].

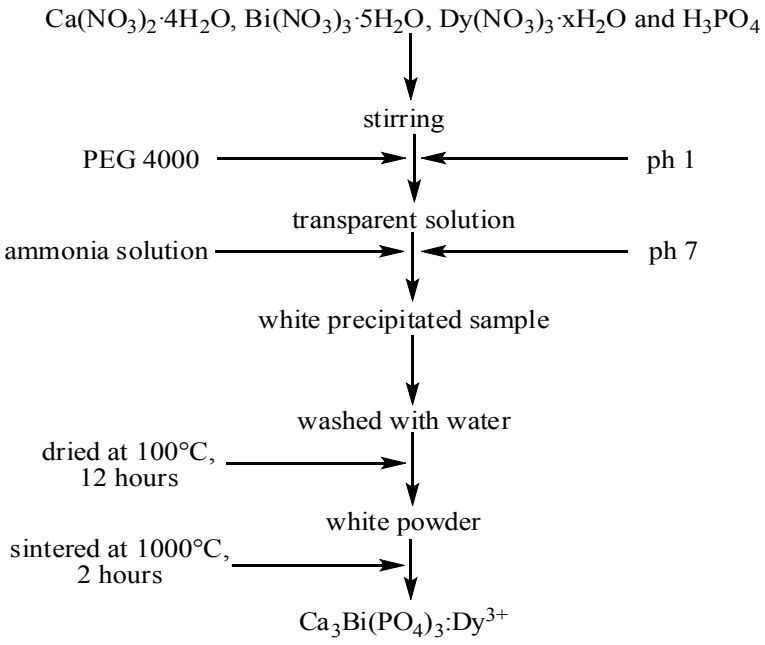

Fig. 2 Synthesis procedure of $Ca_3Bi(PO_4)_3:Dy^{3+}$ phosphor by using co-precipitation method [109]

White light emitting doped $Ca_3Bi(PO_4)_3:Dy^{3+}$ phosphor was successfully synthesized for the first time via the co-precipitation method in the work published in [109]. $Ca(NO_3)_2{\cdot}4H_2O$, $Bi(NO_3)_3{\cdot}5H_2O$, $Dy(NO_3)_3{\cdot}xH_2O$ and H_3PO_4 were used as reagents. The scheme of the used co-precipitation synthesis is presented in Fig. 2.

After 2 h the precipitation was complete. The precipitate was filtered and dried at 100 °C for 12 h, and further sintered at 1000 °C for 2 h. The excitation spectra proved that $Ca_3Bi(PO_4)_3:Dy^{3+}$ phosphor could be excited by NUV radiation and blue LED chips, showing a blue emission at 484 nm and a yellow emission at 575 nm [109]. Savvin et al. [110] used together the rare-earth metals Y, Gd and Eu in a co-precipitation synthesis for obtaining rare-earth phosphates-based co-doped phosphors. The synthesis was performed at room temperature and at 4.5 ph. Yttrium gadolinium co-doped phosphates were synthesized using an aqueous solutions of YCl_3, $KH_2PO_4{\cdot}2H_2O$ and $Gd(NO_3)_3$. Europium was introduced also in the form of $Eu(NO_3)_3$. The obtained precipitates $Y_{1-x-y}Gd_xEu_yPO_4$ were washed, dried for 12 h at 100 °C and further heated in air, in three steps: at 600 and 800 °C for 40 h, and at 1000 °C for 8 h [110]. The classical co-precipitation method was also employed for the synthesis of different phosphate-based phosphors containing Nd^{3+} [111], Ce^{3+} or Tb^{3+} [112–114]. Those phosphors showed a green emission at the wavelength of 547 nm, when excited by UV radiation [111–114].

In the same time, europium doped phosphate phosphors can be synthesized by microwaves co-precipitation, as reported in [115–117]. The $Sr_5(PO_4)_2(SiO_4):Eu^{3+}$ phosphor synthesized in the work of Roh et al. [115] by using microwaves, emitted an intense red light. To add Eu^{3+} into $Sr_5(PO_4)_2(SiO_4)$ phosphors by a microwave controlled reaction, $Sr(NO_3)_2$, $NH_4H_2PO_4$, SiO_2 nanoparticles (60–70 nm), $Eu(NO_3)_3{\cdot}6H_2O$ and NaOH were used as precursors. The reaction was performed under microwave irradiation at relatively low temperature (200 °C) for 2 h. It was observed that the microwave reaction decreases the temperature necessary for the crystallization. When the P/Si ratio was close to 1, the intensity of its red luminescence increased. The highest intensity of the red emission was found at the wavelength of 614 nm. In comparison with Eu^{2+} doped apatite phosphors, the luminescence of Eu^{3+}-doped apatite phosphors have different emission spectrum (in this case an electric-dipole transition was the main reason for the luminescence change) [22]. Therefore, the $Sr_5(PO_4)_2(SiO_4):Eu^{3+}$ phosphor synthesized by the microwave-assisted reaction is a promising red phosphor compound, with potential applications for WLEDs [115].

On the other hand, Yang et al. [116] obtained novel red-emitting $LiSrPO_4:Eu^{3+}$ phosphors also by using microwaves (900 W), but at a higher temperature (1200 °C). The reagents Li_2CO_3, $SrCO_3$, $NH_4H_2PO_4$ and Eu_2O_3 were mixed with alcohol as solvent, and then ball-milled for 1 h with zirconia balls. The synthesized $LiSr_{1-x}PO_4:xEu^{3+}$ phosphors showed several emissions, at 581, 595, 617, 656 and 700 nm. When the Eu^{3+} molar concentration was 0.05 the highest photoluminescence intensity was observed [116]. Dong et al. [117] synthesized a novel series of $La_{1-x-y}PO_4:xEu^{3+}/yTb^{3+}$ phosphors (where x = 0, 0.01, 0.02, 0.03, 0.04, 0.05; y = 0, 0.05, 0.10, 0.15, 0.20) by using the microwave-assisted co-precipitation method and diammonium hydrogen phosphate as precipitant. Under UV irradiation with the wavelength of 350 nm, the co-doped $LaPO_4:Eu^{3+}/Tb^{3+}$ phosphors showed a green light emission at 543 nm and in the same time a red light emission at 591 nm. The green emission is due to Tb^{3+} ion and the red emission is characteristic for Eu^{3+} ion. On Eu^{3+}/Tb^{3+} co-doped phosphors synthesized in the work published in [117] Tb^{3+} ions behaves as sensitizer for Eu^{3+} ions.

In addition to phosphors doped with europium, the microwave-assisted synthesis was used in the recent years also to obtain Y, Gd, or Dy co-doped phosphates. Those phosphors were synthesized via urea-based microwave-assisted homogeneous precipitation method, starting from Y_2O_3, Gd_2O_3, and Dy_2O_3 as reagents. The used oxides reacted with HNO_3 in order to obtain the corresponding nitrates [118]. Then, H_3PO_4, urea, C_{16}TAB and ethylene glycol (EG) were dissolved in the mixed solution of Y, Gd, and Dy nitrates. The solution, with ph adjusted at 0.75 was then heated at 100 °C for 10 min in a microwave oven. The resultant colloidal particles were collected via centrifugation, washed with water and ethanol, and dried in air at 50 °C for 24 h. The Y/Gd/Dy co-doped phosphate-based phosphor obtained after calcination, showed two main emissions: one at 483 nm in the blue region, and one at 575 nm in the yellow region [118].

6 Hydrothermal Synthesis

The hydrothermal synthesis represents the techniques of crystallizing substances from high-temperature aqueous solutions, at high pressure [119]. As we previously described in the present review, in general the most used rare-earth metal for obtaining phosphors, is europium. It is also the case when the hydrothermal method was employed for the synthesis of phosphor materials. The main reasons are that europium is the most reactive lanthanide, the softest also, and it is relatively non-toxic in comparison with other heavy metals. The hydrothermal syntheses performed for obtaining europium doped phosphorus-based phosphors, used both Eu^{2+} [120, 121] and Eu^{3+} ions [122–125]. Zhang et al. [120] described the hydrothermal preparation of the co-doped $Ca_9Y(PO_4)_7:Eu^{2+},Mn^{2+}$ nanophosphors. They have studied the influence of pH, as well as of Eu^{2+} and Mn^{2+} concentrations on the morphologies and on the properties of the synthesized materials. When the ph increased, the samples morphology showed a transition from rod to spherical shape. $Ca(NO_3)_2{\cdot}4H_2O$ was dissolved in water, Eu_2O_3 and Y_2O_3 were dissolved in nitric acid, and MnO_2 was dissolved in a mixture of nitric acid and H_2O_2. Then H_3PO_4 was added and the obtained solution was heated at 180 °C in an autoclave for 24 h. The final products were washed and subsequently heated at 900 °C for 3 h. On the co-doped obtained phosphor $Ca_9Y(PO_4)_7:Eu^{2+},Mn^{2+}$ an energy transfer between Eu^{2+} and Mn^{2+} ions occurred. The work of Zhang et al. [120] can be used to provide reference for the development of ultraviolet (especially NUV) phosphors for LEDs. Also a series of novel green-emitting phosphate-based doped phosphors $Sr_8ZnY(PO_4)_7:Eu^{2+}$ (abbreviated SZYP:Eu^{2+}) and $Sr_{7.98}ZnY_{0.98}(PO_4)_7:0.02Eu^{2+},0.02Ln^{3+}$ co-doped phosphors (where Ln = Pr, Tm or Yb), was synthesized by Zhong et al. [121] with hydrothermal method. A mixture of $Sr(NO_3)_2$, $Zn(NO_3)_2$, $Y(NO_3)_3$, $(NH_4)_2HPO_4$ and $Eu(NO_3)_3$ were transferred into an autoclave and heated at 200 °C for 12 h. The obtained precursors were sintered at 1300 °C for 5 h, in reductive atmosphere (90% N_2; 10% H_2). The SZYP:Eu^{2+} and SZYP:Eu^{2+},Ln^{3+} phosphors obtained with the above mentioned hydrothermal method, showed under NUV light an emission in the green region, around the wavelength of 520 nm. It was proved that co-doping lanthanide ions as Pr^{3+}, Tm^{3+} or Yb^{3+}, improved the thermal stability of the synthesized phosphorus-based phosphors. Green phosphor is an essential component in phosphor-converted white light-emitting diodes (PC-LEDs). With the increase of Eu^{2+} content, a small red shift (with around 4 nm) in the emission spectra of the synthesized SZYP:Eu^{2+} was observed [121].

In addition to Eu^{2+} phosphors, also Eu^{3+}-doped compounds were synthesized by using the hydrothermal method [122–125]. $BiPO_4:Eu^{3+}$ phosphors for example, were synthesized by hydrothermal route using Teflon-autoclaves at different temperatures, for 5–8 h. The intensity of the emission light increased with the hydrothermal temperature [123, 124]. Moreover, on the work of Hachani et al. [125] new luminescent materials emitting in the red and orange regions were described. They have synthesized YPO_4 doped with Gd^{3+}0.25% and/or Eu^{3+}0.5% by a hydrothermal method based on the reaction between rare-earth oxides, orthophosphoric acid and water,

at 200 °C for 4 h, within a stainless steel autoclave with Teflon chamber. After the reaction was complete, the product was dried and further heated at 850 °C and at 1000 °C for 2 h. Under excitation at 394 nm by using a Xenon lamp, the synthesized YPO_4:Gd^{3+}0.25%, Eu^{3+}0.50% phosphors showed an orange-red emission [125, 126].

7 Miscellaneous

In addition to the above mentioned methods, for the syntheses of phosphorus-based phosphors compounds, more techniques could be involved, as for instance ultrasonic spray pyrolysis [127, 128], extraction pyrolytic technique [41], hydrolysis [122], decomposition [125], molten salt synthesis [7, 8], conventional glass melting method [37], activated glasses and classic ceramic method [38]. In this last section of the chapter, we will focus on the description of these methods. In the work published by Galvez-Sandoval et al. [127] zinc phosphate films doped with Ce^{3+}, Tb^{3+}, Mn^{2+}, and co-doped with Ce^{3+}/Tb^{3+} and Ce^{3+}/Tb^{3+}/Mn^{3+}, were deposited at 500 °C by using the ultrasonic spray pyrolysis method. Spray pyrolysis is a low cost deposition technique which brings several advantages, as obtaining small particle size and high purity [127–129]. The films deposited by using spray pyrolysis make them excellent candidates for applications in lightning system technologies. Few examples of the emissions characteristic for such films deposited with spray pyrolysis technique, are: blue emission of Ce^{3+} singly doped film under 280 nm excitation, neutral white light emission of Mn^{2+} singly doped film under 410 nm excitation, green emission of Tb^{3+} singly doped film under excitation at 377 nm, yellowish-green emission of films co-doped with Ce^{3+} and Tb^{3+} under excitation at 280 nm, yellow-white emission of the triply doped films with Ce^{3+}, Tb^{3+} and Mn^{2+} when excited with 280 nm radiation, and so on. All of these make the Mn^{2+} and Ce^{3+}/Tb^{3+}/Mn^{2+}-doped zinc phosphate films, potential candidates for UV-blue LEDs pumped white phosphors [127]. In several publications it was proved that Ce^{3+} ions can be excited by UV LEDs [130–134]. The intense broad absorption bands of Ce^{3+} ion are due to its 4f → 5d parity. Therefore, in co-doped materials, Ce^{3+} ions are excellent sensitizers of different activators, as Tb^{3+} or Mn^{2+}, for obtaining white light emission under UV excitation [130–134]. Moreover, Tb^{3+} and Yb^{3+} ions could be used for spectral conversion in solar photovoltaic cells, due to the photon down-conversion process [135]. The Tb^{3+} ions absorb an UV photon and then give two photons to the Yb^{3+} ion. As a consequence, two NIR emissions occurred. The weak absorption of the Tb^{3+} 4f–4f transitions could be overcome by adding Ce^{3+} ions as sensitizers. It is well known that an efficient energy transfer between sensitizer and activator ions can only occurs when sensitizer (donor) emissions overlap with activator (acceptor) absorption bands. Tb^{3+} and Mn^{2+} ions can be excited by Ce^{3+} ions, due to the strong overlapping between the Ce^{3+} emissions and Tb^{3+}/Mn^{2+}absorption bands [131, 132, 136, 137].

Park and Kim [128] synthesized $(La_{1-x}Gd_x)_{0.94}PO_4$:$Tb_{0.06}$ ($0 \leq x \leq 1$) green phosphors by using ultrasonic spray pyrolysis technique. La_2O_3 and Gd_2O_3 powders

were dissolved in HNO_3 and the obtained solutions were heated to 80 °C until solid nitrates of La^{3+} and Gd^{3+} were formed. Tb_2O_3 powders, used as an activator source, were dissolved in HCl and further heated at 80 °C. This leads to the formation of solid Tb^{3+} chloride. The obtained La^{3+} and Gd^{3+} nitrates, as well as Tb^{3+} chloride, were added to an aqueous solution containing H_3PO_4, ethylene glycol and citric acid. Ethylene glycol and citric acid were used as additives. The ultrasonic spray pyrolysis system consisted of an ultrasonic nebulizer (1.75 MHz), a hot furnace tube reactor (1000 °C) and a precipitator containing a ceramic filter. The phosphor powders were subsequently heated at 1100 °C, for 4 h. They have observed that a higher Gd^{3+} content yielded a smaller lattice parameter. The synthesized phosphors showed four green emissions at 489, 543, 585 and 621 nm. Among the obtained $(La_{1-x}Gd_x)0.94PO_4{:}Tb_{0.06}$ phosphors, the strongest emission intensity was observed when x was 0.75 [128].

Steblevskaya et al. [41] used the pyrolysis extraction method to obtain terbium and europium doped phosphates. The synthesized phosphors exhibited red and green emission, due to Tb^{3+} and Eu^{3+} ions. Terbium and europium were extracted into mixed benzene solutions of acetylacetone and organophosphorus neutral ligands, as triphenylphosphine oxide or tributyl phosphate, in the presence of tris(hydroxymethyl)aminomethane. The Eu^{3+} and Tb^{3+} concentration in the initial aqueous phase was 6 mM. The organic phase was concentrated and pyrolysed at 700–800 °C in a muffle furnace [41].

Another method used for the synthesis of phosphorus-based phosphors is the hydrolysis. Soni et al. [122] used in their work for the synthesis of phosphors, in addition to hydrothermal methods, also urea hydrolysis and ammonia hydrolysis. In a typical urea hydrolysis used for the synthesis of 5% Eu^{3+}-doped $SrMoO_4$ nanoparticles, the processes were performed in four steps, as follows:

- Step 1: Eu_2O_3 and $SrCO_3$ were dissolved in concentrated HNO_3 solution, in order to obtain their nitrates
- Step 2: $MoCl_5$ was dissolved in methanol under heating at 80 °C and the resulted solution was transferred into the solution obtained at step 1
- Step 3: ethylene glycol (EG) and urea were added, and the whole mixture was put in the sonication 1 h, for obtaining a completely homogeneous solution
- Step 4: the reaction mixture was kept at 150 °C for 3 h in reflux conditions until the precipitation was complete

Urea was used as source for obtaining OH^- ions, from its decomposition at 60–100 °C. The generated OH^- ions reacted with Sr^{2+} and Mo^{5+} to finally yield the $SrMoO_4$ molecule. The reactions are showed in Fig. 3 [122].

For the synthesis by using ammonia hydrolysis, the same procedure was used as described in the case of urea hydrolysis in ethylene glycol, except the step 3 in which urea was replaced with ammonia solution. In both cases of urea hydrolysis and ammonia hydrolysis, the Eu^{3+}-doped phosphate phosphor $SrMoO_4{:}Eu^{3+}$ was obtained. It was suggested that such compounds can be potential red phosphors for UV excitation [122].

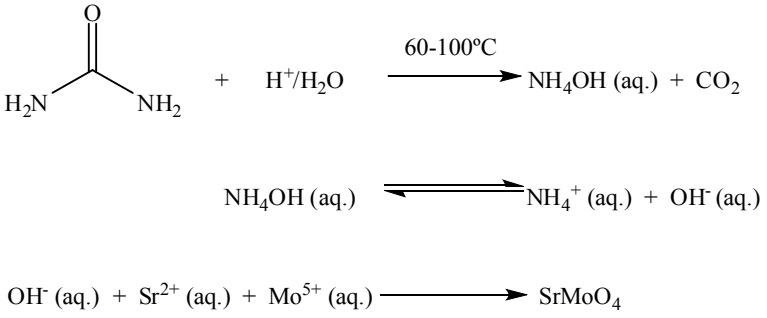

Fig. 3 Scheme of using urea as source for obtaining OH^- ions [122]

In order to solve the issue of the WLEDs luminescent efficiency decreasing in time, coupling of a NUV or blue emitting LED with one activated phosphor glass was performed. The phosphor glass was activated with NUV-blue light-absorbing ions [138]. One such example is represented by the calcium-zinc phosphate glasses doped with Tb_2O_3, or Eu_2O_3, or co-doped with both Tb_2O_3 and Eu_2O_3 [137]. Tb^{3+} is one of the most efficient rare-earth metals for obtaining green emission (at a wavelength of around 541 nm) [139]. Moreover, Tb^{3+} ions can act also as good sensitizers of NUV-blue radiation to different activator ions. Additionally, phosphors doped with Eu^{3+} ions can generate red or orange-red light [140–145].

In recent years, low melting temperature glasses were of great interest as hosts for phosphor converted white light emitting diodes (PC-WLED). A series of trivalent europium doped tin fluorophosphates glasses were prepared by the classical melting method. SnF_2, $NH_4H_2PO_4$, SnO and Eu_2O_3 were melted at 350 °C for 20 min, in alumina crucibles. After that, the glass melts were poured into a cold stainless-steel mold and cooled to room temperature [37]. Such phosphate glasses avoids the yellowing and aging issues, which leads to luminescence decreasing and color shifting in WLEDs in time [146–152]. On the other hand, the tin fluorophosphates glasses doped with rare-earth metals has been also proved to be a promising host for obtaining photon conversion in solar cell applications [153]. It was proved that co-doped $LnPO_4$:RE^{3+} systems (Ln = Y^{3+}, La^{3+} and Gd^{3+}; RE = Eu, Tb and Ce) offer better photoluminescence properties [154].

Hachani et al. [125, 155] in addition to hydrothermal method used also the decomposition synthesis for obtaining phosphorus-based phosphors. They have synthesized YP_3O_9 doped with Sm^{3+}0.25% and/or Eu^{3+}0.50% by ultraphosphate decomposition reaction. LnP_5O_{14} ultraphosphates is converted into $Ln(PO_3)_3$ polyphosphates, by heating at 900 °C. The YP_5O_{14} transparent crystals doped with Sm^{3+} and/or Eu^{3+} were obtained at 450 °C after 150 h [125, 155]. Finally, the ultraphosphate decomposition reaction was used to develop yttrium polyphosphates at 870 °C for 4 h in air, as presented in Fig. 4.

Yttrium polyphosphate powder was further calcinated at 900 °C. Under UV radiation, at the wavelength of around 404 nm, YP_3O_9:Sm^{3+}0.25%,Eu^{3+}0.50% phosphor

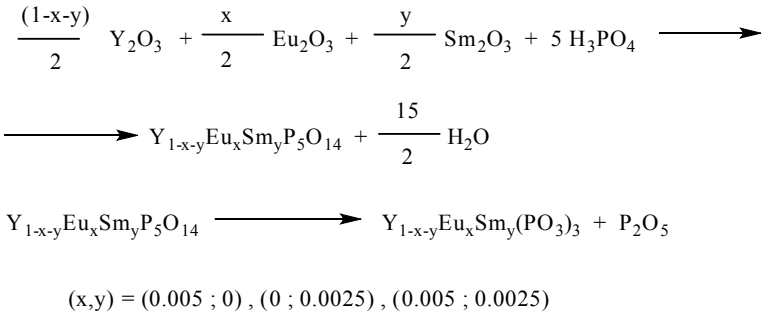

Fig. 4 The decomposition reaction used by Hachani et al. [125]

emits orange-red light, and therefore could have applications as orange-red emitting phosphor for Hg-free fluorescent lamps and plasma display panel (PDP) [125]. The fluorescent glass can transform cool white light into warm white light by changing the excitation wavelength.

Tian et al. [7] and Zhang et al. [8] obtained phosphorus-based phosphors by using molten salt synthesis. A mixture of calcium nitrate, ammonia phosphate, terbium nitrate hexahydrate, sodium nitrate and potassium nitrate, was heated at 350 °C for 3 h. Finally, after cooling and washing, the product was dried at 80 °C in air for 10 h. Under UV light, the α-$Ca_2P_2O_7$:Tb^{3+} phosphors prepared by molten salt synthesis showed a green emission, due to Tb^{3+} ion [7]. On the other hand, Zhang et al. [8] used a combination of molten salt method and flux method for obtaining phosphorus-based phosphors, as follows: a solute-flux mixture of KH_2PO_4, HfO_2, Dy_2O_3, $KF{\cdot}2H_2O$ was heated at 860 °C for 5 h and then cooled to room temperature. The product was washed and the colorless crystals of $K_2DyHf(PO_4)_3$ were obtained after drying (with the size around 0.16 mm) [8]. Moreover, the doped $Li_2BaP_2O_7$:Er^{3+} pyrophosphate was obtained by using the classic ceramic method in the work of Beltaif et al. [38] Stoichiometric amounts of lithium carbonate (Li_2CO_3), barium carbonate ($BaCO_3$), erbium oxide (Er_2O_3) and ammonium dihydrogen phosphate ($NH_4H_2PO_4$) were mixed and slowly heated at 320 °C for 8 h in order to expel the gases. The obtained powder was further pressed into cylindrical pellets and subsequently heated at 750 °C for 10 h. The obtained $Li_2BaP_2O_7$:x%Er^{3+} (where x = 0.1, 1, 3 and 5) phosphor showed green light emissions under UV excitation (at a wavelength of around 400 nm) [38].

8 Conclusions

In the last decades, rare-earth (RE) doped phosphorus-based materials attracted much attention for their potential applications in laser and WLEDs technologies, plasma display panel (PDP), medicine, or as light sources for agriculture, and so on [156–159]. The PDP for example has become a promising candidate for the large flat-displays in the recent years, because it provides a rapid response and a large viewing angle [160, 161]. In a PDP, a mixed Ne–Xe gas is mainly subjected to discharge between two glass panels to generate vacuum ultraviolet (VUV) light. The three-color rare-earth doped phosphate-based phosphors absorb this VUV radiation and as a consequence emit visible light. The phosphate-based phosphors exhibit high efficiency under VUV excitation due to their high absorption in comparison with silicate, borate and oxide-based phosphors [160–165].

Inorganic phosphors contain in general a crystalline material as host, doped with a relatively small amount of rare-earth metal ions, commonly called activators. Those RE metal ions convert the light from shorter wavelength (usually UV radiation) to longer wavelength (visible spectrum) via electronic transitions. This change of the wavelength is called the Stokes shift. In the case of LED lighting, the short wavelength excitation is provided by a blue LED or a NUV LED, and as a consequence, radiation in this spectral range must be strongly absorbed [166]. The increasing interest for RE-doped phosphates has been observed since such phosphors could be used in laser devices, not only in the form of single crystals, but also in powder and glass forms [167–172]. White light-emitting diodes (WLEDs) have become the main lighting source nowadays. WLEDs bring a lot of advantages as environmental protection, energy saving and high efficiency [173]. A typical WLED light source is comprised of a PN junction chip and a phosphor compound to generate the white light emission. The most popular phosphors are in general comprised of an activated ion and a host matrix, including oxides, rare-earth sulfur oxides, rare-earth halogen oxides and so on. An excellent phosphor should involve characteristics of rich spectral lines, narrow emission bands and concentrated luminous energy in the visible spectrum [174–178]. In comparison with other host materials, phosphates offer advantages as simple synthesis condition, low price, as well as good chemical and thermal stabilities [38, 118, 179–181]. Therefore the rare-earth doped phosphates are important nowadays especially due to their interesting optical applications. The luminescence properties are significantly influenced and mainly determined by the rare-earth metal, the host, the method of synthesis, the molar ratio of the reagents, the concentration of the dopant ions, and nevertheless the temperature. Most of the phosphorus-based phosphors are synthesized by using the high temperature conventional solid-state method. In the last years also other synthesis routes were developed, as combustion method, sol–gel method, co-precipitation method, hydrothermal method, ultrasonic spray pyrolysis, extraction pyrolytic technique, hydrolysis, decomposition, and so on. Among the rare-earths ions, Eu^{3+} is one of the most preferred sources of red light emission. In the same time, its reduced form (Eu^{2+}) showed a blue emission. Blue emitting phosphors can be very useful for solid-state lighting if they can be excited

by a NUV LED. Further they convert the radiation in the range 380–410 nm to visible light centered in the blue region (420–500 nm), including part of the violet light. For green emitting phosphors, also Tb^{3+} and Mn^{3+} were used. They convert the radiation in the ranges of 380–410 nm or 450–480 nm, to green light centered in the region of 520–565 nm [166]. The Dy^{3+} ions have been used in recent years, because they can offer both blue and yellow emissions. Tb^{3+} and Er^{3+} ions are employed in the synthesis of phosphors due to their green emission, and Sm^{3+} ions are used because they are emitting an orange light. Some materials are obtained by co-doping the phosphate host with two or three rare-earth metals. By combining rare-earth metals in co-doped phosphorus-based phosphors and by changing their position, ratio and concentration, emissions on the whole visible spectrum could be obtained.

References

1. Kumari, P., Baitha, P.K., Manam, J.: Structural and photoluminescence properties of red-light emitting YVO_4:Eu^{3+} phosphor synthesized by combustion and solid-state reaction techniques: a comparative study. Indian J. Phys. **89**, 1297–1306 (2015)
2. Zhang, F., Zhang, W., Zhang, Z., et al.: Luminescence characteristics and energy transfer of a red-emitting YVO_4:Sm^{3+}, Eu^{3+} phosphor. J. Lumin. **152**, 160–164 (2014)
3. Tyminski, A., Grzyb, T.: Enhancement of the up-conversion luminescence in $LaVO_4$ nanomaterials by doping with M^{2+}, M^{4+} ($M^{2+} = Sr^{2+}$, Ba^{2+}, Mg^{2+}; $M^{4+} = Sn^{4+}$) ions. J. Alloys Compd. **782**, 69–80 (2019)
4. Bhatkar, V.B.: Synthesis and luminescent properties of yttrium vanadate based phosphors. Int. J. Eng. Sci. Innov. Technol. **2**, 426–429 (2013)
5. Cavalli, E., Angiuli, F., Belletti, A., et al.: Luminescent spectroscopy of YVO_4:Ln^{3+}, Bi^{3+} ($Ln^{3+} = Eu^{3+}$, Sm^{3+}, Dy^{3+}) phosphors. Opt. Mater. **36**(10), 1642–1648 (2014)
6. Su, X.Q., Yan, B.: The synthesis and luminescence of $YP_xV_{1-x}O_4$:Dy^{3+} microcrystalline phosphors by in situ co-precipitation composition of hybrid precursors. Math. Chem. Phys. **93**(2–3), 552–556 (2005)
7. Tian, Y., Fang, Y., Tian, B., et al.: Molten salt synthesis, energy transfer, and temperature quenching fluorescence of green-emitting β-$Ca_2P_2O_7$:Tb^{3+} phosphors. J. Mater. Sci. **50**(18), 6060–6065 (2015)
8. Zhang, S.-R., Zhao, D., Fan, Y.-C., Ma, Z., Xue, Y.-L., Li, Y.-N.: Color tunability and energy transfer studies of a new Eu^{3+} doped langbeinite-type phosphate phosphor for lighting applications. J. Solid State Chem. **279**, 120965 (2019)
9. Minakova, T., Mjakin, S., Bakhmetyev, V., et al.: High efficient $YVPO_4$ luminescent materials activated by europium. Crystals **9**, 658–672 (2019)
10. Kim, M., Kobayashi, M., Kato, H., et al.: A highly luminous $LiCaPO_4$:Eu^{2+} phosphor synthesized by a solution method employing a water-soluble phosphate ester. Opt. Photonics J. **3**(6A), 13–18 (2013)
11. Marciniak, L., Guyot, Y., Hreniak, D., et al.: The impact of Eu^{3+} concentration on charge transfer and f–f transitions in $KLa_{1-x}Eu_xP_4O_{12}$ nanocrystals. J. Lumin. **169**, 238–244 (2016)
12. Zhang, Z., Tang, W.: Dual energy transfers and color tunable emission in Eu^{2+}/Tb^{3+}/Mn^{2+}-tri activated $Mg_{21}Ca_4Na_4(PO_4)_{18}$ phosphors. J. Lumin. **169**, 367–373 (2016)
13. Li, Y., Ma, H., Hua, Y., et al.: Tunable luminescence of Ce^{3+}/Li^+, Eu^{2+} co-doped $Ca_4(PO_4)_2O$ phosphor for white light emitting diodes. J. Rare Earths **34**(1), 7–11 (2016)
14. Wani, J.A., Dhoble, N.S., Kokode, N.S., et al.: Synthesis and luminescence property of $Li_2BaP_2O_7$:Ln^{3+} (Ln = Eu, Sm) phosphors. J. Lumin. **147**, 223–228 (2014)

15. Wani, J.A., Dhoble, N.S., Lochab, S.P., et al.: Luminescence characteristics of C^{5+} ions and ^{60}Co irradiated $Li_2BaP_2O_7:Dy^{3+}$ phosphor. Nucl. Instrum. Methods Phys. Res. Sect. B Beam Interact. Mater. Atoms **349**, 56–63 (2015)
16. Saito, A., Kato, H., Kobayashi, M., et al.: Development of a novel green-emitting phosphate phosphor $KSrY(PO_4)_2:Eu^{2+}$. Opt. Photonics J. **3**(6A), 19–24 (2013)
17. Patil, Y.S., Chaudhari, K.G., Poornachandra Rao, N.V., et al.: Synthesis & photoluminescence study of $LaPO_4$:Eu, Tb phosphor. Arch. Phys. Res. **2**(3), 110–115 (2011)
18. Lin, X., Feng, A., Zhang, Z., et al.: VUV spectroscopic properties of rare-earth (RE = Eu, Tb and Dy)-doped $A_2Zr(PO_4)_2$ (A = Li, Na or K) phosphates. J. Rare Earths **32**(10), 946–951 (2014)
19. Verma, B.R., Baghel, R.N.: A review on luminescence properties in Eu doped phosphate phosphors. Int. J. Mater. Sci. **12**(3), 483–489 (2017)
20. Pawade, V.B., Zanwar, A., Birmod, R.P., et al.: Optical and bandgap study of rare earth doped phosphate phosphor. J. Mater. Sci. Mater. Electron. **28**(21), 16306–16313 (2017)
21. Petkov, V.I.: Complex phosphates formed by metal cations in oxidation states I and IV. Russ. Chem. Rev. **81**(7), 606–637 (2012)
22. Tsai, B.-S., Chang, Y.-H., Chen, Y.-C.: Synthesis and luminescent properties of MgIn2-xGaxO4:Eu3+ phosphors. Electrochem. Solid State Lett. **8**(7), H55–H57 (2005)
23. Woodcock, D.A., Lightfoot, P.: Comparison of the structural behaviour of the low thermal expansion NZP phases $MTi_2(PO_4)_3$ (M = Li, Na, K). J. Mater. Chem. **9**(11), 2907–2911 (1999)
24. Butyagin, P.Y.: Problems in mechanochemistry and prospects for its development. Russ. Chem. Rev. **63**(12), 965–976 (1994)
25. Reisfeld, R.: New Materials for Nonlinear Optics, Optical and Electronic Phenomena in Sol-Gel Glasses and Modern Applications, Structure and Bonding. Springer (1996)
26. Rosas Camacho, A., de Carrillo Romo, J.F., García Murillo, A., et al.: Sol-gel synthesis and up-conversion luminescence of $GdPO_4$–$Gd_3PO_7:Yb^{3+}$, Ln^{3+} (Ln = Er, Ho, Tm) phosphor. Mater. Lett. **226**, 34–37 (2018)
27. Hawkins, H.T., Spearing, D.R., Veirs, D.K., et al.: Synthesis and characterization of Uranium(IV)-bearing members of the [NZP] structural family. Chem. Mater. **11**(10), 2851–2857 (1999)
28. Di Vona, M.L., Traversa, E., Licoccia, S.: Non-hydrolytic routes for the synthesis of NASICON. J. Sol-Gel Sci. Technol. **19**(1–3), 463–467 (2000)
29. Kanunov, A.E., Orlova, A.I.: Phosphors based on phosphates of $NaZr_2(PO_4)_3$ and langbeinite structural families. Rev. J. Chem. **8**(1), 1–33 (2018)
30. Lakshmi, M., Vineet, K.R.: Thermally stable red emitting xenotime phosphate nanophosphors for displays. Mater. Res. Bull. **121**, 110628 (2020)
31. Pechini, M.P.: US Patent 3330697 (1967)
32. Lee, H., Hong, M., Bae, S., et al.: A novel approach to preparing nano-size Co_3O_4-coated Ni powder by the Pechini method for MCFC cathodes. J. Mater. Chem. **13**(10), 2626–2632 (2003)
33. Barré, M., Crosnier-Lopez, M.P., Le Berre, F., et al.: Room temperature crystal structure of $La_{1/3}Zr_2(PO_4)_3$, a NASICON-type compound. Chem. Mater. **17**(26), 6605–6610 (2005)
34. Tretyakov, Y.D., Putlyaev, V.I.: Vvedenie v khimiyu tverdofaznykh materialov (Introduction to the Chemistry of Solid State Materials). Nauka, Moscow (2006)
35. Simulescu, V., Crasmareanu, E., Ilia, G.: Synthesis, properties and structures of phosphorus-nitrogen heterocycles. Heterocycles **83**(2), 275–291 (2011)
36. Ilia, G., Simulescu, V., Mak, C.A., et al.: The use of transesterification method for obtaining phosphorus-containing polymers. Adv. Polym. Technol. **33**(S1), 21437 (2014). https://doi.org/10.1002/adv.21437
37. Mao, W., Cai, M., Xie, W., et al.: Tunable white light in trivalent europium single doped tin fluorophosphates ultra-low melting glass. J. Alloys Compd. **805**, 205–210 (2019)
38. Beltaif, M., Koubaa, T., Kallel, T., et al.: Synthesis, structure and optical properties of erbium-doped lithium barium phosphate. Solid State Sci. **90**, 21–28 (2019)

39. Byrappa, K., Pushcharovsky, D.Y.: Crystal chemistry and its significance on the growth of technological materials: part I; silicates, phosphates and their analogues. Prog. Cryst. Growth Charact. Mater. **24**(4), 269–359 (1992)
40. Byrappa, K., Pushcharovsky, D.Y.: Crystal chemistry and its significance on the growth of technological materials: part II; octahedrally coordinated compounds. Prog. Cryst. Growth Charact. Mater. **24**(4), 361–421 (1992)
41. Steblevskaya, N.I., Medkov, M.A., Belobeletskaya, M.V.: Luminophores based on lanthanide phosphates obtained by extraction pyrolytic method. Russ. J. Inorg. Chem. **60**(2), 214–218 (2015)
42. Fujino, S.: US Patent 5614783 (1997)
43. Menon, S.N., Dhabekar, B.S., Kadam, S., et al.: Fading studies in $LiMgPO_4$:Tb, B and synthesis of new $LiMgP_O4$ based phosphor with better fading characteristics. Nucl. Instrum. Methods Phys. Res. Sect. B Beam Interact. Mater. Atoms **436**, 45–50 (2018)
44. Dhabekar, B., Menon, S.N., Alagu Raja, E., et al.: $LiMgPO_4$:Tb, B—a new sensitive OSL phosphor for dosimetry. Nucl. Instrum. Methods Phys. Res. Sect. B Beam Interact. Mater. Atoms **269**(16), 1844–1848 (2011)
45. Gai, M.Q., Chen, Z.Y., Fan, Y.W., et al.: Synthesis of $LiMgPO_4$:Eu, Sm, B phosphors and investigation of their optically stimulated luminescence properties. Radiat. Meas. **78**, 48–52 (2015)
46. Gai, M.Q., Chen, Z.Y., Fan, Y.W., et al.: Synthesis and luminescence in $LiMgPO_4$:Tb, Sm, B phosphors with possible applications in real-time dosimetry. J. Rare Earths **31**(6), 551–554 (2013)
47. Marczewska, B., Bilski, P., Wróbel, D., et al.: Investigations of OSL properties of $LiMgPO_4$:Tb, B based dosimeters. Radiat. Meas. **90**, 265–268 (2016)
48. Zhang, S., Huang, Y., Seo, H.J.: The spectroscopy and structural sites of Eu^{2+} ions doped $KCaPO_4$ phosphor. J. Electrochem. Soc. **157**, 261–266 (2010)
49. Fang, H., Huang, S., Wei, X., et al.: Synthesis and luminescence properties of $KCaPO_4$:Eu^{2+}, Tb^{3+}, Mn^{2+} for white-light-emitting diodes (WLED). J. Rare Earths **33**(8), 825–829 (2015)
50. Palan, C.B., Koparkar, K.A., Bajaj, N.S., et al.: A novel high sensitivity $KCaPO_4$:Ce^{3+} phosphor for radiation dosimetry. Res. Chem. Intermed. **42**(10), 7637–7649 (2016)
51. Malik, C., Kumar Meena, R., Rathi, P., et al.: Effect of dopant concentration on luminescence properties of a phosphor, $KCaPO_4$:Dy. Radiat. Phys. Chem. **168**, 108561 (2020)
52. Hu, Z., Zhang, Y., Liang, W., et al.: Insight into the photoluminescence properties and formation mechanism of $Ca_4(PO_4)_2O$ crystal: design of Eu^{2+}-doped multi-color phosphors. J. Lumin. **210**, 383–391 (2019)
53. Reddy Prasad, V., Damodaraiah, S., Devara, S.N., et al.: Photoluminescence studies on holmium (III) and praseodymium (III) doped calcium borophosphate (CBP) phosphors. J. Mol. Struct. **1160**, 383–392 (2018)
54. Jaya Raja, B., Rajesh Yadav, M., Manjari, V.P., et al.: Spectral investigations on Cu^{2+}-doped $Li_2CaAl_4(PO_4)_4F_4$ phosphors. Appl. Magn. Reson. **46**(8), 953–964 (2015)
55. Wang, T., Hu, Y.-H., Chen, L., et al.: Luminescence properties and energy transfer of a red-emitting $Ca_3(PO_4)_2$:Sm^{3+}, Eu^{3+} phosphor. J. Mater. Sci. Mater. Electron. **26**(7), 5360–5367 (2015)
56. Zhang, Z., Han, C.-L., Shi, W.-W., et al.: Enhanced novel white emission in $Ca_3(PO_4)_2$:Dy^{3+} single-phase full-color phosphor by charge compensation. J. Mater. Sci. Mater. Electron. **26**(3), 1923–1931 (2015)
57. Liang, L., Mei, L., Liu, H., Wang, C., Liao, L.: Intense broad-band absorption and blue-emitting $Ca_9La(PO_4)_5(SiO_4)Cl_2$:$Eu^{2+}$ phosphor under near-ultraviolet excitation. J. Lumin. **206**, 154–157 (2019)
58. Leng, Z., Yang, W., Huang, W., et al.: A novel $Ba_4Gd_3K_3(PO_4)_6F_2$:Eu^{2+} blue-white emitting phosphor for near ultraviolet excited light-emitting diodes. J. Lumin. **213**, 133–139 (2019)
59. Ye, H., He, M., Zhou, T., et al.: A novel reddish-orange fluorapatite phosphor La_6-$xBa_4(SiO_4)6F_2$:xSm^{3+}—structure, luminescence and energy transfer properties. J. Alloys Compd. **757**, 79–86 (2018)

60. Malysa, B., Meijerink, A., Jüstel, T.: Temperature dependent photoluminescence of Cr^{3+} doped $Sr_8MgLa(PO_4)_7$. Opt. Mater. **85**, 341–348 (2018)
61. Chen, K.-H., Weng, M.-H., Yang, R.-Y., et al.: New $NaSrPO_4:Sm^{3+}$ phosphor as orange-red emitting material. Bull. Mater. Sci. **39**(5), 1171–1176 (2016)
62. Han, B., Liu, B., Zhang, J., et al.: Luminescence properties of a novel single-phase white-emitting phosphor based on Dy^{3+} doped strontium tetraphosphate. J. Mater. Sci. Mater. Electron. **27**(10), 10742–10746 (2016)
63. Gao, Y., Long, Q., Nong, R., et al.: Strain-induced enhancement of Eu^{3+} emission in red phosphor $NaMgPO_4:Eu^{3+}$, A^{l3}+. J. Electron. Mater. **46**(2), 911–916 (2017)
64. Zhu, J., Xiang, J., Yang, D., et al.: Low-temperature solid-state synthesis and luminescent performance of a novel $Li_2NaBP_2O_8$-based phosphor activated with europium (III). Ceram. Int. **46**(1), 844–849 (2020)
65. Xia, Y., Huang, Y., Li, Y., et al.: $LaPO_4$:Ce, Tb, Yb phosphor-synthesis and kinetics study for thermal process of precursor by Vyazovkin, OFW, KAS, Starink, and Mastplosts methods. J. Therm. Anal. Calorim. **120**(3), 1635–1643 (2015)
66. Smet, P.F., Botterman, J., Van den Eeckhout, K., et al.: Persistent luminescence in nitride and oxynitride phosphors: a review. Opt. Mater. **36**(11), 1913–1919 (2014)
67. Gawande, A.W., Sonekara, R.P., Omanwar, S.K.: Luminescent properties and particle morphology of $Ca_3(PO_4)_2:Gd^{3+}$, Pr^{3+} phosphor powder prepared by microwave assisted synthesis. Mater. Res. Bull. **60**, 285–291 (2014)
68. Balakrishna, A., Reddy, L., Ntwaeaborwa, O.M., et al.: Remarkable influence of alkaline earth ions on the enhancement of fluorescence from Eu^{3+} ion doped in sodium ortho-phosphate phosphors. J. Mol. Struct. **1203**, 127375 (2020)
69. Bedyal, A.K., Kunti, A.K., Kumar, V., et al.: Effects of cationic substitution on the luminescence behavior of Dy^{3+} doped orthophosphate phosphor. J. Alloys Compd. **806**, 1127–1137 (2019)
70. Bedyal, A.K., Ramteke, D.D., Kumar, V., Swart, H.C.: Blue photons excited highly chromatic red light emitting $K_3La(PO_4)_2:Pr^{3+}$ phosphors for white light emitting diodes. Mater. Res. Bull. **103**, 173–180 (2018)
71. Shinde, K.N., Dhoble, S.J.: Luminescence in Dy^{3+} and Eu^{3+} activated $K_3Al_2(PO_4)_3$. J. Fluoresc. **21**(6), 2053–2056 (2011)
72. Wanjun, T., Tingting, F.: Luminescence and energy transfer in Eu^{2+}, Mn^{2+} codoped $N_a2BaMg_P2_O8$ phosphor. Appl. Phys. A **114**(3), 931–935 (2014)
73. Min, L., Wanjun, T., Kejian, D.: Synthesis and luminescence properties of Eu^{2+}-activated $Ca_4Mg_5(PO_4)_6$ for blue-emitting phosphor. Bull. Mater. Sci. **35**(1), 119–122 (2012)
74. Shanshan, H., Wanjun, T.: Synthesis and luminescence properties of Eu^{2+}- and Mn^{2+}-activated $Mg_{21}Ca_4Na_4(PO_4)_{18}$ phosphors. J. Mater. Sci. **48**(17), 5840–5845 (2013)
75. Zhang, S., Nakai, Y., Tsuboi, T., et al.: The thermal stabilities of luminescence and microstructures of Eu^{2+}-doped $KBaPO_4$ and $NaSrPO_4$ with β-K_2SO_4 type structure. Inorg. Chem. **50**(7), 2897–2904 (2011)
76. Park, K., Heo, M.H., Seo, H.J.: Improvement in photoluminescence properties of (Y, Gd)$(V_{1-x}P_x)O_4:Eu^{3+}$ phosphors by doping Al^{3+}. Electron. Mater. Lett. **12**(2), 315–322 (2016)
77. Krutko, V.A., Komova, M.G., Pominova, D.V.: Combustion synthesis of germanium phosphates $Gd_{11-x-y}Yb_xEr_yGeP_3O_{26}$ and their luminescence properties. Russ. J. Inorg. Chem. **62**(12), 1558–1562 (2017)
78. Patel, N.P., Srinivas, M., Modi, D., et al.: Optimization of luminescence properties of Tb^{3+}-doped a-$Sr_2P_2O_7$ phosphor synthesized by combustion method. Rare Metals **37**(7), 587–593 (2018)
79. Henning, A.H., Michael, D., Brohmer, M.C.: Coactivation of α-$Sr(PO_3)_2$ and $SrM(P_2O_7)$ (M = Zn, Sr) with Eu^{2+} and Mn^{2+}. Chem. Mater. **19**(25), 6358–6362 (2007)
80. Kohale, R.L., Dhoble, S.J.: Eu^{2+} luminescence in $SrCaP_2O_7$ pyrophosphate phosphor. J. Biol. Chem. Lumin. **28**(5), 656–661 (2013)
81. Xu, M., Wang, L., Jia, D., et al.: Tuning the color emission of $Sr_2P_2O_7:Tb^{3+}$, Eu^{3+} phosphors based on energy transfer. J. Am. Ceram. Soc. **98**(5), 1536–1541 (2015)

82. Hao, Z., Zhang, J., Zhang, X., et al.: Phase dependent photoluminescence and energy transfer in $Ca_2P_2O_7$:Eu^{2+}, Mn^{2+} phosphors for white LEDs. J. Lumin. **128**(5–6), 941–944 (2008)
83. Ye, S., Liu, Z.S., Jing, W.J.G.X.P., et al.: Luminescent properties of $Sr_2P_2O_7$:Eu, Mn phosphor under near UV excitation. Mater. Res. Bull. **43**(5), 1057–1065 (2008)
84. Judeinstein, P., Sanchez, C.: Hybrid organic-inorganic materials: a land of multidisciplinarity. J. Mater. Chem. **6**(4), 511–525 (1996)
85. Sanchez, C., Ribot, F., Lebeau, B.: Molecular design of hybrid organic-inorganic nanocomposites synthesized via solgel chemistry. J. Mater. Chem. **9**(1), 35–44 (1999)
86. Schubert, U., Husing, N., Lorenz, A.: Hybrid inorganicorganic materials by sol-gel processing of organofunctional metal alkoxides. Chem. Mater. **7**(11), 2010–2027 (1995)
87. Mackenzie, J.D., Bescher, E.: Some factors governing the coating of organic polymers by sol-gel derived hybrid materials. J. Sol-Gel Sci. Technol. **27**(1), 7–14 (2003)
88. Kumar, V., Singh, S., Chawla, S.: Fabrication of dual excitation, dual emission nanophosphor with broad UV and IR excitation through simultaneous doping of triple rare earth ions Er^{3+}, Yb^{3+}, Eu^{3+} in $GdPO_4$. Superlattices Microstruct. **79**, 86–95 (2015)
89. de Sousa Filho, P.C., Serra, Q.A.: Tripolyphosphate as precursor for $REPO_4$:Eu^{3+} (RE = Y, La, Gd) by a polymeric method. J. Fluoresc. **18**(2), 329–337 (2008)
90. Nair, G.B., Kumar, A., Swart, H.C., et al.: Improved steady-state photoluminescence derived from the compensation of the charge-imbalance in $Ca_3Mg_3(PO_4)_4$:Eu^{3+} phosphor. Ceram. Int. **45**(17), 21709–21715 (2019)
91. Game, D.N., Palan, C.B., Ingale, N.B., et al.: Synthesis and photoluminescence properties of Eu doped $LiBaPO_4$ phosphors for solid state lighting. J. Mater. Sci. Mater. Electron. **28**(12), 8777–8783 (2017)
92. Kanunov, A., Glorieux, B., Orlova, A., et al.: Synthesis, structure and luminescence properties of phosphates $A1_{3x}Eu_xZr_2(PO_4)_3$ (A-alkali metal). Bull. Mater. Sci. **40**(1), 7–16 (2017)
93. Wu, X., Liang, Y., Zhang, M., et al.: Uniform $KCaY(PO_4)_2$:Eu^{3+} phosphors: sol–gel method, morphology and luminescence properties. J. Mater. Sci. Mater. Electron. **26**(10), 7324–7330 (2015)
94. Glorieux, B., Jubera, V., Orlova, A.I., et al.: Phosphors based on $NaZr_2(PO_4)_3$ type calcium and strontium phosphates activated with Eu^{2+} and Sm^{3+}. Inorg. Mater. **49**(1), 82–88 (2013)
95. Orlova, A.I., Pleskova, S.N., Malanina, N.V., et al.: $Ca_3(PO_4)_2$:Er^{3+}, Yb^{3+}: an upconversion phosphor for in vivo imaging. Inorg. Mater. **49**(7), 696–700 (2013)
96. Bao, A., Song, Z., Haschaolu, O., et al.: Hydrothermal synthesis and photoluminescent properties of hierarchical $GdPO_4{\cdot}H_2O$:Ln^{3+} (Ln^{3+} = Eu^{3+}, Ce^{3+}, Tb^{3+}) flower-like clusters. J. Cryst. Growth **483**, 44–51 (2018)
97. Kunghatkar, R.G., Barai, V.L., Dhoble, S.J. Synthesis route dependent characterizations of CaMgP2O7: Gd^{3+} phosphor. Results Phys. **13**, 102295 (2019)
98. Palan, C.B., Omanwar, S.K.: Synthesis and preliminary OSL studies of $NaCaPO_4$: Ce phosphor for radiation dosimetry. Res. Chem. Intermed. **43**, 4043–4050 (2017)
99. Orlova, A.I., Kanunov, A.E., Gorshkova, E.N., et al.: Synthesis, luminescence, and biocompatibility of calcium- and lanthanide-containing $NaZr_2(PO_4)_3$-type compounds. Inorg. Mater. **49**(1), 89–94 (2013)
100. Bingol, B., Jannasch, P.: Phosphorus-based polymers-from synthesis to applications. In: Monge, S., David, G. (eds.), 1st edn, Royal Society of Chemistry, Cambridge (2014)
101. Abueva, C.D., Lee, B.T.: Poly(vinylphosphonic acid) immobilized on chitosan: a glycosaminoglycan-inspired matrix for bone regeneration. Int. J. Biol. Macromol. **64**, 294–301 (2014)
102. Kretlow, J.D., Hacker, M.C., Klouda, L., et al.: Synthesis and characterization of dual stimuli responsive macromers based on poly(*N*-isopropylacrylamide) and poly(vinylphosphonic acid). Biomacromolecules **11**(3), 797–805 (2010)
103. Kim, E.-H., Park, S.-H., Chi, S.-Y., et al.: Enhancement effect of cell adhesion on titanium surface using phosphonated low-molecular-weight chitosan derivative. Macromol. Res. **24**(2), 99–103 (2016)

104. Vahabi, H., Ferry, L., Longuet, C., et al.: Theoretical and empirical approaches to understanding the effect of phosphonate groups on the thermal degradation for two chemically modified PMMA. Eur. Polym. J. **48**(3), 604–612 (2012)
105. Queffélec, C., Petit, M., Janvier, P., et al.: Surface modification using phosphonic acids and esters. Chem. Rev. **112**(7), 3777–3807 (2012)
106. Yang, S.-H., Yang, C.-K., Yan, J.-H., et al.: Improvement of the luminescence of red $LaPO_4$:Eu nanophosphors for a near-UV LED. J. Electron. Mater. **43**(9), 3593–3600 (2014)
107. Van, H.N., Hoan, B.T., Nguyen, K.T., et al.: Controlling blue and red light emissions from europium (Eu^{2+})/manganese (Mn^{2+})-codoped beta-tricalcium phosphate [β-$Ca_3(PO_4)_2$(TCP)] phosphors. J. Electron. Mater. **47**(5), 2964–2969 (2018)
108. Van, H.N., Tam, P.D., Pham, V.-H.: Red and yellow luminescence of Eu^{3+}/Dy^{3+} co-doped hydroxyapatite/β-tricalcium phosphate single phosphors synthesized using coprecipitation method. J. Appl. Spectrosc. **85**(4), 738–742 (2018)
109. Sahu, M.K., Mula, J.: White light emitting thermally stable bismuth phosphate phosphor $Ca_3Bi(PO_4)_3$:Dy^{3+} for solid-state lighting applications. J. Am. Ceram. Soc. **102**(10), 6087–6099 (2019)
110. Savvin, Y.N., Babayevskaya, N.V., Oleinik, S.S., et al.: Luminescent properties of europium-activated yttrium gadolinium phosphates. Inorg. Mater. **45**(4), 423–427 (2009)
111. Watanabe, M., Yamamoto, N., Matsuo, T., et al.: Enhancement of near-infrared emission of neodymium-doped monoclinic gadolinium phosphate nanophosphors by surface coating with calcium phosphate. J. Asian Ceram. Soc. **7**(4), 509–517 (2019)
112. Ma, C.-G., Zheng, W., Jin, L.-G., et al.: Fluorescence and preparation of $Sr_2(P_2O_7)$:Ce, Tb phosphate by co-precipitation method. Rare Metals **32**(4), 420–424 (2013)
113. Yan, S.: Synthesis and luminescence of $BiPO_4$:Ln^{3+} (Ln = Ce^{3+}, Tb^{3+}) phosphors. J. Mater. Sci. Mater. Electron. **25**(6), 2803–2807 (2014)
114. Ji, X., Zhu, F.-J., Zhai, H.-L., et al.: The luminescent enhancement of $LaPO_4$:Ce^{3+}, Tb^{3+} nanophosphors by radial aggregation. Front. Mater. Sci. China **4**(4), 382–386 (2010)
115. Roh, H.-S., Lee, S., Caliskan, S., et al.: Luminescence and electric dipole in Eu^{3+} doped strontium phosphate: effect of SiO_4. J. Alloys Compd. **772**, 573–578 (2019)
116. Yang, R.-Y., Peng, Y.-M., Su, Y.-K.: Novel red-emitting microwave-assisted-sintered $LiSrPO_4$: Eu^{3+} phosphors for application in near-UV white light-emitting diodes. J. Electron. Mater. **42**(10), 2910–2914 (2013)
117. Dong, W., Zhang, X., Shi, H., et al.: Preparation and Luminescence properties of color-tunable single-phased $LaPO_4$:Eu^{3+}/Tb^{3+} phosphors. Chem. Res. Chin. Univ. **32**(2), 248–252 (2016)
118. Xu, Z., Zhu, Q., Li, X., et al.: White-light emitting (Y, Gd)P_O4:Dy^{3+} microspheres: Gd^{3+} mediated morphology tailoring and selective energy transfer and correlation of photoluminescence behaviors. Mater. Res. Bull. **110**, 149–158 (2019)
119. Feng, S.-H., Li, G.-H.: Chapter 4—Hydrothermal and solvothermal syntheses. In: Modern Inorganic Synthetic Chemistry (2nd edn), pp. 73–104. (2017)
120. Zhang, H., Yu, X., Sun, H., et al.: Hydrothermal preparation and luminescence properties of $Ca_9Y(PO_4)_7$:Eu^{2+}, Mn^{2+} nanocrystals. J. Cryst. Growth **522**, 61–67 (2019)
121. Zhong, Y., Gai, S., Yang, Y., et al.: A novel green phosphor $Sr_8ZnY(PO_4)_7$:Eu^{2+}, Ln^{3+} (Ln = Pr, Tm, Yb) with broad emission band for high color rendering white-lighting-emitting diodes. J. Lumin. **214**, 116600 (2019)
122. Soni, A.K., Joshi, R., Jangid, K., et al.: Low temperature synthesized $SrMoO_4$:Eu^{3+} nanophosphors functionalized with ethylene glycol: a comparative study of synthesize route, morphology, luminescence and annealing. Mater. Res. Bull. **103**, 1–12 (2018)
123. Yan, S.-Q.: Effect of pH on the microstructure and luminescence of Eu^{3+}-doped $BiPO_4$ phosphors. J. Mater. Sci. Mater. Electron. **26**(6), 3744–3749 (2015)
124. Zhang, S., Yang, Y.: Hydrothermal synthesis and luminescent properties of $BiPO_4$:Eu^{3+} phosphors. J. Electron. Mater. **43**(2), 389–392 (2014)
125. Hachani, S., Guerbous, L.: Synthesis, luminescence, and energy transfer properties of YPO_4:Gd^{3+}, Eu^{3+}, YP_3O_9:Sm^{3+}, Eu^{3+} phosphors. J. Fluoresc. **29**(3), 665–672 (2019)

126. Zhou, X., Xiong, Z., Xue, H., et al.: Hydrothermal synthesis and photoluminescent properties of $Li_2Sr_{0.996}SiO_4:Pr^{3+}{}_{0.004}$ phosphors for white-LED lightings. J. Rare Earths **33**(3), 244–248 (2015)
127. Gálvez-Sandoval, J.L.N., Camarillo, I., Muñoz, G., et al.: Optical spectroscopy of zinc phosphate films activated with Ce^{3+}, Tb^{3+} and Mn^{2+} ions for white LED applications. Opt. Mater. **84**, 879–887 (2018)
128. Park, K., Kim, K.Y.: VUV photoluminescence of $La_{1-x}Gd_xPO_4:Tb^{3+}$ green phosphors synthesized by ultrasonic spray pyrolysis. Metals Mater. Int. **17**(5), 797–800 (2011)
129. Jacobi, K.: Handbook of Thin Film Process Technology. Institute of Physics Publishing (2001)
130. El Jouhari, N., Parent, C., Le Flem, G.: Photoluminescence of Ce^{3+}, Tb^{3+}, and Mn^{2+} in glasses of base composition $LaMgB_5O_{10}$. J. Solid State Chem. **123**(2), 398–407 (1996)
131. González-Ortega, J.A., Tejeda, E.M., Perea, N., et al.: White light emission from rare earth activated yttrium silicate nanocrystalline powders and thin films. Opt. Mater. **27**(7), 1221–1227 (2005)
132. Martínez-Martínez, R., Álvarez, E., Speghini, A., et al.: White light generation in $Al_2O_3:Ce^{3+}:Tb^{3+}:Mn^{2+}$ films deposited by ultrasonic spray pyrolysis. Thin Solid Films **518**(20), 5724–5730 (2010)
133. Martínez-Martínez, R., Álvarez, E., Speghini, A., et al.: Cold white light generation from hafnium oxide films activated with Ce^{3+}, Tb^{3+}, and Mn^{2+} ions. J. Mater. Res. **25**(3), 484–490 (2010)
134. Lim, C.S., Aleksandrovsky, A., Molokeev, M., et al.: Microwave sol-gel synthesis and upconversion photoluminescence properties of $CaGd_2(WO_4)_4:Er^{3+}/Yb^{3+}$ phosphors with incommensurately modulated structure. J. Solid State Chem. **228**, 160–166 (2015)
135. Florêncio, L.D.A., Gómez-Malagón, L.A., Lima, B.C., et al.: Efficiency enhancement in solar cells using photon down-conversion in Tb/Yb-doped tellurite glass. Solar Energy Mater. Solar Cells **157**, 468–475 (2016)
136. Martínez-Martínez, R., García, M., Speghini, A., et al.: Blue-green-red luminescence from $CeCl_3$ and $MnCl_2$ doped hafnium oxide layers prepared by ultrasonic spray pyrolysis. J. Phys. Condens. Matter **20**(39), 395205 (2008)
137. Trápala-Ramírez, A.U., Gálvez-Sandoval, J.L.N., Lira, A., et al.: Calcium-zinc phosphate glasses activated with Tb^{3+}/Eu^{3+} for laser and white LED applications. J. Lumin. **215**, 116621 (2019)
138. Meza-Rocha, A.N., Lozada-Morales, R., Speghini, A., et al.: White light generation in $Tb^{3+}/Eu^{3+}/Dy^{3+}$ triply-doped $Zn(PO_3)_2$ glass. Opt. Mater. **51**, 128–132 (2016)
139. Yamashita, T., Ohishi, Y.: Optical amplification at 0.54 μm by Tb^{3+}-doped fluoride fibre. Electron. Lett. **43**(2), 88–90 (2007)
140. Krupke, W.F.: Optically-pumped ~620 nm europium doped solid state laser. Patent US 2006/0153261 A1 (2006)
141. Caldiño, U., Lira, A., Meza-Rocha, A.N., et al.: Development of sodium-zinc phosphate glasses doped with Dy^{3+}, Eu^{3+} and Dy^{3+}/Eu^{3+} for yellow laser medium, reddish-orange and white phosphor applications. J. Lumin. **194**, 231–239 (2018)
142. Lira, A.C., Martín-Rodríguez, E., Martínez-Martínez, R., et al.: Spectroscopy of the $Bi_4Si_3O_{12}:Er^{3+}$ glass for optical amplification and laser application. Opt. Mater. **32**(9), 1266–1273 (2010)
143. Zhang, R., Wang, B., Zhou, P., et al.: A novel $Ce^{3+}:Y_3Al_5O_{12}$ and $Eu^{2+}:Sr_2Si_5N_8$ dual phosphors-in-glass thick film for warm white LED. Mater. Lett. **221**, 31–34 (2018)
144. Meza-Rocha, A.N., Bordignon, S., Speghini, A., et al.: Zinc phosphate glasses activated with $Dy^{3+}/Eu^{3+}/Sm^{3+}$ and $Tb^{3+}/Eu^{3+}/Sm^{3+}$ for reddish-orange and yellowish white phosphor applications. J. Lumin. **203**, 74–82 (2018)
145. Zhong, H., Chen, G., Yao, L., et al.: The white light emission properties of $Tm^{3+}/Tb^{3+}/Sm^{3+}$ triply doped SrO–ZnO–P_2O_5 glass. J. Non-Crystal. Solids **427**, 10–15 (2015)
146. Ehrt, D.: Phosphate and fluoride phosphate optical glasses properties, structure and applications. Phys. Chem. Glasses Eur. J. Glass Sci. Technol. B **56**(6), 217–234 (2015)

147. Bobkova, N.M., Trusova, E.E.: Low-melting bismutheborate glass: composition development. Glass Ceram. **68**(11–12), 349–352 (2012)
148. Varghese, J., Siponkoski, T., Teirikangas, M.: Structural dielectric and thermal properties of Pb free molybdate based ultralow temperature glass. ACS Sustain. Chem. Eng. **4**(7), 3897–3904 (2016)
149. Cai, M., Mao, W., Calvez, L.: Broadband blue emission from ZnO amorphous nanodomains in zinc phosphate oxynitride glass. Opt. Lett. **43**(23), 5845–5848 (2018)
150. Xiang, X., Wang, B., Lin, H.: Towards long-lifetime high-performance warm w-LEDs: fabricating chromaticity-tunable glass ceramic using an ultra-low melting Sn-PFO glass. J. Eur. Ceram. Soc. **38**(4), 1990–1997 (2018)
151. Lin, H., Hu, T., Cheng, Y.: Glass ceramic phosphors: towards long-lifetime highpower white light-emitting-diode applications-a review. Laser Photon. Rev. **12**(6), 1700344 (2018)
152. Yang, L., Chen, M., Lv, Z.: Preparation of a YAG: Ce phosphor glass by screenprinting technology and its application in LED packaging. Opt. Lett. **38**(13), 2240–2243 (2013)
153. York-Winegar, J., Harper, T., Brennan, C.: Structure of SnF_2-SnO-P_2O_5 glasses. Phys. Proc. **44**, 159–165 (2013)
154. Wang, D., Wang, Y.: Luminescence properties of $LaPO_4$:Tb^{3+}, Me^{3+} (Me = Gd, Bi, Ce) under VUV excitation. Mater. Res. Bull. **42**(12), 2163–2169 (2007)
155. Hachani, S., Moine, B., El-akrmi, A., et al.: Luminescent properties of some ortho- and pentaphosphates doped with Gd^{3+}-Eu^{3+}: potential phosphors for vacuum ultraviolet excitation. Opt. Mater. **31**(4), 678–684 (2009)
156. Xu, D., Zhou, W., Li, S., et al.: $Ba_3LaNa(PO_4)_3F$:Tm^{3+}, Dy^{3+}: a tunable blue-white color emitting phosphor via energy transfer for UV white LEDs. Chin. Chem. Lett. **31**(2), 575–578 (2020)
157. Wen, M., Wu, H., Yu, H., et al.: The first rare-earth lead phosphates $Pb_3AP_3O_{12}$ (A = Sc, Gd) with remarkable SHG enhancement. J. Solid State Chem. **286**, 121276 (2020)
158. Dousti, M.R., Poirier, G.Y., de Camargo, A.S.S.: Tungsten sodium phosphate glasses doped with trivalent rare earth ions (Eu^{3+}, Tb^{3+}, Nd^{3+} and Er^{3+}) for visible and near-infrared applications. J. Non-Crystal. Solids **530**, 119838 (2020)
159. Anand, A.: Synthesis of rare earth compounds from phosphor coating of spent fluorescent lamps. Sep. Purif. Rev. (2020). https://doi.org/10.1080/15422119.2020.1754240
160. Rao, R.P., Devine, D.J.: RE-activated lanthanide phosphate phosphors for PDP applications. J. Lumin. **87–89**, 1260–1263 (2000)
161. Kim, C.J., Kwon, M.S.: Effects of water content in an ethanol-based solvent on sol-gel synthesis of Zn_2SiO_4: Mn phosphors. Electron. Mater. Lett. **5**(3), 113–117 (2009)
162. Di, W., Wang, X., Chen, B., et al.: Preparation, characterization and VUV luminescence property of YPO_4: Tb phosphor for a PDP. Opt. Mater. **27**(8), 1386–1390 (2005)
163. Wang, Y., Wu, C., Wei, J.: Hydrothermal synthesis and luminescent properties of $LnPO_4$:Tb, Bi (Ln = La, Gd) phosphors under UV/VUV excitation. J. Lumin. **126**(2), 503–507 (2007)
164. Wu, X., You, H., Cui, H., et al.: Vacuum ultraviolet optical properties of (La, Gd)PO_4:RE^{3+} (RE = Eu, Tb). Mater. Res. Bull. **37**(9), 1531–1538 (2002)
165. Wu, C., Wang, Y., Jie, W.: Hydrothermal synthesis and luminescent properties of $LnPO_4$:Tb (Ln = La, Gd) phosphors under VUV excitation. J. Alloys Compd. **436**(1–2), 383–386 (2007)
166. Lin, Y.-C., Karlsson, M., Bettinelli, M.: Inorganic phosphor materials for lighting. Top Curr. Chem. Z **374**(2), 21 (2016)
167. Li, H., Baikie, T., Pramana, S.S., et al.: Hydrothermal synthesis, structure investigation, and oxide ion conductivity of mixed Si/Ge-based apatite-type phases. Inorg. Chem. **53**(10), 4803–4812 (2014)
168. Yu, S., Xia, Z., Molokeev, M.S., et al.: Synthesis and luminescence properties of blue-emitting phosphor $Li_3Sc_2(PO_4)_3$:Eu^{2+}. J. Solid State Sci. Technol. **3**(8), R159–R163 (2014)
169. Wang, Z., Xia, Z., Molokeev, M.S., et al.: Blue-shift of Eu^{2+} emission in (Ba, Sr)3Lu$(PO_4)3$:Eu^{2+} eulytite solid-solution phosphors resulting from release of neighbouring-cation-induced stress. Dalton Trans. **43**(44), 16800–16804 (2014)

170. Lim, C.S., Atuchin, V., Aleksandrovski, A., et al.: Microwave sol-gel synthesis of $CaGd_2(MoO_4)_4:Er^{3+}/Yb^{3+}$ phosphors and their upconversion photoluminescence properties. J. Am. Ceram. Soc. **98**(10), 3223–3230 (2015)
171. Lim, C.S., Aleksandrovsky, A.S., Molokeev, M.S., et al.: Microwave synthesis and spectroscopic properties of ternary scheelite-type molybdate phosphors $NaSrLa(MoO_4)_3:Er^{3+}$, Yb^{3+}. J. Alloys Compd. **713**, 156–163 (2017)
172. Dobrowolska, A., Bos, A.J.J., Dorenbos, P.: Charge carrier storage properties and the vacuum referred binding energy scheme for $Li_2BaP_2O_7$:Ln (Ln = Ce, Eu, TB, Yb). J. Lumin. **170**(2), 497–504 (2016)
173. Jiang, S., Luo, X., Liu, Y., et al.: Warm white light emission of apatite-type compound $Ca_4Y_6O(SiO_4)_6$ doped with Dy^{3+}. Mater. Res. Bull. **106**, 428–432 (2018)
174. Xue, Y., Zhao, D., Zhang, S., et al.: A new disordered langbeinite-type compound, $K_2Tb_{1.5}Ta_{0.5}P_3O_{12}$, and Eu^{3+}-doped multicolour light-emitting properties. Acta Crystal. Sect. C Struct. Chem. **75**, 213–220 (2019)
175. Barbosa Junior, G.J., Sousa, A.M., de Freitas, S.M., et al.: Investigation of Europium dopant in the orthophosphate $KMPO_4$ (M¼ Ba and Sr) compounds. J. Phys. Chem. Solids **130**, 282–289 (2019)
176. Sun, X., Han, T., Wu, D., et al.: Investigation on luminescence properties of Dy^{3+}, Eu^{3+}-doped, and Eu^{3+}/Dy^{3+}-codoped $SrGd_2O_4$ phosphors. J. Lumin. **204**, 89–94 (2018)
177. Yu, M., Zhang, W., Qin, S., et al.: Synthesis and luminescence properties of single-component $Ca_5(PO_4)_3F:Dy^{3+}$, Eu^{3+} white-emitting phosphors. J. Am. Ceram. Soc. **101**(10), 4582–4590 (2018)
178. Vijayakumar, R., Guo, H., Huang, X.: Energy transfer and color-tunable luminescence properties of Dy^{3+} and Eu^{3+} co-doped $Na_3Sc_2(PO_4)_3$ phosphors for near-UV LED based warm white LEDs. Dyes Pigments **156**, 8–16 (2018)
179. Han, S., Li, H., Yang, Z., et al.: Three new phosphates, $Cs_8Pb_4(P_2O_7)_4$, $CsLi_7(P_2O_7)_2$ and $LiCa(PO_3)_3$: structural comparison, characterization and theoretical calculation. Dalton Trans. **48**(24), 8948–8954 (2019)
180. Malinowski, M., Kaczkan, M.: Absorption intensity analysis and emission properties $KEu(PO_3)_4$ and $KEu_xY_{1-x}(PO_3)_4$ crystals. J Lumin. **211**, 138–143 (2019)
181. Zhu, J., Xiang, J., Hu, L., et al.: Synthesis and red emitting properties of $NaAlP_2O_7:Pr^{3+}$ polycrystal for blue chip-excited WLEDS. Results Phys. **12**, 771–775 (2019)

Progress and Prospects of Graphitic Structure—Based Phosphors

Velayudhan Prajitha, Keloth Paduvilan Jibin, K. S. Sisanth, Jesiya Susan George, and Sabu Thomas

1 Introduction

Graphite and its derivatives are at the forefront of scientific curiosity. Graphene structure considered to be one atom thick two-dimensional honeycomb layer of sp^2 carbon atoms [1]. Also, its derivatives graphene oxide, reduced graphene oxide, thermally expanded graphene oxide and graphene quantum dots etc. having exceptional electrical, optical and mechanical properties. They are the recent thought-provoking materials in countless applications such as field-effect transistors, transparent conducting films, sensors, photovoltaic, separation membranes, catalysis, biomedical applications etc. [2–9]. Generally, luminescent materials are an amalgamation of both host lattice and activator, rare earth and transition elements are the activators in phosphors which can emit light after excitation [10]. Developing new hybrid composites with these graphitic structures and phosphor materials having hydrogen bond and electrostatic interactions unleash the new spectrum of applications predominantly in optoelectronics, photocatalysis and fluorescence sensors [11–14].

V. Prajitha · K. P. Jibin (✉) · K. S. Sisanth · J. S. George · S. Thomas
International and Inter University Centre for Nano Science and Nanotechnology, Mahatma Gandhi University, Kottayam 686560, Kerala, India

V. Prajitha · K. P. Jibin · J. S. George · S. Thomas
School of Chemical Sciences, Mahatma Gandhi University, Kottayam 686560, Kerala, India

© Springer Nature Switzerland AG 2022

K. Upadhyay et al. (eds.), *Hybrid Phosphor Materials*, Engineering Materials,
https://doi.org/10.1007/978-3-030-90506-4_6

2 Synthesis

2.1 Graphene Oxide Based Phosphor

Graphene oxide is synthesized by chemical exfoliation of graphite with strong oxidants under acidic condition and major accepted method is modified hummers method. Which includes oxygen functionalities like carbonyl, epoxy and hydroxyl groups, supported on the surface of a monolayer graphene sheet [15]. Due to the presence of oxygen-containing functional groups makes the graphene oxide sheet defective. Because of the defects present in the graphene oxide, it shows less fluorescence so it can be enhanced by functionalizing with rare earth complexes [16]. Cao et al. non covalently functionalised the graphene oxide with red-luminescent [Eu (DBM)2(Phen)(SA)] (DBM = dibenzoyl methane, Phen = 1,10-phenanthroline, SA = stearic acid) to form GO –RE complex hybrids [17].

They have successfully synthesised the bright red luminescent GO–RE complex (Figs. 1, 2) and appealed that it has a large prospective in countless arenas such as biological labelling and anti-counterfeiting.

Efficient photoluminescence is required for optoelectronic devices; Rani et al. improved the efficiency of photoluminescence by synthesising GO-Phosphor nanoscrolls with enhanced chemical and physical properties. Rani et al. used $SrBaSi_2O_2N_2$: Eu^{2+} as phosphor which is embedded into GO solution employing modest chemical practice. And the GO-Phosphor solution is spin-coated and annealed at different temperatures. The phosphor particles attached to the graphene sheets spontaneously twist the GO sheets. At 180° GO sheets entwined due to the presence of phosphor which makes it very challenging to maintain the high aspect ratio of the two-dimensional structure (Fig. 3). These hybrids exhibited extremely robust luminescence emission in the violet and green regions (Fig. 4) [16].

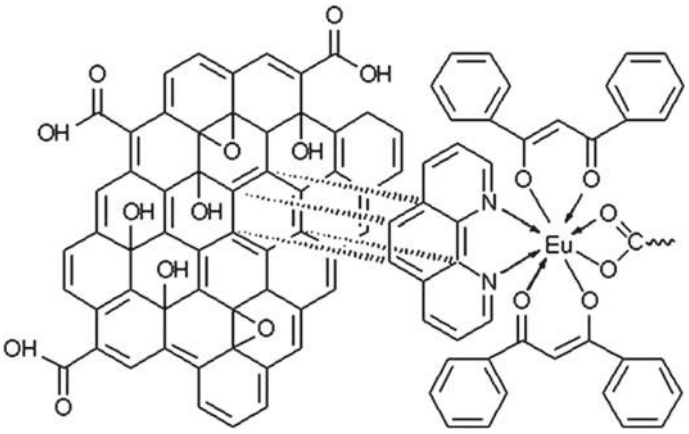

Fig. 1 Schematic sketch of GO–RE complex hybrids

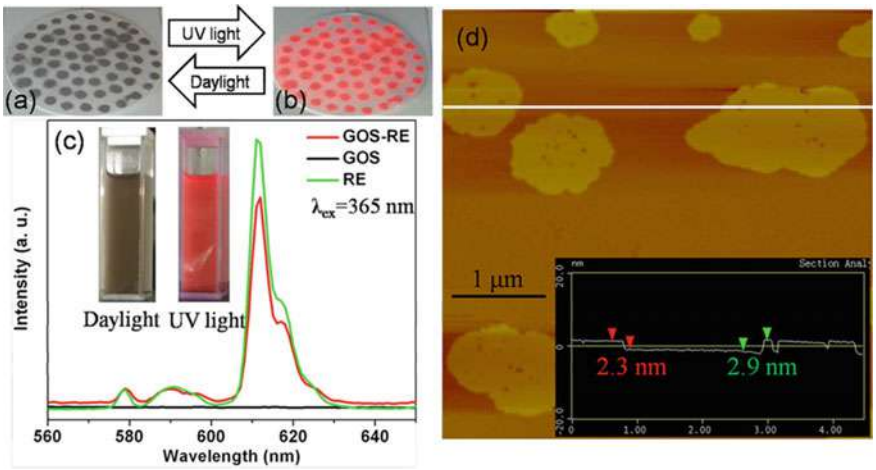

Fig. 2 Digital depictions of GO–RE complex hybrids under **a** daylight and **b** 365 nm UV light. **c** Luminescence emission spectra (kex = 365 nm) of GO–RE complex hybrids, GOSs and RE complexes in their dispersions. Inset in **c** snapshots of the THF dispersion of GO–RE complex hybrids under (left) daylight and (right) 365 nm UV light. **d** AFM image of GO–RE complex hybrids with (inset) a height profile [17]

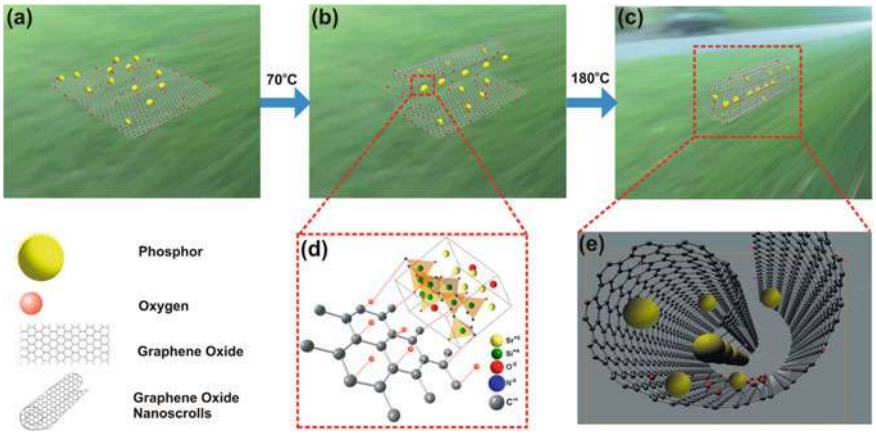

Fig. 3 Representation drawing display **a** phosphor particles attached to GO sheets, **b** the GO sheets just flinch to scroll, **c** GO sheets wholly scrolled at 180 °C, **d** the bonding amongst GO and phosphor, and **e** 3D interpretation of a lone GO-phosphor scroll [16]

Also, Fan et al. decorated surface carboxylated graphene oxide with luminescent Sm^{3+} complexes (tris-(2-thenoyltrifluoroacetone) mono-1,10-phenanthroline-Sm3) via covalent functionalization (Fig. 5) these red-emitting complex can be used as drug carriers and biomarkers [18].

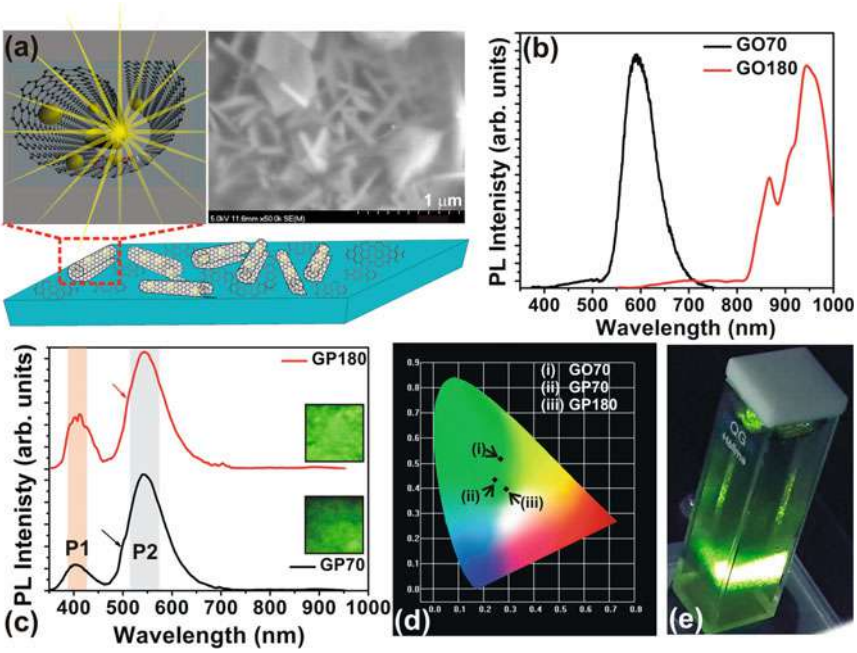

Fig. 4 **a** SEM image and graphic displaying the GO-phosphor hybrid nanoscrolls in GP180, PL emission spectra of **b** GO70 and GO180 films, **c** GP70 and GP180 films measured with an excitation wavelength of 280 nm. **d** CIE chromaticity coordinates of the PL emission from the synthesized thin films and **e** digital image of the strong PL emission from the GO-phosphor hybrid solution [16]

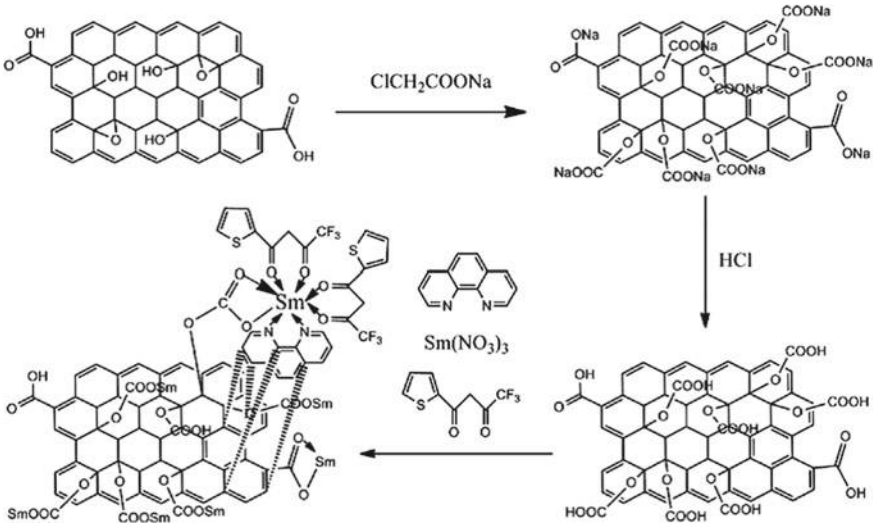

Fig. 5 Schematic diagram depicting the synthesis of GO-COOH-RE complex hybrids [18]

Zhang et al. improved the luminescence efficiency of graphene oxide by the non-covalent modification by using Eu^{3+}-2-thenoyltrifluoroacetone (TTA)-pyromellitic acid (PMA) complex. They have deposited this rare earth complex into the surface of graphene oxide sheets and these hybrid resources result in a high enrichment in luminescence and proposed the application as biosensors, optical devices etc. [19].

2.2 Reduced Graphene Oxide (rGO) Based Phosphor

Highly oxidized graphene oxide is reduced by physical or chemical treatments and results in partially deoxygenated sheets, called reduced graphene oxide which is having high surface area and thermal stability [20]. Hybrids of rare-earth complex and reduced graphene oxide are synthesised on the way to improve photo thermal possessions for biomedical significance. Yang et al. covalently attached vancomycin (Van) an antibiotic and a luminescent rare-earth complex (Eu+) to the surface of rGO (Fig. 6). They developed a novel approach to trace the pathogen as well as to kill the bacteria under near-infrared (NIR) laser beam [21]. Naderi et al. developed Yb_2O_3/RGO hybrid materials via simple sonication method (Fig. 7) to improve the super capacitive performance. They found that the synthesized Yb-rGO hybrid nanocomposite having super capacitance value about 240 F g^{-1} at the scan rate of 2 mV s^{-1}; greater than that of pure Yb_2O_3 and RGO electrodes has potential use as high-performance supercapacitor electrodes. Anoop et al. addressed the instability

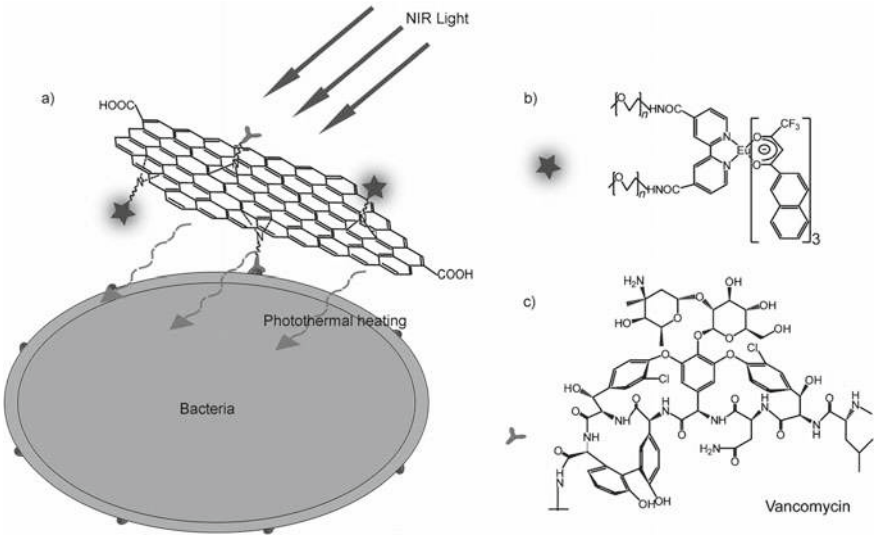

Fig. 6 **a** Design of Eu-Van-rGO for targeted bacteria imaging and photothermal killing; **b** the construction of the Eu complex; **c** the structure of vancomycin [21]

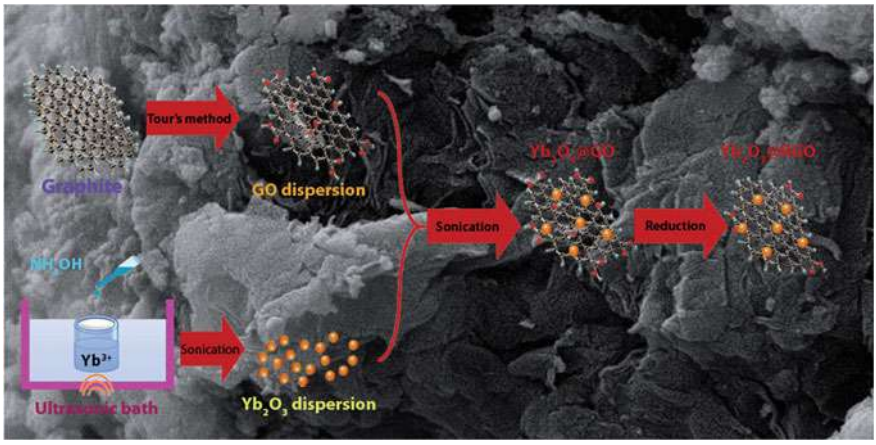

Fig. 7 Schematic drawing for the synthesis of the Yb_2O_3–RGO nanocomposite [22]

of commercially available phosphor-converted light-emitting diodes. To improve the thermal stability, they wrapped the phosphor ($(SrBa)Si_2O_2N_2$: Eu^{2+}) with rGO sheet by annealing with different temperature. This rGO wrapped phosphor shows superior oxidation defiance because of the passage of surplus heat through rGO layers [22].

Rather than constructing hybrid composites with two compounds nowadays scientists are interested in ternary nanocomposites. Rostami et al. developed ternary nanocomposite La/TiO_2@La/ZnO-15 wt% B–RGO for improved photocatalytic activity. Boron is doped into RGO by hydrothermal method and mixed with La/TiO_2@La/ZnO by ultra-sonication (Fig. 8) [13]. Also, Shukla et al. developed tertiary nanohybrid material [(La–Y_2O_3)–MoS_2–(Methionine functionalised rGO)] for thin film lubrication (Fig. 9) [23].

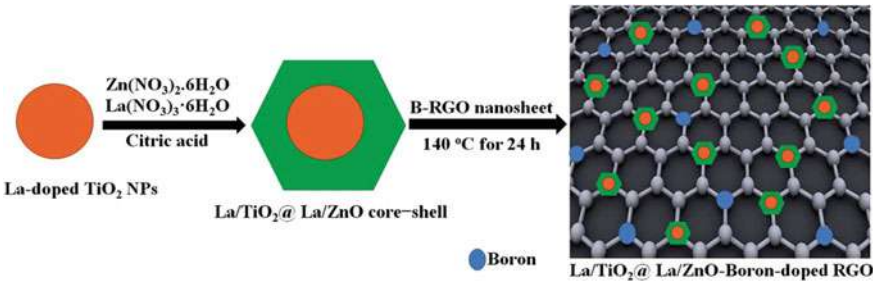

Fig. 8 Method of preparation of La/TiO_2@La/ZnO–B–RGO ternary nanocomposites [13]

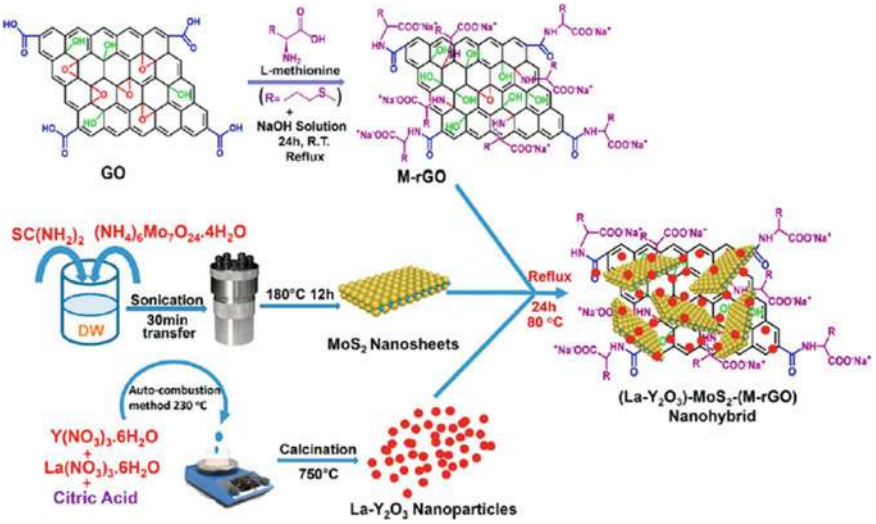

Fig. 9 Synthesis protocols of the Ternary Nanohybrid (La–Y_2O_3)–MoS_2–(M-rGO) [23]

2.3 Graphene Quantum Dots (GQDs) Based Phosphor

Zero-dimensional graphene quantum dots possess very good biocompatibility, tuneable photoluminescence which makes it as a potential material for bioimaging and sensing application [24].

Luo et al. synthesised a novel phosphor white light- emanating graphene quantum dots by way of microwave assisted hydrothermal synthesis which is having high luminescence and current density at the applied voltage 11–14 V [25]. Yin et al. fabricated yellow-green emitting GQD for optoelectronic application [26].

3 Applications

3.1 Sensors

Eu decorated graphene quantum dots were synthesized by Lin et al. for the determination of Cu^{2+} and L-cysteine (L-Cys) by using fluorescence "off–on" approach with high selectivity and sensitivity [27] (Fig. 10).

Devdas et al. fabricated an electrochemical sensor composed of a lutetium hexacyanoferrate (LuHCF) which is dispersed on to a reduced graphene oxide supported in glassy carbon electrode for the detection of salicylic acid [28]. Yu et al. developed a multi-layer hybrid film composed of (phthalocyanine) (porphyrinato) europium (III) triple-decker compound (Pc)Eu(Pc)Eu[trans-T($COOCH_3$)$_2$PP] (1) and graphene oxide (GO) using the solution-processing QLS method for the detection of H_2O_2 [29]. Manavalan et al. synthesized an H_2O_2 sensor which can detect very low concentration (1.57 nM) of H_2O_2 by using Gd_2O_3 nanoparticles decorated reduced

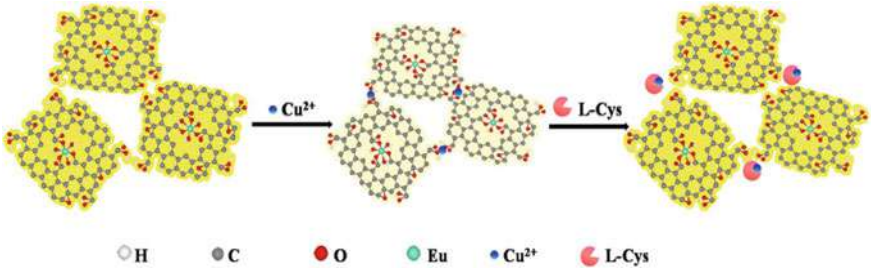

Fig. 10 Analysis of Cu^{2+} and L-Cys using Eu-GQDs—a schematic representation [27]

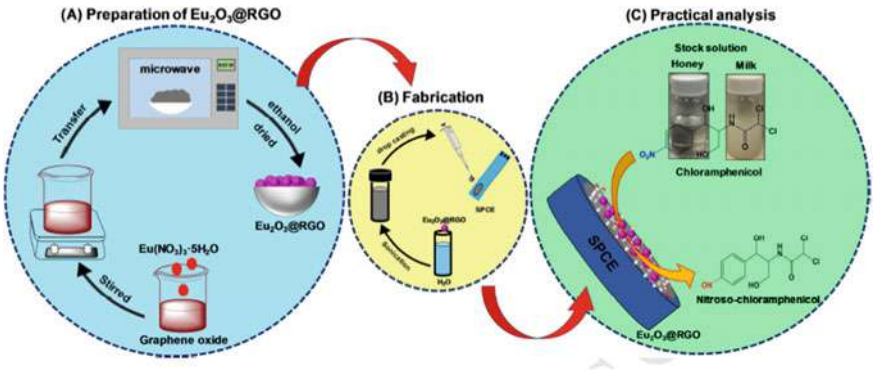

Fig. 11 Pictorial representation of fabrication of Eu2O3@RGO (**a**). Fabrication of Sensor (**b**) and the electrocatalytic performance toward CAP sensing in real samples (**c**)

graphene oxide nanocomposite (Gd_2O_3 NPs@RGO) [30]. From the same group Rajaji et al. synthesised a Eu_2O_3 nanoparticles decorated reduced graphene oxide through microwave-assisted route and developed an amperometric sensor for the detection of chloramphenicol (CAP) (Fig. 11) [31].

Rong et al. fabricated a fluorescence sensor as graphene oxide as acceptor and β-$NaYF_4$: Yb, Er UCNPs as the fluorescence donor for the detection of diazinon which has potential use in pesticide determination in food sample [32].

3.2 Optoelectronics

Mondal et al. developed a device which is composed of Diamino pyridine functionalized graphene oxide containing Eu^{2+} which is attached electrostatically to the nitrogen which results in a bright blue-green emission, which can potentially use as an optoelectronic device (Fig. 12) [33].

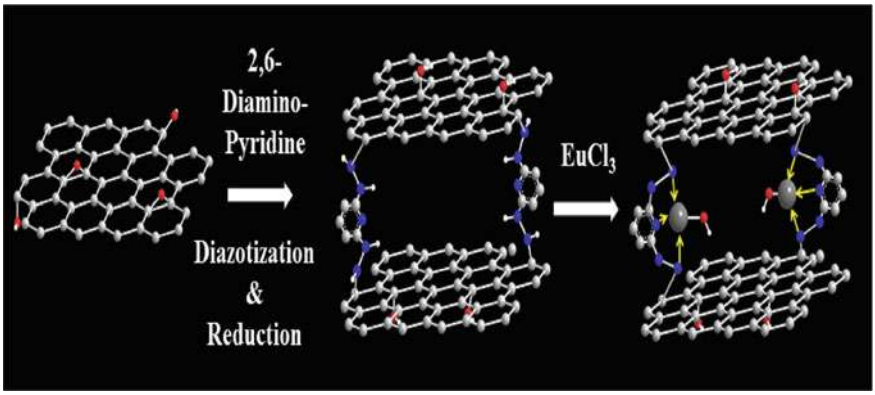

Fig. 12 Schematic diagram of RGO-Amino-Pyridine-Eu^{2+} composite through the functionalization of GO [33]

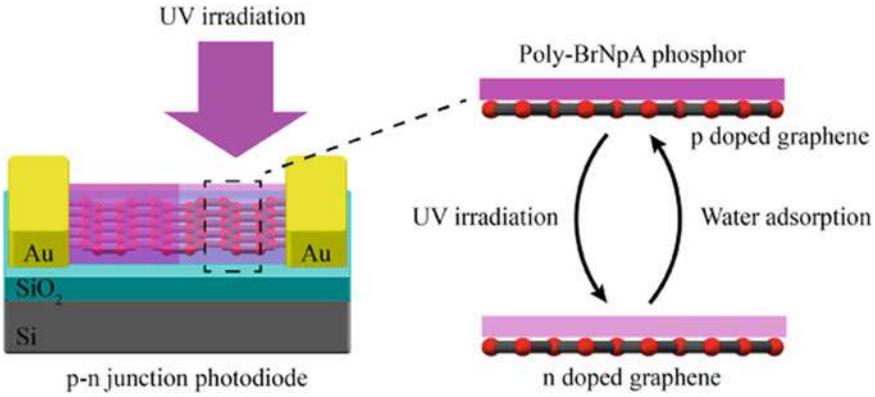

Fig. 13 Schematic representation of p–n junction photodiode [34]

Li et al. effectively manufactured a novel graphene-based bright rewritable p-n intersection photodiode which is made out of graphene-covered with a formless phosphor of 4-Bromo-1,8-naphthalic anhydride subordinate polymer (poly-BrNpA) (Fig. 13) which can be handily deleted by a sticky nitrogen flush and furthermore shows UV rewritable attributes [34].

3.3 Catalysis

Rostami et al. built up a ternary nanocomposite made out of La/TiO_2@La/ZnO-15 wt% B–RGO for improved visible light photocatalytic action (Fig. 14) [13].

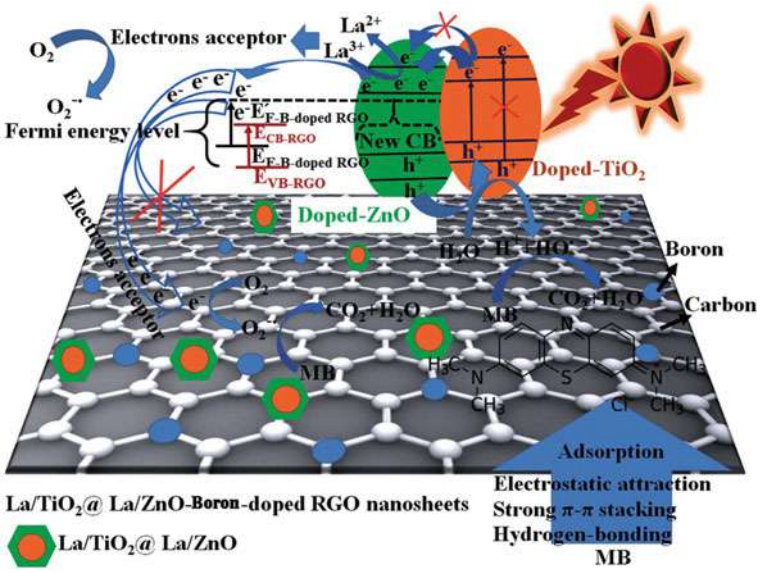

Fig. 14 Schematic outline of proposed photocatalysis and band-hole narrowing mechanism, photo-excited and accepted electrons, adsorption of MB, and electron and hole transfer of La/TiO_2@La/ZnO–B–RGO TNCs under sunlight irradiation [13]

4 Conclusion

Graphitic structure-based hybrid phosphors were studied extensively by various scientists. The covalent and noncovalent functionalisation of both graphene oxide and reduced graphene oxide with a phosphor material has an expected application in various territories, for example biomedical, sensing, catalysis and optoelectronics.

References

1. Gass, M.H., Bangert, U., Bleloch, A.L., Wang, P., Nair, R.R., Geim, A.K.: Free-standing graphene at atomic resolution. Nat. Nanotechnol. **3**, 676–681 (2008). https://doi.org/10.1038/nnano.2008.280
2. Zhu, Y., Murali, S., Cai, W., Li, X., Suk, J.W., Potts, J.R., Ruoff, R.S.: Graphene and graphene oxide: Synthesis, properties, and applications. Adv. Mater. **22**, 3906–3924 (2010). https://doi.org/10.1002/adma.201001068
3. Yang, C., Yu, Y., Xie, Y., Zhang, D., Zeng, P., Dong, Y., Yang, B., Liang, R., Ou, Q., Zhang, S.: One-step synthesis of size-tunable gold nanoparticles/reduced graphene oxide nanocomposites using argon plasma and their applications in sensing and catalysis. Appl. Surf. Sci. **473**, 83–90 (2019). https://doi.org/10.1016/j.apsusc.2018.12.125

4. Novodchuk, I., Kayaharman, M., Ibrahim, K., Al-Tuairqi, S., Irannejad, M., Abdel-Rahman, E., Sanderson, J., Bajcsy, M., Yavuz, M.: B/N co-doped graphene oxide gel with extremely-high mobility and ION/IOFF for large-area field effect transistors. Carbon N. Y. **158**, 624–630 (2020). https://doi.org/10.1016/j.carbon.2019.11.034
5. Yang, T., Lin, H., Loh, K.P., Jia, B.: Fundamental transport mechanisms and advancements of graphene oxide membranes for molecular separation. Chem. Mater. **31**, 1829–1846 (2019). https://doi.org/10.1021/acs.chemmater.8b03820
6. Deng, T., Zhang, Z., Liu, Y., Wang, Y., Su, F., Li, S., Zhang, Y., Li, H., Chen, H., Zhao, Z., Li, Y., Liu, Z.: Three-dimensional graphene field-effect transistors as high-performance photodetectors. Nano Lett. **19**, 1494–1503 (2019). https://doi.org/10.1021/acs.nanolett.8b04099
7. Kim, M., Nabeya, S., Han, S.M., Kim, M.S., Lee, S., Kim, H.M., Cho, S.Y., Lee, D.J., Kim, S.H., Kim, K.B.: Selective atomic layer deposition of metals on graphene for transparent conducting electrodea application. ACS Appl. Mater. Interfaces. **12**, 14331–14340 (2020). https://doi.org/10.1021/acsami.9b23261
8. Wei, Q., Pei, S., Wen, G., Huang, K., Wu, Z., Liu, Z., Ma, W., Cheng, H.M., Ren, W.: High yield controlled synthesis of nano-graphene oxide by water electrolytic oxidation of glassy carbon for metal-free catalysis. ACS Nano **13**, 9482–9490 (2019). https://doi.org/10.1021/acsnano.9b04447
9. Rosli, N.N., Ibrahim, M.A., Ahmad Ludin, N., Mat Teridi, M.A., Sopian, K.: A review of graphene based transparent conducting films for use in solar photovoltaic applications. Renew. Sustain. Energy Rev. **99**, 83–99 (2019). https://doi.org/10.1016/j.rser.2018.09.011.
10. Guo, C., Suo, H.: Design of single-phased multicolor-emission phosphor for LED (2016). https://doi.org/10.1007/978-3-662-52771-9_15
11. Kang, Y., yong Chu, Z., Ma, T., Ping Li, W., Jiu Zhang, D., Yu Tang, X.: Red photoluminescence BCNO synthesized from graphene oxide nanosheets. Optoelectron. Lett. **12**, 1–4 (2016). https://doi.org/10.1007/s11801-016-5227-y.
12. Junaid, M., Khir, M.H.M., Witjaksono, G., Ullah, Z., Tansu, N., Mohamed Saheed, M.S., Kumar, P., Hing Wah, L., Magsi, S.A., Siddiqui, M.A.: A review on graphene-based light emitting functional devices. Molecules **25** (2020). https://doi.org/10.3390/molecules25184217
13. Rostami, M.: Construction of La-doped TiO2@La-doped ZnO-B-doped reduced graphene oxide ternary nanocomposites for improved visible light photocatalytic activity. RSC Adv. **7**, 43424–43431 (2017). https://doi.org/10.1039/c7ra06767d
14. Zhu, P., Li, S., Zhao, C., Zhang, Y., Yu, J.: 3D synergistical rGO/Eu(TPyP)(Pc) hybrid aerogel for high-performance NO_2 gas sensor with enhanced immunity to humidity. J. Hazard. Mater. **384** (2020). https://doi.org/10.1016/j.jhazmat.2019.121426
15. Dimiev, A.M., Eigler, S.: Graphene Oxide: Fundamentals and Applications (2016). http://ir.obihiro.ac.jp/dspace/handle/10322/3933
16. Rani, J.R., Oh, S.I., Woo, J.M., Tarwal, N.L., Kim, H.W., Mun, B.S., Lee, S., Kim, K.J., Jang, J.H.: Graphene oxide-phosphor hybrid nanoscrolls with high luminescent quantum yield: synthesis, structural, and x-ray absorption studies. ACS Appl. Mater. Interfaces. **7**, 5693–5700 (2015). https://doi.org/10.1021/am507342w
17. Cao, Y., Yang, T., Feng, J., Wu, P.: Decoration of graphene oxide sheets with luminescent rare-earth complexes. Carbon N. Y. **49**, 1502–1504 (2011). https://doi.org/10.1016/j.carbon.2010.11.014
18. Fan, X., Shang, K., Sun, B., Chen, L., Ai, S.: Decoration of surface-carboxylated graphene oxide with luminescent Sm 3+-complexes. J. Mater. Sci. **49**, 2672–2679 (2014). https://doi.org/10.1007/s10853-013-7975-4
19. Zhang, X., Zhang, W., Li, Y., Li, C.: Hybrid luminescent materials of graphene oxide and rare-earth complexes with stronger luminescence intensity and better thermal stability. Dye. Pigment. **140**, 150–156 (2017). https://doi.org/10.1016/j.dyepig.2017.01.019
20. Smith, A.T., LaChance, A.M., Zeng, S., Liu, B., Sun, L.: Synthesis, properties, and applications of graphene oxide/reduced graphene oxide and their nanocomposites. Nano. Mater. Sci. **1**, 31–47 (2019). https://doi.org/10.1016/j.nanoms.2019.02.004

21. Yang, X., Li, Z., Ju, E., Ren, J., Qu, X.: Reduced graphene oxide functionalized with a luminescent rare-earth complex for the tracking and photothermal killing of drug-resistant bacteria. Chem. A Eur. J. **20**, 394–398 (2014). https://doi.org/10.1002/chem.201303964
22. Naderi, H.R., Ganjali, M.R., Dezfuli, A.S., Norouzi, P.: Sonochemical preparation of a ytterbium oxide/reduced graphene oxide nanocomposite for supercapacitors with enhanced capacitive performance. RSC Adv. **6**, 51211–51220 (2016). https://doi.org/10.1039/c6ra02943d
23. Shukla, N., Verma, D.K., Singh, A.K., Kumar, B., Kavita, Rastogi,, R.B.: Ternary composite of methionine-functionalized graphene oxide, lanthanum-doped yttria nanoparticles, and molybdenum disulfide nanosheets for thin-film lubrication. ACS Appl. Nano Mater. **3**, 8012–8026 (2020). https://doi.org/10.1021/acsanm.0c01468.
24. Liu, B., Xie, J., Ma, H., Zhang, X., Pan, Y., Lv, J., Ge, H., Ren, N., Su, H., Xie, X., Huang, L., Huang, W.: From graphite to graphene oxide and graphene oxide quantum dots. Small **13**, 1–7 (2017). https://doi.org/10.1002/smll.201601001
25. Luo, Z., Qi, G., Chen, K., Zou, M., Yuwen, L., Zhang, X., Huang, W., Wang, L.: Microwave-assisted preparation of white fluorescent graphene quantum dots as a novel phosphor for enhanced white-light-emitting diodes. Adv. Funct. Mater. **26**, 2739–2744 (2016). https://doi.org/10.1002/adfm.201505044
26. Yin, L., Zhou, J., Li, W., Zhang, J., Wang, L.: Yellow fluorescent graphene quantum dots as a phosphor for white tunable light-emitting diodes. RSC Adv. **9**, 9301–9307 (2019). https://doi.org/10.1039/c8ra10353d
27. Lin, L., Song, X., Chen, Y., Rong, M., Wang, Y., Zhao, L., Zhao, T., Chen, X.: Analytica chimica acta europium-decorated graphene quantum dots as a fluorescent probe for label-free, rapid and sensitive detection of Cu(2+) þ and L-cysteine, Anal. Chim. Acta. 1–8 (2015). https://doi.org/10.1016/j.aca.2015.08.011.
28. Devadas, B., Madhu, R., Chen, S.M., Yeh, H.T.: Controlled electrochemical synthesis of new rare earth metal lutetium hexacyanoferrate on reduced graphene oxide and its application as a salicylic acid sensor. J. Mater. Chem. B. **2**, 7515–7523 (2014). https://doi.org/10.1039/c4tb01325e
29. Yu, Z., Zou, L., Chen, Y., Jiang, J.: (Pc)Eu(Pc)Eu[trans-T(COOCH3)2PP]/GO Hybrid Film-Based Nonenzymatic H2O2 Electrochemical Sensor with Excellent Performance. ACS Appl. Mater. Interfaces. **8**, 30398–30406 (2016). https://doi.org/10.1021/acsami.6b08760
30. Manavalan, S., Rajaji, U., Chen, S.M., Chen, T.W., Ramalingam, R.J., Maiyalagan, T., Sathiyan, A., Hao, Q., Lei, W.: Microwave-assisted synthesis of gadolinium(III) oxide decorated reduced graphene oxide nanocomposite for detection of hydrogen peroxide in biological and clinical samples. J. Electroanal. Chem. **837**, 167–174 (2019). https://doi.org/10.1016/j.jelechem.2019.02.023
31. Rajaji, U., Manavalan, S., Chen, S.M., Govindasamy, M., Chen, T.W., Maiyalagan, T.: Microwave-assisted synthesis of europium(III) oxide decorated reduced graphene oxide nanocomposite for detection of chloramphenicol in food samples. Compos. Part B Eng. **161**, 29–36 (2019). https://doi.org/10.1016/j.compositesb.2018.10.043
32. Rong, Y., Li, H., Ouyang, Q., Ali, S., Chen, Q.: Rapid and sensitive detection of diazinon in food based on the FRET between rare-earth doped upconversion nanoparticles and graphene oxide, Spectrochim. Acta Part A Mol. Biomol. Spectrosc. S1386–1425 (n.d.)
33. Mondal, S., Gupta, A., Shaw, B.K., Saha, S.K.: Photo-induced conductivity in 2, 6-diaminopyridine functionalized graphene oxide containing Eu^{2+} for optoelectronic applications. Opt. Mater. (Amst) **73**, 555–562 (2017). https://doi.org/10.1016/j.optmat.2017.09.013
34. Li, H., Su, S., Liang, C., Zhang, T., An, X., Huang, M., Tao, H., Ma, X., Ni, Z., Tian, H., Chen, X.: UV Rewritable Hybrid Graphene/Phosphor p-n Junction Photodiode. ACS Appl. Mater. Interfaces. **11**, 43351–43358 (2019). https://doi.org/10.1021/acsami.9b14461

Synthesis, Properties and Applications of Polymeric Matrix-Based Phosphor Hybrids

Samit Kumar Ray, Amritanshu Banerjee, Bidyut Kumar Bhangi, Barnali Dutta, and Debapriya Pyne

Abstract Phosphors are special types of compounds which emit lights when exposed to visible light, ultraviolet radiation or electron beam. In general, these compounds are prepared from inorganic transition metal or rare earth compounds. The radiation causes movement of its valence electron to the conduction or exciton band leaving behind a hole in the valence band. The electron–hole pairs moves to the impurities in the crystal of the phosphor which rapidly de-excite by emitting light. The inhomogeneity in the crystal structure of phosphor is created by addition of the impurities or dopants which is also called activator. Accordingly, a phosphor consists of a host which is oxides, nitrides, sulfides, halides, silicates or selenides of Zn, Cd, Mn, Al, Si or different rare earth metals and an activator metal such as Cu or Ag activated ZnS or Bi activated CaS phosphor. Apart from inorganic phosphors, more energy efficient phosphors for lighting and other optoelectronic applications are prepared from metal–organic frameworks (MOF) or coordination polymers. MOF consists of single metal ions or clusters of metal ions linked by organic ligands having multiple binding sites to form extended network structures. However, the inorganic or MOF based phosphors have several drawbacks like limited resources, high toxicity and also high cost. In contrast to inorganic or MOF based phosphors, metal-free small organic molecules or polymer based room temperature phosphors (RTP) are environment friendly and easy to process. These two types of RTPs are characterized by its long-lived triplet excitons and larger Stokes shift. However, easy processing, good flexibility and stretching ability, low cost, excellent electron mobility and thermal conductivity have made polymer based RTPs more attractive than small organic molecules based RTPs. Thus, Polymer based RTPs are widely used in organic light emitting diodes, solar cells, field effect transistors, memory devices and many other similar applications. The phosphors are prepared by (1) intersystem crossing (ICS) from the lowest excited singlet state (S_1) to a triplet state (T_n) and (2) radiative transition from the lowest excited triplet state (T_1) to the ground state (S_0). The emission from T_1 state is quenched at room temperature under ambient conditions. Accordingly, the challenge to get efficient RTP is to suppress

S. K. Ray (✉) · A. Banerjee · B. K. Bhangi · B. Dutta · D. Pyne
Department of Polymer Science and Technology, University of Calcutta, 92, A.P.C. Road, Kolkata 700009, India
e-mail: dskrpoly@caluniv.ac.in

© Springer Nature Switzerland AG 2022

K. Upadhyay et al. (eds.), *Hybrid Phosphor Materials*, Engineering Materials,
https://doi.org/10.1007/978-3-030-90506-4_7

nonradiative decay. Polymers are of high molecular weight with long chains that can cause entanglement and a high degree of rigidity making them ideal candidates to observe phosphorescence from organic lumiphores. In this book chapter synthesis, properties and applications of (1) non-doped and (2) doped polymer based RTPs will be discussed with reference to recent literature with the following possible.

1 Introduction

1.1 History, Origin, Definition and Types

About 20% of electricity is consumed for lighting. Thus, an energy efficient and environment friendly solid state lighting (SSL) based on phosphor converted light emitting diode (pc-LED) is of great importance [1]. This very word 'Phosphor' originates from Greek mythology of morning star Venus meaning 'light bearer' [2]. Phosphors are characterized with emission of 'Luminescence' or 'cold light'. These compounds emit light on exposure to different kinds of radiations such as photons, electrons with a high or low kinetic energy and X-rays [3]. A phosphor consists of a host which is oxides, nitrides, sulfides, halides, silicates or selenides of Zn, Cd, Mn, Al, Si or different rare earth metals and an activator metal such as Cu or Ag activated ZnS or Bi activated CaS phosphor. Apart from inorganic phosphors, there exist more efficient inorganic–organic hybrid, organic and polymer based phosphors. Japanese first prepared phosphors from seashells as reported in Chinese documents of tenth century. In seventeenth century an alchemist Casciarolo of Bologna, Italy fired a glossy stone obtained from a volcano with an objective to obtain a noble metal. However, the stone emitted light in the dark. In fact, the stone was a barite or $BaSO_4$ which on firing turned to BaS, now well known as one of the phosphor materials. In 1866 a young French Chemist Théodore Sidot first prepared ZnS type phosphor for television tube. From late nineteenth century to early twentieth century, Lenard and co-workers synthesized various phosphors based on sulfides and selenides of alkaline earth metals. Pohl and coworkers explored thallium activated single-crystal phosphors of alkali halide with extensive spectroscopic studies in twenties and thirties of twentieth century [2]. The modern luminescence physics is based on their research work only. After second World war-II there was a significant development on research of phosphor compounds with the progress in optical microscopy of transition and rare earth metal ions and also semiconductor physics. Apart from inorganic phosphors, more energy efficient phosphors for lighting and other optoelectronic applications are prepared from metal–organic frameworks (MOF) or coordination polymers. MOF consists of single metal ions or clusters of metal ions linked by organic ligands having multiple binding sites to form extended network structures. In the last few decades, there was significant development of white light phosphors based on coordination compounds of small organic molecules, MOF, non-metal polymer and polymer nanocomposites [4].

1.2 Theory and Mechanism of Light Emission

The cold radiation or luminescent of a phosphor is caused by either the host lattice or the activator impurity. In general, the emission takes place in the impurity or activator ion. However, the luminescence efficiency of a phosphor decreases at higher concentration of the activator (concentration quenching). When the emission is low from the activator (forbidden transition), a second 'sensitizer' is added. The sensitizer absorbs the energy and transfers it to the activator. The energy transfer from sensitizer (S) to activator (A) strongly depends on electrostatic and exchange interaction between S and A. The optical absorption leading to emission can also takes place by host lattice itself where energy is transferred from host lattice to activator. The color of the radiation is adjusted by changing the activator without changing the host lattice where the activator is added [5]. The emission mechanism from a phosphor is schematically shown in Fig. 1. The luminescence consists of both sharp emission bands of around 1 nm width and broad bands with >50 nm band width. Sharp bands are characterized with optical transitions involving same chemical bonding character in ground and excited state and also for optical transition between electronic states without any chemical bonding, e.g. for f–f transition in rare earth metal ions. In contrast, broad bands occur when the nature of chemical bonding differs considerably in ground and excited states as in the case of partly filled d orbitals of transition metal ions (d–d transition), transition between 5d and 4f orbitals of rare earth ions (4f–5d transition) and for emission on S orbitals (S2 ions) of metal ions like ions of lead, antimony and thallium. For a good phosphor the elapsed time between excitation and emission should be very short to avoid afterglow which is

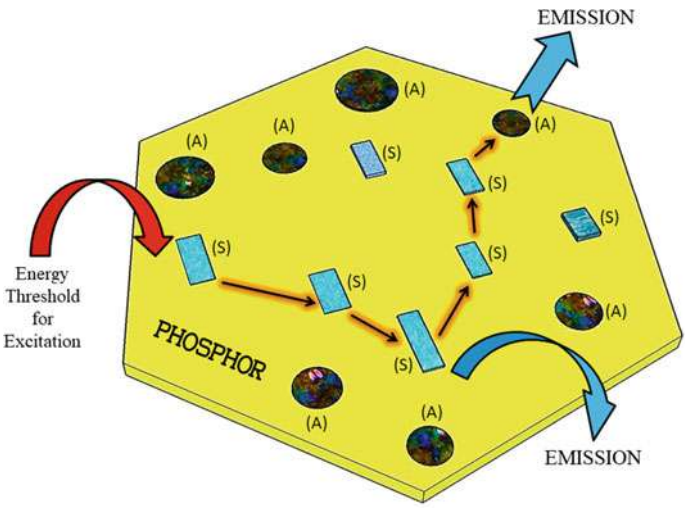

Fig. 1 Emission from a phosphor-containing activator (A) and sensitizer (S) [Adapted from Fig. 1.1 of Ref. [5], copyright ©2008 Wiley-VCH, ISBN 978-3-527-31402-7]

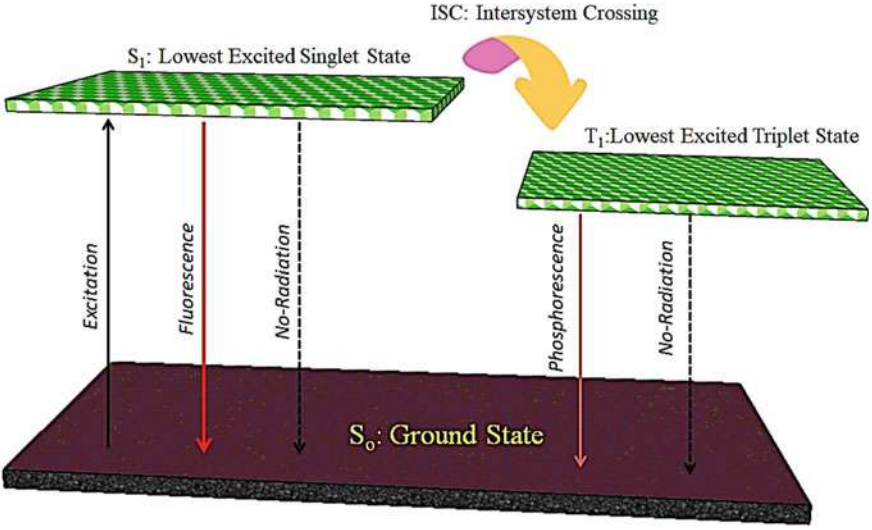

Fig. 2 Jablonski diagram of photoluminescence of RTP [Adapted from Fig. 2 of Ref. [6], 0010-8545/©Elsevier B.V., 2017]

efficiently met with rare earth metal based phosphor with 4f–5d transition. The 4f states of these phosphors weakly interact with the host lattice resulting in constant energy difference. For room temperature phosphors (RTP) consisting of metal free organic molecules or polymer based RTP, the phosphorescence includes inter system crossing (ISC) from the lowest excited singlet state (S_1) to a triplet state (T_n) and (ii) radiative transition from the lowest excited triplet state (T_1) to the ground state [6, 7] as shown in Fig. 2 in Jablonski diagram for polymer based phosphor. For these systems the emissions is easily quenched at room temperature. The only challenge for these systems is to reduce nonradiative decay and promote ISC. Polymers with its high molecular weight and hence long entangled chains and rigidity show good phosphorescence from organic lumiphores. It behaves like a crystalline lattice to control the molecular vibration and rotation of RTP. The polymer support of the RTP also reduces quenching effect of oxygen and moisture allowing triplet excitons of organic compounds for emission at room temperature.

1.3 Inorganic and MOF Based Phosphor

Inorganic phosphors consists of a crystalline host materials such as oxides, nitrides, sulfides, halides, silicates or selenides of Zn, Cd, Mn, Al, Si or different rare earth metals doped with a small amounts of impurities such as rare earth or transition metal ions, called an activator. The activator shows Stokes shift by converting light

from shorter to longer wavelength by electronic transition. For developing new inorganic phosphors the following systematic strategies, i.e., (i) screening suitable candidate from inorganic crystal structure database (ICSD), (ii) combinational chemistry screening with high throughput experimentation, (iii) chemical unit co-substitution based on a structural model and (iv) single particle diagnosis approach are considered [8]. Based on ICSD several inorganic phosphors have already been commercialized with various applications such as Ca-α-SiAlON:Eu^{+2} emitting yellow, β-SiAlON:Eu^{2+} emitting green and CaAlSiN3:Eu^{2+} emitting red light [9–11]. Similarly, novel phosphors such as $Ca_{15}Si_{20}O10N30:Eu^{2+}$, $La_{4-x}Ca_xSi_{12}O_{3+x}N_{18-x}:Eu^{2+}$, $Ca_{1.5}Ba_{0.5}Si_5N_6O_3:Eu^{2+}$ and $Ba(Si, Al)_5(O,N)_8:Eu^{2+}$ were developed based on combinational chemistry screening [12–15]. Similarly, based on the structural model several phosphors were developed, i.e., UCr_4C_4 model gave birth to different narrow-band phosphors such as red emitting nitride phosphors [16]. Nitride phosphors such as $BaSi_4Al_3N_9:Eu^{+2}$ and $Ba_5Si_{11}Al_7N_{25}:Eu^{+2}$ were developed based on single particle diagnosis approach [17]. Inorganic phosphors may be suitably modified to a more efficient phosphor by incorporating organic ligands which is bonded to a single or clusters of metal ions by its multiple binding sites. These kinds of phosphors are called metal–organic framework (MOF) or coordination polymer (CP) based phosphors. In fact, these coordination compounds are the largest family of known white light phosphors [4]. They are more diverse than inorganic phosphors since the organic ligands, metal centers and their coordination geometry can be designed in different ways. The structures of these crystalline phosphors are characterized with diffraction. The porous nature of MOF or CP allows easy encapsulation of guest species [6]. In general, rare-earth metals are selected for these inorganic–organic hybrid compounds since rare-earth metals easily show white light emission. The emission of light may be from the ligand, metal center or the guest molecules present in these phosphors. Luminescent CP (LCP) or MOF (LMOF) are used for imaging [18, 19], sensing [20, 21], optoelectronics [22, 23] and also in solid state lighting (SSL) device. These apart, MOF and CP based phosphors with its multi-functionalities are also reported for gas separation and storage [24, 25], catalysis [26, 27], proton conduction [27, 28] and also in drug delivery [29, 30].

1.4 Organic Metal Free Phosphors

The inorganic and inorganic–organic hybrid such as MOF or CP based phosphors has several drawbacks such as limited resources and hence high cost and use of toxic metal ions. In contrast, room temperature (RT) metal free low cost phosphors prepared from small organic molecules and polymers are environment friendly, non-toxic and easy to process. For metal based phosphors including MOF, the two critical steps in phosphorescence, viz., spin flipping from the excited singlet state to a triplet state and subsequent radiative decay from the excited triplet state (T_1) to the ground state occurs by spin–orbit coupling of the metal. Though organic phosphors are cheaper than metal phosphors, they are weaker and show long lived triplets. These

triplets are easily consumed by vibrational effects which reduces emissive decay. The vibrational dissipation from T_1 to the ground state must be reduced as it competes with phosphorescent decay. Aromatic ketone such as benzophenon is used as base compound for most of the organic phosphors [31] based on small organic molecules. For these compounds triplet T_2 level is close in energy with singlet S_1. Further, spin orbit coupling is localized at the carbonyl oxygen. The unwanted vibrational dissipation of benzophenon based phosphors may be reduced by introducing some heavy atoms like bromine or incorporating crystallinity [31]. Introduction of long chain rigid polymer backbone also reduces vibrational dissipation. Polymer based phosphors are more flexible and possess much better mechanical properties than small organic compound based phosphors because of its high molecular weight and long chain length. In fact, polymer based phosphors finds widespread applications in electronics such as organic light-emitting diodes, solar cells, field-effect transistors, memory devices, etc. In this book chapter various polymer based RT phosphors developed in recent years will be discussed in detail in terms of its preparation, properties, characterization and applications.

2 Polymer Based Phosphors

2.1 General Properties, Characteristics and Classification

Metal free room-temperature organic phosphors (RTP) are blessed with fascinating properties with widespread applications in the field of bio-imaging, sensing and display materials [32]. This new class of organic emitters is characterized with long decay time (millisecond to second), inefficient spin-orbit coupling (SOC) and large Stokes shifts which causes spectral separation of excitation and emission wavelength and thus measurements at low interference [33]. However, high costs, toxicity and instability in aqueous solutions limit applications of some of the RTPs. On the other hand a pure organic compound—small molecules or polymers could be a very good RTP provided it meets the following requirements—(1) some functional groups present in the organic compound should favor n-π^* transition with efficient intersystem crossing (ICS) from the lowest excited singlet state (S_1) to a triplet state (T_n), (2) it should have a very good packing or rigid structure in the solid state to stabilize the triplet excitons since it results in much reduction in radiative transition from the lowest excited triplet state (T_1) to the ground state (S_0) [34]. Polymer based RTPs are very efficient because of the presence of the polymer structure. The long coiled chains of high molecular weight polymer backbone provide rigidity in the structure which inhibits undesirable nonradiative relaxation. The coiled structure of polymer easily isolates oxygen and humidity resulting in reduced triplet excitons [7, 35]. Further, the polymer based RTPs have excellent properties such as non-toxicity, very good flexibility, stretchability, easy processing, low cost (in comparison to inorganic or MOF phosphors) and also good thermal stability [36]. A polymer may be converted to a

RTP by incorporation of some phosphor functionalities such as naphthalene imide, 4-bromobenzaldehyde or difluoroboron dibenzoylmethane in the polymer as 'guest' [37]. These functionalities also restrain intramolecular motions so that the room-temperature phosphorence properties are efficiently manifested. Polymer based RTP are prepared by non-covalent, i.e., physical encapsulation of the phosphor guests in the polymer or by chemical modification of the polymer where the phosphor functionalities are covalently bonded to the main chain, side chain or at terminal groups of the polymers [37]. These are schematically explained in Fig. 3. In physically encapsulated polymer based RTP, the host (polymer)-guest (phosphor groups) interaction is governed by electrostatic, hydrogen bond or Van der Waal forces. Covalent crosslinking between polymer and phosphors is also employed to further enhance its rigidity as required for a good RTP [38]. Based on these criteria, the polymer based RTPs are classified in two broad categories-namely (1) Non-doped polymer based RTP where the phosphor lies in the backbone of the polymer itself and thus there is no need for additional matrix bearing phosphor and (2) doped polymer based RTP

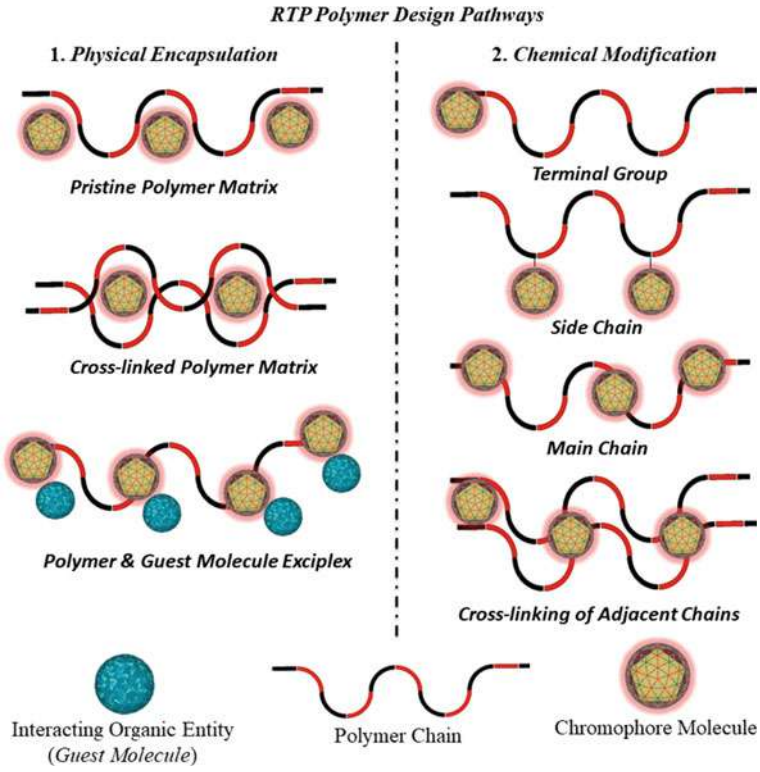

Fig. 3 Design strategy for polymer based RTP [Adapted from Fig. 2 of Ref. [37], © Chinese Chemical Society Institute of Chemistry, Chinese Academy of Sciences SpringerVerlag GmbH Germany, part of Springer Nature 2019]

where the polymer is not phosphor but a phosphor is incorporated (doped) in the polymer matrix [36].

3 Non-doped Polymer Based RTP

3.1 Polyurethane Based RTP

Long persistent or afterglow luminescent phosphors show visible light emission for a long period of time even after the excitation has stopped [39]. These long afterglow phosphors are widely used as night-vision materials for various important applications such as in traffic signs, display device, emergency signage, medical diagnostics, military and also for solar energy utilization [40–43]. Most of the commercial long lasting persistent phosphors are prepared from Eu^{2+} doped with aluminate or silicate. However, in these phosphors the emission color is restricted from blue to green region only [39]. This narrow color range could be widened by using polymer based persistent phosphors. Several specialty polymers such as polyurethane may be suitably modified to prepare these kinds of long persistent luminescent phosphors with wide range of color emission.

Polyurethanes (PUs) are one of the most important functional polymers with unique properties such as excellent mechanical strength, toughness, abrasion resistance, corrosion resistance, low temperature flexibility and easy processability. Thus, PUs are applied in a wide range of applications such as textile laminating, leather/synthetic leather finishing, foams, coatings and adhesives [44]. Multifunctional PUs are also used as long persistent luminescent phosphors. PUs consist of urethane (–NHCOO–) repeating unit in its structure produced from the reaction of isocyanate (–NCO) and polyols (–OH) along with some other additives. Depending on the type of isocyanate, polyol or crosslinker, PUs may be used as soft and hard segments, elastomers, adhesives, coatings and foams. PUs based phosphors may be classified as fluorescent and long persistent afterglow [44]. Fluorescence is also generated by radiation. However, it stops immediately after the incident radiation ceases [45]. For preparing fluorescent PUs, fluorescent dyes or pigments are mixed with PUs where it is chemically bonded to Pus [39]. Hu reported [46] fluorescent polymer dye prepared by reaction of a waterborne PU with disperse violet 26 dye (DV26). The waterborne PU was prepared by reaction of 2.4 toluene diisocyanate (TDI), polypropylene glycol (PPG) and dimethylol propionic acid (DMPA). The DV 26 was covalently bonded to the PU polymer by reacting with NCO groups of the prepolymer. This polymer dye is reported to show stable fluorescence with little change of fluorescence spectrum after storage at ambient temperature for one month. In a similar way PU-acrylic hybrid dye was also prepared by core shell emulsion polymerization where the dye monomer 6- amino-2-cyclohexylbenz[de]isoquinone-1,3dione was anchored on the PU shell. This PU dye is also reported to show stable fluorescence stability for three months

[47]. Amino functionalized $SrAl_2O_4:Eu^{2+}$, Dy^{3+} is a persistent luminescent phosphor having an afterglow time of 10 h with high luminescent intensity. It emits green color at a wavelength of 520 nm. This phosphor and a red fluorescers 1-[(2-hydrocyethly) amino]anthraquinone (HAA) was chemically bonded to the PU prepared from isophorone diisocyanate, (IPDI), 1,6-diisocyanatohexane (H12MDI), PPG and 1,4-Butanediol (1,4-BDO). This photochromic long persistent luminescent polyurethane (PLPLPU) shows red in daylight and yellow in darkness with persistent luminescence effect as shown in Fig. 4. In this PU, the antraquinone (HAA) part acts as color conversion agent and the yellow color in darkness is generated by mixing red of HAA with green of the inorganic phosphor [38]. Instead of HAA, a thermochromic pigment and $SrAl_2O_4:Eu^{2+}$, Dy^{3+} were incorporated in a similar PU prepared from isophorone diisocyanate (IPDI), 1, 6 diisocyanatohexane and PPG. This thermochromic PU shows an intense red color at room temperature which turns to white when the temperature rises to 35 °C. In darkness it shows yellow light at low temperature which changes to green at higher temperature [48]. From these results it is evident that a luminescent dye or pigment and long afterglow inorganic phosphors may be chemically bonded to functional PUs. In tune with these works, PUs were prepared by polymerization of a luminophore (a) as shown in Fig. 5 [49].

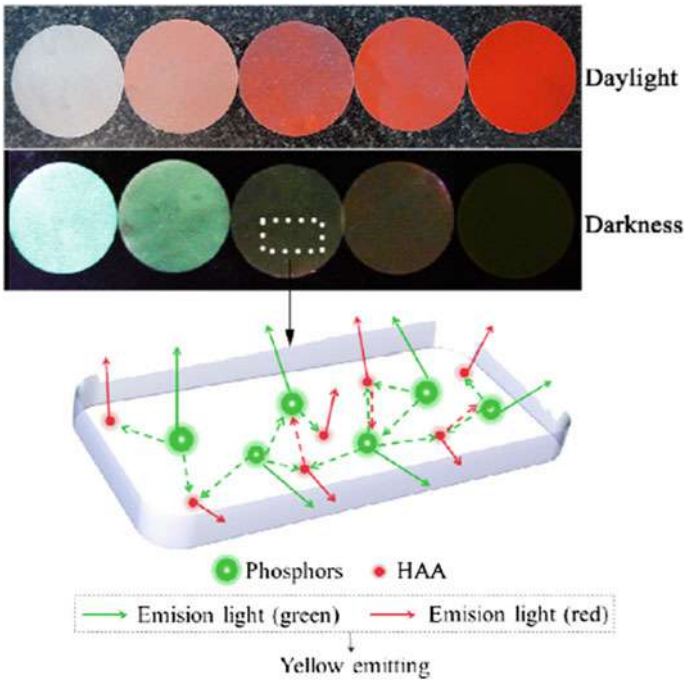

Fig. 4 Photograph and emission of photochromic long persistent luminescent polyurethane [Reproduced by combining Figs. 5 and 7 of Ref. [39] © The Royal society of Chemistry, https://doi.org/10.1039/C7NJ02607B]

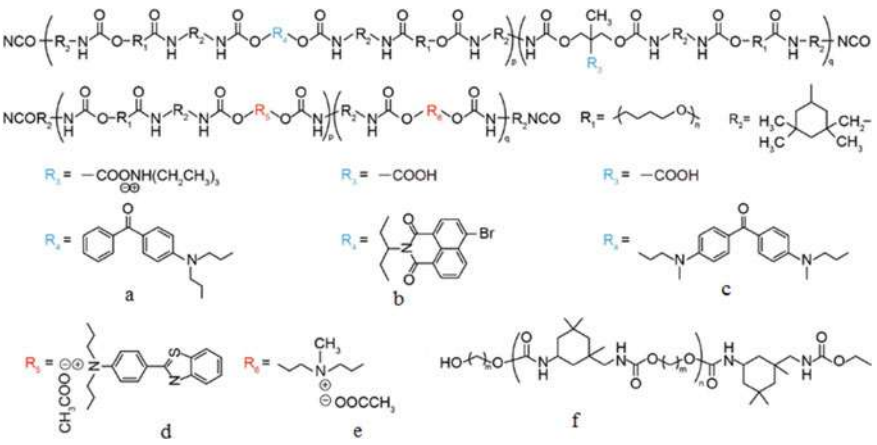

Fig. 5 Structure of some PU based RTP [Reproduced from Scheme 2 of Ref. [7], © 2018 WILEY-VCH Verlag GmbH & Co. KGaA, Weinheim]

Because of polymerization the energy level between singlet and triplet excited state decreases resulting in enhanced intersystem crossing (ISC). Similar emission properties were reported from polymer b and c as shown in Fig. 5 [50, 51]. The ratio of chromophore was increased in polymer film d (Fig. 4) and it showed a new phosphorescence band at around 520 nm with a lifetime up to microsecond. Apart from these structurally modified PUs, external stimuli also generated RTP from PUs. Thus, protonated thioflavin derivative was incorporated into a strongly polar PU matrix 'e' as shown in Fig. 5 [52]. The unprotonated form failed to show any RTP. In fact, the protonation causes lower lying intramolecular charge transfer (ICT) with more efficient ISC [7]. Similarly, green light emitting RTP with a lifetime of 0.5 s was obtained from nonaromatic polymer of 'f' (Fig. 5). This PU can be used for detection of explosive and also for cellular imaging because of its emission in concentrated solution and also in solid state [53].

3.2 Polyacrylonitrile (PAN) Based RTP

PAN is one of the most widely used thermoplastics around the world. The realm of its applicability extends from ultrafiltration (UF) membranes to the manufacture (precursor) of high-quality acrylic and carbon fibres. Being a non-conjugated polymer, PAN exhibits bleak chances of providing sustainable RTP emission and conceiving it still remains a daunting task. However, few reports have stated their observations of luminescence in some non-conjugated polymers and termed it as aggregation-induced photonic emissions (AIE) [54–56]. The exhibition of AIE emission by PAN has been reasoned in the reports as the clustering of –C≡N groups of

PAN as well as the overlap of their π and lone pair electrons which results in rigidified conformation facilitating RTP emissions. An older perspective towards the issue states that the heteroatom of nitrogen of PAN being electron-rich could facilitate RTP emissions. The structure of PAN along with its Jablonski diagram for different states of emission is shown in Fig. 6. To justify this presumption an exhaustive report by Zhou et al. [57] was published which demonstrated luminescence in a series of concentrated nano-emulsions of PAN in DMF/DCM solvents which was not apparent in the dilute solutions of the same. This observation exhibited the AEI property of PAN. In the same study, RTP emission peaks were observed in solid powders as well ranging between 440–484 nm. The plausible reason for the later event was depicted by clustering-triggered emission (CTE) mechanism where the role of the chromophore was played by the –C≡N groups of PAN. The RTP was induced by the overlapping π and n electrons which rigidified the conformation of the molecule such that lone pairs can initiate spin–orbit coupling, thereby facilitating the ISC between the energy levels. Similar report was published by Chen et al. [58], where the CTE mechanism for RTP was accepted and implemented to explain the phosphorescence of a poly-amino acid of ε-poly-L-lysine (ε-PLL); which is a non-aromatic compound. In the mid-2019, Kopeć et al. [59] reported surface-grafted PAN brushes with solid-state AIE properties. PAN was synthesized and grafted on silicon wafers by copper-mediated photo-induced atom transfer radical polymerization (ATRP). It was reported that AIE was more pronounced in low molecular weight (Mn < 10 k) PAN as well as in thin (d < 15 nm), surface-grafted polymer brushes. The revelation was unique since AIE properties in low molecular weight PAN can be henceforth be applied to other non-aromatic polymers as well as structural analogues like block copolymers or molecular brushes etc.

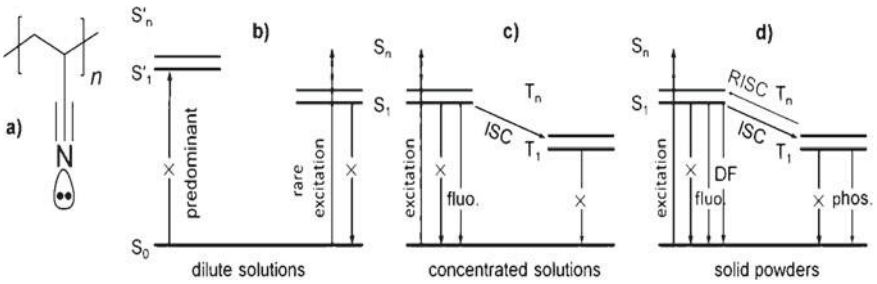

Fig. 6 Structure of PAN along with Jablonski diagram for different states of PAN [Reproduced from Fig. 1 of Ref. [57], https://doi.org/10.1002/smll.201601545 © 2016 WILEY-VCH Verlag GmbH & Co. KGaA, Weinheim]

3.3 Polyamide/Polyimide Based RTP

High performance polymers such as polyamides and polyimides are characterized with high crystallinity, regularity, rigidity, melting and strong chain-chain interaction. In fact, multiple hydrogen bondings in the structure of polyamide/polyimide contribute to its structure rigidity which efficiently stabilizes the triplet excitons resulting in generation of RTP [7]. Because of its rigid repeating unit, these engineering plastics have excellent thermal, mechanical, environmental and radiation stability [60]. These polymers are widely used in aerospace industries, electronics, photonics, microelectronics and also as RTP because of photoluminescence (PL) properties of some of the polyamides and polyimides. Polyacrylamide is a water soluble low cost polymer which can also be used as RTP. Accordingly, the following three metal free polyacrylamide based RTPs (Fig. 7 a–c) with high emissive efficiencey were reported [61]. The quantum yield (Φ_p) of these three RTPs increased significantly (11.4%, 8.1% and 7.4%, respectively) after incorporation of heavy

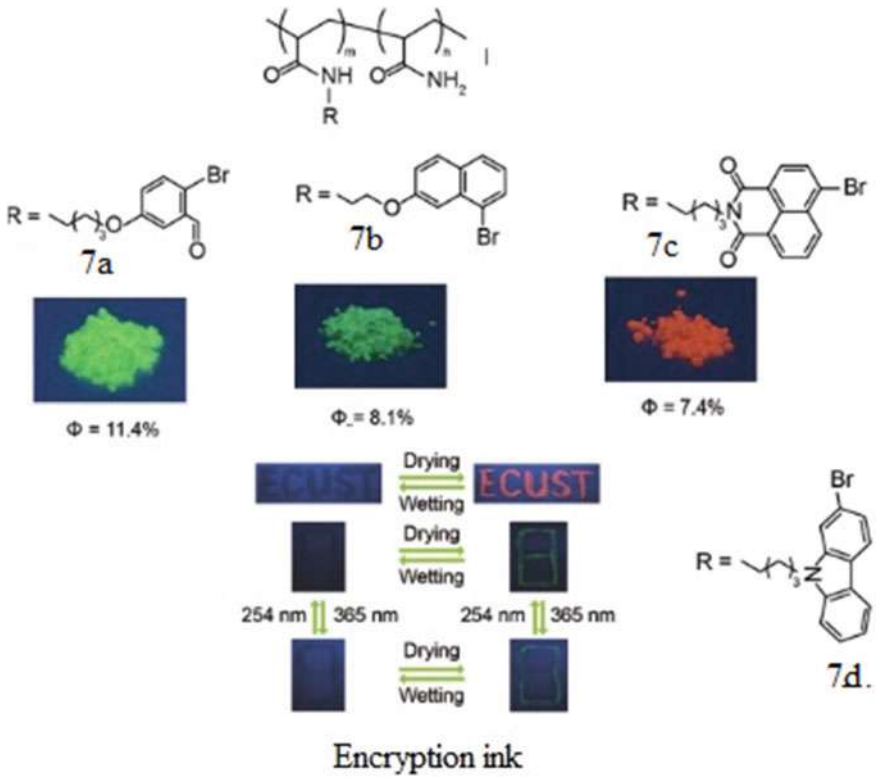

Fig. 7 Polyacrylamide based RTP, structure, solid powder and encryption ink based on these RTP [Reproduced combining Figs. 2 and 5 of Ref. [61], https://doi.org/10.1002/adom.201600427 © 2016 WILEY-VCH Verlag GmbH & Co. KGaA, Weinheim]

bromine (Br) atom in the polymer. In these cases the strong hydrogen bonding between the polymer chain not only reduce the undesirable nonradiative transition but also make it a water responsive RTP. The emission of the substituted polyacrylamide as shown in Fig. 7a occurs at 254 and 365 nm while the other two amides as shown in Fig. 7b, c shows emission at only 254 and 365 nm, respectively. Hence, these polyamides can be used in encryption ink. The polyacrylamide based RTP with bromine substitution as shown in Fig. 7d showed blue purple RTP at 453 nm with a Φ_p of 4.83% in air [62]. The photographs of these amorphous polyamide based RTP along with the encryption ink is also shown in Fig. 7

From the above discussion it is evident that the presence of heavy halogen atom such as Br increases chain rigidity resulting in improved RTP. However, the presence of halogen in the structure also shortens the phosphorescence lifetime by increasing the rate of radiative and nonradiative transition of triplet excitations [7]. Incorporation of oxygen containing functional groups instead of Br atom provided excellent emission performance with a life time of 537 ms and a high phosphorescence efficiency of 15.39% [63]. The quantum yield (Φ_p) of aromatic polyimides prepared from aromatic dianhydrides and diamines are very low (Φ_p much less than 0.01) because of very strong charge transfer (CT) interaction between the aromatic diamine and the aromatic dianhydride [64]. For improved PL properties, the CT interaction is to be reduced. Thus, instead of aromatic diamine, alicyclic diamine was employed and the resulting polyimide film with reduced CT interaction showed much higher PL [65]. However, the energy gap between the excitation and the emission wavelength, i.e., the Stokes shift for these polyimides (PI) are low. Polyimide with higher Stokes shift was reported where the polyimide was synthesized with a pyromellitic dianhydride containing –OH functionality. In this case higher Stokes shift occurred due to intramolecular proton transfer from the excited state (ESIPT) [66–68]. Similarly, a series of CoPIs were prepared by copolymerizing 3, 3′, 4, 4′-biphenyltetracarboxylic dianhydride (BPDA) and 1,4-dibromopyromellitic dianhydride (DBrPMDA) with 4,4′-diaminocyclohexylmethane (DCHM) as a diamine. These CoPIs showed excellent PL properties [60].

3.4 Polylactic Acid-Based Phosphors

Polylactic acid (PLA) is a biodegradable thermoplastic obtained from the fermentation of agricultural products such as corn, potato, sugar beet and other organic wastes which produce lactic acid (precursor) [69]. PLA is also reported to have similar mechanical properties of commodity plastics like polyethylene (PE), polyethylene terephthalate (PET), polypropylene (PP) and polystyrene (PS) [70]. Hence, an investigation of PLA's rigid molecular structure to exhibit RTP was a necessity. From the sporadic research on the luminescence of PLA, it was revealed that PLA could yield RTP emission and also possess a dual emissive property in communion with some functionalized luminophores having two-photon absorption and a large extinction

coefficient value. Zang et al. [71] have reported luminescent property of a biocompatible polymer called boron difluoride dibenzoylmethane (BF2dbm)—PLA, which is perhaps the fundamental work about the topic under review. Upon investigation, BF2dbm coupled with PLA showed several facets of emission which included delayed to intense fluorescence along as well as green RTP having a lifetime of 0.17 s. The team also reported having remarkably achieved RTP persisting for about 10s even after the excitations were stopped. The staggered RTP was reasoned to have occurred possibly due to the rigid structure of PLA harbouring BF2dbm that resulted in restrained triplet excitons from thermal decay. More than half a decade later, DeRosa et al. [72] investigated several halide substituents of BF2dbm-PLA and arrived at the conclusion that the heavier was the halogen substituent, the more efficiently BF2dbm-PLA performed ISC. The heavy atom effect increased manifold the RTP intensity only at the cost of a decreased lifetime. DeRosa et al. further opined on the influence of molecular weight (M_w) of BF2dbm-PLA on RTP emission wavelength and stated that an increase in M_w can increase the singlet-triplet energy gap thereby decreasing ISC, which resulted in long RTP lifetime. A research article by Zhang et al. [73] gives an insight into the structural contribution of a luminophore in RTP. The hydroxyl-functionalized aromatic diketone, dibenzoylmethane (dbmOH), under investigation showed weakly fluorescence in the solid-state and was surprisingly non-fluorescent in solution while its difluoroboron complex (BF2dbmOH) as highly emissive in both states. The results depict that boron was contributory towards enhancing RTP but the diketone structure initiates phosphorescence. Zhang et al. [74] focused their investigations on PLA stereochemistry which could influence RTP properties. The research team was able to synthesize BF2dbmPCL-PLA (D, L-Lactide) and BF2dbmPCL-PLLA (L-Lactide) block copolymers respectively and brought them under the ambit of RTP study. RTP measurements gave an uncanny result; both D, L-Lactide and L-Lactide had a persistent green emission with similar lifetimes but with different intensities. It can be asserted from the given observation that the PLA segments reduce the local crystallinity as well as the micro-cavities inherently present in the polymer. The resultant molecular vibrations and rotations are restrained and thermal decay pathways are reduced. This resulted in RTP emissions in the D, L-PLA system to be appreciably brighter than L-PLA (PLLA) systems.

Molecular aggregates of organometallic compounds exhibit very efficient ISC. The resultant phenomena are called ligand localized ($^3\pi$–π^*) phosphorescence. It is mediated by the metal to-ligand or ligand-to-metal charge transfer (CT) present in such molecular systems. Extending this paradigm, Chen et al. [75] attempted to introduce an intra-molecular ICT in NNI-based PLAs for the initiation and enhancement of RTP as shown in Fig. 8. Their investigations revealed that to obtain an effective ISC resulting into a sustained RTP, PLA should be endowed with a heavy atom viz. Cl, Br etc. or an ICT state must be introduced in the same. Chen et al. had reported that out of the several NNI-based PLAs under their research ambit, only the molecular species of 1, 2-OPh-PLA exhibited intense RTP due to the obvious reasons that the referred species possessed the highest ICT due to the large singlet-triplet energy gap (ΔEST) which is inherent to the π–π^* transitions.

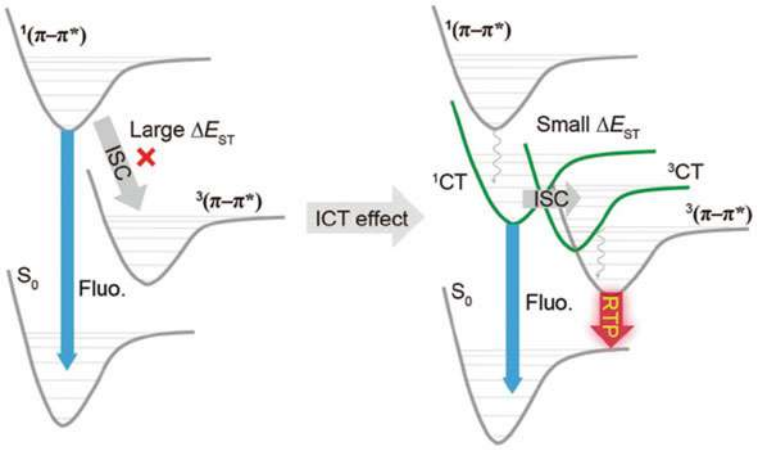

Fig. 8 Introduction of ICT state in PLA based phosphors for sustained RTP emissions Ref. [Reproduced from Scheme 2 of Ref. [75] © 2016 Wiley–VCH Verlag GmbH & Co. KGaA, Weinheim]

The noteworthy contribution of nanotechnology (NT) in the field of phosphorescence is worth mentioning. From a deluge of reports based on phosphorescent nanoparticles (NPs), an investigation on green RTP emission by BF2dbmPLA NPs by Pfister et al. [76] provides an insight into the applicability of the synthesized NPs in the field of cell internalization as well as imaging. Surprisingly, the NPs had similar phosphorescent properties as BF2dbmPLA polymer at 22 °C. The RTP lifetime of 200 ms bestowed on the NPs was also found to be analogous to that of the polymer in the solid-state under vacuum. Kerr et al. [77] carried out further investigations on difluoroboron β-diketonate polylactic acid (BF2bdkPLA) NPs. In their study the used four dyes with varying π-conjugation (phenyl, naphthyl) and donor groups, viz., −OMe, −NMe2 coupled to PLLA−PEG block copolymers by post-polymerization had achieved full RTP emission along with sustained lifetimes of phosphorescence. The NPs exhibited red-shifted RTP ranging from 520 to 556 nm which was long-lived to be utilized in oxygen concentration imaging.

3.5 Other Non-doped Polymer Based RTP

Polystyrene sulfonic acid is an ion exchange resin used in chemical industries for separation of metal ions and also as drug for removal of excess potassium from human body suffering from kidney disease. This resin has also the potential of being used as RTP. Ogoshi [78] and coworkers reported a polystyrene sulfonic acid based RTP showing one of the longest life time (1.22 s) among reported non-doped organic RTP. The long life time was ascribed to the presence of sulfonic acid group in the

polymer. Similarly, terephthalic acid and its derivatives shows crystallization induced dual emission (CIDE) which prevents non-radiative motion and quenching of triplet excitons by oxygen or humidity [37]. Accordingly, Yuan and coworkers reported a polymer prepared from terephthalic acid, i.e., poly(ethylene terephthalate) (PET) based RTP. It showed concentration enhanced emission and also aggregation induced emission [79]. In recent years phosphors based on nano material filled polymers, polymer carbon dots (PCdots) and covalent organic framework (COF) have also been reported. Kim and coworkers [80] synthesized a polymer nanoparticle (PNPs) in a non-rigid matrix showing bright green RTP in argon rich water. The PNPs dispersed in aqueous solution showed high sensitivity to oxygen and hence it could be used for oxygen quantification in various environments. In PCdots the carbon dots provide excellent phosphorescence properties while the polymer acts as the matrix support. Thus, a blue–green afterglow emission was reported from a covalently crosslinked and rigid PCdots with a very long life time of 658.11 ms [81]. Wang reported a COF with H aggregation emitting yellow phosphorescence with a life time of 0.69 ms [82].

4 Doped Polymer Based RTP

From the above discussion it is evident that several functional polymers may be suitably modified as non-doped RTP where the phosphor, e.g., different dyes molecules is chemically bonded with the polymer. The phosphorescence is originated from the molecular center of the non-doped polymers. However, the requirement of the chemical reaction and subsequent bond formation between the guest phosphor and the host polymer, maintaining stringent reaction conditions, use of expensive catalyst for these kinds of selective reactions limit the widespread development and applications of non-doped RTP. To eliminate these problems, doped RTP was developed where the guest phosphor is physically mixed with the host polymer. In doped polymer based RTP the function of the host polymer is to provide a rigid atmosphere so that the nonradiative transitions are reduced. Further, rigid structure has lower probability of rotation and possible collisions causing better phosphorescence performance [83]. In this case the phosphorescence originates only from the guest molecule which is physically bonded with the host polymers. In general, polymers such as polymethyl methacrylate (PMMA), polyvinyl alcohol (PVA), polylactic acid (PLA) with transparency and hydrogen bonding ability is chosen as host matrix to encapsulate the small organic RTP as guest. Accordingly, the following doped polymer based RTP are widely reported for various applications.

4.1 Polymethyl Methacrylate (PMMA) Based RTP

PMMA or Plexiglas has been a lucrative choice in the fabrication of several luminescent devices in the last three-four decades. PMMA is bestowed with excellent transparency particularly in the near-UV to the near-IR spectral regions. The thermal stability and easy processing make it a robust and cheap alternative. An inert polymer, PMMA finds applicability as a base material in fabricating phosphorescent devices due to its structural robustness along with a wide band gap [84] which enables the polymer matrix to confine the molecular-motion essential for RTP emissions. To add to these accolades, PMMA has very close solubility parameter values towards several organic molecules (dopants) which results in the formation of several doped phosphorescent materials which are easy to fabricate and are frequently used across the orient. This decade has perhaps witnessed some prolific work on RTP research, where Reineke et al. [85] have reported high yielding dual emissions of fluorescence and phosphorescence at room temperatures from a PMMA film doped with a semiconducting molecule; (N,N′-bis(4-benzoyl-phenyl)-N,N′-diphenyl-benzidine). This work exhibited a slow lifetime of decay of about 208 ms with an estimated high Φ_p value of 50%. The result was in contrast to the general observation as the total phosphorescence intensity at room temperatures was appreciably higher than what has been observed at 77 K or below. This anomaly can be addressed by the fact that in the present study the coupling of the triplet state to the intermolecular motion was very weak and the ISC had to be assisted thermally to initiate phosphorescence. Reineke et al. report was in agreement to the presumption that PMMA provides rigid structure at low temperatures to restrict molecular mobility making RTP conducive and emission of different colours ranging from 550–470 nm was observed from the doped matrices. Lee et al. [31] had published an exhaustive report depicting a highly efficient RTP with a quantum yield of around 7.5%. The study was based on the host–guest material interactions in amorphous PMMA matrix and also helped to establish the fact that the tacticity of PMMA had a pivotal role in enhancing RTP emissions. Lee and co-workers introduced a guest molecule of Br6A (2,5-hexyloxy-4-bromobenzaldehyde) into an isotactic PMMA (iPMMA) matrix and had witnessed nearly ten times brighter RTP when compared with its syndiotactic or atactic isomers. The percent dosing of iPMMA was increased gradually, the Φ_p escalated from 0.7 to 7.5%. This observation was substantiated from the fact that the triplet excitons lead to the vibrational losses which are remarkably suppressed due to the reduced β-relaxation in iPMMA structure. This structural facet of iPMMA enables the guest molecule phosphorescence quite efficiently. The Br6A-doped iPMMA matrix was then employed in a microfluidic device meant for temperature sensing. It consisted of a polydimethyl siloxane (PDMS) rubber channel on a glass slide coated with Br6A-doped iPMMA as shown in Fig. 9. Hot and cold water was made to flow through microchannels of the device which resulted in setting up of a temperature gradient, the outcome of which was phosphorescence occurring at room temperatures. RTP emissions increase almost linearly across the temperature gradient which served to be the prototype for RTPs to be utilized as temperature sensors. The versatile PMMA

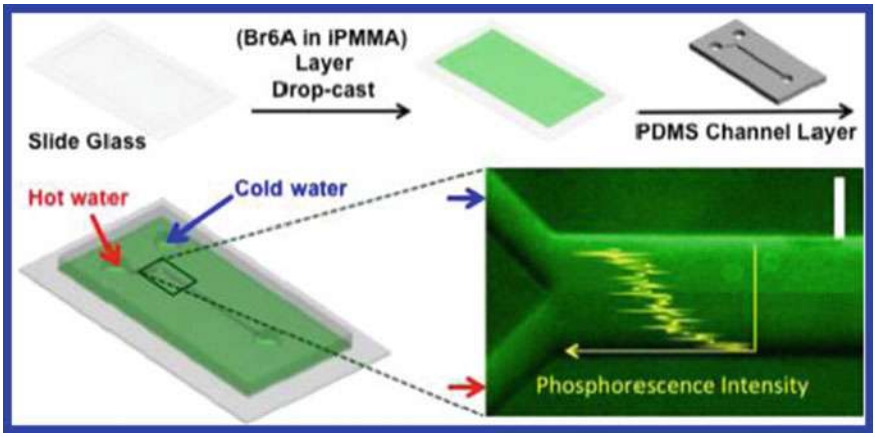

Fig. 9 Microfluide device containing Br6A embedded iPMMA coated on a glass slide on a PDMS channel. [Reproduced from Fig. 6 of Ref. [31] © American Chemical society, 2013]

matrix was again put to use by Joshi et al. [86], they employed conformational control and tried to incorporate some contributory.

functional groups to a bichromophoric molecule called CBIQD; (2-(6-chlorobenzo[d]thiazol-2-yl)-1H-benzo[de]isoquinoline-1,3(2H)-dione) and altered its emissive properties, especially phosphorescence. The study revealed that an interesting fact that planar and non-planar conformation of CBIQD molecule influenced RTP emissions. The planar conformation contributed to fluorescence; while nonplanar one aided in phosphorescence. The rigid PMMA matrix induced the essential triplet state emission to initiate RTP by hindering nonradiative pathways and restricting intermolecular motions of CBIQD respectively. On a similar footing, coronene (a polycyclic aromatic hydrocarbon or super-benzene) doped PMMA was studied by Mieno et al. [87] and they shared their observations by stating that both aggregative and non-radiative transitions of planar coronene were restricted by the rigid PMMA matrix. Mieno and co-workers witnessed a sustained RTP for about 5.58 ms by introducing only 0.6wt% of planar coronene into the PMMA matrix. An unhackneyed approach was suggested by Koch et al. [88] which utilized singlet fission to amplify phosphorescence. The study was based on seven metal and heavy atom-free boron compounds synthesized from hydroxy-vinyl imines and were introduced into PMMA. The report showed over 100% absolute quantum yield for some of the candidate compounds within the purview of the study. Upon thorough investigation, the study revealed a striking facet that singlet fission can be induced by $\pi-\pi$ stacking interactions as well as tailored electronic structures present in PMMA matrix, which are primarily responsible for high-efficiency emissions. The idea established a benchmark to be used in several optoelectronic applications in near future. A comparative study based on mainly two luminescent compounds, viz. 1-naphthoic acid (1NA) and 2-naphthoic acid (2NA) was undertaken by Gahlaut et al. [83] to investigate the implications of several polymer microdomains consisting of PVA,

PMMA & CA on the optical properties of the resultant compound. The result enunciated a striking conclusion that even for the same guest organic molecule different polymers exhibit different RTP properties. It was quite apparent in the case of PMMA, which exhibited negligible phosphorescence under nitrogen atmosphere perhaps due to weak hydrogen bonding.

4.2 Polyvinyl Alcohol (PVA) Based RTP

PVA is a good film forming water soluble polymer with excellent hydrogen bonding capabilities. PVA film is crystalline due to extensive intra and intermolecular hydrogen bonding. However, the intermolecular and intramolecular hydrogen bonding of PVA is lost and it turns to amorphous when a small organic phosphor guest, a substituted functional aromatic compound containing –OH, C=O and Br (marked as G1) is encapsulated in PVA matrix as shown in Fig. 10 [89]. As a host, PVA shows multiple hydrogen bonding interactions with the guest phosphor which also reduces the thermal motion of the guest molecules. The heavy halogen atom, Br of the organic phosphor also undergoes strong hydrogen bonding interaction with

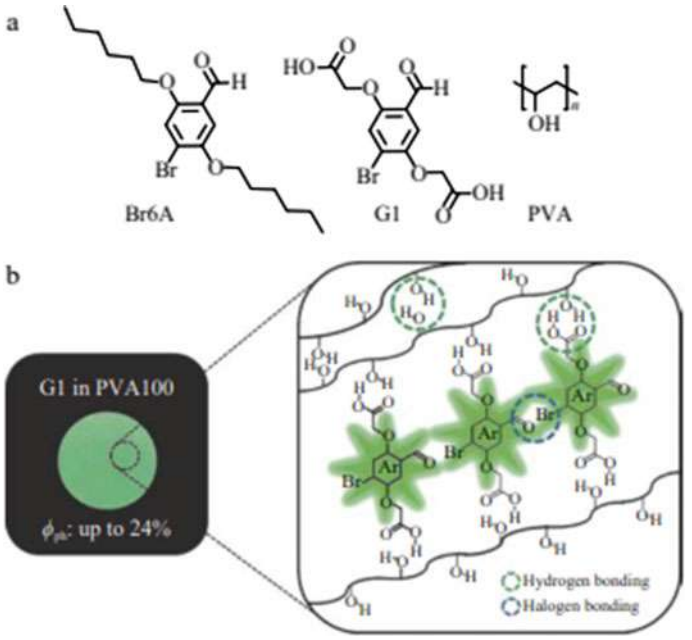

Fig. 10 Structure and image of PVA based RTP [taken from Fig. 13 of Ref. [7] © 2018, WILEY-VCH Verlag GmbH & Co. KGaA, Weinheim]

the PVA matrix. It results in increase in rigidity of the polymer host, increased spin–orbit coupling and intersystem crossing (ISC) between singlet and triplet states. As a result this PVA encapsulated phosphor showed a very good quantum yield of 24% with a life time of 5.9 ms at ambient condition [89]. As G1 is replaced with another phosphor, 2,5-dihexyloxy-4-bromobenzaldehyde (noted in Fig. 10 as Br6A), the quantum yield of the phosphor decreased to 12% due to reduction in hydrogen bonding with this (in comparison to G1) phosphor having higher substitution. On the other hand crosslinking in PVA further increases its rigidity and hence the organic phosphor doped crosslinked PVA showed higher quantum yield [90]. Similarly, more functional organic phosphor such as hexa-(4-carboxyl-phenoxy)-cyclotriphosphazene containing six benzoic acid arms in its structure showed extensive hydrogen bonding with PVA. Further, the carbonyl functionalities of the six aromatic rings provide enough *n* orbitals for easy ISC from singlet to triplate states. However, small amount of this phosphor when encapsulated in PVA showed poor RTP with a life time of 0.28 ms and quantum yields of only 2.85%.

However, after irradiation for 65 min at 254 nm light the life time and quantum yield increased to 0.71 ms and 11.23%, respectively. These results indicate that crosslink polymer under external stimulus efficiently improved the performance of physically encapsulated RTP [37, 90]. Similarly, Gahlaut et al. [83] observed strong RTP with a life time of 55 ms for 1, naphthoic acid phosphor encapsulated in PVA because of strong hydrogen bonding interaction between the guest 1, naphthoic acid and PVA. Oxygen was also found to quench the RTP significantly. PVA based RTP was further attached to carbon dot (C dots) to further improves its phosphorescence properties. In fact, the carbonyl groups of C dots s contributes to increased phosphorescence while the PVA matrix protects the triplet excitons from rotational and vibrational decay through rigid hydrogen bonding. Accordingly, PVA-Cdots composite green RTP was reported by Deng et al. [91] in 2013 which showed a long life time of 380 ms. Amphiphilic carbon dots (ACdots)/PVA was also reported to show a very long life time of 450 ms [92]. Patir and Gogoi prepared another Cdots-PVA which showed green phosphorescence with a life time of 503.43 ms [93]. Because of strong phosphorescence as well as water solubility Cdots-PVA can be used as anti-counterfeiting and secret information carrier on various packages [91].

4.3 Polylactic Acid (PLA) Based RTP

Exhaustive research has been undertaken in the recent past to demonstrate the viability of PLA to be used as a non-doped RTP emitter. The promising results have resurrected the urge to investigate further into the realm of doping and utilizing PLA as the host polymer matrix. PLA in its amorphous state provides a rigid environment to restrict the thermal decay and impedes quenching molecules to interfere with the triplet excitons conducive to RTP. Aromatic difluoroboron β-diketonate complexes (BF2bdks) can be termed as the most frequently used class of fluorescent compounds which has fed the insatiable thirst of RTP research over the years.

Accordingly, several BF2bdk derivatives were brought under research ambit by Xu et al. [94] to investigate the RTP properties of doped PLA films within a dye concentration range of 0.05–0.5%. Their report stated distinct green/yellow RTP emissions being observed by all BF2bdks blended with PLA. In these phosphors a slight red shift in phosphoresce was sighted with a higher dye load. The methoxyl (electron donor) substituted BF2bdks were found to be accountable for the apparent red-shift in RTP when compared with the non-substituted ones which have higher lifetimes of phosphorescence. Not remaining restricted to BF2dbm complexes, a report by Zang et al. [95] narrates an observation of dual RTP emissions from aromatic ketones incorporated into PLA. Several Lewis acids like $AlCl_3$, BCl_3, BF_3, and $GdCl_3$ were chosen to fabricate dual emissive material because they have a strong binding affinity towards the aromatic ketone. The researchers witnessed a prolonged RTP emission under the nitrogen environment even after UV irradiation was halted. They asserted the plausible cause of their observation was due to rigidness of the PLA matrix which could suppress thermal decay or loss at room temperatures. Daly et al. [96] brought a new perspective to the topic under review and highlighted the stereochemistry of luminescent compounds. They reported the synthesis of BF2dibenzoylmethane (BF2dbm) dyes with dodecylalkoxy chains in either the para- or meta-position on one aryl moiety of the dye, with the opposing phenyl ring substituted with a halide. When these dyes were incorporated into PLA, emission shifting to blue spectrum was perceived with very short lifetimes as compared to the meta-counterparts. This investigation revealed that apart from ICT state contribution, the location of substitution played a key role in tuning phosphorescence. Under the purview of BF2bdks inclusion into PLA as unsymmetrical guest species, Liu et al. [97] demonstrated the scrupulous tuning of phosphorescence by substituting a heavy atom on the naphthyl unit (major) of BF2bdks. Secondly, by positioning a bromide ion on the phenyl unit of the same molecule, the authors represented a surge in triplet species population initiating RTP.

4.4 Molecularly Imprinted Polymers (MIPs)

The advent of MIPs (molecularly imprinted polymers) has enriched the field of materials research to great extent by penetrating several domains like chemical/biological sensors, dye separation, artificial antibodies (pharmacological application), catalysis, etc. The molecular imprinting of polymers is based on a simple principle [98], where a functional monomer and an imprint molecule (often termed to be a template) are combined and ultimately co-polymerized in presence of a chemical cross-linker. The covalent interaction between functional monomer and the imprint takes place before the polymerization. After polymerization, the template rebinding occurs due to non-covalent interactions. These non-covalent interactions are responsible for the molecular recognition phenomenon between the template molecule and polymer due to their flexible rebinding and reversibility. Removal of the template

molecule from the crosslinked polymer results in the formation of template recognition sites complementary to a ligand, shape and size of the template. Thus, molecular imprinting is a facile method to impart molecular memory in a candidate polymer. The rigid environment of the MIPs yielded by the crosslinked internal structure can be put to deliverance for RTP emissions. Yet the topic has been explored to a limited extent. Salinas-Castillo et al. [99] reported the use of tetra-iodo-bisphenol A and diphenylmethane-4,4′-di-isocyanate (MDI) as functional monomers and fluoranthene substantiated as the template molecule. The recipe was chosen for sensing PAHs (polycyclic aromatic hydrocarbons) which are known to exhibit RTP emissions in the presence of fluoranthene. The investigation revealed that fluoranthene entrapped by the non-iodinated MIP did not exhibit any RTP emissions, but a contrary result was obtained for the iodinated one. RTP emission peaks were witnessed at around 550–593 nm for the iodinated MIP. It can be asserted that RTP emission was due to the iodine (heavy atom) contained in the rigid environment of the MIP which induced efficient RTP emission in the presence of an oxygen scavenger. Sanchez-Barragan et al. [100] in 2005 extended the heavy atom effect analogy. The MIP was synthesized using the aforementioned recipe for sensing several PAHs. The sensor demonstrated high fluoranthene specificity and the detection limit for the target analyte of 35 ng/L. Recently, a MIP-based nanosensor [101] for fish aflatoxins (AFs) detection was reported as also shown in Fig. 11.

The MIP was synthesized using DMSO (dimethyl sulfoxide) with the template DMC (5,7-dimethoxycoumarin), divinylbenzene(DVB) and methacrylic acid (MA) in-situ coated on PEG (polyethylene glycol)-Mn-doped ZnS QDs (quantum dots) en route polymerization. Synthesized nanosensors exhibited intense RTP with a total decay time of 0.004 s as the AFs interacted with the recognition cavities of the MIPS attached to the phosphorescent QDs. The RTP was found ranging from 520 to 720 nm (highest peak intensity of 594 nm) after excitation. The prepared MIPs exhibited high

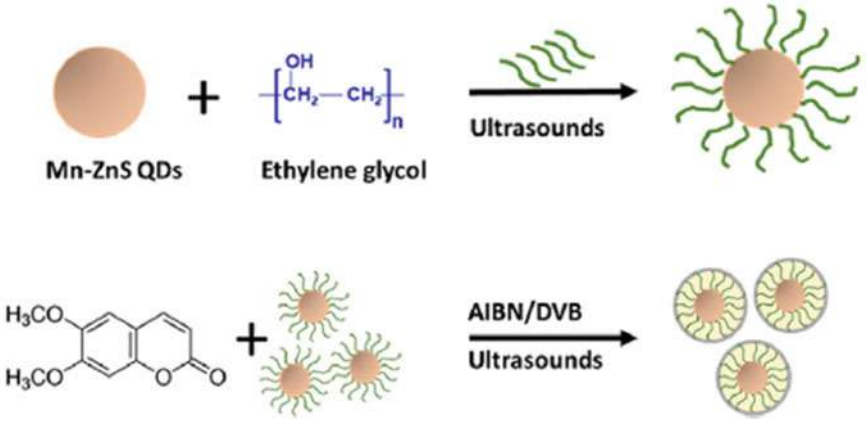

Fig. 11 Schematic diagram of MIP-QDs synthesis [Reproduced from Fig. 1 of Ref. [101], https://doi.org/10.1016/j.aca.2019.12.060 © 2019 Elsevier B.V. All rights reserved.]

adsorption capacity against non-imprinted QDs, demonstrating high adsorption of AFs.

4.5 Zeonex Phosphors

Zeonex is the trade name given to a group of cyclo-olefin polymers [102]. This class is bestowed with the optical transparency and flexibility in processing generally associated with polymers. Zeonex is transparent to ultraviolet A (UV-A) and near infrared (IR) wavelengths similar to glass. To add to its merits Zeonex is gifted with low haze and very little affinity towards moisture. It finds its applicability from optical mirrors or lenses to optical fibers used in telecommunication. Zeonex exhibits dimensional stability at room temperatures and has a glass transition temperature of 138 °C. It has pronounced air permeability and is virtually impermeable to oxygen. Thus, Zeonex can serve a suitable candidate having both rigidity and inertness to exhibit RTP emissions. Several thianthrene derivatives were studied by Pander and co-workers [103]. Their investigation was based on the blending of such derivatives in Zeonex and reported their RTP emissions or behaviors. They witnessed strong yellow phosphorescence from one of the derivatives bearing an Φ_P value of nearly 40%. Doped Zeonex films have exhibited noticeable sensitivity to oxygen, which tends to open an operational window for prospective use in sensing applications.

5 Conclusion and Future Prospect

In this review report the recent works carried out on polymer based room temperature phosphors (RTP) have been discussed. The metal free organic phosphors including polymer based RTPs are highly promising in terms of its different applications. These RTPs may be undoped, i.e., the phosphor is covalently bonded with the polymer or doped where the phosphor is physically encapsulated with the polymer with hydrogen bonding or other similar ionic interactions. From the above discussion it is evident that non-doped RTPs are limited to few polymers such as polyurethane, polylactic acid (PLA), polyamide/imide, polyacrylonitrile, some nanocomposites, polystyrene sulfonic acid ion exchange resins, polyethylene terephthalate (PET) derivatives, carbon dots and some covalent organic framework (COF) polymers while doped polymer RTP are limited to polymethyl methacrylate, polyvinyl alcohol (PVA), PLAs, some molecularly imprinted polymers (MIF) and few cyclo-olefin polymers (zeonex). However, there are many limitations of polymer based RTPs. The exact structure of the polymer based RTP, its mechanism of phosphorescence, role of polymer and the phosphor component and their structure properties relationship are yet to be fully explored. The application areas of polymer based RTPs are also narrower than inorganic or small organic compound based phosphor. In fact, the color range of polymer based RTPs is not as wide as observed for non-polymer phosphors,

e.g., polymer based RTPs with blue or red emission is very rare. The application areas are also limited to only data encryption and sensing materials. Because of the absence of efficient red or near- infrared emission in aqueous solution, polymer based RTP cannot be used for most of the biomedical applications. Extensive research is going on for eliminating these limitations. Once the structure–property relationship between phosphor and the polymer component as well as phosphorescence mechanism are rightly established, more polymers will be explored for development of new polymer based doped and undoped RTP with wide range of applications.

References

1. European Commission (2011) Green Paper Lighting the Future: Accelerating the deployment of innovative lighting technologies. http://ec.europa.eu/newsroom/dae/document.cfm?doc_id=1127. Accessed 30 Mar 2016
2. Shionoya, S.: Introduction to the hand book. In: William, M., Shionoya, Y.S. (Deceased), Yamamoto, H. (eds.) Phosphor Handbook. CRC Press. Taylor & Francis Group, 6000 Broken Sound Parkway NW, Suite 300, Boca Raton, FL 33487–2742, pp. 3–8 (2007)
3. Yi, G., Sun, B., Chen, D.: Nanocrystalline phosphors, vol 6. In: Nalwa, H.S. (ed.) Encyclopedia of nanoscience and nanotechnology. American Scientific Publishers, pp. 465–476. ISBN: 1-58883-062-4 (2004)
4. Wang, M., Guo, G.: Inorganic–organic hybrid white light phosphors chem. Commun. (2013). https://doi.org/10.1039/C6CC03184F
5. Ronda, C.R.: Emission and excitation mechanisms of phosphors. In: Chapter 1 Luminescence: From Theory to Applications. Edited by Cees Ronda, WILEY-VCH Verlag GmbH & Co. KGaA, Weinheim. ISBN: 978-3-527-31402 (2008)
6. William, P.: Lustig, Jing Li, Luminescent metal–organic frameworks and coordination polymers as alternative phosphors for energy efficient lighting devices. Coord. Chem. Rev. **373**, 116–147 (2018)
7. Gan, N., Shi, H., An, Z., Huang, W.: Recent advances in polymer-based metal-free room-temperature phosphorescent materials. Adv. Funct. Mater. **28**, 1802657 (2018)
8. Li, S., Xie, R.J.: Review—data-driven discovery of novel phosphors. ECS J. Solid State Sci. Technol. **9**, 016013 (2020)
9. Xie, R.-J., Hirosaki, N., Sakuma, K., Yamamoto, Y., Mitomo, M.: Appl. Phys. Lett. **84**(26), 5404 (2004)
10. Hirosaki, N., Xie, R.J., Kimoto, K., Sekiguchi, T., Yamamoto, Y., Suehiro, T., Mitomo, M.: Appl. Phys. Lett. **86**(21), 211905 (2005)
11. Uheda, K., Hirosaki, N., Yamamoto, Y., Naito, A., Nakajima, T., Yamamoto, H.: Electrochem. Solid State Lett. **9**(4), H22 (2006)
12. Park, W.B., Singh, S.P., Yoon, C., Sohn, K.-S.: J. Mater. Chem. **22**, 14068 (2012)
13. Park, W.B., Shin, N., Hong, K.-P., Pyo, M., Sohn, K.-S.: Adv. Funct. Mater. **22**, 2258 (2012)
14. Park, W.B., Singh, S.P., Yoon, C., Sohn, K.-S.: J. Mater. Chem. C **1**, 1832 (2013)
15. Park, W.B., Singh, S.P., Sohn, K.-S.: J. Am. Chem. Soc. **136**, 2363 (2014)
16. Pust, P., Wochnik, A.S., Baumann, E., Schmidt, P.J., Wiechert, D., Scheu, C., Schnick, W.: Chem. Mater. **26**, 3544 (2014)
17. Hirosaki, N., Takeda, T., Funahshi, S., Xie, R.-J.: Chem. Mater. **26**, 4280 (2014)
18. Yang, Y., Zhao, Q., Feng, W., Li, F.: Chem. Rev. **113**, 192–270 (2013)
19. Taylor-Pashow, K.M.L., Della Rocca, J., Huxford, R.C., Lin, W.: Chem. Commun. **46**, 5832–5849 (2010)
20. Wei, Z., Gu, Z.-Y., Arvapally, R.K., Chen, Y.-P., McDougald, R.N., Ivy, J.F., Yakovenko, A.A., Feng, D., Omary, M.A., Zhou, H.-C.: J. Am. Chem. Soc. **136**, 8269–8276 (2014)

21. Lustig, W.P., Mukherjee, S., Rudd, N.D., Desai, A.V., Li, J., Ghosh, S.K.: Chem. Soc. Rev. **46**, 3242–3285 (2017)
22. Heine, J., Muller-Buschbaum, K.: Chem. Soc. Rev. **42**, 9232–9242 (2013)
23. Stavila, V., Talin, A.A., Allendorf, M.D.: Chem. Soc. Rev. **43**, 5994–6010 (2014)
24. Bao, Z., Chang, G., Xing, H., Krishna, R., Ren, Q., Chen, B.: Energy Environ. Sci. (2016). https://doi.org/10.1039/C6EE01886F
25. He, Y., Zhou, W., Krishna, R., Chen, B.: Chem. Commun. **48**(2012), 11813–11821 (1831)
26. Morozan, A., Jaouen, F.: Energy Environ. Sci. **5**, 9269–9290 (2012)
27. Liu, J., Chen, L., Cui, H., Zhang, J., Zhang, L., Su, C.-Y.: Chem. Soc. Rev. **43**, 6011–6061 (2014)
28. Song, B.Q., Wang, X.L., Yang, G.S., Wang, H.N., Liang, J., Shao, K.Z., Su, Z.M.: Cryst. Eng. Comm. **16**, 6882 (2014)
29. Ke, F., Yuan, Y.-P., Qiu, L.-G., Shen, Y.-H., Xie, A.-J., Zhu, J.-F., Tian, X.-Y., Zhang, L.-D.: J. Mater. Chem. **21**, 3843–3848 (2011)
30. Ray Chowdhuri, A., Bhattacharya,D., Sahu, S.K.: Dalton Trans. **45**, 2963–2973 (2016)
31. Lee, D., Bolton, O., Kim, B.C., Youk, J.H., Takayama, S., Kim, J.: Room temperature phosphorescence of metal-free organic materials in amorphous polymer matrices. J. Am. Chem. Soc. **135**, 6325 (2013)
32. Mukherjee, S., Thilagar, P.: Chem. Commun. **51**, 109988–111003 (2015)
33. Yu, Y., Kwon, M.S., Jung, J., Zeng, Y., Kim, M., Chung, K., Gierschner, J., Youk, J., Borisov, S.M., Kim, J.: Room-temperature-phosphorescence-based dissolved oxygen detection by core-shell polymer nanoparticles containing metal-free organic phosphors. Angew. Chem. **129**, 16425–16429 (2017)
34. Fang, M., Yang, J., Xiang, X., Xie, Y., Dong, Y.Q., Peng, Q., Li, Q., Li, Z.: Unexpected room temperature phosphorescence from nonaromatic pure organic molecule with low molecular weight of 85: how the intermolecular hydrogen bond creates wonderful flash mater. Chem. Front. (2018). https://doi.org/10.1039/C8QM00396C
35. Wu, W., Tang, R., Li, Q., Li, Z.: Functional hyperbranched polymers with advanced optical, electrical and magnetic properties. Chem. Soc. Rev. **44**, 3997–4022 (2015)
36. Tian, R., Xu, S.M., Xu, Q., Lu, C.: Large-scale preparation for efficient polymer-based room-temperature phosphorescence via click chemistry. Sci. Adv. **6**, eaaz6107 (2020)
37. Fang, M.-M., Yang, J., Lia, Z.: Recent advances in purely organic room temperature phosphorescence polymer. Chin. J. Polym. Sci. **37**, 383–393 (2019)
38. Kwon, M.S., Yu, Y., Coburn, C., Phillips, A.W., Chung, K., Shanker, A., Jung, J., Kim, G., Pipe, K., Forrest, S.R., Youk, J.H., Gierschner, J., Kim, J.: Nat. Commun. **6**, 8947 (2015)
39. Tian, S., Fan, H., Yi., Chen, Yan, J., Sun, J., Qin, D.: A photochromic long persistent luminescent polyurethane based on colour conversion process. New J. Chem. **00**, 1–3 (2013). https://doi.org/10.1039/C7NJ02607B
40. Bessiere, A., Sharma, S.K., Basavaraju, N., Priolkar, K.R., Binet, L., Viana, B., Bos, A.J.J., Maldiney, T., Richard, C., Scherman, D., Gourier, D.: Chem. Mater. **26**, 1365–1373 (2014)
41. Pan, Z., Lu, Y.-Y., Liu, F.: Nat. Mater. **11**, 58–63 (2012)
42. Chenu, S., Veron, E., Genevois, C., Garcia, A., Matzen, G., Allix, M.: J. Mater. Chem. C **2**, 10002–10010 (2014)
43. Gao, Yan, D.: Chem. Sci. **8**, 590–599 (2017)
44. Tian, S.: Recent advances in functional polyurethane and its application in leather manufacture: a review. Polymers **2020**, 12 (1996). https://doi.org/10.3390/polym12091996
45. Hu, X., Ding, Y., Liu, J., Deng, Y., Cheng, C.: Synthesis and fluorescence properties of a waterborne polyurethane–acrylic hybrid polymeric dye. Polym. Bull. **74**, 555–569 (2016)
46. Hu., Xianhai, Zhang, X., Liu, J., Dai, J.: Synthesis, characterization and fluorescence performance of a waterborne polyurethane-based polymeric dye. J. Lumin. **142**, 23–27 (2013)
47. Hu, X., Ding, Y., Liu, J., Deng, Y., Cheng, C.: Synthesis and fluorescence properties of a waterborne polyurethane–acrylic hybrid polymeric dye. Polym. Bull. https://doi.org/10.1007/s00289-016-1729-9

48. Tian, S., Wen, J., Fan, H., Chen,Y., Yan, J.: A thermochromic luminous polyurethane based on long persistent luminescent phosphors and thermochromic pigment. New J. Chem. https://doi.org/10.1039/c7nj04951j
49. Zhou, C., Xie, T., Zhou, R., Trindle, C.O., Tikman, Y., Zhang, X., Zhang, G., Appl. A.C.S.: Mater. Interfaces **7**, 17209 (2015)
50. Wang, T., Zhang, X., Deng, Y., Sun, W., Wang, Q., Xu, F., Huang, X.: Polymers **9**, 411 (2017)
51. Wang, T., Zhou, C., Zhang, X., Xu, D.: Polym. Chem. **9**, 1303 (2018)
52. Sun, W., Wang, Z., Wang, T., Yang, L., Jiang, J., Zhang, X., Luo, Y., Zhang, G.: J. Phys. Chem. A **121**, 4225 (2017)
53. Chen, X., Liu, X., Lei, J., Xu, L., Zhao, Z., Kausar, F., Xie, X., Zhu, X., Zhang, Y., Yuan, W.Z.: Mol. Syst. Des. Eng. **3**, 364 (2018)
54. Song, L., Zhu, T., Yuan, L., Zhou, J., Zhang, Y., Wang, Z., Tang, C.: Ultra-strong long-chain polyamide elastomers with programmable supramolecular interactions and oriented crystalline microstructures. Nat. Commun. **10**, 1315 (2019)
55. Zhao, E., Lam, J.W.Y., Meng, L., Hong, Y., Deng, H., Bai, G., Huang, X., Hao, J., Tang, B.Z.: Poly[(maleic anhydride)-alt-(vinyl acetate)]: a pure oxygenic nonconjugated macromolecule with strong light emission and solvatochromic effect. Macromolecules **48**, 64–71 (2015)
56. Lu, H., Feng, L., Li, S., Zhang, J., Lu, H., Feng, S.: Unexpected strong blue photoluminescence produced from the aggregation of unconventional chromophores in novel siloxane–poly(amidoamine) dendrimers. Macromolecules **48**, 476–482 (2015)
57. Zhou, Q., Cao, B., Zhu, C., Xu, S., Gong, Y., Yuan, W.Z., Zhang, Y.: Clustering-triggered emission of nonconjugated polyacrylonitrile. Small **12**, 6586 (2016)
58. Chen, X., Luo, W., Ma, H., Peng, Q., Yuan, W.Z., Zhang, Y.: Prevalent intrinsic emission from nonaromatic amino acids and poly(amino acids). Sci. China Chem. **61**, 351–359 (2017)
59. Kopeć, M., Pikiel, M., Vancso, G.J.: Surface-grafted polyacrylonitrile brushes with aggregation-induced emission properties. Polym. Chem. **11**, 669–674 (2020)
60. Nara, M., Orita, R., Ishige, R., Ando, S.: White-light emission and tunable luminescence colors of polyimide copolymers based on FRET and room-temperature phosphorescence. ACS Omega
61. Chen, H., Yao, X., Ma, X., Tian, H.: Adv. Opt. Mater. **4**, 1397 (2016)
62. Zhang, T., Chen, H., Ma, X., Tian, H.: Ind. Eng. Chem. Res. **56**, 3123 (2017)
63. Ma, X., Xu, C., Wang, J., Tian, H.: Angew. Chem., Int. Ed. **57**, 10854 (2018)
64. Hasegawa, M., Horie, K.: Photophysics, photochemistry, and optical properties of polyimides. Pergamon **26**, 259–335 (2001)
65. Wakita, J., Sekino, H., Sakai, K., Urano, Y., Ando, S.: Molecular design, synthesis, and properties of highly fluorescent polyimides. J. Phys. Chem. B **113**, 15212–15224 (2009)
66. Wakita, J., Inoue, S., Kawanishi, N., Ando, S.: Excited-state intramolecular proton transfer in imide compounds and its application to control the emission colors of highly fluorescent polyimides. Macromolecules **43**, 3594–3605 (2010)
67. Kanosue, K., Shimosaka, T., Wakita, J., Ando, S.: Polyimide and imide compound exhibiting bright red fluorescence with very large stokes shifts via excited-state intramolecular proton transfer. Macromolecules **48**, 1777–1785 (2015)
68. Kanosue, K., Augulis, R., Peckus, D., Karpicz, R., Tamulevičius, T., Tamulevičius, S., Gulbinas, V., Ando, S.: Polyimide and imide compound exhibiting bright red fluorescence with very large stokes shifts via excited-state intramolecular proton transfer II. Ultrafast proton transfer dynamics in the excited state. Macromolecules **49**, 1848−1857 (2016)
69. Yuniarto, K., Welt, B.A., Irawan, C.: Morphological, thermal and oxygen barrier properties plasticized film polylactic acid. J. Appl. Packag. Res. **9**(3)(6), 1–9 (2017)
70. Anderson, K.S., Schreck, K.M., Hillmyer, M.A.: Toughening polylactide. Polym. Rev. **48**, 85–108 (2008)
71. Zhang, G., Chen, J., Payne, S.J., Kooi, S.E., Demas, J.N., Fraser, C.L.: Multi-emissive difluoroboron dibenzoylmethane polylactide exhibiting intense fluorescence and oxygen-sensitive room-temperature phosphorescence. J. Am. Chem. Soc. **129**, 8942–8943 (2007)

72. DeRosa, C.A., Kerr, C., Fan, Z., Kolpaczynska, M., Mathew, A.S., Evans, R.E., Zhang, G., Fraser, C.L.: Tailoring oxygen sensitivity with halide substitution in difluoroboron dibenzoylmethane polylactide materials. ACS Appl. Mater. Interfaces **7**, 23633–23643 (2015)
73. Zhang, G., Evans, R.E., Campbell, K.A., Fraser, C.L.: Role of boron in the polymer chemistry and photophysical properties of difluoroboron−dibenzoylmethane polylactide. Macromolecules **42**, 8627–8633 (2009)
74. Zhang, G., Fiore, G.L., Clair, T.L.S., Fraser, C.L.: Difluoroboron dibenzoylmethane pcl-pla block copolymers: matrix effects on room temperature phosphorescence. Macromolecules **42**, 3162–3169 (2009)
75. Chen, X., Xu, C., Wang, T., Zhou, C., Du, J., Wang, Z., Xu, H., Xie, T., Bi, G., Jiang, J., Zhang, X., Demas, J.N., Trindle, C.O., Luo, Y., Zhang, G.: Versatile room-temperature-phosphorescent materials prepared from n-substituted naphthalimides: emission enhancement and chemical conjugation. Angew. Chem., Int. **55**(34), 9872–9876 (2016)
76. Pfister, A., Zhang, G., Zareno, J., Horwitz, A.F., Fraser, C.L.: Boron polylactide nanoparticles exhibiting fluorescence and phosphorescence in aqueous medium. ACS Nano **2**(6), 1252–1258 (2008)
77. Kerr, C., Derosa, C.A., Daly, M.L., Zhang, H., Palmer, G.M., Fraser, C.L.: Luminescent difluoroboron β-diketonate pla–peg nanoparticle. Biomacromol **18**, 551–561 (2017)
78. Ogoshi, T., Tsuchida, H., Kakuta, T., Yamagishi, T.-A., Taema, A., Ono, T., Sugimoto, M., Mizuno, M.: Adv. Funct. Mater. **29**, 1707369 (2018)
79. Chen, X., He, Z., Kausar, F., Chen, G., Zhang, Y., Yuan, W.: Aggregation-induced dual emission and unusual luminescence beyond excimer emission of poly (ethylene terephthalate). Macromolecules **51**, 9035–9042 (2018)
80. Yu, Y., Kwon, M.S., Jung, J., Zeng, Y., Kim, M., Chung, K., Gierschner, J.,. Youk, J.H., Borisov, S., Kim, J., Angew. Chem., Int. Ed. **56**, 16207 (2017)
81. Tao, S., Lu, S., Geng, Y., Zhu, S., Redfern, S.A.T., Song, Y., Feng, T., Xu, W., Yang, B., Angew. Chem., Int. Ed. **57**, 2393 (2018)
82. Wang, S., Ma, L., Wang, Q., Shao, P., Ma, D., Yuan, S., Lei, P., Li, P., Feng, X., Wang, B.: J. Mater. Chem. C **6**, 5369 (2018)
83. Gahlaut, R., Joshi, H.C., Joshi, N.K., Pandey, N., Arora, P., Rautela, R., Suyal, K., Pant, S.: Luminescence characteristics and room temperature phosphorescence of naphthoic acids in polymers. J. Lumin. **138**, 122–128 (2013)
84. Hess, S., Becker, A., Baluschev, S., Yakutkin, V., Wegner, G.: A comparative study of oxygen permeabilities of film-forming polymers by quenching of platinum porphyrin phosphorescence. Macromol. Chem. Phys. **208**(19–20), 2173–2188 (2007)
85. Reineke, S., Seidler, N., Yost, S.R., Prins, F., Tisdale, W.A., Baldo, M.A.: Highly efficient, dual state emission from an organic semiconductor. Appl. Phys. Lett. **103**, 093302 (2013)
86. Joshi, R., Meitei, O.R., Jadhao, M., Kumar, H., Ghosh, S.K.: Conformation controlled turn on–turn off phosphorescence in a metal-free biluminophore: thriving the paradox that exists for organic compounds. Phys. Chem. Chem. Phys. **18**, 27910–27920 (2016)
87. Mieno, H., Kabe, R., Notsuka, N., Allendorf, M.D., Adachi, C.: Long-lived room temperature phosphorescence of coronene in zeolitic imidazolate framework ZIF-8 Adv. Opt. Mater. **4**(7), 1015–1021 (2016)
88. Koch, M., Perumal, K., Blacque, O., Garg, J.A., Saiganesh, R., Kabilan, S., Balasubramanian, K.K., Venkatesan, K.: Metal-free triplet phosphors with high emission efficiency and high tenability. Angew. Chem., Int. **53**(25), 6378 (2014)
89. Kwon, M., Lee, D., Seo, S., Jung, J., Kim, J.: Tailoring intermolecular interactions for efficient room-temperature phosphorescence from purely organic materials in amorphous polymer matrices. Angew. Chem. Int. Ed. **53**(11177–11181), 38 (2014)
90. Su, Y., Phua, S., Li, Y., Zhou, X., Jana, D., Liu, G., Lim, W.Q., Ong, W., Yang, C., Zhao, Y.: Ultralong room temperature phosphorescence from amorphous organic materials toward confidential information encryption and decryption. Sci. Adv. **4**, eaas9732 (2018)
91. Deng, Y., Zhao, D., Chen, X., Wang, F., Song, H., Shen, D.: Chem. Commun. **49**, 5751 (2013)

92. Tan, J., Zhang, J., Li, W., Zhang, L., Yue, D.: J. Mater. Chem. C **4**, 10146 (2016)
93. Patir, K., Gogoi, S.K.: ACS sustainable Chem. Eng. **6**, 1732 (2018)
94. Xu, S., Evans, R.E., Liu, T., Zhang, G., Demas, J.N., Trindle, C.O., Fraser, C.L.: Aromatic difluoroboron β-diketonate complexes: effects of π-conjugation and media on optical properties. Inorg. Chem. **52**(7), 3597–3610 (2013)
95. Zhang, X., Xie, T., Cui, M., Yang, L., Sun, X., Jiang, J., Zhang, G.: General design strategy for aromatic ketone-based single-component dual-emissive materials. ACS Appl. Mater. Interfaces. **6**(4), 2279–2284 (2014)
96. M. L. Daly, C. Kerr, C. A. Derosa, C. L. Fraser, Meta-alkoxy-substituted difluoroboron dibenzoylmethane complexes as environment-sensitive materials. ACS Applied Materials & Interfaces, *ACS Appl. Mater. Interfaces*, 9, 2017, 32008–32017.
97. Liu, T., Zhang, G., Evans, R.E., Trindle, C.O., Altun, Z., Derosa, C.A., Wang, F., Zhuang, M., Fraser, C.L.: Phosphorescence tuning through heavy atom placement in unsymmetrical difluoroboron β-diketonate materials. Chem. Eur. J. **24**(8), 1859–1869 (2018)
98. Bhogal, S., Kaur, K., Malik, A.K., Sonne, C., Lee, S.S., Kim, K.H.: Core-shell structured molecularly imprinted materials for sensing applications. TrAC Trends in Analy. Chem. 116043 (2020)
99. Salinas-Castillo, A., Sanchez-Barragan, I., Costa-Fernandez, J.M., Pereiro, R., Ballesteros, A., Gonzalez, J.M., Segura-Carretero, A., Fernandez-Gutierrez, A., Sanz-Medel, A.: Iodinated molecularly imprinted polymer for room-temperature phosphorescence optosensing of fluoranthene. Chem. Commun. **25**, 3224–3226 (2005)
100. Sanchez-Barragan, I., Costa-Fernandez, J.M., Pereiro, R., Sanz-Medel, A., Salinas, A., Segura, A., Fernandez-Gutierrez, A., Ballesteros, A., Gonzalez, J.M.: Molecularly imprinted polymers based on iodinated monomers for selective room-temperature phosphorescence optosensing of fluoranthene in water. Anal. Chem. **77**(21), 7005–7011 (2005)
101. Madurangika Jayasinghe, G.D.T., Domínguez-González, R., Bermejo-Barrera, P., Moreda-Piñeiro, A.: Room temperature phosphorescent determination of aflatoxins in fish feed based on molecularly imprinted polymer—Mn-doped ZnS quantum dots. Analy. Chim. Act. **1103** 183–191 (2020)
102. Woyessa, G., Rasmussen, H.K., Bang, O.: Zeonex—a route towards low loss humidity insensitive single-mode step-index polymer optical fibre. Opt. Fiber Technol. **57**, 102231 (2020)
103. Pander, P., Swist, A., Soloducho, J., Dias, F.B.: Room temperature phosphorescence lifetime and spectrum tuning of substituted thianthrenes. Dyes Pigm. **142**, 315–322 (2017)

Applications

Upconversion Hybrid Phosphors for Biological Applications

Kaushal Kumar, Sachin Kumar Maurya, and Manoj Kumar Mahata

1 Introduction

The photoluminescence emission in rare earth (lanthanide) materials has already been explained in previous chapters of this book and here only a short introduction specific to the frequency upconversion emission phosphors is provided to make consistency of this chapter. The most attractive feature of the rare earth luminescent compounds is the atomic line like emissions at several wavelengths (rare earth ions possesses large numbers of energy levels). The emission wavelength shifts are also found less sensitive to the host matrices and there is only the change in radiative/non-radiative transition rates if one goes from one host to another. The rare earth (RE) ion luminescence is widely investigated and underline emission processes are well resolved [1]. Rare earth ions based frequency upconversion phosphor (UC) technology has grown mature and is an interesting subject for fluorescence application community. Thanks to the advances in chemical preparation routes and nanotechnology, the size and shape controlled nano-particles synthesis has now become possible. Use of UC emission phosphors/particles in photo-thermal cancer therapy, bio-imaging, latent fingerprint detection, and temperature sensing in nano/micro-volumes are the stunning ideas, generated recently. The fact is how wisely one can mold the upconversion materials for these applications. Recent research in cancer therapy is focused on the development of target specific tools to detect and cure the cancer cells simultaneously with minimal harm to healthy cells. Trials of using optically functionalized magnetic (magnetic hyperthermia) and plasmonic (photothermal) nanoparticles

K. Kumar (✉) · S. K. Maurya
Department of Physics, Indian Institute of Technology (Indian School of Mines), Dhanbad 826004, Jharkhand, India
e-mail: kkumar@iitism.ac.in

M. K. Mahata
III. Physikalisches Institut-Biophysik, Georg-August-Universitat Gottingen, Gottingen 37077, Germany

© Springer Nature Switzerland AG 2022

K. Upadhyay et al. (eds.), *Hybrid Phosphor Materials*, Engineering Materials,
https://doi.org/10.1007/978-3-030-90506-4_8

(NPs) for multimodal detection and destruction of cancerous cells have given very appreciable results. Such studies will be continuing and will lead to advancement in medical science.

Here it is customary to differentiate between the two emission modes viz. frequency downconversion and frequency upconversion emission modes as in this chapter applications of both the emission modes are discussed and particularly the upconversion emission mode as it finds more comfortable home for biological applications.

1.1 Frequency Downconversion Luminescence

The downconversion (or downshifting) luminescence follows well-known Stoke's law principle, is an emission process where a high frequency photon is converted into low frequency photon. This energy difference between the absorbed photon and emitted photon is termed as Stoke shift. The downconversion emission process can easily be understood from Fig. 1. The emission (red colour in figure) has higher wavelength than the excitation wavelength (blue colour) and hence is called down-shifting emission. This emission mode is most common, widely studied and has many practical applications such as lamp phosphors, white light emitting diodes etc. One of the best examples is the red emitting Eu^{3+} doped Y_2O_3 phosphor under UV excitation. Almost all rare earth ions in their trivalent or divalent valence states possess this property. Sometimes two different rare earth ions are used in conjunction to get the enhanced luminescence. In this case one rare earth ion act as sensitizer (transfer its energy) and another works as activator (receives energy). The sensitizer ion adequately transfers its energy to the activator ion and this process enhances luminescence efficiency (intensity). For downshifting phosphors the Ce^{3+} ion is most commonly used ascodoping ion to enhance the luminescence intensity of RE (RE = Eu^{3+}, Tb^{3+}, Dy^{3+}, Sm^{3+}) ions, as emission wavelength of Ce^{3+} ion well matches with several f − f transitions of RE ions. The Ce^{3+} − RE^{3+} combination has been used in many hostslike $NaGdF_4$, $BaYF_5$, YPO_4, GdF_3, and $Sr_3Y_2(BO_3)_4$.

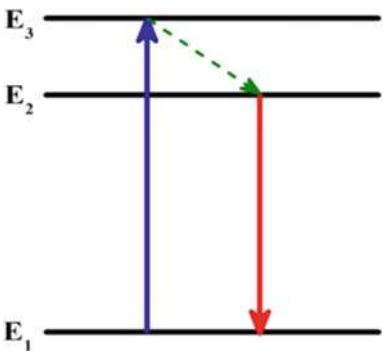

Fig. 1 Schematic diagram for downconversion luminescence process

1.2 Frequency Upconversion Luminescence

Contrary to the downconversion emission the upconversion emission produces photon of higher frequency (energy) than the excitation photon and the process involves sequential absorption of two or more low energy photons. Such emission is called anti-Stokes emission in its basic statement in physics language. If one compares the upconversion emission pattern with the downconversion emission patterns then it can easily be noticed that Stokes shift for upconversion emission is higher than the downconversion emission and this large Stokes shift makes upconversion emission materials superior over conventional luminescence. The large Stokes shift enhances the signal to noise ratio which helps to record high contrast upconversion emission image of the object. This upconversion emission finds novel applications in photonic devices, temperature sensors, bioimaging, biomedical diagnostics and therapy, security etc. Bloembergen in year 1959 had proposed an infrared quantum counter (IRQC) where super excitation of the energy levels was used as a detector to detect and count the infrared (IR) photons [2]. After that F. Auzel in year 1966 had suggested that energy exchange between the two excited rare earth ions could lead frequency upconversion emission [3]. This discovery has opened a new area of research and thereafter many novel applications of frequency upconversion emission were proposed. The frequency upconversion is the property of the rare earth ions and no other inorganic element/ion/compound possesses this property. However, similar frequency upconversion is observed in few organic compounds but with different mechanism and is not a part of the present discussion. There are several dynamical processes which result upconversion emission in rare earth ions and are discussed in short below.

1.2.1 Excited State Absorption (ESA)

The ESA process was first proposed in 1959 by Bloembergen [2]. In ESA there is successive absorption of two or more incident photons by a single atom/ion. The schematic process of ESA involving two successive absorptions is shown in Fig. 2a. Under the resonant excitation, the ground state 1 absorbs incident photon and reaches to the metastable level 2, the excited state 2 then absorbs second incident photon and reach to final state 3. Condition is that level 2 and level 3 should be resonant with incident energy (energy mismatch $\equiv$800 cm^{-1} could be compensated either by phonon absorption or by phonon emission, whichever is the condition). When the electronde-excites from the level 3 to the ground level 1, the upconversion emission happens. Generally in rare earth ions ESA is observed in samples containing low active ion concentration.

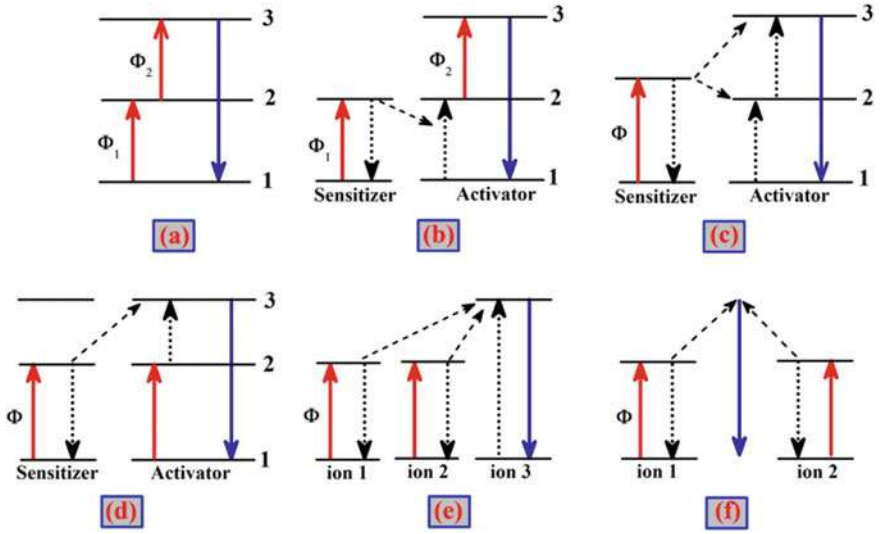

Fig. 2 General upconversion emission processes: **a** excited state absorption, **b** energy transfer followed by excited state absorption; **c** successive energy transfer; **d** cross relaxation process; **e** cooperative sensitization; **f** and cooperative emission (from virtual level) phenomenon

1.2.2 Energy Transfer Upconversion (ETU)

Energy transfer upconversion (ETU) is rather different from the ESA process explained above. The ESA works within a single RE ion while ETU requires two different RE ions, one RE ion acts as sensitizer (or donor) and other works as activator (or acceptor). In this process the sensitizer ion is in one of its excited state and activator ion is in its ground state and the interaction between the two transfers the excitation energy from donor to acceptor ion. ETU is treated as the most efficient UC process. Such ET upconversion processes have been reported in many materials which were codoped with two types of RE ions e.g. Yb^{3+}/Er^{3+}, Yb^{3+}/Ho^{3+}. There are five different types of ETU processes as illustrated in Fig. 2b–f. These are the energy transfer process (ET) followed by excited state absorption, successive energy transfer, cross relaxation process, cooperative sensitization and cooperative emission. The cases (b), (c) and (d) of Fig. 2 do not involve any cooperative effect. For example, the second process in Fig. 2b is the energy transfer followed by excited-state absorption in which sensitizer in its excited state transfers its excitation energy to the ground state of activator and the excited activator absorbs a second input photon and excited to a higher excited state 3. The third process in Fig. 2c contains successive energy transfer from sensitizer to the activator ion and raising the activator to a high energy state. This is the process where only sensitizer absorbs photon from the incident beam and then then transfers to two different levels of activator. Figure 2d represents a process which might be termed as cross-relaxation (CR) upconversion. The donar decays to ground state and acceptor absorbs that energy to reach from

state 2 to state 3. Further details of the basic upconversion mechanism can be found elsewhere [3].

The last two UC processes (Fig. 2e, f) involve cooperative effects. In the case of cooperative sensitization (Fig. 2e), the energy accumulated in two excited donors is transferred to one acceptor ion. The excited ion reaches to state which is just sum of the energy of two donor ions. Figure 2f shows the case of cooperative emission where two excited ions itself combines their energy and sum of the energy is emitted from the virtual level. In this process second type of ion is not required. This case is found in Yb^{3+} ions. Any mismatch between the energy levels of the sensitizer and that of the activator can be counter balanced by phonons. In practice, energy difference consideration is used to identify the excitation and emission processes. This may also permit a method to distinguish between ET and ESA. ET mechanism has an advantage over ESA, as only one pump beam is necessary and this permits a simpler pumping configuration. However, RE concentration in the host should be high enough so that ion-ion interactions can induce energy transfer.

2 Surface Modified Hybrid Phosphors

Most of the RE emission studies have done on either inorganic lanthanide phosphors iron molecular lanthanide compounds. The ever increasing demand of high performance phosphors and advancement in science and technology had further widened the research on phosphors and we have witnessed so called organic–inorganic hybrid materials with RE ions as active centers. In such materials either an organic lanthanide complex is embedded in an inorganic host matrix or an inorganic lanthanide phosphor is embedded in an organic matrix (say polymer). Likewise, inorganic RE phosphor particles can be coated with organic compounds and this strategy has been found quite useful for biological applications. However, there is no clear distinction among these classes and a combination of inorganic–organic components of a phosphor can be treated under the hybrid phosphors. Most of the applications described here in this chapter have utilized inorganic lanthanide core coated/functionalized with organic part. Other classes of hybrid phosphors have uses in applications such as optical waveguides, amplifiers, OLEDs, displays etc.).

The biological applications have little bit different requirements than the other applications for example bio-imaging using the phosphors requires phosphor sample to be in dispersible form having particle size less than 100 nm. Now-a-days it is not a difficult task to produce nanometer size particle size. Soft chemistry routes have advanced enough to produce size and shape controlled nanoparticles of RE compounds. Most laboratory synthesized inorganic phosphors are toxic to the bio cells and hence further they need to be made in biocompatible form. So, for this purpose rare earth doped nanoparticles are coated with long chain organic molecules. The organic coating also improves the colloidal stability of the nanoparticles (NPs). The organic coating isolates the nanoparticles from interacting with other nanoparticles and thus avoids particle aggregation which leads to segregation. The attachment

of organic molecules or metal complexes through covalent bonding to the surface of nanoparticles can also be done and this results additional functionality in the phosphor. It is also possible to attach luminescent RE complexes via a linking group on non-luminescent nanoparticles such as Gold. The $NaYF_4$:(Tm^{3+}/Yb^{3+}) nanoparticles functionalized with glucose have been developed as fluorescent labels for the determination of glucose in blood [4]. Liu et al. [5] have proposed a glucose detection scheme using polydopamine (PDA) coated upconversion nanoparticles (UCNPs). In this scheme, first oleate group capped UCNPs were prepared through high temperature coprecipitation method and then oleate group was removed from surface through acid treatment. The oleic acid during synthesis was used to control the particle size. After removing of the oleate group the bare UCNPs were mixed with dopamine monomer and after polymerization PDA capped UCNPs were obtained. PDA has strong absorbance in the visible region and thus promotes luminescence quenching in UCNPs. The presence of H_2O_2 in solution inhibits the polymerization of DA monomers and leads intense upconversion emission from UCNPs under 976/980 nm excitation. The UCNPs-PDA system can be well explored as effective bioassay nanoplatform for glucose detection that produces H_2O_2 through the reaction with glucose oxidase (GOx) enzyme. The concentration of glucose can be monitored by measuring the emission intensity. Liu et al. have found that upconversion emission intensity of the UCNPs-PDA system increases linearly with glucose concentration from 0 to 300 mM and having limit of detection (LOD) of 0.8 mM. The proposed scheme is applicable for human serum and whole blood with high accuracy and precision. In a similar way Chen et al. [6] have reported a nanosensor using UCNPs and squaric acid (SQA)-iron (III) combination for high sensitivity glucose detection in human serum. In the assay formed, GOx-catalyzed oxidization of glucose produces gluconic acid and hydrogen peroxide (H_2O_2). The H_2O_2then catalytically oxidize iron (II) to iron (III) which rapidly (<1 min) coordinate with the SQA to produce (SQA)-iron (III). The absorption band of (SQA)-iron (III) largely overlap with the emission band of UCNPs and hence there is emission quenching of UCNPs. The glucose level can be monitored by measuring the SQA-iron (III). The fluorescence quenching is found to show linear response with glucose concentration in 7–340 μM range and detection limit of 2.3 μM. The developed technique was further applied to monitor glucose levels in human. Compared with other fluorescence methods, this method has displayed high sensitivity and signal-to-noise ratio. In Fig. 3 one such scheme of the use of UCNPs in glucose detection has shown. There are numerous other schemes available in literature where upconversion emission of UCNPs is utilized to sense the biological objects [7–9].

Before start of the discussion on biological applications of the hybrid phosphors, here it is customary to mention the specific benefits of the upconversion emission in biological applications over the conventional downconversion emission found in semiconductor quantum dots, carbon nanoparticles and RE phosphors. Upconversion emission has following advantages:

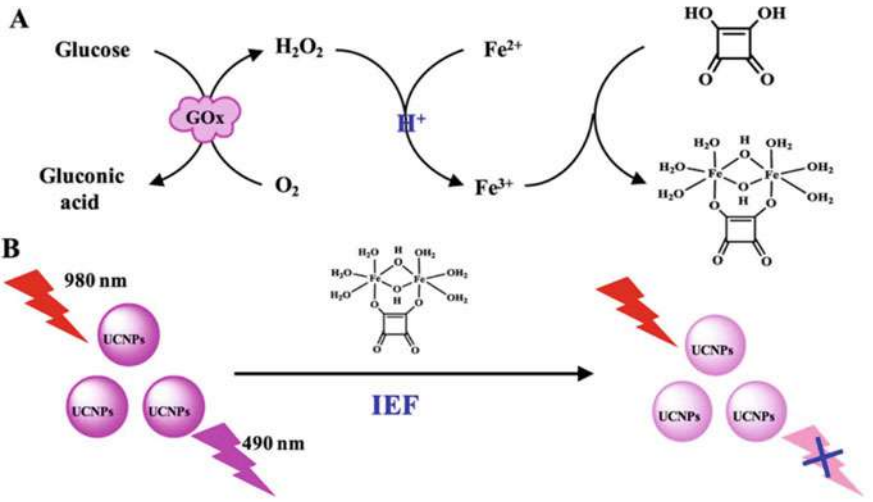

Fig. 3 Schematic mechanism showing how UCNPs can be used in glucose detection after surface modification. Reproduced with permission [6] Copyright 2016, Elsevier

1. Upconversion emission in rare earth ions has large Stoke's shift (e.g. excitation wavelength: 980 nm; emission wavelength: 550 nm for Er^{3+} ion) and hence factors such as excitation light scattering do not affect the detection of emission.
2. The biological samples are prone to give fluorescence on visible excitation and hence can interfere in the detection process. The upconversion emission can only be produced from rare earth ions and hence in principle there is no background emission in upconversion emission mode. It gives high contrast and high signal to noise ratio.
3. The UCNPs are quite stable under high excitation powers and there is no unwanted photoblinking as found in luminescent quantum dots.
4. The upconversion phosphors are excited around near infrared (NIR) region and biological samples are transparent to NIR wavelengths except at certain wavelengths (water absorption bands). Hence NIR radiation receives more penetration depth inside the tissue cells than the visible radiation.
5. Rare earth phosphors can emit at several wavelengths with sharp bands and hence detection can be done at the choice of wavelength.

In the following table a comparative chart is provided which shows the superiority of UCNPs over the other luminescent tools used for various biological applications (Table 1).

Table 1 A comparison of specialties of UCNPs with other luminescent probes used for biological applications

Types of emission probes/parameter	Organic dyes	Silica nanoparticles with dye	Quantum dots	Lanthanide chelates	UCNPs
Size (nm)	5–10 nm	25–500 nm	2–6 bare Up to 30 nm with functional groups	5–10 nm	20–200 nm (size does not impact emission property)
Cost	Low	Low	High	Medium	Medium
Applications					
Cell imaging	High	Low	Medium	Medium	High
Tissue/animal imaging	Low	Low	Low	Low	High
High resolution imaging	Medium	Low	High	Low	High
Therapies	PDT	–	PHT	PDT	PDT, PHT
Excitation	UV–Vis	UV–Vis	UV–Vis	UV–Vis	NIR
Background emission interference	High	High	High	Medium	NIL
Photostability	Very low	Medium	High photoblinking	High	Very high
Chemical stability	Medium	Medium	High	Medium	High
Detection mode	E	E	E	E	E/MRI
Clearance from body	Fast	–	–	Fast	Few days
Biocompatibility	Very high	High	Medium	Medium	Low; biocompatible shell required

Symbols: PDT: photodynamic therapy, PHT: photo-thermal therapy, E: fluorescence emission, MRI: magnetic Resonance Imaging

3 Synthesis Methods of Upconversion Hybrid Phosphors

Preparation of mono-dispersed upconversion nanoparticles is the major challenge for practical applications of UCNPs. For biological applications, the UCNPs should have narrow size distribution, dispersible and stable in aqueous medium [10–12]. Among the studied upconversion host materials, the fluorides have been found most suitable for the strong upconversion emission because they have low phonon frequency and good chemical stability. For example, $NaYF_4$:Yb^{3+}/Er^{3+} and $NaYF_4$:Yb^{3+}/Tm^{3+} have been found most efficient upconversion materials to give intense green, red

and blue emission [13, 14]. Recent research focus has been done on the improvement of synthesis methods, surface modifications and colloidal stability to improve the efficacy for different applications. Out of several synthesis methods for fluoride based UCNPs, the coprecipitation, hydrothermal and thermal decomposition methods are most popular and are discussed here. Other important preparation methods are tabulated in Table 2.

Table 2 Ln-doped UCNPs can be made using variety of synthetic approaches. Here some important methods are described along with some of their benefits and drawbacks

Synthetic method	Process	Benefits	Drawbacks
Precipitation	Chemical reaction forces soluble salts to precipitate in the form of compound within a template or in a confined space	Easy to handle, fast reaction, cost effective, require low/moderate temperature and pressure	Less control on particle size and shape, aggregation is obvious, needs postreaction annealing to remove organic content, annealing leads to further growth in size
Combustion synthesis	Nitrate salts are burnt in the presence of organic fuels which produce oxide compounds	Easy to work, rapid synthesis, cost effective and low cost	Almost no control on particle size and shape, high degree of aggregation, less possibility of phase purity repeatability
Sol–gel method	Dissolved salts are converted to gel through hydrolysis and polymerization processes. Chemical reaction produce metal oxides	Simple reactions, suitable to prepare thin coatings, easy to control doping, slow reaction leads high degree of homogeneity and purity	Pure metal acetates/metal alkoxides precursors are little expansive, Little control over shape and size of particles
Microwave synthesis	Uses microwaves to produce heat to start reaction	Fast reaction rates and uniform heating, Low energy consumption, high reproducibility	Requires microwave generator, limited solvent choice
Spray pyrolysis/Flame synthesis	Liquid solution with hydrocarbon fuel is sprayed and passed through a flame source. Burning produce fine crystalline powder	High-purity samples, Fine size distribution, cost effective and fast synthesis, good control on shape, high yield	Considerable aggregation is observed, synthesis of complex materials is difficult

3.1 Coprecipitation Method

The coprecipitation method is a simplest method to prepare the samples as it has simple reaction conditions, effortless protocols and fast reaction rate. The coprecipitation method does not require expansive equipment; only few glassware items are required. In the technique, the metal precursors are taken in the form of salt and mixed altogether in water medium. Base (e.g. NH_4OH) is then added dropwise in the solution to form metal hydroxide. The metal hydroxides are insoluble and can be separated from the solution via centrifugation.

The release of anions and cations during the reaction can be regulated with the help of reaction arrestors (e.g. Ethylenediaminetetraacetic acid EDTA, a long chain hydrocarbon) to control nucleation and particle growth kinetics. This control could produce desired size and shape of the particles; however it is little bit difficult in this technique. In order to get better control on the particle size and shape several modifications such as use of surfactants, sonochemical methods etc. are proposed.

The collected precipitate could be dried in an oven to get the desired compound. Drying process removes the hydroxide from the sample. If one considers the suitability of this method for upconversion emission phosphors then it is found that samples prepared through this technique produce low upconversion emission because of the small presence of volatile compounds in the sample. Hence, in order to get the desired upconversion emission intensity samples need to go for heat treatment. This heat treatment although removes the volatile impurity but in same time increases the particle size and agglomeration. Hence, for biological applications this technique is not so useful. Yi et al. have reported the synthesis of $NaYF_4$:Yb^{3+}/Er^{3+} phosphor through this method [15] and used EDTA to obtain controlled size particles.

3.2 Hydrothermal/Solvothermal Method

Due to the simplicity and capability of producing colloidal particles, the hydrothermal method is evolved as a popular synthesis technique. In this technique chemical reactions occur in a sealed environment under high temperature and pressure, usually above the critical point of the solvent. The reaction vessel is known in various names as hydrothermal synthesis reactor, digestion bomb, high temperature and pressure digestion vessel, teflon lined autoclave etc. and is made up of thick stainless steel to handle water temperature upto 250 °C and pressure upto 2–3 Mpa. The precursors are taken in the form of nitrates, fluorides, and chlorides. In order to control size &shape surfactants like ethylenediaminetetraacetic acid (EDTA), cetyltrimethylammonuim bromide (CTAB), trisodium citrate (Na_3Cit), linoleate acid, oleic acid etc. are utilized. Using this technique various shapes of $NaYF_4$ crystals such as rod, prism, tube, disk, octa dechedral shapes etc. were obtained [16–18] and used for various applications. In Fig. 4 it is shown that how just precursor pH changes the morphology of $NaYF_4$ UCNPs and it is the beauty of hydrothermal synthesis.

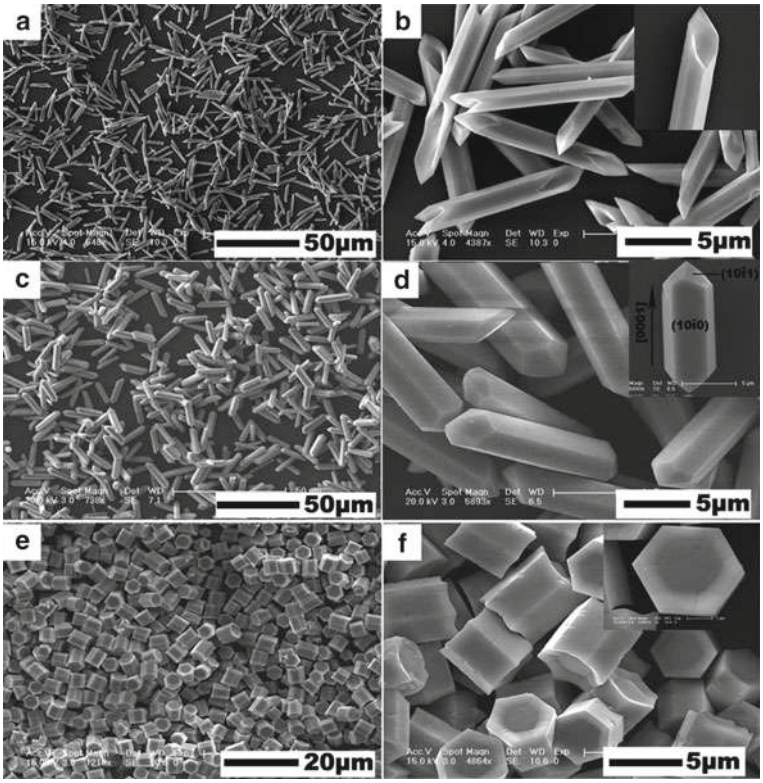

Fig. 4 The effect of pH on the morphology of $NaYF_4$ crystals containing NH_4F as the fluoride source. **a** and **b** At pH = 3, prismatic microrods with fractured ends were produced. **c**, **d** At pH = 7, prismatic microrods with conical ends were produced. **e** and **f** At pH = 10, hexagonal microprisms were produced. These samples were treated hydrothermally for 24 h at 180 °C (1:1 molar ratio for Cit^{3-}/Y^{3+}). Reproduced with permission from [18], Copyright 2007, American Chemical Society

The hydrothermal route has the advantages as: (a) use of simple instrumentation (b) relatively low reaction temperature (commonly below 200 °C) (c) easy control on size, and shape of particles (d) good yield and (f) high reproducibility. The UCNPs prepared through this technique may contain hydrophobic organic ligands (for example, OA) at the surface of the nanoparticles and hence biological applications require further surface modifications of these particles.

3.3 Thermal Decomposition Method

The hydrothermal method uses water as a reaction medium and hence synthesized UCNPs may contain water molecules which reduce the upconversion emission drastically. The thermal decomposition or thermolysis process uses organic liquids as

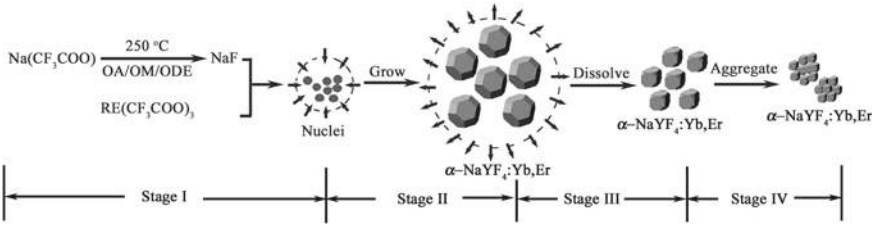

Fig. 5 Representative steps shows how α-$NaYF_4$:Yb^{3+}/Er^{3+} nanocrystals grow via nucleation process. Reproduced with permission from [30], Copyright 2007, American Chemical Society

a reaction medium and hence prepared UCNPs are free from water molecules. The preparation of –OH free samples through thermal decomposition route produces high upconversion emission intensity and hence this technique is mostly used in upconversion phosphor research. Many alkali lanthanide tetrafluoride ($AREF_4$) UCNPs such as $LiYF_4$ [19], $NaYF_4$ [20, 21], $NaGdF_4$ [22, 23], $NaLuF_4$ [24], $KGdF_4$ [25], $BaYF_5$ [26] and CaF_2 [27] have been synthesized through this route. This method also provides best control on the particle size and shape with comparatively faster reaction time [28]. The method employs thermolysis of organometallic precursors like Ln-trifluoroacetates [12, 20, 29] in a high boiling point organic medium such as 1-octadecene (ODE). The reaction solution needs to be heated upto 300 °C in oxygen free environment to form crystalline particles. During the reaction, nucleation and particle growth happen and organic ligands present in solution encapsulate grown particles and further particle growth sustains [12, 20, 29–31]. Synthesis stages of cubic $NaYF_4$:Yb^{3+}/Er^{3+} UCNPs are depicted in Fig. 5. Different shapes and sizes of $NaYF_4$:Yb^{3+}/Er^{3+} UCNPs can be obtained by varying the reagent concentrations, reaction duration, and reaction temperature.

3.4 Surface Functionalization of UCNPs and Biocompatibility Testing

The surface modification of the rare earth doped upconverting nanoparticles is required to develop a bioconjugation of the nanoparticles. Thus, the UCNPs may gain functional groups or become strongly charged on the surface that helps to conjugate biomolecules. Such modification improves colloidal stability of the UCNPs and generates a nanoplatform for biological applications [32–35]. Several bioconjugation strategies are used for UCNPs. Out of which chemical binding is one of the specific compared to the physical interaction (e.g. electrostatic adsorption method). A number of strategies have been proposed so far for surface modification of UCNPs which includes layer-by-layer self-assembly method, ligand exchange, ligand oxidation reaction, and amphyphilic polymers coating. In ligand exchange process, original ligand is displaced by bifunctional polymeric molecules on the

nanocrystal substrate which results hydrophilic surface and proficient for bioconjugation. Recent study found that the $NaYF_4$:Yb/Er can be used for obtaining carboxyl-functionalized water-soluble surface [36]. On the other hand, the ligand oxidation process involves carbon–carbon double bond oxidation of the ligand by Lemieux-von Rudloff reagent. The oxidation process converts carbon–carbon double bond into carboxylic acid group and that provides reactive functional moieties following biofunctionalization. A simple and versatile strategy for converting hydrophobic UCNPs into water dispersible sample is reported using this platform in reference [37]. Using the oppositely charged linear polyions, another group developed a layer-by-layer assembly strategy which can produce water-soluble UCNPs. In this technique electrostatic absorption of alternately charged polyions occurs and is useful for hydrophilic nanocrystals. Silica coating on the surface of nanocrystal produced by hydrolysis and condensation of siloxane monomers can be also functionalized. Zhang et al. have reported that polyvinyl-pyrrolidone stabilized $NaYF_4$nanocrystals could be directly coated with silica to facilitate a suitable surface for bioconjugation [33].

4 Biological Applications of Hybrid Phosphors

Conventional fluorescence-based probes/agents including organic dyes, quantum dots etc. have no longer importance in biological applications and in place of newer generation inorganic–organic hybrid fluorescent particles are receiving attention. Organic fluorescent dyes undergo photo-bleaching and long-term applications including live-cell bioimaging become troublesome. Also with organic dyes multicolor labeling and imaging is not possible. Same is also true for inorganic luminescent quantum dots. The organic dyes also suffer change in excitation and emission wavelengths with the change in pH, temperature etc. of the analyte. Rare earth based upconversion emission probes as mentioned above overcome these limitations and hence gaining their importance. Few interesting applications of UCNPs in biology are discussed below.

4.1 UCNPS as Biomolecule Sensors

Biomolecule sensors are developed based on FRET (fluorescence resonant energy transfer) technique where the donor's fluorescence is quenched by the acceptors in the nanometer distance range. A large number of experiments have been dedicated to design such novel sensors. Initialy, Wang et al. have constructed a FRET system using UCNPs as energy donors and gold nanoparticles as acceptors for the detection of trace amounts of avidin [38]. The sensor's principle was utilizing gold NPs as quencher for UCNPs. A separate study on cyclodextrin-decorated UCNPs platform to

detect cysteine has been done by Ni et al. [39]. Rhodamine-oxaldehyde conjugated β-$NaYF_4$:Yb^{3+}/Er^{3+} FRET model were developed to detect cysteine in aqueous solution through FRET method. Here, rhodamine-oxaldehyde and β-$NaYF_4$:Yb^{3+}/Er^{3+} were used as an donor and acceptor respectively (Fig. 6).

Increasing the concentration of cysteine, the quenching of UC luminescence was observed increasing upon NIR light excitation and was testified by absorption spectroscopy. The developed cysteine nanosensor is a potential biomolecular sensor due to avoiding background fluorescence interference which is because of the NIR excitation source. It was reported that graphene oxide (GO) quenches significantly through light emission of DNA-functionalized UCNPs, where β-$NaYF_4$:Yb, Er were used as

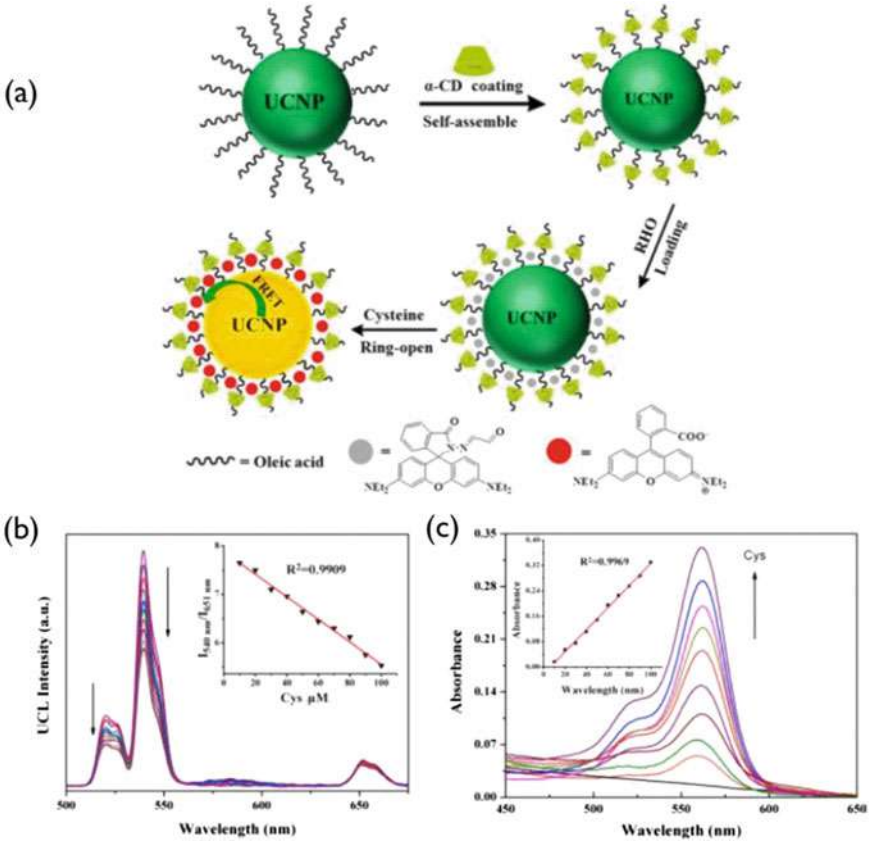

Fig. 6 **a** Surface modification and FRET: donor UCNPs and acceptor rhodamine. **b** UC emission spectra under 980 nm, (Inset: the variation of relative upconversion emission at 540–651 nm ratio upon various amount of Cys.) and **c** titration spectra of UV–Vis absorption (Inset shows the response of the ratio with Cys concentration.) of Rhodamine-oxaldehyde functionalized UCNPs with gradual increment of Cys. Reproduced with permission from [39], Copyright 2015, Royal Society of Chemistry

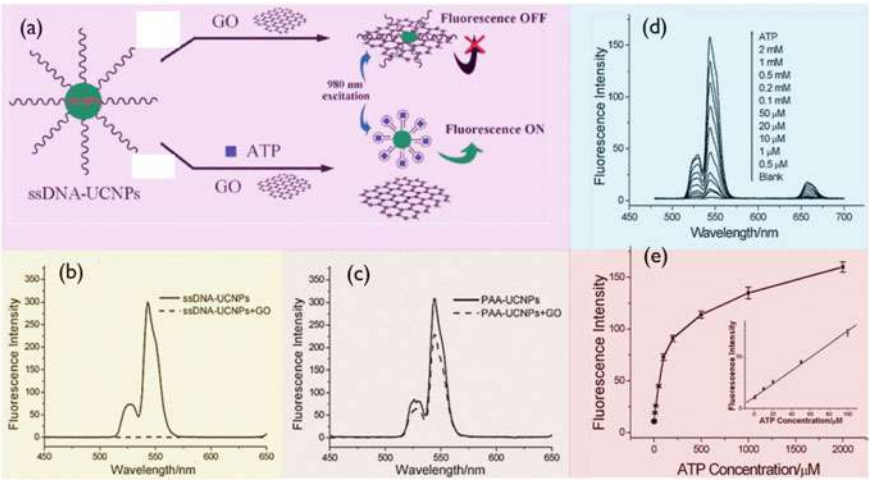

Fig. 7 **a** Scheme for upconversion FRET between GO and ssDNA-UCNPs for ATP sensing. **b** Upconversion spectra of ssDNA-UCNPs before (solid line) and after (dashed line) addition with GO. **c** Upconversion spectra of PAA-UCNPs before (solid line) and after (dashed line) addition of GO. Reproduced with permission from [40], Copyright 2011, Royal Society of Chemistry

the donor [40]. Furthermore, surface of the β-$NaYF_4$:Yb, Er UCNPs were functionalized by polyacrylic acid which is a carboxylic acid group. Under 980 nm excitation, the ssDNA as adenosine triphosphate-specific aptamer exhibit upconversion luminescence which can be quenched when GO is added. When adenosine triphosphate is added, the luminescence is recovered (Fig. 7).

This study also infers that the assay of UCNPs-GO can be used as a probe for various target molecules by cross-linking suitable aptamers and UCNPs. The UCNPs-based sensing is useful for tyrosine detection based on photo induced electron-transfer mechanism between melanin-like polymers and UCNPs [41]. Moreover, Guo et al. have developed UCNP-based sensing material for glycoprotein detection [42]. These works suggest that UCNPs can be applied to different biomolecules detection, and it has also been proven to exhibit good sensitivity in a range of chemical and biological analysis. Less toxicity of polymer coated UCNPs permits long-term live imaging monitoring. Hence, UCNPs are promising materials for imaging probes or sensors in biomedical application [43, 44].

The UCNPs can also be functionalized with proteins and such system can be used to the detection of antigen and antibody. Zijlmans et al. [45] have first time utilized UCNPs as markers to detect specific antigens in cells and tissue sections through solid phase immunologic fluorescent assay (IFA) and immunohistochemistry methods, respectively. The researchers have also used specific primary antibodies to target the antigens and biotin-conjugated antibodies as the secondary antibody. UCNPs coated avidin was then allowed to bind with secondary antibody. The obtained images had shown morphology of the tissue and cells and were easily marked because of the absence of fluorescence interference. This study shows feasibility of UCNPs for

fluorescent staining of proteins. However, researchers have given extensive effort to the development of such designs. The detection speed is comparatively faster than other techniques like enzyme-linked immunosorbent assay (ELISA). Thus, it is stated that UCNPs are potential for designing rapid diagnosis methods [46]. Several other researchers have used similar schemes to detect different virus and bacteria e.g. respiratory syncytial virus [47], hepatitis B virus [48], human immunodeficiency virus, and human cytomegalovirus [49], Mycoplasma tuberculosis bacteria [49], Yersinia pestis bacteria [50] and Brucella bacteria [51].

4.2 UCNPs as ROS (Reactive Oxygen Species) Sensors

The ROS has significant effects in cell signalling and homeostasis and its high level can lead lipid peroxidation, DNA, RNA, and amino acids oxidation. Thus, the amount of reactive oxygen species is important in biosystem. As natural by products ROS are formed by normal metabolism. Some of the examples of reactive oxygen species are H_2O_2, HClO, –OH, etc. To detect H_2O_2 and glucose, Shuang Wu's group has fabricated UCNPs based hybrid system [52]. In that work, nanocomposite was developed by combination of DNA-templated silver nanoparticles (DNA-AgNPs) and $NaYF_4$:Yb/Tm@$NaYF_4$ UCNPs where DNA-AgNPs acts as quencher and $NaYF_4$:Yb/Tm@$NaYF_4$ as donor. On the other hand, to obtain bare UCNPs, OA ligands coated $NaYF_4$:Yb/Tm@$NaYF_4$were treated with HNO_3. A cytosine rich DNA sequence was used for nucleation of AgNPs and to increase the accessibility to UCNPs, poly (adenine) sequence was added at the 3′ end of the C-rich sequence. To form DNA-AgNPs/UCNP nanocomposite based on the interactions between the negatively charged phosphonate groups of DNA-AgNPs and the RE ions on UCNPs, DNA-AgNPs could be assembled on UCNP's surface. This design is based on modulation of H_2O_2 of DNA-AgNPs induced luminescence quenching of UCNPs (Fig. 8).

A spectral match between the blue upconversion and the DNA-AgNPs's absorption was observed from absorption spectrum of DNA-AgNPs and upconversion spectrum of the $NaYF_4$:Yb/Tm@$NaYF_4$, as a result UC luminescence can be quenched by DNA-AgNPs as shown in Fig. 8b. With the addition of H_2O_2 the UC luminescence can be recovered. Researchers [53] have reported MnO_2^- modified UCNP sensor for detection of H_2O_2 and glucose in human blood. This design works on H_2O_2 modulation of luminescence quenching of UCNPs. $NaYF_4$:Yb,Tm@$NaYF_4$ was employed in this scheme as energy donar and MnO_2nanosheets on the UCNP acted as quencher. Absorption band of MnO_2 nanosheets in 250–500 nm range overlaps the blue emission of UCNPs, whereas UCNPs emission is quenched by H_2O_2, that help to form Mn^{2+} from MnO_2, and the glucose is detected from the enzymatic conversion of glucose by glucose oxidase for the generation of H_2O_2.

The –OH radical can damage biomolecules in living systems therefore, monitoring of –OH radical is very important to understand its physiological roles. Researchers

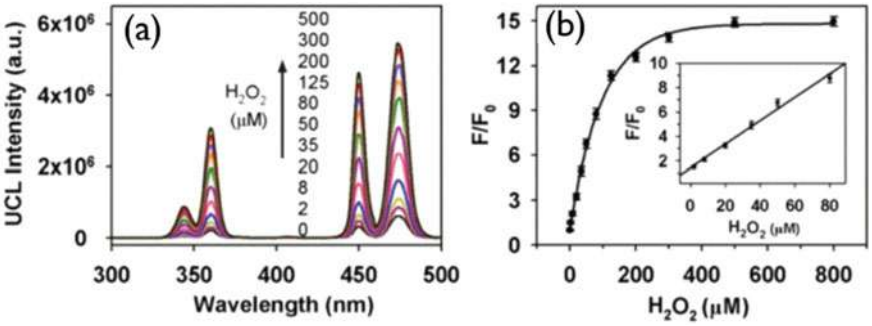

Fig. 8 **a** H_2O_2 concentration dependent spectra of DNA-AgNPs/UCNP, **b** variation of F/F_0 with changing the amount of H_2O_2 in DNA-AgNPs/UCNP; F and F_0 are emission intensity in the presence and absence of H_2O_2, respectively. Reproduced with permission from [52], Copyright 2016, Royal Society of Chemistry

have developed UCNP probe to detect the –OH radicals [54]. In this mechanism the UC emission from the UCNP is suppressed due to carminic acid and can be recovered in the presence of –OH. In 2017, a high-sensitive multifunctional probe was reported by Zhou and co-workers to detect –OH concentration in a broad linear detection range [55]. Hypochlorous acid (HOCl) is an important microbicidal agent in the immune systems but its misproportion could damage the tissues. Therefore, many efforts have been done on developing HOCl sensor. Zhang's group has reported a novel UCNP-based probe for ratiometric detection of HClO [56]. In this work, a water-soluble detection system containing rhodamine modified UCNPs were synthesized.

4.3 UCNPs in Intra-Cellular pH

Detection of cellular pH is of great importance in biomedical research and designing appropriate pH nanoprobes that work under NIR excitation [92]. Optical pH sensors are usually based on the of materials that are sensitive to pH [91]. UCNPs based pH sensor was first suggested by the group of Wolfbeis in 2009 [56]. They designed a sensor film (~12 μm) by using $NaYF_4$: Er, Yb nanorods, pH indicator- bromothymol blue. The pH probe exhibited a large spectral shift and specific color change with pH. In a separate study, a ratiometric pH probe was developed by combining porphyrin derivatives and $NaYF_4$:Yb, Er UCNPs [58]. In this work, it has been reported that by monitoring the change in the red/green ratio of upconversion, pH can be detected. Mahata et al. [59] have reported a rationally designed and effective upconversion system (Fig. 9) that combines $NaYF_4$:Yb^{3+}/Tm^{3+} @ $NaYF_4$:Yb^{3+} @ $NaYF_4$:Yb^{3+}/Nd^{3+} ore-shell-shell UCNPs with fluorescein-5-isothiocyanate (FITC) dye and evaluated its pH sensing ability upon NIR light excitations, as illustrated in Fig. 9. The blue upconversion luminescence bands from the Tm^{3+}-ions showed

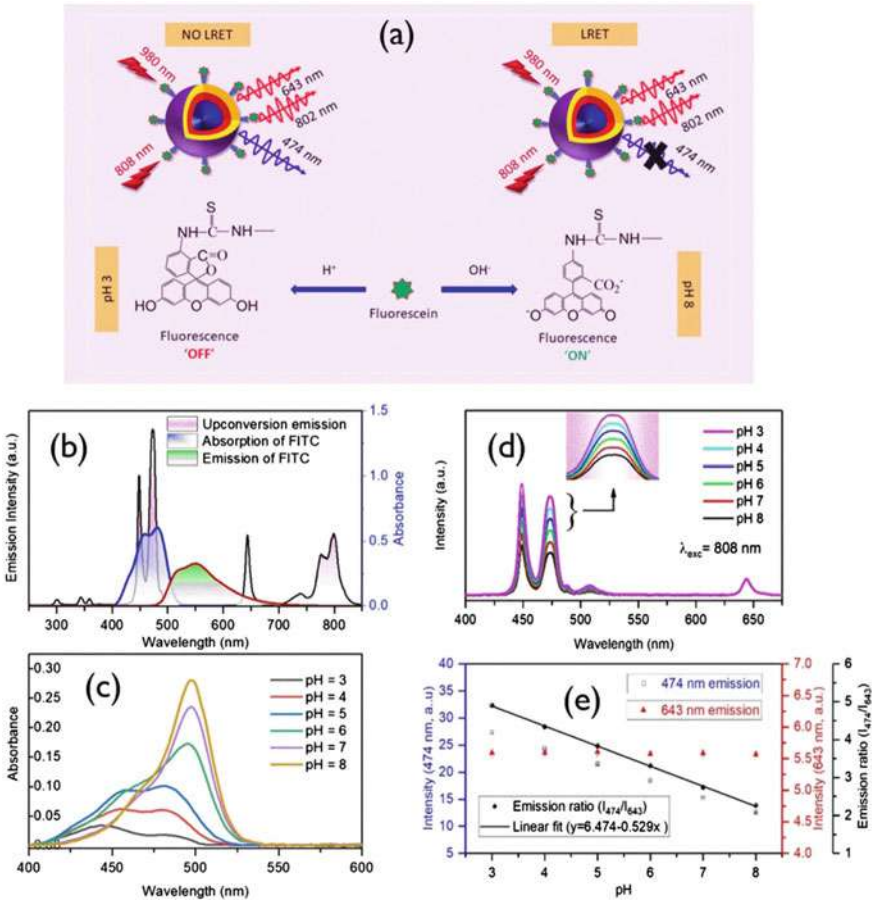

Fig. 9 **a** Design of the nanoprobe and its working principle, **b** black line- upconversion emission upon 980 nm, blue line-absorption spectrum of FITC, redline-FITC emission upon 488 nm laser excitation; **c** absorption spectra of FITC at various pH, **d** variation of 808 nm excited upconversion emission spectra of FITC conjugated nanoprobes with pH; inset shows the 474 nm band. **e** pH dependent variation of 474, 643 nm and their ratio (474–643 nm). Reproduced with permission from [59], Copyright 2019, Royal Society of Chemistry

pH dependent variation because of absorption of blue light by the FITC molecules while the other bands at the red or near-infrared regions remained unchanged. Thus, a ratiometric and self-referenced sensor was developed by considering 474, 643, and 802 nm emission bands upon longwave light excitations. The black line fit of the experimental points in Fig. 9 indicates a linear relation of the ratio (474 to 643 nm) and pH. This approach will help to broaden the applications in pH sensing for further development of nano-bio probes.

4.4 UCNPs as Contrast Agent in OCT Imaging

The potential of UCNPs can be utilized by several ways due to the versatility of these particles. The UCNPs can be made to work in multi-modal/-functional way. As an example $NaGdF_4:Er^{3+}/Yb^{3+}$ UCNPs can show at least two properties, (1) frequency upconversion optical emission and (2) paramagnetic property. First belongs to the optical functionality and second belongs to the magnetic functionality and both can be explored at the same time. This has introduced multimodal imaging using UCNPs in biology. Gadolinium (Gd^{3+}) host based compounds are commonly employed as contrast agents for magnetic resonance imaging (MRI) [60–62]. The Gd^{3+} is among those four elements that can be magnetized at room temperature (gadolinium, nickel, iron, and cobalt). This offers alternatives to high energy ionizing radiation methods of tomographic imaging such as computed tomography and positron emission tomography. Several groups have utilized lanthanide UCNPs as multimodal imaging [63, 64]. It is not limited to here and further UCNPs have potential to work as contrast agent for multiple bio-imaging techniques. The UCNPs can generate heat (due to non-radiative transitions) on suitable excitation and hence can be used to enhance the photoacoustic imaging [65]. In a very recent study UCNPs were used to enhance the contrast of images recorded by optical coherence tomography (OCT). This is indeed an important study and the results of the study are summarized here.

Optical coherence tomography (OCT) has evolved as an important imaging technology for biomedical imaging of the skin, blood vessels (angiography), malignant tumours, and other tissues. The OCT uses near-infrared light to provide unrivalled spatial resolution without sacrificing penetration depth [66–68]. OCT generally has two configurations; one uses broadband excitation source and a grating for dispersion and other uses swept source (varying wavelength) excitation, popularly known as SSOCT. The SSOCT works on the principle of Fourier transform interferometry and has increased sensitivity over the conventional OCT [69]. The SSOCT in itself is not free from shortcoming, at many occasions it also produces lower contrast and hence researchers are further trying to enhance the image contrast with various additive methods. The use of contrast agents is one of those methods to improve the contrast. The idea behind using of UCNPs was that when nanoparticles come close to the cell surface there is a mismatch in the refractive index and it results phase-contrast between the two different region [70]. The refractive index mismatch can induce light scattering and may enhance the contrast [71]. The Gold nanoparticles (with visible wavelength plasmon band) were used for the purpose and idea has worked but low penetration depth of visible light into tissue has not increased depth resolution. If one tries to select the excitation within the biological transparency window (650–1300 nm) then more depth resolution could be achieved. This NIR window could efficiently be used with UCNPs and particularly Er^{3+}/Yb^{3+} doped UCNPs excited with 976 nm wavelength. Jiyoung et al. have investigated $NaGdF_4$: Er^{3+}/Yb^{3+} nanoparticles on HeLa cells for in vitro imaging application [72]. They have observed that colloidal stability of UCNPs is an important factor for imaging and the presence of polar functional groups e.g. –OH, –COOH and $–NH_2$ usually enhance the colloidal

stability. Maurya et al. [73] have prepared $NaGdF_4:Er^{3+}/Yb^{3+}$ through solvo thermal method using ethyleneglycol (EG) and oleic acid (OA) as the reaction medium. Two samples viz. polyvinylpyrrolidone (PVP) coated $NaGdF_4:Er^{3+}/Yb^{3+}$ (sample named as NaGdF-I) and oleic acid coated $NaGdF_4:Er^{3+}/Yb^{3+}$ (sample named as NaGdF-II) were prepared for this purpose. Two thin slices (about 12 mm) of chicken breast tissue were prepared for in vitro tissue imaging. NaGdF-I and -II concentrations of 50 μg/mL were prepared separately in ultra pure ethanol. To see if UCNPs might be used as an OCT contrast agent, a tissue sample without UCNPs was scanned first using the SSOCT system (control experiment). Following that, few drops of NaGdF-I and –II colloidal solution were placed on the tissue surface and then were allowed to penetrate deeper into tissue layers. The imaging of tissue was done using 1060 nm wavelength but this wavelength does not excite UCNPs and hence 976 nm wavelength radiation is required to excite UCNPs during the imaging. OCT images were recorded at the intervals of 0, 5, 10, 20, and 30 min after placing of UCNPs. During the recording, images were recorded with and without the use of excitation (976 nm) of UCNPs, means one image of tissue was taken without 976 nm excitation and at the same time another image was taken with 976 nm excitation. The SSOCT B-scan pictures of the control sample are shown in Fig. 10a, d. Figure 10b, e shows the SSOCT image after a 30-min interval without excitation of NaGdF-I & -II, respectively. Figure 10c, f shows a high-contrast SSOCT image taken while NaGdF-I & -II were excited at 976 nm. SSOCT images demonstrate increased depth of penetration and high contrast image indicating the diffusion of UCNPs into inner layers of tissue after a 30-min period.

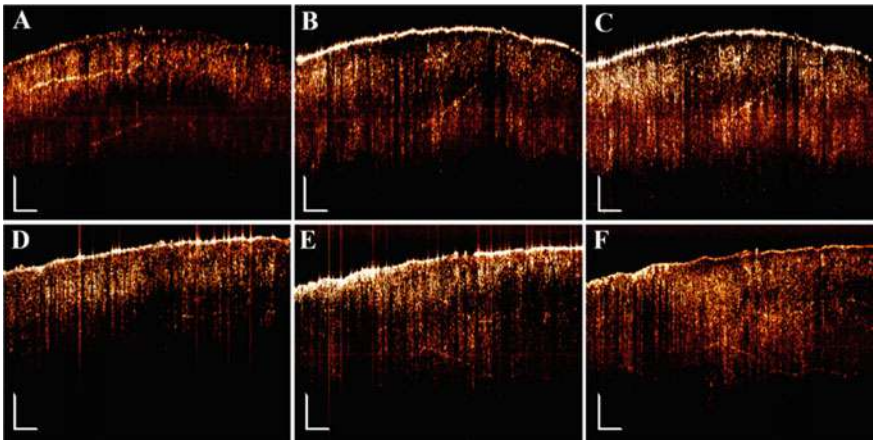

Fig. 10 SSOCT B-Scan images of chicken breast tissue; **a** control sample for first sample; **b** without excitation of NaGdF-I UCNPs after 30 min of application; **c** excitation of NaGdF-I UCNPs after 30 min of application; **d** control sample for the second experiment; **e** without excitation of NaGdF-II UCNPs after 30 min of application; **f** with excitation of NaGdF-II UCNPs after 30 min of application (Scale: 200 μm). Reproduced with permission from [73], Copyright 2020, American Chemical Society

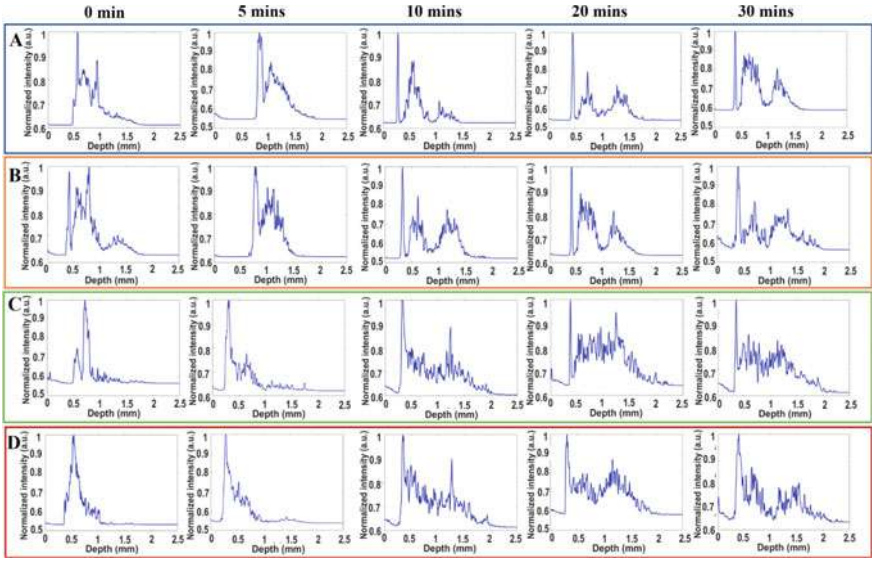

Fig. 11 Averaged A-scan profile plot of SSOCT image over region of interest at different interval of time 0, 5, 10, 20 and 30 min. A-scan for sample with **a** NaGdF-I without excitation; **b** NaGdF-I with excitation; **c** NaGdF-II without excitation; **d** NaGdF-II with excitation. The X-axis in all spectra represents depth in millimetres, whereas the Y axis represents normalised intensity in arbitrary units (au). Reproduced with permission from [73], Copyright 2020, American Chemical Society

The B-scan pictures could not be easily read and hence A-scan pictures were created from B-scans. Figure 11 shows A-scan profiles corresponding to Fig. 10. From the figure it can easily be observed that as time increases from 0 to 30 min the second peak shifts towards higher depth. It indicates incremental penetration of UCNPs with time. Moreover intensity of the second peak is found higher when sample is excited with 976 nm (Fig. 11b). The increase in intensity indicates the increase scattering of recording wavelength (1060 nm) from excited UCNPs. Comparison of Fig. 11b, d gives that NaGdF-I UCNPs are superior over NaGdF-II UCNPs as intensity is found higher for the case of NaGdF-I. The studies made here are the just initial efforts to extend the application of UCNPs in OCT imaging and the results are inspiring. It is expected that further investigations may lead to real world application.

4.5 UCNPs in Photodynamic and Photothermal Therapy

The applications of UCNPs are not limited to sensing and imaging areas but further extended to targeted drug delivery systems and maligned cell destruction through photothermal therapy. The non-targeted drug administration e. g. oral drugs work

equally on healthy and unhealthy cells and hence possess severe side effects, general chemotherapy is one example. Chemotherapy works on two principles: photodynamic effect and photothermal effect. In photodynamic therapy (PDT) there is in-situ generation of singlet oxygen which kills the cells, on the other hand in photothermal therapy (PHT) generated heat destroys the cells. The PDT has long been used in clinical practice while PHT is still under the research stage. For cancer treatment various diagnosis techniques like X-rays imaging, computed tomography (CT) scan, magnetic resonance imaging (MRI), positron emission tomography (PET) scan and fluorescence imaging are used. These techniques are complete in it but just are in situ diagnosis techniques. The present day need is more than this and we need multi-modal techniques that could diagnose and treat the targeted area simultaneously. The imaging probes attached with the drugs have been investigated much for this purpose and several efficient schemes were proposed [74]. The UCNPs-based drug delivery systems possess good therapeutic value and enable tracking and drug release in real-time. The magnetic nanoparticles based drug delivery systems works efficiently under magnetic hyperthermia effect but magnetic nanoparticles do not possess luminescence itself and designed system needs additional luminescence entity for real time imaging. On the other hand UCNPs can produce luminescence as well as heat (or singlet oxygen) on photo-excitation and hence here single entity performs two jobs simultaneously. This makes UCNPs more useful for multimodal cancer treatment.

Wang et al. have shown how folic acid (FA) attached onto the surface of PEI-modified UCNPs and loaded with camptothecin (CPT)/doxorubicin (DOX) can efficiently be used for targeted cancer treatment [74]. In this review article more details about the use of UCNPs in therapeutics could be found. Yang et al. have used UCNPs with a mesoporous shell to create a photoresponsive drug release device [75]. Bao et al. have attached UCNPs and DOX on starch-based gel nanoparticle. The PEI and 2,3-dimethyl maleic anhydride (DMMA) were also used to decorate the nanoparticle. Their results show that multiple modifications in system enhance the circulation time of drug in the body as well as chances of drug to reach the tumor site [76]. In Fig. 12 the scheme of drug carrier structure preparation and processes of drug release and cell destruction is shown [76].

Along with the use of UCNPs the long persistence luminescence nanophosphors (LPNP) have also gained interest in biological applications [77]. Indeed, long-lasting luminescence could be valuable for scientific research including cell tracking, cell development, and medication release monitoring. The mesoporous silica-coated long persistence phosphors could be employed for medication administration and tumour imaging, according to the study [78]. After UV stimulation followed by red LED, the afterglow of the folic acid (FA) modified-$Zn_{1.1}Ga_{1.8}Ge_{0.1}O_4:Cr^{3+}:Eu^{3+}@SiO_2$ has lasted up to 15 days. The DOX was first placed into the mesoporous silica shell, and then the LPNP was delivered intravenously into the mouse. The in-vivo and in-situ monitoring of DOX in the H22 tumor-bearing mice has shown in Fig. 13a. The afterglow signal was detected at the tumor site, as illustrated by the yellow arrow, due to FA's targeting capacity. Figure 13b shows the identical image after 2 min

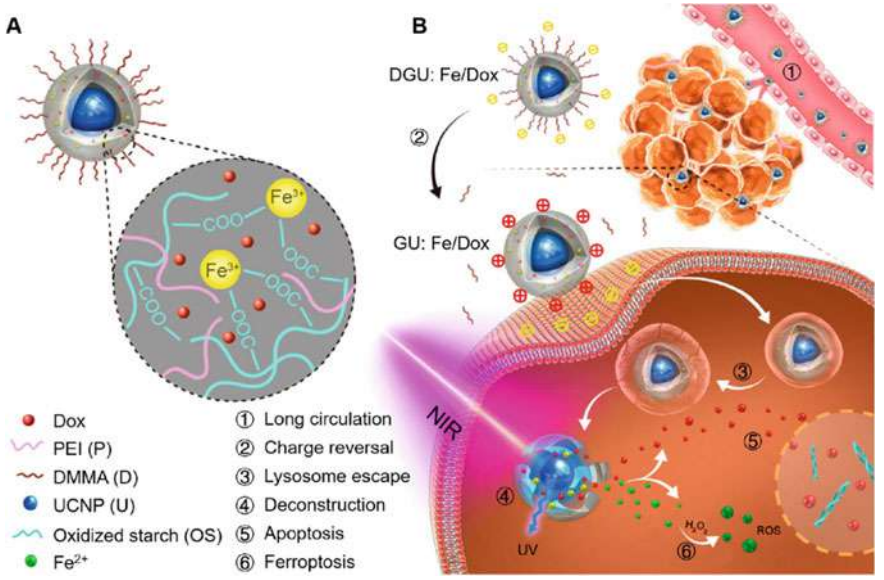

Fig. 12 **a** Figure showing Fe^{3+} linked UCNPs as core and DOX drug attached at the polymer shell. **b** Figure showing anticancer mechanism of created structure. (1) Accumulation and circulation of particles in channel. (2) Conversion of –ve charged particle to +ve charge particle at tumor site through pH change and cellular uptake. (3) Lysosome escape through proton sponge effect. (4) Deconstruction of structure through NIR radiation. (5) Released of DOX and (6) Ferroptosis process. Reproduced with permission from [76], Copyright 2019, American Chemical Society

of secondary stimulation with a red LED. Studies indicate that long-persistence phosphors can be promising candidates for trackable drug delivery.

As discussed above UCNPs are appealing materials for phototherapies. The photodynamic therapy (PDT) requires photon sensitizer to produce oxygen singlet ($^1O_2$) in order to kill tumors [79], whereas photothermal therapy (PHT) requires photon sensitizer to produce heat in order to kill tumours via an extensive heating effect [80]. The NIR-activated phototherapies have greater penetration depth than UV/visible light-activated phototherapies [81]. For improved PDT, Idris et al. have created a hybrid system with $NaYF_4$ UCNPs and two photon sensitizers, merocyanine 540 (MC540) and zinc(II)phthalocyanine (ZnPc) [82]. The good spectral overlap of the upconversion emission and absorption spectra of MC540 and ZnPc allowed for efficient production of $^1O_2$. Furthermore, the tumour suppression effect was evaluated by measuring tumour volumes in different treatment groups of mice over a two-week period. Other researchers have presented similar findings on the use of $NaYF_4$-ZnPC for in-vivo PDT applications [83]. In this experiment, ZnPC is the key element for producing $^1O_2$, and they have discovered that the nanocomposite can achieve PDT for tumours with a depth of 1 cm. Cheng et al. have used a layer-by-layer growth method to create coreshell-shell multifunctional nanoparticles (MFNPs) with a $NaYF_4$:Yb/Er core/iron oxide shell/gold nanoshell structure [84]. Unlike other reported PHT work,

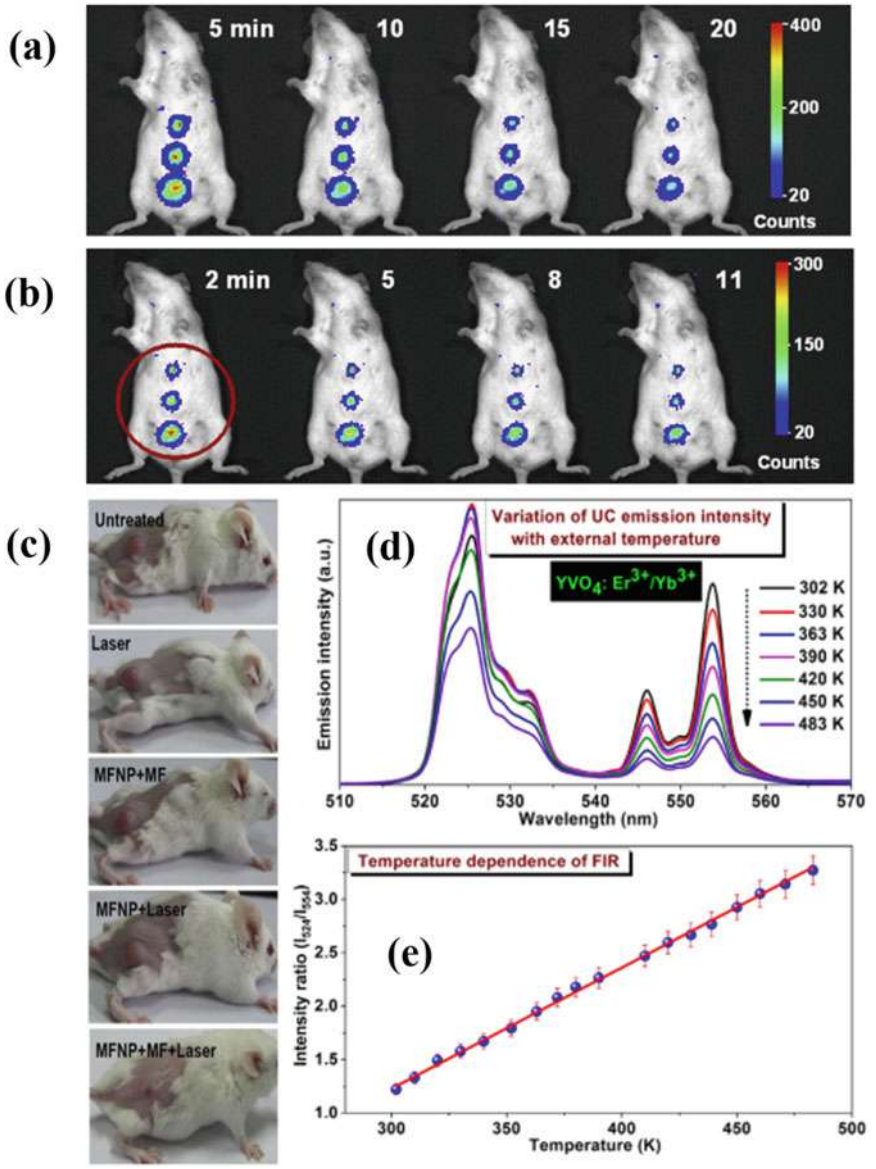

Fig. 13 **a** In-vivo luminescence images of H22 tumor-bearing mice after giving intravenous injection of (FA)-$Zn_{1.1}Ga_{1.8}Ge_{0.1}O_4$:$Cr^{3+}$/$Eu^{3+}$@$SiO_2$ with DOX drug. Reproduced with permission [78] Copyright 2015, Elsevier. **b** Secondary excitation by red LED for 2 min after 2 h of circulation. The yellow arrow in the figure indicates the tumor site. Reproduced with permission [78] Copyright 2015, Elsevier. **c** 4T1 tumor bearing mice photos in different test groups with different treatment. Reproduced with permission [84] Copyright 2012, Elsevier. **d** Pattern of change in UC emission of green bands with temperature of $NaGdF_4$:Er^{3+}/Yb^{3+}sample, Reproduced with permission [87] Copyright 2014, Elsevier. **e** Variation of fluorescence intensity ratio (FIR) with external temperature. Reproduced with permission [87] Copyright 2014, Elsevier

this nanocomposite can execute magnetically guided PHT under magnetic field. Figure 13c depicts 4T1 tumor-bearing mice in various testing groups. The mouse with injected MFNPs clearly showed significant tumour shrinkage under magnetic guidance and laser illumination for PHT. Authors have also observed no tumour regrowth after 40 days. Furthermore, $NaYF_4$:Yb^{3+}/Er^{3+}@Ag core/shell nanocomposites for upconversion imaging and PHT applications were created [85]. The silver shell not only gives PHT but also reduces its toxicity. PDT and PHT are undeniably effective tumor-suppressing agents. As a result, combining the two phototherapeutic techniques has the potential to improve their theranostics capabilities. It is demonstrated that the two techniques can be used in tandem to produce a core–shell UCNPs-nanographene oxide/ZnPC composite [86]. For bioimaging and PHT applications, 808 nm laser excitation is absorbed, whereas PDT is triggered by 630 nm laser illumination. In comparison to PDT and PHT alone, combined PDT and PHT can improve cancer therapy efficacy.

4.6 UCNPs in Micro Volume Temperature Sensing

As mentioned above that UCNPs can generate heat and hence this property could also be used to measure the temperature of the environment. The UCNPs can be prepared upto several nano/micrometer diameter and a single micro-particle can be sufficient to measure the temperature. The microvolume temperature measurement is the need for biomedical field. The use of luminous microsized particle at the tip of scanning thermal probe or at the tip of an optical fibre has been searched for the past decade. Two commonly used approaches, decay time and fluorescence intensity ratio (FIR), are used to determine the temperature sensing through UC materials. The FIR technique uses temperature dependent variation of UC intensity ratio of two thermally connected levels and is the most widely accepted method for temperature sensing due to its simplicity. The FIR approach uses low excitation power or short pulsed radiation to excite the sample. Er^{3+} has thermally linked $^2H_{11/2}$ and $^4S_{3/2}$ levels and is the most studied ion for temperature sensing applications. Figure 13d compares temperature dependent upconversion spectra of Er^{3+}/Yb^{3+}codopedYVO_4sample [87]. Thermally coupled electronic multiplets exhibit a noticeable change in emission intensity. The plot of the intensity ratio vs. absolute temperature is shown in Fig. 13e. The system displays the Boltmann distribution of populations at the $^2H_{11/2}$ and $^4S_{3/2}$ levels, which is as expected. Few submicron scale luminous thermometers have been successfully demonstrated for temperature sensing with a scanning microscope [88–90]. In coming years more advances in this filed is expected to come in light.

References

1. Dieke, G.H.: Spectra and energy levels of rare-earth ions in crystals. In: Crosswhite, H.M. (eds.) Interscience Publishers (1968)
2. Solid, B.N., Counters, S.I.Q.: Phys. Rev. Lett. **2**, 84–85 (1959)
3. Auzel, F.: Upconversion and anti-Stokes processes with f and d ions in solids. Chem. Rev. **104**, 139–173 (2004)
4. Wu, S., Kong, X.-J., Cen, Y., Yuan, J., Yu, R.-Q., Chu, X.: Nanoscale **8**, 8939–8946 (2016)
5. Liu, Y., Tu, D., Zheng, W., Lu, L., You, W., Zhou, S., Huang, P., Li, R., Chen, X.: Nano Res. **11**(6), 3164–3174 (2018)
6. Chen, H., Fang, A., He, L., Zhang, Y., Yao, S.: Talanta **164**, 580–587 (2017)
7. Resch-Genger, U., Gorris, H.H.: Anal. Bioanal. Chem. **409**, 5855–5874 (2017)
8. Yuan, J., Cen, Y., Kong, X.J., Wu, S., Liu, C.L., Yu, R.Q., Chu, X.: ACS Appl. Mater. Interfaces **7**, 10548–10555 (2015)
9. Wang, H., Yi, J., Yu, Y., Zhou, S.: Nanoscale **9**, 509–516 (2017)
10. Pound, G.M., Mer, V.K.L.: J. Am. Chem. Soc. **74**, 2323–2332 (1952)
11. LaMer, V.K., Dinegar, R.H.: J. Am. Chem. Soc. **72**, 4847–4854 (1950)
12. Wang, H.-Q., Nann, T., Luminescence, L., Hänninen, H.H (eds.) Springer, Berlin, Heidelberg, pp. 115–132 (2011)
13. Vetrone, F., Mahalingam, V., Capobianco, J.A.: Chem. Mater. **21**, 1847–1851 (2009)
14. Page, R.H., Schaffers, K.I., Waide, P.A., Tassano, J.B., Payne, S.A., Krupke, W.F., et al.: J. Opt. Soc. Am. B **15**, 996–1008 (1998)
15. Yi, G.S., Lu, H.C., Zhao, S.Y., Yue, G., Yang, W.J., Chen, D.P., et al.: Nano Lett. **4**, 2191–2196 (2004)
16. Li, C., Yang, J., Quan, Z., Yang, P., Kong, D., Lin, J.: Chem. Mater. **19**, 4933–4942 (2007)
17. Li, C., Quan, Z., Yang, J., Yang, P., Lin, J.: Inorg. Chem. **46**, 6329–6337 (2007)
18. Li, C., Yang, J., Quan, Z., Yang, P., Kong, D., Lin, J.: Chem. Mater. **19**(20), 4933–4942 (2007)
19. Liu, Y., Tu, D., Zhu, H., Chen, X.: Chem. Soc. Rev. **42**, 6924–6958 (2013)
20. Boyer, J.-C., Vetrone, F., Cuccia, L.A., Capobianco, J.A.: J. Am. Chem. Soc. **128**, 7444–7445 (2006)
21. Boyer, J.-C., Cuccia, L.A., Capobianco, J.A.: Nano Lett. **7**, 847–852 (2007)
22. Vetrone, F., Naccache, R., Mahalingam, V., Morgan, C.G., Capobianco, J.A.: Adv. Func. Mater. **19**, 2924–2929 (2009)
23. Naccache, R., Vetrone, F., Mahalingam, V., Cuccia, L.A., Capobianco, J.A.: Chem. Mater. **21**, 717–723 (2009)
24. Liu, Q., Sun, Y., Yang, T., Feng, W., Li, C., Li, F.: J. Am. Chem. Soc. **133**, 17122–17125 (2011)
25. Wong, H.-T., Vetrone, F., Naccache, R., Chan, H.L.W., Hao, J., Capobianco, J.A.: J. Mater. Chem. **21**, 16589–16596 (2011)
26. Vetrone, F., Mahalingam, V., Capobianco, J.A.: Chem. Mater. **21**, 1847–1851 (2009)
27. Quan, Z., Yang, D., Yang, P., Zhang, X., Lian, H., Liu, X., Lin, J.: Inorg. Chem. **47**, 9509–9517 (2008)
28. Haase, M., Schäfer, H.: Angew. Chem. Int. Ed. **50**, 5808–5829 (2011)
29. Wang, F., Liu, X.: Chem. Soc. Rev. **38**, 976–989 (2009)
30. Mai, H.-X., Zhang, Y.-W., Sun, L.-D., Yan, C.-H.: J. Phys. Chem. C **111**, 13730–13739 (2007)
31. Lin, M., Zhao, Y., Wang, S., Liu, M., Duan, Z., Chen, Y., Li, F., Xu, F., Lu, T.: Biotechnol. Adv. **30**, 1551–1561 (2012)
32. Wang, H.F., Liu, X.: J. Am. Chem. Soc. **130**, 5642 (2008)
33. Li, Z., Zhang, Y.: Angew. Chem. Int. Ed. **45**, 7732 (2006)
34. Mai, H., Zhang, Y., Sun, L., Yan, C.: J. Phys. Chem. C **111**, 13721 (2007)
35. Lu, Q., Guo, F., Sun, L., Li, A., Zhao, L.: J. Appl. Phys. **103**, 123533 (2008)
36. Yi, G., Chow, G.: Adv. Funct. Mater. **16**, 2324 (2006)
37. Chen, Z., Chen, H., Hu, H., Yu, M., Li, F., Zhang, Q., Zhou, Z., Yi, T., Huang, C.: J. Am. Chem. Soc. **130**, 3023 (2008)

38. Wang, L., Yan, R., Huo, Z., Wang, L., Zeng, J., Bao, J., Wang, X., Peng, Q., Li, Y.: Angew. Chem. Int. Ed. **44**, 6054–6057 (2005)
39. Ni, J., Shan, C., Li, B., Zhang, L., Ma, H., Luo, Y., Song, H.: Chem. Commun. **51**, 14054 (2015)
40. Liu, C., Wang, Z., Jia, H., Li, Z.: Chem. Commun. **47**, 4661–4663 (2011)
41. Wu, Q., Fang, A., Li, H., Zhang, Y., Yao, S.: Biosens. Bioelectron. **77**, 957–962 (2016)
42. Guo, T., Deng, Q., Fang, G., Yun, Y., Hub, Y., Wang, S.: Biosens. Bioelectron. **85**, 596–602 (2016)
43. Gu, B., Zhang, Q.: Adv. Sci. **5**, 1700609 (2018)
44. Li, Z., Yuan, H., Yuan, W., Su, Q., Li, F.: Coord. Chem. Rev. **354**, 155–168 (2018)
45. Zijlmans, H., Bonnet, J., Burton, J., Kardos, K., Vail, T., Niedbala, R.S., Tanke, H.J.: Anal. Biochem. **267**, 30–36 (1999)
46. Guo, H., Sun, S.: Nanoscale **4**, 6692 (2012)
47. Mokkapati, V.K., Sam Niedbala, R., Kardos, K., Perez, R.J., Guo, M., Tanke, H.J., Corstjens, P.L.A.M.: Ann. N. Y. Acad. Sci. **1098**, 476–485 (2007)
48. Li, L., Zhou, L., Yu, Y., Zhu, Z., Lin, C., Lu, C., Yang, R.: Diagn. Microbiol. Infect. Dis. **63**(165–172), 21400 (2009)
49. Corstjens, P.L.A.M., Chen, Z., Zuiderwijk, M., Bau, H.H., Abrams, W.R., Malamud, D., Sam Niedbala, R., Tanke, H.J.: Ann. N. Y. Acad. Sci. **1098**, 437–445 (2007)
50. Yan, Z., Zhou, L., Zhao, Y., Wang, J., Huang, L., Hu, K., Liu, H., Wang, H., Guo, Z., Song, Y., Huang, H., Yang, R.: Sens. Actuators B105 Chem. **119**, 656–663 (2006)
51. Qu, Q., Zhu, Z., Wang, Y., Zhong, Z., Zhao, J., Qiao, F., Du, X., Wang, Z., Yang, R., Huang, L., Yu, Y., Zhou, L., Chen, Z.: J. Microbiol. Methods **79**, 121–123 (2009)
52. Wu, S., Kong, X.J., Cen, Y., Yuan, J., Yu, R.Q., Chu, X.: Nanoscale **8**, 8939 (2016)
53. Yuan, J., Cen, Y., Kong, X.J., Wu, S., Liu, C.L., Yu, R.Q., Chu, X., Appl, A.C.S.: Mater. Interfaces **7**, 10548–10555 (2015)
54. Li, Z., Liang, T., Lv, S.W., Zhuang, Q.G., Liu, Z.H.: J. Am. Chem. Soc. **137**, 11179 (2015). Guo, H.Q.W., Liu, Y.X., Jia, Q., Zhang, G., Fan, H.M., Liu, L.D., Zhou, J.: Anal. Chem. **89**, 4986 (2017)
55. Zhou, Y., Pei, W., Wang, C., Zhu, J., Wu, J., Yan, Q., Huang, L., Huang, W., Yao, C., Loo, J.S.C., Zhang, Q.: Small **10**(17), 3560–3567 (2014)
56. Sun, L.N., Peng, H., Stich, M.I.J., Achatz, D., Wolfbeis, O.S.: Chem. Commun. 5000 (2009)
57. Soni, A.K., Rai, V.K., Mahata, M.K.: Mater. Res. Bull. **89**, 116 (2017)
58. Esipova, T.V., Ye, X., Collins, J.E., Sakadzic, S., Mandeville, E.T., Murray, C.B., Vinogradov, S.A.: Proc. Natl. Acad. Sci. U.S.A. **109**, 20826–20831 (2012)
59. Mahata, M.K., Lee, K.T.: Nanoscale Adv. **1**, 2372–2381 (2019)
60. Zhou, J., Liu, Q., Feng, W., Sun, Y., Li, F.: Chem. Rev. **115**(1), 395–465 (2015)
61. Cheng, L., Wang, C., Liu, Z.: Nanoscale **5**(1), 23–37 (2013)
62. Tiwari, S.P., Maurya, S.K., Yadav, R.S., Kumar, A., Kumar, V., Joubert, M.-F., Swart, H.C.: J. Vac. Sci. Technol. B Nanotechnol. Microelectron. Mater. Process. Meas. Phenom. **36**(6), 060801 (2018)
63. Chen, J., Zhao, J.X.: Sensors **12**(3), 2414–2435 (2012)
64. Wang, C., Tao, H., Cheng, L., Liu, Z.: Biomaterials **32**(26), 6145–6154 (2011)
65. Brezinski, M.E., Fujimoto, J.G.: IEEE. J. Sel. Top. Quantum Electron. **5**(4), 1185–1192 (1999)
66. Boppart, S.A., Luo, W., Marks, D.L., Singletary, K.W.: Breast Cancer Res. Treat. **84**(2), 85–97 (2004)
67. Poddar, R., Kim, D.Y., Werner, J.S., Zawadzki, R.J.: J. Biomed. Opt. **19**(12), 126010 (2014)
68. Huang, D., Swanson, E., Lin, C., Schuman, J., Stinson, W., Chang, W., Hee, M., Flotte, T., Gregory, K., Puliafito, C., et al.: Science (Washington, DC, U. S.) **254**(5035), 1178−1181 (1991)
69. Choma, M., Sarunic, M., Yang, C., Izatt, J.: Opt. Express **11**(18), 2183 (2003)
70. Fitzgerald, R.: Phase-sensitive X-ray imaging. Phys. Today **53**(7), 23–26 (2000)
71. Tanev, S., Sun, W., Pond, J., Tuchin, V.V., Zharov, V.P.: J. Biophotonics **2**(8–9), 505–520 (2009)

72. Ryu, J., Park, H.-Y., Kim, K.; Kim, H.; Yoo, J. H.; Kang, M.; Im, K.; Grailhe, R.; Song, R. J. Phys. Chem. C 114 (49), 21077−21082 (2010)
73. Maurya, S.K., Mohan, M., Poddar, R., Senapati, D., Singh, S., Roy, A., Munirathnappa, A., Joaquim, K., Esteves da Silva, C.G., Kumar, K.: J. Phys. Chem. C **124**(33), 18366–18378 (2020)
74. Wang, F., Banerjee, D., Liu, Y., Chen, X., Liu, X.: Analyst **135**, 1839 (2010)
75. Yang, Y., Velmurugan, B., Liu, X., Xing, B.: Small **9**, 2937 (2013)
76. Bao, W.E., Liu, X., Lv, Y., Lu, G.H., Li, F., Zhang, F., Liu, B., Li, D., Wei, W., Li, Y.: ACS Nano **13** (2019)
77. Li, Z., Zhang, Y., Wu, X., Huang, L., Li, D., Fan, W., Han, G.: J. Am. Chem. Soc. **137** (2015)
78. Shi, J., Sun, X., Li, J., Man, H., Shen, J., Yu, Y., Zhang, H.: Biomaterials **37**, 260 (2015)
79. Wang, C., Tao, H., Cheng, L., Liu, Z.: Biomaterials **32**, 6145 (2011)
80. Cheng, L., Yang, K., Li, Y., Chen, J., Wang, C., Shao, M., Lee, S.-T., Liu, Z.: Angew. Chem. Int. Ed. **123**, 7523 (2011)
81. Chatterjee, D.K., Zhang, Y.: Nanomedicine **3**, 73 (2008)
82. Idris, N.M., Gnanasammandhan, M.K., Zhang, J., Ho, P.C., Mahendran, R., Zhang, Y.: Nat. Med. **18**, 1580 (2012)
83. Cui, S., Yin, D., Chen, Y., Di, Y., Chen, H., Ma, Y., Achilefu, S., Gu, Y.: ACS Nano **7**, 676 (2013)
84. Cheng, L., Yang, K., Li, Y., Zeng, X., Shao, M., Lee, S.-T., Liu, Z.: Biomaterials **33**, 2215 (2012)
85. Dong, B., Xu, S., Sun, J., Bi, S., Li, D., Bai, X., Wang, Y., Wang, L., Song, H.: J. Mater. Chem. **21**, 6193 (2011)
86. Wang, Y., Wang, H., Liu, D., Song, S., Wang, X., Zhang, H.: Biomaterials **34**, 7715 (2013)
87. Mahata, M.K., Kumar, K., Rai, V.K.: Sensor Actuat. B Chem. **209**, 775–780 (2015)
88. Peng, H.S., Stich, M.I.J., Yu, J.B., Sun, L.N., Fischer, L.H., WolĠeis, O.S.: Adv. Mater. **22**, 716–719 (2010)
89. Vetrone, F., Naccache, R., Zamarron, A., Juarranz de la Fuente, A., Sanz-Rodríguez, F., Maestro, L.M., et al.: ACS Nano. **4**, 3254–3258 (2010)
90. Debasu, M.L., Ananias, D., Pastoriza-Santos, I., Liz-Marzan, L.M., Rocha, J., Carlos, L.D.: Adv. Mater. **25**, 4868–4874 (2013)
91. Mahata, M.K., Bae, H., Lee, K.T.: Upconversion luminescence sensitized pH-Nanoprobes. Molecules **22**(12), 2064 (2017). https://doi.org/10.3390/molecules22122064
92. Mahata, M.K., De, R., & Lee, K.T.: Near-infrared-triggered upconverting nanoparticles for biomedicine applications. Biomedicines, **9**(7), 756 (2021)

Biological Application of Hybrid Phosphors

Sajjad Husain Mir, M. K. Mohammad Ziaul Hyder, and A. M. Masudul Azad Chowdhury

Abstract Hybrid phosphors have gained large interest in the field of biomedical systems owing to their excellent physicochemical features. The potentiality of hybrid phosphors also lies in gathering favourable features of varied nanoforms in a single construct. An advantage of polymer as one of the components as host material for luminescent phosphors is their simple method of preparation, superior mechanical properties, higher flexibility and lighter density. The polymer films are prepared by melt casting or spin coating and materials of any desirable size or shape can be prepared from polymers. Moreover, manufacturing of polymers is cheaper and the energy consumption of making polymers is much lower. Different types of optically transparent polymers can easily be incorporated with phosphors. In a hybrid matrix it has higher thermal stability and luminescence output. Besides, being an agent for in-vivo imaging, hybrid phosphor based fluorescent materials also demonstrate several advantages for use in bioassay and therapy. Amongst different phosphor-based nanomaterials, upconversion phosphors are potential optical contrast agents for uses in biomedical appliance due to their long emission lifetime, sharp emission peaks, and their photostability. In this chapter, a comprehensive overview on hybrid upconversion phosphor is discussed with the basic conceptions that include the mechanisms for the illustration of different fluorescent behaviours, the different methods applied for the preparation of these phosphors, and finally the uses of these materials in biological arena. In addition, new trends in these type of materials are summarized with future perspectives.

S. H. Mir (✉)
Advanced Materials and Bioengineering Research Center (AMBER), School of Chemistry, Trinity College Dublin, Dublin 2, Dublin, Ireland

M. K. Mohammad Ziaul Hyder
Department of Chemistry, Chittagong University of Engineering & Technology, Chittagong, Bangladesh

A. M. M. A. Chowdhury
Department of Genetic Engineering and Biotechnology, University of Chittagong, Chattogram, Bangladesh

© Springer Nature Switzerland AG 2022

K. Upadhyay et al. (eds.), *Hybrid Phosphor Materials*, Engineering Materials,
https://doi.org/10.1007/978-3-030-90506-4_9

1 Introduction

Luminescent nanomaterials have attracted large interest of research community owing to their excellent utilizations in innumerable area. Recent development of fluorescent elements have been focused on their improved design and diverse applications such as metal complexes [1], organic dyes [2], metal nanoparticles [3], fluorescent proteins [4], polymers [5] metal organic frameworks (MOF) [6], etc. have been modelled and improved for diverse applications [7]. Upconversion (UC) phosphors have found applications in multifunctional hybrid nanocomposites. The addition of different subject matters into the nanocomposite materials can utilize UC nanophosphor as a wavelength transformation matters to further enhance the functional range of the additional matters or integrating the additional active elements in one nanocomposite materials. This increases the field of potentiality in applications of UC nanomaterials.

Most of the conventional nanomaterials are downconversion (DC) fluorophores because they demonstrate fluorescence emission through emitting light of longer wavelength into shorter wavelength. Therefore, provide desirable properties such as, greater molar extinction coefficient, wide excitation spectra, tuneable emission peak and enhanced fluorescence lifespan, etc. [8]. However, there are specific disadvantages for example, little permeation into the biological cells because of the excitement of light at high energy, wide band of emission, auto fluorescence, short Stokes-shift overlaps of emission and excitation bands and phototoxicity, etc. [9]. Near infrared light is invisible, non-destructive, and huge abundance in nature compared to other electromagnetic radiations of light. Furthermore, when in laser radiation it can be produced simply compared to visible and ultraviolet radiations. Therefore, it is considered suitable source of electromagnetic radiation for the excitement of luminescent material [10]. The indicated challenges mentioned above for conventional fluorophores could be subdued by applying phosphors that are capable of irradiating with lower energy light irradiation to emit high energy radiations [11]. The materials of these kinds are known as anti-Stokes shift or up-conversion (UPC) phospors. Near infra-red radiation is utilized as a source of excitement for emitting ultraviolet or visible radiationst [12]. In contrast, long lifetime is presumed to be required for upholding more higher density for the absorption of the second excitation energy from transitional excited states [13]. Upconversion happens for the sequential absorption of low energy radiations to excite the photon to the higher energy levels and also for having longer life-time. Radiative relaxation delivers higher energy-light emissions from the higher energy levels which lie in the wavelengths of 800–300 nm. Illustration of conventional UC luminescence is shown in Fig. 1 [13].

The photon UC process is an in testing phenomenon due to the emission of the higher-energy visible (Vis) and ultraviolet (UV) photons from the lower energy and near infrared (NIR) photons [14]. This strange anti-Stokes emission makes the way to wide scope of uses spanning deep tissue imaging [15], light-triggered nanomedicine [16], and optogenetics [17]. UC nanoparticles (UCNPs) systems depend on the various ladder-like and long-lived electronic states to allow wide anti-Stokes shifts

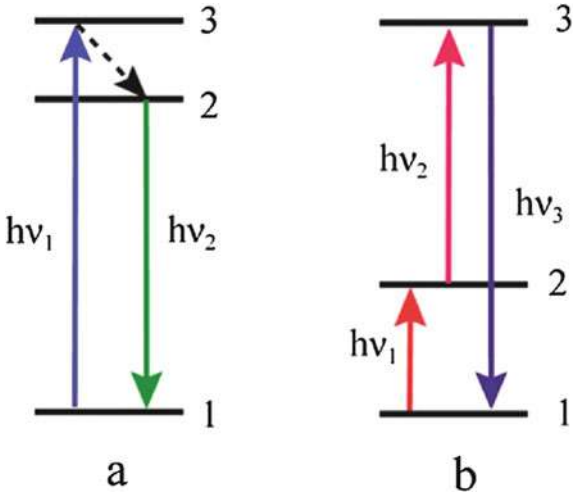

Fig. 1 **a** Conventional photoluminescence and **b** UC luminescence processes. [13] Reprinted with permission. Copyright 2015, American Chemical Society

from near infra-red excitation to the visible and ultraviolet light emission [14]. Moreover, upconversion nanoparticles absorb the radiation very inadequately, and their comprehensive UC efficiency are often <5%. Therefore, the aim is to develop well-built methods which enable the system in photon sensitization with higher energy that leads to higher brightness and enables conversion of broadband near infra-red light into visible and ultraviolet, to correspond with the essential requisition of the desired appliance explained earlier. For this, integrative researches have commenced to design and synthesize hybrid UC nanosystems (HUCNs) [18, 19], which can change UC properties that are not possible in their homogeneous parent molecules. In this book chapter, we mention recent advancement in HUCNs. Organic–inorganic nanohybrids constituting of organic and inorganic components [20–26] have gained intense attention in the field of bio-related systems owing to their favourable physicochemical properties [26–31].

1.1 Synthetic Methods

(i) **Thermal Decomposition Method (TDM)**: Thermal decomposition method is a promising method to produce superior nanocrystals less than 10 nm in size, which nanocrystals can be effectively removed from the human body and the application of upper dose is permitted [32]. This organic-phase synthetic process is carried out in absence of oxygen, which contains dissolving organic templates into the organic solvents of high boiling point temperatures with the help of surfactants and the decomposition of those templates at higher temperature. Mostly, organic templates are organic acid salts, for example, trifluoroacetate, acetylacetonate, oleate, and acetate. Non-coordinating octadecene

of high boiling point (315 °C) is applied to produce the high temperature environ. Oleylamine and oleic acid with polar capping elements and long chain of hydrocarbon are used as surfactants and coordination solvent. For successful synthesis, both the choice of fine-tuning of coordination behavior of the solvents and organic templates are important and mostly acceptable.

(ii) **Solvo/hydrothermal Synthesis (SHS)**: This method is utilized for the preparation of UCNPs because of simple operation and requirement of very little experimental skills (Fig. 2). In SHS method, high pressure and high temperature above critical point are needed; that allows the significant increment of the solubility of solids fastens the reaction for the nucleation of nanoscaled nanoparticles [33]. But the temperature applied in this method is lower than that of TDM [34]. The morphology and size of NPs can be fine-tuned with the control over the reaction atmosphere such as template-concentrations, pH value of the solvent, temperature and time, etc. [35]. By adding the capping agents that show heat resistivity, narrow-size distribution with surface functionalized NPs are possible in one-pot process [32].

(iii) **Coprecipitation Method**: Compared to TDM, coprecipitation method is facile and simple approach without the application of severe reaction conditions, expensive arrangement and complicated systems [36]. Growth of nanocrystals is controlled by adding capping ligands like PVP, EDTA, PEI

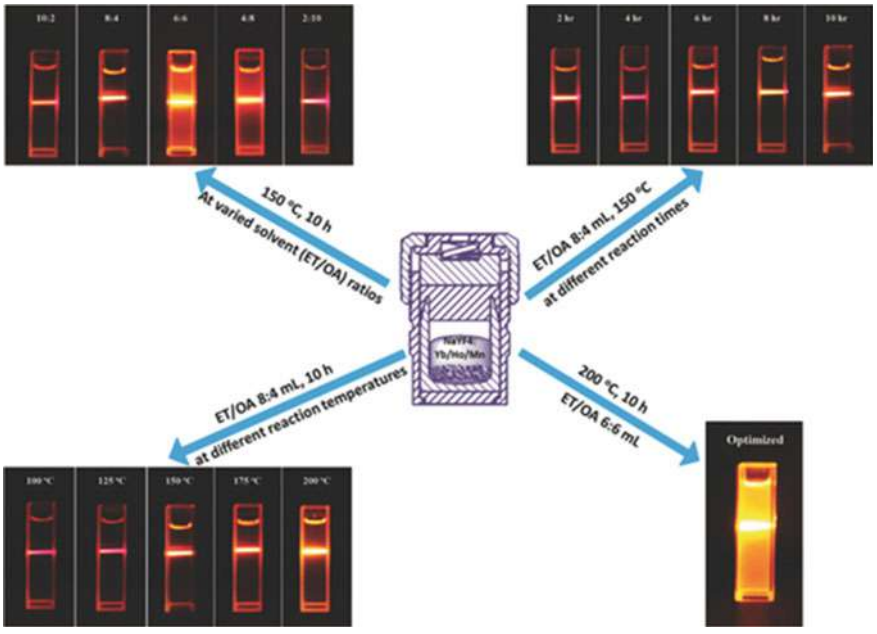

Fig. 2 Synthesis of $NaYF_4$:Yb/Ho/Mn in different conditions. [34] Reprinted with permission. Copyright 2017, ACS Publishers

etc. [37, 38]. This method can be applied for the synthesis of Ln-doped $NaYF_4$ crystals as well as for the synthesis of Ln-ions doped $YbPO_4$ and $LuPO_4$ NCs. In order to get high grade crystals for improved UC emissions, post fabrication heat treatment is essential [39].

(iv) **Microwave Synthesis (MS)**: This approach possesses two processes, liquid and solid microwave, namely. In the process of liquid microwave, Ln-complex salts and fluorides are first diffused in solvent and then microwave is applied to heat the total solution to obtain NPs in the solvent. On the other hand, Ln-oxides are added to fluorides to obtain NPs directly from microwave in solid microwave process. Monodispersed Ln-doped $NaYF_4$ and other fluorides (GdF3, PrF3, etc.) with various kinds of morphology have been obtained through microwave [40]. The advantages of applying microwave for the fabrication of UCNPs are, (i) it consumes less energy to generate rapid heat (Fig. 3), (ii) free of the by-products as microwave provides heat to the entire system uniformly, and (iii) the properties and structures of UCNPs can be enhanced by the addition of suitable surfactant [41].

(v) **Flaming Synthesis (FS)**: In FS method, all reactions happen in gaseous state and take place in four steps for example, precursor reaction, seeding, polymer growth and ion deposition, for fine powder containing NPs. The basic advantage of FS approach is time-efficient, inexpensive, and mass production of NPs. Besides oxide NPs, this method cannot be applied for other host material (vanadate, fluoride, phosphate, etc.) for UCNPs preparations [42].

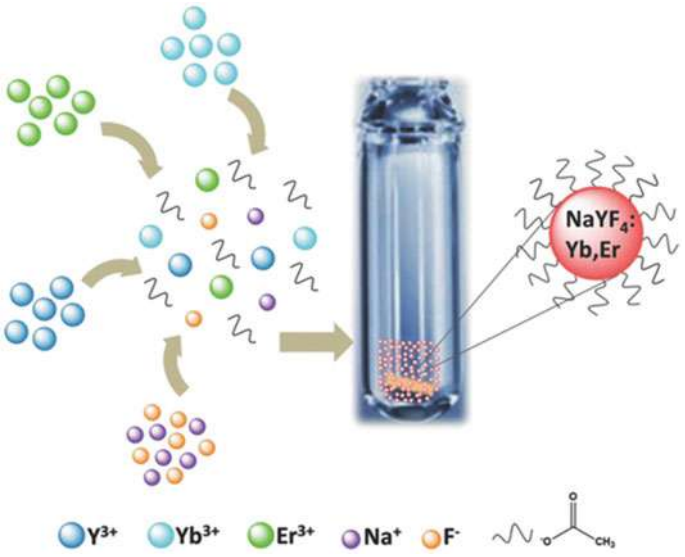

Fig. 3 Schematic of the microwave-supported fabrication of NaYF4:Yb/Er UC NPs. [41] Reprinted with permission. Copyright 2017, Springer Publishers

(vi) **Mechanochemical Preparation (MP)**: Mechanochemistry is a quick way for the fabrication of monodispersed NPs by easy grinding and mixing an of the precursor substances. $NaYF_4$:Gd^{3+}/Yb^{3+}/Tm^{3+} and SrFCl:Yb^{3+}/Er^{3+} NCs were prepared through the ball milling at the ambient temperature. Hexagonal phased NCs ~20 nm size were obtained [43]. Mechanochemical approach was applied for the synthesis of rare earth oxide UCNPs. Such as Y_2O_3:Er^{3+}/Yb^{3+} nanocrystals size ~25 nm, employing ball milling technique [44].

(vii) **Ionic-Liquids-Based Synthesis (ILBS)**. Ionic liquids (ILs) are organic salts that are non-volatile, non-flammable, and have the thermal stability. ILs are represented as "green solvents" which is a replacement of organic solvents in number of chemical reactions due to their uncommon properties, such as lower viscosity, melting point lower than100 °C, low viscosity, broad electrochemical site, moreover adaptable polarity of solvent [45]. ILs contain great tendency for the dissolution and acquiring the stability of metal ions, which gives them the greater chance of playing role as solvents, surfactants or capping agents in inorganic synthesis [46].

1.2 Luminescent Properties of phosphors

1.2.1. Down-Conversion Luminescence (DCL): Down-conversion luminescence particles consists of activated Ln^{3+} doping ions and an inorganic matrix and [47]. The inorganic matrix holds the Ln^{3+} ions tightly as a host crystal and also but also sensitizes the luminescent properties. Different types of inorganic materials, such as rare-earth oxides, fluoride, oxysulfide, vanadate, and phosphate have been utilized as host matrix. Activators are implanted deep into the host lattice in lower concentration ($\leq$5 mol %) to decrease the concentration quenching of luminescence, and not allow any alteration in the crystal lattice of the host materials [48].

1.2.2. Up-Conversion Luminescence (UCL): UCL is an effective system to produce visible electromagnetic radiation from the low energy excitation of near infra-red radiation. The utilization of long wave length excitation is connected with various favourable benefites, such as insignificant photodecomposition to living organisms, high radiation excitation deep penetration with high light excitation and low autofluorescence background [49]. These types of anti-Stokes UC methods can be classified into the three categories in Fig. 4: excited state absorption (ESA), photon avalanche (PA), and energy transfer up-conversion (ETU). ETU has been hugely utilized to generate up-conversion luminescence. In contrast, PA is subjected to pump power and manifests steady feedback to excitation, while ESA shows very less efficiency [50].

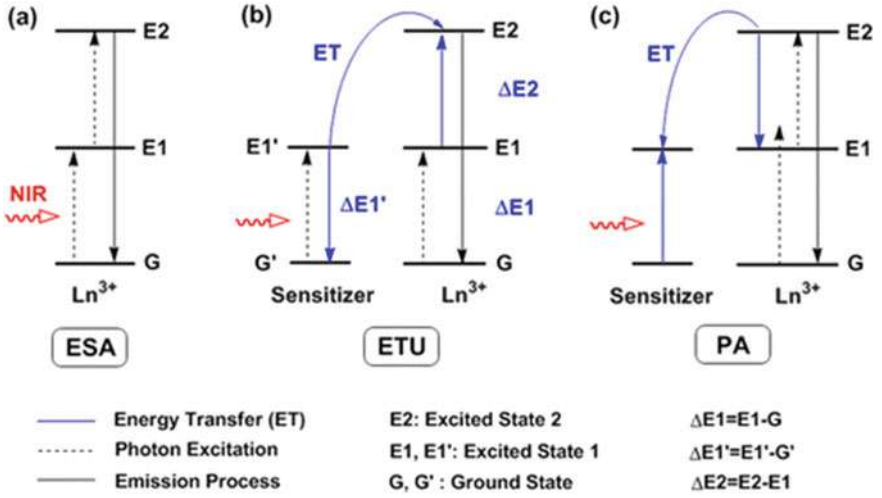

Fig. 4 UC processes for Ln^{3+} doped crystals. Reproduced with permission [50]. Copyright 2014, ACS Publishers

2 Hybrid Phosphors

2.1 Polymer Materials

2.1.1. Polymeric Blends with Complexes: Simple processability of polymer using as a host material makes them suitable for luminescent lanthanide complexes blend. Polymer films are easy to fabricate through melt casting or spin coating and materials of any wanted size (sheets, fibers, rods etc.) or structure can be obtained from polymer. Polymeric materials have numerous benefits compared to glasses in addition to higher flexibility and lighter density as well as the better processability. The requirements of lesser energy to produce polymers than that of glasses make it cost effective. Lanthanide (Ln) compounds can be inserted in many polymers which are optically transparent. For example, polystyrene (PS), poly(vinyl alcohol) (PVA), poly(methyl methacrylate) (PMMA), polyethylene (PE) [51], polyurethanes, polyimides,, polyesters, epoxy resins and polycarbonates. Fluorinated or deuterated polymeric materials are considered as the important materials for IR luminescent Ln complexes as a host matrix (Scheme 1).

2.1.2. Polymer Matrix Covalently Bonded to the Complexes: This is the favourable method to decrease the aggregation of Ln ions in polymer matrix compared to the blending of Ln compound with the polymer matrix (Fig. 5) [52]. Ligand having the ability of polymerized is primarily copolymerized with a polymer matrix. The pendant-coordinating group of the polymer-matrix is then reacted with a Ln salt of the complex to obtain the final product. Moreover, it is probable to obtain Ln complexes with the active groups combined to a polymer with the active groups themselves [52, 53].

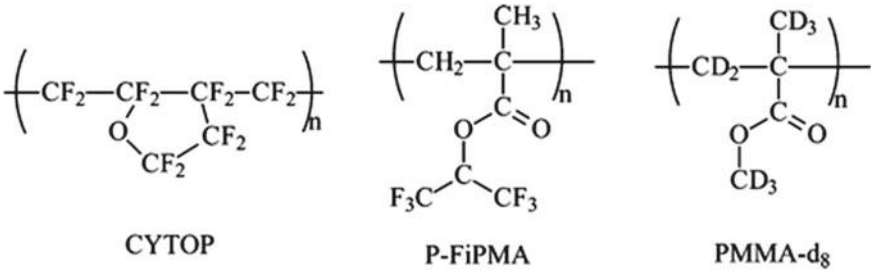

Scheme 1 Fluorinated and deuterated polymeric materials applied as host for NIR emitting lanthanide complexes

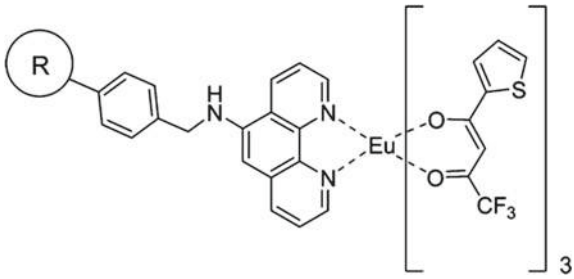

Fig. 5 [Eu(tta)$_3$(phen)] [52] covalently attached to a Merrifield resin moiety

2.1.3. Dendrimeric LigandsComplexes: Aggregation of Ln ions is a drawback for Ln ions dispersion in polymers or sol–gel derivative materials due to the cooperative energy-transfer processes. This aggregation may quench the luminescence effect by non-radiative relaxation of the excited states. Organic ligands are used to decrease the aggregation of Ln ions by capping the ions. The organic ligands capping are more advantageous in decreasing the impact of aggregation, as organic ligands have tendency to hold and exchange excitation energy by protecting the Ln ion to make coordination complex with H_2O_2 ligand or with other ligands having high-energy vibrations (Fig. 6) [54, 55].

2.1.4. Coordination Polymers Complexes: The coordination polymers containing Ln have been researched upon more than a decade [56]. The attention has mostly gone to the characterization of the structure of these compounds and investigation on luminescent of these compounds have been overlooked until very recent time [57]. Moreover, there are certain coordination polymers with carboxylate ligands that exhibit standard luminescence features. Similarly, coordination polymers with pores such as metal–organic frameworks [58] allow the fine-tuning of luminescence behavior by entrapping in the network pores (Fig. 7).

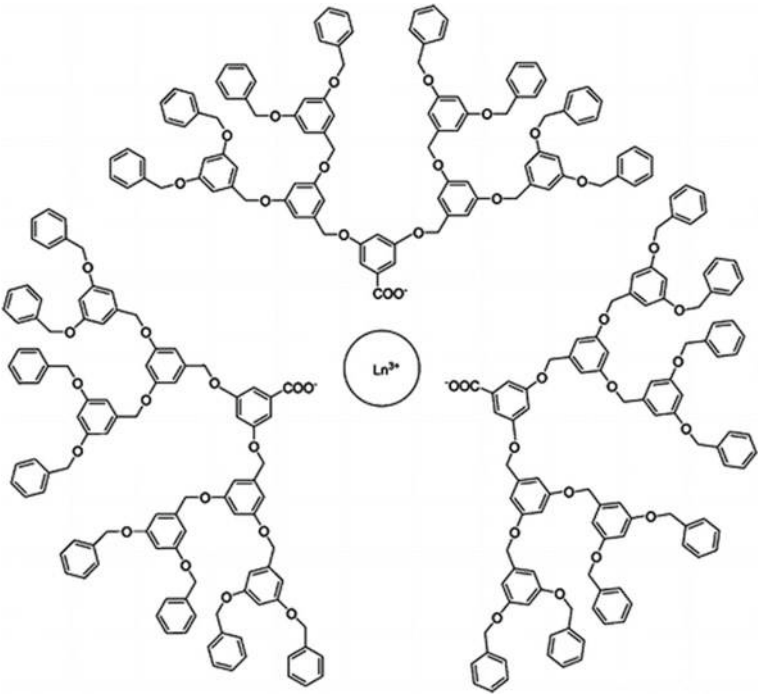

Fig. 6 Lanthanide complexes having dendritic polymers with carboxylate groups (Ln = Eu, Tb, Er) [55]

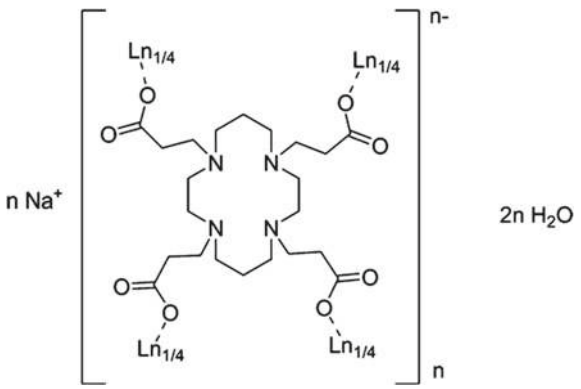

Fig. 7 Ln-containing coordination polymers obtained from tetraazacyclotetradecane-tetraproprionic acid. Ln = La, Sm, Eu, or Gd

2.2. Organo-gels and Hydrogels: Organo-gels and hydrogels and are kind of substances which are synthesised by immobilization of organic solvents and/or water with the use of gelator [59]. Commonly gelator is a organic compound with lower molecular mass, that forms self-assembly polymer-like fibres with dimensions that is

length on the micrometre scale and diameter on the nanometre range. The entanglement of the fibres allows the creation of a framework that binds solvent particles in the fibrillar networks respectively. The organogels or hydrogels synthesised by gelators with low molar mass are known as supramolecular-gels or physical gels. There is an another class of gels known as *polyelectrolyte gels*, for example from poly(acrylic acid) or by poly(methacrylic acid) [60], are synthesised by polymeric materials like poly(*N*,*N*-dimethyl-acrylamide) (PNIPAM). The gels are generally very viscoelastic, where solvent is the bigpart. Luminescent hydrogels and organogels are possible to avail by mixing of luminescent compounds in the water phase or organic solvent phase or by integrating of luminophores in the gelator. Hydrogel prepared from cross-linking alginic acid in water by (paramagnetic) Ho^{3+} ions was exhibited to be responsive to an outside magnetic field. But no luminescence of these materials was observed, these were latter added with emissive Ln ions to convert into luminescent magnetic-field-responsive matters [61].

2.3. Nanocomposite Materials: Nanoparticles with luminescent properties dispersed in a polymer backbone have attracted attention because they impart the extra advantage to both polymeric materials (fine mechanical characteristics and better processability) and inorganic luminescent (long-term chemical stability and high luminescence tendency). Microsized polymers particles show powerful light scattering, whereas nanoparticles polymers are more transparent [62]. Nanoparticles less than 40 nm in size are good to decrease the Rayleigh scattering to obtain transparent materials. However, size requirements also depend on the variation of refractive index between the nanoparticles and polymer matrix, as larger the difference, higher the light scattering happens. Goubart et al. studied on green-emitting poly(ethylene oxide) films which were doped with Gd_2O_3/Tb^{3+}NPs [63]. Dekker et al. synthesised near-IR emitting PMMA films which were doped with LaF_3/Nd^{3+}NPs [64].

3 Biomedical Applications

3.1 Bioimaging

Photoluminescence (PL) imaging has found significant applications in biomedical studies, for example they are effective for screening, prior identification and image-guided therapy of life-taking diseases [65]. Fluorophores of stoke-shifted (fluorescent proteins, metal complexes and organic fluorophores,) or quantum dots were not suitable for bioimaging because excitation was in the visible or UV region, which has restricted light penetration and gives rise to a powerful imaging framework (that means light scattering and strong autofluorescence) (Fig. 8) [66].

3.1.1. In Vitro and In Vivo Toxicity Assessment: The toxicity of UCNPs in vitro cytotoxic functionality and long-term in vivo toxicity has been screened

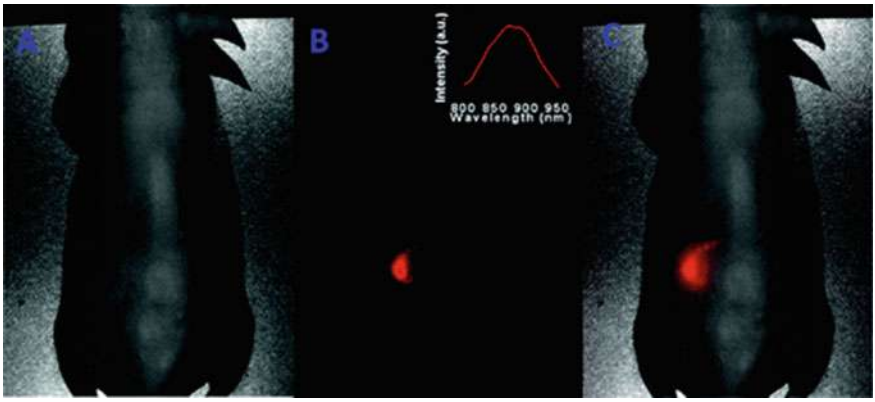

Fig. 8 **a** Image of bright field, **b** image of PL, and **c** image of superimposition (spectrally unmixed and PL image bright field image). [66] Reprinted with permission. Copyright 2017, ACS Publishers

[67]. Methyl thiazolyl tetrazolium (MTT), 3-(4,5-dimethylthiazol-2-yl)-5-(3-carboxymethoxyphenyl)-2-(4-sulfophen-yl)-2H-tetrazolium, sodium salts (MTS), and CCK-8 mitochondrial metabolic functionality studies are employed to check different verities of cells such as human breast cancer MCF-7 cells, human pancreatic cancer Panc-1 cells (HPC), human glioblastoma U87MG cells, and human nasopharyngeal epidermal carcinoma cells (KB cells) [67, 68]. Incubation of UCNPs with cells for atleast 24 h, then cellular viabilities were screened, which were found to be higher than 90% at upper doses, showing the less cytotoxicity of UCNPs [67, 68]. The in vivo toxicity of UCNPs is must for theranostic applications of UCNPs [69, 70].

3.1.2. Whole-Body Photoluminescent (PL) Imaging: PL imaging has shown the potential of UCNPs for different kinds of tiny animal imaging and the bio-distribution features of UCNPs. Tail vein or subcutaneous injection was applied to administer the dose of upconversion nanoparticles into smaller animals to observe in vivo upconversion photoluminiscent imaging. Surface-engineered dendritic upconverting nanoparticles are also capable to work with CW laser sources of low-power for in vivo multiphoton microscopic vascular imaging [71].

3.1.3. Active Targeting: Active targeting of the tumor is crucial for the detection of cancer and possible therapy, where the target-specific recognition is facilitated by antigen – antibody interactions and specific ligand – receptor. Here, bioconjugation chemistry plays an important role to present precise recognition biomolecules onto the surface of UCNPs. Active targeting of specific framework in vivo has been in focus. Nevertheless, in vitro target imaging uses a wide spectrum of recognition biomolecules but it is limited to the conjugation of FA and RGD peptides with UCNPs.

3.2 *Applications of Hybrid Phosphors for Drug Delivery and Therapy*

3.2.1. Drug Delivery: The incorporation of luminescence in drug delivery (DD) have explored significant prospective theranostics [72]. Carrying drugs to deliver at particular area with the tracking of luminescence properties is excellent for efficient treatment, and as such tracking DD efficiency (Scheme 2). Additional to the applications of Ln-doped UCNPs in bioimaging, these are also applied for DD uses in cancer therapies [73]. Different processes are employed for transporting the drug, for example deposition of drug in nanopores of silica coated on UCNPs, loading drug in hollow sphere of UCNP with porous shell [73, 74]. The release of drug in the delivery system have been reported to be activated with various parameters such as magnetic field, near infra-red radiation, pH and temperature [75]. These stimuli were introduced to confirm drug release at specific site. Due to the strong penetration depth of near infra-red radiation, photodynamic therapies (PDT) have been proved effective therapies for cancers [76].

3.2.2. ***Upconversion Nanocomposites for Chemotherapy***: Chemotherapy is a therapeutic treatment through chemical drugs for cancer cells treatment [77, 78]. At present, numerous investigation has been carried out using UCNPs as a drug delivering agent due to their upconversion luminescence, distinctive physicochemical properties and their size, and uses in vitro and in vivo becauseeasy tailoring surface chemistry to drug-delivery [79]. Basically, three approachesof drug delivery method based on UCNP are designed: (1) UCNPs encapsulated by hollow mesoporous-coated spheres. (2) UCNPs integrated with mesoporous SiO_2, and ((3) UCNPs capped with polymer.

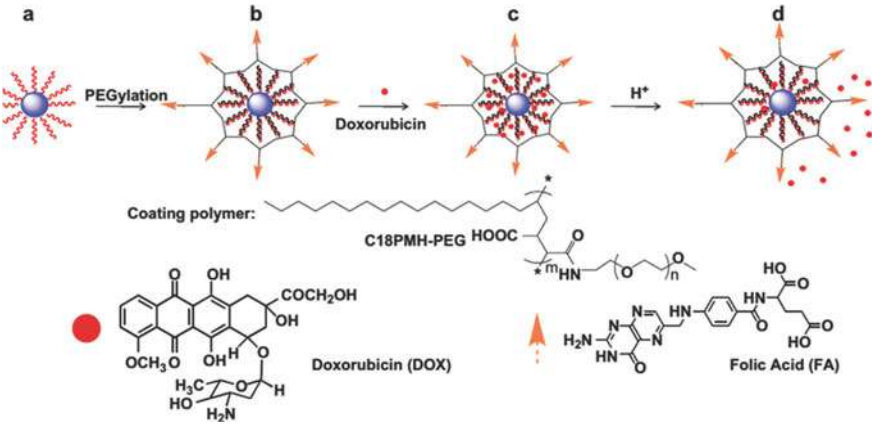

Scheme 2 Schematics of surface functionalized UCNP-based DDS. Reproduced with permission 76]. Copyright 2011, Elsevier Publisher

3.2.3. Future Directions for Therapeutics One of the major hinderance of UCNPs in biomedical application is the long-period bioeffects on the human body. Specifically, when we have to consider the complexity of several kinds of theranostic systems based on UCNP, whether structures would be stabilized enough in the harsh biological environment for long time raises a biosafety question. Therefore, it is imperative to study the long-period degradability of UCNPs in biological systems. Moreover, when UCNP-based nanoparticles are disinterred, how they interact with nervous and immune system and work in body requires a thorough investigation. Hence, the way in which the UCNPs make interaction in system and control the action of different kinds of cells needs deeper study. Developing novel strategies and suitable architectures to synthesise small and brighter UCNPs is one of the approaches for the future research. For example, emission dye-sensitization method makes way to greater quantum yield increment in smaller UCNPs [80], which inspires new UCNP architecture and throughs open practical approach to improve UC performance of tiny UCNPs.

4 Conclusion and Outlook

Therapeutic applications based on UCNP have demonstrated success in DDS, light-controlled drug release, PDT, and PTT. Moreover, therapeutic experiments were performed extensively in vitro buts in vivo there are limited works. Therapeutic research of UCNPs in rodents will further explore the details. In order to enhance the chemotherapeutic efficiency, new constructs of therapeutic agents based on UCNPs are necessary, with higher dose of drugs and facilitate targeted therapeutic drugs release. Moreover, it is highly recommended theragnostic materials for simultaneous medical diagnosis and therapy is required in the future. An immense investigation of imaging-guided drug delivery or therapy for cancer treatment or malignancy treatment will be desirable to research.

References

1. Reddy, K.L., Kumar, A.M., Dhir, A., Krishnan, V.: Selective and sensitive fluorescent detection of picric acid by new pyrene and anthracene based copper complexes. J. Fluoresc. **26**, 2041–2046 (2016). https://doi.org/10.1007/s10895-016-1898-9
2. Venkateswarulu, M., Gaur, P., Koner, R.R.: Sensitive molecular optical material for signaling primary amine vapors. Sens. Actuators B Chem. **210**, 144–148 (2015). https://doi.org/10.1016/j.snb.2014.12.082
3. Xu, C.T., Svenmarker, P., Liu, H., Wu, X., Messing, M.E., Wallenberg, L.R., Andersson-Engels, S.: High-resolution fluorescence diffuse optical tomography developed with nonlinear upconverting nanoparticles. ACS Nano **6**, 4788–4795 (2012). https://doi.org/10.1021/nn3015807
4. Liu, X., Yan, C.-H., Capobianco, J.A.: Photon upconversion nanomaterials. Chem. Soc. Rev. **44**, 1299–1301 (2015). https://doi.org/10.1039/C5CS90009C

5. Yi, G.-S., Chow, G.-M.: Water-soluble NaYF4:Yb, Er(Tm)/NaYF4/Polymer core/shell/shell nanoparticles with significant enhancement of upconversion fluorescence. Chem. Mater. **19**, 341–343 (2007). https://doi.org/10.1021/cm062447y
6. Huang, R.-W., Wei, Y.-S., Dong, X.-Y., Wu, X.-H., Du, C.-X., Zang, S.-Q., Mak, T.C.W.: Hypersensitive dual-function luminescence switching of a silver-chalcogenolate cluster-based metal-organic framework. Nat. Chem. **9**, 689–697 (2017). https://doi.org/10.1038/nchem.2718
7. Auzel, F.: Upconversion and anti-stokes processes with f and d ions in solids. Chem. Rev. **104**, 139–174 (2004). https://doi.org/10.1021/cr020357g
8. Stanisavljevic, M., Krizkova, S., Vaculovicova, M., Kizek, R., Adam, V.: Quantum dots-fluorescence resonance energy transfer-based nanosensors and their application. Biosens. Bioelectron. **74**, 562–574 (2015). https://doi.org/10.1016/j.bios.2015.06.076
9. Resch-Genger, U., Grabolle, M., Cavaliere-Jaricot, S., Nitschke, R., Nann, T.: Quantum dots versus organic dyes as fluorescent labels. Nat. Methods **5**, 763–775 (2008). https://doi.org/10.1038/nmeth.1248
10. Haase, M., Schäfer, H.: Upconverting nanoparticles. Angew. Chem. Int. Ed. Engl. **50**, 5808–5829 (2011). https://doi.org/10.1002/anie.201005159
11. Upconversion nanoparticles: design, nanochemistry, and applications in theranostics. Chem. Rev. https://doi.org/10.1021/cr400425h. Accessed 24 Sept 2020
12. Wu, S., Butt, H.-J.: Near-infrared-sensitive materials based on upconverting nanoparticles. Adv. Mater. **28**, 1208–1226 (2016). https://doi.org/10.1002/adma.201502843
13. Zhou, J., Liu, Q., Feng, W., Sun, Y., Li, F.: Upconversion luminescent materials: advances and applications. Chem. Rev. **115**, 395–465 (2015). https://doi.org/10.1021/cr400478f
14. Zhou, B., Shi, B., Jin, D., Liu, X.: Controlling upconversion nanocrystals for emerging applications. Nat. Nanotechnol. **10**, 924–936 (2015). https://doi.org/10.1038/nnano.2015.251
15. Xu, J., Yang, P., Sun, M., Bi, H., Liu, B., Yang, D., Gai, S., He, F., Lin, J.: Highly emissive dye-sensitized upconversion nanostructure for dual-photosensitizer photodynamic therapy and bioimaging. ACS Nano **11**, 4133–4144 (2017). https://doi.org/10.1021/acsnano.7b00944
16. Song, R., Murphy, M., Li, C., Ting, K., Soo, C., Zheng, Z.: Current development of biodegradable polymeric materials for biomedical applications. Drug. Des. Devel. Ther. **12**, 3117–3145 (2018). https://doi.org/10.2147/DDDT.S165440
17. Wu, X., Zhang, Y., Takle, K., Bilsel, O., Li, Z., Lee, H., Zhang, Z., Li, D., Fan, W., Duan, C., Chan, E.M., Lois, C., Xiang, Y., Han, G.: Dye-sensitized core/active shell upconversion nanoparticles for optogenetics and bioimaging applications. ACS Nano **10**, 1060–1066 (2016). https://doi.org/10.1021/acsnano.5b06383
18. Wang, X., Valiev, R.R., Ohulchanskyy, T.Y., Ågren, H., Yang, C., Chen, G.: Dye-sensitized lanthanide-doped upconversion nanoparticles. Chem Soc Rev **46**, 4150–4167 (2017). https://doi.org/10.1039/C7CS00053G
19. Nienhaus, L., Wu, M., Bulović, V., Baldo, M.A., Bawendi, M.G.: Using lead chalcogenide nanocrystals as spin mixers: a perspective on near-infrared-to-visible upconversion. Dalton Trans. **47**, 8509–8516 (2018). https://doi.org/10.1039/C8DT00419F
20. Mir, S.H., Ochiai, B.: Fabrication of polymer-Ag honeycomb hybrid film by metal complexation induced phase separation at the air/water interface. Macromol. Mater. Eng. **301**, 1026–1031 (2016). https://doi.org/10.1002/mame.201600035
21. Mir, S.H., Ochiai, B.: Conductive polymer-Ag honeycomb thin film: the factors affecting the complexity of the microstructure. J. Electrochem. Soc. **165**, B3030 (2018). https://doi.org/10.1149/2.0031808jes
22. Akinoglu, G.E., Mir, S.H., Gatensby, R., Rydzek, G., Mokarian-Tabari, P.: Block copolymer derived vertically coupled plasmonic arrays for surface-enhanced Raman spectroscopy. ACS Appl. Mater. Interfaces **12**, 23410–23416 (2020). https://doi.org/10.1021/acsami.0c03300
23. Sciortino, F., Mir, S.H., Pakdel, A., Oruganti, A., Abe, H., Witecka, A., Shri, D.N.A., Rydzek, G., Ariga, K.: Saloplastics as multiresponsive ion exchange reservoirs and catalyst supports. J. Mater. Chem. A **8**, 17713–17724 (2020). https://doi.org/10.1039/D0TA05901C
24. Mir, S.H., Ebata, K., Yanagiya, H., Ochiai, B.: Alignment of Ag nanoparticles with graft copolymer bearing thiocarbonyl moieties. Microsyst. Technol. **24**, 605–611 (2018). https://doi.org/10.1007/s00542-017-3418-5

25. Khosla, A., Shah, S., Shiblee, M.N.I., Mir, S.H., Nagahara, L.A., Thundat, T., Shekar, P.K., Kawakami, M., Furukawa, H.: Carbon fiber doped thermosetting elastomer for flexible sensors: physical properties and microfabrication. Sci. Rep. **8**, 12313 (2018). https://doi.org/10.1038/s41598-018-30846-3
26. Mir, S.H., Rydzek, G., Nagahara, L.A., Khosla, A., Mokarian-Tabari, P.: Review—recent advances in block-copolymer nanostructured subwavelength antireflective surfaces. J. Electrochem. Soc. **167**, 037502 (2019). https://doi.org/10.1149/2.0022003JES
27. Mir, S.H., Ochiai, B.: Development of hierarchical Polymer@Pd nanowire-network: synthesis and application as highly active recyclable catalyst and printable conductive ink. ChemistryOpen **5**, 213–218 (2016). https://doi.org/10.1002/open.201600009
28. Mir, S.H., Ochiai, B.: One-pot fabrication of hollow Polymer@Ag nanospheres for printable translucent conductive coatings. Adv. Mater. Interfaces **4**, 1601198 (2017). https://doi.org/10.1002/admi.201601198
29. Mir, S.H., Hasan, P.M.Z., Danish, E.Y., Aslam, M.: Pd-induced phase separation in poly(methyl methacrylate) telopolymer: synthesis of nanostructured catalytic Pd nanorods. Colloid Polym. Sci. (2020). https://doi.org/10.1007/s00396-020-04630-7
30. Mir, S.H.: Development of organic-inorganic hybrid functional nanomaterials by metal-complexation induced self-assembly processes. 山形大学 (2016)
31. Mir, S.H., Nagahara, L.A., Thundat, T., Mokarian-Tabari, P., Furukawa, H., Khosla, A.: Review—organic-inorganic hybrid functional materials: an integrated platform for applied technologies. J. Electrochem. Soc. **165**, B3137–B3156 (2018). https://doi.org/10.1149/2.0191808jes
32. Wang, L., Zhang, Y., Zhu, Y.: One-pot synthesis and strong near-infrared upconversion luminescence of poly(acrylic acid)-functionalized YF3:Yb3+/Er3+ nanocrystals. Nano Res. **3**, 317–325 (2010). https://doi.org/10.1007/s12274-010-1035-z
33. Feng, S., Xu, R.: New materials in hydrothermal synthesis. Acc. Chem. Res. **34**, 239–247 (2001). https://doi.org/10.1021/ar0000105
34. Lingeshwar Reddy, K., Srinivas, V., Shankar, K.R., Kumar, S., Sharma, V., Kumar, A., Bahuguna, A., Bhattacharyya, K., Krishnan, V.: Enhancement of luminescence intensity in red emitting NaYF4:Yb/Ho/Mn upconversion nanophosphors by variation of reaction parameters. J. Phys.. Chem. C **121**, 11783–11793 (2017). https://doi.org/10.1021/acs.jpcc.7b01334
35. Zhang, F., Li, J., Shan, J., Xu, L., Zhao, D.: Shape, size, and phase-controlled rare-Earth fluoride nanocrystals with optical up-conversion properties. Chemistry **15**, 11010–11019 (2009). https://doi.org/10.1002/chem.200900861
36. Du, H., Zhang, W., Sun, J.: Structure and upconversion luminescence properties of BaYF5:Yb3+, Er3+ nanoparticles prepared by different methods. J. Alloy. Compd. **509**, 3413–3418 (2011). https://doi.org/10.1016/j.jallcom.2010.12.101
37. Yi, G., Lu, H., Zhao, S., Ge, Y., Yang, W., Chen, D., Guo, L.-H.: Synthesis, characterization, and biological application of size-controlled nanocrystalline NaYF4:Yb, Er infrared-to-visible up-conversion phosphors. Nano Lett. **4**, 2191–2196 (2004). https://doi.org/10.1021/nl048680h
38. Wu, X., Liu, H., Liu, J., Haley, K.N., Treadway, J.A., Larson, J.P., Ge, N., Peale, F., Bruchez, M.P.: Immunofluorescent labeling of cancer marker Her2 and other cellular targets with semiconductor quantum dots. Nat. Biotechnol. **21**, 41–46 (2003). https://doi.org/10.1038/nbt764
39. Xu, Z., Li, C., Yang, P., Hou, Z., Zhang, C., Lin, J.: Uniform Ln(OH)3 and Ln2O3 (Ln = Eu, Sm) submicrospindles: facile synthesis and characterization. Cryst. Growth Des. **9**, 4127–4135 (2009). https://doi.org/10.1021/cg9003559
40. Mi, C., Tian, Z., Cao, C., Wang, Z., Mao, C., Xu, S.: Novel microwave-assisted solvothermal synthesis of NaYF4:Yb, Er upconversion nanoparticles and their application in cancer cell imaging. Langmuir **27**, 14632–14637 (2011). https://doi.org/10.1021/la204015m
41. Reddy, K.L., Prabhakar, N., Arppe, R., Rosenholm, J.M., Krishnan, V.: Microwave-assisted one-step synthesis of acetate-capped NaYF4:Yb/Er upconversion nanocrystals and their application in bioimaging. J. Mater. Sci. **52**, 5738–5750 (2017). https://doi.org/10.1007/s10853-017-0809-z

42. Abram, C., Mezhericher, M., Beyrau, F., Stone, H.A., Ju, Y.: Flame synthesis of nanophosphors using sub-micron aerosols. Proc. Combust. Inst. **37**, 1231–1239 (2019). https://doi.org/10.1016/j.proci.2018.06.040
43. Zhang, J., Riesen, N., Riesen, H.: Mechanochemically prepared SrFCl nanophosphor co-doped with Yb3+ and Er3+ for detecting ionizing radiation by upconversion luminescence. Nanoscale **9**, 15958–15966 (2017). https://doi.org/10.1039/C7NR05108E
44. Martín-Rodríguez, R., Valiente, R., Pesquera, C., González, F., Blanco, C., Potin, V., Marco de Lucas, M.C.: Optical properties of nanocrystalline-coated Y2O3:Er3+, Yb3+ obtained by mechano-chemical and combustion synthesis. J. Lumin. **129**, 1109–1114 (2009). https://doi.org/10.1016/j.jlumin.2009.05.012
45. Pârvulescu, V.I., Hardacre, C.: Catalysis in ionic liquids. Chem. Rev. **107**, 2615–2665 (2007). https://doi.org/10.1021/cr050948h
46. Lovingood, D.D., Strouse, G.F.: Microwave induced in-situ active ion etching of growing InP nanocrystals. Nano Lett. **8**, 3394–3397 (2008). https://doi.org/10.1021/nl802075j
47. Wang, F., Tan, W.B., Zhang, Y., Fan, X., Wang, M.: Luminescent nanomaterials for biological labelling. Nanotechnology **17**, R1–R13 (2005). https://doi.org/10.1088/0957-4484/17/1/R01
48. Wang, W., Cheng, Z., Yang, P., Hou, Z., Li, C., Li, G., Dai, Y., Lin, J.: Patterning of YVO4:Eu3+ luminescent films by soft lithography. Adv. Func. Mater. **21**, 456–463 (2011). https://doi.org/10.1002/adfm.201001467
49. Abdul Jalil, R., Zhang, Y.: Biocompatibility of silica coated NaYF4 upconversion fluorescent nanocrystals. Biomaterials **29**, 4122–4128 (2008). https://doi.org/10.1016/j.biomaterials.2008.07.012
50. Gai, S., Li, C., Yang, P., Lin, J.: Recent progress in rare earth micro/nanocrystals: soft chemical synthesis, luminescent properties, and biomedical applications. Chem. Rev. **114**, 2343–2389 (2014). https://doi.org/10.1021/cr4001594
51. Hao, J., Cocivera, M.: Blue cathodoluminescence from Ba2B5O9Cl: Eu phosphor thin films on glass substrates. Appl. Phys. Lett. **81**, 4154–4156 (2002). https://doi.org/10.1063/1.1525879
52. Lenaerts, P., Driesen, K., Van Deun, R., Binnemans, K.: Covalent coupling of luminescent Tris(2-thenoyltrifluoroacetonato)lanthanide(III) complexes on a Merrifield Resin. Chem. Mater. **17**, 2148–2154 (2005). https://doi.org/10.1021/cm0486868
53. Pei, J., Liu, X.-L., Yu, W.-L., Lai, Y.-H., Niu, Y.-H., Cao, Y.: Efficient energy transfer to achieve narrow bandwidth red emission from Eu3+-grafting conjugated polymers. Macromolecules **35**, 7274–7280 (2002). https://doi.org/10.1021/ma020529b
54. Vicinelli, V., Ceroni, P., Maestri, M., Balzani, V., Gorka, M., Vögtle, F.: Luminescent lanthanide ions hosted in a fluorescent polylysin dendrimer. Antenna-like sensitization of visible and near-infrared emission. J. Am. Chem. Soc. **124**, 6461–6468 (2002). https://doi.org/10.1021/ja017672p
55. Kawa, M., Fréchet, J.M.J.: Self-assembled lanthanide-cored dendrimer complexes: enhancement of the luminescence properties of lanthanide ions through site-isolation and antenna effects. Chem. Mater. **10**, 286–296 (1998). https://doi.org/10.1021/cm970441q
56. Pan, L., Adams, K.M., Hernandez, H.E., Wang, X., Zheng, C., Hattori, Y., Kaneko, K.: Porous lanthanide-organic frameworks: synthesis, characterization, and unprecedented gas adsorption properties. J. Am. Chem. Soc. **125**, 3062–3067 (2003). https://doi.org/10.1021/ja028996w
57. Allendorf, M.D., Bauer, C.A., Bhakta, R.K., Houk, R.J.T.: Luminescent metal–organic frameworks. Chem. Soc. Rev. **38**, 1330–1352 (2009). https://doi.org/10.1039/B802352M
58. Férey, G.: Hybrid porous solids: past, present, future. Chem. Soc. Rev. **37**, 191–214 (2007). https://doi.org/10.1039/B618320B
59. Sangeetha, N.M., Maitra, U.: Supramolecular gels: functions and uses. Chem. Soc. Rev. **34**, 821–836 (2005). https://doi.org/10.1039/B417081B
60. Kramarenko, E.Yu., Philippova, O.E., Khokhlov, A.R.: Polyelectrolyte networks as highly sensitive polymers. Polym. Sci. Ser. C **48**, 1 (2006). https://doi.org/10.1134/S1811238206010012
61. Winkleman, A., Bracher, P.J., Gitlin, I., Whitesides, G.M.: Fabrication and manipulation of ionotropic hydrogels cross-linked by paramagnetic ions. Chem. Mater. **19**, 1362–1368 (2007). https://doi.org/10.1021/cm062626f

62. Althues, H., Henle, J., Kaskel, S.: Functional inorganic nanofillers for transparent polymers. Chem. Soc. Rev. **36**, 1454–1465 (2007). https://doi.org/10.1039/B608177K
63. Goubard, F., Vidal, F., Bazzi, R., Tillement, O., Chevrot, C., Teyssié, D.: Synthesis and luminescent properties of PEO/lanthanide oxide nanoparticle hybrid films. J. Lumin. **126**, 289–296 (2007). https://doi.org/10.1016/j.jlumin.2006.07.009
64. Dekker, R., Klunder, D.J.W., Borreman, A., Diemeer, M.B.J., Wörhoff, K., Driessen, A., Stouwdam, J.W., van Veggel, F.C.J.M.: Stimulated emission and optical gain in LaF3: Nd nanoparticle-doped polymer-based waveguides. Appl. Phys. Lett. **85**, 6104–6106 (2004). https://doi.org/10.1063/1.1840110
65. Introduction to Biophotonics. Wiley. In: Wiley.com. https://www.wiley.com/en-us/Introduction+to+Biophotonics-p-9780471287704. Accessed 26 Sept 2020
66. Chen, G., Ohulchanskyy, T.Y., Liu, S., Law, W.-C., Wu, F., Swihart, M.T., Ågren, H., Prasad, P.N.: Core/shell NaGdF4:Nd3+/NaGdF4 nanocrystals with efficient near-infrared to near-infrared downconversion photoluminescence for bioimaging applications. ACS Nano **6**, 2969–2977 (2012). https://doi.org/10.1021/nn2042362
67. Xiong, L., Yang, T., Yang, Y., Xu, C., Li, F.: Long-term in vivo biodistribution imaging and toxicity of polyacrylic acid-coated upconversion nanophosphors. Biomaterials **31**, 7078–7085 (2010). https://doi.org/10.1016/j.biomaterials.2010.05.065
68. Nyk, M., Kumar, R., Ohulchanskyy, T.Y., Bergey, E.J., Prasad, P.N.: High contrast in vitro and in vivo photoluminescence bioimaging using near infrared to near infrared up-conversion in Tm3+ and Yb3+ doped fluoride nanophosphors. Nano Lett. **8**, 3834–3838 (2008). https://doi.org/10.1021/nl802223f
69. Chatterjee, D.K., Rufaihah, A.J., Zhang, Y.: Upconversion fluorescence imaging of cells and small animals using lanthanide doped nanocrystals. Biomaterials **29**, 937–943 (2008). https://doi.org/10.1016/j.biomaterials.2007.10.051
70. Ostrowski, A.D., Chan, E.M., Gargas, D.J., Katz, E.M., Han, G., Schuck, P.J., Milliron, D.J., Cohen, B.E.: Controlled synthesis and single-particle imaging of bright, sub-10 nm lanthanide-doped upconverting nanocrystals. ACS Nano **6**, 2686–2692 (2012). https://doi.org/10.1021/nn3000737
71. Esipova, T.V., Ye, X., Collins, J.E., Sakadžić, S., Mandeville, E.T., Murray, C.B., Vinogradov, S.A.: Dendritic upconverting nanoparticles enable in vivo multiphoton microscopy with low-power continuous wave sources. PNAS **109**, 20826–20831 (2012). https://doi.org/10.1073/pnas.1213291110
72. Xu, C.T., Svensson, N., Axelsson, J., Svenmarker, P., Somesfalean, G., Chen, G., Liang, H., Liu, H., Zhang, Z., Andersson-Engels, S.: Autofluorescence insensitive imaging using upconverting nanocrystals in scattering media. Appl. Phys. Lett. **93**, 171103 (2008). https://doi.org/10.1063/1.3005588
73. Xu, Z., Li, C., Ma, P., Hou, Z., Yang, D., Kang, X., Lin, J.: Facile synthesis of an up-conversion luminescent and mesoporous Gd 2 O 3: Er 3+ @ n SiO 2 @ m SiO 2 nanocomposite as a drug carrier. Nanoscale **3**, 661–667 (2011). https://doi.org/10.1039/C0NR00695E
74. Yang, D., Ma, P., Hou, Z., Cheng, Z., Li, C., Lin, J.: Current advances in lanthanide ion (Ln3+)-based upconversion nanomaterials for drug delivery. Chem. Soc. Rev. **44**, 1416–1448 (2015). https://doi.org/10.1039/C4CS00155A
75. Liu, J., Bu, W., Pan, L., Shi, J.: NIR-triggered anticancer drug delivery by upconverting nanoparticles with integrated azobenzene-modified mesoporous silica. Angew. Chem. Int. Ed. **52**, 4375–4379 (2013). https://doi.org/10.1002/anie.201300183
76. Lu, F., Yang, L., Ding, Y., Zhu, J.-J.: Highly emissive Nd3+-sensitized multilayered upconversion nanoparticles for efficient 795 nm operated photodynamic therapy. Adv. Func. Mater. **26**, 4778–4785 (2016). https://doi.org/10.1002/adfm.201600464
77. Wang, C., Cheng, L., Liu, Z.: Drug delivery with upconversion nanoparticles for multi-functional targeted cancer cell imaging and therapy. Biomaterials **32**, 1110–1120 (2011). https://doi.org/10.1016/j.biomaterials.2010.09.069
78. Chabner, B.A., Roberts, T.G.: Chemotherapy and the war on cancer. Nat. Rev. Cancer **5**, 65–72 (2005). https://doi.org/10.1038/nrc1529

79. Liu, J., Bu, W., Pan, L., Zhang, S., Chen, F., Zhou, L., Zhao, K., Peng, W., Shi, J.: Simultaneous nuclear imaging and intranuclear drug delivery by nuclear-targeted multifunctional upconversion nanoprobes. Biomaterials **33**, 7282–7290 (2012). https://doi.org/10.1016/j.biomaterials.2012.06.035
80. Wisser, M.D., Fischer, S., Siefe, C., Alivisatos, A.P., Salleo, A., Dionne, J.A.: Improving quantum yield of upconverting nanoparticles in aqueous media via emission sensitization. Nano Lett. **18**, 2689–2695 (2018). https://doi.org/10.1021/acs.nanolett.8b00634

Hybrid Phosphor Materials for Optoelectronic Application

Jemy James, Sharin Maria Thomas, Ajeesh Kumar Somakumar, Blessy Joseph, Nandakumar Kalarikkal, and Sabu Thomas

Abstract You might be reading the article on a computer screen or on a book. On both the cases, light is required, be it the light on screen or the light required for reading. You might go to a supermarket and now you may not need to stay in large ques, thanks to the modern laser scanners and barcode readers. You might be browsing the internet, Thanks to the fibre amplifier in optical cables. When you think of hybrid phosphor materials in daily life, you will be able to see many devices helping you directly or indirectly in many ways. This chapter gives a short insight into the Luminescent thin films, Polymer optical amplifiers and LEDs.

1 Introduction

The eyes are one of the natures wonders. Similarly, photosynthesis. Each has its own science to say. As the mankind progressed many innovations happened and one of it was light emitting diodes (LEDs). The LEDs came into picture around 1960s where even though they were highly inefficient, expensive and tiny, they were used as indicator lamps on machines, especially the red and green. Its been a long journey for LEDS and White LEDs (WLED) rule the world of lighting with an enormous decrease in cost and increase in efficiency. But the current WLEDs are based on toxic phosphors which are inorganic like Cd Qds, or rare earth elements, which can cause critical issues related to the sustainable development. Hybrid WLEDs based

J. James (✉) · B. Joseph · N. Kalarikkal
International and Inter University Centre for Nanoscience and Nanotechnology, Mahatma Gandhi University, Kottayam 686560, India

S. M. Thomas
Centre for Nanotechnology Research, Vellore Institute of Technology, Vellore 632014, India

A. K. Somakumar
Institute of Physics, Polish Academy of Sciences, Aleja Lotnikow 32/46, 02-668 Warsaw, Poland

S. Thomas
School of Energy Materials, Mahatma Gandhi University, Kottayam 686560, India

© Springer Nature Switzerland AG 2022

K. Upadhyay et al. (eds.), *Hybrid Phosphor Materials*, Engineering Materials,
https://doi.org/10.1007/978-3-030-90506-4_10

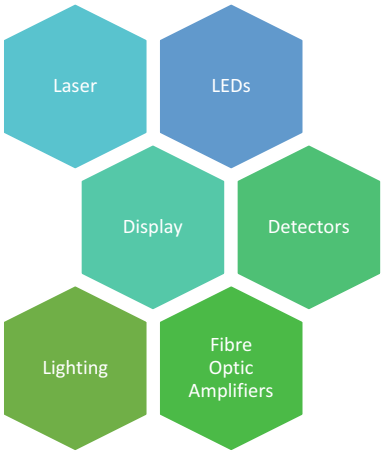

Fig. 1 Various application of hybrid phosphors for optoelectronic applications

Table 1 Some materials used for LED and their emission wavelengths

Material	Emission wavelength	Colour
AlInGaP	626–630 nm 615–621 nm 605 nm 590–592 nm	Red Red–orange Orange Amber
InGaN	525 nm 498–505 nm 470 nm	Green Blue green Blue

on coordination complexes, or organic phosphors, conjugate polymers need to be developed as alternative to existing manufacturing materials for lighting (Fig. 1).

Some of the conventional LED materials are shown below with their emission wavelength (Table 1).

In the case of AlInGaP LEDs, as the temperature of the LED P–N junction increases, the luminous intensity decreases, and also the dominant wavelength shift towards longer wavelength whereas in the case of InGaN LEDs, as the LED current increases, the dominant wavelength moves towards shorter wavelength. There is a need for a more stable, eco-friendly, energy efficient, LEDs. Hybrid Phosphors are the answer to this need of the hour.

2 Detectors

During the early 1980's there was many problems associated with the semiconductor industry. AW White describes in detail the issues associated with the materials and its development [1]. The interaction of visible and infrared radiation is initiated by three different ways.

Fig. 2 Detectors

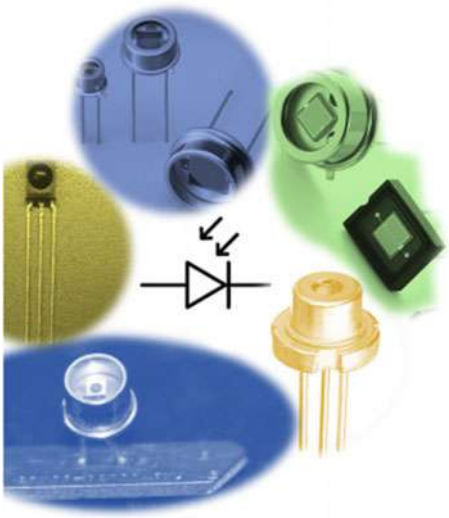

Table 2 Some materials for detectors and their mode of detection

Materials	Mode of detection
GaAsCr	Photoconductivity
GaAsAl	Schottky junction
InAs	P–N junction
InSb	P–N junction

1. Thermal effect
2. Optical effect
3. Electro Magnetic Wave interaction.

In the thermal effect, the temperature change caused due to the absorption of the photons can be used for sensing. In the second case, the photons interact with electrons after transferring their energy. In the third case the E.M. field causes field dependent parameters to change (Fig. 2).

Some parameters of binary-semiconductor detectors are given below (Table 2).

3 Luminescent Thin Films

Luminescent thinfilms are particular type of thinfilms having a dimension of few hundred microns coated or packed with luminescent materials. These films show visible color emission when they are excited with energy sources [1]. The major applications of luminescent thinfilms are lighting, display, sensors, solarcells, electrochromic windows, scintillating screens etc. Generally these films are of two types,

either coated on glass, quartz, silicon and polyethylene terephthalate (PET) like substrates or as a free standing film [2–6]. Not only the single layer films but also multi-layer films are getting popular since these films are stacked as very thin layers so that the thickness and the interface between layers offer some unique properties which are inaccessible in their bulk form [7]. These films are commonly prepared by dipcoating, spin coating spray pyrolysis, thermal evaporation, atomic layer deposition (ALD), pulse laser deposition (PLD) and chemical vapor deposition (CVD) and various types of epitaxial growth methods. Good quality luminescent thin films must have following features such as, the films should be thin and transparent in nature, no substrate emission, very low surface roughness, multicolor emission, film flexibility and good quality emission. Luminescent films are always consist of a material which is highly sensitive to light and that particular inorganic material is either purely coated as a film or applied along with some other agents like polymers. These light emitting materials are commonly called as phosphor materials. The material's band gap, doping and selection of substrate have an important role in the development of luminescent thinfilms [2–9] (Fig. 3).

Rare-earth and transition metal based materials, some inorganic halides and some highly luminescent P3HT like polymeric compounds are the major building blocks used for thin film making. The sharp luminescence emission bands, extreme quantum efficiencies and the presence of 4f-4f and 4f-5d transitions in rare-earth materials make them an ideal candidate for opto-electronic applications [10]. The polymer like materials which are inherently not so luminescent can be turned in to luminescent materials by doping them with rare-earths [11, 12]. For example, the Fig. 4 shows the multicolor luminescence emission from a rare-earth nano-phosphor (Eu^{3+})—polymer (PVA) composite film on a glass substrate. The film shows different emission colors from two different luminescent centers. The film shows a blue emission from

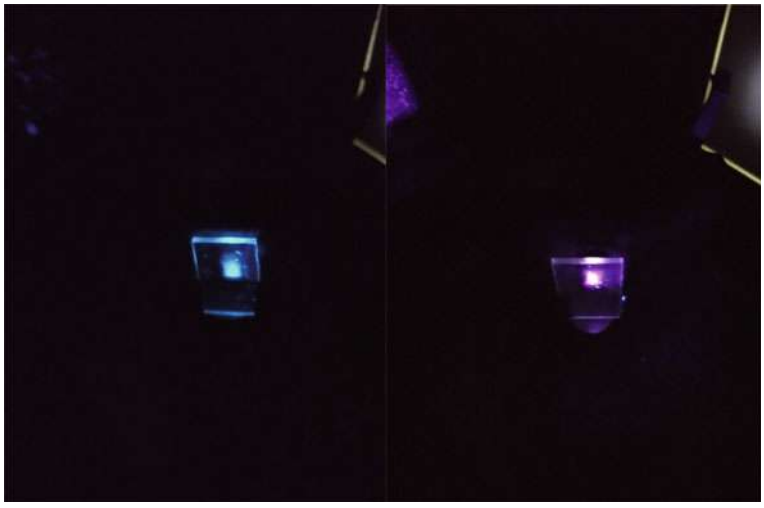

Fig. 3 Multi-color emission from a dip coated polymer rare-earth nano-phosphor film

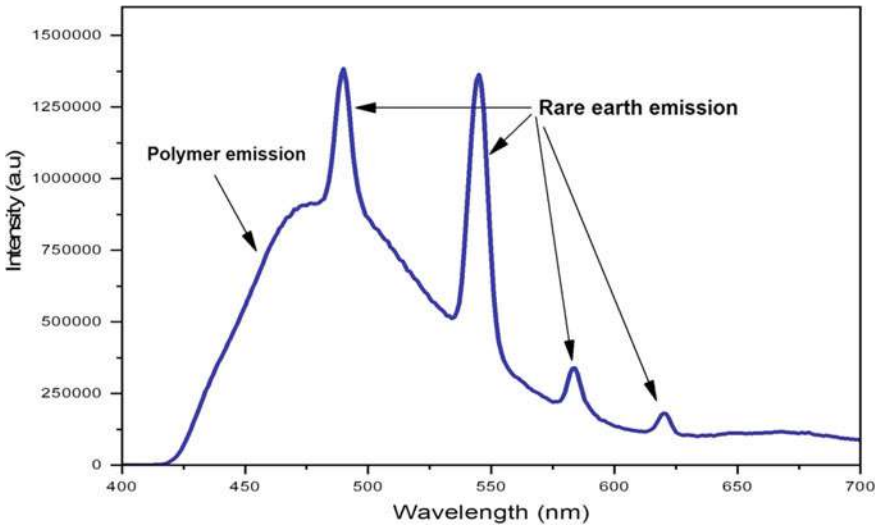

Fig. 4 Photoluminescence emission spectra of a polymer rare-earth nano-phosphor film on glass substrate

the polymer when it is excited with 360 nm wavelength and shows purple color by the direct excitation (393nmof Eu^{3+}) of rare-earth. The usage of quartz substrate instead of glass substrate can guarantee a very good and sharp red emission at 616 nm by eliminating blue emission which is incorporated due to the glass substrate since glass is a very good absorber of UV radiation. Figure 4 shows the photoluminescence spectra of a polymer- nano phosphor composite thin film.

But nowadays researchers are in search of new rare-earth alternatives due their high cost and toxicity. Transition metal ion based phosphors are the front runners in this category [13]. Manganese is a well-known and promising rare-earth alternative in this group since it shows multicolor emission for various oxidation states ($Mn^{+2, +3, +4, +6, \text{and } +7}$). Perovskite based materials doped with rare-earths and transition metal ions are also popular in making luminescent thinfilms [14, 15]. The luminescent centers in phosphor have an important role in the emission properties of thin films. The infrared (IR) emission exhibited by some thin films can also be exploited for highly sensitive applications such as, night vision devices, IR sensors in military and photodynamic therapy in cancer treatment. The photo response of phosphor contained films towards x-rays, alpha and gamma irradiation can be used for fabricating scintillating screens. These scintillating thin film materials have paramount potential applications such as big particle detectors, x-ray imaging of cancer tissues, radiation monitoring and gamma energy harvesters [16–19].

3.1 Polymer Optical Amplifier (POA)

Optical amplifiers are utilized in fiber optical transmission lines to magnify the signals and hence minimize the unavoidable attenuation amid transmissions. Optical amplifiers can also be named repeaters, when the device regenerates the optical signal directly without conversion to an electronic signal [20]. Apart from the conventionally availed inorganic materials, organic polymers are more sought after material due to their flexibility, easy processibility, low-cost and significant mechanical strength [21]. Different polymers of varying characteristics are exploited according to its desired properties in order to facilitate effective transmission. Photorefractive (PR) polymers are used as optical amplifier due to its distinct two-beam coupling effect. Independent of the active layers, the beam will be amplified due to the energy transfer from the pumping source beam alone. One such example of PR is a high performance polymer composite PVK:PDCST:BBP:C_{60} [poly (n-vinyl carbazole)]: chromophore: plasticizer: fullurene C_{60} [22]. Broadband amplifiers have been reported using semiconducting Conjugate Polymers (CP). A CP such as poly [2-methoxy-5-(2', 6'-dimethyloctylloxy)-paraphenylene vinylene]-[OC_1 C_{10}-PPV] was reported as a cost-effective amplifier medium for short haul data transmissions [23]. Moderately solid-state polymer amplifiers are found to be more probable amplifiers than liquid solutions [24].

3.2 How Is Hybrid Phosphor Used in POA?

Hybrid materials are advantageous due to the combination of distinct optical responses along with various mechanical properties. Hybrid phosphor is promising due to the combined benefits from an industrial and environmental perspective. They facilitate less transmission loss and for greater bandwidth essentially in the visible and NIR region [25]. On comparison with the organic counterpart, the hybrid phosphor is significant due to photosensitivity that permits direct writing [7], tunability in large refractive index, enhanced photo stability at the expense of greater incorporation of ions as Ln^{3+} [26]. One of the main bottlenecks is the reduction of numbers of OH, CH, NH and CO oscillators in the hybrids. These oscillators display strong radiation absorption in the NIR spectral region within the telecommunication window i.e., 1330–1550 nm, thus leading to increased attenuation and propagation losses [27]. The hybrid phosphors are useful mainly in case of fiber to home solution and for short haul telecommunications [28].

3.3 Polymer Optical Fiber Amplifier (POFA)

Polymer Optical Fiber Amplifier with a multimode graded index (GI) have been first developed via an interfacial gel based polymerization technique [29]. When an organic dye is doped in polymer optical fiber (POF), the amplifier will have a gain in the visible region and can emit fluorescence. Rhodamine B dyes [30] and Er^{3+} in GeO_2-SiO_2 [31] are a few examples of dyes that lead to high efficiency light amplification. The main aim is to achieve a high gain with high conversion efficiency [32]. In addition to organic dyes, rare earth elements are also used in POFA. The organic corresponding part is sought-after as the dye doped POFA due to its high saturation power is independent of the input signal power. At an optimal length, the gain is amplified. The pump and signal wavelength can also determine the amplification gain. At an optimal wavelength, range of 550–600 nm is best suited for the signal amplification. A high power pump like Nd-YAG laser is required due to the low metastable lifetime [33].

3.4 Polymer Optical Fiber Lasers and Detectors

Tunable fiber lasers can be devised due to the spectral shift of the emission in POF. The Amplified Spontaneous Emission (ASE) gives information about the wavelength that provides high power in POF laser. The POF laser doesn't require an input signal rather it is pumped [34]. One of the prominent examples of dye doped POF laser was reported by Kuriki et al. [35]. They fabricated GI POF with a diameter of 0.6 and 1 mm, which was doped by various organic dyes. At an optimal length of 5 cm, the POF was transversely pumped using millijoule pulses at 532 nm. The laser performance is highly dependent on the resonator quality and doping concentrations to recognize the suited configurations for effective lasing. Figure 5 displays a RB (Rhodamine B)-POF laser, studied by Spelthamm et al. [36]. This 10 mm dye doped POF generated an OC efficiency of 35%, upon greater slope efficiency (56 and 50% lifetime) produced high output energy (1.65 mJ).

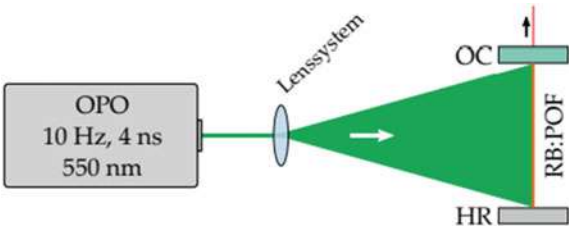

Fig. 5 Schematic of the RB:POF laser transversally pumped with an optical parametric oscillator (OPO). The resonator mirrors are both butt coupled to the fiber facets. OC: output coupler; HR: high reflective mirror [36]

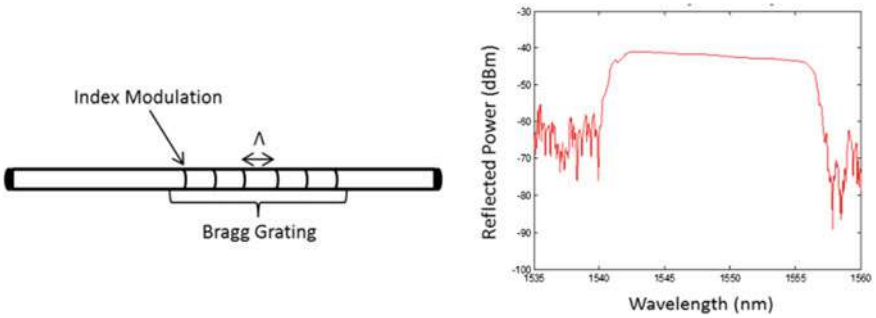

Fig. 6 Overview of FBG sensing and the effect on the transmitted spectrum [37]

Due to low acoustic impedance, higher acoustic sensitivity and reduced Youngs Modulus at 1 and 10 MHz, Polymer optical fibers are utilized for detectors and sensors [37]. POF with intrinsic configurations such as Braggs grating [38], Fabry Perot cavities [39], interferometric fiber sensors [40], micro ring resonators [41] are well suited for point detection applications. POF laser finds application in opto-acoustic endoscopic imaging with possibility for a customizable bandwidth. Figure 6 shows a Bragg Grating inscribed Fiber (FBG) that generates a stop band around the Braggs wavelength in the transmission spectrum. Upon reflection, a pass band is generated at the Bragg wavelength. When the fiber is under strain or pressure, there is a phase change in FBG profile due to the shift in the refractive index of fiber. This method possesses low attenuation and greater repeatability. Integrating detectors based on photoacoustic imaging, the POF displayed high sensitivity and yield compared to the glass fiber [42]. pH sensors based POF was demonstrated wherein a pH sensitive fluorescence dye-doped cellulose acetate thin film was synthesized. The detector displayed varying fluorescence intensities at pH range of 2.5–4.5 [43]. Ultrasonic wide band sensors based on single mode POF with potential biomedical applications were studied. The single-mode PMMA showed high ultrasonic phase sensitivity 12 times greater than silica in 1–5 MHz range [44].

3.5 Erbium Doped Fiber Amplifier (EDFA)

Erbium Doped Fiber Amplifier (EDFA) is a vital technology used to lessen the loss during long distance optical transmissions. It operates in the C-band and L-band of the telecom optical wavelength. EDFA plays multiple roles as booster, in-line and pre- amplifier in the transmission. These are placed in several kilometres as seen in Fig. 7. The change in energy levels of Er^{3+} ions directly influence the amplification of Er doped fiber. The more the energy absorbed, higher the energy level attained. The absorption of pump photons will lead to the excitation of Er^{3+} ions to greater energy states. Depending on the configurations EDFA can be categorized as one stage

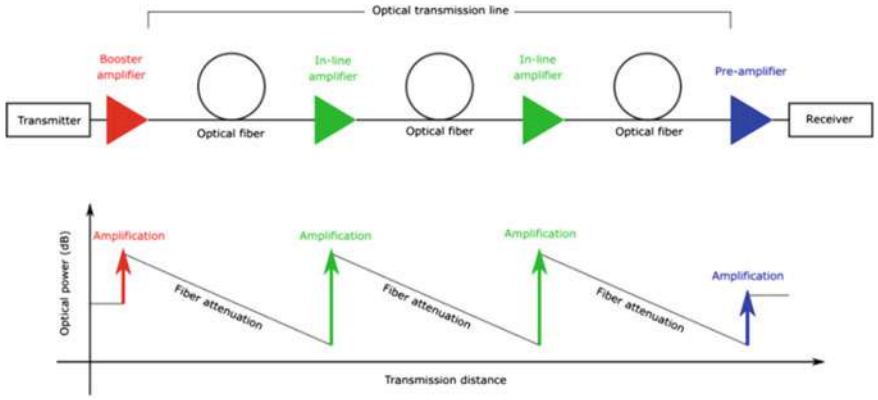

Fig. 7 Booster, inline, and pre-amplifier EDFAs used in optical transmission line [46]

EDFA, Single pass, Double pass, Triple pass, Quadruple pass etc. The light emission can be attributed to either spontaneous emission or stimulated emissions. The light generated by stimulated emission is of the same polarization, frequency, and phase due to the identical energies produced. There is an additional liberated energy due to the stimulation that adds up for constructive amplification. Several amendments on various performance parameters are being investigated to optimize the EDFA for different applications. EDFA doped with Zr, Yt, Al was evaluated against Silica doped EPFA. Zr-EDFA displayed higher gain and low noise at longer wavelength in varying configurations. A flat gain of 19.5 dB was attained for single pass and gain of 17.5–21 dB at low noise for double pass configuration was prominent [45]. The main challenge is to reduce the noise at high pump power and to control the performance parameters for high gain. The transmission can be enhanced by high pump power, however due to the non-linear effects of transmission fiber, the system performance deteriorates.

3.6 Latest Advances in the Field of POA

The integration of polymers in the optical telecommunication have been highly beneficial due to low-cost, flexibility and ease in processing [47]. Low-cost waveguide amplifiers based on Er-doped nanocomposite thin films have been reported [48]. High gain fiber amplifiers doped with Yb^{3+} ions have been reported. Various parameters such as fiber core diameter, numerical aperture, dopant concentration, etc. govern the threshold power for transverse mode instability [49]. Wave guide optical amplifier with ability to act as filter for signal communications and as channels when in case of communication are devised for highly secure transmissions [50]. Organic

ligands facilitate high optical gain due o the high efficiency in absorption of the polymers compared to inorganic structures i.e. absorption is of 10^{-22} and $10^{-23}m^2$ at 405 nm. Advanced POFA functioning in 614 nm have been developed for in-house communication systems.

4 Prospects

The new challenges to the hybrid phosphor is to incorporate multiple properties and functionalities to these materials. A recent work by Zhang et al., on optical-electrical response in 2D hybrid perovskites throw some light into this area. The integration of luminescence and dielectric switching properties was achieved on the 2D hybrid perovskites. Thus, a slight mechanical stimulus results in the formation of the materials with dielectric switching ability and luminescence control, which can in future lead to low cost high efficient electronics. There is also newer research into the leadfree materials for the development of perovskites in optoelectronic applications. Li et al., has described about the lead free halide perovskites (LFHP) due to the environment friendly nature and good optoelectronic properties. Another aspect to look is the integration of the new generation luminescent material using artificial intelligence. Zhuo et al., has discussed deeply on the option and possibilities for the integration of these materials using artificial intelligence [AI], which can lead to sole some of the challenges in the employment of the AI in the lighting industry. There are plethora of applications for the hybrid phosphor materials for optoelectronic applications and it's the scientific community along with the industrial fraternity who constantly improves the technology and thus enabling better life for the people (Fig. 8).

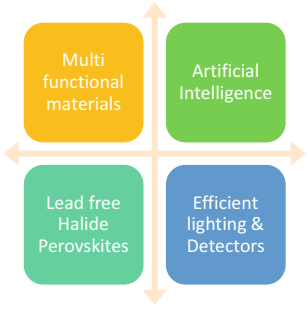

Fig. 8 Future prospects

References

1. White, A.M.: Problems in optoelectronic semiconductors. J. Mater. Sci. **10**(4), 714–726 (1975). https://doi.org/10.1007/BF00566581
2. Fujihara, S.: Luminescent thin films: fundamental aspects and practical applications. Chemical Solution Deposition of Functional Oxide Thin Films, pp. 725–745 (2013)
3. Huang, X., et al.: Visible-emitting hybrid sol–gel materials comprising lanthanide ions: thin film behaviour and potential use as phosphors for solid-state lighting. New J. Chem. **38**(12), 5793–5800 (2014)
4. Zhuo, N., Zhang, N., Jiang, T., Chen, P., Wang, H.: Effect of particle sizes and mass ratios of a phosphor on light color performance of a green phosphor thin film and a laminated white light-emitting diode. RSC Adv. **9**(47), 27424–27431 (2019)
5. Alex, et al.: Substrate temperature induced effect on microstructure, optical and photocatalytic activity of ultrasonic spray pyrolysis deposited MoO3 thin films. Mater. Res. Exp. **6**(6), 66421 (2019)
6. Kang, M.J., Santoro, E.G., Kang, Y.S.: Enhanced efficiency of functional smart window with solar wavelength conversion phosphor-photochromic hybrid film. ACS Omega **3**(8), 9505–9512 (2018)
7. Gao, R., Yan, D.: Ordered assembly of hybrid room-temperature phosphorescence thin films showing polarized emission and the sensing of VOCs. Chem. Commun. **53**(39), 5408–5411 (2017)
8. Güner, T., Köseoğlu, D., Demir, M.M.: Multilayer design of hybrid phosphor film for application in LEDs. Opt. Mater. **60**, 422–430 (2016)
9. Zhang, Y., Hao, J.: Metal-ion doped luminescent thin films for optoelectronic applications. J. Mater. Chem. C **1**(36), 5607–5618 (2013)
10. Thomas, K., et al.: Intrinsic red luminescence of Eu3+-activated lanthanum molybdate: insights into the spectroscopic features using Judd–Ofelt theoretical analysis. J. Phys. Chem. Solids **137**, 109212 (2020)
11. Ilmi, R., Anjum, S., Haque, A., Khan, M.S.: A new brilliant red emitting Eu (III) ternary complex and its transparent flexible and photostable poly (urethane) hybrid thin film for optoelectronic applications. J. Photochem. Photobiol. A Chem. **383**, 111968 (2019)
12. Dar, W.A., Iftikhar, K.: Phase controlled colour tuning of samarium and europium complexes and excellent photostability of their PVA encapsulated materials. Structural elucidation, photophysical parameters and the energy transfer mechanism in the Eu 3+ complex by Sparkle/PM3 calc. Dalton Trans. **45**(21), 8956–8971 (2016)
13. Zhang, X., Liu, W., Wei, G.Z., Banerjee, D., Hu, Z., Li, J.: Systematic approach in designing rare-earth-free hybrid semiconductor phosphors for general lighting applications. J. Am. Chem. Soc. **136**(40), 14230–14236 (2014)
14. Zhou, G., et al.: Optically modulated ultra-broad-band warm white emission in Mn2+-doped (C6H18N2O2) PbBr 4 hybrid metal halide phosphor. Chem. Mater. **31**(15), 5788–5795 (2019)
15. Ebrahimi, S., Yarmand, B., Naderi, N.: High-performance UV-B detectors based on MnxZn1-xS thin films modified by bandgap engineering. Sens. Actuators A Phys. **303**, 111832 (2020)
16. Sengupta, D., Miller, S., Marton, Z., Chin, F., Nagarkar, V., Pratx, G.: Bright Lu2O3: Eu thin-film scintillators for high-resolution radioluminescence microscopy. Adv. Healthc. Mater. **4**(14), 2064–2070 (2015)
17. Nikl, M.: Nanocomposite, Ceramic, and Thin Film Scintillators. CRC Press (2016)
18. Dujardin, C., et al.: Needs, trends, and advances in inorganic scintillators. IEEE Trans. Nucl. Sci. **65**(8), 1977–1997 (2018)
19. Riva, F., Douissard, P.-A., Martin, T., Carlá, F., Zorenko, Y., Dujardin, C.: Epitaxial growth of gadolinium and lutetium-based aluminum perovskite thin films for X-ray micro-imaging applications. CrystEngComm **18**(4), 608–615 (2016)
20. Choudhury, P.K.: Introductory chapter: a revisit to optical amplifiers. Optical Amplifiers: A Few Different Dimensions, p. 1 (2018)

21. Bastos, A., et al.: Flexible optical amplifier for visible-light communications based on organic–inorganic hybrids. ACS Omega **3**(10), 13772–13781 (2018)
22. Grunnet-Jepsen, A., Thompson, C.L., Moerner, W.E.: Spontaneous oscillation and self-pumped phase conjugation in a photorefractive polymer optical amplifier. Science **277**(5325), 549–552 (1997)
23. Lawrence, J.R., Turnbull, G.A., Samuel, I.D.W.: Broadband optical amplifier based on a conjugated polymer. Appl. Phys. Lett. **80**(17), 3036–3038 (2002)
24. Shi, J., Suarez, L.E.A., Yoon, S.J., Varghese, S., Serpa, C., Park, S.Y., Lüer, D., Roca-Sanjuán, D., Milián-Medina, B., Gierschner, J.: Solid state luminescence enhancement in π-conjugated materials: unraveling the mechanism beyond the framework of AIE/AIEE. J. Phys. Chem. C **121**, 23166–23183 (2017)
25. Sanchez, C., Lebeai, B., Chaput, F., Boilot, J.-P.: Adv. Mater. **15**, 1969 (2003)
26. Carlos, L.D., Ferreira, R.A.S., de Z. Bermudez, V., Ribeiro, S.J.L.: Lanthanide-containing light-emitting organic–inorganic hybrids: a bet on the future. Adv. Mater. **21**(5), 509–534 (2009)
27. Bunzli, J.-C.G.: Lanthanide luminescence for biomedical analyses and imaging. Chem. Rev. **110**(5), 2729–2755 (2010)
28. Carlos, L.D., Ferreira, R.A.S., de Zea Bermudez, V., Julian-Lopez, B., Escribano, P.: Progress on lanthanide-based organic–inorganic hybrid phosphors. Chem. Soc. Rev. **40**(2), 536–549 (2011)
29. Ishigure, T., et al.: Formation of the refractive index profile in the graded index polymer optical fiber for gigabit data transmission. J. Lightwave Technol. **15**(11), 2095–2100 (1997)
30. Sahar, E., Treves, D.: Excited singlet-state absorption in dyes and their effect on dye lasers. IEEE J. Quantum Electron. **13**(12), 962–967 (1977)
31. Fleming, S.C., Whitley, T.J.: Measurement of pump induced refractive index change in erbium doped fibre amplifier. Electron. Lett. **27**(21), 1959–1961 (1991)
32. Tayaga, A., Koike, Y., Kinoshita, T.: Polymer optical fiber amplifier EJ-I. Appl. Phys. Lett. **63**(7), 883–885 (1993)
33. Karimi, M., Granpayeh, N., Farshi, M.K.M.: Erratum to: analysis and design of a dye-doped polymer optical fiber amplifier. Appl. Phys. B **78**(3), 387–396 (2004)
34. Arrue, J., Jiménez, F., Ayesta, I., Illarramendi, M.A., Zubia, J.: Polymer-optical-fiber lasers and amplifiers doped with organic dyes. Polymers **3**(3), 1162–1180 (2011)
35. Kuriki, K., et al.: High-efficiency organic dye-doped polymer optical fiber lasers. Appl. Phys. Lett. **77**(3), 331–333 (2000)
36. Spelthann, S., et al.: Towards highly efficient polymer fiber laser sources for integrated photonic sensors. Sensors **20**(15), 4086 (2020)
37. Broadway, C., et al.: A compact polymer optical fibre ultrasound detector. In: Photons Plus Ultrasound: Imaging and Sensing 2016, vol. 9708, p. 970813 (2016)
38. Rosenthal, A., Razansky, D., Ntziachristos, V.: High-sensitivity compact ultrasonic detector based on a pi-phase-shifted fiber Bragg grating. Opt. Lett. **36**(10), 1833–1835 (2011)
39. Cox, B.T., Beard, P.C.: The frequency-dependent directivity of a planar Fabry-Perot polymer film ultrasound sensor. IEEE Trans. Ultrason. Ferroelectr. Freq. Control **54**(2), 394–404 (2007)
40. Lamela, H., Gallego, D., Oraevsky, A.: Optoacoustic imaging using fiber-optic interferometric sensors. Opt. Lett. **34**(23), 3695–3697 (2009)
41. Chen, S.-L., Huang, S.-W., Ling, T., Ashkenazi, S., Guo, L.J.: Polymer microring resonators for high-sensitivity and wideband photoacoustic imaging. IEEE Trans. Ultrason. Ferroelectr. Freq. Control **56**(11), 2482–2491 (2009)
42. Gruen, H., Berer, T., Burgholzer, P., Nuster, R., Paltauf, G.: Three-dimensional photoacoustic imaging using fiber-based line detectors. J. Biomed. Opt. **15**(2), 21306 (2010)
43. Yang, X.H., Wang, L.L.: Fluorescence pH probe based on microstructured polymer optical fiber. Opt. Express **15**(25), 16478–16483 (2007)
44. Gallego, D., Lamela, H.: High-sensitivity ultrasound interferometric single-mode polymer optical fiber sensors for biomedical applications. Opt. Lett. **34**(12), 1807–1809 (2009)

45. Markom, A.M., et al.: Performance comparison of enhanced Erbium–Zirconia–Yttria–Aluminum co-doped conventional erbium-doped fiber amplifiers. Optik **132**, 75–79 (2017)
46. Fiberlabsus_admin 投稿者: Erbium-Doped Fiber Amplifier (EDFA). Fiberlabs Inc. https://www.fiberlabs.com/glossary/erbium-doped-fiber-amplifier/. Accessed 23 Apr 2021
47. Fischer, U.H.P., Haupt, M., Joncic, M., Predeep, P.: Optical transmission systems using polymeric fibers. Optoelectronics—Devices and Applications (2011)
48. Kumi Barimah, E., et al.: Erbium-doped nanoparticle–polymer composite thin films for photonic applications: structural and optical properties. ACS Omega **5**(16), 9224–9232 (2020)
49. Antipov, O., Kuznetsov, M., Tyrtyshnyy, V., Alekseev, D.: Low-threshold mode instability in few-mode Yb3+-doped fiber amplifiers: an overview of recent results. In: Fiber Lasers XVIII: Technology and Systems, vol. 11665, p. 116650T (2021)
50. Nayak, S.K., Bhuyan, K.C., Mohanty, M.N.: Optical wave guide: fast and secure communication for next-generation technology. Advances in Electronics, Communication and Computing, pp. 227–237. Springer (2021)

Functionalised (ZnO:Dy@AuNP) Nanoassembly for Sensing Nitro Aromatic Compound

G. L. Praveen, Kanchan Upadhyay, Sony George, and Sabu Thomas

Abstract Sensing of analyte molecules via monitoring the turn-on fluorescence produced by magneto-luminescent and plasmonic nanoassembly for the analyte, when present in aqueous medium is depicted in this study. Donor–acceptor FRET phenomenon first provides a turn-off fluorescence followed by a turn-on fluorescence exhibited as a consequence of meisenheimer complex formation between the functionalized AuNp of the nanoassembly and nitro groups of the analyte. Here, UV–Visible, Photoluminescence, TCSPC, TEM, DLS, zeta potential, and FT-IR analytical techniques were employed for substantiating the observed phenomenon.

1 Introduction

Advance material science employed gold nanoparticle (AuNP) in its various branches for its applications in the field of catalysis, medicine, environmental science, electronics, optics and photovoltaic [1–3]. Size, shape, interparticle distance and interaction mechanism matters well for AuNps extensive usages. Optical band (absorption band) of AuNps in the visible region of the electromagnetic spectrum is called surface plasmons formulated by Mie, and is so called Mie theory [4, 5]. Collective oscillation of free conduction electrons occurs as a result of resonant electromagnetic field is notes as surface plasmons (SP). The SP results in a dipole formation which vastly depends on a number of parameters such as nanoparticle composition, morphology, concentration, solvent refractive index, surface charge, and temperature [6, 7].

Depending on the angle of the electric field, plasmons appears as transverse and longitudinal bands. Transverse plasmons occurs at a wavelength region close to that of spherical AuNps and longitudinal band spans between 600–900 nm as per the AuNps aspect ratio. Colorimetric sensor for identifying food suitability were already established through AuNps [8]. Detection of proteins, pollutants, and other molecules free to label make use of surface enhanced raman spectroscopic (SERS) applications of AuNps.

G. L. Praveen (✉) · K. Upadhyay · S. George · S. Thomas
International and Inter University Center for Nanoscience and Nanotechnology, Mahatma Gandhi University, Kottayam, India

© Springer Nature Switzerland AG 2022

K. Upadhyay et al. (eds.), *Hybrid Phosphor Materials*, Engineering Materials,
https://doi.org/10.1007/978-3-030-90506-4_11

Among the different metal oxide nanoparticles, Zinc oxide (ZnO) nanoparticles were well established for its applications in gas-chemical sensor, biological sensors, drug delivery systems and in electrical devices [9, 10]. At room temperature, properties of ZnO lies on 3.37 eV wide band gap, large band strength and large exciton binding energy of 60 meV. Electromagnetic coupled sensors and actuators make use of ZnO for its piezoelectric property [11]. With narrow and tunable emission lines, higher photostability along with high quantum yield allows the QDS to overrule molecular dyes from their both physical and biological senseronic fields of application [12, 13]. In addition the distance dependent fluorescence emission quenching and enhancement of QD by nearby metal NPs were also explored [17]. Distance between single class QD and metal nanoparticles (MNPs) plays a vital role in QD emission-quenching by forming an assembly between them [14]. The nonradiative energy decipation mechanisms happens between dipoles through fÖrster resonance energy transfer (FRET) [15] and nanometal surface energy transfer (NSET) [16, 17] comes into play for the quenching process of QDs-MNPs nanoassembly.

Dexter mechanism starts once the wave functions of donor and acceptor molecules overlaps leads to charge carrier exchange. Unlike dexter transfer, FRET needs a high spectral overlap with low concentration of donor to acceptor moieties (Scheme 1). In FRET mechanism the QD and AuNPacts as point dipoles and for a pair the energy transfer rate is expressed as:

$$k_{FRET} = \tau_D^{-1}\left(\frac{R_0}{r_{DA}}\right)^6$$

where

$\tau_D = (K_{nr} + K_r)^{-1}$ is the intrinsic lifetime of the quantum dot emission decay.

r_{DA} is the center to center separation between the QD and AuNP. R_0 is the Förster radius. Where, 50%, energy transfer happens. This efficient Resonance energy

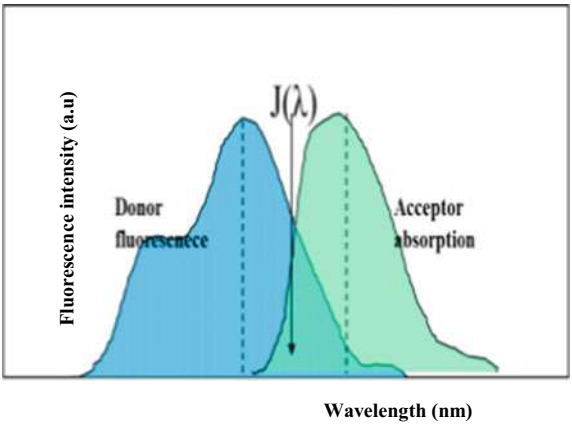

Scheme 1 Criteria of fluorescence resonance energy transfer (FRET)

transfer is possible only when the donor and acceptor molecules are separated by a distance of 100 A^0.

The Förster radius is given by

$$R_0 = 0.0211\left(\frac{k^2 QY}{n^4} J\right)^{1/6}$$

K^2 is the orientation factor of the dipole. QY is the photoluminescence (PL) quantum yield of the QDs and n is the refractive index of the surrounding medium.

$$J = \int_0^\infty \hat{i}_{QD}(\lambda).\varepsilon_{AuNP}(\lambda)\lambda^4 d\lambda$$

where, $\hat{i}_{QD}$ is the normalized donor emission spectrum of the QD, ε_{AuNP} is the acceptor (AuNP) molar extinction coefficient and J is the spectral overlap of the area normalized donor QD emission spectrum and the acceptor AuNP extinction spectrum.

To detect a bright signal in a dark back ground is quite easy and precise, which overruled the turn-off sensors from the scenario. The pictorial representation of the turn-on sensing mechanism of nitro aromatic compounds by the quantum dot-plasmonic nanoassembly is shown in Scheme 2. The amine-terminated AuNP ($\lambda_{absorption}$ = 526 nm) and carboxyl-terminated ZnO:Dy ($\lambda_{emission}$ = 536 nm) first form an assembly through amine-carboxyl electrostatic interaction, switch on to FRET between QD to AuNPs and almost complete emission of the QD is quenched. Next, the added 2,4,6-trinitrotoluene (TNT) molecules break the assembly and replace the QDby forming

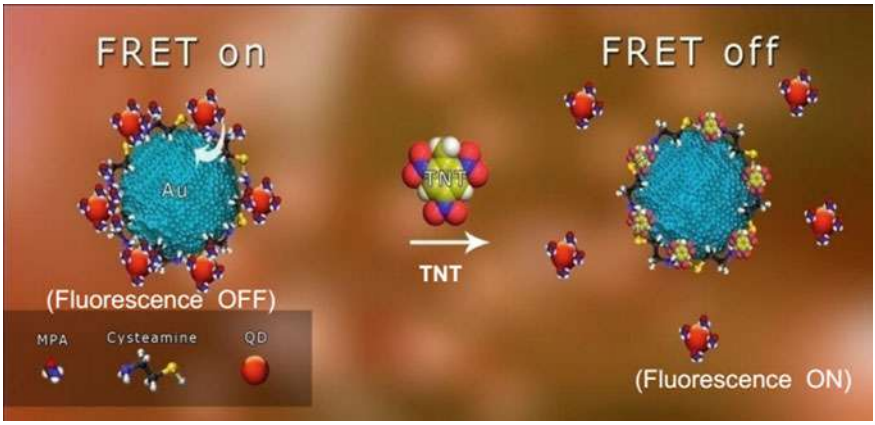

Scheme 2 Pictorial representation of FRET ON and FRET OFF as part of Meisenhiemer complex formation

a meisenheimer complex between TNT and the primary amines of the cysteamine capped AuNPs [18]. This complex formation breaks FRET and a corresponding fluorescence recovery is obtained. The magnitude of fluorescence recovery depicts the concentration of the analyte molecule present.

2 Results and Discussion

2.1 Photoluminescence Study of MPA Capped ZnO:Dy

The emission spectrum of dysprosium doped ZnOQD capped with mercaptopropionic acid was derived through 367 nm range excitation entity.

Figure 1 depicts the emission profile of Dy doped ZnO QD capped with MPA. Maximum fluorescence emission is recorded at a spectral range of 536 nm. As part of 5d-4f transition and the 5d state is easily affected by the outer crystal field [19], the fluorescence of Dy^{3+} ions happens. The luminescence efficiency of rare earth doped materials depends mostly on the host matrix nature. When Dy^{3+} ion (0.99A˚) are introduced into ZnO host (0.75A˚), only a minor fraction of Dy^{3+} could substitute the Zn^{2+} sites and the major fraction resided on the surface or on the grain boundaries of the ZnO nanocrystals yielding optimum strain relief [20]. The characteristic QD emission is confirmed by obtaining green light from the aqueous sample irradiated with 367 nm UV light as shown in the digital photograph.

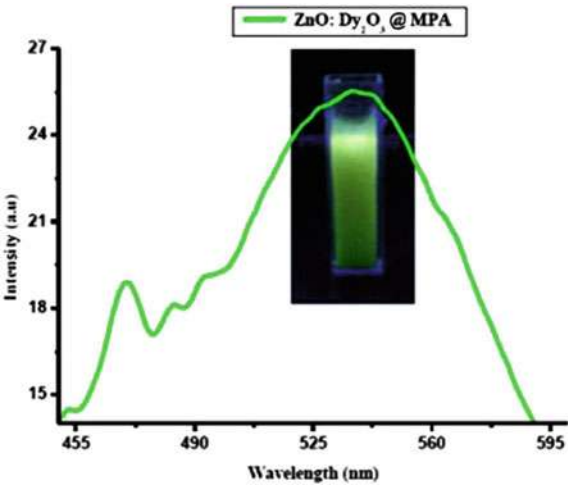

Fig. 1 Emission spectrum of Dy doped ZnO capped with MPA and the direct photograph showing its fluorescence under the UV lamp

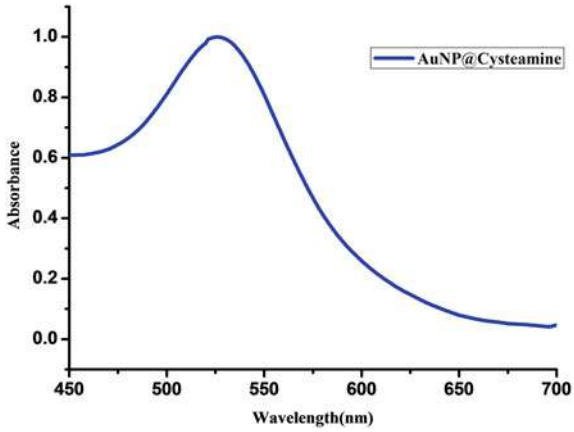

Fig. 2 Absorption spectrum of AuNP@cysteamine

2.2 *UV–Visible Absorption Study of Cysteamine Capped AuNP*

The Fig. 2 shows that cysteamine capped AuNP exhibits the absorption maximum at the wavelength region of 526 nm. Usually AuNPs exhibit surface plasmon resonance at UV–Visible region approximately at 520 nm which corresponds to the transverse oscillation of the free-conduction electrons induced by an interacting electromagnetic field, and their resonances (Mie 1998). Here, the cysteamine capped AuNP gave the absorption band which is almost matched with emission band of Dy:ZnO@MPA.

In order to analyse surface functionalisation done on the donor and acceptor moieties of the nanoassembly FT-IR spectral studies were carried out.

2.3 *Functional Group Analysis of MPA Capped QD Using FT-IR*

The Fig. 3 shows the FT-IR spectrum of MPA modified ZnO:Dy QD. The absorption peak occurs at 3170 cm^{-1} corresponding to O–H stretching of –COOH group, and absorption peak at 637 cm^{-1} corresponding to C-S vibrations of mercaptopropionic acid respectively. In MPA modified ZnO:Dy, the characteristic peak of S–H vibration around 2650 cm^{-1} is absent which indicates the successful binding of the MPA towards the ZnO:Dy QD surfaces. The peaks observed around 3500 cm^{-1} and 562 cm^{-1} corresponds to free –COOH group and the metal-oxide (Zn–O) vibration respectively.

The surface charge obtained for the MPA capped ZnO:DyQD was evaluated using *zeta potential* (ξ) measurements which is shown in Fig. 4. It was found that the particles were negatively charged having a *zeta potential* value of −35.4 mV. The obtained negative potential depicts the stability and successful MPA capping.

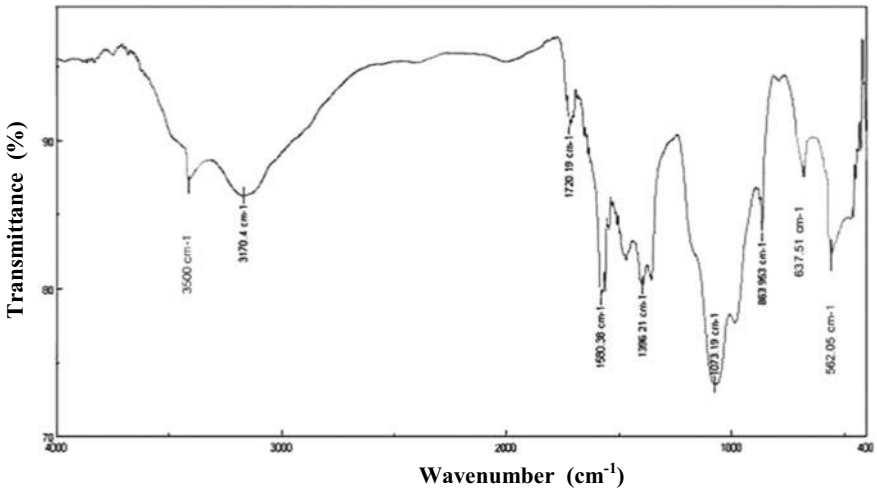

Fig. 3 FT-IR spectrum of MPA modified ZnO:Dy

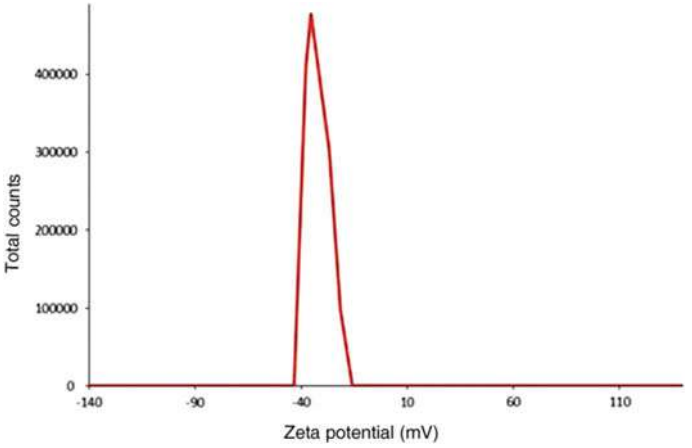

Fig. 4 Surface charge analysis of MPA capped ZnO:Dy

2.4 Functional Group Analysis of Cysteamine Capped AuNP Using FT-IR

Figure 5 shows the FT-IR spectrum of cysteamine modified AuNP. The characteristic peak of–NH_2 vibration in cysteamine was observed at 3403 cm^{-1}. The characteristic peak of S–H vibration around 2650 cm^{-1} is absent which indicates the successful binding of the cysteamine towards the AuNP surfaces.

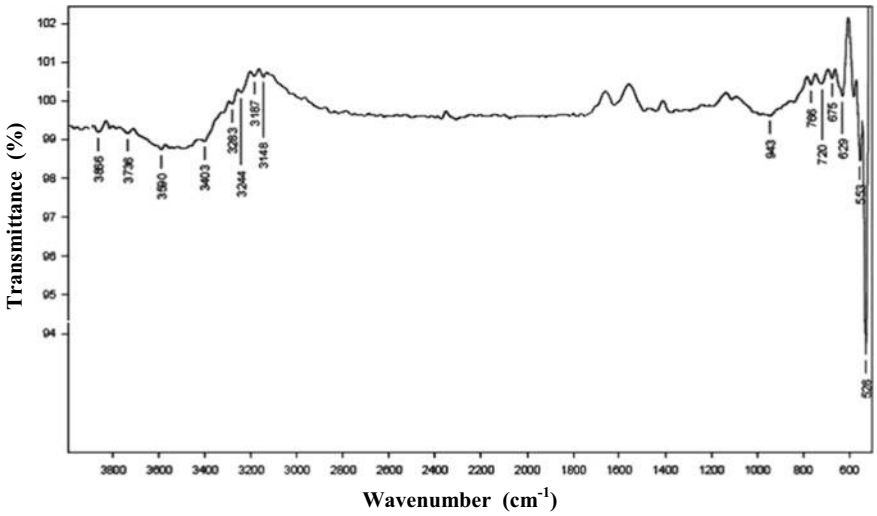

Fig. 5 FT-IR spectrum of AuNP@cysteamine

The surface charge obtained for the cysteamine capped AuNP was evaluated using *Zeta potential* (ξ) measurements which is shown in Fig. 6. It was found that the particles were positively charged having a *Zeta potential* value of +27.7 mV. The obtained positive potential depicts the successful MPA capping.

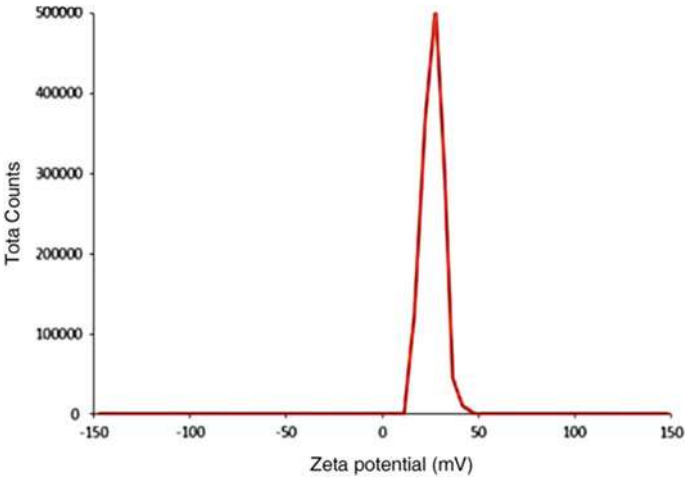

Fig. 6 Surface charge analysis of cysteamine capped AuNPs

2.5 *Quenching Studies of Dy:ZnO@MPA and AuNP@cysteamine Assembly*

The FT-IR and *zeta potential* spectral data supports well for QD and AuNP possessing oppositively charged surface groups. Thus the amine terminated AuNPs stands as a good scaffold for the negatively charged QDs. The quenching studies between QD-AuNps nanoassembly is achieved by the merging of emission–absorption peaks of QD-AuNps respectively. Figure 7 shows the emission and absorption peaks merging obtained for the as optimised (QD_{536}) and ($AuNP_{526}$) nanoassembly depicts the possibilities of FRET within our system.

Addition of picomolar (pM) concentrations of AuNP to the nanomolar (nM) concentrations of QD within a constant volume of the system resulted in quenching studies by keeping the volume of the system a constant. The spectra thus obtained are shown in Fig. 8. As the concentration of AuNP grows the emission intensity of QD is deminishes. The maximum quenching of the emission intensity of QD was observed for 12.6 pM concentration of AuNP added system. It is evident from the spectrum that a turn-off mechanism via FRET is operating between the surface modified QDs and AuNPs [21].

If the QDisin the close proximity of metal nanoparticle i.e. AuNP (less than a few nm), then the possibility exists that the excited state QD electron and hole can tunneled to the AuNP through non-radiative relaxation [22]. Thus in this system with a reasonably good spectral overlaps between the donor and acceptor moieties which results in the prevailence of non-radiative energy transfer between QD to the AuNP causing the quenching of the fluorescence of QD molecules (Donor moieties). The computational studies calculated that the length of cysteamine and MPA are 0.40 and 0.48 nm respectively [21]. Thus, the MPA modified QDs and cysteamine modified

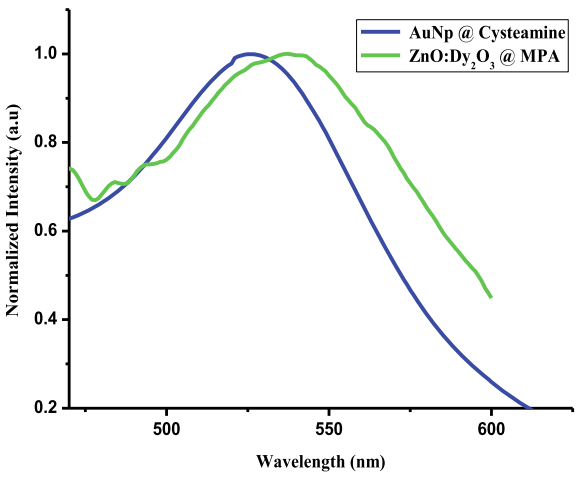

Fig. 7 Graphical representation of FRET mechanism

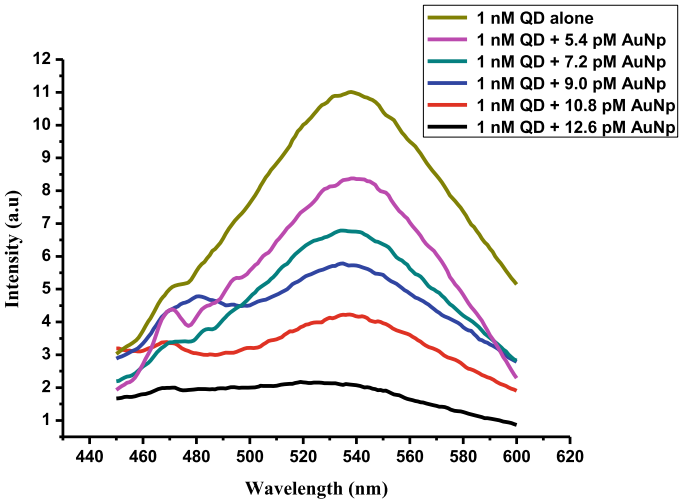

Fig. 8 Concentration dependent fluorescence emission quenching in QD-AuNp assembly

AuNPs will be almost far apart by anm. Hence, it will provide an effective electrostatic attraction between AuNP and QD resulting in a high FRET efficiency system.

Stern–Volmer equation $\frac{Fo}{F} = 1 + \text{kq}\ \tau_0\ [\text{Q}]$ opens the picture of quenching of QD fluorescence in the presence of AuNP. Here F_0 and F are the fluorescence intensity of ZnO:Dy QD in the non-availability and availability of AuNP respectively. τ_0 is the life time of nanophosphors in the absence of quencher. Q is the concentration of AuNP and k_q is the quenching constant. A linear Stern–Volmer plot is obtained when $\frac{Fo}{F}$ is plotted against concentration of AuNp as shown in Fig. 9.

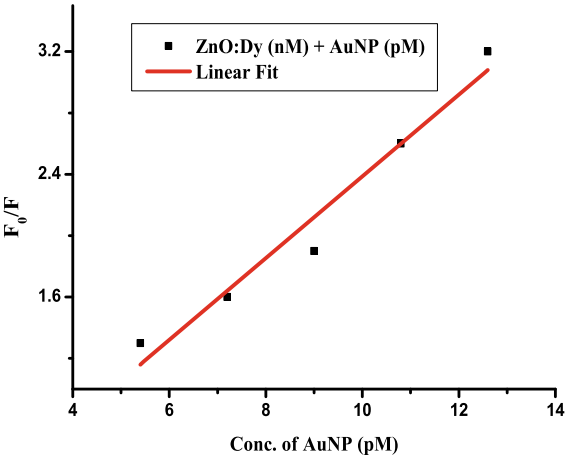

Fig. 9 Stern–Volmer plot for the fluorescence quenching of QDs with variable concentration of AuNP

A linear Stern–Volmer plot is an indication of the accessibility of quencher (AuNP) for the single class of fluorophores (ZnO:Dy). The quenching mechanism is also explained from the measurement of fluorescent life time studies, a method to distinguish static and dynamic quenching.

2.6 Detection of the Analyte (TNT)

Addition of variable nM concentrations of TNT molecules towards the nanoassembly of the donor–acceptor (ZnO:Dy@AuNP) moiety caused highest quenching of the donor luminescence. These spectral changes (emission recovery) is evaluated using PL emission data as are shown in Fig. 10. An increase in the QD luminescence from the maximum quenched nanoassembly is observed for each nM concentrations of TNT addition. Hence a clear linear increase in the amount of fluorescence turn-on is seen with an increasing amount of analyte concentration (TNT) in the aqueous medium.

The fluorescence enhancement is attained as the TNT molecules break AuNP-QD assembly and switch off the FRET from QD towards AuNP (Scheme 1). TNT molecules fall in love with primary amines of the cysteamine capped AuNP and form Meisenheimer complex and this covalent interaction is stronger than electrostatic binding between amine and carboxyl groups of the cysteamine functionalised MNP

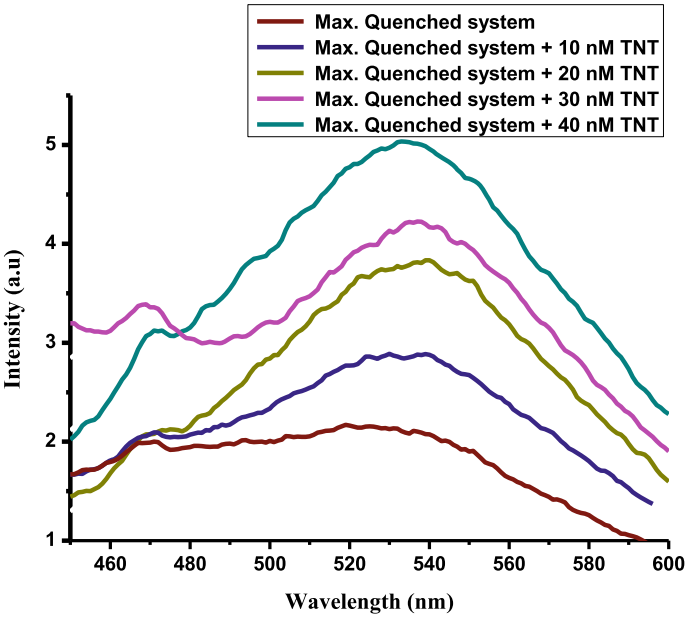

Fig. 10 QD replacement by TNT analyte (fluorescence recovery)

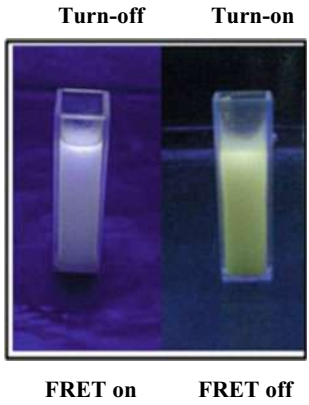

Fig. 11 The direct UV photograph of the system which enabled maximum fluorescence quenching (FRET on) and fluorescence recovery (FRET off)

and the MPA capped QD respectively [23]. Thus, QD electrostatically attracted towards AuNPs were substituted by TNT molecules. The recovery of the green emission of the QD through the replacement of AuNPs by the analyte molecule can be clearly visualized from the direct photographs taken under 367 nm UV radiation (Fig. 11) of the samples which enabled maximum FRET on and FRET off.

Detection limit for analyte was calculated using the following equation

$$\text{Limit of detection (LOD)} = \frac{3 \times \text{standard deviation} \times \text{lower limit}}{\text{volume taken in cuvette} \times \text{emission intensity in lower limit}}$$

The fluorescence turn-on is immediate and the limit of detection is as low as 1.46×10^{-8} M. Observations such as fluorescence recovery of 45.45% with a high quenching constant (Ksv) of $1.25 + 0.01 \times 10^{10}$ M^{-1} depicts the sensitivity acceptability of developed sensors.

2.7 Selectivity Study

The fluorescence response and selectivity of the nanoassembly (AuNP-ZnO:Dy)in the detection of the analyte 2,4,6-trinitrotoluene is tested by taking the fixed volume of an aqueous solution which contained analogue molecules of TNT such as nitrobenzene (NB) and 2-nitrophenol (2-NP), along with commonly seen metal ion impurities such as alkali (K^+), alkaline earth (Ba^{2+}) and transition metal ion (Fe^{3+}). The selectivity responses obtained were shown in Fig. 12. The corresponding fluorescence response of the system is shown in Fig. 13. The excellent selectivity of the nanoassembly towards TNT is because the fact that high electrostatic interactions between the carboxyl terminated QD and the amine terminated AuNP, which lacks in the case of NB and 2-NP. Here only one electron withdrawing groups is present in each aromatic rings.

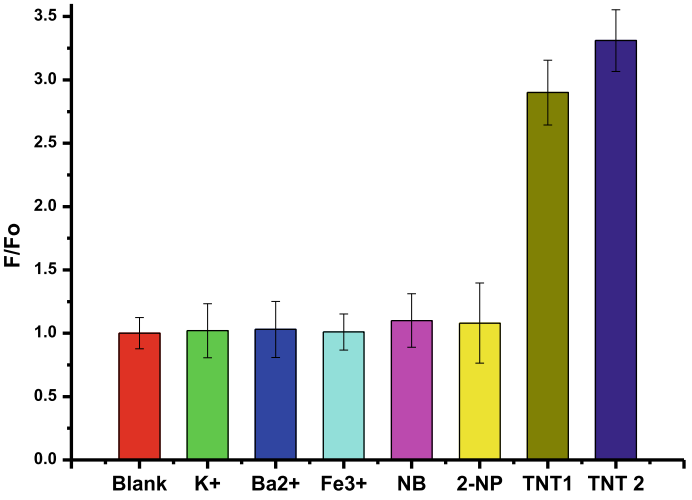

Fig. 12 Response of Fluorescence of AuNP-QD assembly to cations (K^+, Ba^{2+} and Fe^{3+}) and nitro aromatic (NB, 2-NP) compounds. The concentration of K^+, Ba^{2+} and Fe^{3+} are 10 μM and NB and 2-NP are 40 nM

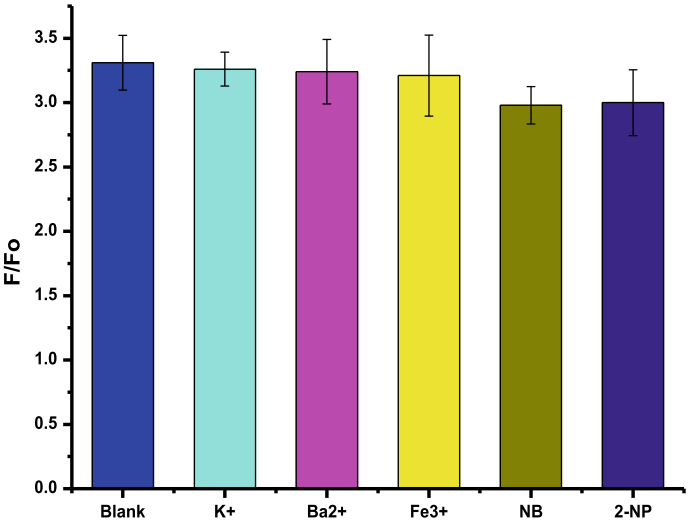

Fig. 13 The selectivity of AuNP-QD assembly for TNT in the presence of cations (K^+, Ba^{2+} and Fe^{3+}) and nitroaromatics (NB and 2-NP). The concentration of K^+, Ba^{2+} and Fe^{3+} are 10 μM and NB and 2-NP are 40 nM. F_0 and F are the fluorescence intensities of AuNP-QD assemblies before and after addition of corresponding substances. The concentration of AuNP is 12.6 pM and QD is 1 nM

2.8 Morphological Study

To visualise the AuNP@QD nanoassembly and the replacement of QD by TNT we go for the TEM study.

From the Fig. 14 it is clear that both the nanoparticles are spherical in shape. The TEM studies were carried out on three types of samples (1) AuNP alone Fig. 14a (2) AuNP+QDnanoassembly Fig. 14b and c corresponds to maximum quenching concentration of AuNP (12.6 pM) added system and (3) AuNP+QD+TNT system. Figure 14d corresponds to maximum turn-on enabling concentration (40 nM) of TNT added system. From the given scale of TEM images the average size of AuNP is calculated to be 30 nm and QD to be 10 nm. From Fig. 14b and c it is clear that the QDs and AuNPs are very much close together ought to the electrostatic interaction among them. The replacement of QD by TNT can be clearly visualised from the corresponding sample (Fig. 14d).

Thus, the TEM study clearly substantiates the turn-off and turn-on phenomenon working in our chemosensor.

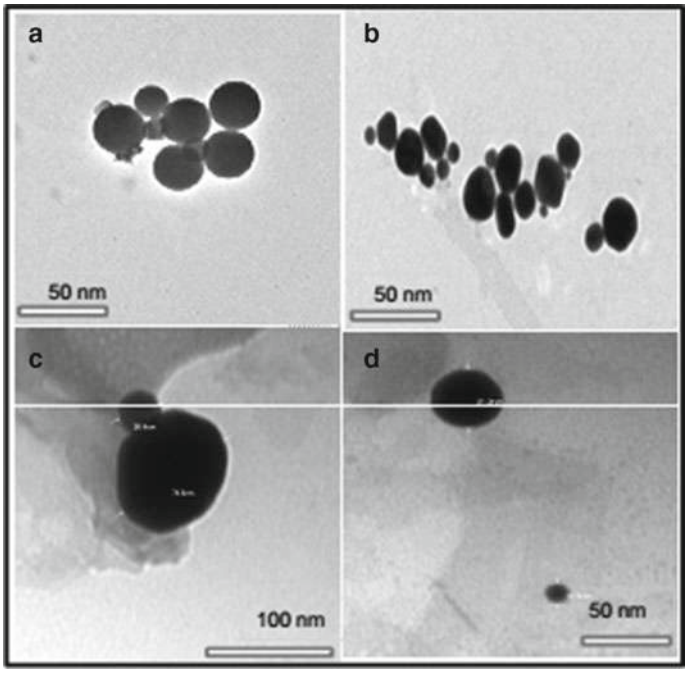

Fig. 14 TEM images of **a** AuNP@cysteamine **b** Dy: ZnO@MPA+AuNP@cysteamine quenched (turn-off) system **c** specified region of the quenched system **d** The quenched+TNT added (turn-on) system

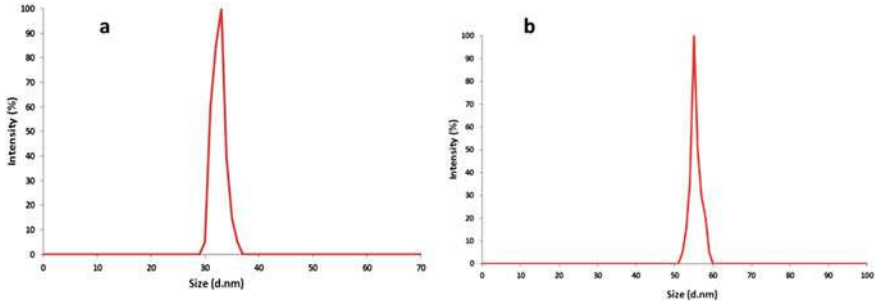

Fig. 15 Size distribution curve of functionalised **a** AuNP alone **b** AuNP+ZnO:Dy

2.9 Size Distribution Analysis

Dynamic light scattering (DLS) analysis is an important method for determining the size of particle present in solution. DLS works by shining a laser at sample solution and observing the scattered light. Figure 15a shows the DLS distribution curve of cysteamine modified AuNP alone which gave the characteristic peak at 33 nm indicates its hydrodynamic diameter, and Fig. 15b shows the DLS distribution curve of the cysteamine capped AuNP in presence of MPA modified ZnO:Dy QD which gave a characteristic peak at 55 nm. This increase in the AuNP size can be attributed to the fact that due to electrostatic attraction the MPA modified QDs come close to the oppositively charged cysteamine modified AuNP and act as a single system.

Thus the DLS profile further substantiates the proposed turn-off phenomenon working in our chemosensor.

2.10 Fluorescence Life Time Study

ZnO:Dy@MPA system and the ZnO:Dy@AuNP were subjected for Time correlated single photon counting, the decrease in emission intensity at high metal nanoparticle concentrations (AuNP) is underlined by measurements of the emission life times of the QD with and without the AuNPs. The QD without AuNP exhibited bi-exponential lifetime decay but the QD with maximum AuNP quenching concentration showed tri-exponential decays, which were summarised in Table 1 and Fig. 16.

Emission quenching and decay life time shortening is evidenced by the occurrence of non-radioactive energy transfer in the optical emitter [24].

Table 1 Fluorescent life time of the pristine QD, QD+AuNP and QD+AuNP+TNT

Samples	τ_1(ns)	τ_2(ns)	τ_3(ns)	A_1	A_2	A_3	$\chi 2$
ZnO:Dy alone	8.249	5.645	–	53.44	46.56	–	0.995
ZnO:Dy@AuNP	5.342	5.008	6.028	61.65	10.73	27.62	0.954
ZnO:Dy@AuNP@TNT	7.098	5.591	6.961	64.84	7.96	27.20	1.01

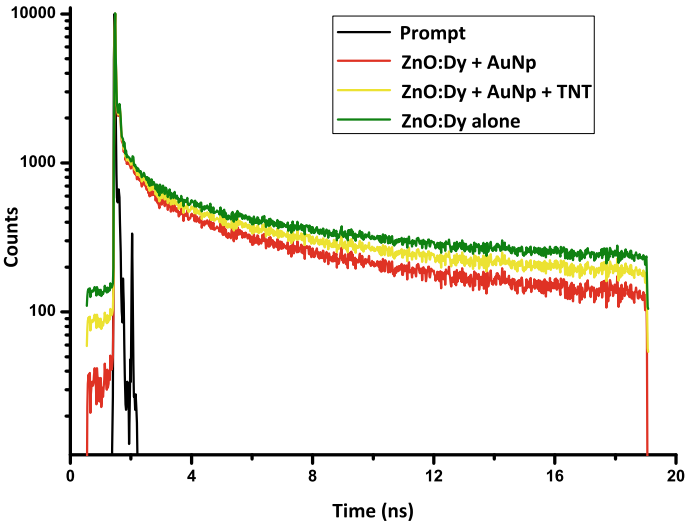

Fig. 16 TCSPC spectra of ZnO:Dy alone, ZnO:Dy+AuNP and ZnO:Dy+AuNP+TNT

Our study support these two characteristics in QD-AuNP assembly at optimal quenching concentration. The emission life time measurements emphasises the existence of distinctive states for the QD-AuNP at the maximum AuNP quenching concentrations in the nano assembly shown in Table 1. By concentration increase of AuNPs a subset of excited state QDs transfer the excited electron and hole to the AuNP by non radiative relaxation.

In the case of MPA capped ZnO:Dy a bi-exponential pathway is dominant. The first is of ZnO:Dy ($\tau_1 = 8.249$ ns) and the second is contributed by the capping agent ($\tau_2 = 5.645$ ns). Here the capping agent can change the luminescence of QD. When AuNP is introduced to the system the decay profile exhibits a tri-exponential pathway, the third decay channel is provided by AuNPs. Moreover, the decay time changes from $\tau_1 = 8.249$ ns to 5.342 ns and $\tau_2 = 5.645$ ns to 5.008 ns. The decrease of lifetime points that luminescence of QD gets quenched by the acceptor AuNPs. The shortening of life time is dynamic as only the excited state of the fluorophore is affected. When the analyte TNT was introduced to the AuNP-QD system, it also gave a tri-exponential decay and a good recovery in the fluorescent lifetime was obtained ($\tau_1 = 5.342$ ns to 7.098 ns and $\tau_2 = 5.008$ ns to 5.591 ns). A good recovery of lifetime indicates that the additional decay channel becomes less strengthened with

the disintegration of the hybrid assemblies between QD and AuNP ($\tau_3 = 6.028$ ns to 6.961 ns).

2.11 Magnetic Measurements of Mercaptopropionic Acid Capped ZnO and ZnO:Dy Quantum Dots

Magnetization curves as shown in the Fig. 17 are measured on powder sample of QD@MPA nanoparticles at room temperature using vibration sample magnetometer (VSM). Magnetic hysteresis [M-H] curve of undopped ZnO nanoparticle recorded at room temperature is shown in the Fig. 17a. The sample shows diamagnetic behavior. Figure 17b reveal hysteresis with enhancement in saturation magnetization for 5% Dy doped ZnO nanocrystals. The saturation magnetization (Ms) value, obtained for the Dy doped ZnO nanocrystals was 21.41 emu/g and the undoped ZnO nanocrystals was only 4.634 emu/g. ZnO is a promising host material for ferromagnetic doping at room temperature [25, 26]. By Dy doping the diamagnetic undoped ZnO nanoparticle is changed to paramagnetic substances. That is increase in concentration of Dy^{3+} ions in ZnO nanocrystals leads to an increase in paramagnetic behavior may be due to presence of Dy at near surface sites. This paramagnetic nature of the donor moiety can be explored for the magnetic concentration of the analyte molecules which will even increase the accuracy of the detection of analyte from natural surroundings.

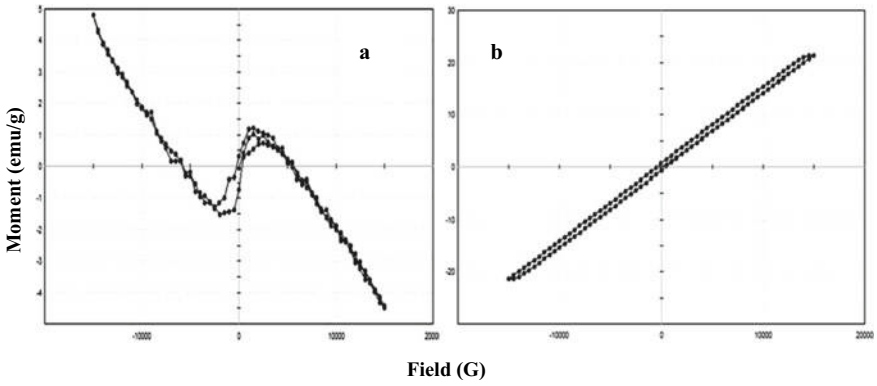

Fig. 17 Magnetization curve for MPA capped **a** ZnO **b** ZnO:Dy QDs

3 Conclusions

In summary, Meticulous optimisation of the emission wavelength of Magnetic-Luminescent nanoparticles with the absorption wavelength of plasmonic nanoparticles provides promising FRET enabled nanosensors.

4 Experimental

4.1 Reagents

Zinc acetate dehydrate [$(CH_3COO)_2Zn{\cdot}2H_2O$], dysprosium (III) chloride hydrate [$DyCl_3$], hydrogen tetrachloroaurate [$HAuCl_4{\cdot}3H_2O$] and N-Cetyl N,N,N trimethyl ammonium bromide [CTAB] were used of Oxford Laboratory, Alfa Aesar, Aldrich, and Otto respectively. Sodium borohydride [$NaBH_4$], sodium hydroxide [NaOH], potassium hydroxide [KOH], methanol [CH_3OH], ascorbic acid [Vitamin C], mercaptopropionic acid [MPA] and cysteamine hydrochloride employed were of Spectrochem. Hydrochloric acid [HCl] and nitric acid [HNO_3] were purchased from Spectrum, tri sodiumcitrate [$C_6H_5Na_3O_7{\cdot}2H_2O$] from Nice and TNT [2,4,6-trinitro toluene] was obtained from Forensic Laboratory. Milli-Q water was used to prepare all the solutions in this study. All the materials and chemicals were used as received.

4.2 Synthesis of MPA Capped Dysprosium Doped ZnO QD

In order to synthesis dysprosium doped ZnO first prepared dysprosium oxide from lanthanide halides i.e.; dysprosium chloride. For that added 1.5 mL (0.05 M) NaOH solution to the 5 mL (0.005 M) $DyCl_3$. White precipitate will obtained indicate the presence of Dy_2O_3. The above obtained Dy_2O_3 is added to 9 mL (0.1 M) of precursor complex such as zinc acetate dihydrate ($ZnAc_2{\bullet}2H_2O$). Stirred vigorously for about 10 min. To the stirred solution added 1 M KOH (22 mL) drop by drop and magnetically stirred for about 1 h. Then centrifuged, washed three times with 1:1 methanol water solution. The resultant product is the dysprosium doped ZnO, (ZnO:Dy). It is then dried and powered. To this added 40 mL (0.1 M) MPA and stirred for about 10 h then centrifuged and washed with 1:1 ethanol water solution. The resultant product is the MPA capped dysprosium doped ZnO (ZnO:Dy@MPA).

4.3 Synthesis of Cysteamine Functionalised AuNPs

AuNPs are prepared in aqueous solution using a seeded growth protocol with slight modification [21]. Specifically the seed solution was first made by addition of 0.01 M $HAuCl_4$ solution (0.25 mL) into 0.1 M CTAB (9.75 mL) in a 15 mL plastic tube. The solution was gently mixed by inversion. A freshly prepared ice cold 0.01 M $NaBH_4$ solution (0.6 mL) was then injected quickly into the mixture solution followed by rapid inversion for 2 min. The resultant seed solution was kept at 30 °C for 2 h before use. To grow AuNPs0.01 M $HAuCl_4$ (2 mL) was first mixed with 0.1 M CTAB (40 mL) in a 100 mL beaker mix gently. 1 M HCl (0.8 mL) was then added for adjusting the pH, followed by the addition of 0.01 M ascorbic acid (0.32 mL) and mixed well by inversion. After the growth solution was mixed by inversion the CTAB stabilized seed solution (0.096 mL) was rapidly injected. The resultant solution was gently mixed for 10 sand kept undisturbed for 12 h in 30 °C water bath.

Amine terminated AuNPs were obtained by a modified literature procedure (Wang and Irudayaraj 2010). Briefly 5 mL of AuNP sample was centrifuged twice at 10,000 rpm for 15 min to remove CTAB and other ions in the solution. The precipitate was redispersed in water (5 mL) and subsequently an aqueous solution of cysteamine (20 mM, 10.5 mL) was added drop wise under vigorous stirring. The mixture was sonicated for 0.5 h at 50 °C, which was further heated in a 50 °C water bath for 3 h. The resultant AuNPs were collected by centrifugation twice at 13,000 rpm for 15 min to remove excess cysteamine and desorbed CTAB. The purified amine-terminated AuNPs were dried under vacuum at 40 °C overnight. The cysteamine-AuNPs were then redispersed in water.

4.4 The Spectrofluorometric Determination of Turn-Off Fluorescence

Different volumes of AuNP (1.0×10^{-9} M) solution such as 27, 36, 45, 54, and 63 μL were placed in a series of 10 mL calibrated test tubes. Various amounts of ZnO@MPA (1.0×10^{-7} M) were mixed with the test tubes. The mixture was then diluted to 5 mL with water and mixed thoroughly. Five minutes later, the mixed solutions were transferred into the quartz cuvette and the fluorescence was measured at an excitation wavelength of 367 nm.

4.5 The Spectrofluorometric Detection of 2,4,6-Trinitrotoluene

72 μL of AuNP (1.0×10^{-9} M) were placed in a series of 10 mL calibrated test tubes. Then ZnO@MPA (1.0×10^{-7} M) of various amounts were mixed with the solution.

Five minutes later the analyte (TNT) with different concentrations (10, 20, 30, and 40 nM) from 1.0×10^{-6} M TNT solution with volumes respectively were added to the mixture. The mixtures were then diluted to 5 mL with water and mixed thoroughly. After 5 min the mixed solution were transferred to the quartz cuvette. Their fluorescence spectra were recorded by operating the fluorescence spectrophotometer at an excitation wavelength of 367 nm.

References

1. Narayanan, R., El-Sayed, M.A.: Catalysis with transition metal nanoparticles in colloidal solution: nanoparticle shape dependence and stability. J. Phys. Chem. B. **109**, 12663–12673 (2005)
2. Nash, M.A., Waitumbi, J.N., Hoffman, A.S., Yager, P., Stayton, P.S.: Multiplexed enrichment and detection of malarial biomarkers using a stimuli-responsive iron oxide and gold nanoparticle reagent system. ACS Nano **6**, 6776–6787 (2012)
3. Bedford, E.E., Spadavecchia, J., Pradier, C.M., Gu, F.X.: Surface plasmon resonance biosensors incorporating gold nanoparticles. Macromol. Biosci. **12**, 724–735 (2012)
4. Mayer, K.M., Hafner, J.H.: Localized surface plasmon resonance sensors. Chem. Rev. **111**, 3828–3838 (2011)
5. Mie, G.: Contribution to the optics of turbid media, especially colloidal metal suspensions. Ann. Phys. **25**, 377–445 (1908)
6. Link, S., El-Sayed, M.A.: Spectral properties and relaxation dynamics of surface plasmon electronic oscillations in gold and silver nanodots and nanorods. J Phys. Chem. B **103**, 8410–8426 (1999)
7. Rodriguez-Gonzalez, B., Sanchez-Iglesias, A., Giersig, M., Liz-Marzan, L.M.: Au-Ag bimetallic nanoparticles: formation, silica-coating and selective etching. Faraday Discuss. **125**, 133–140 (2004)
8. Ali, M.E., Hashim, U., Mustafa, S., Man, Y.B.C., Islam, K.N.: Gold nanoparticle sensor for the visual detection of pork adulteration in meatball formulation. J. Nanomater. **2011**, 1–7 (2012)
9. Baxtex, Aydil, E.S.: Growth of comb-like ZnO nanostructures for dye-sensitized solar cells applications. Appl. Phys. Lett. **86**, 53114–53117 (2005)
10. Huang, M.H., Mao, S., Feick, H., Yan, H.Q., Wu, Y., Kind, H., Weber, E., Russo, R., Yang, P.: Room-temperature ultraviolet nanowire nanolasers. Science **292**, 1897–2109 (2001)
11. Minne, S.C., Manalis, S.R., Quate, C.F.: Centimeter scale atomic force microscope imaging and lithography. Appl. Phys. Lett. **67**, 3918–3929 (1995)
12. Clapp, A.R., Medintz, I.L., Mattoussi, H.: Förster resonance energy transfer investigations using quantum-dot fluorophores. Chem. Phys. Chem. **7**, 47–57 (2006)
13. Resch-Genger, U., Grabolle, M., Cavaliere-Jaricot, S., Nitschke, R., Nann, T.: Quantum dots versus organic dyes as fluorescent labels. Nat. Methods **5**, 763–775 (2008)
14. Wargnier, R., Baranov, A.V., Maslov, V.G., Stsiapura, V., Artemyev, M., Pluot, M., Sukhanova, A., Nabiev, I.: Energy transfer in aqueous solutions of oppositely charged CdSe/ZnS core/shell quantum dots and in quantum dot a nanogold assemblies. Nano Lett. **4**, 451–457 (2004)
15. Haldar, K., Sen, T., Patra, A.: Metal conjugated semiconductor hybrid nanoparticle-based fluorescence resonance energy transfer. J. Phys. Chem. C **114**, 4869–4874 (2010)
16. Jennings, T.L., Singh, M.P., Strouse, G.F.: Flourescent lifetime quenching near d=1.5 nm gold nanoparticles. J. Am. Chem. Soc. **128**, 5462–5467 (2006)
17. Pons, T., Medintz, I.L., Sapsford, K.E., Higashiya, S., Grimes, A.F., English, D.S., Mattoussi, H.: On the quenching of semiconductor quantum dot photoluminescence by proximal gold nanoparticles. Nano Lett. **7**, 3157–3164 (2007)

18. Walker, N.R., Linman, M.J., Timmers, M.M., Dean, S.L., Burkett, C.M., Lloyd, J.A., Keelor, J.D., Baughman, B.M., Edmiston, P.L.: Selective detection of gas-phase TNT by integrated optical waveguide spectrometry using molecularly imprinted sol-gel sensing films. Anal. Chim. Acta **593**, 82–91 (2007)
19. Gu, F., Wang, S.F., Lu, M.K., Zhou, G.J., Xu, D., Yuan, D.R.: Structure evaluation and highly enhanced luminescence of Dy^{3+}-doped ZnO nanocrystals by Li^{+} doping via combustion method. Langmuir **20**, 3528 (2004)
20. Ghosh, P., Sadhu, S., Patra, A.: Preparation and photoluminescence properties of $Y_2SiO_5:Eu^{3+}$ nanocrystals. Phys. Chem. Chem. Phys. **8**, 3342 (2006)
21. Xia, Y., Song, L., Zhu, C.: Turn-on and near-infrared fluorescent sensing for 2,4,6-trinitrotoluene based on hybrid (gold nanorod)−(quantum dots) assembly. Anal. Chem. **83**, 1401–1407 (2011)
22. Kulakovich, O., Strekal, N., Yaroshevich, A., Maskevich, S.: Enhanced luminescence of CdSe quantum dots on gold colloids. Nano Lett. **2**, 1449–1452 (2002)
23. Jehuda, Y., Johonson, V.J., Bernier, R., Yost, U., Mayfield, A.R., Mahone, T.H., Vorbeck, W.C.: Reactions in the mass spectrometry of a hydride meisenheimer complex of 2,4,6-trinitrotoluene (TNT). J Mass Spectrom. **30**, 715–722 (2005)
24. Chandra, S., Doran, J., McCormack, S.J., Kennedy, M., Chatten, A.J.: Enhanced quantum dot emission for luminescent solar concentrators using plasmonic interaction. Sol. Energy Mater. Sol. Cells. **98**, 385–390 (2012)
25. Dietl, T.: Ferromagnetic semiconductors. Sci. Technol. **17**, 377–383 (2002)
26. Spaldin, N.A.: Absence of ferromagnetism in Mn- and Co-doped ZnO. Phys. Rev. B. **69**, 125201–125210 (2004)

Hybrid Nanostructures for Biomedical Applications

R. Rajakumari, Abhimanyu Tharayil, Sabu Thomas, and Nandakumar Kalarikkal

Abstract Nanoparticles have great potential in the biomedical field owing to its superior properties. Hybrid nanomaterials can be used to perform both diagnostic and therapeutic function by a single system. These materials will have the synergistic beneficial features of the different nanomaterials incorporated. In this chapter, we have categorised the inorganic/organic hybrid nanomaterials which are being developed in the field of biomedical applications. In addition, summarized the most recently reported hybrid nanomaterials, nanoparticles and nanocomposites with their synthesis methods and physicochemical properties. This chapter will summarize the recent advances in the synthesis, design and applications of hybrid nanomaterials in the biomedical field. The applications especially the imaging, drug delivery and cancer therapeutic applications will be highlighted.

Keywords Medical imaging · Theranostic · Cancer therapy · Liposomes · Nanoparticles

R. Rajakumari · A. Tharayil · S. Thomas (✉) · N. Kalarikkal (✉)
International and Inter-University Centre for Nanoscience and Nanotechnology, Mahatma Gandhi University, Kerala 686560, India
e-mail: sabuchathukulam@yahoo.co.uk

N. Kalarikkal
e-mail: nkkalarikkal@mgu.ac.in

S. Thomas
School of Chemical Sciences, Mahatma Gandhi University, Kerala 686560, India

N. Kalarikkal
School of Pure and Applied Physics, Mahatma Gandhi University, Kerala 686560, India

A. Tharayil · S. Thomas
School of Energy Materials, Mahatma Gandhi University, Kerala 686560, India

© Springer Nature Switzerland AG 2022

K. Upadhyay et al. (eds.), *Hybrid Phosphor Materials*, Engineering Materials,
https://doi.org/10.1007/978-3-030-90506-4_12

1 Introduction

The biomaterials such as polymers, metals, ceramics and composites are used in the biomedical applications for the treatment of various diseases. There are different types of polymers are established in the biomedical field because of its improved biocompatibility and biodegradability. In the biomedical applications, these biomaterials are used in the field of drug delivery, drug targeting, imaging, theranostics. There are several polymer based drug delivery systems which are available commercially and also few are clinically approved for the medicinal use [1–5].

The inorganic biomaterials which are used for the biomedical applications such as minerals, metals, metal oxides, glasses, ceramics and other inorganic components. These type of materials have number of advantages than the organic materials which includes mechanical, thermal, magnetic, optical properties and the porous structures [6]. There are also other class of biomaterials which is called as hybrid biomaterials or functionalised biomaterials which contains a mixture of organic and inorganic materials used for the biomedical applications [7, 8]. The inorganic nanoparticles such as gold, iron oxide nanoparticles, carbon dots, quantum dots etc. is easily dispersible in the water with the organic polymers for the surface modification. This type of hybrid biomaterials are used for the diagnostic and therapeutic purposes. Moreover, this type of hybrid materials leads to prepare a novel therapeutic molecules which can be used for imaging because of the excellent properties of inorganic nanoparticles and the surface modification. For fabricating bone graft materials the hybrid biomaterials were used which contains the inorganic ceramic nanoparticles along with the polymer nanocomposites [9, 10].

These hybrid materials containing the organic polymer and the inorganic materials are used particularly in the manufacturing of pharmaceuticals such as drug delivery carriers, scaffolds for tissue engineering etc., and medical devices such as dental implants, vascular stents etc. The organic/inorganic hybrid biomaterials are classified as nanoparticles and nanocomposites and these materials were prepared by many synthesis methods [11]. The reported methods are complex and difficult to process in an industrial level whereas the current scenario demands simpler, cost effective and also requires reproducibility. In addition, there are also some studies they are in continuous efforts to develop a novel class of hybrid materials by overcoming the drawbacks and limitations of the already existing methods. As it is used for the biomedical applications, it should be used safely by all for the clinical purposes. So, it is very important to use the biocompatible materials and also the *in-vivo* studies are very important to know the pharmacodynamics and pharmacokinetic behaviour of the molecules. Moreover, the interaction studies should be performed with the biological cells, tissues and proteins to understand the complexity and nature of the biomaterials [12, 13].

The hybrid biomaterials containing organic and inorganic nanomaterials were used for the drug delivery applications with different imaging concepts. This approach can also be useful for the theranostic applications for the treatment of various diseases. Therefore, this approach represents a novel strategy for the cancer

immunotherapy with the application of hybrid biomaterials. And also, the very novel artificial intelligence is an emerging technology which can contribute in developing personalised biomaterials with the mixture of polymer and inorganic materials. Thus, multidisciplinary approach by involving experts in various fields from biotechnology, medicine, physics, chemistry, pharmacy professionals are necessary for the clinical development of hybrid nanomaterials [14].

2 Organic/Inorganic Hybrid Nanomaterials

The organic/inorganic hybrid nanomaterials can be divided into two groups based on their interaction between the organic and inorganic moieties. The hybrid materials interacts very strongly by formation of covalent bonds or ionic bonds between the organic and inorganic components. This type of materials comes under type 2 hybrid materials in which they can be used to synthesise new materials from alkoxide, minimises the separation of phases and easier to identify the interface between the organic and inorganic components. The type 1 materials are classified as the hybrid materials which interacts with the organic and inorganic components very weakly by the van der Waals, hydrogen and electrostatic bonds. These type of hybrid materials were divided into hybrid nanoparticles and hybrid nanocomposites. The hybrid nanoparticles consists of organic and inorganic nanoparticles or nanomaterials where the hybrid nanocomposites consists of organic and inorganic components which are larger than or in the micro scale. Based on the bonding strength and the process through which they are formulated, these kind of materials were further divided into two different classes [15, 16].

2.1 Hybrid Nanoparticles

Generally the nanoparticles are in the size range of 1–100 nm which can be of organic or inorganic materials. This category of nanoparticles affords a wide range of opportunities to examine the material properties with respect to the particle size. For the biomedical applications, mostly the metal groups consists of Au, Ag and Cu nanoparticles were used because of their unique optical, catalytic and electrical properties based on their size [17, 18]. This kind of nanoparticles differ completely from the category of nanocomposites or bulk materials which completely depends on their shape, size, distance and the nature. If these nanoparticles has to be used in the bioapplications it is very important that these particles should be completely dispersed in the aqueous phase. They should have very good chemical stability and it also should be devoid of oxidation or sintering (avoidance of degradation process). To make it stable the polymer stabilizers were used in the synthesis of inorganic nanoparticles in which it improves the dispersion in the aqueous phase and thereby improving the

chemical stability. Moreover, these hybrid nanoparticles also improves the processability and biocompatibility of the materials by surface modification process. These kind of nanoparticles have the unique characteristics such as it can behave as both inorganic and organic nanomaterials. Therefore, this type of hybrid nanoparticles could be useful in different kinds of biological applications which also includes imaging, photodynamic therapy. Image assisted delivery, drug delivery applications [19–21].

2.2 Hybrid Nanocomposites

Generally the nanocomposites are combination of organic and inorganic nanomaterials. This type of nanocomposites consists of homogenous and heterogenous structures of organic and inorganic materials. Each organic and inorganic material domains are in the range of nanometer scale. Because of the synergy between the organic and inorganic nanomaterials they are considered to be the stronger hybrid nanocomposites. The physicochemical properties of the hybrid nanomaterials depend upon their nature and contents of the individual components of the organic and inorganic materials. When compared to the individual organic and inorganic components, the hybrid nanocomposites have very good mechanical and thermal stability. Moreover, the physicochemical properties (magnetic, electrical, redox) of the hybrid nanocomposites were controlled by the inorganic components because of their porous network. These porous nanostructures of the hybrid materials were used as a suitable candidate for the drug delivery applications. In addition, the hybrid nanocomposites as scaffolds can also be used in tissue regeneration and cell therapy. The porous structures of the hybrid nanomaterials are useful for encapsulation of osteoinductive components which stimulate the cells differentiation for the regeneration of tissues. For example, the hydrogels containing organic and inorganic materials that can be used in an extensive range of biomedical applications [22]. The organic and inorganic hybrid nanocomposites are categorised as matrix materials and hydrogels which are explained in detail below.

2.3 Hybrid Nanomaterials

The studies prove that the researches have utilised the both organic and inorganic nanoparticles for the biomedical applications. To achieve the desirable properties, the position, design and arrangement of individual nanoparticles should be controlled to use in the different fields. There are various synthetic methods were used and they are self-assembly, surface modification, physical blending, metal–organic frameworks (MOFs) and *in-situ* deposition. These methods are utilised to obtain the desired physicochemical properties by modifying the surface properties and thereby controlling its arrangement. The surface incompatibility between the polymer materials and

nanoparticles can be overcome by introduction of polymer or small molecules on the surface of the nanoparticles and this process is called as surface modification. This process improves the nanoparticles dispersion in the polymer matrix and also facilitates the modifications in the matrix which is useful for the wide range of applications [23, 24]. There are several methods to control the aligning of nanoparticles with respect to their physicochemical properties. Hence, there are different kinds of hybrid nanoparticles have been formulated to control the arrangements of nanoparticles using metal organic frameworks (MOFs) and self-assembly methods. Likewise there are methods to develop nanocomposites with the polymer matrix for the improvement of mechanical and other physicochemical properties. The nanoparticles should be well dispersed in the polymer matrix with a high stability to get the desired nanocomposites with the well-defined properties [25, 26]. The homogenous hybrid nanocomposites were categorised into two major classes such as physical and chemical. The synthetic methods of preparing hybrid nanocomposites by means of physical means involves solution and melt blending process and chemical process involves the *in-situ* deposition methods.

2.3.1 Hybrid Nanoparticles

The surface properties of the inorganic nanoparticles such as the colloidal stability and biocompatibility were not suitable for the biomedical applications. Because of their high surface area to volume ratio, the inorganic components are susceptible to the formation of agglomerates and aggregates. Thereby these inorganic nanoparticles undergoes a very rapid clearance by the reticuloendothelial system (RES). So to improve the biocompatibility, circulation time and stability of the inorganic nanoparticles, it is very important to modify the physicochemical properties by coating with organic polymers. And also, this section deals with the methods like surface modification, metal organic frameworks (MOFs) and self-assembly for polymers hybridization and stabilise the inorganic nanoparticles [27, 28].

Surface Modification Method

The inorganic nanoparticle surfaces could be improved by two different kinds of methods consists of adsorption (physical) and grafting (chemical) methods (Table 1). The surface modifications by physical methods were attained by the surface adsorption and reaction with the small molecules. And the surface modifications by chemical methods were achieved by the grafting of polymer molecules in which the functional groups acts as a site for chemical bonding (Fig. 1). The most common agent used for the inorganic nanoparticles are the silane coupling agents which has bifunctional groups forms a bridge/bond between the two phases [29]. The silane coupling agent contains R–Si-$(OR)_3$ in which the R = CH_3O–, CH_3CH_2O– acts as an anchor and it reacts with the –OH groups present on the surface of the metal oxides (M) forming a Si–O–M bond. The R forms an alkyl bridge between the functional group

Table 1 Synthesis of hybrid nanomaterials by surface modification method

	Polymer	Inorganic material
Hybrid nanoparticles (surface modification)	APTES, TEOS	$SrAl_2O_4:Eu^{2+}$ [34]
	DSPE-PEG	Fe_3O_4 [35]
	Poly(*N*-isopropyl acrylamide)	AuNPs [36]
	PMAGal-b-(PMAGal-co-PPyMA)	β-Fe_2O_3 [37]
	Poly(2-(methylsulfonyl)ethyl acrylate)	Fe_3O_4 [38]
	PEG-PEI-Chitosan	Fe_3O_4 [39]
	Aminosilane, PEG	Fe_3O_4 [40]
	Carboxyl methylated PVA	Fe_3O_4 [41]

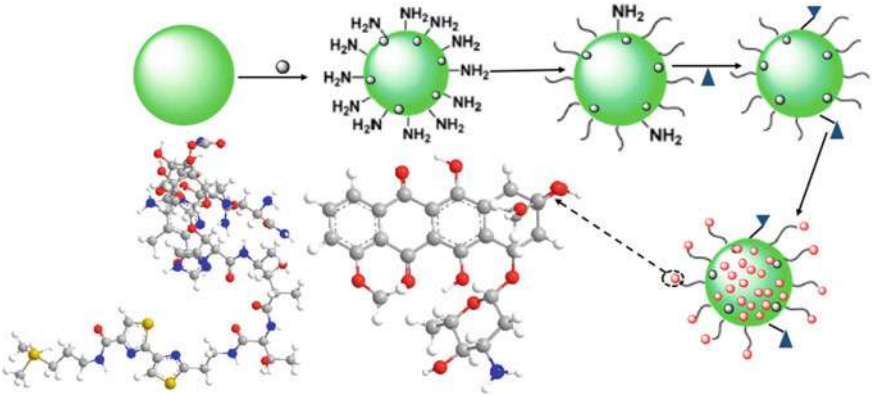

Fig. 1 Surface modification of nanoparticles for biomedical applications (reprinted with permission from MDPI nanomaterials [42])

and the silicon atom through a condensation reaction. The surface modification by the silane molecules undergoes by the four different types and they are (i) the alkoxyl groups should be hydrolysed in the water for the liberation of alcohols and producing a reactive silane molecule, (ii) self-condensation of silanol groups takes place during hydrolysis, (iii) the reactive silane groups were adsorbed by means hydrogen bond formation in the hydroxy groups of the metal oxide surfaces, (iv) and these molecules liberates water during heating then the remaining silane groups condensed with metal oxide groups through the conversion of hydrogen bonds into covalent bonds. Chen et al. prepared a nanoscintillator which is silica coated for the photodynamic therapy. For the synthesis of nanoscintillator, nanoparticles SrAl2O4:Eu^{2+} (SAO) were coated with silane precursors such ad tetra ethyl orthosilicate (TEOS) and aminopropyltriethoxysilane (APTES). These nanoscintillator which are coated with silica have a large number of functional amine group results in positively charged surface [30].

Table 2 Synthesis of hybrid nanoparticles by self-assembly

	Polymer	Inorganic material
Hybrid nanoparticles (self-assembly)	Diethylene glycol Tetra thiafulvalene	AuNPs [39]
	PEG-PBLA-Ce6	Fe_3O_4 [8]
	Gd-DTTA, polystyrenesulfonate	$[Ru(bpy)_3]Cl_2$ [48]
	NH_2–Leu–Aib–Tyr–OMe peptide	AuNPs[49]
	Diethylene glycol dioxynaphthalene	AuNPs [50]

Chemical method is another approach for the surface modification of nanoparticles. It includes the grafting of polymers to the surface that improves the functional characteristics and modifies the surface morphology of the inorganic nanoparticles [31]. There are two methods for chemical grafting and the first one is that it links the polymers with the surface of the inorganic nanoparticle. This process tends to low grafting density because of the reactivity of the functionalised polymer chains. The second approach is that to increase the grafting density the surface initiated polymerisation process is involved. This process includes radical, cationic, anionic polymerisation methods which involves the distribution of the functionalised grafted polymers from the nanoparticle surface. The monomers which are polymerised from the inorganic nanoparticle surface in the grafting method. They will easily penetrate the aggregated nanoparticles which reacts on the activated surface on the polymer because of its low molecular weight. The density and the thickness of the polymer could be controlled by the rate of polymerisation and the nature of monomer. In a study they have grafted poly (2-(methylsulfonyl) ethyl acrylate) using 12-(2-bromoisobutyramido) dodecanoic acid on the surface of superparamagnetic iron oxide nanoparticles through the polymerisation reaction [32, 33].

Self-Assembly

This method involves the controlling of accumulation of inorganic nanoparticles by improving their properties in a controlled way (Table 2). The nanoparticles or other distinct constituents in which they unite together via directly or indirectly through the specific interactions [43, 44]. The block copolymers play an important role in self-assembly of nanoparticles because ABA triblock chemical structures along with the nanoparticles provides well-defined interactions. Through the specific interactions these block copolymers self-assemble into the ordered nanostructures. Those specific interactions occurs by the block copolymers and they are dipole–dipole, covalent, non-covalent, steric hindrance, columbic attraction or repulsion. Balancing the hydrophilic and lipophilic balance (HLB) of the block copolymer has a great influence on the self-assembly of nanoparticles. Moreover, by controlling the HLB of the block copolymer, the morphology of the self-assembled nanoparticles can be maintained. In addition to the block copolymers, the inorganic nanoparticles

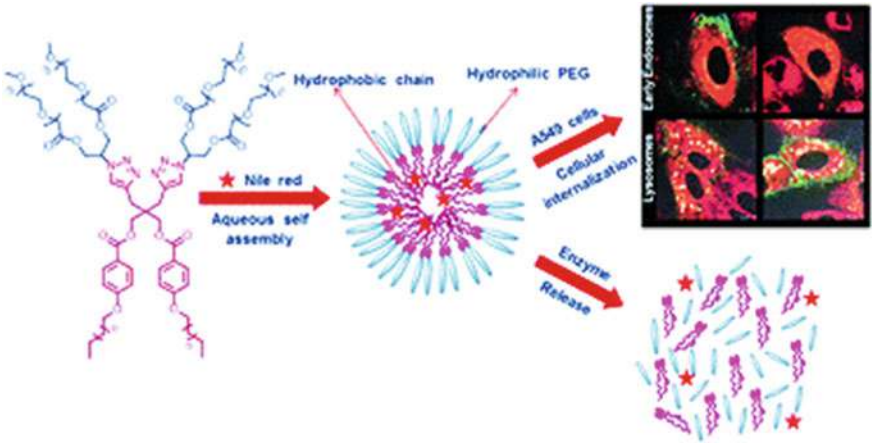

Fig. 2 Self-assembly nanomaterials for biomedical applications (reprinted with permission from RSC advances [51])

are also used for the functionalization or as the templates to provide stable self-assembled nanostructures. Mostly, the magnetic nanoparticles were combined with the block copolymers to produce a well-defined nanostructures. In a report, they have used pH sensitive magnetic nanoparticles (PMNs) as a functionalising agent on the block copolymers to obtain a self-assembled iron oxide nanoparticles. PMNs exhibited improved imaging for targeting the cancer cells through the self-assembly of iron oxide nanoparticles. This is because of the selective targeting ability of the PMNs which also showed photodynamic activity which kills and prevent the growth of cancer cells (Fig. 2) [45–47].

Metal–Organic Frameworks (MOFs)

The MOFs has the ability to protect the active moieties from degradation and also it improves the drug loading efficiency. Because of their even porosity, it has a good pore volume and shell surface to increase the drug loading capacity. And also, the metals are connected by the strong coordination bonds with the multidentate organic ligands which results in the high mechanical and thermal stability [52]. There are various functional materials such as graphene based materials, carbon nanotubes, quantum dots, metal nanoparticles and biomolecules were combined to form the hybrid nanomaterials (Table 3). So, it will be easy for the drug molecules in which it can be loaded in the MOFs which acts as a drug carriers to target the disease region and also it improves the stability. This leads to the commercialisation of few nanodrugs such as Abraxane, Ambisome and Doxil [53, 54]. In addition, MOFs can be attained by the single-component nanostructures with good physicochemical properties, intriguing morphological structures, improved BET (Brunauer–Emmett–Teller) surfaces and high porosity. Moreover, the fabrication methods for the MOFs

Table 3 Synthesis of hybrid nanomaterials by MOFs method

	Polymer	Inorganic material
Hybrid nanoparticles (metal organic frameworks (MOFs))	Terephthalic acid, 1,3,5-tris(4-carboxyphenyl)benzene	Zn_4O cluster [63]
	BTC	Fe_3O trimer [64]
	Naphthalene-2,6-dicarboxylic acid	Zinc nitrate [65]
	Lipoic acid, PEG	Zirconium nodes, AuNPs
	AzTPDC	Zinc nitrate [66]
	2-methylimidazole	Zinc nitrate [67]
	Amino-TPDC	$Zrcl_4$ [68]

include solution, diffusion and hydrothermal techniques [55]. The solution method is the most widely used method in which it contains organic ligands, metal elements and other materials in a solvent were stirred at a specified time and temperature. The purification process involves the filtration method in which the solvent is evaporated and whereas the diffusion method involves the long reaction process under mild condition which can be of liquid, gas or gel diffusion. Firstly, the gel diffusion method is a process in which the organic ligands are dispersed in the gel containing metal ion solution which forms a crystals of MOFs. Secondly, in the liquid diffusion process the organic ligands are dissolved in the solvent containing metal ions to form MOF crystals. Thirdly, the gas diffusion involves the process of mixing metal ion with the volatile organic ligand solution to form MOFs. An another method of preparing MOFs is the hydrothermal method in which it can be obtained by involving the organic ligands, metal ions, solvents and the other required materials in the polytetrafluoroethylene liner. These materials are kept in the high temperature reactor for the initiation of reaction process to form MOFs [56–59]. In a study, they have used an autophagy inhibitor 3-methyladenine (MA) in the MOFs (zeolitic imidazole framework) which has high drug loading capacity and they found that it has a strong anticancer activity. The MOFs have high encapsulating efficiency, particles with uniform size and shape, exceptional biocompatibility and high stability. Furthermore, the MA-ZIF exhibits strong anticancer effect by inhibiting the autophagy in the tumour bearing mice and also delivers the drug in a controlled manner with improved permeability. In addition, because of the improved permeability and retention, the active molecule accumulates in the tumour tissue more than normal because of the angiogenesis in the tumour tissue (Fig. 3) [60–62].

2.4 Hybrid Nanocomposites

The hybrid nanocomposites are intended to increase the optical, magnetic, electrical, rheological and mechanical properties. In this type of nanocomposites, the inorganic nanoparticles such as metal and metal oxides were incorporated in the polymer

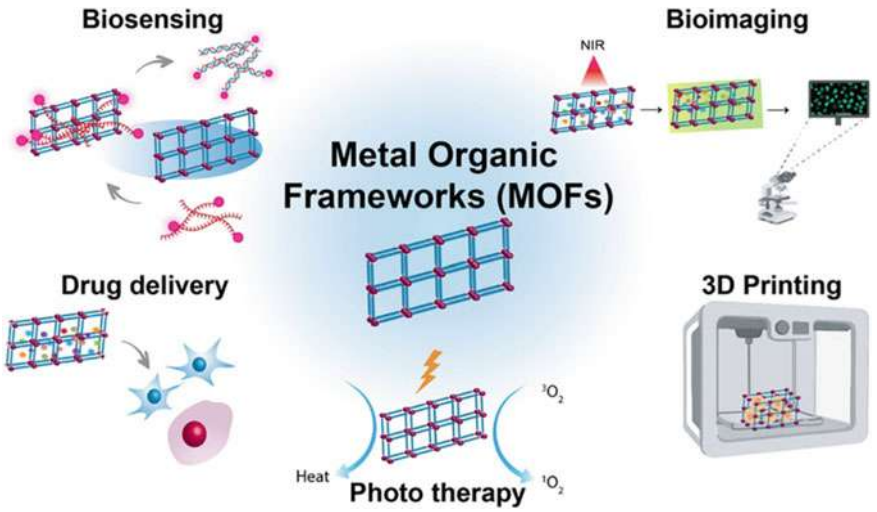

Fig. 3 Biomedical applications of MOFs (reprinted with permission from Wiley Interdisciplinary Reviews: Nanomedicine and Nanobiotechnology [69])

matrices. The only disadvantage in this type of hybrid nanocomposites is that it undergoes agglomeration if there is any inadequate distribution of nanoparticles in the polymer matrices. And also, this may leads to affect the physico chemical properties of the nanocomposites. Therefore, to increase the dispersion behaviour, the surface modification process is followed to create a strong repulsion between the nanoparticles on the polymer matrices. There are different methods were developed to get a well-defined characteristics to obtain an improved physico chemical properties [29].

2.4.1 Physical Blending

The conventional method for the preparation of hybrid nanocomposites is physical blending and this consists of solution and melt blending. Solution blending involves the direct mixing of polymer and inorganic nanoparticles in the solvent [29]. Then the hybrid nanocomposites is obtained by precipitation, filtration and removal of solvents. The main disadvantage of the solution blending method is that identifying a suitable solvent, its removal and the toxicity of the solvents. In a study, they have prepared polystyrene-zinc oxide nanocomposites by solution blending method and then they were casted as film. Firstly, the ZnO nanoparticles dissolved in the dimethylacetamide and polystyrene with vigorous stirring. After mixing, the obtained polystyrene-zinc oxide mixture were casted into films at 90 °C to get the nanocomposite film. This technique evenly distribute the ZnO nanoparticles in the polymer matrix and it also has improved stability [70].

Table 4 Synthesis of hybrid nanomaterials by physical blending method

	Polymer	Inorganic material
Hybrid nanoparticles (physical blending)	PMMA, PVPh	POSS [73]
	Polydopamine	AuNR [74]
	PS	ZnO [70]
	PP	SiO_2 [72]
	Polybenzoxazine	POSS [75]
	OBT, OBA	POSS [76]

2.4.2 Melt Blending

This technique is a very simple, cost-effective method which effectively removes the toxic solvents. In this method, the inorganic nanoparticles are dispersed in the polymer which is melted by the extrusion technology [71]. Because of the high viscosity of the polymers, it's difficult to regulate the dispersion of inorganic nanoparticles in the polymer matrix. In a study they have used polypropylene incorporated with nano silica by melt blending method with the addition of maleic anhydride which forms an amino functionalised polypropylene silica nanoparticles (Table 4). The grafting was done by condensation method by the incorporating maleic anhydride functionalised polypropylene and amino functionalised silicon dioxide. Then these blended mixture is dispersed in the polypropylene matrix using Haake Polylab at 140 °C which is refluxed with xylene and completed the blending at 200 °C. The rheological results proved that it increased the melt strength of polypropylene [72].

2.4.3 *In-Situ* Deposition

The *in-situ* deposition technique is one of the simple and effective method for dispersing the inorganic nanoparticles in the polymer matrix (Table 5). In this method the nanoparticles are uniformly distributed inside the polymer matrices and this method does not involves the usage of solvents [71]. Firstly, the inorganic nanoparticles are mixed with the monomer and this mixture is incorporated into the polymers through the liquid or the gas phase. The *in-situ* deposition method are prepared by

Table 5 Synthesis of hybrid nanomaterials by *in-situ* deposition method

	Polymer	Inorganic material
Hybrid nanoparticles (*in-situ* deposition)	Polylactic acid	AgNPs, GO [78]
	Polyaniline	MnO_2, Cr_2O_3 [79]
	Polypyrrole, Polyaniline	Fe_3O_4 [80]
	BisGMA-TEGDMA resin mixture	Silver 2-ethylhexanoate [77]
	Polyindole, PVA	$ZnFe_2O_4$ [81]

the methods such as stirring, ultrasonication and UV curing (photo initiation) which contains the blend of inorganic nanoparticles with the monomers. In addition, the hybrid nanocomposites or the polymer which cannot be processed under the melt mixing or the solution method can be fabricated by the *in-situ* deposition method [29]. In a study by Cheng et al., the preparation method involves the mixing of crosslinked dimethacrylate and silver nanoparticles through the photo initiated free radical polymerisation. The silver 2 ethyl hexanoate is mixed with the resin mixture BisGMA-TEGDMA (bisphenol A glycerolate methacrylate-triethylene glycol dimethacrylate) and this mixture undergoes photo polymerisation reaction using visible light. The X-ray photoelectron spectroscopy (XPS) and the morphological analysis proved that the silver nanoparticles are dispersed on the surface of the polymer matrix [77].

3 Biomedical Applications

3.1 Detection and Treatment of Cancer

Hybrid nanoparticles contain two or more different materials in the nanometer dimension, which will have the advantages of both individual nanoparticles (Table 6). In the medical field it is believed that this material will have superior properties of individual nanoparticles and is very useful in cancer detection and treatment [82, 83]. Many nanoparticles are manufactured which have the ability to circulate in the blood stream and detect cancer causing tumors [83]. Nanoparticles are used as a drug delivery agent as it can carry comparatively higher drug loads and deliver at targeted tumor sites [84]. Liposomes based on lipid bi layer have high load carrying capability combined with minimum toxicity [85]. Similarly the inorganic mesoporous silica nanoparticles were used and were proven to have targeted drug delivery properties [86]. Nanoparticles can also be engineered to produce thermal energy from optical or radio frequency sources and can be used in photothermal therapy to destroy malignant tumors (Fig. 4) [87]. The nanoparticles produce outstanding results in the treatment of cancer, but the single functionality limits their use; as a result a synergistic multi component system is required to detect, monitor and treat malignancies that arises [88, 89]. This is where the hybrid systems come into play where multiple nanostructures and components are integrated into a single component to form a therapeutic and diagnostic system commonly referred to as theranostic device [90–93].

The functional nanostructures which are used as a contrast agent, fluorescence imaging etc. are incorporated onto the surface to the another inner compartment of another structural nanocomponents[94]. These structural nanocomponents could be a polymer, liposome, micelle etc. that serve as a drug carrier or components like gold nanoparticles that can be used in photothermal therapy [95, 96]. These hybrid nanostructures when administered intravenously should circulate in the blood stream for more than two hours and have the ability to be readily filtered out by the

Table 6 Hybrid nanostructure based systems for theranostic applications

Nanocomponent	Functional nanocomponents	Function	Target cells/area	Referencess
Phospholipid liposome	Gold NP	Plasmonic investigation, optical imaging	Jurkat cells	[144, 145]
DSPC/DPPC phospholipid liposome calcein drug	Gold NP	Light triggered drug release	ARPE 19 cells	[146]
Phospholipid liposome [6-carboxyfluorescein drug]	Gold NP	Photothermal drug release	NA	[147]
Phospholipid liposome [xylenol orange sodium salt drug]	Superparamagnetic iron oxide nanodots	Ultra sound triggered MRI	NA	[148]
Bilayer decorated magneto liposomes	Hydrophobic superparamagnetic iron oxide nanoparticle	NP heating using AC electromagnetic fields		[149]
PEGylated liposome JPM 565	Ferrimagnetic iron oxide	Non-invasive drug delivery	MMTV-PyMT tumour	[150]
Phospholipid liposome	Quantum dot	Optical imaging	A549 lung cells	[151]
Phospholipid liposome doxorubicin	NA	NA	MCF-7/HER 2 cells	[152]
Polybutyl cyanoacrylate microbubbles/paclitaxel	Iron oxide nanoparticles	Magnetic resonance and ultrasound imaging	MLS human epithelial ovarian cancer cells	[153]
MAL-PEG-PLA block MPEG-PLA/doxorubicin	Superparamagnetic iron oxide nanoparticles	Magnetic resonance imaging	SLK cells, Avβ3 integrins	[154]
Phospholipid micelle	Oleic acid coated magnetic nanocrystal		MKN-74	[155]
PEG-PAsp(DIP)-CA/Paclitaxel	Quantum dot	Optical imaging	Bel 7402 human carcinoma cells	[156]
PEG-phospholipid micelle	Magnetic nanoparticle, TOP coated quantum dot	Optical and magentic resonance imaging	MDA-MB-435 human cancer cells	[157]
PS(16)-b-PAA(10)/doxorubicin	Magnetic nanocrystal	Optical imaging	4T1 cancer cells	[158]
Adenovirus	MnMEIO magnetic nanoparticle	Gene delivery	CAR positive cells	[104]
HIV-1	DNA-Au nanoparticles	Photothermal imaging	NA	[159]

(continued)

Table 6 (continued)

Nanocomponent	Functional nanocomponents	Function	Target cells/area	Referencess
PLGA/methotrexate	RGD attached gold nanoparticles	Photothermal healing	A 431 carcinoma cells	[160]
PS-PLGA/paclitaxel	QD and Iron oxide nanoparticles	Optical and magnetic resonance imaging	LNCaP prostrate cancer cells	[161]
Magnetic gold nanoshells and PEG linker	Iron oxide nanoparticles	Magnetic resonance imaging	SKBR3 and H520 cells	[162]
SWNT/cisplatin	Quantum dots	Optical imaging	EGFR antibody	[163, 164]

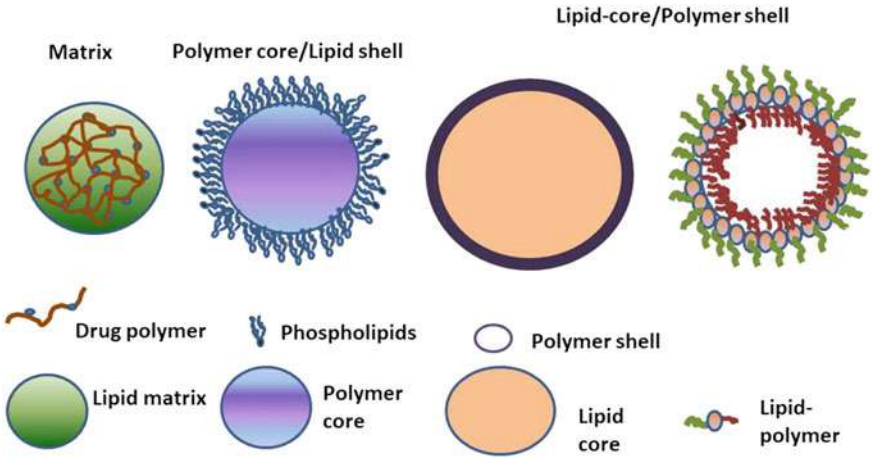

Fig. 4 Polymer-Lipid hybrid nanocarrier system showing the monolithic polymer matrix and the core shell type (redrawn from [143])

liver and kidneys [97]. The theranostic agents provide both diagnosis and treatment with the same material. A hybrid nanoparticle composite of doxorubicin and calcium carbonate hybrid nanoparticles were used for chemotherapy and cancer related imaging applications [98]. The enhanced permeability and retention effect causes the nanomaterial to selectively attach to the tumor tissues [99]. In the *in-vivo* studies the hybrid nanomaterial composites showed excellent anticancer properties. Antigens were encapsulated inside nanoparticles and delivered to improve the B and T cell responses. These materials can directly act on antigen presenting cells thereby triggering the activation of antigen specific T cells [100].

A uniform core shell spherical nanoparticles made of bovine serum albumin and polymethylmethacrylate core was made. This protein hydrophobic polymer conjugate functions as a drug delivery agent and possess additional features owing to their amphiphilic molecular structures and island growth. In the *in-vivo* studies camptothecin encapsulated BSA/PMMA nanohybrid material showed enhanced anti tumor activity [101]. Kang et al. prepared gold nanoparticle based vaccines where conjugated with a recombinant ovalbumin for the analysis of CD^{8+} T cell response and delivery into lymph nodes [102]. The *in-vivo* mice study showed remarkable tumor inhibition properties and a higher interferon gamma production. The study also showed the importance of nanoparticle size in the therapeutical applications. In another study, Zhang et al. constructed a novel mannose targeting LPNP vaccine system based on a biodegradable polymer PCL-PEG-PCL and cationic lipid DOTAP for the delivery of an antigen and a toll like receptor (TLR 7/8). The vaccine had a hydrophobic inner core of PCL-PEG-PCL with imiquimod, a lipid layer, a cationic DOTAP lipid and a mannose targeting moiety. The vaccine delivery with Monophosphoryl lipid A (MPLA) and imiquimod (IMQ) with a hybrid nanoparticle system showed promising antigen delivery [103].

Yong Min Huh et al. developed adenovirus based hybridised magnetic nanoparticle system based on manganese doped iron oxide that had the capabilities of targeted infection and magnetic resonance imaging. The adenovirus was selected as it showed specificity to the cells with overexpression of coxsackievirus receptor and outstanding gene delivery capability [104]. Polydopamine coated nano star shaped gold nanoparticles showed improved photothermal efficiency. When doxorubicin were administered along with polydopamine coated gold nanoparticle the material showed remarkable antitumor immune response. The *in-vivo* studies also showed a long term anti tumor immunity response [105]. In another study by Wu et al. gold nanoflowers with Chlorin e6 and a polydopamine coating was used in the photothermal therapy applications. The material showed lower cytotoxicity and phototoxicity and had a combined effect for killing cancer cells [106]. A poly (ethylene glycol)/ poly (ethylene imine) co grafted iron nanoparticles were prepared and shown to have improved tumor resistance. This magnetic hyperthermia based material produced tumor associated antigens and elicited anti tumor immune response [107].

Photosensitizers used in the non-invasive photodynamic therapy has low selectivity for tumors and also aggregates under physiological conditions [108]. Lanthanide ion doped upconversion nanoparticles acts as a transducer by up converting absorbed near infra-red light to the high energy visible light. A highly efficient NIR-triggered PDT system based on $LiYF_4$: Yb/Er upconversion nanoparticles were coupled with a photosensitizer of a β-carboxyphthalocyanine zinc (ZnPc-COOH) molecule by a direct electrostatic interaction, which produced singlet oxygen ($^1O_2$). This helps in the deep tissue penetration of visible light to treat deep tumors. The infra-red photons absorbed by lanthanide ions in a host lattice produces high energy photon [109]. Nano scintillated ionizing radiation was used which overcame the issue of low skin penetration depth in the photodynamic therapy [110]. The ionizing X-rays showed tissue penetration which was multiple times deeper than

infrared radiations. The interaction of high energy X ray photons with nano scintillator occurs through a cascading of photo electric effect and Compton scattering that generates many electron hole pairs [111]. This trapping of electron and hole creates luminescence and leads to the production of $^1O_2$ which is cytotoxic in nature [112]. The microenvironment of the tumor plays a big role in the efficacy of the photodynamic therapy as a low oxygen microenvironment increase tumor metasis and promote resistance to chemotherapy [113, 114].

Perfluorocarbon based oxygen nanoparticles were delivered to improve the hypoxic tumor microenvironment even though the efficiency is quite less as the oxygen quantity is less [115]. Human serum albumin, chlorin e6, and manganese di oxide nanoparticles (HSA-MnO_2-Ce6) were prepared to overcome tumor related hypoxia and treat bladder cancer by a photodynamic therapy. Manganese dioxide nanoparticles reacted with hydrogen peroxide improved the PDT efficiency by the production of O_2. These were performed in an *in-vivo* mouse experiment and showed good PDT efficiency [116]. Hyperthermia is another factor that causes destruction of cancer cells [117]. The thermal gradient that develops will be maximum at the body surface and reduces as it penetrates the tissues. Indocyanine green (ICG) dye in combination with a nanocarrier is used to improve its photothermal efficiency. These was shown in an *in-vivo* study when the ICG nanohybrid particles targeted large tumor particles. An Indocyanine green, 1,2 distearoyl-sn-glycero-3-phosphethanolamine-*N*-[methoxy (polyethylene glycol) coated iron oxide nanoparticles were constructed for dual modal imaging as a theranostic agent. The hybrid material showed excellent photostability and temperature increment upon treatment with NIR laser [118].

A gene editing nanohybrid system prepared by Mout et al. had a CRISPR/Cas9-ribonucleoprotein with cationic arginine gold nanoparticle based system. The system showed an improved cytoplasmic delivery for the gene editing system [119]. A nanohybrid containing PEGylated triangular gold nanoparticles conjugated with a peptide P_{75} was prepared (TGN-PEG-P_{75}). The system had an affinity towards epidermal growth factor receptor and is overexpressed in non-small cell lung cancer (NSCLC) cells due to the interaction between anti-epidermal growth factor receptor (EGFR) and the peptide. The material behaved as an efficient theranostic device showing visual guidance and inhibition of the NSCLC cells by the photothermal therapy effect [120]. A 3D bioprinting method was adopted to produce nanohybrids of PEGDA, laponite and hydroxyapatite. The material was intended for usage as a bone scaffold [121]. A nanocomposite scaffold made of 3D printed porous calcium phosphate polylactic acid conjugated with human bone morphogenetic protein-2 (rhBMP-2) showed delivery of both rhBMP-2 and calcium ions and promoted differentiation of stem cells [122].

In another study functionalized graphene oxide (GO) nanosheets that has angiogenic genes incorporated into GelMA hydrogel showed good revascularization in the diseased heart [123]. Also, graphene oxide and reduced graphene oxide embedded PEG/PA hydrogel showed good chondrogenesis and adipogenesis [124]. Liu et al. prepared crosslinked functionalized graphene oxide acrylate (Goa) with CNT and poly (ethylene glycol) acrylate with oligo (polyethylene glycol) fumarate

hydrogel. The material showed excellent biocompatibility as enhanced proliferation and spreading of PC12 cells were observed on the conducting hydrogels [125]. Gold nanoparticles embedded in GelMA to form hybrid nanostructures and showed improved cell matrix adhesion. The amount of gold nanoparticles decides the proliferation and osteogenic differentiation of the stem cells [126].

A hybrid nanostructure based scaffold made of PLGA/$Mg(OH)_2$ showed good anti-inflammatory properties. In the *in-vivo* study using a mouse model the hybrid material showed regeneration of renal glomerular tissue and had a very low inflammatory response [127]. Starch modified hyperbranched polyurethane with carbon dot silver nanomaterials based hybrid structures shows improved thermal, mechanical properties along with high biocompatibility and infection resistance [128]. Owing to these features the material can be used as a material for self-expandable stents. A vascular stent made of cobalt-chromium, Sirolimus loaded PLGA with a surface modified coating of $Mg(OH)_2$ nanoparticles showed less inflammatory response by in stent restenosis as part of intimal hyperplasia [129]. Improving the endothelialisation is one of the most sought after way to improve the efficiency of the vascular stent implantation [130]. A collagen/gold nanocomposite material showed excellent biomechanical and thermal properties [131]. The *in-vivo* studies in a rat model showed excellent vascular regeneration, higher antifibrotic ability and anti-inflammatory responses. A polyhedral oligomeric silsesquioxane poly (carbonate-urea) urethane nanocomposite was attached with anti CD34 antibodies to improve endothelialisation by capturing the endothelial progenitor cells. Thus this material can be used as an ideal coating for catheter stents due to its superior biocompatibility and biophysical properties [132].

Naturally occurring viral nanoparticles like cowpea mosaic virus and bacteriophage Qβ particles were linked with C60 fullerenes to improve their solubility. The bio conjugation was realised by a click chemistry involving poly (ethylene glycol) modified propargyl-O-PEG C60 units. This material had the potential to be used in photo activated tumor therapy applications [133]. A nanohybrid system comprising of a hydrophobic PLGA core loaded with fluorescent quantum dots and with a positive charged glycol chitosan shell. The loaded DNA was released as the pH of the system changes. An *in-vivo* study using a mouse model confirmed the transfection of DNA into the Langerhans cells present on the skin surface [134]. A treatment device for Rheumatoid arthritis was developed by making a methotrexate drug loaded PLGA with RGD conjugated gold half shell nanoparticles. The developed nanohybrid was injected into an arthritic mouse and the nanoparticles selectively adhered at the inflammation sites. The drug was delivered by a photothermal method after being exposed by near infrared radiation (NIR). The nanohybrid material showed excellent therapeutic efficiency even when smaller dosage of drug is used [135]. A ferromagnetic iron oxide nanoparticle prepared using saline crystal hydrate were encapsulated in a steric stable PEGylated liposome. The intracellular delivery of the targeted ferri liposome in an *in-vivo* mice mammary tumor cell was observed with a significant reduction in tumor growth [136]. A dumbbell like gold-iron oxide hybrid nanoparticles were prepared and coupled with Herceptin and platin complex. These material could be used as potential nanocarriers for theranostic applications [137].

In a study by Zhu et al. a bifunctional iron oxide silver ^{125}I heterodimers were prepared to be used as imaging modules. The $Fe_3O_4/Ag/^{125}I$ heterostructured radionuclide nanoparticles showed high radiolabeling combined with a low cell toxicity, where ^{125}I served as the contrast agent. The SPECT images of mice *in-vivo* study showed the nanoparticles were taken readily by liver and spleen [138]. An Ag–Fe_3O_4 heterodimer nanocomposite heterodimer system was prepared where nanocrystal sizes could be varied by the synthesis conditions. This material has the advantage for simultaneous two photon fluorescence imaging and magnetic manipulation [139]. A multimodal contrast agent's i.e. thiol modified gold nanocages and iron oxide nanoparticles were prepared for simultaneous T_1–T_2 contrast imaging. The prepared hybrid nanoparticles showed excellent biocompatibility with very less aggregation and has good contrast properties [140].

Li etc. prepared gold coated iron oxide nanoroses which can be used in optical imaging, magnetic resonance imaging, photothermal therapy, chemotherapy and aptamer based targeting. The anticancer drug doxorubicin is integrated with nanoroses and is released due to a rise in temperature when near infrared light is absorbed by the gold shell. The aptamers present on the surface provides efficient and selective drug delivery and imaging with high specificity [141]. A theranostic device made of Polystyrene which was embedded with superparamagnetic iron oxide nanoparticles and the drug paclitaxel was loaded in a poly (lactic-co-glycolic acid). The targeting was by conjugating nanocarriers with anti-prostrate specific membrane antigen. The detection studies and the nanocarrier binding activity was carried out in the LNCaP prostrate cancer cells. This material has the advantage of dual modality within the same nanosystem for cancer diagnosis and chemotherapy [142].

4 Conclusions and Clinical Prospects

The hybrid nanoparticle based systems have made significant development in the field of biomedical applications especially cancer therapy. These hybrid nanoparticles show significant function in *in-vitro* based studies, but once testing is done inside the body environment the behaviour of these materials change. Inside the dynamic body environment the nanoparticles interact with many cells, tissues, proteins and majority of them are cleared out from the body before reaching the targeted site. It requires careful engineering of the chemical and surface properties to improve the efficiency and residence time of these materials. The hybrid nanomaterials will have a combined size larger than individual nanomaterials and are designed in such a way so that they can accumulate preferentially at the tumor sites due to the enhanced permeation and retention (EPR) effect. The biggest challenge is that all the components of the hybrid system should work in tandem and coherently to achieve the desired biomedical function. All the materials individually and together should not elicit any adverse reactions and cause an immunological response. Thus it is imperative to have reliable and biocompatible material and the design and its *in-vivo* behaviour should be given considerable weightage.

References

1. Qiu, L.Y., Bae, Y.H.: Polymer architecture and drug delivery. Pharm. Res. **23**, 1–30 (2006)
2. Huebsch, N., Mooney, D.J.: Inspiration and application in the evolution of biomaterials. Nature **462**, 426–432 (2009)
3. Bobo, D., Robinson, K.J., Islam, J., Thurecht, K.J., Corrie, S.R.: Nanoparticle-based medicines: a review of FDA-approved materials and clinical trials to date. Pharm. Res. **33**, 2373–2387 (2016)
4. Allen, T.M., Cullis, P.R.: Drug delivery systems: entering the mainstream. Science **303**(80), 1818–1822 (2004)
5. Ramakrishna, S., Mayer, J., Wintermantel, E., Leong, K.W.: Biomedical applications of polymer-composite materials: a review. Compos. Sci. Technol. **61**, 1189–1224 (2001)
6. Nicole, L., Rozes, L., Sanchez, C.: Integrative approaches to hybrid multifunctional materials: from multidisciplinary research to applied technologies. Adv. Mater. **22**, 3208–3214 (2010)
7. Mir, S.H., Nagahara, L.A., Thundat, T., Mokarian-Tabari, P., Furukawa, H., Khosla, A.: Organic-inorganic hybrid functional materials: an integrated platform for applied technologies. J. Electrochem. Soc. **165**, B3137 (2018)
8. Ling, D., Park, W., Park, Y.I., Lee, N., Li, F., Song, C., et al.: Multiple-interaction ligands inspired by mussel adhesive protein: synthesis of highly stable and biocompatible nanoparticles. Angew. Chemie. Int. Ed. **50**, 11360–11365 (2011)
9. Liu, H., Webster, T.J.: Mechanical properties of dispersed ceramic nanoparticles in polymer composites for orthopedic applications. Int. J. Nanomed. **5**, 299 (2010)
10. Hong, Z., Reis, R.L., Mano, J.F.: Preparation and *in-vitro* characterization of scaffolds of poly (L-lactic acid) containing bioactive glass ceramic nanoparticles. Acta Biomater. **4**, 1297–1306 (2008)
11. Ates, B., Koytepe, S., Balcioglu, S., Ulu, A., Gurses, C.: Biomedical Applications of Hybrid Polymer Composite Materials. Elsevier Ltd (2017). https://doi.org/10.1016/B978-0-08-100785-3.00012-7
12. Tsuru, K., Hayakawa, S., Osaka, A.: Medical Applications of Hybrid Materials. Weinheim. Wiley-VCH Verlag GmbH & Co. KGaA, Weinheim (2007)
13. Sanchez, C., Shea, K.J., Kitagawa, S.: Medical applications of organic–inorganic hybrid materials within the field of silica-based bioceramics. Chem. Soc. Rev. **40**, 596–607 (2011). https://doi.org/10.1039/c0cs00025f
14. Chimene, D., Alge, D.L., Gaharwar, A.K.: Two-dimensional nanomaterials for biomedical applications: emerging trends and future prospects. Adv. Mater. **27**, 7261–7284 (2015)
15. Adnan, M.M., Dalod, A.R.M., Balci, M.H., Glaum, J., Einarsrud, M.-A.: *In-situ* synthesis of hybrid inorganic–polymer nanocomposites. Polymers (Basel) **10**, 1129 (2018)
16. Sanchez, C., Ribot, F., Lebeau, B.: Molecular design of hybrid organic-inorganic nanocomposites synthesized via sol-gel chemistry. J. Mater. Chem. **9**, 35–44 (1999)
17. Daniel, M.-C., Astruc, D.: Gold nanoparticles: assembly, supramolecular chemistry, quantum-size-related properties, and applications toward biology, catalysis, and nanotechnology. Chem. Rev. **104**, 293–346 (2004)
18. Magdolenova, Z., Collins, A., Kumar, A., Dhawan, A., Stone, V., Dusinska, M.: Mechanisms of genotoxicity. A review of *in-vitro* and *in-vivo* studies with engineered nanoparticles. Nanotoxicology **8**, 233–278 (2014)
19. Kelly, K.L., Coronado, E., Zhao, L.L., Schatz, G.C.: The optical properties of metal nanoparticles: the influence of size, shape, and dielectric environment (2003)
20. El-Sayed, M.A.: Small is different: shape-, size-, and composition-dependent properties of some colloidal semiconductor nanocrystals. Acc. Chem. Res. **37**, 326–333 (2004)
21. Zhao, N., Yan, L., Zhao, X., Chen, X., Li, A., Zheng, D., et al.: Versatile types of organic/inorganic nanohybrids: from strategic design to biomedical applications. Chem. Rev. **119**, 1666–1762 (2018)
22. Vallet-Regí, M., Colilla, M., González, B.: Medical applications of organic–inorganic hybrid materials within the field of silica-based bioceramics. Chem. Soc. Rev. **40**, 596–607 (2011)

23. Oun, A.A., Shankar, S., Rhim, J.-W.: Multifunctional nanocellulose/metal and metal oxide nanoparticle hybrid nanomaterials. Crit. Rev. Food Sci. Nutr. **60**, 435–460 (2020)
24. Liu, X., Zhang, Q., Knoll, W., Liedberg, B., Wang, Y.: Rational design of functional peptide-gold hybrid nanomaterials for molecular interactions. Adv. Mater. **32**, 2000866 (2020)
25. Makvandi, P., Wang, C., Zare, E.N., Borzacchiello, A., Niu, L., Tay, F.R.: Metal-based nanomaterials in biomedical applications: Antimicrobial activity and cytotoxicity aspects. Adv. Funct. Mater. 1910021 (2020)
26. Park, W., Shin, H., Choi, B., Rhim, W.-K., Na, K., Han, D.K.: Advanced hybrid nanomaterials for biomedical applications. Prog. Mater. Sci. 100686 (2020)
27. Xiao, M.-C., Chou, Y.-H., Hung, Y.-N., Hu, S.-H., Chiang, W.-H.: Hybrid polymeric nanoparticles with high zoledronic acid payload and proton sponge-triggered rapid drug release for anticancer applications. Mater. Sci. Eng. C **116**, 111277 (2020)
28. Pieretti, J.C., Rolim, W.R., Ferreira, F.F., Lombello, C.B., Nascimento, M.H.M., Seabra, A.B.: Synthesis, characterization, and cytotoxicity of Fe_3O_4@Ag hybrid nanoparticles: promising applications in cancer treatment. J. Clust. Sci. **31**, 535–547 (2020)
29. Kango, S., Kalia, S., Celli, A., Njuguna, J., Habibi, Y., Kumar, R.: Surface modification of inorganic nanoparticles for development of organic–inorganic nanocomposites—a review. Prog. Polym. Sci. **38**, 1232–1261 (2013)
30. Xie, Y., Hill, C.A.S., Xiao, Z., Militz, H., Mai, C.: Silane coupling agents used for natural fiber/polymer composites: a review. Compos. Part A. Appl. Sci. Manuf. **41**, 806–819 (2010)
31. Hideshima, S., Hinou, H., Ebihara, D., Sato, R., Kuroiwa, S., Nakanishi, T., et al.: Attomolar detection of influenza A virus hemagglutinin human H1 and avian H5 using glycan-blotted field effect transistor biosensor. Anal. Chem. **85**, 5641–5644 (2013)
32. Basuki, J.S., Esser, L., Zetterlund, P.B., Whittaker, M.R., Boyer, C., Davis, T.P.: Grafting of P (OEGA) onto magnetic nanoparticles using Cu(0) mediated polymerization: comparing grafting "from" and "to" approaches in the search for the optimal material design of nanoparticle MRI contrast agents. Macromolecules **46**, 6038–6047 (2013)
33. Chatterjee, S., Karam, T.E., Rosu, C., Wang, C.-H., Youm, S.G., Li, X., et al.: Silica–conjugated polymer hybrid fluorescent nanoparticles: preparation by surface-initiated polymerization and spectroscopic studies. J. Phys. Chem. C **122**, 6963–6975 (2018)
34. Chen, H., Wang, G.D., Chuang, Y.-J., Zhen, Z., Chen, X., Biddinger, P., et al.: Nanoscintillator-mediated X-ray inducible photodynamic therapy for *in-vivo* cancer treatment. Nano. Lett. **15**, 2249–2256 (2015)
35. Tong, S., Hou, S., Zheng, Z., Zhou, J., Bao, G.: Coating optimization of superparamagnetic iron oxide nanoparticles for high T2 relaxivity. Nano. Lett. **10**, 4607–4613 (2010)
36. Raula, J., Shan, J., Nuopponen, M., Niskanen, A., Jiang, H., Kauppinen, E.I., et al.: Synthesis of gold nanoparticles grafted with a thermoresponsive polymer by surface-induced reversible-addition-fragmentation chain-transfer polymerization. Langmuir **19**, 3499–3504 (2003)
37. Pfaff, A., Schallon, A., Ruhland, T.M., Majewski, A.P., Schmalz, H., Freitag, R., et al.: Magnetic and fluorescent glycopolymer hybrid nanoparticles for intranuclear optical imaging. Biomacromol **12**, 3805–3811 (2011)
38. Yan, J., Li, S., Cartieri, F., Wang, Z., Hitchens, T.K., Leonardo, J., et al.: Iron oxide nanoparticles with grafted polymeric analogue of dimethyl sulfoxide as potential magnetic resonance imaging contrast agents. ACS Appl. Mater. Interfaces **10**, 21901–21908 (2018)
39. Kievit, F.M., Veiseh, O., Bhattarai, N., Fang, C., Gunn, J.W., Lee, D., et al.: PEI–PEG–chitosan-copolymer-coated iron oxide nanoparticles for safe gene delivery: synthesis, complexation, and transfection. Adv. Funct. Mater. **19**, 2244–2251 (2009)
40. Cole, A.J., David, A.E., Wang, J., Galbán, C.J., Hill, H.L., Yang, V.C.: Polyethylene glycol modified, cross-linked starch-coated iron oxide nanoparticles for enhanced magnetic tumor targeting. Biomaterials **32**, 2183–2193 (2011)
41. Liong, M., Shao, H., Haun, J.B., Lee, H., Weissleder, R.: Carboxymethylated polyvinyl alcohol stabilizes doped ferrofluids for biological applications. Adv. Mater. **22**, 5168–5172 (2010)
42. Zhu, N., Ji, H., Yu, P., Niu, J., Farooq, M.U., Akram, M.W., et al.: Surface modification of magnetic iron oxide nanoparticles. Nanomaterials **8**, 810 (2018)

43. Li, F., Lu, J., Kong, X., Hyeon, T., Ling, D.: Dynamic nanoparticle assemblies for biomedical applications. Adv Mater **29**, 1605897 (2017)
44. Nie, Z., Petukhova, A., Kumacheva, E.: Properties and emerging applications of self-assembled structures made from inorganic nanoparticles. Nat. Nanotechnol. **5**, 15–25 (2010)
45. Ling, D., Hackett, M.J., Hyeon, T.: Surface ligands in synthesis, modification, assembly and biomedical applications of nanoparticles. Nano. Today **9**, 457–477 (2014)
46. Grzelczak, M., Vermant, J., Furst, E.M., Liz-Marzán, L.M.: Directed self-assembly of nanoparticles. ACS Nano **4**, 3591–3605 (2010)
47. Ling, D., Lee, N., Hyeon, T.: Chemical synthesis and assembly of uniformly sized iron oxide nanoparticles for medical applications. Acc. Chem. Res. **48**, 1276–1285 (2015)
48. Kim, J.S., Rieter, W.J., Taylor, K.M.L., An, H., Lin, W., Lin, W.: Self-assembled hybrid nanoparticles for cancer-specific multimodal imaging. J. Am. Chem. Soc. **129**, 8962–8963 (2007)
49. Si, S., Raula, M., Paira, T.K., Mandal, T.K.: Reversible self-assembly of carboxylated peptide-functionalized gold nanoparticles driven by metal-ion coordination. Chem. Phys. Chem. **9**, 1578–1584 (2008)
50. Klajn, R., Olson, M.A., Wesson, P.J., Fang, L., Coskun, A., Trabolsi, A., et al.: Dynamic hook-and-eye nanoparticle sponges. Nat. Chem. **1**, 733–738 (2009)
51. Prasad, S., Achazi, K., Böttcher, C., Haag, R., Sharma, S.K.: Fabrication of nanostructures through self-assembly of non-ionic amphiphiles for biomedical applications. RSC Adv. **7**, 22121–22132 (2017)
52. Horcajada, P., Gref, R., Baati, T., Allan, P.K., Maurin, G., Couvreur, P., et al.: Metal–organic frameworks in biomedicine. Chem. Rev. **112**, 1232–1268 (2012)
53. He, C., Liu, D., Lin, W.: Nanomedicine applications of hybrid nanomaterials built from metal–ligand coordination bonds: nanoscale metal–organic frameworks and nanoscale coordination polymers. Chem. Rev. **115**, 11079–11108 (2015)
54. Moon, H.R., Lim, D.-W., Suh, M.P.: Fabrication of metal nanoparticles in metal–organic frameworks. Chem. Soc. Rev. **42**, 1807–1824 (2013)
55. Wang, L., Zheng, M., Xie, Z.: Nanoscale metal–organic frameworks for drug delivery: a conventional platform with new promise. J. Mater. Chem. B **6**, 707–717 (2018)
56. Wu, M., Yang, Y.: Metal–organic framework (MOF)-based drug/cargo delivery and cancer therapy. Adv. Mater. **29**, 1606134 (2017)
57. Stock, N., Biswas, S.: Synthesis of metal-organic frameworks (MOFs): routes to various MOF topologies, morphologies, and composites. Chem. Rev. **112**, 933–969 (2012)
58. Chen, B., Yang, Z., Zhu, Y., Xia, Y.: Zeolitic imidazolate framework materials: recent progress in synthesis and applications. J. Mater. Chem. A **2**, 16811–16831 (2014)
59. Xuan, W., Zhu, C., Liu, Y., Cui, Y.: Mesoporous metal–organic framework materials. Chem. Soc. Rev. **41**, 1677–1695 (2012)
60. Fang, J., Nakamura, H., Maeda, H.: The EPR effect: unique features of tumor blood vessels for drug delivery, factors involved, and limitations and augmentation of the effect. Adv. Drug Deliv. Rev. **63**, 136–151 (2011)
61. Greish, K.: Enhanced Permeability and Retention (EPR) Effect for Anticancer Nanomedicine Drug Targeting, pp. 25–37. Springer, Cancer Nanotechnol. (2010)
62. Nichols, J.W., Bae, Y.H.E.P.R.: Evidence and fallacy. J. Control Release **190**, 451–464 (2014)
63. Koh, K., Wong-Foy, A.G., Matzger, A.J.: A crystalline mesoporous coordination copolymer with high microporosity. Angew. Chemie. Int. Ed. **47**, 677–680 (2008)
64. Han, L., Qi, H., Zhang, D., Ye, G., Zhou, W., Hou, C., et al.: A facile and green synthesis of MIL-100 (Fe) with high-yield and its catalytic performance. New. J. Chem. **41**, 13504–13509 (2017)
65. Miller, M.A., Wang, C.-Y., Merrill, G.N.: Experimental and theoretical investigation into hydrogen storage via spillover in IRMOF-8. J. Phys. Chem. C **113**, 3222–3231 (2009)
66. Ishiwata, T., Furukawa, Y., Sugikawa, K., Kokado, K., Sada, K.: Transformation of metal–organic framework to polymer gel by cross-linking the organic ligands preorganized in metal–organic framework. J. Am. Chem. Soc. **135**, 5427–5432 (2013)

67. Chen, X., Tong, R., Shi, Z., Yang, B., Liu, H., Ding, S., et al.: MOF nanoparticles with encapsulated autophagy inhibitor in controlled drug delivery system for antitumor. ACS Appl. Mater. Interfaces **10**, 2328–2337 (2018)
68. He, C., Lu, K., Liu, D., Lin, W.: Nanoscale metal–organic frameworks for the co-delivery of cisplatin and pooled siRNAs to enhance therapeutic efficacy in drug-resistant ovarian cancer cells. J. Am. Chem. Soc. **136**, 5181–5184 (2014)
69. Arun Kumar, S., Balasubramaniam, B., Bhunia, S., Jaiswal, M.K., Verma, K., Khademhosseini, A., et al.: Two-dimensional metal organic frameworks for biomedical applications. Wiley Interdiscip. Rev. Nanomed. Nanobiotechnol. e1674 (2020)
70. Chae, D.W., Kim, B.C.: Characterization on polystyrene/zinc oxide nanocomposites prepared from solution mixing. Polym. Adv. Technol. **16**, 846–850 (2005)
71. Li, S., Meng Lin, M., Toprak, M.S., Kim, D.K., Muhammed, M.: Nanocomposites of polymer and inorganic nanoparticles for optical and magnetic applications. Nano. Rev. **1**, 5214 (2010)
72. Yuan, W., Wang, F., Chen, Z., Gao, C., Liu, P., Ding, Y., et al.: Efficient grafting of polypropylene onto silica nanoparticles and the properties of PP/PP-g-SiO_2 nanocomposites. Polymer (Guildf) **151**, 242–249 (2018)
73. Chen, W.-C., Lin, R.-C., Tseng, S.-M., Kuo, S.-W.: Minimizing the strong screening effect of polyhedral oligomeric silsesquioxane nanoparticles in hydrogen-bonded random copolymers. Polymers (Basel) **10**, 303 (2018)
74. Zhang, L., Su, H., Cai, J., Cheng, D., Ma, Y., Zhang, J., et al.: A multifunctional platform for tumor angiogenesis-targeted chemo-thermal therapy using polydopamine-coated gold nanorods. ACS Nano **10**, 10404–10417 (2016)
75. Hu, W.-H., Huang, K.-W., Chiou, C.-W., Kuo, S.-W.: Complementary multiple hydrogen bonding interactions induce the self-assembly of supramolecular structures from heteronucleobase-functionalized benzoxazine and polyhedral oligomeric silsesquioxane nanoparticles. Macromolecules **45**, 9020–9028 (2012)
76. Wu, Y.-C., Kuo, S.-W.: Self-assembly supramolecular structure through complementary multiple hydrogen bonding of heteronucleobase-multifunctionalized polyhedral oligomeric silsesquioxane (POSS) complexes. J. Mater. Chem. **22**, 2982–2991 (2012)
77. Cheng, Y., Zeiger, D.N., Howarter, J.A., Zhang, X., Lin, N.J., Antonucci, J.M., et al.: *In-situ* formation of silver nanoparticles in photocrosslinking polymers. J. Biomed. Mater. Res. Part B. Appl. Biomater. **97**, 124–131 (2011)
78. Shen, X.-J., Yang, S., Shen, J.-X., Ma, J.-L., Wu, Y.-Q., Zeng, X.-L., et al.: Improved mechanical and antibacterial properties of silver-graphene oxide hybrid/polylactid acid composites by *in-situ* polymerization. Ind. Crops Prod. **130**, 571–579 (2019)
79. Mohammad Shafiee, M.R., Sattari, A., Kargar, M., Ghashang, M.: MnO_2/Cr_2O_3/PANI nanocomposites prepared by *in-situ* oxidation polymerization method: optical and electrical behaviors. J. Appl. Polym. Sci. **136**, 47219 (2019)
80. Liu, C., Zhang, L., Liu, H., Cheng, K.: Delivery strategies of the CRISPR-Cas9 gene-editing system for therapeutic applications. J. Control Release **266**, 17–26 (2017)
81. Ramesan, M.T., Anjitha, T., Parvathi, K., Anilkumar, T., Mathew, G.: Nano zinc ferrite filler incorporated polyindole/poly (vinyl alcohol) blend: Preparation, characterization, and investigation of electrical properties. Adv. Polym. Technol. **37**, 3639–3649 (2018)
82. Thakor, A.S., Gambhir, S.S.: Nanooncology: The future of cancer diagnosis and therapy. CA Cancer J. Clin. (2013). https://doi.org/10.3322/caac.21199
83. Padmanabhan, P., Kumar, A., Kumar, S., Chaudhary, R.K., Gulyás, B.: Nanoparticles in practice for molecular-imaging applications: an overview. Acta Biomater. (2016). https://doi.org/10.1016/j.actbio.2016.06.003
84. Pang, L., Zhang, C., Qin, J., Han, L., Li, R., Hong, C., et al.: A novel strategy to achieve effective drug delivery: exploit cells as carrier combined with nanoparticles. Drug Deliv. (2017). https://doi.org/10.1080/10717544.2016.1230903
85. Bulbake, U., Doppalapudi, S., Kommineni, N., Khan, W.: Liposomal formulations in clinical use: an updated review. Pharmaceutics (2017). https://doi.org/10.3390/pharmaceutics9020012

86. Baeza, A., Colilla, M., Vallet-Regí, M.: Advances in mesoporous silica nanoparticles for targeted stimuli-responsive drug delivery. Expert Opin. Drug Deliv. (2015). https://doi.org/10.1517/17425247.2014.953051
87. Doughty, A.C.V., Hoover, A.R., Layton, E., Murray, C.K., Howard, E.W., Chen, W.R.: Nanomaterial applications in photothermal therapy for cancer. Materials (Basel) (2019). https://doi.org/10.3390/ma12050779
88. Levchenko, I., Bazaka, K., Keidar, M., Xu, S., Fang, J.: Hierarchical multicomponent inorganic metamaterials: intrinsically driven self-assembly at the nanoscale. Adv. Mater. (2018). https://doi.org/10.1002/adma.201702226
89. Silva, C.O., Pinho, J.O., Lopes, J.M., Almeida, A.J., Gaspar, M.M., Reis, C.: Current trends in cancer nanotheranostics: metallic, polymeric, and lipid-based systems. Pharmaceutics (2019). https://doi.org/10.3390/pharmaceutics11010022
90. Murugan, C., Sharma, V., Murugan, R.K., Malaimegu, G., Sundaramurthy, A.: Two-dimensional cancer theranostic nanomaterials: synthesis, surface functionalization and applications in photothermal therapy. J. Control Release (2019). https://doi.org/10.1016/j.jconrel.2019.02.015
91. Tan, Y.Y., Yap, P.K., Xin Lim, G.L., Mehta, M., Chan, Y., Ng, S.W., et al.: Perspectives and advancements in the design of nanomaterials for targeted cancer theranostics. Chem. Biol. Interact. (2020). https://doi.org/10.1016/j.cbi.2020.109221
92. Bejarano, J., Navarro-Marquez, M., Morales-Zavala, F., Morales, J.O., Garcia-Carvajal, I., Araya-Fuentes, E., et al.: Nanoparticles for diagnosis and therapy of atherosclerosis and myocardial infarction: evolution toward prospective theranostic approaches. Theranostics (2018). https://doi.org/10.7150/thno.26284
93. Ali, E.S., Sharker, S.M., Islam, M.T., Khan, I.N., Shaw, S., Rahman, M.A., et al.: Targeting cancer cells with nanotherapeutics and nanodiagnostics: current status and future perspectives. Semin. Cancer Biol. (2020). https://doi.org/10.1016/j.semcancer.2020.01.011
94. Li, Z., Ye, E., David, L.R., Loh, X.J.: Recent advances of using hybrid nanocarriers in remotely controlled therapeutic delivery. Small (2016). https://doi.org/10.1002/smll.201601129
95. Das, S.S., Bharadwaj, P., Bilal, M., Barani, M., Rahdar, A., Taboada, P., et al.: Stimuli-responsive polymeric nanocarriers for drug delivery, imaging, and theragnosis. Polymers (Basel) (2020). https://doi.org/10.3390/polym12061397
96. Kim, H.S., Lee, D.Y.: Photothermal therapy with gold nanoparticles as an anticancer medication. J. Pharm. Investig. (2017). https://doi.org/10.1007/s40005-016-0292-6
97. Poon, W., Zhang, Y.N., Ouyang, B., Kingston, B.R., Wu, J.L.Y., Wilhelm, S., et al.: Elimination pathways of nanoparticles. ACS Nano (2019). https://doi.org/10.1021/acsnano.9b01383
98. Wu, J.L., Wang, C.Q., Zhuo, R.X., Cheng, S.X.: Multi-drug delivery system based on alginate/calcium carbonate hybrid nanoparticles for combination chemotherapy. Colloids Surfaces B Biointerfaces (2014). https://doi.org/10.1016/j.colsurfb.2014.09.047
99. Nakamura, Y., Mochida, A., Choyke, P.L., Kobayashi, H.: Nanodrug delivery: is the enhanced permeability and retention effect sufficient for curing cancer? Bioconjug. Chem. (2016). https://doi.org/10.1021/acs.bioconjchem.6b00437
100. Zhang, Z., Tongchusak, S., Mizukami, Y., Kang, Y.J., Ioji, T., Touma, M., et al.: Induction of anti-tumor cytotoxic T cell responses through PLGA-nanoparticle mediated antigen delivery. Biomaterials (2011). https://doi.org/10.1016/j.biomaterials.2011.01.067
101. Ge, J., Lei, J., Zare, R.N.: Bovine serum albumin—poly(methyl methacrylate) nanoparticles: an example of frustrated phase separation. Nano Lett. (2011). https://doi.org/10.1021/nl201303q
102. Kang, S., Ahn, S., Lee, J., Kim, J.Y., Choi, M., Gujrati, V., et al.: Effects of gold nanoparticle-based vaccine size on lymph node delivery and cytotoxic T-lymphocyte responses. J. Control Release (2017). https://doi.org/10.1016/j.jconrel.2017.04.024
103. Zhang, L., Wu, S., Qin, Y., Fan, F., Zhang, Z., Huang, C., et al.: Targeted codelivery of an antigen and dual agonists by hybrid nanoparticles for enhanced cancer immunotherapy. Nano. Lett. (2019). https://doi.org/10.1021/acs.nanolett.9b00030

104. Huh, Y.M., Lee, E.S., Lee, J.H., Jun, Y.W., Kim, P.H., Yun, C.O., et al.: Hybrid nanoparticles for magnetic resonance imaging of target-specific viral gene delivery. Adv. Mater. (2007). https://doi.org/10.1002/adma.200701952
105. You, Y.H., Lin, Y.F., Nirosha, B., Chang, H.T., Huang, Y.F.: Polydopamine-coated gold nanostar for combined antitumor and antiangiogenic therapy in multidrug-resistant breast cancer. Nanotheranostics (2019). https://doi.org/10.7150/ntno.36842
106. Wu, F., Liu, Y., Wu, Y., Song, D., Qian, J., Zhu, B.: Chlorin e6 and polydopamine modified gold nanoflowers for combined photothermal and photodynamic therapy. J. Mater. Chem. B (2020). https://doi.org/10.1039/c9tb02646k
107. Schweiger, C., Pietzonka, C., Heverhagen, J., Kissel, T.: Novel magnetic iron oxide nanoparticles coated with poly(ethylene imine)-g-poly(ethylene glycol) for potential biomedical application: synthesis, stability, cytotoxicity and MR imaging. Int. J. Pharm. (2011). https://doi.org/10.1016/j.ijpharm.2010.12.046
108. Park, W., Cho, S., Han, J., Shin, H., Na, K., Lee, B., et al.: Advanced smart-photosensitizers for more effective cancer treatment. Biomater. Sci. (2018). https://doi.org/10.1039/c7bm00872d
109. Wang, M., Chen, Z., Zheng, W., Zhu, H., Lu, S., Ma, E., et al.: Lanthanide-doped upconversion nanoparticles electrostatically coupled with photosensitizers for near-infrared-triggered photodynamic therapy. Nanoscale (2014). https://doi.org/10.1039/c4nr01826e
110. Morgan, N.Y., Kramer-Marek, G., Smith, P.D., Camphausen, K., Capala, J.: Nanoscintillator conjugates as photodynamic therapy-based radiosensitizers: Calculation of required physical parameters. Radiat. Res. (2009). https://doi.org/10.1667/RR1470.1
111. Kamkaew, A., Chen, F., Zhan, Y., Majewski, R.L., Cai, W.: Scintillating nanoparticles as energy mediators for enhanced photodynamic therapy. ACS Nano (2016). https://doi.org/10.1021/acsnano.6b01401
112. Bos, A.J.J.: Thermoluminescence as a research tool to investigate luminescence mechanisms. Materials (Basel) (2017). https://doi.org/10.3390/ma10121357
113. Jing, X., Yang, F., Shao, C., Wei, K., Xie, M., Shen, H., et al.: Role of hypoxia in cancer therapy by regulating the tumor microenvironment. Mol. Cancer (2019). https://doi.org/10.1186/s12943-019-1089-9
114. Senthebane, D.A., Rowe, A., Thomford, N.E., Shipanga, H., Munro, D., Al Mazeedi, M.A.M., et al.: The role of tumor microenvironment in chemoresistance: to survive, keep your enemies closer. Int. J. Mol. Sci. (2017). https://doi.org/10.3390/ijms18071586
115. Yang, G., Tian, J., Chen, C., Jiang, D., Xue, Y., Wang, C., et al.: An oxygen self-sufficient NIR-responsive nanosystem for enhanced PDT and chemotherapy against hypoxic tumors. Chem. Sci. (2019). https://doi.org/10.1039/c9sc00985j
116. Lin, T., Zhao, X., Zhao, S., Yu, H., Cao, W., Chen, W., et al.: O_2-generating MnO_2 nanoparticles for enhanced photodynamic therapy of bladder cancer by ameliorating hypoxia. Theranostics (2018). https://doi.org/10.7150/thno.22465
117. Jha, S., Sharma, P.K., Malviya, R.: Hyperthermia: role and risk factor for cancer treatment. Achiev. Life Sci. (2016). https://doi.org/10.1016/j.als.2016.11.004
118. Wang, H., Li, X., Tse, B.W.C., Yang, H., Thorling, C.A., Liu, Y., et al.: Indocyanine green-incorporating nanoparticles for cancer theranostics. Theranostics (2018). https://doi.org/10.7150/thno.22872
119. Mout, R., Ray, M., Yesilbag Tonga, G., Lee, Y.W., Tay, T., Sasaki, K., et al.: Direct cytosolic delivery of CRISPR/Cas9-ribonucleoprotein for efficient gene editing. ACS Nano (2017). https://doi.org/10.1021/acsnano.6b07600
120. Zhao, Y., Liu, W., Tian, Y., Yang, Z., Wang, X., Zhang, Y., et al.: Anti-EGFR peptide-conjugated triangular gold nanoplates for computed tomography/photoacoustic imaging-guided photothermal therapy of non-small cell lung cancer. ACS Appl. Mater. Interfaces (2018). https://doi.org/10.1021/acsami.7b19013
121. Chang, C.W., Van Spreeuwel, A., Zhang, C., Varghese, S.: PEG/clay nanocomposite hydrogel: a mechanically robust tissue engineering scaffold. Soft Matter (2010). https://doi.org/10.1039/c0sm00067a

122. Zhao, L., Tang, M., Weir, M.D., Detamore, M.S., Xu, H.H.K.: Osteogenic media and rhBMP-2-induced differentiation of umbilical cord mesenchymal stem cells encapsulated in alginate microbeads and integrated in an injectable calcium phosphate-chitosan fibrous scaffold. Tissue Eng. Part A (2011). https://doi.org/10.1089/ten.tea.2010.0521
123. Paul, A., Hasan, A., Kindi, H.A., Gaharwar, A.K., Rao, V.T.S., Nikkhah, M., et al.: Injectable graphene oxide/hydrogel-based angiogenic gene delivery system for vasculogenesis and cardiac repair. ACS Nano (2014). https://doi.org/10.1021/nn5020787
124. Noh, M., Kim, S.H., Kim, J., Lee, J.R., Jeong, G.J., Yoon, J.K., et al.: Graphene oxide reinforced hydrogels for osteogenic differentiation of human adipose-derived stem cells. RSC Adv. (2017). https://doi.org/10.1039/c7ra02410j
125. Liu, X., Miller, A.L., Park, S., Waletzki, B.E., Terzic, A., Yaszemski, M.J., et al.: Covalent crosslinking of graphene oxide and carbon nanotube into hydrogels enhances nerve cell responses. J. Mater. Chem. B (2016). https://doi.org/10.1039/c6tb01722c
126. Navaei, A., Saini, H., Christenson, W., Sullivan, R.T., Ros, R., Nikkhah, M.: Gold nanorod-incorporated gelatin-based conductive hydrogels for engineering cardiac tissue constructs. Acta Biomater. (2016). https://doi.org/10.1016/j.actbio.2016.05.027
127. Lih, E., Park, W., Park, K.W., Chun, S.Y., Kim, H., Joung, Y.K., et al.: A bioinspired scaffold with anti-inflammatory magnesium hydroxide and decellularized extracellular matrix for renal tissue regeneration. ACS Cent. Sci. (2019). https://doi.org/10.1021/acscentsci.8b00812
128. Duarah, R., Singh, Y.P., Gupta, P., Mandal, B.B., Karak, N.: High performance bio-based hyperbranched polyurethane/carbon dot-silver nanocomposite: a rapid self-expandable stent. Biofabrication (2016). https://doi.org/10.1088/1758-5090/8/4/045013
129. Jeong, D.W., Park, W., Bedair, T.M., Kang, E.Y., Kim, I.H., Park, D.S., et al.: Augmented re-endothelialization and anti-inflammation of coronary drug-eluting stent by abluminal coating with magnesium hydroxide. Biomater. Sci. (2019). https://doi.org/10.1039/c8bm01696h
130. Bassous, N., Cooke, J.P., Webster, T.J.: Enhancing stent effectiveness with nanofeatures. Methodist. Debakey Cardiovasc. J. (2016). https://doi.org/10.14797/mdcj-12-3-163
131. Akturk, O., Kismet, K., Yasti, A.C., Kuru, S., Duymus, M.E., Kaya, F., et al.: Collagen/gold nanoparticle nanocomposites: a potential skin wound healing biomaterial. J. Biomater. Appl. (2016). https://doi.org/10.1177/0885328216644536
132. Tan, A., Farhatnia, Y., Goh, D., Natasha, G., de Mel, A., Lim, J., et al.: Surface modification of a polyhedral oligomeric silsesquioxane poly(carbonate-urea) urethane (POSS-PCU) nanocomposite polymer as a stent coating for enhanced capture of endothelial progenitor cells. Biointerphases (2013). https://doi.org/10.1186/1559-4106-8-23
133. Steinmetz, N.F., Hong, V., Spoerke, E.D., Lu, P., Breitenkamp, K., Finn, M.G., et al.: Buckyballs meet viral nanoparticles: candidates for biomedicine. J. Am. Chem. Soc. (2009). https://doi.org/10.1021/ja902293w
134. Lee, P.W., Hsu, S.H., Tsai, J.S., Chen, F.R., Huang, P.J., Ke, C.J., et al.: Multifunctional core-shell polymeric nanoparticles for transdermal DNA delivery and epidermal Langerhans cells tracking. Biomaterials (2010). https://doi.org/10.1016/j.biomaterials.2009.11.100
135. Ha, Y.J., Lee, S.M., Mun, C.H., Kim, H.J., Bae, Y., Lim, J.H., et al.: Methotrexate-loaded multifunctional nanoparticles with near-infrared irradiation for the treatment of rheumatoid arthritis. Arthritis Res. Ther. (2020). https://doi.org/10.1186/s13075-020-02230-y
136. Askari, A., Tajvar, S., Nikkhah, M., Mohammadi, S., Hosseinkhani, S.: Synthesis, characterization and *in-vitro* toxicity evaluation of doxorubicin-loaded magnetoliposomes on MCF-7 breast cancer cell line. J. Drug Deliv. Sci. Technol. (2020). https://doi.org/10.1016/j.jddst.2019.101447
137. Xu, C., Wang, B., Sun, S.: Dumbbell-like Au-Fe_3O_4 nanoparticles for target-specific platin delivery. J. Am. Chem. Soc. (2009). https://doi.org/10.1021/ja900790v
138. Gu, H., Zheng, R., Zhang, X.X., Xu, B.: Facile one-pot synthesis of bifunctional heterodimers of nanoparticles: a conjugate of quantum dot and magnetic nanoparticles. J. Am. Chem. Soc. (2004). https://doi.org/10.1021/ja0496423
139. Jiang, J., Gu, H., Shao, H., Devlin, E., Papaefthymiou, G.C., Ying, J.Y.: Bifunctional Fe_3O_4-Ag heterodimer nanoparticles for two-photon fluorescence imaging and magnetic manipulation. Adv. Mater. (2008). https://doi.org/10.1002/adma.200800498

140. Wang, G., Gao, W., Zhang, X., Mei, X.: Au nanocage functionalized with ultra-small Fe_3O_4 nanoparticles for targeting T1–T2 dual MRI and CT imaging of tumor. Sci. Rep. (2016). https://doi.org/10.1038/srep28258
141. Li, C., Chen, T., Ocsoy, I., Zhu, G., Yasun, E., You, M., et al.: Gold-coated Fe_3O_4 nanoroses with five unique functions for cancer cell targeting, imaging, and therapy. Adv. Funct. Mater. (2014). https://doi.org/10.1002/adfm.201301659
142. Ganipineni, L.P., Ucakar, B., Joudiou, N., Bianco, J., Danhier, P., Zhao, M., et al.: Magnetic targeting of paclitaxel-loaded poly(lactic-co-glycolic acid)-based nanoparticles for the treatment of glioblastoma. Int. J. Nanomed. (2018). https://doi.org/10.2147/IJN.S165184
143. Zhang, R.X., Ahmed, T., Li, L.Y., Li, J., Abbasi, A.Z., Wu, X.Y.: Design of nanocarriers for nanoscale drug delivery to enhance cancer treatment using hybrid polymer and lipid building blocks. Nanoscale (2017). https://doi.org/10.1039/c6nr08486a
144. Sailor, M.J., Park, J.H.: Hybrid nanoparticles for detection and treatment of cancer. Adv. Mater. (2012). https://doi.org/10.1002/adma.201200653
145. Ba, H., Rodríguez-Fernández, J., Stefani, F.D., Feldmann, J.: Immobilization of gold nanoparticles on living cell membranes upon controlled lipid binding. Nano. Lett. (2010). https://doi.org/10.1021/nl101454a
146. Paasonen, L., Sipilä, T., Subrizi, A., Laurinmäki, P., Butcher, S.J., Rappolt, M., et al.: Gold-embedded photosensitive liposomes for drug delivery: triggering mechanism and intracellular release. J. Control Release (2010). https://doi.org/10.1016/j.jconrel.2010.07.095
147. Wu, G., Mikhailovsky, A., Khant, H.A., Fu, C., Chiu, W., Zasadzinski, J.A.: Remotely triggered liposome release by near-infrared light absorption via hollow gold nanoshells. J. Am. Chem. Soc. (2008). https://doi.org/10.1021/ja802656d
148. Liu, T.Y., Huang, T.C.: A novel drug vehicle capable of ultrasound-triggered release with MRI functions. Acta Biomater. (2011). https://doi.org/10.1016/j.actbio.2011.06.038
149. Chen, Y., Bose, A., Bothun, G.D.: Controlled release from bilayer-decorated magnetoliposomes via electromagnetic heating. ACS Nano (2010). https://doi.org/10.1021/nn100274v
150. Mikhaylov, G., Mikac, U., Magaeva, A.A., Itin, V.I., Naiden, E.P., Psakhye, I., et al.: Ferri-liposomes as an MRI-visible drug-delivery system for targeting tumours and their microenvironment. Nat. Nanotechnol. (2011). https://doi.org/10.1038/nnano.2011.112
151. Al-Jamal, W.T., Al-Jamal, K.T., Tian, B., Lacerda, L., Bomans, P.H., Frederik, P.M., et al.: Lipid - Quantum dot bilayer vesicles enhance tumor cell uptake and retention *in-vitro* and *in-vivo*. ACS Nano (2008). https://doi.org/10.1021/nn700176a
152. Weng, K.C., Noble, C.O., Papahadjopoulos-Sternberg, B., Chen, F.F., Drummond, D.C., Kirpotin, D.B., et al.: Targeted tumor cell internalization and imaging of multifunctional quantum dot-conjugated immunoliposomes *in-vitro* and *in-vivo*. Nano. Lett. (2008). https://doi.org/10.1021/nl801488u
153. Li, H., Wang, J., Huang, G., Wang, P., Zheng, R., Zhang, C., et al.: Multifunctionalized microbubbles for cancer diagnosis and therapy. Anticancer Agents Med. Chem. (2013). https://doi.org/10.2174/18715206113130300004
154. Accardo, A., Tesauro, D., Morelli, G.: Peptide-based targeting strategies for simultaneous imaging and therapy with nanovectors. Polym. J. (2013). https://doi.org/10.1038/pj.2012.215
155. Namiki, Y., Namiki, T., Yoshida, H., Ishii, Y., Tsubota, A., Koido, S., et al.: A novel magnetic crystal-lipid nanostructure for magnetically guided *in-vivo* gene delivery. Nat. Nanotechnol. (2009). https://doi.org/10.1038/nnano.2009.202
156. Wang, W., Cheng, D., Gong, F., Miao, X., Shuai, X.: Design of multifunctional micelle for tumor-targeted intracellular drug release and fluorescent imaging. Adv. Mater. (2012). https://doi.org/10.1002/adma.201104066
157. Park, J.H., Von Maltzahn, G., Ruoslahti, E., Bhatia, S.N., Sailor, M.J.: Micellar hybrid nanoparticles for simultaneous magnetofluorescent imaging and drug delivery. Angew. Chemie. Int. Ed. (2008). https://doi.org/10.1002/anie.200801810
158. Xu, H., Cheng, L., Wang, C., Ma, X., Li, Y., Liu, Z.: Polymer encapsulated upconversion nanoparticle/iron oxide nanocomposites for multimodal imaging and magnetic targeted drug delivery. Biomaterials (2011). https://doi.org/10.1016/j.biomaterials.2011.08.053

159. Vieweger, M., Goicochea, N., Koh, E.S., Dragnea, B.: Photothermal imaging and measurement of protein shell stoichiometry of single HIV-1 Gag virus-like nanoparticles. ACS Nano (2011). https://doi.org/10.1021/nn202184x
160. Lee, S.M., Kim, H.J., Ha, Y.J., Park, Y.N., Lee, S.K., Park, Y.B., et al.: Targeted chemo-photothermal treatments of rheumatoid arthritis using gold half-shell multifunctional nanoparticles. ACS Nano (2013). https://doi.org/10.1021/nn301215q
161. Cho, H.S., Dong, Z., Pauletti, G.M., Zhang, J., Xu, H., Gu, H., et al.: Fluorescent, superparamagnetic nanospheres for drug storage, targeting, and imaging: A multifunctional nanocarrier system for cancer diagnosis and treatment. ACS Nano (2010). https://doi.org/10.1021/nn101000e
162. Wang, C., Chen, J., Talavage, T., Irudayaraj, J.: Gold Nanorod/Fe3O4 nanoparticle "nano-pearl- necklaces" for simultaneous targeting, dual-mode imaging, and photothermal ablation of cancer cells. Angew. Chemie. Int. Ed. (2009). https://doi.org/10.1002/anie.200805282
163. Bhirde, A.A., Patel, V., Gavard, J., Zhang, G., Sousa, A.A., Masedunskas, A., et al.: Targeted killing of cancer cells *in-vivo* and *in-vitro* with EGF-directed carbon nanotube-based drug delivery. ACS Nano (2009). https://doi.org/10.1021/nn800551s
164. Bertrand, N., Wu, J., Xu, X., Kamaly, N., Farokhzad, O.C.: Cancer nanotechnology: the impact of passive and active targeting in the era of modern cancer biology. Adv. Drug Deliv. Rev. (2014). https://doi.org/10.1016/j.addr.2013.11.009

Progress on Lanthanide Ion-Activated Inorganic Hybrid Phosphors: Properties and Applications

Preeti Padhye Kulkarni, Monika Malik, and Pankaj Poddar

Abstract The exploration of multifunctional platforms for diverse applications has gained tremendous advancement towards the designing and engineering of numerous versatile materials with many functions combined into nanostructured hybrid systems. Such materials combine the benefits of different components to improve the efficiency, reliability, cost-efficiency, and scalability of the hybrid system. Trivalent lanthanide ion (Ln^{3+})-activated hybrid phosphors are important for designing new multifunctional materials with modulated optical and magnetic properties. Thus, their studies open up new directions in material sciences and related technologies. This chapter presents a broad overview of the recently investigated various Ln^{3+}-based inorganic hybrid materials. It covers the hybrids of Ln^{3+}-doped inorganic phosphors, including oxides, fluorides, phosphates, vanadates, sulfides, with materials such as (a) semiconductors (TiO_2/ZnO), (b) magnetic nanoparticles (Fe_3O_4), (c) metal/plasmonic nanoparticles (Au/Ag), (d) graphene and its derivatives, (e) quantum dots, (f) polymers, and others. We will present the study of these materials for their modulated luminescence efficiency and respective advantages in the applications of sensing, optical telecommunication, energy harvesting, multimodal imaging, biomedicine, etc. Furthermore, this chapter will also focus on the synthesis methods and approaches, including surface functionalization and modification, core–shell processing, controlled assembly, and the relationship between the composition, structure, and properties. We anticipate that a fusion of distinctive structural aspects and integrated functions will compel researchers to create smart hybrid materials and exploit this opportunity in all three realms of science: physics, chemistry, and biology.

P. P. Kulkarni
Microtron Accelerator Laboratory, Department of Physics, Savitribai Phule Pune University, Pune 411007, India

M. Malik · P. Poddar (✉)
Physical and Materials Chemistry Division, CSIR-National Chemical Laboratory, Pune 411008, India

Academy of Scientific and Innovative Research (AcSIR), Uttar Pradesh, Sector 19, Kamla Nehru Nagar, Ghaziabad 201002, India

© Springer Nature Switzerland AG 2022

K. Upadhyay et al. (eds.), *Hybrid Phosphor Materials*, Engineering Materials,
https://doi.org/10.1007/978-3-030-90506-4_13

1 Introduction

1.1 Lanthanide Ion-Activated Inorganic Phosphors

The research on lanthanide ion (Ln^{3+})-doped inorganic phosphor materials is motivated by a fundamental significance in the optical properties and the promise for broad-ranging applications in various technologies. Ln^{3+}-doped phosphors stand dominant among various optically active materials because of unique and riveting electronic and optical features. Their intricate spectroscopic properties emerge from their parity forbidden *f–f* transitions, which are shielded by filled 5*s* and 5*p* orbitals [1]. This electronic configuration renders intriguing features that involve emissive transitions in the broad spectral region, least sensitivity from the surrounding, narrow emission linewidth (with FWHM ~ 10 nm), tunable emission with long luminescent lifetime (ranging from microseconds up to several milliseconds), large anti-Stokes and Stokes shift (>200 nm; down/upconversion), high photostability, low autofluorescence, low cytotoxicity, and low photo-blinking [2–6]. These features make Ln^{3+}-activated luminescent materials as efficient complementarities and companions to dyes, biological fluorophores, and semiconductors. Accordingly, Ln^{3+}-doped phosphors uphold their dominant position in the widespread applications in optical waveguides, opto-electronics, solid-state lasers, light-emitting diodes, biomedical diagnostics and imaging, sensing, catalysis, photovoltaics, anti-counterfeiting, security printing, and so on [7–12]. Despite significant optical properties and research progress, Ln^{3+}-activated phosphors generally suffer from low quantum efficiencies, mainly because of low molar absorption coefficients ($\varepsilon = 1–10\ M^{-1}\ cm^{-1}$) [13], as a limited amount of radiation is absorbed by the direct excitation in the 4*f* levels of lanthanide ions. Some of the innovative approaches developed to enhance luminescence efficiency include manipulation in Ln^{3+}-doped phosphor systems *via* surface passivation, host lattice manipulation, surface plasmon coupling, photonic crystals, *etc.*

1.2 Significance of Ln^{3+}-Activated Inorganic Phosphors Based Hybrids

Recent technological breakthroughs and the aspiration for new functions render an extensive demand for advanced materials. Research in advanced novel multifunctional hybrid materials, their new structures, and exploration of the structure–property-performance relations is a rapidly growing area and are the fundamental driving forces that are fetching hybrid science into a new era [14–17]. The development of multifunctional hybrid materials has allowed the researchers to engineer diverse nanomaterials with multiple discrete functions of different constituents integrated into one system to overcome the limitation of single-mode applications [18]. They have the ability to tailor and acquire improved properties and functions as

well as to enhance the effectiveness of diverse types of targeted applications. The strategy to prepare hybrid materials is to intentionally combine two or more different active functional materials into a composite form while maintaining the beneficial aspects of each constituent. Thus, they are expected to possess the caliber to exhibit additional functions that should be better than their components. Hybrid materials typically consist of two or three components connected to each other with physical and/or chemical interactions. Hybrid materials are generally classified according to the possible interfacial interactions between the components present in the material. One class of materials demonstrates weak interactions between the two components, such as hydrogen bonding, van der Waals, or weak electrostatic interactions. The other class of hybrid materials exhibits strong chemical interactions between the two components, such as covalent bonding, and differentiation can also be made on the basis of their composition [19].

The research of hybrid materials is constantly and rapidly expanding, connecting diverse research communities together with their specific subjects and approaches [20, 21]. It is worth noticing that the multifunctional materials of Ln^{3+}-doped phosphors that unite many characteristics have come to the forefront. Indeed, the exploitation of Ln^{3+}-activated phosphors-based hybrids has strongly emerged in the last decade [22–24]. The need for materials demonstrating improved efficiency, reliability, possessing superior physical, chemical, thermal and optical properties, and being highly suitable for new functions has progressed. The study of the distinctively luminescent Ln^{3+}-based phosphors in hybrid materials is not only of fundamental interest due to their modulated properties but also of the potential for widespread applications in biological and material sciences. It is also evident that to realize even more opportunities for Ln^{3+}-doped phosphors, the fabrication or tuning of their hybrid materials is required to acquire improved or multifunctional properties. In particular, the synergistic combination of Ln^{3+}-activated phosphors with different active materials has high luminescence output and better processability and application, which are unattainable by either of the individual materials [25].

The integration of phosphors with other functional components using chemical approaches mainly includes surface modification and functionalization, core–shell processing, and controlled assembly. This chapter targets to review the various types of Ln^{3+}-based inorganic hybrid materials and their different applications. Here, the attention is primarily focused on the multicomponent assembly of the Ln^{3+}-based phosphors with different nanomaterials or other photoactive materials, which includes semiconductors (TiO_2/ZnO), magnetic nanoparticles (Fe_3O_4), metal nanoparticles (Au/Ag), graphene and its derivatives, quantum dots (QDs), metal–organic frameworks (MOFs), polymers, etc. Here, Fig. 1 gives an illustration of the components used for the design and functions of multicomponent Ln^{3+}-based hybrids in this chapter. The literature has been covered until September 2020. We wish to mention here that while browsing the literature for this chapter, we realized that in

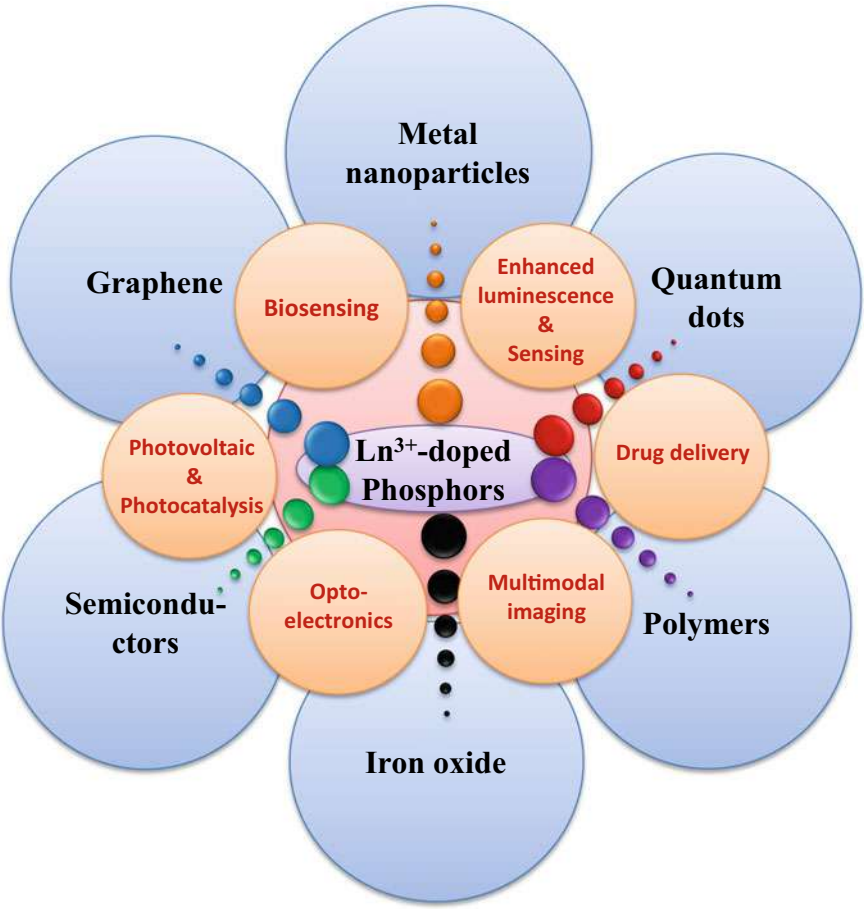

Fig. 1 Various hybrids of lanthanide ion-doped phosphors for their enhanced applications

many reports, the term hybrid is used in a broader aspect spanning a wide area of different materials with or without the interactions between the components. So, to maintain the flow, we are delimiting to use this broadly used term by considering the other terms such as composites, where bonding in the nanomaterials is not well defined.

2 Various Types of Ln^{3+}-Based Inorganic Hybrid Materials and Applications

2.1 Ln^{3+}-doped Phosphor-Semiconductor Hybrids for Energy Applications

2.1.1 Ln^{3+}-doped Phosphor-Semiconductor Hybrids for Photovoltaics

It is a challenge to develop and design the materials for broad region solar radiation absorption with increased efficiency for most of the energy applications such as solar cells, water splitting, and photocatalysis. Generally, the photon-absorbing species, such as dyes, semiconductors, perovskite materials, QDs, etc., absorb photons only in a particular spectral region. Thus, the major constraint in enhancing the energy conversion efficiency in solar cells and photocatalysis lies in the underutilization of the photons of the incoming solar light and the bandgap of the photoactive semiconductor materials. The visible and near-infrared (NIR) lights occupy about ~45% and ~50% of the solar light, respectively, while the percentage of UV light is only ~5%. Owing to the wide bandgap of the conventional semiconductors used in the photovoltaic applications, they can utilize energy only in the UV region, which is nearly 5% of the solar radiation impinging on the surface of Earth crust. Modified or doped semiconductors can absorb in the visible region of the solar energy as well; however, the NIR portion (~50%) of clean and sustainable solar energy remains unutilized [26]. Contrarily, to attain the harvesting of NIR photons, novel sensitizers such as thienothiophene- and thiophene-based dyes, indoline-based dyes, and squaraine dyes, QDs, and co-sensitizers have been utilized [27–29]. However, the dyes easily degrade, and the QDs are sensitive to the surrounding chemical species such as ions, water, and oxygen to a certain extent [30]. Thus, to harvest the complete solar spectrum, Ln^{3+}-doped phosphors-semiconductor hybrids have been developed. Lanthanide-doped materials are the leading candidates for efficient spectral conversion owing to their rich electronic structures that permit facile photon management [31]. Specially, composites of TiO_2 with upconverting (UC) phosphors are popular, wherein UC phosphors absorb NIR and convert it to UV and visible light via anti-Stokes emission by sequential absorption of two or more photons. These photons are absorbed by UV–vis photoactive materials such as dyes or semiconductors, consequently harvest the complete solar spectrum and enhance photocatalysis and solar cell efficiency. Thus, the utilization of UC phosphors is the simplest approach to enhance the performance in all the classes of solar cells, including gallium arsenide solar cells, crystalline and amorphous silicon-based solar cells, dye-sensitized solar cells (DSSC), and all other types of solar cells. Although, in this overview, we are primarily discussing the DSSCs.

Demopoulos and co-workers in the year 2010 made an important effort on developing the Ln^{3+}-based solar upconverters [30]. They first explored the upconversion effect by utilizing LaF_3: Yb, Er UC nanocrystals in DSSCs. They proposed

a multiple-layer structure for enhancing the harvesting of NIR photons in conventional DSSCs. In this approach, LaF_3: Yb,Er phosphors were integrated with TiO_2; and so formed LaF_3: Yb,Er-TiO_2 nanocomposites were utilized as the UC layer to construct a "triple-layer" working electrode on fluorine-doped tin oxide (FTO) glass. Four kinds of working electrodes were prepared and studied to optimize the UC-TiO_2 layer modified working electrode structure. The four different arrangements of solar cell devices were as follows: (i) FTO/UC-TiO_2/transparent TiO_2/scattering TiO_2/Pt/FTO; (ii) FTO/transparent TiO_2/UC-TiO_2/scattering TiO_2/Pt/FTO; (iii) FTO/UC-TiO_2/scattering TiO_2/Pt/FTO and; finally device (iv) FTO/transparent TiO_2/scattering TiO_2/Pt/FTO was taken as a control, i.e., without UC-TiO_2 composite layer. In all the structures, the transparent layer of TiO_2 consists of control TiO_2 nanoparticles (NPs) of ≡10 nm–15 nm size, and the scattering TiO_2-layer contained ≡350 nm–450 nm sized TiO_2 particles. Among the four different tested devices, arrangement (ii) showed an improved performance. In experimental arrangements (i) and (iii), the UC-TiO_2 nanocomposites were incorporated directly on the FTO-glass that resulted in the electronic conduction of the UC itself, affecting the separation of charges in the DSSCs. Thus, the enhancement in the photocurrent was not observed in such an arrangement. This indicated that the incorporation of the UC layer at an appropriate place in the DSSC structure plays a crucial role. Since the presence of the UC layer at the wrong place may lead to counterproductive recapturing of the photoinjected electrons by the electrolyte. In this study, the authors conveyed that the introduction of the layer of UC-TiO_2 nanocomposites between scattering and transparent layers in a multiple-layer DSSC structure yielded the best performance. Wherein, the LaF_3: Yb,Er UC phosphors converted the NIR light to high energy photons in visible and UV regions, which was further absorbed by the dyes/sensitizers, such as N719 dye, which subsequently injected electrons to TiO_2. This mechanism improved the current output and conversion efficiency of the DSSCs. However, the overall efficiency of the DSSCs was not that appreciable, probably due to the recombination of charge-carrier at the interfaces of the triple-layer. Thus, the same group further tried to enhance the photovoltaic efficiency by tuning the morphology of the Ln^{3+}-doped inorganic phosphor. They developed a novel DSSC configuration, wherein they applied a layer of $NaYF_4$: Yb,Er hexagonal nanoplatelets as an external layer, and a single internal transparent TiO_2 layer [32]. In this arrangement, the photocurrent and overall DSSC efficiency were improved by approximately 10%, which were attained by adding the UC external layer, which exhibited two roles, i.e., light reflection and harvesting of NIR light. In addition, to allow complete utilization of the upconverted light and simultaneously avoid the charge recombination, the research progressed towards constructing hybrids via core–shell nanostructures, morphology, and composition tuning of UC hybrids and other modifications to improve the solar cell efficiency further. In general, these hybrids mainly eliminated or diminished the serious recombination of electrons and holes, causing loss of the photocurrent. Some of the examples are discussed here. Liang and co-workers designed β-$NaYF_4$: Er,Yb@SiO_2@TiO_2 core/double-shell (CDS) structured hexagonal submicroprisms abbreviated as NYEY@S@T HSMs [33]. This structure consisted of β-$NaYF_4$: Yb,Er HSM as a core having ~400 nm diameter, ~10 nm thick amorphous

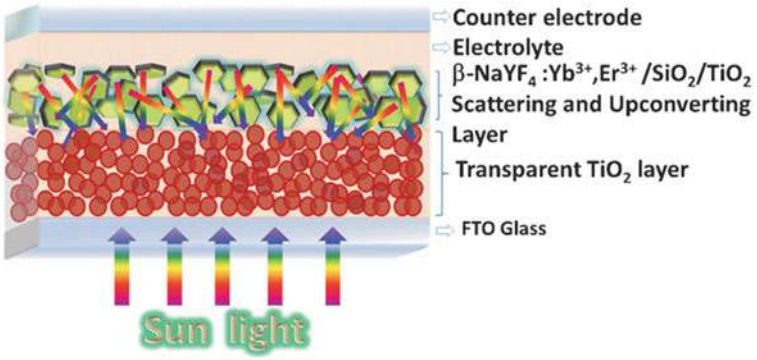

Fig. 2 Schematic diagram of bilayer DSSC photoanodes with β-$NaYF_4$: Yb,Er/SiO_2/TiO_2 submicroplates for light scattering. Reprinted with permission from Ref. [34]. Copyright 2013 The Royal Society of Chemistry

insulating SiO_2 as inner shell, and ~30 nm thick interconnected grains of anatase phased TiO_2 as an outer shell. For device configuration, optimization was done by introducing various amounts of these HSMs into TiO_2 NPs of size (20–40) nm to form nano/submicrometer composites that to be deposited on a transparent TiO_2 layer. The mixing ratio of β-NYEY@S@T HSMs corresponding to mass-fraction levels with respect to TiO_2, changed from X = 5% to 20% (DSC-NYEY@S@T-X), and their photovoltaic performances were compared with the reference cell (DSC-NYEY@S@T-0), which was constructed in the absence of HSMs. When the mixing ratio was 10%, the DSSC efficiency was improved by 10.9% in contrast to the reference cell. Additionally, the efficiency of this system was improved by 120% as compared to that of the device made up of bare $NaYF_4$: Yb,Er crystals. In parallel, the same group fabricated double-shell β-$NaYF_4$: Yb,Er@SiO_2@TiO_2 microplates, which were sandwiched between a transparent TiO_2 layer and a counter electrode as shown in Fig. 2, and the system achieved nearly 29.4% increment in DSSCs efficiency [34]. In this hybrid structure, β-$NaYF_4$: Yb,Er played a role as scattering and upconverting layer, and so, the β-$NaYF_4$: Yb,Er core absorbed the NIR light and re-emitted visible-light, which matched the absorption of the N719 dye. Thus the absorption spectrum was broadened, and more photogenerated electrons can be produced to amplify the photocurrent. Moreover, the submicron dimensions of plates like structures acted as efficient Mie scatterers, which lead to an overall improvement in the light-harvesting capability. Further, the recombination effect was eliminated by insulating the SiO_2 layer, which isolated the UC cores from the external environment. The outer TiO_2-shells facilitated the electron diffusion. In this way, such composite constructor film can increase the harvesting of the photons of the solar spectrum in the NIR region and generate significant light scattering by incorporating UC phosphors. The studies and results discussed and revealed that the concentration, morphology, and size of UC phosphors, as well as SiO_2 and TiO_2-shell thicknesses, play a critical role in increasing the overall efficiency of DSSCs.

In 2016, our group attempted to develop a broad-spectrum responsive photoactive multifunctional platform based on β-$NaGdF_4$: Yb,Er, and mesoporous anatase TiO_2 ($m TiO_2$) composite for biomedical and energy applications [35]. Wherein, β-$NaGdF_4$: Yb,Er/$m TiO_2$ nanocomposites were developed to improve the absorption of photons in a broader region of the solar spectrum. The UC phosphors harvested NIR photons and stimulated visible emission; at the same time, $m TiO_2$ absorbed UV and weak visible light, thus increased the overall photon-capture for photocatalysis and photon conversion efficiency (PCE) for DSSC. Furthermore, it was estimated that the $m TiO_2$ could increase the number of active sites, thereby improved the photocatalytic activity and enhanced the dye adsorption in the DSSC. In addition, it was also expected to increase the drug-loading capacity for photodynamic therapy (PDT) and chemotherapy for cancer treatment. Concurrently, the upconverting nanoparticles (UCNPs), β-$NaGdF_4$: Yb,Er, can favor the cancer therapy guided by luminescence- and magnetic resonance-based imaging. The as-synthesized nanocomposites exhibited an enhancement in the photocurrent density and solar cell efficiency by ~24% and ~17%, respectively, in comparison to pristine $m TiO_2$. For photocatalysis, the Rhodamine B (RhB) dye was degraded ~99% in the presence of β-$NaGdF_4$: Yb,Er/$m TiO_2$ nanocomposites under the sunlight irradiation for 50 min. The dye mixture was also efficiently degraded to about 89% by the nanocomposite system. In another work, Yu et al. designed YbF_3: Ho/TiO_2 (UC/TiO_2) nanoheterostructures and analyzed them as an effective photoelectrode material rendering enhanced performance of DSSCs [36]. The overall PCE showed ~23% increment as compared to the pristine devices. The surface and transient photovoltage techniques were utilized to study the photogenerated charge transfer properties of UC/TiO_2 nanoheterostructures. Moreover, the electrochemical impedance spectra and open-circuit photovoltage decay techniques were used to investigate the interfacial dynamics of charge transfer and recombination processes in DSSCs. In another approach, $Na_xGdF_yO_z$: Yb,Er@TiO_2 shell/shell hollow spheres were fabricated by W. Liao et al., where they showed an improved solar cell performance via harvesting of NIR photons from the solar spectrum [37]. In all of these studies mentioned above, the main aim behind utilizing Ln^{3+}-activated inorganic phosphors in their respective systems is to improve the harvesting of photons across the solar spectrum viz. UV, visible, and NIR regions. These materials also act as a scattering layer, which ultimately helps to produce more photoelectrons to improve the PCE of the solar cell. A similar notable study was reported by P. Ramasamy et al., wherein a rear reflector structure was utilized that combined β-$NaGdF_4$: Yb,Er,Fe UCNPs for harvesting of NIR light, and silver (Ag) particles for light reflection to improve the DSSC performance [38]. The PCE of DSSC with a rear reflector increased by ~21.3% when compared with the cell without a rear reflector. The doping of Fe-ions in β-$NaGdF_4$ increased the luminescence efficiency by 30 times, which ultimately improved the photon-trapping of the system. Moreover, the presence of Ag particles increased the upconversion emission intensities, and this effect was predominantly attributed to significant scattering and surface plasmon coupling (explained in subsequent sections). Similarly, Y_2O_3: Er/Au@TiO_2 (SYE/A@T) composite, exhibiting star-like morphology, was developed, which displayed effective upconversion and light scattering when used

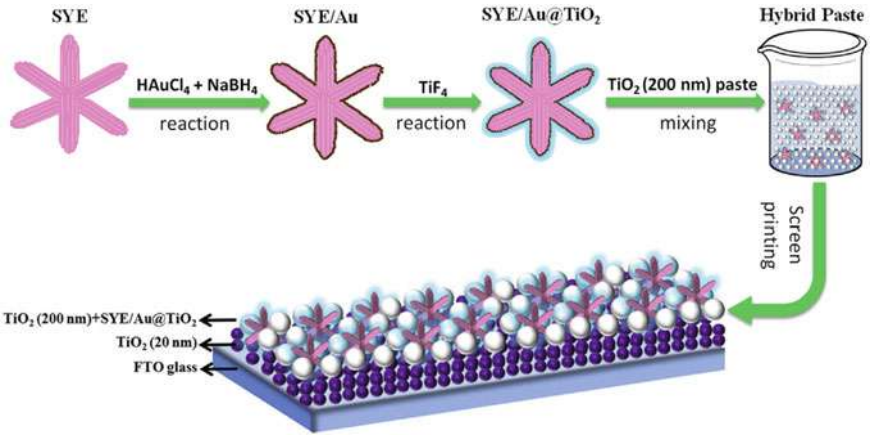

Fig. 3 Schematic representation of the synthesis procedure for SYE/Au@TiO_2 and the photoanode configuration of DSSCs. Reprinted with permission from Ref. [39]. Copyright 2016 Elsevier

in DSSCs [39]. The schematic representation of the synthesis procedure and configuration of the photoanode film is shown in Fig. 3. In the synthesis method, firstly, the star-like Y_2O_3: Er (SYE) was prepared, followed by the Au layer on the surface of Y_2O_3: Er NPs. Finally, the core–shell structured Y_2O_3: Er/Au@TiO_2 composite was synthesized via solvothermal process at 180 °C for 6 h. This was followed by the calcination reaction at 500 °C for 3 h. The TiO_2-shell reduced the recombination of charges on the SYE surface, while the Au-NPs layer increased the light absorption at around 515 nm due to the local electric field enhancement effect, thereby increasing the UCL. This overall significantly improved the PCE of DSSC by 27.6% as compared to the pristine cell.

In parallel, Luoshan and co-workers developed multi-shell-coated β-$NaYF_4$: Yb,Er—NFYE@SiO_2@Au@TiO_2 (NSAT) hexagonal submicroprisms decorated by Au-NPs, which were incorporated into the DSSCs as photoanodes [40]. The overall efficiency was enhanced by 28.1% in comparison to the DSSC with pure TiO_2. The improved efficiency of this system was expected owing to the high emission efficiency of hexagonal phase $NaYF_4$ compared to other hosts. The coating of SiO_2-shell provided insulation to the UC core, and thus the electron trapping induced by surface defects and luminescence quenching from ligands of bare β-$NaYF_4$: Yb,Er crystals can be avoided effectively. Further, the coating by Au-NPs improved the upconversion luminescence (UCL) by surface plasmon resonance (SPR) effect. This configuration enhanced the utilization of upconverted photons and ultimately enhanced the solar cell efficiency.

A variety of other hybrid materials based on Ln^{3+}-doped phosphors for photovoltaic applications have been presented by different research groups, such as β-$NaYF_4$: Yb,Er@TiO_2 composites [41], Y_2O_3: Yb,Er UCNPs and TiO_2 composite with PCE of 6.68% [42], $NaYF_4$: Yb,Er@$NaYF_4$ core–shell and TiO_2 composite with PCE of 12.5% sensitized with N749 dye [43], Y_2CaZnO_5: Yb,Er and TiO_2

composite with maximum PCE of 7.21% [44], $NaYF_4$: Yb,Er with TiO_2 hollow microspheres [45], β-$NaYF_4$: Yb,Er and TiO_2 composite with PCE of 7.17% [46], Y_2O_3: Yb,Ho and TiO_2 composite with PCE of 10.33% [47], etc.

2.1.2 Ln^{3+}-doped Phosphor-Semiconductor Hybrids for Photocatalysis

Similar to photovoltaics, photocatalytic systems with Ln^{3+}-doped phosphors as energy converters can improve the photocatalytic efficiency by the same working principle as described earlier. Wherein the drawback of insufficient sunlight utilization and photogenerated charge separation and the poor quantum efficiency of single-component semiconductor photocatalyst is reasonably overcome by the implementation of a multicomponent composite photocatalyst system. In 2010, Qin and co-workers developed a NIR to UV upconverting system—YF_3: Yb, Tm/TiO_2 core–shell nanostructure as an efficient photocatalyst [48]. The efficient energy-transfer from the UC core to the TiO_2-shell helped to improve photocatalytic activity. The core–shell YF_3: Yb,Tm/TiO_2 NPs were prepared using a modified hydrolysis process employing polyvinylpyrrolidone (PVP) as a coupling agent. In the beginning, in the dye decolorization process, Yb^{3+} ions absorbed the NIR light, and then the energy was transferred to Tm^{3+} ions, which emitted the UV light. The UV emissions from Tm^{3+} ions activated TiO_2-layers to generate reductive electrons and oxidative holes. The hole reacted with H_2O adsorbed on the surface to produce a free radical ·OH and H^+. The radical ·OH and e^- were able to destroy the chromophore of methylene blue (MB). The as-fabricated hybrid system led to about 61% photodegradation of MB upon 980 nm illumination for 30 h, while the pure TiO_2 used as a control did not show noticeable photocatalytic activity. Among the various UC phosphors, the $NaREF_4$ (RE = Y, Gd), specifically, hexagonal $NaYF_4$ is considered as one of the excellent host materials with better luminescence efficiency due to its low lattice phonon energy and wide bandgap [49]. Thus, it is observed that many researchers have predominantly utilized the judicial coupling of β-$NaYF_4$ based phosphors with other photoactive material in this field for achieving enhanced efficiency in their respective applications. Guo et al. reported β-$NaYF_4$: Yb,Tm@ZnO composites synthesized using the thermolysis method [50]. The composite showed 65% RhB degradation in 30 h under NIR irradiation. They also compared the photocatalytic activity of $NaYF_4$: Yb,Tm, and ZnO mixture; the activity was found to be only 35% under constant experimental conditions. The generation of ·OH radical, in the presence of $NaYF_4$: Yb,Tm@ZnO composites under NIR illumination, were monitored using terephthalic acid (TA) as a fluorescence probe. TA does not exhibit any fluorescence, although when it reacted with ·OH radical, it produced hydroxyterephthalic acid that emitted fluorescence upon excitation at 312 nm. Luminescence dynamic curves determined the energy-transfer efficiencies of pristine, mixture, and composites. Wu et al. presented $NaYF_4$: Yb,Er/C-TiO_2 hybrid as a promising potential photocatalyst for NO_x gas destruction induced by UV light and also weak visible and NIR lights [51]. The composite was synthesized via a calcination-assisted solvothermal route. The improved efficiency was resulted from the increased carbon doping in

TiO_2 and effective energy-transfer between UC phosphor and C-doped TiO_2. The composite possessed NO_x destruction ability much greater than P25 titania, C-TiO_2, and $NaYF_4$: Yb,Er/N-TiO_2 hybrid, due to the promising synergistic effect of $NaYF_4$: Yb,Er and C-TiO_2. In another work, core–shell $NaYF_4$: Yb,Tm@TiO_2 composites were prepared by a wet-chemical method [52]. The core $NaYF_4$: Yb,Tm for UCL was formed by a solvothermal process, while the anatase TiO_2-shell was synthesized through controlled hydrolysis and condensation of a titanium alkoxide in ethanol solution (Stöber's process). This process was followed by a solvothermal method for the crystalline shell of TiO_2. The core–shell $NaYF_4$: Yb,Tm@TiO_2 composites showed 65% MB degradation, which was 2 times greater than the physical mixture. This was ascribed to efficient energy migration in a core–shell structure, where $NaYF_4$: Yb,Tm, and anatase TiO_2 were in proximity forming the compact interfaces, hence, exhibited efficient FRET processes. While, no contact interfaces were present in the physical mixture of TiO_2 and $NaYF_4$: Yb,Tm particles, and thus, TiO_2 was excited via radiation-reabsorption. The schematic shown in Fig. 4 explained the dye-degradation mechanism for MB. The $NaYF_4$: Yb,Tm absorbed NIR light and emitted UV light, which activated the TiO_2 via FRET. The activated-TiO_2 produced electrons and holes in the conduction band (CB) and valence band (VB), respectively.

The electrons and holes reacted with water and oxygen adsorbed on the TiO_2 surface and generated reactive oxygen species (ROS). The CB of TiO_2 is located above the redox potential of MB ($E^{\circ}_{MB\cdot+/MB} = 1.08$ V vs. standard hydrogen electrode), which allowed TiO_2 to be catalytically active. Consequently, the ROS, such as $O_2^{\cdot-}$, ·OH, and H_2O_2, especially ·OH, oxidized the organic molecules and

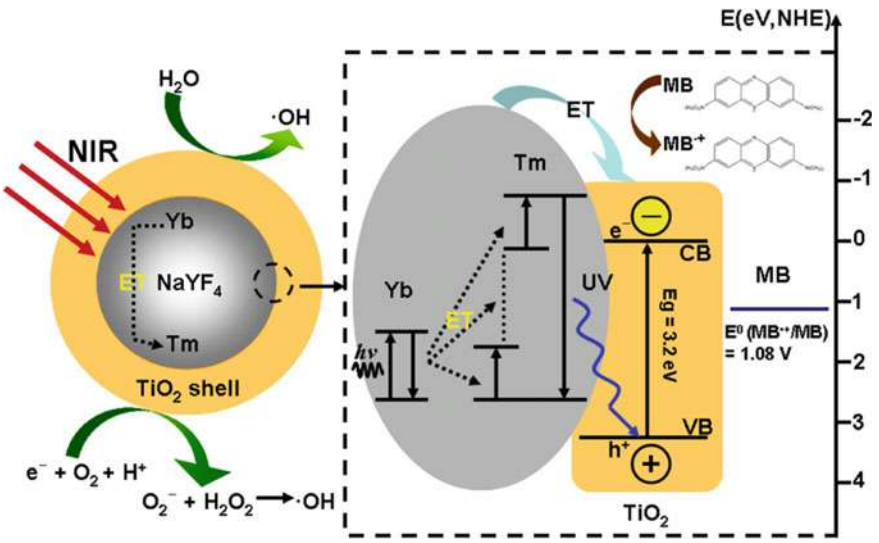

Fig. 4 Illustrative diagram showing energy-transfer process among Yb^{3+}, Tm^{3+} ions, and TiO_2, and the generation of ·OH radicals via reaction of electron and hole with the surface species of TiO_2. Reprinted with permission from Ref. [52]. Copyright 2013 American Chemical Society

performed photocatalysis. In another study, the $NaLuF_4$: Gd,Yb,Tm/TiO_2 composite was designed, and degradation of dyes including MB, RhB, and methyl orange (MO), dye mixtures, and dye wastewater were evaluated under irradiation using simulated solar light [53]. The $NaLuF_4$: Gd,Yb,Tm was synthesized by solvothermal route, and then the anatase phased TiO_2 NPs were attached to $NaLuF_4$: Gd,Yb,Tm nanocrystals via hydrolysis process and hydrothermal method. The degradation ratio of RhB, MB, and MO were 98.7%, 95.5%, and 82.9%, respectively, in the presence of the as-prepared composite under the Xe lamp illumination for 250 min. The photocatalytic activity of the nanocomposites $NaLuF_4$: Gd,Yb,Tm/TiO_2 was observed to be 1.7 times higher than their physical mixture due to the efficient energy-transfer between them in the nanocomposite. In another work, a β-$NaLuF_4$: Gd,Yb,Tm@SiO_2@TiO_2: Mo double-shell-structured nanocomposite as a potent photocatalyst was designed by Yin et al. [54]. The nanocomposite consisted of β-$NaLuF_4$: Gd,Yb,Tm UC nanocrystals as a core, SiO_2 as a middle-shell, and anatase TiO_2 as the outer-shell modified by Mo-doping. This modification narrowed the bandgap of TiO_2. Consequently, TiO_2 acted as an electron-trap which resulted in the improvement of overall light absorption and reduction in the rate of recombination of the photogenerated charge carriers. A different model for improved NIR photocatalysis was proposed by preparing $NaYF_4$: Yb,Tm/CdS/TiO_2 composites, wherein TiO_2 and CdS nanocrystals were linked to the surface of $NaYF_4$: Yb,Tm microcrystals to form a heterojunction structure [55]. The energy-transfer between $NaYF_4$: Yb,Tm, and the semiconductors CdS and TiO_2 was explored. It was observed that the combined adherence of TiO_2 and CdS on the surface of $NaYF_4$: Yb,Tm particle displayed significantly higher catalytic activities than the individual adhesion of TiO_2 or CdS on the surface of $NaYF_4$: Yb,Tm NPs. The higher activity of the system was mostly ascribed to the effective electron–hole pair separation due to the charge transfer across the CdS-TiO_2 interface which was driven by the difference in the band potential between them. In another report, $NaYF_4$: Yb,Tm UCNPs were modified with a carbon-layer using reverse-micelle method. This carboneous polymer shell consisted of cross-linked aromatic compounds and other functional groups such as –OH, –COOH, and –CHO, rendering hydrophilicity and surface functionality to the UCNPs [56]. Thus, the carbon-shell on the UCNPs provided a suitable substrate for the in situ generation of CdS nanoclusters on the surface. The developed $NaYF_4$: Yb,Er@C@CdS hybrid displayed significant visible light-induced photocatalytic activity. Zhang et al. reported $NaYF_4$: Yb,Tm@TiO_2 core–shell composite photocatalysts where $NaYF_4$: Yb,Tm microrods, and nanorods were coated with highly crystalline and thickness-tunable TiO_2-shells [57]. The crystallinity and controlled thickness of the shell was essential for efficient photocatalysis performance. It was demonstrated by Fig. 5 that if the polycrystalline TiO_2-shell is too thick, it may decrease a considerable amount of the incoming NIR light; concurrently, the TiO_2 surface was less activated since the UV light arrived at the external surface was weakened. The synthesis process is shown in Fig. 5b. Firstly, the $NaYF_4$: Yb,Tm microrods were prepared by the hydrothermal route. Then, PVP was coated on the surface by adding microrods into the PVP solution with ultra-sonication and stirred to stabilize them. The PVP coating ensured the uniform nucleation of TiO_2 nanocrystals on the rods. Then, TiF_4 as Ti precursor was added into the solution under

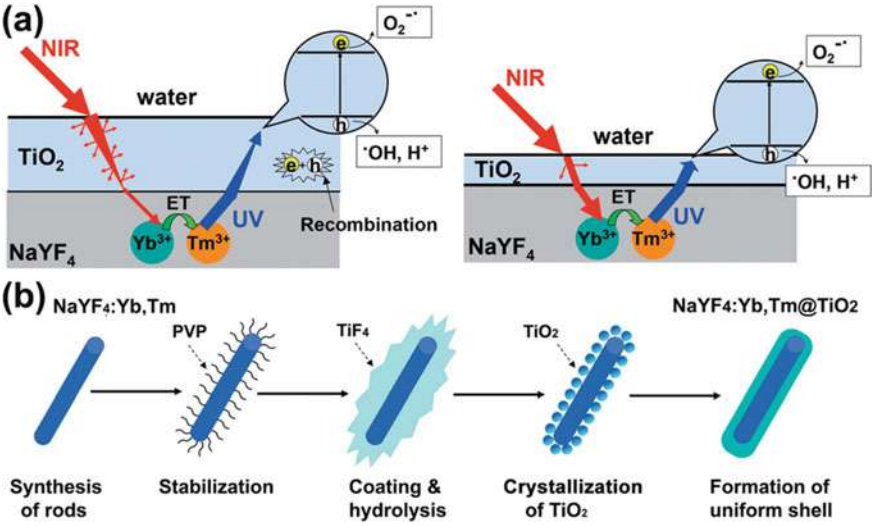

Fig. 5 Schematic describing **a** the upconversion-based photocatalysis process with different shells thicknesses (left: thick shell, right: moderate shell), **b** synthesis of core–shell $NaYF_4$: Yb,Tm@TiO_2 composites. Reprinted with permission from Ref. [57]. Copyright 2013 The Royal Society of Chemistry

constant stirring, as it mildly hydrolyzed under hydrothermal conditions. In the final step, the resultant suspension was heated hydrothermally at 180 °C for 4 h. The thicknesses of the TiO_2-shell were tuned by changing the ratio of Ti precursors and fluorides. This work discussed the significance of shell thickness in light absorption, surface quenching process, trapping of electron–hole pair and recombination which ultimately modified the photocatalytic efficiency. Controlling shell-thickness is an important parameter for enhanced photocatalytic efficiency. It is quite challenging to tune shell-thickness and is a significant research area for the material scientists working in the field of energy applications.

In another approach, Wu reported UC phosphors coupled BiOBr composites for nitric oxide (NO) gas degradation [58]. In their study, oxygen vacancies enriched BiOBr NPs, a typical p-type photocatalyst with a narrow bandgap, were utilized for photocatalytic degradation of toxic NO gas in the visible region. The as-prepared composite displayed superior deNO_x ability under irradiation of UV, visible, and NIR lights. A. Kumar designed and developed a multicomponent photocatalyst system by rationally combining UCNPs, plasmonic metals, semiconductors, and carbonaceous support as a promising method for the effective photon-conversion of the broadband spectrum [59]. The structure was formed of core–shell nanostructures $NaYF_4$@CdS decorated with Au-NPs, which were supported on reduced graphene oxide (RGO) nanosheets. Compared to bare counterparts, these quaternary nanocomposites exhibited better photocatalytic activity for degradation of a typical pharmaceutical drug pollutant, non-photosensitizing ciprofloxacin, under visible and NIR

light. This was ascribed to synergistic effects of (a) NIR absorption by UC phosphors, (b) spectral-overlap of UC emission and CdS absorption in core–shell structures, (c) emission enhancement of UC via SPR effect owing to the presence of Au-NPs (d) RGO supporting the catalyst and acting as electron-acceptor, electron-transporter, and an adsorbent for the pollutant. The photocatalytic activity was investigated for ciprofloxacin degradation under visible and NIR light with varied RGO content (1–5 wt%) in the nanocomposites. The concentration of RGO also affects the absorption of pollutants; that parameter also played a significant role in improving the photocatalytic properties. A similar kind of system was fabricated as UC Ln^{3+}-doped nanophosphors; $NaYF_4$: Yb,Tm were coated with a porous semiconductor TiO_2, and then decorated with bimetallic plasmonic Ag–Cu NPs [60]. Apart from the plasmonic effect from Ag–Cu bimetallic NPs, they also served to utilize visible light emitted from active core–shell UCNPs, playing the role of co-catalyst. Thus, the photocatalytic activity was improved, ascribed to the cooperative effect brought in by the upconverting properties of UC core, the semiconducting properties of TiO_2, and the SPR effect of Ag–Cu bimetallic NPs.

Other rare-earth compound based photocatalysts and hybrids, including oxides, oxysulfides, etc., have also been studied by various groups; some of them mentioned are $Y_3Al_5O_{12}$: Er^{3+}/TiO_2–ZrO_2 composite as visible-light active photocatalyst [61], integration of Y_2O_3: Er,Yb crystals into TiO_2/CdSe heterostructured photoanodes for H_2 generation with NIR photons [62], Y_2O_2S: Eu–ZnO composite photocatalyst [63], and so forth. A consolidated list of composites reported for photovoltaics and photocatalysts is given in Table 1.

Furthermore, the hybrid/composites of TiO_2 and Ln^{3+}-doped UC phosphors were also studied for biomedical applications [64, 65]. In a noticeable study by Xu et al., Anti-cAngptl4 Ab-conjugated N-TiO_2/$NaYF_4$: Yb,Tm hybrid was reported for NIR-induced drug release and targeted cancer cell destruction by ROS mechanism [66]. This is an important study providing a gateway for the utilization and development of semiconductor-based Ln^{3+}-activated inorganic hybrids for applications in theranostics. In another study by Hou et al., a NIR-activated photosensitizer for PDT based on UCNPs@TiO_2 core–shell nanocomposites was designed [67]. In this work, $NaYF_4$: Yb,Tm@$NaGdF_4$: Yb core–shell UCNPs converted NIR light to UV emission under 980 nm illumination. The UV emission matched well with the absorption of the TiO_2. The as-prepared nanocomposites could produce intracellular ROS under NIR light, which decreased the potential of the mitochondrial membrane to release cytochrome *c* into the cytosol. This activated caspase 3 to induce cancer cell apoptosis and inhibited the growth of tumors in vivo. The results in this work showed that the nanocomposites could serve as a potential photosensitizer for NIR-activated PDT in antitumor therapy as well as prospective CT and MRI contrast agents. Chen and group reported UCNPs@m$HTiO_2$ as a nanoplatform for chemo/PDT and imaging based on the UCNPs, $NaYF_4$: Yb,Tm@$NaYF_4$ as core, coated with hollow, mesoporous-TiO_2 [68]. The hollow structure helped to store the antitumor drug doxorubicin (DOX) and thus promoted chemotherapy efficiency. Under NIR irradiation, UV-emission obtained from UCNPs excited TiO_2 to produce ROS and to achieve PDT. The results

Table 1 A list of composites reported for photovoltaics and photocatalysts with their efficiency

S. No	Hybrid material	Enhancement in photovoltaic efficiency	Enhancement in photocatalytic efficiency	References
1	$NaYF_4$: Yb,Er hexagonal nanoplatelets as an external layer and a single internal transparent TiO_2 layer	10%		[32]
2	Core/double-shell β-$NaYF_4$: Yb,Er@SiO_2@ TiO_2 submicron hexagonal prism	10.9%		[33]
3	β-$NaYF_4$: Yb,Er@SiO_2@ TiO_2 microplates	29.4%		[34]
4	β-$NaGdF_4$: Yb,Er/*m*TiO_2	17%	99% RhB degradation in 50 min under sunlight	[35]
5	YbF_3: Ho/TiO_2 nano-heterostructures	23%		[36]
6	$Na_xGdF_yO_z$: Yb,Er@TiO_2	11.3%		[37]
7	Y_2O_3: Er/Au@TiO_2	27.6%		[39]
8	$NaYF_4$@SiO_2@Au	28.1%		[40]
9	YF_3: Yb,Tm@TiO_2		61% MB degradation in 30 h under NIR irradiation	[48]
10	β-$NaYF_4$: Yb,Tm@ZnO		65% RhB degradation in 30 h under NIR irradiation	[50]
11	$NaYF_4$: Yb,Er/C-TiO_2		8.5% of NOx gas destruction for NIR, 30% for 445 nm LED, and 19% by the red LED	[51]
12	$NaYF_4$: Yb,Tm@TiO_2 core–shell		65% MB degradation under NIR irradiation	[52]
13	$NaLuF_4$: Gd,Yb,Tm/TiO_2		98% degradation of RhB, 95.5% MB, 82.9% MO degradation in 250 min under Xe lamp	[53]

(continued)

Table 1 (continued)

S. No	Hybrid material	Enhancement in photovoltaic efficiency	Enhancement in photocatalytic efficiency	References
14	$NaLuF_4$:Gd,Yb,Tm@SiO_2@TiO_2:Mo		99% RhB degradation in 210 min under Xe lamp and almost complete degradation under NIR 980 nm light	[54]
15	$NaYF_4$: Yb,Tm/CdS/TiO_2		100% degradation of MB in 50 h under NIR light	[55]
16	$NaYF_4$: Yb,Er-BiOBr composite		2.5% deNOx ability under NIR light, 1.92% deNOx ability under NIR light	[58]
17	$NaYF_4$: Yb,Er@CdS-Au-RGO (RGO concentration 3 and 4%)		90% degradation of ciprofloxacin under visible light and 69% degradation in 180 min under NIR light	[59]
18	$NaYF_4$: Yb,Er@CdS-Ag–Cu (For 0.5 wt% Ag–Cu concentration)		96% degradation of MB in 60 min under UV light, and 65% degradation of MB in 180 min under NIR light	[60]

Note: Enhancement refers to improved efficiency compared to the reference cell without the UC materials or compared to the pristine individual counterparts

showed that the cooperative effect of chemotherapy and PDT enhanced the cytotoxicity to the cancer cells. These studies offer ample scope in designing and developing novel materials to show promising applications in biological sciences.

2.2 Ln^{3+}-doped Phosphor-Magnetic Material Hybrids for Multimodal Imaging Applications

Trivalent lanthanide ion-doped NPs are promising candidates as bioprobes in cell imaging due to their intriguing merits of luminescent properties, as discussed in the introduction part. Although optical imaging provides excellent sensitivity for in vitro imaging, but still possesses the shortcoming of low penetration depth and is incapable of acquiring physiological and anatomical details in in vivo imaging. Diversely, magnetic resonance imaging (MRI) renders a great spatial resolution and penetration depth for bioimaging and gives detailed anatomical information; however, it suffers from limited sensitivity [69]. The integration of the potential benefits of MRI and optical imaging can fill gaps in sensitivity and depth of imaging between these two modalities and offer the way to overcome the current limitations of individual imaging. Luminescent-magnetic hybrids based on fluorescent QDs or organic fluorophore and magnetic iron oxide are able to fulfil the bimodal imaging capabilities. However, as discussed earlier about the limitations of QDs/fluorophores, their respective hybrids suffer photobleaching and cause photodamage to the biological tissues. On the other hand, Ln^{3+}-doped inorganic phosphors, specifically UC phosphors, offer deeper tissue penetration, reduced photodamage, and prolonged photostability. Moreover, these also eliminate the autofluorescence from the biological samples during imaging. These aspects stimulated the development of Ln^{3+}-activated inorganic hybrids with magnetic nanoprobes as a new approach in drug delivery, bioseparation, and medical theranostics.

Zhang et al., in 2008, developed magnetic-luminescent nanocomposite $Fe_3O_4@SiO_2/Y_2O_3$: Tb by combining $Fe_3O_4@SiO_2$ core–shell nanostructures with Y_2O_3: Tb nanorods [70]. The as-synthesized nanocomposite integrated the advantages of luminescence and superparamagnetism and thus was expected to find applications in bioimaging and drug delivery. Another system, multifunctional $Fe_3O_4@Y_2O_3$: Eu core–shell structure, was synthesized by Gowd et al. via facile wet-chemical route followed by annealing [71]. The as-synthesized core–shell structure possessed a small size of ~30 nm NPs with red emission at 612 nm and superparamagnetic behavior at room temperature. The NPs were expected to possess a prospect for drug delivery and multimodal bio-imaging applications. Later, Wu et al. fabricated the Gd^{3+} co-doped $Fe_3O_4@Y_2O_3$: Eu bifunctional core–shell NPs, that is $Fe_3O_4@(Y_{1-x}Gd_x)_2O_3$: Eu composite via urea-based homogeneous precipitation method [72]. The sample exhibited the amplified photoluminescence intensity, which was almost 2.7 times more than the undoped composite because of the effective energy-transfer between Gd^{3+} and Eu^{3+}. This system possessed strong red luminescence and good saturation magnetization. A multicomponent sandwich structured $Fe_3O_4@nSiO_2@mSiO_2@YVO_4$: Eu hybrid microspheres were developed with mesoporous, luminescent, and magnetic properties by Yang et al. [73]. In this approach, firstly, Fe_3O_4 microspheres were synthesized hydrothermally, and then these microspheres were encapsulated with nonporous silica followed by mesoporous silica layer using the sol–gel method. The outer silica-shell surface was

further coated by YVO_4: Eu phosphors. The storage and release properties were studied for this drug-carrier multifunctional system, wherein ibuprofen was used as a drug. This system was reported to be utilized as a targeted drug delivery system, where the amount of drug release can be observed with the change in the luminescence intensity of Eu^{3+} ions, since the Eu^{3+} luminescence intensity increased with the released amount of drug. In another effort, a luminescence-magnetic hybrid of YVO_4: Eu/Fe_2O_3 was synthesized, which was investigated for hyperthermia and bioimaging in the cancer cells [74]. The hyperthermia temperature of 42 °C was achieved and the red emission of Eu^{3+} was used for bioimaging applications.

In another commendable attempt, Lu et al. described a method of synthesizing UC-fluorescent magnetic NPs with covalently-coupled streptavidin (sAv). Yb and Er co-doped $NaYF_4$ was deposited on Fe_2O_3 NPs by co-precipitation of lanthanide salts in the presence of ethylenediaminetetraacetic acid (EDTA) [75]. Then, fluorescent/magnetic NPs were coated with a SiO_2 layer, formed by the hydrolysis of tetraethyl orthosilicate (TEOS) and 3-aminopropyltrimethoxysilane. These NPs were covalently-coupled with sAv after the activation with glutaraldehyde. The hybrid NPs possessed magnetic response and green/red upconversion luminescence. The sAv-coated UC fluorescent magnetic NPs can be easily linked with biomolecules such as proteins, antibodies, and nucleic acids, etc., via streptavidin/biotin interactions; thus can be used to detect target molecules in samples. In another report, Mi et al. synthesized magnetic/luminescent multifunctional Fe_3O_4/$NaYF_4$: Yb,Er nanocomposites by linking carboxylic-functionalized superparamagnetic Fe_3O_4 NPs with amine-functionalized silica-coated luminescent $NaYF_4$: Yb,Er UCNPs via covalent linkage using EDC/NHS (EDC: *N*-ethyl-*N*′-[2-(dimethylamino)propyl]carbodiimide hydrochloride and NHS: *N*-hydroxysuccinide) coupling chemistry [76]. The obtained nanocomposites exhibited chemically active amine and carboxylic groups on the surface, which were beneficial for facile conjugation with biomolecules. In this report, $NaYF_4$: Yb,Er UCNPs were utilized for bioimaging in response to irradiation by NIR light. Furthermore, the nanocomposites were conjugated with transferrin as there were active functional groups on the surface, which helped in the conjugation. The conjugated nanocomposites specifically recognized the transferrin receptors overexpressed in HeLa cancer cells, and thus can be used for biolabeling and bioimaging of HeLa cells. NIR light possesses deep penetration into the biological samples without damaging them, and its use can avoid autofluorescence from biological tissue. Thus, the UCNPs and superparamagnetic NPs presence in the nanocomposites will endow them in simultaneous bioimaging and separation applications. Another approach was developed by Shen et al., where they synthesized Fe_3O_4/$NaYF_4$: Yb,Er hetero-NPs via a cross-linker anchoring process with dual properties of upconversion emission and superparamagnetism [77]. The cross-linker, 11-mercaptoundecanoic acid (MUA) or 1,10-decanedicarboxylic acid (DDA), was incorporated for anchoring Fe_3O_4 NPs onto the $NaYF_4$: Yb,Er hexagonal prismatic NPs surface, as shown in Fig. 6. In the synthesis protocol, firstly, $NaYF_4$: Yb,Er nanocrystals capped with oleic acid (OA) were prepared possessing the uniform size and high dispersibility. These bound OA could be substituted further with DDA or MUA via ligand exchange with the

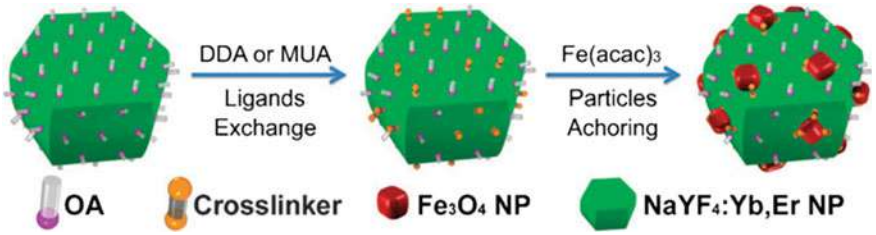

Fig. 6 Schematic showing cross-linker anchoring strategy for bifunctional Fe_3O_4/$NaYF_4$: Yb,Er hetero-NPs. Reprinted with permission from Ref. [77]. Copyright 2010 The Royal Society of Chemistry

simultaneous anchoring of the Fe_3O_4 NPs during the thermolysis reaction. It was proposed that the cross-linker is necessary to couple UCNPs and Fe_3O_4 NPs to yield hetero-NPs, as in a control experiment without cross-linkers; hetero-structure was not formed. In comparison with other processes for chemical linkage, this cross-linker anchoring strategy was found to be facile, irreversible and stable, thus it is effective for the construction of hetero-NPs. This coordination-based method is also not restricted by lattice mismatch for different functional constituents, which is usually regarded as the prerequisite for the synthesis of hetero-structures.

In another work, Fe_3O_4/$NaYF_4$ hetero-submicrorods with a bifunctional magnetic-luminescent property were developed via EDTA-assisted hydrothermal route [78]. The Fe_3O_4 NPs were strongly attached to the $NaYF_4$ submicrorods surface, generating a hetero-structure. The Fe_3O_4/$NaYF_4$ hetero-submicrorods possessed a saturated magnetization value of 9.4 emu g^{-1} and were able to emit bright green luminescence under irradiation at 980 nm. It is well studied that the limitation of low penetration depth of the incident light in photoluminescent imaging can be resolved by MRI as well as X-ray computed tomography (CT). Many studies have utilized bi-modal imaging of luminescence and MRI. But, it is noticeable that CT also provides better spatial resolution and 3D tomography detail about deep anatomic structures with different contrast and imaging depth than that of MRI. Thus, a tri-modal imaging sole probe can be helpful in different areas of application. Zhu et al. synthesized Fe_3O_4@$NaLuF_4$: Yb,Er/Tm core–shell nanostructures (abbreviated as MUCNP) as can be seen in Fig. 7, utilized as a CT, MR, and UCL tri-modality imaging probe [79].

The hybrid exhibited superparamagnetic property with a saturation magnetization of 15 emu g^{-1}, and T_2-enhanced MRI capability, resulting from the Fe_3O_4 cores. Since Lu atom has the highest atomic number among the lanthanides, a high degree of X-ray absorption by the $NaLuF_4$-based UCNPs was expected. Thus, the $NaLuF_4$-based UCNPs provided excellent X-ray attenuation (CT imaging) and UCL under excitation at 980 nm. An in vitro toxicity assay and in vivo CT and MRI imaging experiments were performed in this work. Another kind of facile method was presented by Hu et al. for the construction of $NaYF_4$: Yb,Er/Tm@SiO_2@Fe_3O_4 core–shell structured nanocomposites [80]. In this approach, the $NaYF_4$: Yb,Tm/Er

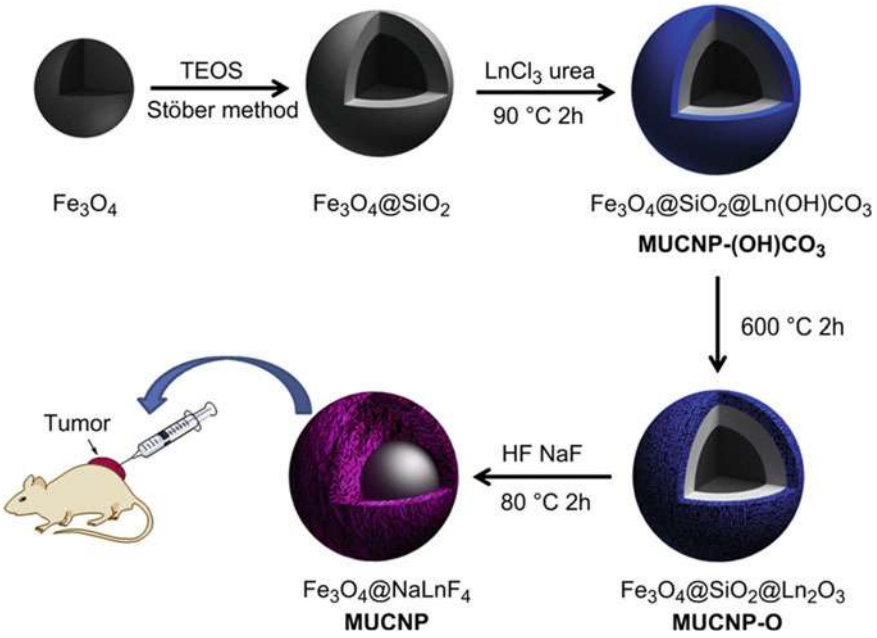

Fig. 7 Schematic illustration of the synthetic approach of the core–shell Fe_3O_4@$NaLuF_4$: Yb,Er/Tm NPs. Reprinted with permission from Ref. [79]. Copyright 2012 Elsevier

NPs capped with EDTA were mixed with the OA-modified Fe_3O_4 NPs in isopropyl alcohol. This step was followed by the addition of TEOS and ammonium hydroxide, and the solution was mixed for 2 h at room temperature. The $NaYF_4$: Yb,Er/Tm@SiO_2@Fe_3O_4 core–shell nanocomposites, with $NaYF_4$: Yb,Er/Tm as core and SiO_2-Fe_3O_4 as hybrid shell, were yielded directly. Otherwise, the other methods of core–shell structure fabrication require multiple steps of functionalization and coatings. In another report, Zhong et al. demonstrated the fabrication of monodispersed, magnetic, and luminescent core–shell structured Fe_3O_4@$NaGdF_4$: Yb,Er@$NaGdF_4$: Yb,Er NPs by a seed-growth thermolysis process [81]. Firstly, Fe_3O_4 core NPs capped with OA were prepared by the thermal decomposition of the iron-oleate precursors. Then, as-synthesized Fe_3O_4 NPs were served as the seeds for the growth of $NaGdF_4$: Yb,Er shell in the presence of OA, and 1-octadecene. Besides, a luminescent shell was grown using the as-prepared Fe_3O_4@$NaGdF_4$: Yb,Er as seeds. In another effort by Cheng et al., the UCNP-IONP-Au multifunctional nanocomposite fabricated via layer-by-layer self-assembly was developed [82]. The schematic representation of the synthesis process of this multifunctional nanocomposite is shown in Fig. 8. The superparamagnetic iron oxide nanoparticles (IONPs) were adsorbed on the $NaYF_4$ surface by electrostatic interaction to form UCNP-IONP complex. A thin shell of Au was formed via the seed-induced reduction growth method on top of the complex. The IONPs layer between the UCNPs and the Au-shell rendered magnetic properties along with the luminescence enhancement of UCNPs

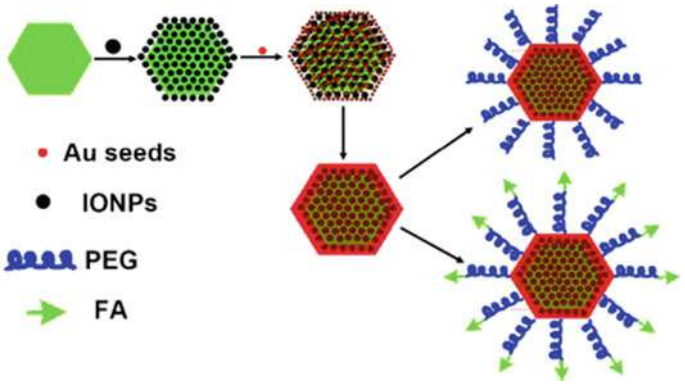

Fig. 8 Schematic showing the strategy for multifunctional NPs synthesis and functionalization. Adapted with permission from Ref. [83]. Copyright 2020 The Royal Society of Chemistry

by surface plasmon coupling via maintaining FRET distance. The UCNP-IONP-Au multifunctional NPs were then coated with poly(ethylene glycol) (PEG) to impart stability to the particles in physiological solutions used for in vitro targeted MR, UCL, and dark-field light scattering imaging. The folic acid was conjugated further to the multifunctional NPs through PEG linker to target the folate receptor, which is usually up-regulated in cancer cells. The contribution of Au-shell in the composite was employed for dual-targeted photothermal ablation of cancer cells through SPR absorption. In vivo UCL/MR dual-modal imaging was further validated in animal imaging experiments. The proposed multifunctional nanocomposites may have great use in multimodality biomedical imaging and therapy.

We have attempted to cover significant and broad types of magnetic-luminescent hybrid materials fabricated by different chemical approaches. A variety of other magnetic-luminescent hybrid materials have been presented by different research groups, for example, Fe_3O_4@$GdPO_4$: Eu nanoneedles hybrids [84], $NaYF_4$: Yb,Tm@Fe_xO_y with 20 nm $NaYF_4$: Yb,Tm NPs as a core and 5 nm Fe_xO_y NPs as a shell [85], Fe_3O_4@nSiO_2@mSiO_2@$NaYF_4$: Yb,Er [86], etc.

2.3 Ln^{3+}-doped Phosphor-Plasmonic Metal Hybrids for Luminescence Enhancement and Sensing Applications

Ln^{3+}-activated phosphors have demonstrated significant potential in many fields, including biosensing, bioimaging, and solar energy conversion, as mentioned earlier; however, some bottlenecks such as lower upconversion efficiency should be overcome. Using plasmonic nanostructures with phosphors presents a promising route to highly efficient down/upconversion luminescence. Therefore, plenty of reports have

been published in recent years to enhance the luminescence of the Ln^{3+}-doped materials by coupling them with Au or Ag NPs/films [87–89]. The collective oscillations of free electrons are called plasmons, and the oscillations at the interface between a dielectric material and the material with free electrons are known as surface plasmons. The coupling of these oscillations causes the incoming light highly confined near the interface, which may lead to the enhancement of the radiative decay rates and absorption cross-sections. Overall, the enhancement of luminescence of phosphor materials due to their proximity with metal NPs may be ascribed to two probable factors: (1) a substantial increment of effective excitation/absorption flux around lanthanide emitting ions induced by local electric-field enhancement (LFE) associated with plasmonic resonance; (2) improvement of luminescence efficiency due to the coupling of the down/upconversion emission with the plasmonic resonance peak of metal NPs increase the radiative decay rate and consequently the emission rate, resulting in surface plasmon coupled emission (SPCE) [90, 91]. Tuning of SPR peaks of metal NPs resonant to the absorption and emission wavelength of the phosphors can be the main principle to improve the emission efficiency of the phosphors. Further, the effect of the spacing between UCNPs and the surface of metal NPs controls the interactions and the enhancement factor. These hybrid structures also bestow a potential platform for improved applications in biological imaging, photothermal therapy (PTT), sensing, and detection. To date, the phenomenon of enhanced emission intensity, due to metallic (especially Ag and Au) NPs, has been well established, and researchers have adopted many methods to obtain Ln^{3+}-doped down/upconverting NPs with high brightness via incorporation of noble metals NPs due to their effective modulation of the spectral properties [92–95].

For example, in 2009, the luminescence of Y_2O_3: Yb thin films deposited on sapphire substrates was improved from 970 to 1070 nm range using the Au-NPs arrays with different aspect ratios [96]. The resonance of longitudinal localized SPR peaks of Au NPs with multiple transition lines of Yb^{3+} ions enhanced the luminescence efficiency. The findings indicated that the Y_2O_3: Yb is a promising frequency-shifting material and thus applicable for the harvesting of solar photons. Zhang et al. reported a facile procedure to construct core/spacer/shell metal-core enhanced materials [97]. The group synthesized $Ag@SiO_2@Y_2O_3$ nanostructures and optimized the thickness of the spacer, silica. The nanostructure synthesis is schematically shown in Fig. 9a, where Ag-NPs were coated with a layer of silica through the modified Stöber method to obtain $Ag@SiO_2$ composite. The resulting composite with ~50 nm Ag NP positioned at the center has a diameter of ~190 nm (Fig. 9b). Then, the layer of Y, $Er(OH)CO_3 \cdot H_2O$ was coated over $Ag@SiO_2$ spheres through a precipitation method at 90 °C for 2 h. Further heating at 700 °C for 3 h transformed Y, $Er(OH)CO_3 \cdot H_2O$ layer to the cubic phase of Y_2O_3. The results revealed that the luminescence intensity of the nanostructures was sensitive to the distance between the Ag-NP and Y_2O_3: Er shell, with a maximum increment obtained at an optimal thickness of the spacer of 30 nm. The reason for the increment was referred to as the higher emission rate of Er^{3+} ions induced by the strong plasmon resonance scattering.

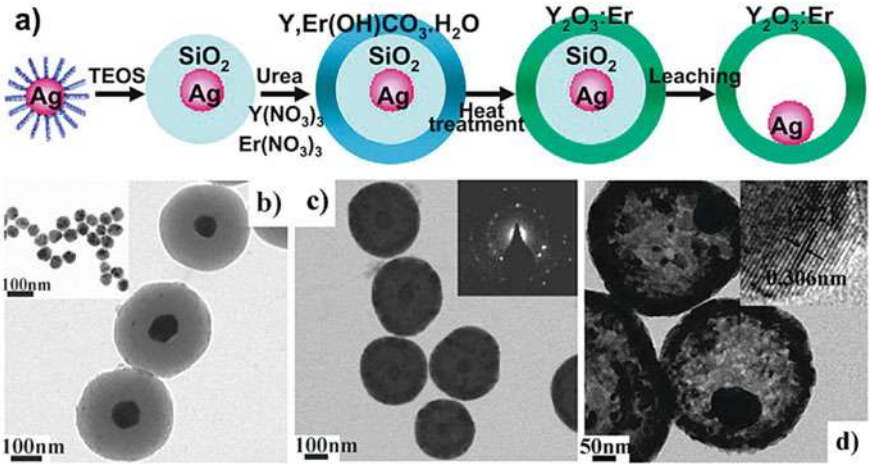

Fig. 9 **a** Schematic showing the synthetic approach of the $Ag@SiO_2@Y_2O_3$: Er nanostructures. TEM images of **b** Ag-50 nm@SiO_2 nanospheres, with inset showing 50 nm Ag NPs; **c** Ag-50 nm@SiO_2@Y_2O_3: Er nanospheres, with inset showing SAED patterns recorded on the Y_2O_3: Er layer; **d** Ag-50 nm@Y_2O_3: Er hollow nanospheres, with inset showing HRTEM of the Y_2O_3: Er layer. Reprinted with permission from Ref. [97]. Copyright 2010 American Chemical Society

In 2014, Ag-SiO_2-ErO_3 hybrid was fabricated where the interaction of E_2O_3 with surface-plasmon of Ag-NPs enhanced the UCL remarkably [98]. It was interesting to observe that the luminescence was improved by order of 10^0 to 10^4, which depended on the power density of excitation wavelength under 980 nm illumination. The prepared hybrid was promised to be useful at extreme conditions such as high temperature and high pumping power.

In the case of fluoride phosphors, a study was reported with an overall fivefold improvement of UCL in $NaYF_4$: Yb,Er crystals when coupled with Au-island films [90]. It was shown that a continuous Au-film featured a plasmonic resonance peak in the NIR range where the absorption for the upconversion process is located (980 nm). The spectroscopic studies in this work showed that there was an increase in the excitation flux, which was originated from LFE and hence resulted in the improvement of the UCL intensity. Another approach was demonstrated to modulate the upconversion luminescence through the heterointegration of $NaYF_4$: Yb,Tm UCNPs with Au-nanostructures [91]. It was shown that Au-NPs on the UCNPs surface could function as the seeds for the growth of Au-nanoshells. $NaYF_4$: Yb,Tm NPs were prepared by the thermal decomposition method with OA as a ligand providing hydrophobic character to the surface. This was followed by the ligand-exchange treatment with poly(acrylic acid) (PAA), rendering the negative charge to the NPs. For the positive charge on the surface, an extra layer of poly(allylamine hydrochloride) was coated. Further, the attachment of Au-NPs and the growth of Au-nanoshells were performed in an aqueous solution. Au-NPs were shown to increase the luminescence intensity

by more than twofold, while the Au-nanoshells suppressed the upconversion emission intensity due to the excitation radiation scattering. These results, to modulate the emission intensity, impacted the areas of biomedical imaging, sensing, therapeutics, as well as energy harvesting and conversion, as mentioned in the above sections. In another similar study in 2012 conducted by Li et al., plasmon-enhanced UCL in $NaYF_4$: Yb,Er,Gd nanorods was achieved using Au-NPs or Au-nanoshells [99]. A process for $NaYF_4$/Au core–shell nanostructures was proposed with dispersed Au-NPs and Au-nanoshell on the surface of nanorods. In the system with Au-NPs on the surface, more than threefold improvement in the luminescence intensity was observed at 540 nm under 980 nm diode laser, whereas the formation of a continuous shell around the nanorods suppressed the intensity. Schietinger and group showed the plasmon enhancement in single $NaYF_4$: Yb,Er nanocrystal with the emission peaks in the green and red regions under the excitation at 973 nm [100]. In this work, single $NaYF_4$ nanocrystal and Au nanospheres (30 nm and 60 nm in diameter) were fabricated in a combined confocal and atomic force microscope setup. An enhancement factor of 3.8 was achieved in this system. In another work, multicolor UCL increment was achieved using the hybrid nanostructures Au@$NaYF_4$: Yb,Tm, synthesized using trisodium citrate as a surfactant [101]. The enhancement factor at the emission wavelengths of 291 nm and 345 nm were 73.7 and 109.0, respectively. The main reason for this improved luminescence intensity was the plasmon field enhancement effect or LFE. As non-linear optical materials, UCNPs normally require high excitation power densities for better emission intensity, which might cause damage to the biological tissues in the applications. Consequently, the NPs for such kind of applications should be of low pumping threshold in power density and should able to possess high efficiency for the upconversion emission, which was achieved in this system. In a work by Priyam and group, an improvement of UCL was achieved for silica-coated $NaYF_4$: Yb, Er when coated with Au-nanoshell [102]. The tuning of the SPR peak of Au-nanoshell was done in the NIR region, which increased the excitation flux via the LFE effect and thereby increased the emission intensity. The system thus prepared was promised to be used for upconversion luminescence and dark-field light scattering imaging. In another interesting work by Kannan et al. [103], Au-nanorods were decorated on 'polyamidoamine generation 1 dendrimer'-functionalized $NaYF_4$: Yb,Tm UCNPs by seed-mediated growth of Au-nanorods. The UCL of $NaYF_4$:Yb,Tm@Au was improved using the shell-like structures up to 27 times, suggesting the decoration of individual Au-nanorods to be a good way for improving the luminescence. This system was further modified with 2-thiouracil for the uric acid detection with a detection limit of 1 pM. In the subsequent year, amplification of emission intensity of $NaYF_4$:Yb,Tm and $NaYF_4$: Yb,Er UCNPs was observed in the presence of metal NPs [104]. In this work, a configuration was presented where UCNPs were separated from metal NPs (Ag or Au) by the oxide (Al_2O_3) layer grown by atomic layer deposition. This geometry was used to investigate the role of the thickness of the spacer-layer on the enhancement process in which the spacer thickness was varied from 2 to 15 nm for distinct metal-UCNPs combinations. It was expected that the luminescence improvements would be relied on the oxide-layer thickness and the type of metal NPs used with the enhancement

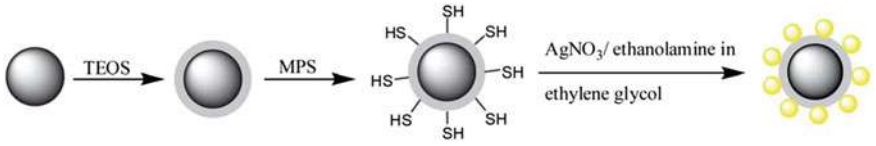

Fig. 10 Schematic describing the synthesis process of $NaYF_4$: Yb,Er@SiO_2@Ag nanocomposites. Reprinted with permission from Ref. [105]. Copyright 2012 The Royal Society of Chemistry

up to 5.2-fold with Au NPs and up to 45-fold with Ag-NPs. To study the impact of the oxide spacer-layer to modulate the emission intensity of UCNPs, in another study by Yuan et al., core–shell hybrid $NaYF_4$: Yb,Er@SiO_2@Ag was prepared with different SiO_2 thicknesses [105]. For the preparation of core–shell structure, firstly, $NaYF_4$: Yb,Er UCNPs were prepared with OA as surfactant followed by a coating of silica on the surface with TEOS as shown in Fig. 10. Ag-NPs were synthesized in two sizes: 15 and 30 nm. The extent of modulation of emission intensity was greatly dependent on the separation between the UCNPs and Ag-NPs, which was attributed to the competition between radiative decay rates and energy-transfer process. An increment of 14.4-fold was noticed when Ag-NPs of size 15 nm were used with a 10 nm separation distance, while 10.8-fold enhancement was observed when Ag-NPs of size 30 nm were used. This system was further modified with DNA to improve their biocompatibility to demonstrate the biological imaging of B16F0 cells.

In another exciting work, the colloidal core–shell hybrid Au–Ag nanocage@$NaYF_4$@$NaYF_4$: Yb,Er nanostructures were fabricated with a different intermediate $NaYF_4$ shell thickness and tunable SPR peaks of metals [106]. After optimization, an overall increment of 25-fold was achieved with ~7.5 nm intermediate spacer thickness and localized SPR peak of metal NPs at ~950 nm. The results indicated that the improvement in UCL in Ag nanocube@$NaYF_4$@$NaYF_4$: Yb,Er was observed with increasing the thickness of the intermediate shell, which was ascribed to the inhibition of energy-transfer to Ag nanocubes from Er^{3+} ions. This increment also originated from the coupling of Au–Ag nanocages with the excitation wavelength of the UCNPs.

Plasmonic modulation of luminescence was well known, where the plasmonic nanostructures concentrated the incident light into the localized electric fields close to the surface of the NPs. Since this is a near-field effect and thus exponentially decays as we move far from the surface of the metal. Also, if the metal NPs density is not high and the distance between them is larger, then the UCNPs will not be able to interact with the metal NPs effectively. However, in the proximity of the metal NPs, the plasmonic resonance can modify both re-radiative decay rates and non-radiative decay rates, which stimulate the enhancement and lead to the quenching of luminescence, respectively. In order to achieve stability, reproducibility, and high efficiency of UCL through plasmon coupling and to increase the scattering of the metal NPs, a porous Ag-film that consisted of randomly distributed Ag-NPs of more than 100 nm was prepared [107]. The improved UCL of $NaYF_4$: Yb,Er was observed by using the near-field coupling of SPR of Ag-NPs and far-field coupling

of poly(methyl methacrylate), PMMA opal photonic crystals. Photonic crystals can control the propagation of electromagnetic waves and can be utilized to modulate the luminescence intensity. A porous Ag-film was designed consisting of Ag-NPs to effectively control the interaction distance between SPR and UCNPs, which was a pivotal point to obtain high luminescence. The porosity in the film not only decreased the interaction between Ag-film and UCNPs but also suppressed the local thermal effects caused by the laser irradiation. In the far-field coupling of photonic crystals, PMMA photonic stop band was tuned to 980 nm, which precisely matched with the excitation light. An enhancement factor of 60-fold was observed in a hybrid system with PMMA/Ag NPs/$NaYF_4$: Yb,Er, while a 50-fold enhancement was noticed with a hybrid consisting of Ag-NPs/$NaYF_4$: Yb,Er. Overall, this work offered the fundamental understanding of the UCL improvement through the coupling of SPR of metals, which have potential in photoelectric devices. In another effort, arrays of nanoholes in Au-films were constructed and were utilized as a template to localize and increase the UCL of $NaYF_4$: Yb,Er UCNPs [108]. The thin metallic layers of Au-nanoholes arrays were designed in such a way that the nanohole could take up only one UCNP upon filling. They employed the squeegee method to precisely position the single UCNP inside each nanohole array. The luminescence increment of up to 35-fold was noted due to the combined effect of generation of the enhanced electromagnetic field in nanohole arrays at resonance and increase in the radiative decay rate of the emitters. In a work by Wang et al., 2D Au-NPs arrays of various periodicities were prepared, which improved the UCL from $NaYF_4$: Yb,Er,Gd nanorods (UC NR) [109]. The red emission at ~660 nm from UC NR under the excitation at 980 nm was significantly increased by 1.4-fold due to the interaction with Au-NPs arrays. The Au-NPs arrays were prepared on indium tin oxide-coated glass by electron beam lithography. The SEM images in Fig. 11a, b show the top- and side-views of the arrays. The UC NRs were formed by a liquid–solid reaction in ethanol and OA; and then, the thin film was prepared by spin-coating on the Au-NPs arrays, as shown in Fig. 11c with the substrate tilted at 60°. The relative enhancement of the green and red emission was manipulated by varying the periodicity of 2D Au-NPs arrays. It was demonstrated in this work that the SPR-assisted diffractive coupling in Au-NPs arrays contributed to the overall improvement in the emission. These results suggested that the plasmonic-excitation-emission interactions can be controlled, and UCL can therefore be modulated accordingly.

In another effort, lithographically-fabricated metal–insulator-metal (MIM) nanostructures were reported, which showed over the 1000-fold enhancement of UCL of $NaYF_4$: Yb,Er [110]. It was further demonstrated that the system had potential use in bioimaging the bladder cancer cell by dispersing the MIM into water. Recently, the plasmonic Au-nanohole-nanoplate bilayer arrays (PABAs) were designed by Zhan et al. to generate the local field. This generated local field then coupled with excitation and emission field of $NaGdF_4$: Yb,Er@$NaYF_4$ core–shell UCNPs [111]. The theoretical simulation indicated that the PABA could generate a steady-state electric field in the nanoholes of the arrays that overlapped efficiently with the green emission of the UCNPs, which led to the LFE. The as-prepared PABA-supported core–shell

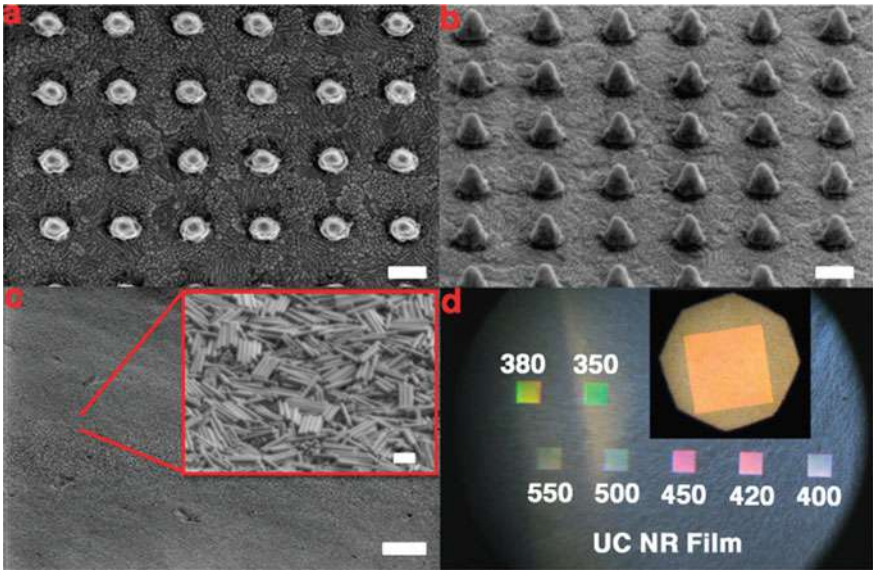

Fig. 11 **a** Top view SEM image of Au-NP arrays, and **b** side view of Au-NPs on ITO substrate (substrate titled at 45°) **c** UC NRs film covering Au-NP arrays (substrate titled at 60°) and the close view of the UC NRs film **d** optical microscope images of a UC NRs film covered Au-NP arrays; each array showed different color under white light illumination at a titled angle; the numbers indicated the periodicities of each array; the inserted image showed one UC NR film covered array under higher magnification. Dimensions: scale bars (**a**) and **b** 200 nm; **c** 20 mm and 200 nm on the whole surface and inserted SEM, respectively; **d** 100 × 100 mm^2 for each Au-NP arrays square. Reprinted with permission from Ref. [109]. Copyright 2015 Physical Chemistry Chemistry Physics Owner Societies

UCNPs were utilized as a sensor to detect acetic acid with much higher sensitivity and a detection limit of 81 nmol mL^{-1}.

Some of the other examples in this field are Al_2O_3: Er on Ag island films [112], Au/SiO_2/Y_2O_3: Yb,Er [113], Ag NPs embedded La_2O_3: Yb,Er phosphors [114], YVO_4: Yb,Er@Ag hybrid colloid [115], $NaGdF_4$: Yb,Er@SiO_2/Au NPs hybrid for bioimaging applications [116], $NaYF_4$: Yb,Er@Ag core–shell nanocomposites [117], Au-nanoshell coated $NaYF_4$ [102], Ag metal-capped $NaGd_{0.3}Yb_{0.7}F_4$: Er [118], hybrid of $NaYF_4$: Yb,Er@$NaYF_4$ and Au nanorods for PTT [119], and so forth.

2.4 Ln^{3+}-doped Phosphor-Graphene (and Its Derivatives) Hybrids for FRET Based-Sensing, and Drug Delivery Applications

Carbon-based materials such as graphite, carbon black, carbon nanotubes (CNT), graphene, graphene oxide (GO), graphene quantum dots (GQDs), and so on possess unique physicochemical properties. Among them, nanomaterials such as graphene, GO, GQDs and CNTs have engaged significant attention in the last decade in view of their advantageous properties such as high specific surface area, mechanical strength, high electrical and thermal conductivity due to excellent mobility of charge carriers, high thermal stability, low density, and environmental friendliness [120, 121]. Thus, they have fascinated a considerable interest in fundamental science and potential applications in various new opto-electronic devices, sensors, and energy systems. It is worth noting that various reports of carbon-based materials with Ln^{3+}-doped phosphors are known until now for their biosensing, bioimaging, drug delivery, anti-counterfeiting, opto-electronic and photocatalytic applications [122–125].

The coupling of Ln^{3+}-doped phosphors with graphene showed excellent and amplified electrogenerated chemiluminescent intensity by taking advantage of the electrical conduction of graphene, as depicted in Fig. 12 [126]. In this work, an in situ one-step method was reported to fabricate ultrathin graphene and $NaYF_4$: Yb,Er UCNPs hybrid material with amplified electrogenerated chemiluminescence enhanced by fivefold. The electrogenerated chemiluminescent-based sensing application shares many superior advantages in analytical science, such as simpler instrumentation and low limit of detection arisen from the low background emission.

Another exciting example includes the new generation hybrid material based on UCNPs and GO covalently bonded together. The short distance described by this covalent bond assured that the energy from the UCNPs could be effectively transferred to GO, resulting in superior optical limiting performance [127]. The superior optical limiting effect suggested applications in opto-electronic devices and in making high-performance laser protecting products. In another study, a new approach was demonstrated using core–shell $NaYF_4$: Yb,Er,Nd@$NaYF_4$: Nd UCNPs, and monolayer graphene hybrid for broadband photodetection utilizing the multi-energy

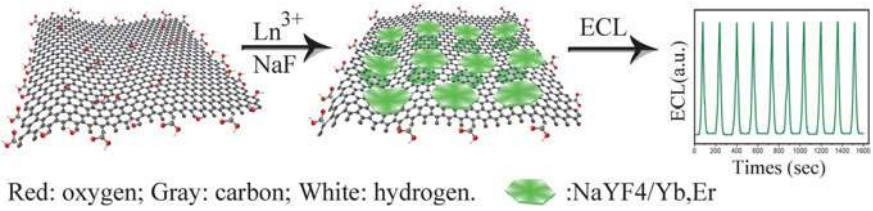

Fig. 12 Schematic representation of the preparation procedure of the nanohybrid graphene-$NaYF_4$: Yb,Er, and its electrogenerated chemiluminescent property. Reprinted with permission from Ref. [126]. Copyright 2012 The Royal Society of Chemistry

levels of lanthanides [128]. In this system, the hybrid photodetector showed photoresponsitivity of 190 AW^{-1} under the 808 nm irradiation. This was due to the presence of a rippled structured graphene, which enabled high photon absorption. The UCNPs showed broad absorption spectra over UV, visible, and IR regions, as shown in Fig. 13a, making them suitable for broadband photodetection. The as-prepared hybrid was used on prestrained poly(dimethylsiloxane) (PDMS) substrate to construct a planar structure photodetector. To get the hybrid UCNP/rippled graphene photodetector, prestrained PDMS substrate was released later. The SEM image of rippled graphene after being released is shown in Fig. 13b. The rippled structured graphene facilitated the photon absorption for UCNPs due to the multiple scattering adding to the value of photoresponsivity, as can be seen in schematic in Fig. 13c. The hybrid photodetection on PDMS substrate exhibited great stretchability, wearability, flexibility, and durability with high photoresponsivity. In another similar kind of study in 2019, a hybrid based on silica-coated UCNPs, $NaYF_4$: Yb,Er@SiO_2, and graphene

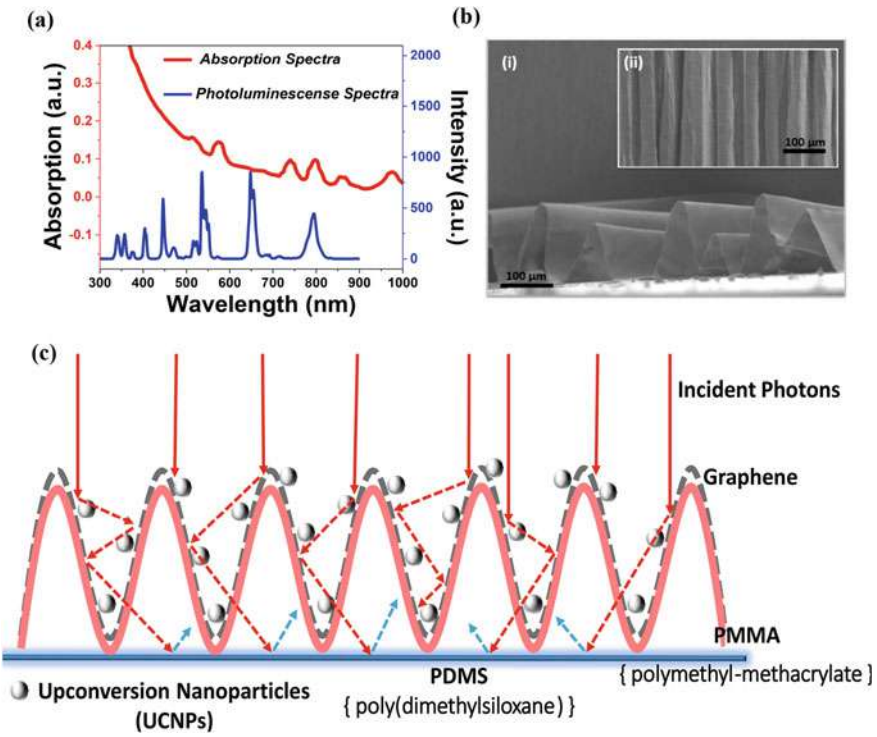

Fig. 13 **a** Absorption and photoluminescence spectra of $NaYF_4$: Yb,Er,Nd@$NaYF_4$: Nd core–shell UCNPs in cyclohexane. **b** (i) Cross-sectional SEM image and (ii) lateral SEM image of the rippled structure. **c** Schematic diagram of the rippled structure of the hybrid photodetector showing multiple internal reflections. Adapted with permission from Ref. [128]. Copyright 2018 American Chemical Society

[129] was fabricated for broadband photodetection under 980 nm illumination with photoresponsivity of 2.7×10^4 AW^{-1}.

Ln^{3+}-based phosphors hold promise as NIR light converters to improve the efficiency of the solar cells. Despite their value, their use in solar cells is restricted by their low emission efficiency and poor electrical conductivity. Thus, graphene and graphene oxide can be used to achieve good electrical conductivity. Taking this road, in 2012, $NaYF_4$: Yb,Er-graphene composites were prepared by growing UCNPs in interlayers of expanded graphite. This was accompanied by the exfoliation of expanded graphite under PVP-assisted hydrothermal reaction [130]. A large number of UCNPs homogeneously cover the surface of multi-layered graphene sheets. More importantly, the as-prepared hybrid was used to form TiO_2-$NaYF_4$: Yb,Er-graphene hybrid photoanodes, which had the capability to enhance the efficiency of the solar cell. In a similar kind of study, reduced GO (rGO) and $NaYF_4$: Yb,Er hybrids were designed to achieve better electrical conductivity because of the high charge carrier mobility of rGO [131]. The hybrid of UCNPs and rGO were synthesized in situ by the hydrothermal approach, which was followed by the reduction method. Then, the as-prepared hybrid was incorporated into the photoanode of the solar cell, which improved the efficiency by 10% and short-circuit current density. These studies opened new opportunities for extending the use of Ln^{3+}-based hybrid phosphors in the areas of solar energy harvesting.

Development of optical pH sensors based on the flexible free-standing optical hybrid film was composed using GO and polyethylenimine (PEI)-coated $NaYF_4$: Yb,Er NPs (Fig. 14a–c). In this work, the high specific surface area, luminescence quenching ability, mechanical stability of GO were used as the platform for pH sensing [132]. Here, GO served as an acceptor in the energy-transfer pair between GO and UCNPs hybrid and as a matrix for the free-standing film. The interaction between the $NaYF_4$: Yb,Er NPs and GO becomes stronger with increasing pH, which led to the significant luminescence quenching of UCNPs. The admirable mechanical properties of the hybrid film endowed the pH sensor with higher stability and superior repeatability and thus promised to be a good candidate for biological applications.

For biomedical applications, fluorescence resonance energy-transfer (FRET)-based energy-transfer is used for sensing different biomolecules by utilizing UCNPs and graphene and its derivatives. There have been many reports where non-radiative energy-transfer from an excited donor (UCNPs) to an acceptor (GO) through electrostatic dipole–dipole interactions takes place [133–136]. In one study in 2012, an aptasensor for mycotoxins was presented based on the FRET between multicolor UCNPs, $BaYF_5$: Yb,Tm, and $BaYF_5$: Yb,Er as a donor, and GO as an acceptor [137]. The UNCPs $BaYF_5$: Yb,Tm, and $BaYF_5$: Yb,Er were functionalized with immobilized ochratoxin A (OTA) aptamers and fumonisin B_1 (FB_1) aptamers, respectively. These UCNPs modified with aptamer were brought in the vicinity to the surface of GO due to the β–β stacking interactions between aptamers nucleobases and sp^2 carbon atoms of GO. This resulted in the luminescence quenching of the UCNPs because of the significant overlap of absorption of GO and emission of UCNPs in that region. The aptamers on the UCNPs surface preferred to attach to their corresponding mycotoxins in the presence of OTA and FB_1, leading to a change in the aptamers formation.

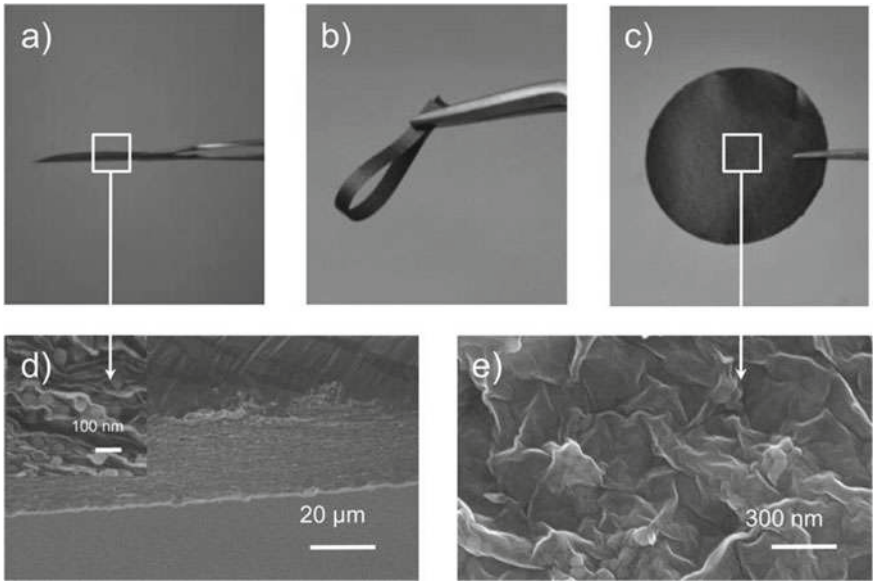

Fig. 14 **a–c** Photographs of free-standing hybrid film GO-PEI-$NaYF_4$: Yb,Er. **d** Low and high-resolution SEM images of the hybrid film (side view). **e** The SEM image of the hybrid film on the surface. Adapted with permission from Ref. [132]. Copyright 2014 The Royal Society of Chemistry

Consequently, UCNPs modified with aptamers were at a distance from the surface of GO, leading to an increase in the UCL intensity, as schematically shown in Fig. 15. The limit of detection observed for OTA and FB_1 was 0.02 ng mL^{-1} and 0.1 ng mL^{-1}, respectively.

In a separate study, GQDs and single-stranded DNA (ssDNA) linked UCNP@SiO_2 based sensor was designed for the detection of specific microRNA (miRNA) sequence [138]. The developed sensor deliberated the interactions between the sp^2 carbon atoms of GQDs and DNA nucleobases linked to the UCNPs, which brought GQDs near to the surface of ssDNAUCNP@SiO_2. The UCNPs capacity to interact with GQDs through β-β stacking was hindered by ssDNA in the presence of a complementary miRNA sequence, which resulted in the reduction of the fluorescent intensity-dependent of miRNA sequence. This outcome was utilized to design a sensor with a limit of detection of 10 fM. For bioimaging applications, multifunctional multi-walled CNT (MWCNT)-$NaGdF_4$: Yb,Er,Eu hybrid was developed for simultaneous optical and magnetic imaging by $NaGdF_4$: Yb,Er,Eu NPs and photothermal conversion from MWCNT [139]. Wang et al. reported a multifunctional platform where core–shell structured UCNPs were covalently grafted with nanographene oxide (NGO) via PEG followed by loading of phthalocyanine (ZnPc) on the NGO surface [140]. Firstly, $NaYF_4$: Yb,Er,Tm@$NaYF_4$ core–shell type of structure was prepared using the thermal decomposition procedure with OA as a capping agent. In order to further utilize them, the ligand exchange method was

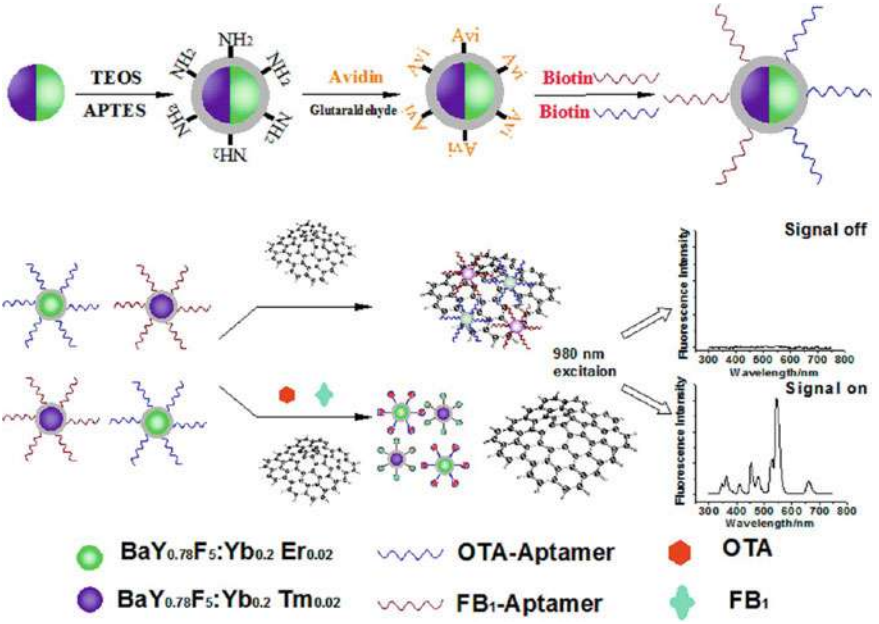

Fig. 15 Schematic representation of the upconversion fluorescence resonance energy-transfer (FRET) between aptamers-UCNPs and GO for the detection of OTA and FB_1. Reprinted with permission from Ref. [137]. Copyright 2012 American Chemical Society

adopted for the amine functionalization on the UCNPs surface with poly(allylamine). To bestow the UCNPs with multimodal therapeutic functions, NGO was grafted with UCNPs, which served as PTT agent and carrier for photosensitizer. This was done via carbodiimide cross-linking reactions between the amino group present in UCNPs-NH_2 and the carboxylic group of NGO-PEG to yield UCNPs-NGO composite, as shown in Fig. 16a. This was finally followed by the loading of the drug ZnPc to yield UCNPs-NGO/ZnPc composite. The obtained UCNPs-NGC/ZnPc composite was used for diagnosis as an imaging probe with high contrast. The integration of PTT, PDT, and imaging functions into a single hybrid nanostructure acted as a theranostic probe, as illustrated in Fig. 16b. The combined treatment of PDT and PTT exhibited a synergistic effect which resulted in higher therapeutic efficacy for the in vitro cancer treatment by decreasing the tissue damage by over-heating and dosage-limiting toxicity.

Recently, one concept for the fabrication of histidine and octadecylamine-functionalized GQDs and $NaYF_4$: Yb,Er UCNPs hybrid nanocage was proposed, which was adequate for drug loading towards the controlled delivery and cancer theranostics [141]. In this work, the biomimetic drug delivery system was developed, which consisted of hybrid nanocage and Au-NPs and MGC-803 cell membranes as the core and the shell, respectively. This system exhibited the DOX loading capacity

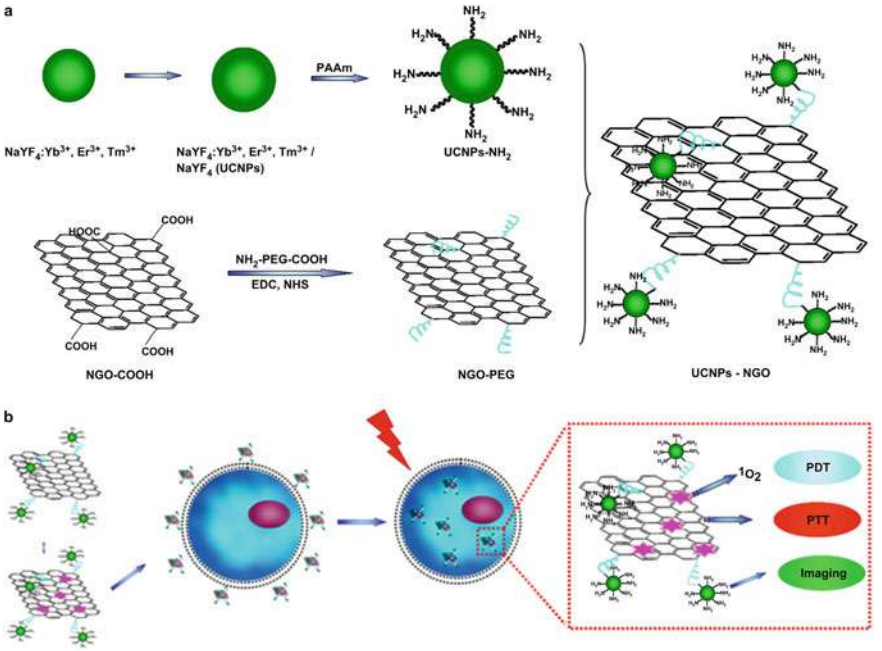

Fig. 16 Schematic representation of the **a** synthesis process for UCNPs-NGO where numbers of core–shell UCNPs being covalently grafted with NGO via bifunctional PEG; **b** UCNPs-NGO/ZnPc hybrid as a multifunctional theranostic nanoplatform for cancer treatment. Reprinted with permission from Ref. [140]. Copyright 2013 Elsevier

of 461.2% at nearly 100% of encapsulation efficiency. It also exhibited the selective targeting of homotypic tumor cells showing both with pH and light-stimulated drug release. The nanocage hybrid remarkably improved the photothermal effect of Au-NPs, which helped accelerate the NIR-triggered drug release. This study opens a pathway to develop and synthesize ideal nanocarriers for cancer theranostics.

A range of other hybrid materials with graphene and its derivatives for different applications have been reported by various research groups, for example, GO-oxynitride phosphor ($SrBaSi_2O_2N_2$: Eu) hybrid for opto-electronic device applications [142], $NaYF_4$: Yb,Er-GO hybrid for glucose determination [143], $NaYF_4$: Yb,Er-graphene for DSSC [144], graphene oxide quantum dots and $NaYF_4$: Yb,Tm@$NaGdF_4$ hybrid for PDT [145], and so forth.

2.5 Ln^{3+}-doped Phosphor-Quantum Dot Hybrids for Bioimaging, FRET-Based Biosensing, and Energy Applications

Quantum dots (QDs) have been largely analyzed because of their distinct optical properties such as large emission/absorption cross-sections, tunable emissions, and multiplexing capabilities [146, 147]. Also, QDs are widely studied as FRET energy-donors or acceptors in various applications. Bednarkiewicz et al. demonstrated the efficient FRET between UC phosphor $NaYF_4$: Yb,Er as a donor, and CdSe QDs as an acceptor [148]. The green upconverted emission at ~540 nm from Er^{3+} ion was quenched by QDs; on the other hand, the orange emission from QDs appeared simultaneously due to an energy-transfer from $NaYF_4$: Yb,Er donor to QDs acceptor. They studied the FRET efficiency using lifetime measurements. The authors proposed that this system can be utilized as nanolabels in the biodetection field. In a work by Chang et al., $NaYF_4$: Yb,Tm/CdS nanoheterostructures were developed, and they observed that the red and NIR emissions of $NaYF_4$: Yb,Tm phosphors were amplified by 7.3 times, whereas the blue emission was attenuated [149]. They proposed that the energy-transfer process between Tm^{3+} ions and CdS QDs was very efficient. They also synthesized $NaYF_4$: Yb,Tm/CdSe nanoheterostructures to analyze the effect of other QDs on the UCL of $NaYF_4$: Yb,Tm, and found that in this case also the NIR emission of $NaYF_4$: Yb,Tm improved greatly. The UCNP-to-QD FRET system using biotin-streptavidin interaction as a prototype was demonstrated by Mattsson et al., which can be used for rapid homogeneous optical biosensing [147]. $NaYF_4$: Yb,Er-streptavidin (sAv) acted as a donor and biotinylated CdSe/ZnS core–shell (biot) QDs acted as an acceptor to form UCNP-sAv-biot-QD system. Biotin-streptavidin recognition was utilized in the development of a competitive replacement assay to modulate the UCNP-to-QD energy-transfer upon varying biotin concentration. This competitive replacement assay principle is shown in Fig. 17. In this study, the biot-QD and UCNP-sAv concentrations were optimized, resulting in a very low limit of detection. Such technology of UCNPs and QDs based FRET system can be employed for the biological interactions detection. Antoniak et al. studied spectrally-resolved femtosecond non-linear optical properties in the range 950–1350 nm for $NaYF_4$: Yb,Er/CdSe hybrid [150]. In this work, the size of CdSe QDs decorated on the surface of core $NaYF_4$: Yb,Er phosphors were varied, and the FRET efficiency between them varied depending on the size of CdSe QDs. The two-photon-induced luminescent properties and the switching of multimodal luminescence of $NaYF_4$: Yb,Er/CdSe hybrid nanomaterials were demonstrated. Continuous wave 980 nm laser was used for $NaYF_4$: Yb,Er UCNPs emission, while NIR femtosecond laser was used for emission of CdSe QDs.

The multimodal luminescent properties of these hybrid nanomaterials were proposed to be potentially utilized for 2D anti-counterfeiting applications. In another report published in the year 2016, $NaYF_4$: Yb,Tm/CdSe nanostructures were synthesized where the emission from Tm^{3+} ions at 797 nm was observed under 980 nm irradiation with no UV and blue emissions from it [151]. It was indicated that the

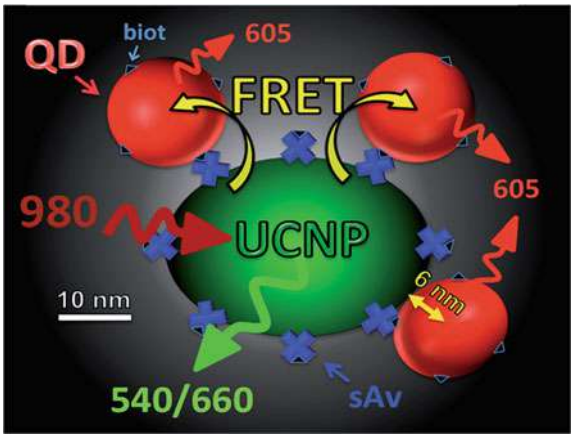

Fig. 17 Schematic representation of principle of the homogeneous UCNP-to-QD FRET biotin replacement assay. Excitation at 980 nm leads to emission from UCNPs and FRET to QDs, which resulted in QD luminescence. Reprinted with permission from Ref. [147]. Copyright 2015 The Royal Society of Chemistry

energy was first transferred from Yb^{3+} ions to Tm^{3+} ions when excited with 980 nm laser. Then, it was transferred to CdSe QDs partially from Tm^{3+} ions, which excited CdSe QDs returns/gives back to Tm^{3+} ions. The NIR emission from Tm^{3+} was greatly enhanced, and no emission peaks of CdSe QDs appeared. In this work, the excitation wavelength and the emission wavelength were both located in the NIR region (700–1100 nm), which is considered as the "optical window" of biological tissues. Hence, such nanoheterostructures are expected to possess eminent potential in the field of biological and biomedicine applications. S. Cui designed $NaYF_4$: Yb,Er/CdTe UCNPs/QDs composite as a probe for the Hg^{2+} ions detection in serum [152]. The PEI-capped $NaYF_4$: Yb,Er UCNPs were prepared via solvothermal procedure. The CdTe QDs were then grafted on the $NaYF_4$: Yb,Er UCNPs surface. The system was irradiated by 980 nm NIR light, which was able to overcome the interfering autofluorescence from the serum. A FRET-based biosensor was able to detect Hg^{2+} ions effectively with a limit of detection of 15 nM. The core–shell $NaYF_4$: Yb,Tm@CdS composite was demonstrated for photocatalytic application by Feng et al. [153]. As compared to pure CdS, the photocatalytic activity of $NaYF_4$: Yb,Tm@CdS composite was enhanced under vis–NIR irradiation by improving the absorption of sunlight.

Some other hybrid materials with QDs for different applications includes—$NaYF_4$: Yb,Er and CdSe QDs nanoheterostructures [154], Ag_2Se QDs-$NaYF_4$: Yb,Gd,Er@$NaYF_4$: Nd,Yb nanocomposite for PDT [155], etc.

2.6 Ln^{3+}-doped Hybrid Phosphors with Other Materials

The other composites of Ln^{3+}-doped phosphors with several other materials of interest, such as metal–organic frameworks (MOFs), polymers, dichalcogenides, etc., have also been studied by various scientific groups.

MOF: Typically, MOFs are highly porous crystalline materials comprising metal ions or clusters coordinately interconnected by organic-linkers. An exceptionally high surface area of up to 8000 $m^2\ g^{-1}$ and tunable pore sizes can be obtained due to the resultant void within these materials [156]. Due to these properties, MOFs have been one of the most studied materials in the areas of biomedicines, photocatalysis, sensing, etc. Specifically, the biomedical applications requiring controlled drug release, high drug-loading capacities, and optimal stability, the MOFs can improve the treatment efficacy [157]. The performance of MOFs can be improved by linking them or encapsulating them with other active materials such as Ln^{3+}-doped phosphors. Li et al. developed core–shell UCNPs@MOF: $NaYF_4$: Yb,Er@Fe-MIL-101_NH_2 nanoprobes for luminescent/magnetic dual-mode targeted imaging [158]. The framework Fe-MIL-101 comprises terephthalate linkers and Fe_3O-carboxylate trimers with octahedrally-coordinated metal ions. The core–shell nanostructures simultaneously presented the optical property of the UCNPs core and the T_2-MRI property of the MOF-shell. The UCNPs core was coated with amine-functionalized octahedral iron carboxylate MOF-shell, giving the nanostructures good water dispersibility along with easier conjugation to PEG. The surface of the core–shell nanostructures was further modified with poly(ethylene glycol)-2-amino ethyl ether acetic acid and folic acid (FA), which resulted in PEGylated core–shell UCNP@Fe-MIL-101_NH_2@PEG-FA nanostructures. It was believed that the core–shell structures open up new ways to combine the advantages of UCNPs and MOF for various functions. Deng et al. reported an aptamer-conjugated core–shell $NaYF_4$: Yb,Er@Fe-MIL100 composite for the targeted delivery of DOX and for cell imaging [159]. Here, UCNPs chosen as optical labels, emitted intense green light under 980 nm excitation, while the MOF based on the iron carboxylate MOF, Fe-MIL-100 possessed high porosity and low cytotoxicity, which was beneficial for the drug delivery. The anticancer aptamer, AS1411 (a 26-mer guanine-rich oligonucleotide), was conjugated covalently on the surface of the UCNP@MOF, which helped in targeting the cancer cell and enhancing the intracellular uptake. This system promised targeted cancer theranostics. Yuan et al. [160] demonstrated in situ self-assembly method for the synthesis of the nanocomposites of MOFs and UCNPs driven by only electrostatic interactions. The schematic illustration of the synthesis procedure is shown in Fig. 18. Firstly, OA-capped β-$NaYF_4$: Yb,Er was synthesized by the thermal co-precipitation method followed by the acid treatment to remove the surface ligands. The ligand-free UCNPs were mixed with the MOF precursors to yield the nanocomposite having octahedral geometry with small UCNPs decorated on the surface of MOF. This was further used to construct core–shell-shell, MOF@UCNPs@MOF sandwiched nanocomposites via epitaxial growth of MOF

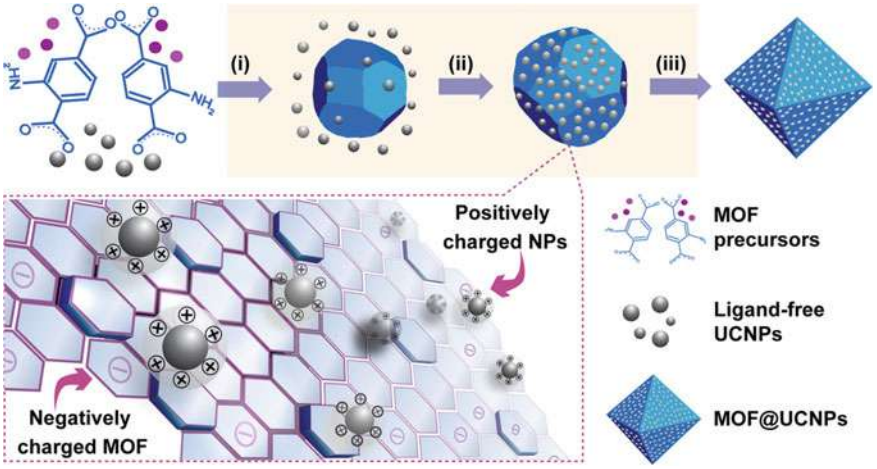

Fig. 18 Schematic illustration of the fabrication of UCNPs and MOF nanocomposites. The reaction precursors of MOF and ligand-free UCNPs were mixed directly, and the nanocomposites were formed in situ. Shaded steps show the proposed formation mechanisms: (i) MOF nucleation, (ii) attachment of NPs onto MOFs through electrostatic interactions, and (iii) nanocomposite formation. Reprinted with permission from Ref. [160]. Copyright 2018 American Chemical Society

layers for the potential use in drug delivery, optical sensing, anti-counterfeiting, and PDT.

Wang et al. developed multifunctional water-dispersible $NaLnF_4$@MOF-Ln (Ln = Y, Yb, Tm, Eu) nanocomposites for dual-mode luminescent properties where MOF-Ln is a type of hybrid porous material composed of Ln^{3+} ion clusters and organic ligands bonded through coordinate bonds [161]. The as-prepared nanocomposite showed unique Stokes (red) and anti-Stokes (blue) emission from mesoporous MOF-Ln and $NaYF_4$: Tm,Yb UCNPs, respectively, under laser excitation at a specific wavelength. Thus, the nanocomposite offered luminescence imaging capabilities. In another work, UCNPs@MIL-53/FA dual-function system has been developed that integrated bioimaging and drug delivery. For this purpose, H.L. Cong and group prepared core–shell $NaYF_4$: Yb,Er@$NaYF_4$: Nd@MIL-53 microsphere system via layer-by-layer self-assembly method [162]. Herein, $NaYF_4$: Yb,Er@$NaYF_4$: Nd UCNPs were used for bioimaging under NIR light. MIL-53 acted as a drug carrier for delivery of DOX, and further FA was functionalized as a targeting agent, which was encapsulated to the core–shell structure to yield UCNPs@MIL-53/FA. Similarly, in another interesting work, a core-satellite structure of $NaGdF_4$: Yb,Er@$NaGdF_4$: Nd,Yb UC phosphor with UiO-68-NH_2 MOF system for trimodal, MR/UCL imaging functions, and PDT was deliberated [163]. In a work by Li et al., MIL-53(Fe)/UCNP composites were developed, which were expected to exhibit the enhanced performance of photocatalytic activity under the vis–NIR light [164]. In this work, firstly, the Fe-based MOF; octahedral MIL-53(Fe) with uniform concave facets, was prepared by the microwave-assisted method. To this interesting structural geometry

of MIL-53(Fe), UCNPs $NaYF_4$: Yb,Tm were anchored on their concave surface. The nanocomposite showed efficient photocatalysis by extending its light utilization in the solar spectrum. The same group developed core–shell $NaYF_4$: Yb,Tm@MIL-53(Fe) composite structure and explored their photocatalytic performances systematically [165]. In this approach, PVP modified $NaYF_4$: Yb,Tm nanoplates were first prepared, and then MIL-53(Fe) shell was employed on the as-prepared nanoplates via a layer-by-layer growing procedure. The thickness of the MOF-shell was tuned, and also modification of the MOF-shell was done with amino groups to improve the photocatalytic efficiency. There are various other reports for hybrids based on UCNPs and MOFs, for e.g., $NaYF_4$: Yb,Tm@MIL-100(Fe)-PEG for pH-responsive drug delivery and dual-mode imaging [166], $NaGdF_4$: Yb,Er@MIL-53(Fe)/FA for tumor-targeted chemotherapeutic delivery [167], and so forth.

Polymer: The ease of polymer processing with Ln^{3+}-doped phosphors was demonstrated in various reports to synthesize UCNP-polymer hybrids [168, 169]. In the year 2007, OA-capped LaF_3: Yb,Er NPs were prepared with a mean diameter of ~7 nm and showed excellent dispersibility in the PMMA matrix [170]. The resulted UCNPs-polymer hybrid material exhibited emission in the telecommunication window (1500 nm) and therefore acted as a promising material for optical waveguide amplifiers. Boyer and group presented a technique to synthesize OA-stabilized UCNPs/PMMA bulk polymer composite via in situ polymerization of PEG-monooleate ligand [171]. The PMMA polymerization in the presence of PEG-monooleate ligand resulted in the formation of transparent bulk polymer-UCNPs composite, as shown in Fig. 19. This also prevented their phase separation. The tech-

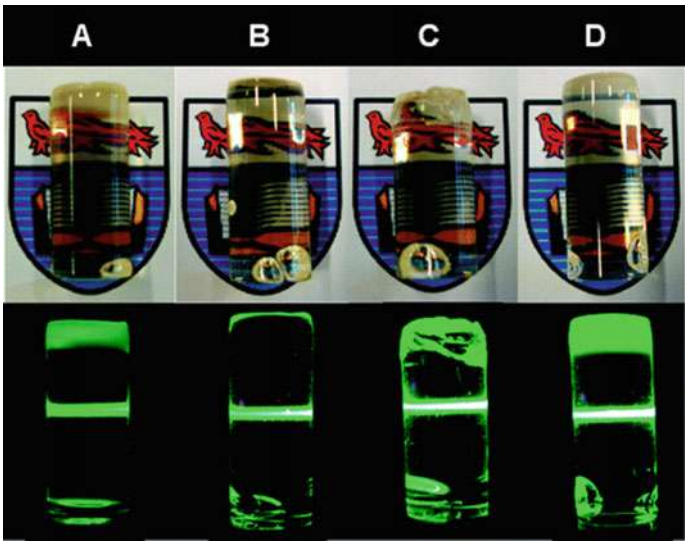

Fig. 19 Photographs of UCNP-PMMA composites under ambient light (top) and 980 nm laser irradiation (bottom) **a** 0.5 wt%, **b** 1 wt%, **c** 2 wt%, and **d** 3 wt% $NaYF_4$: Yb,Er UCNPs in PMMA. Reprinted with permission from Ref. [171]. Copyright 2009 American Chemical Society

nique used in this work may also be extended to different types of NPs, such as Fe_2O_3, QDs, semiconductor NPs. Kim et al. synthesized $LiYF_4$: Eu, $LiYF_4$: Ce,Tb@$LiYF_4$: Eu and $LiYF_4$: Eu@$LiYF_4$: Ce,Tb core–shell and $LiYF_4$: Eu,Ce,Tb nanophosphors and luminescence properties of these architectures were analyzed [172]. Among these, $LiYF_4$: Eu,Ce,Tb nanophosphors exhibited intense green and red emission peaks, which were controlled by adjusting the concentration of Eu^{3+} ions. With the increase in the concentration of Eu^{3+}, $LiYF_4$: Eu,Ce,Tb exhibited multicolor emission from green to orange, as clearly shown in Fig. 20. These nanophosphors were incorporated into PDMS polymer to yield a transparent composite that presented excellent, bright multicolor tunability for the application in transparent display devices.

The polymer-based $BaGd_2ZnO_5$: Er/PMMA and $NaYF_4$: Er/PMMA composites were demonstrated by Fan et al. as an efficient system to determine the

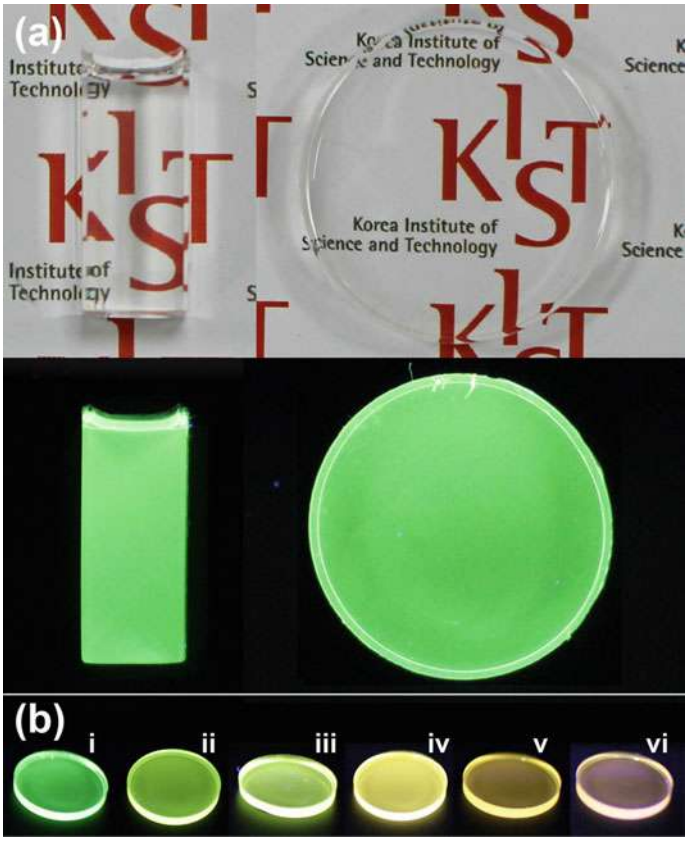

Fig. 20 Photographs of **a** $LiYF_4$: Ce (13%), Tb (14%), Eu (0%)-PDMS bar (left) and disk (right) under room light (upper panel) and UV lamp (lower panel) and **b** $LiYF_4$: Ce, (13%), Tb (14%), Eu (0–5%)-PDMS disks under UV lamp illumination [i: 0%, ii: 1%, iii: 2%, iv: 3%, v: 4%, and vi: 5%]. Reprinted with permission from Ref. [172]. Copyright 2015 Springer Nature

Judd–Ofelt parameters [173]. The intense emission at 1553 nm was noticed upon 980 nm excitation. Using the Judd–Ofelt theory, the radiative transition probability and lifetime of the optical transitions were calculated. The results revealed the potentiality of these composites in broadband optical amplifier application. Li developed nanohybrids of UCNPs, and fluorescent conjugated polymer for NIR-mediated antibacterial performance based on FRET [174]. In this approach, NIR light-absorbing PAA-functionalized β-$NaYF_4$:Yb,Tm UCNPs, and a fluorescent conjugated polymer, poly[9,9-bis(6,6-(*N*,*N*,*N*-trimethylaminium)-fluorene-2,7-ylenevinylene-co-alt-2,5-dicyano-1,4-phenylene] (PFVCN) was used for the fabrication of UCNP/PFVCN nanohybrid for the enhanced antibacterial activity. Highly effective FRET from UCNPs (donor) to PFVCN (acceptor) took place. The NIR-mediated antibacterial mechanism was demonstrated for *Escherichia coli* (*E. coli*) bacterium. Here, the cationic PFVCN was easily anchored on the negatively charged PAA-UCNPs surface via electrostatic interaction to form the UCNP/PFVCN nanohybrids. Moreover, there existed good spectral overlap between UCNPs and PFVCN to enable FRET. Upon excitation at 980 nm, UCNPs exhibited intense emission at 470 nm; on the other hand, PFVCN displayed emission at 560 nm upon absorption at 473 nm. Thus, PFVCN could also be excited via FRET upon excitation of UCNPs by 980 nm light; it could then generate ROS to kill *E. coli*. Further, FRET efficiency, fluorescence imaging, and antibacterial studies of UCNP/PFVCN nanohybrids were demonstrated in this work. An important study by Dai et al., wherein inorganic–organic hybrid microspheres was reported, which involved luminescent $NaYF_4$: Yb,Er as the core coated with pH-induced thermo-sensitive smart hydrogel P(NIPAM-co-MAA) as the shell [175]. The core–shell microspheres $NaYF_4$: Yb,Er@SiO_2@P(NIPAM-co-MAA) showed bright UCL under 980 nm laser illumination that is employed in the cell imaging. The hybrid microspheres were loaded with the drug DOX. The cytotoxicity and cellular uptake were studied in SKOV3 ovarian cancer cells. The drug release behavior is pH-induced thermally sensitive. Upon changing the pH from normal physiological pH (7.4) to mildly acidic microenvironment (endosome/lysosomes) at physiological temperature, the structure of the shell deformed and collapsed, which resulted in the release of a large number of DOX from the microspheres. This system showed pH-induced thermally controlled drug release properties. The synthesis process and DOX release mechanism of $NaYF_4$: Yb,Er@SiO_2@P(NIPAM-co-MAA) microsphere is presented in Fig. 21. First, the $NaYF_4$: Yb,Er microspheres were prepared using the hydrothermal route. Then after a layer of silica was coated onto the as-prepared $NaYF_4$: Yb,Er microspheres by the sol–gel process. Then, the silica surface was modified with the coupling agent MPS, which reacted with the monomer of a polymer in aqueous phase radical polymerization. This was followed by the polymerization of NIPAM, MAA, and BIS on the silica surface in deionized water. Apart from nanoparticles/nanocomposites or core–shell preparation, researchers are also working in the formations of thin-films, which is specifically crucial for optical applications. The thin-films UCNPs can certainly be prepared using approaches such as dip coating, dispersion casting, spray drying, etc. However, such films may possess poor adhesion, lack of thickness control, and can consequently degrade device performance.

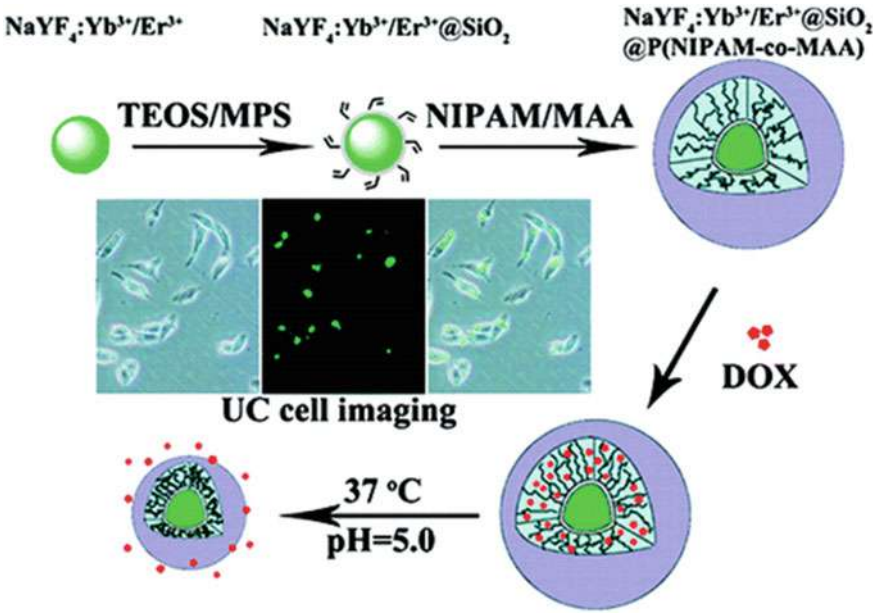

Fig. 21 Schematic illustration of the preparation process of $NaYF_4$: Yb^{3+}/Er^{3+}@SiO_2@P(NIPAM-co-MAA) hybrid microspheres and controlled release of DOX. MPS: methacryloxypropyltrimethoxysilane, NIPAM: N-isopropylacrylamide, MAA: Methacrylic acid, BIS: N,N'-methylenebisacrylamide, KPS: potassium peroxodisulfate, DOX: doxorubicin hydrochloride. Reprinted with permission from Ref. [175]. Copyright 2012 American Chemical Society

The pulse laser deposition (PLD), atomic/molecular layer deposition (ALD/MLD), etc., are emerging techniques for the fabrication of thickness-controlled fine thin films. A. M. Darwish and group demonstrated the fabrication of PMMA: $NaYF_4$: Tm,Yb composite film deposited using double-beam pulsed laser deposition (DPLD) technique [176]. Similarly, PMMA: $NaYF_4$: Er,Yb and PMMA: $NaYF_4$: Ho,Yb were also prepared, and the effectiveness of the deposition was investigated. The prepared polymer-UC composite films showed bright emission under NIR excitation. The same group later demonstrated the fabrication of the nanocomposite film of PMMA + $NaYF_4$: Yb,Er + aluminum-doped ZnO (AZO). The films were deposited using concurrent matrix-assisted pulsed laser evaporation (MAPLE) for PMMA and PLD for UCNPs and AZO [177]. Thus, triple beams, an IR 1064-nm laser beam for the MAPLE and two 532-nm laser beams for the PLD targets, were concomitantly used in the process. The proposed system was found to possess better control for the deposition of different nature of materials. In a work by Tan et al., luminescent polymer UCP/PVA composite films were fabricated using an aqueous solution casting method wherein poly(vinyl alcohol) (PVA) was employed as a matrix polymer and $NaYF_4$: Yb, Er UCNPs were used as the filler [178]. Firstly, water-soluble branched structured $NaYF_4$: Yb,Er UCNPs were prepared via hydrothermal method using hexadecyl pyridinium chloride (CPC) and trisodium citrate (Na_3Cit)

as a capping agent. Then, the UCNPs/PVA hybrid composite films were prepared by solution casting method. The UCNPs were well-dispersed in the polymer matrix because of the presence of intermolecular hydrogen bonding between O–H group of the PVA and pyridine ring in the CPC ligand on the surface of UCNPs. The fabricated UCNP/PVA composite films exhibited strong UCL under the 980 nm laser excitation and thus, proposed that these luminescent polymer composite films can be used for anti-counterfeiting applications.

Dichalcogenides: In another category with Ln^{3+}-doped hybrid phosphors, Niu et al. synthesized the transition metal dichalcogenide-based $NaYF_4$: Yb,Er-MoS_2 film for the IR opto-electronic devices [179]. In this study, $NaYF_4$: Yb,Er UCNPs-MoS_2 was synthesized by the thermolysis process in the mixture of oleylamine and OA. For the device fabrication, the film of the composites capped with surfactants was deposited on the glass substrate. This step was followed by the immersion of the film in a dilute solution of $SOCl_2$/DMF in hexane to remove the insulating surface ligands of these nanomaterials. The film showed a negative IR photoresponse to 980 nm illumination, which was higher than that of pure UCNPs. The results obtained in this study showed that the system has the potential for the development of novel IR opto-electronic devices. Zhou et al. fabricated the core–shell structured, $NaYF_4$: Yb,Er@$NaYF_4$: Nd,Yb UCNPs, and monolayer MoS_2-based narrowband wavelength-selective NIR photodetector [180]. In this system, UCNPs acted as IR-light absorbers due to their narrow spectral window, while the MoS_2 was used as a supporter and receiver of energy from UCNPs because of their high specific surface area and superior photoelectric response. They showed the selective detection of 808 and 980 nm NIR radiations and revealed that the doping of the different lanthanides could tune the target wavelengths. This design could revitalize photodetection research, especially in the selective response field.

Also, the utilization of 2D materials in photocatalysis has attracted researchers around the world and has become an important topic of research interest. 2D layered materials exhibit advantages of maximum specific surface area and reduced electron–hole recombination, which can be used to enhance photocatalytic efficiency. High specific surface area increases the number of photocatalytic sites, and the 2D nature minimizes the distance that photogenerated carriers have to migrate, thereby reduce the probable recombination of electrons and holes. MoS_2 is one of the important 2D transition metal dichalcogenides, the structure of which consists of Mo atoms sandwiched between the two layers of hexagonally close-packed sulfur atoms. MoS_2 has a narrow bandgap of 1.8 eV that provides high absorption in the visible light region of the solar spectrum. Therefore, MoS_2 is expected to have the potential for photocatalytic applications. Chatti et al. fabricated NIR active MoS_2-$NaYF_4$: Yb,Er nanocomposites using the hydrothermal method for enhanced photocatalytic performance [181]. The idea behind using MoS_2 was its broad absorption in the visible region, which can effectively use the upconverted emissions. Interestingly, 61% of the RhB was decomposed using the MoS_2-$NaYF_4$: Yb,Er nanocomposites, which was three times greater than the MoS_2-$NaYF_4$: Yb,Er physical mixture (18%). This was due to the presence of different energy-transfer pathways in the

nanocomposites and the mixture. The efficient photocatalytic process from UCNPs-MoS_2 based combination was utilized by Qiao et al. Their work demonstrated the development of β-$NaYF_4$: Yb,Er,Gd nanorods@1 T/2H-MoS_2 nanocomposite for NIR-triggered bactericidal activity [182]. In this work, hexagonal phase negatively charged carboxylic- functionalized β-$NaYF_4$: Yb,Er,Gd nanorods were prepared, and the positively charged PEI-coated 1 T/2H MoS_2 nanosheets were assembled on it through electrostatic attractions. *E. coli* was inactivated effectively (approximately 99.3%) within 15 min upon NIR irradiation at a minimum inhibitory concentration of 40 $\mu g\ mL^{-1}$. Under 980 nm light illumination, β-$NaYF_4$: Yb,Er,Gd efficiently emitted in visible region, which was strongly absorbed by layered 1 T/2H-MoS_2 nanosheets, that were capable to strongly produce reductive electrons and oxidative holes. Thus, the photogenerated electron–hole pairs were further able to react with O_2, H_2O, and OH^- to produce ROS that resulted in the death of bacteria. The in vitro cytotoxicity of the as-formed composites and the antibacterial performance were evaluated.

In principle, as discussed, these hybrid materials possess superior electrical, thermal, luminescent, magnetic, and catalytic properties than the single system of phosphors in multifunctional applications.

3 Summary and Outlook

This chapter has presented significant developments in the lanthanide ion-activated inorganic hybrid phosphors and their applications with a comprehensive overview of the distinctive optical properties, including easy tuning of emission colors, NIR-triggered emission, etc. It is a prerequisite for developing Ln^{3+}-activated phosphor hybrids to investigate their potential in different applications such as biomedicine, environmental remediation, and chemical sensing. The hybrids of Ln^{3+}-doped inorganic phosphors with semiconductors, magnetic NPs, metal NPs, and graphene and its derivatives are reviewed in detail. Some other hybrids with quantum dots, polymers, metal–organic frameworks, dichalcogenides, etc., are also discussed. The synergistic combination of Ln^{3+}-activated inorganic phosphors with different materials possesses superior properties and applications, unattainable by its constituents in isolation. Because of the high versatility in chemical and physical properties, Ln^{3+}-based hybrids open up a field of applications in many areas where their extraordinary optical, electronic, and magnetic properties are fully explored.

The main motivation behind designing Ln^{3+}-activated inorganic phosphor-semiconductor hybrids for energy applications is to extend and improve photon-harvesting across the broad solar spectrum. Ln^{3+}-doped phosphors also act as the efficient photon scattering layer in the fabrication of the solar cell. Better photon absorption leads to the rise in the number of photoelectrons to increase the PCE of solar cells. The capability of energy-transfer efficiency between Ln^{3+}-doped phosphor and semiconductor is the key factor for enhanced photocatalytic efficiency, and core–shell structures are ideal for the same. However, tuning of shell thickness is

crucial and critical to achieve enhanced FRET efficiency and, consequently, photocatalytic activity. These studies are significant, challenging, and rarely explored, thus open for future research studies. We can also further play with the morphological and compositional tuning of Ln^{3+}-doped phosphors to achieve increased photocatalytic and photovoltaic efficiency, as these are the important factors that influence the luminescence intensity.

Upconverting luminescent-magnetic hybrids are significantly advantageous in theranostics owing to their NIR-triggered emission along with superparamagnetic properties. These hybrids are able to bridge the gap in sensitivity and depth of imaging between two modalities by the integration of potential benefits of optical and MRI imaging. As such, this offers the perspective to overcome the current limitations of individual imaging. However, the methods for the synthesis of such multifunctional materials involve a complex and multi-step process. So, without sacrificing optical efficiency, it is imperative to develop more facile protocols to obtain the hybrid materials, e.g., the one-pot method. Morphology, size, and composition tuning are crucial factors to realize the improved efficiency of hybrids. Specifically, biomedical functions and applications are limited by the non-perseverance of the particle size uniformity of hybrid materials. Thus, it is still a significant challenge to design and develop a practical multifunctional probe for the multimodal imaging and targeted drug delivery system to realize the applications in theranostics.

Ln^{3+}-doped UC nanocrystals have a long history of research and development, and they have emerged as an effective and versatile tool for various applications. However, the low upconversion quantum efficiency of these nanocrystals due to forbidden *f-f* transitions and non-radiative processes, which are mediated by bulk and surface defects, limits their applications. The coupling of UCNPs with plasmons offered new avenues to engineer optical processes and enhance the upconversion efficiency of traditional UC materials using the noble metal nanostructures by increasing the light flux in the proximity of the metal surface due to SPR. The enhancement of many folds can be achieved by tuning the SPR peak of the metal NPs to match with the excitation wavelength of dopant ions in UCNPs. Further, the effect of the spacing between the metal NPs surface and UCNPs controls the interactions and the enhancement factor. The incorporation of metal structures in the form of NPs, films, arrays, or shells imparts additional functionalities that provide a wide range of new opportunities for fundamental research and developing new applications such as biomedical imaging, sensing, security ink, and photoswitching, etc. The experimental and theoretical studies are rapidly revealing the mechanism with which the environment of nanophotonics impacts numerous optical processes, such as absorption, luminescence energy-transfer, and non-radiative decays. However, the highly complicated nature of the upconversion process anticipates further explanation. The complete understanding of these complex dynamics in the plasmonic field could allow the design and development of plasmon-enhanced upconversion and thus pave the road to a wide range of applications.

The use of Ln^{3+}-doped UCNPs as FRET donor has allowed their application as sensors when they are integrated with appropriate FRET acceptors. A hybrid of graphene oxide and UCNPs offered a sensitive sensing platform for various

molecules by exploiting the FRET pair formed between GO and UCNPs. The GO-induced FRET quenching occurs due to the overlap of the UCNPs emission and the GO absorption. Moreover, the hybrid of carbon-based nanomaterials with UCNPs enabled the applications in the field of broadband photodetection, solar cells, bioimaging, drug delivery, and theranostics, etc. Some hybrids, along with their excellent performance in different aspects of these fields, have been highlighted in this chapter. Current research developments have clearly revealed a promising prospect for the application of these hybrids in real-life theranostics. However, the biocompatibility and toxicity of such hybrids have not been well addressed, and thus in-depth studies need to be carried out before the real-life applications.

The Ln^{3+}-doped phosphor-quantum dot hybrids are mainly based on FRET between upconversion donor and QD acceptors for the applications in sensing and bioimaging. Due to the high surface area and tunable pore sizes, the capabilities of MOFs can be effectively utilized via UCNP-MOF composite for NIR-triggered theranostics, PDT, and energy applications. In a nutshell, the judicial integration of Ln^{3+}-doped phosphors and other active material possessing appropriate composition, surface modification, and morphology can provide a single platform with multiple discrete functions for a broad range of applications. There is still plenty of room for facile fabrication of hybrids, interface studies and improvements, size control, and enhancing luminescence efficiency to widen the scope of these materials. These also entail collective efforts from scientists and researchers working in different disciplines. In the future, hybrid materials will become increasingly miniaturized, energetically efficient, eco-friendly, reliable, and inexpensive. These materials will undoubtedly play a vital role in cutting-edge technological endeavors. Specifically mentioning the novel developments in luminescent waveguides, micro-optical devices, sensors, and biosensors based on time-resolved fluoroimmunoassays, CT tomography, fluorescence imaging microscopy, bioimaging by using hybrid nanoprobes with NIR luminescence will emerge soon. It is anticipated that this chapter will stimulate the research and development of advanced novel multifunctional materials and provide solutions to a wide range of scientific and technological challenges.

References

1. Werts, M.H.V.: Making sense of lanthanide luminescence. Sci. Prog. **88**, 101–131 (2005). https://doi.org/10.3184/003685005783238435
2. Casanova, D., Giaume, D., Beaurepaire, E., Gacoin, T., Boilot, J.-P., Alexandrou, A.: Optical in situ size determination of single lanthanide-ion doped oxide nanoparticles. Appl. Phys. Lett. **89**, 253103 (2006). https://doi.org/10.1063/1.2405871
3. Wang, Y., Liu, Y., Xiao, Q., Zhu, H., Li, R., Chen, X.: Eu^{3+} doped KYF_4 nanocrystals: synthesis, electronic structure, and optical properties. Nanoscale **3**, 3164 (2011). https://doi.org/10.1039/c1nr10341e
4. Sun, C., Carpenter, C., Pratx, G., Xing, L.: Facile Synthesis of amine-functionalized Eu^{3+}-doped $La(OH)_3$ nanophosphors for bioimaging. Nanoscale Res. Lett. **7**, 1–7 (2010). https://doi.org/10.1007/s11671-010-9768-x

5. Heine, J., Müller-Buschbaum, K.: Engineering metal-based luminescence in coordination polymers and metal-organic frameworks. Chem. Soc. Rev. **42**, 9232 (2013). https://doi.org/10.1039/c3cs60232j
6. Fan, Y., Wang, P., Lu, Y., Wang, R., Zhou, L., Zheng, X., Li, X., Piper, J.A., Zhang, F.: Lifetime-engineered NIR-II nanoparticles unlock multiplexed in vivo imaging. Nat. Nanotechnol. **13**, 941–946 (2018). https://doi.org/10.1038/s41565-018-0221-0
7. Wang, G., Peng, Q., Li, Y.: Lanthanide-doped nanocrystals: synthesis, optical-magnetic properties, and applications. Acc. Chem. Res. **44**, 322–332 (2011). https://doi.org/10.1021/ar100129p
8. Zeng, S., Ren, G., Xu, C., Yang, Q.: High uniformity and monodispersity of sodium rare-earth fluoride nanocrystals: controllable synthesis, shape evolution and optical properties. Cryst. Eng. Comm. **13**, 1384–1390 (2011). https://doi.org/10.1039/C0CE00325E
9. Padhye, P., Alam, A., Ghorai, S., Chattopadhyay, S., Poddar, P.: Doxorubicin-conjugated β-$NaYF_4$: Gd^{3+}/Tb^{3+} multifunctional, phosphor nanorods: a multi-modal, luminescent, magnetic probe for simultaneous optical and magnetic resonance imaging and an excellent pH-triggered anti-cancer drug delivery nanovehicle. Nanoscale **7**, 19501–19518 (2015). https://doi.org/10.1039/C5NR04473A
10. Zhang, J., Li, B., Zhang, L., Jiang, H.: An optical sensor for Cu(II) detection with upconverting luminescent nanoparticles as an excitation source. Chem. Commun. **48**, 4860 (2012). https://doi.org/10.1039/c2cc31642k
11. Malik, M., Padhye, P., Poddar, P.: Downconversion luminescence-based nanosensor for label-free detection of explosives. ACS Omega **4**, 4259–4268 (2019). https://doi.org/10.1021/acsomega.8b03491
12. Meruga, J.M., Cross, W.M., Stanley May, P., Luu, Q., Crawford, G.A., Kellar, J.J.: Security printing of covert quick response codes using upconverting nanoparticle inks. Nanotechnology **23**, 395201 (2012). https://doi.org/10.1088/0957-4484/23/39/395201
13. Sudarsan, V., van Veggel, F.C.J.M., Herring, R.A., Raudsepp, M.: Surface Eu^{3+} ions are different than "bulk" Eu^{3+} ions in crystalline doped LaF_3 nanoparticles. J. Mater. Chem. **15**, 1332–1342 (2005). https://doi.org/10.1039/B413436B
14. Artiles, M.S., Rout, C.S., Fisher, T.S.: Graphene-based hybrid materials and devices for biosensing. Adv. Drug. Deliv. Rev. **63**, 1352–1360 (2011). https://doi.org/10.1016/j.addr.2011.07.005
15. Huang, X., Tan, C., Yin, Z., Zhang, H.: 25th anniversary article: hybrid nanostructures based on two-dimensional nanomaterials. Adv. Mater. **26**, 2185–2204 (2014). https://doi.org/10.1002/adma.201304964
16. Sarkar, J., Ghosh, P., Adil, A.: A review on hybrid nanofluids: recent research, development and applications. Renew. Sustain. Energy Rev. **43**, 164–177 (2015). https://doi.org/10.1016/j.rser.2014.11.023
17. Li, W., Wang, Z., Deschler, F., Gao, S., Friend, R.H., Cheetham, A.K.: Chemically diverse and multifunctional hybrid organic-inorganic perovskites. Nat. Rev. Mater. **2**, 16099 (2017). https://doi.org/10.1038/natrevmats.2016.99
18. Li, X., Zhao, D., Zhang, F.: Multifunctional upconversion-magnetic hybrid nanostructured materials: synthesis and bioapplications. Theranostics **3**, 292–305 (2013). https://doi.org/10.7150/thno.5289
19. Saveleva, M.S., Eftekhari, K., Abalymov, A., Douglas, T.E.L., Volodkin, D., Parakhonskiy, B.V., Skirtach, A.G.: Hierarchy of hybrid materials—the place of inorganics-in-organics in it, their composition and applications. Front. Chem. **7**, 1–21 (2019). https://doi.org/10.3389/fchem.2019.00179
20. Chen, G., Yu, Y., Wu, X., Wang, G., Ren, J., Zhao, Y.: Bioinspired multifunctional hybrid hydrogel promotes wound healing. Adv. Funct. Mater. **28**, 1801386 (2018). https://doi.org/10.1002/adfm.201801386
21. Jian, Y., Hu, W., Zhao, Z., Cheng, P., Haick, H., Yao, M., Wu, W.: Gas sensors based on chemi-resistive hybrid functional nanomaterials. Nano-Micro. Lett. **12**, 71 (2020). https://doi.org/10.1007/s40820-020-0407-5

22. Feng, W., Han, C., Li, F.: Upconversion-nanophosphor-based functional nanocomposites. Adv. Mater. **25**, 5287–5303 (2013). https://doi.org/10.1002/adma.201301946
23. Tian, G., Zhang, X., Gu, Z., Zhao, Y.: Recent advances in upconversion nanoparticles-based multifunctional nanocomposites for combined cancer therapy. Adv. Mater. **27**, 7692–7712 (2015). https://doi.org/10.1002/adma.201503280
24. Wen, S., Zhou, J., Schuck, P.J., Suh, Y.D., Schmidt, T.W., Jin, D.: Future and challenges for hybrid upconversion nanosystems. Nat. Photonics **13**, 828–838 (2019). https://doi.org/10.1038/s41566-019-0528-x
25. Bai, G., Tsang, M.-K., Hao, J.: Luminescent ions in advanced composite materials for multifunctional applications. Adv. Funct. Mater. **26**, 6330–6350 (2016). https://doi.org/10.1002/adfm.201602142
26. Wu, X., Yin, S., Dong, Q., Sato, T.: Blue/green/red colour emitting up-conversion phosphors coupled C-TiO_2 composites with UV, visible and NIR responsive photocatalytic performance. Appl. Catal. B Environ. **156–157**, 257–264 (2014). https://doi.org/10.1016/j.apcatb.2014.03.028
27. Li, S.-L., Jiang, K.-J., Shao, K.-F., Yang, L.-M.: Novel organic dyes for efficient dye-sensitized solar cells. Chem. Commun. **2**, 2792 (2006). https://doi.org/10.1039/b603706b
28. Burke, A., Schmidt-Mende, L., Ito, S., Grätzel, M.: A novel blue dye for near-IR "dye-sensitised" solar cell applications. Chem. Commun. 234–236 (2007). https://doi.org/10.1039/B609266G
29. McDonald, S.A., Konstantatos, G., Zhang, S., Cyr, P.W., Klem, E.J.D., Levina, L., Sargent, E.H.: Solution-processed PbS quantum dot infrared photodetectors and photovoltaics. Nat. Mater. **4**, 138–142 (2005). https://doi.org/10.1038/nmat1299
30. Shan, G.-B., Demopoulos, G.P.: Near-infrared sunlight harvesting in dye-sensitized solar cells via the insertion of an upconverter-TiO_2 nanocomposite layer. Adv. Mater. **22**, 4373–4377 (2010). https://doi.org/10.1002/adma.201001816
31. Wang, F., Liu, X.: Recent advances in the chemistry of lanthanide-doped upconversion nanocrystals. Chem. Soc. Rev. **38**, 976 (2009). https://doi.org/10.1039/b809132n
32. Shan, G.-B., Assaaoudi, H., Demopoulos, G.P.: Enhanced performance of dye-sensitized solar cells by utilization of an external, bifunctional layer consisting of uniform β-$NaYF_4$: Er^{3+}/Yb^{3+} nanoplatelets. ACS Appl. Mater. Interfaces **3**, 3239–3243 (2011). https://doi.org/10.1021/am200537e
33. Liang, L., Liu, Y., Bu, C., Guo, K., Sun, W., Huang, N., Peng, T., Sebo, B., Pan, M., Liu, W., Guo, S., Zhao, X.-Z.: Highly uniform, bifunctional core/double-shell-Structured β-$NaYF_4$: Er^{3+}, Yb^{3+}@SiO_2@TiO_2 hexagonal sub-microprisms for high-performance dye sensitized solar cells. Adv. Mater. **25**, 2174–2180 (2013). https://doi.org/10.1002/adma.201204847
34. Liang, L., Liu, Y., Zhao, X.-Z.: Double-shell β-$NaYF_4$: Yb^{3+}, Er^{3+}/SiO_2/TiO_2 submicroplates as a scattering and upconverting layer for efficient dye-sensitized solar cells. Chem. Commun. **49**, 3958 (2013). https://doi.org/10.1039/c3cc41252k
35. Padhye, P., Sadhu, S., Malik, M., Poddar, P.: A broad spectrum photon responsive, paramagnetic β-$NaGdF_4$: Yb^{3+}, Er^{3+}-mesoporous anatase titania nanocomposite. RSC Adv. **6**, 53504–53518 (2016). https://doi.org/10.1039/C6RA06813H
36. Yu, J., Yang, Y., Fan, R., Wang, P., Dong, Y.: Enhanced photovoltaic performance of dye-sensitized solar cells using a new photoelectrode material: upconversion YbF_3-Ho/TiO_2 nanoheterostructures. Nanoscale **8**, 4173–4180 (2016). https://doi.org/10.1039/C5NR08319B
37. Liao, W., Zheng, D., Tian, J., Lin, Z.: Dual-functional semiconductor-decorated upconversion hollow spheres for high efficiency dye-sensitized solar cells. J. Mater. Chem. A **3**, 23360–23367 (2015). https://doi.org/10.1039/C5TA06238A
38. Ramasamy, P., Kim, J.: Combined plasmonic and upconversion rear reflectors for efficient dye-sensitized solar cells. Chem. Commun. **50**, 879–881 (2014). https://doi.org/10.1039/C3CC47290F
39. Meng, F., Luo, Y., Zhou, Y., Zhang, J., Zheng, Y., Cao, G., Tao, X.: Integrated plasmonic and upconversion starlike Y_2O_3: Er/Au@TiO_2 composite for enhanced photon harvesting in dye-sensitized solar cells. J. Power Sources **316**, 207–214 (2016). https://doi.org/10.1016/j.jpowsour.2016.03.032

40. Luoshan, M., Bai, L., Bu, C., Liu, X., Zhu, Y., Guo, K., Jiang, R., Li, M., Zhao, X.: Surface plasmon resonance enhanced multi-shell-modified upconversion $NaYF_4$: Yb^{3+}, Er^{3+}@SiO_2@Au@TiO_2 crystallites for dye-sensitized solar cells. J. Power Sources **307**, 468–473 (2016). https://doi.org/10.1016/j.jpowsour.2016.01.028
41. Dyck, N.C., Demopoulos, G.P.: Integration of upconverting β-$NaYF_4$: Yb^{3+}, Er^{3+} @TiO_2 composites as light harvesting layers in dye-sensitized solar cells. RSC Adv. **4**, 52694–52701 (2014). https://doi.org/10.1039/C4RA08775E
42. Du, P., Lim, J.H., Leem, J.W., Cha, S.M., Yu, J.S.: Enhanced photovoltaic performance of dye-sensitized solar cells by efficient near-infrared sunlight harvesting using upconverting Y_2O_3: Er^{3+}/Yb^{3+} phosphor nanoparticles. Nanoscale Res. Lett. **10**, 321 (2015). https://doi.org/10.1186/s11671-015-1030-0
43. Chander, N., Khan, A.F., Komarala, V.K., Chawla, S., Dutta, V.: Enhancement of dye sensitized solar cell efficiency via incorporation of upconverting phosphor nanoparticles as spectral converters. Prog. Photovoltaics Res. Appl. **24**, 692–703 (2016). https://doi.org/10.1002/pip.2723
44. Rajeswari, R., Susmitha, K., Jayasankar, C.K., Raghavender, M., Giribabu, L.: Enhanced light harvesting with novel photon upconverted Y_2CaZnO_5: Er^{3+}/Yb^{3+} nanophosphors for dye sensitized solar cells. Sol. Energy **157**, 956–965 (2017). https://doi.org/10.1016/j.solener.2017.09.018
45. Cai, W., Zhang, Z., Jin, Y., Lv, Y., Wang, L., Chen, K., Zhou, X.: Application of TiO_2 hollow microspheres incorporated with up-conversion $NaYF_4$: Yb^{3+}, Er^{3+} nanoparticles and commercial available carbon counter electrodes in dye-sensitized solar cells. Sol. Energy **188**, 441–449 (2019). https://doi.org/10.1016/j.solener.2019.05.081
46. Mao, X., Yu, J., Xu, J., Wan, L., Yang, Y., Lin, H., Xu, J., Zhou, R.: Commercial upconversion phosphors with high light harvesting: a superior candidate for high-performance dye-sensitized solar cells. Phys. Status Solid. **216**, 1900382 (2019). https://doi.org/10.1002/pssa.201900382
47. Tadge, P., Yadav, R.S., Vishwakarma, P.K., Rai, S.B., Chen, T.-M., Sapra, S., Ray, S.: Enhanced photovoltaic performance of Y_2O_3: Ho^{3+}/Yb^{3+} upconversion nanophosphor based DSSC and investigation of color tunability in Ho^{3+}/Tm^{3+}/Yb^{3+} tridoped Y_2O_3. J. Alloys Compd. **821**, 153230 (2020). https://doi.org/10.1016/j.jallcom.2019.153230
48. Qin, W., Zhang, D., Zhao, D., Wang, L., Zheng, K.: Near-infrared photocatalysis based on YF3: Yb^{3+}, Tm^{3+}/TiO_2 core/shell nanoparticles. Chem. Commun. **46**, 2304 (2010). https://doi.org/10.1039/b924052g
49. Padhye, P., Poddar, P.: Static and dynamic photoluminescence and photocatalytic properties of uniform, monodispersed up/down-converting, highly luminescent, lanthanide-ion-doped β-$NaYF_4$ phosphor microcrystals with controlled multiform morphologies. J. Mater. Chem. A **2**, 19189–19200 (2014). https://doi.org/10.1039/C4TA04274C
50. Guo, X., Song, W., Chen, C., Di, W., Qin, W.: Near-infrared photocatalysis of β-$NaYF_4$: Yb^{3+}, Tm^{3+}@ZnO composites. Phys. Chem. Chem. Phys. **15**, 14681 (2013). https://doi.org/10.1039/c3cp52248b
51. Wu, X., Yin, S., Dong, Q., Liu, B., Wang, Y., Sekino, T., Lee, S.W., Sato, T.: UV, visible and near-infrared lights induced NO_x destruction activity of (Yb, Er)-NaY_F4/C-TiO_2 composite. Sci. Rep. **3**, 2918 (2013). https://doi.org/10.1038/srep02918
52. Tang, Y., Di, W., Zhai, X., Yang, R., Qin, W.: NIR-responsive photocatalytic activity and mechanism of $NaYF_4$: Yb, Tm@TiO_2 core-shell nanoparticles. ACS Catal. **3**, 405–412 (2013). https://doi.org/10.1021/cs300808r
53. Wang, C., Song, K., Feng, Y., Yin, D., Ouyang, J., Liu, B., Cao, X., Zhang, L., Han, Y., Wu, M.: Preparation of $NaLuF_4$: Gd, Yb, Tm–TiO_2 nanocomposite with high catalytic activity for solar light assisted photocatalytic degradation of dyes and wastewater. RSC Adv. **4**, 39118–39125 (2014). https://doi.org/10.1039/C4RA05575F
54. Yin, D., Zhang, L., Cao, X., Tang, J., Huang, W., Han, Y., Liu, Y., Zhang, T., Wu, M.: Improving photocatalytic activity by combining upconversion nanocrystals and Mo-doping: a case study on β-$NaLuF_4$: Gd, Yb, Tm@SiO_2@TiO_2: Mo. RSC Adv. **5**, 87251–87258 (2015). https://doi.org/10.1039/C5RA12852H

55. Guo, X., Di, W., Chen, C., Liu, C., Wang, X., Qin, W.: Enhanced near-infrared photocatalysis of $NaYF_4$: Yb, Tm/CdS/TiO_2 composites. Dalt. Trans. **43**, 1048–1054 (2014). https://doi.org/10.1039/C3DT52288A
56. Tou, M., Mei, Y., Bai, S., Luo, Z., Zhang, Y., Li, Z.: Depositing CdS nanoclusters on carbon-modified $NaYF_4$: Yb,Tm upconversion nanocrystals for NIR-light enhanced photocatalysis. Nanoscale **8**, 553–562 (2016). https://doi.org/10.1039/C5NR06806A
57. Zhang, Y., Hong, Z.: Synthesis of lanthanide-doped $NaYF_4$@TiO_2 core-shell composites with highly crystalline and tunable TiO_2 shells under mild conditions and their upconversion-based photocatalysis. Nanoscale **5**, 8930 (2013). https://doi.org/10.1039/c3nr03051b
58. Wu, X., Zhang, K., Zhang, G., Yin, S.: Facile preparation of BiOX (X = Cl, Br, I) nanoparticles and up-conversion phosphors/BiOBr composites for efficient degradation of NO gas: Oxygen vacancy effect and near infrared light responsive mechanism. Chem. Eng. J. **325**, 59–70 (2017). https://doi.org/10.1016/j.cej.2017.05.044
59. Kumar, A., Reddy, K.L., Kumar, S., Kumar, A., Sharma, V., Krishnan, V.: Rational design and development of lanthanide-doped $NaYF_4$@CdS-Au-RGO as quaternary plasmonic photocatalysts for harnessing visible-near-infrared broadband spectrum. ACS Appl. Mater. Interfaces **10**, 15565–15581 (2018). https://doi.org/10.1021/acsami.7b17822
60. Reddy, K.L., Kumar, S., Kumar, A., Krishnan, V.: Wide spectrum photocatalytic activity in lanthanide-doped upconversion nanophosphors coated with porous TiO_2 and Ag-Cu bimetallic nanoparticles. J. Hazard Mater. **367**, 694–705 (2019). https://doi.org/10.1016/j.jhazmat.2019.01.004
61. Yin, L., Gao, J., Wang, J., Luan, X., Kang, P., Li, Y., Li, K., Zhang, X.: Synthesis of Er^{3+}: $Y_3Al_5O_{12}$ and its effects on the solar light photocatalytic activity of TiO_2-ZrO_2 composite. Res. Chem. Intermed. **38**, 523–536 (2012). https://doi.org/10.1007/s11164-011-0368-x
62. Gonell, F., Haro, M., Sánchez, R.S., Negro, P., Mora-Seró, I., Bisquert, J., Julián-López, B., Gimenez, S.: Photon up-conversion with lanthanide-doped oxide particles for solar H_2 generation. J. Phys. Chem. C **118**, 11279–11284 (2014). https://doi.org/10.1021/jp503743e
63. Liu, X., Pan, L., Li, J., Yu, K., Sun, Z., Sun, C.Q.: Light down-converting characteristics of ZnO-Y_2O_2S: Eu^{3+} for visible light photocatalysis. J. Colloid Interface Sci. **404**, 150–154 (2013). https://doi.org/10.1016/j.jcis.2013.04.047
64. Lucky, S.S., Muhammad Idris, N., Li, Z., Huang, K., Soo, K.C., Zhang, Y.: Titania coated upconversion nanoparticles for near-infrared light triggered photodynamic therapy. ACS Nano **9**, 191–205 (2015). https://doi.org/10.1021/nn503450t
65. Tong, R., Lin, H., Chen, Y., An, N., Wang, G., Pan, X., Qu, F.: Near-infrared mediated chemo/photodynamic synergistic therapy with DOX-UCNPs@mSiO_2/TiO_2-TC nanocomposite. Mater. Sci. Eng. C **78**, 998–1005 (2017). https://doi.org/10.1016/j.msec.2017.04.112
66. Xu, Q.C., Zhang, Y., Tan, M.J., Liu, Y., Yuan, S., Choong, C., Tan, N.S., Tan, T.T.Y.: Anti-cAngptl4 Ab-conjugated N-TiO_2/$NaYF_4$: Yb, Tm nanocomposite for near infrared-triggered drug release and enhanced targeted cancer cell ablation. Adv. Healthcare Mater. **1**, 470–474 (2012). https://doi.org/10.1002/adhm.201200055
67. Hou, Z., Zhang, Y., Deng, K., Chen, Y., Li, X., Deng, X., Cheng, Z., Lian, H., Li, C., Lin, J.: UV-emitting upconversion-based TiO_2 photosensitizing nanoplatform: near-infrared light mediated in vivo photodynamic therapy via mitochondria-involved apoptosis pathway. ACS Nano **9**, 2584–2599 (2015). https://doi.org/10.1021/nn506107c
68. Chen, Y., Lin, H., Tong, R., An, N., Qu, F.: Near-infrared light-mediated DOX-UCNPs@m$HTiO_2$ nanocomposite for chemo/photodynamic therapy and imaging. Colloids Surfaces B Biointerfaces **154**, 429–437 (2017). https://doi.org/10.1016/j.colsurfb.2017.03.026
69. Penet, M.-F., Mikhaylova, M., Li, C., Krishnamachary, B., Glunde, K., Pathak, A.P., Bhujwalla, Z.M.: Applications of molecular MRI and optical imaging in cancer. Future Med. Chem. **2**, 975–988 (2010). https://doi.org/10.4155/fmc.10.25
70. Zhang, Y., Pan, S., Teng, X., Luo, Y., Li, G.: Bifunctional magnetic - Luminescent nanocomposites: Y_2O_3/Tb nanorods on the surface of iron oxide/silica core-shell nanostructures. J. Phys. Chem. C **112**, 9623–9626 (2008). https://doi.org/10.1021/jp8015326

71. Gowd, G.S., Patra, M.K., Mathew, M., Shukla, A., Songara, S., Vadera, S.R., Kumar, N.: Synthesis of Fe_3O_4@Y_2O_3: Eu^{3+} core-shell multifunctional nanoparticles and their magnetic and luminescence properties. Opt. Mater. (Amst.) **35**, 1685–1692 (2013). https://doi.org/10.1016/j.optmat.2013.04.029
72. Wu, T., Pan, H., Chen, R., Luo, D., Zhang, H., Shen, Y., Lu, B., Huang, J., Li, Y., Wang, L.: Enhanced photoluminescence of Fe_3O_4@Y_2O_3: Eu^{3+} bifunctional nanoparticles by the Gd^{3+} co-doping. J. Alloys Compd. **666**, 507–512 (2016). https://doi.org/10.1016/j.jallcom.2016.01.130
73. Yang, P., Quan, Z., Hou, Z., Li, C., Kang, X., Cheng, Z., Lin, J.: A magnetic, luminescent and mesoporous core-shell structured composite material as drug carrier. Biomaterials **30**, 4786–4795 (2009). https://doi.org/10.1016/j.biomaterials.2009.05.038
74. Singh, L.P., Jadhav, N.V., Sharma, S., Pandey, B.N., Srivastava, S.K., Ningthoujam, R.S.: Hybrid nanomaterials YVO_4: Eu/Fe_3O_4 for optical imaging and hyperthermia in cancer cells. J. Mater. Chem. C **3**, 1965–1975 (2015). https://doi.org/10.1039/C4TC02636E
75. Lu, H., Yi, G., Zhao, S., Chen, D., Guo, L.-H., Cheng, J.: Synthesis and characterization of multi-functional nanoparticles possessing magnetic, up-conversion fluorescence and bio-affinity properties. J. Mater. Chem. **14**, 1336 (2004). https://doi.org/10.1039/b315103d
76. Mi, C., Zhang, J., Gao, H., Wu, X., Wang, M., Wu, Y., Di, Y., Xu, Z., Mao, C., Xu, S.: Multifunctional nanocomposites of superparamagnetic (Fe_3O_4) and NIR-responsive rare earth-doped up-conversion fluorescent ($NaYF_4$: Yb, Er) nanoparticles and their applications in biolabeling and fluorescent imaging of cancer cells. Nanoscale **2**, 1141 (2010). https://doi.org/10.1039/c0nr00102c
77. Shen, J., Sun, L.-D., Zhang, Y.-W., Yan, C.-H.: Superparamagnetic and upconversion emitting Fe3O4/NaYF4: Yb, Er hetero-nanoparticles via a crosslinker anchoring strategy. Chem. Commun. **46**, 5731 (2010). https://doi.org/10.1039/c0cc00814a
78. Liu, D., Zhao, D., Shi, F., Zheng, K., Qin, W.: Superparamagnetic and upconversion luminescent properties of Fe_3O_4/$NaYF_4$: Yb, Er hetero-submicro-rods. Mater. Lett. **85**, 1–3 (2012). https://doi.org/10.1016/j.matlet.2012.06.023
79. Zhu, X., Zhou, J., Chen, M., Shi, M., Feng, W., Li, F.: Core-shell Fe_3O_4@$NaLuF_4$: Yb, Er/Tm nanostructure for MRI, CT and upconversion luminescence tri-modality imaging. Biomaterials **33**, 4618–4627 (2012). https://doi.org/10.1016/j.biomaterials.2012.03.007
80. Hu, D., Chen, M., Gao, Y., Li, F., Wu, L.: A facile method to synthesize superparamagnetic and up-conversion luminescent $NaYF_4$: Yb, Er/Tm@SiO_2@Fe_3O_4 nanocomposite particles and their bioapplication. J. Mater. Chem. **21**, 11276 (2011). https://doi.org/10.1039/c1jm11172h
81. Zhong, C., Yang, P., Li, X., Li, C., Wang, D., Gai, S., Lin, J.: Monodisperse bifunctional Fe_3O_4@$NaGdF_4$: Yb/Er@$NaGdF_4$: Yb/Er core-shell nanoparticles. RSC Adv. **2**, 3194 (2012). https://doi.org/10.1039/c2ra20070h
82. Cheng, L., Yang, K., Li, Y., Chen, J., Wang, C., Shao, M., Lee, S.-T., Liu, Z.: Facile preparation of multifunctional upconversion nanoprobes for multimodal imaging and dual-targeted photothermal therapy. Angew. Chemie. Int. Ed. **50**, 7385–7390 (2011). https://doi.org/10.1002/anie.201101447
83. Wang, K., Xiang, Y., Pan, W., Wang, H., Li, N., Tang, B.: Dual-targeted photothermal agents for enhanced cancer therapy. Chem. Sci. **11**, 8055–8072 (2020). https://doi.org/10.1039/D0SC03173A
84. Runowski, M., Grzyb, T., Lis, S.: Magnetic and luminescent hybrid nanomaterial based on Fe_3O_4 nanocrystals and $GdPO_4$: Eu^{3+} nanoneedles. J. Nanoparticle Res. **14**, 1188 (2012). https://doi.org/10.1007/s11051-012-1188-7
85. Xia, A., Gao, Y., Zhou, J., Li, C., Yang, T., Wu, D., Wu, L., Li, F.: Core–shell $NaYF_4$: Yb^{3+}, Tm^{3+}@Fe_xO_y nanocrystals for dual-modality T_2-enhanced magnetic resonance and NIR-to-NIR upconversion luminescent imaging of small-animal lymphatic node. Biomaterials **32**, 7200–7208 (2011). https://doi.org/10.1016/j.biomaterials.2011.05.094
86. Gai, S., Yang, P., Li, C., Wang, W., Dai, Y., Niu, N., Lin, J.: Synthesis of magnetic, up-conversion luminescent, and mesoporous core-shell-structured nanocomposites as drug carriers. Adv. Funct. Mater. **20**, 1166–1172 (2010). https://doi.org/10.1002/adfm.200902274

87. Mertens, H., Polman, A.: Plasmon-enhanced erbium luminescence. Appl. Phys. Lett. **89**, 211107 (2006). https://doi.org/10.1063/1.2392827
88. Da Silva, D.M., Kassab, L.R.P., Lüthi, S.R., De Araújo, C.B., Gomes, A.S.L., Bell, M.J.V.: Frequency upconversion in Er^{3+} doped PbO-GeO_2 glasses containing metallic nanoparticles. Appl. Phys. Lett. **90**, 1–4 (2007). https://doi.org/10.1063/1.2679798
89. Som, T., Karmakar, B.: Nanosilver enhanced upconversion fluorescence of erbium ions in Er^{3+}: Ag-antimony glass nanocomposites. J. Appl. Phys. **105**, 013102 (2009). https://doi.org/10.1063/1.3054918
90. Zhang, H., Xu, D., Huang, Y., Duan, X.: Highly spectral dependent enhancement of upconversion emission with sputtered gold island films. Chem. Commun. **47**, 979–981 (2011). https://doi.org/10.1039/C0CC03566A
91. Zhang, H., Li, Y., Ivanov, I.A., Qu, Y., Huang, Y., Duan, X.: Plasmonic modulation of the upconversion fluorescence in $NaYF_4$: Yb/Tm hexaplate nanocrystals using gold nanoparticles or nanoshells. Angew. Chemie. Int. Ed. **49**, 2865–2868 (2010). https://doi.org/10.1002/anie.200905805
92. Feng, W., Sun. L.-D., Yan. C.-H.: Ag nanowires enhanced upconversion emission of $NaYF_4$: Yb,Er nanocrystals via a direct assembly method. Chem. Commun. 4393 (2009). https://doi.org/10.1039/b909164e
93. Zhang, W., Ding, F., Chou, S.Y.: Large enhancement of upconversion luminescence of $NaYF_4$: Yb^{3+}/Er^{3+} nanocrystal by 3D plasmonic nano-antennas. Adv. Mater. **24**, OP236–OP241 (2012). https://doi.org/10.1002/adma.201200220
94. Kannan, P., Rahim, F.A., Teng, X., Chen, R., Sun, H., Huang, L., Kim, D.-H.: Enhanced emission of $NaYF_4$: Yb, Er/Tm nanoparticles by selective growth of Au and Ag nanoshells. RSC Adv. **3**, 7718 (2013). https://doi.org/10.1039/c3ra22130j
95. Jiang, T., Li, J., Qin, W., Zhou, J.: Greatly enhanced Raman scattering and upconversion luminescence of Au-$NaYF_4$ nanocomposites. J. Lumin. **156**, 164–169 (2014). https://doi.org/10.1016/j.jlumin.2014.08.020
96. Lu, Y., Chen, X.: Plasmon-enhanced luminescence in Yb^{3+}: Y_2O_3 thin film and the potential for solar cell photon harvesting. Appl. Phys. Lett. **94**, 193110 (2009). https://doi.org/10.1063/1.3133340
97. Zhang, F., Braun, G.B., Shi, Y., Zhang, Y., Sun, X., Reich, N.O., Zhao, D., Stucky, G.: Fabrication of Ag@SiO_2@Y_2O_3: Er nanostructures for bioimaging: tuning of the upconversion fluorescence with silver nanoparticles. J. Am. Chem. Soc. **132**, 2850–2851 (2010). https://doi.org/10.1021/ja909108x
98. Xu, W., Min, X., Chen, X., Zhu, Y., Zhou, P., Cui, S., Xu, S., Tao, L., Song, H.: Ag-SiO_2-Er_2O_3 nanocomposites: highly effective upconversion luminescence at high power excitation and high temperature. Sci. Rep. **4**, 5087 (2015). https://doi.org/10.1038/srep05087
99. Li, Z.Q., Chen, S., Li, J.J., Liu, Q.Q., Sun, Z., Wang, Z.B., Huang, S.M.: Plasmon-enhanced upconversion fluorescence in $NaYF_4$: Yb/Er/Gd nanorods coated with Au nanoparticles or nanoshells. J. Appl. Phys. **111**, 014310 (2012). https://doi.org/10.1063/1.3676258
100. Schietinger, S., Aichele, T., Wang, H., Nann, T., Benson, O.: Plasmon-enhanced upconversion in single $NaYF_4$: Yb^{3+}/Er^{3+} codoped nanocrystals. Nano. Lett. **10**, 134–138 (2010). https://doi.org/10.1021/nl903046r
101. Liu, N., Qin, W., Qin, G., Jiang, T., Zhao, D.: Highly plasmon-enhanced upconversion emissions from Au@β-$NaYF_4$: Yb,Tm hybrid nanostructures. Chem. Commun. **47**, 7671 (2011). https://doi.org/10.1039/c1cc11179e
102. Priyam, A., Idris, N.M., Zhang, Y.: Gold nanoshell coated $NaYF_4$ nanoparticles for simultaneously enhanced upconversion fluorescence and darkfield imaging. J. Mater. Chem. **22**, 960–965 (2012). https://doi.org/10.1039/C1JM14040J
103. Kannan, P., Abdul Rahim, F., Chen, R., Teng, X., Huang, L., Sun, H., Kim, D.-H.: Au nanorod decoration on $NaYF_4$: Yb/Tm nanoparticles for enhanced emission and wavelength-dependent biomolecular sensing. ACS Appl. Mater. Interfaces **5**, 3508–3513 (2013). https://doi.org/10.1021/am4007758

104. Saboktakin, M., Ye, X., Oh, S.J., Hong, S.-H., Fafarman, A.T., Chettiar, U.K., Engheta, N., Murray, C.B., Kagan, C.R.: Metal-enhanced upconversion luminescence tunable through metal nanoparticle-nanophosphor separation. ACS Nano **6**, 8758–8766 (2012). https://doi.org/10.1021/nn302466r
105. Yuan, P., Lee, Y.H., Gnanasammandhan, M.K., Guan, Z., Zhang, Y., Xu, Q.-H.: Plasmon enhanced upconversion luminescence of $NaYF_4$: Yb, Er@SiO_2@Ag core-shell nanocomposites for cell imaging. Nanoscale **4**, 5132 (2012). https://doi.org/10.1039/c2nr31241g
106. Chen, X., Zhou, D., Xu, W., Zhu, J., Pan, G., Yin, Z., Wang, H., Zhu, Y., Shaobo, C., Song, H.: Fabrication of Au-Ag nanocage@$NaYF_4$@$NaYF_4$: Yb, Er core-shell hybrid and its tunable upconversion enhancement. Sci. Rep. **7**, 41079 (2017). https://doi.org/10.1038/srep41079
107. Xu, W., Zhu, Y., Chen, X., Wang, J., Tao, L., Xu, S., Liu, T., Song, H.: A novel strategy for improving upconversion luminescence of $NaYF_4$: Yb, Er nanocrystals by coupling with hybrids of silver plasmon nanostructures and poly(methyl methacrylate) photonic crystals. Nano. Res. **6**, 795–807 (2013). https://doi.org/10.1007/s12274-013-0358-y
108. Saboktakin, M., Ye, X., Chettiar, U.K., Engheta, N., Murray, C.B., Kagan, C.R.: Plasmonic enhancement of nanophosphor upconversion luminescence in Au nanohole arrays. ACS Nano **7**, 7186–7192 (2013). https://doi.org/10.1021/nn402598e
109. Wang, P., Li, Z., Salcedo, W.J., Sun, Z., Huang, S., Brolo, A.G.: Surface plasmon enhanced upconversion from $NaYF_4$: Yb/Er/Gd nano-rods. Phys. Chem. Chem. Phys. **17**, 16170–16177 (2015). https://doi.org/10.1039/C5CP02249E
110. Das, A., Mao, C., Cho, S., Kim, K., Park, W.: Over 1000-fold enhancement of upconversion luminescence using water-dispersible metal-insulator-metal nanostructures. Nat. Commun. **9**, 4828 (2018). https://doi.org/10.1038/s41467-018-07284-w
111. Zhan, S., Xiong, J., Nie, G., Wu, S., Hu, J., Wu, X., Hu, S., Zhang, J., Gao, Y., Liu, Y.: Steady state luminescence enhancement in plasmon coupled core/shell upconversion nanoparticles. Adv. Mater. Interfaces **6**, 1802089 (2019). https://doi.org/10.1002/admi.201802089
112. Aisaka, T., Fujii, M., Hayashi, S.: Enhancement of upconversion luminescence of Er doped Al_2O_3 films by Ag island films. Appl. Phys. Lett. **92**, 132105 (2008). https://doi.org/10.1063/1.2896303
113. Ge, W., Zhang, X.R., Liu, M., Lei, Z.W., Knize, R.J., Lu, Y.: Distance dependence of gold-enhanced upconversion luminescence in Au/SiO_2/Y_2O_3: Yb^{3+}, Er^{3+} nanoparticles. Theranostics **3**, 282–288 (2013). https://doi.org/10.7150/thno.5523
114. Tiwari, S.P., Kumar, K., Rai, V.K.: Plasmonic enhancement in upconversion emission of La_2O_3: Er^{3+}/Yb^{3+} phosphor via introducing silver metal nanoparticles. Appl. Phys. B **121**, 221–228 (2015). https://doi.org/10.1007/s00340-015-6223-9
115. Xu, W., Chen, B., Yu, W., Zhu, Y., Liu, T., Xu, S., Min, X., Bai, X., Song, H.: The upconversion luminescent properties and silver-modified luminescent enhancement of YVO_4: Yb^{3+}, Er^{3+} NPs. Dalt. Trans. **41**, 13525 (2012). https://doi.org/10.1039/c2dt31435e
116. Liu, S., Chen, G., Ohulchanskyy, T.Y., Swihart, M.T., Prasad, P.N.: Facile synthesis and potential bioimaging applications of hybrid upconverting and plasmonic $NaGdF_4$: Yb^{3+}, Er^{3+}/silica/gold nanoparticles. Theranostics **3**, 275–281 (2013). https://doi.org/10.7150/thno.4983
117. Dong, B., Xu, S., Sun, J., Bi, S., Li, D., Bai, X., Wang, Y., Wang, L., Song, H.: Multifunctional $NaYF_4$: Yb^{3+}, Er^{3+}@Ag core/shell nanocomposites: integration of upconversion imaging and photothermal therapy. J. Mater. Chem. **21**, 6193–6200 (2011). https://doi.org/10.1039/c0jm04498a
118. Li, A.-H., Lü, M., Guo, L., Sun, Z.: Enhanced upconversion luminescence of metal-capped $NaGd_{0.3}Yb_{0.7}F_4$: Er submicrometer particles. Small **12**, 2092–2098 (2016). https://doi.org/10.1002/smll.201502934
119. Zhang, Y., Xu, S., Li, X., Zhang, J., Sun, J., Xia, H., Hua, R., Chen, B.: Fabrication, photothermal conversion and temperature sensing of novel nanoplatform-hybrid nanocomposite of $NaYF_4$: Er^{3+}, Y^{b3}+@NaY_F4 and Au nanorods for photothermal therapy. Mater. Res. Bull. **114**, 148–155 (2019). https://doi.org/10.1016/j.materresbull.2019.03.003

120. Chen, Y., Zhang, B., Liu, G., Zhuang, X., Kang, E.-T.: Graphene and its derivatives: switching ON and OFF. Chem. Soc. Rev. **41**, 4688 (2012). https://doi.org/10.1039/c2cs35043b
121. Park, S., Vosguerichian, M., Bao, Z.: A review of fabrication and applications of carbon nanotube film-based flexible electronics. Nanoscale **5**, 1727–1752 (2013). https://doi.org/10.1039/c3nr33560g
122. Cheng, Z., Chai, R., Ma, P., Dai, Y., Kang, X., Lian, H., Hou, Z., Li, C., Lin, J.: Multiwalled carbon nanotubes and $NaYF_4$: Yb^{3+}/Er^{3+} nanoparticle-doped bilayer hydrogel for concurrent NIR-triggered drug release and up-conversion luminescence tagging. Langmuir **29**, 9573–9580 (2013). https://doi.org/10.1021/la402036p
123. Vilela, P., El-Sagheer, A., Millar, T.M., Brown, T., Muskens, O.L., Kanaras, A.G.: Graphene oxide-upconversion nanoparticle based optical sensors for targeted detection of mRNA biomarkers present in Alzheimer's disease and prostate cancer. ACS Sens. **2**, 52–56 (2017). https://doi.org/10.1021/acssensors.6b00651
124. Giust, D., Lucío, M.I., El-Sagheer, A.H., Brown, T., Williams, L.E., Muskens, O.L., Kanaras, A.G.: Graphene oxide-upconversion nanoparticle based portable sensors for assessing nutritional deficiencies in crops. ACS Nano **12**, 6273–6279 (2018). https://doi.org/10.1021/acsnano.8b03261
125. Lin, F., Jia, M., Sun, Z., Fu, Z.: Highly sensitive self-referencing thermometry probe and advanced anti-counterfeiting based on the CDs/YVO_4: Eu^{3+} composite materials. Scr. Mater. **186**, 298–303 (2020). https://doi.org/10.1016/j.scriptamat.2020.05.015
126. Yin, M., Wu, L., Li, Z., Ren, J., Qu, X.: Facile in situ fabrication of graphene-upconversion hybrid materials with amplified electrogenerated chemiluminescence. Nanoscale **4**, 400–404 (2012). https://doi.org/10.1039/C1NR11393C
127. Wei, W., He, T., Teng, X., Wu, S., Ma, L., Zhang, H., Ma, J., Yang, Y., Chen, H., Han, Y., Sun, H., Huang, L.: Nanocomposites of graphene oxide and upconversion rare-earth nanocrystals with superior optical limiting performance. Small **8**, 2271–2276 (2012). https://doi.org/10.1002/smll.201200065
128. Kataria, M., Yadav, K., Haider, G., Liao, Y.M., Liou, Y.-R., Cai, S.-Y., Lin, H., Chen, Y.H., Paul Inbaraj, C.R., Bera, K.P., Lee, H.M., Chen, Y.-T., Wang, W.-H., Chen, Y.F.: Transparent, wearable, broadband, and highly sensitive upconversion nanoparticles and graphene-based hybrid photodetectors. ACS Photon. **5**, 2336–2347 (2018). https://doi.org/10.1021/acsphotonics.8b00141
129. Thakur, M.K., Gupta, A., Fakhri, M.Y., Chen, R.S., Wu, C.T., Lin, K.H., Chattopadhyay, S.: Optically coupled engineered upconversion nanoparticles and graphene for a high responsivity broadband photodetector. Nanoscale **11**, 9716–9725 (2019). https://doi.org/10.1039/C8NR10280E
130. Li, Y., Wang, G., Pan, K., Jiang, B., Tian, C., Zhou, W., Fu, H.: $NaYF_4$: Er^{3+}/Yb^{3+}-graphene composites: preparation, upconversion luminescence, and application in dye-sensitized solar cells. J. Mater. Chem. **22**, 20381 (2012). https://doi.org/10.1039/c2jm34113a
131. Wu, S., Sun, X., Zhu, J., Chang, J., Zhang, S.: Increasing electrical conductivity of upconversion materials by in situ binding with graphene. Nanotechnology **27**, 345703 (2016). https://doi.org/10.1088/0957-4484/27/34/345703
132. Yan, L., Chang, Y.-N., Yin, W., Liu, X., Xiao, D., Xing, G., Zhao, L., Gu, Z., Zhao, Y.: Biocompatible and flexible graphene oxide/upconversion nanoparticle hybrid film for optical pH sensing. Phys. Chem. Chem. Phys. **16**, 1576–1582 (2014). https://doi.org/10.1039/C3CP54317J
133. Liu, C., Wang, Z., Jia, H., Li, Z.: Efficient fluorescence resonance energy transfer between upconversion nanophosphors and graphene oxide: a highly sensitive biosensing platform. Chem. Commun. **47**, 4661 (2011). https://doi.org/10.1039/c1cc10597c
134. Mendez-Gonzalez, D., Calderón, O.G., Melle, S., González-Izquierdo, J., Bañares, L., López-Díaz, D., Velázquez, M.M., López-Cabarcos, E., Rubio-Retama, J., Laurenti, M.: Contribution of resonance energy transfer to the luminescence quenching of upconversion nanoparticles with graphene oxide. J. Colloid. Interface Sci. **575**, 119–129 (2020). https://doi.org/10.1016/j.jcis.2020.04.076

135. Rong, Y., Li, H., Ouyang, Q., Ali, S., Chen, Q.: Rapid and sensitive detection of diazinon in food based on the FRET between rare-earth doped upconversion nanoparticles and graphene oxide. Spectrochim. Acta Part A Mol. Biomol. Spectrosc. **239**, 118500 (2020). https://doi.org/10.1016/j.saa.2020.118500
136. Alonso-Cristobal, P., Vilela, P., El-Sagheer, A., Lopez-Cabarcos, E., Brown, T., Muskens, O.L., Rubio-Retama, J., Kanaras, A.G.: Highly sensitive DNA sensor based on upconversion nanoparticles and graphene oxide. ACS Appl. Mater. Interfaces **7**, 12422–12429 (2015). https://doi.org/10.1021/am507591u
137. Wu, S., Duan, N., Ma, X., Xia, Y., Wang, H., Wang, Z., Zhang, Q.: Multiplexed fluorescence resonance energy transfer aptasensor between upconversion nanoparticles and graphene oxide for the simultaneous determination of mycotoxins. Anal. Chem. **84**, 6263–6270 (2012). https://doi.org/10.1021/ac301534w
138. Laurenti, M., Paez-Perez, M., Algarra, M., Alonso-Cristobal, P., Lopez-Cabarcos, E., Mendez-Gonzalez, D., Rubio-Retama, J.: Enhancement of the upconversion emission by visible-to-near-infrared fluorescent graphene quantum dots for miRNA detection. ACS Appl. Mater. Interfaces **8**, 12644–12651 (2016). https://doi.org/10.1021/acsami.6b02361
139. Liu, W., Liu, G., Dong, X., Wang, J., Yu, W.: Multifunctional MWCNTs-$NaGdF_4$: Yb^{3+}, Er^{3+}, Eu^{3+} hybrid nanocomposites with potential dual-mode luminescence, magnetism and photothermal properties. Phys. Chem. Chem. Phys. **35**, 22659–22667 (2015). https://doi.org/10.1039/b000000x
140. Wang, Y., Wang, H., Liu, D., Song, S., Wang, X., Zhang, H.: Graphene oxide covalently grafted upconversion nanoparticles for combined NIR mediated imaging and photothermal/photodynamic cancer therapy. Biomaterials **34**, 7715–7724 (2013). https://doi.org/10.1016/j.biomaterials.2013.06.045
141. Ruiyi, L., Zaijun, L., Xiulan, S., Jan, J., Lin, L., Zhiguo, G., Guangli, W.: Graphene quantum dot-rare earth upconversion nanocages with extremely high efficiency of upconversion luminescence, stability and drug loading towards controlled delivery and cancer theranostics. Chem. Eng. J. **382**, 122992 (2020). https://doi.org/10.1016/j.cej.2019.122992
142. Rani, J.R., Oh, S.-I., Woo, J.M., Tarwal, N.L., Kim, H.-W., Mun, B.S., Lee, S., Kim, K.-J., Jang, J.-H.: Graphene oxide-phosphor hybrid nanoscrolls with high luminescent quantum yield: synthesis, structural, and X-ray absorption studies. ACS Appl. Mater. Interfaces **7**, 5693–5700 (2015). https://doi.org/10.1021/am507342w
143. Zhang, C., Yuan, Y., Zhang, S., Wang, Y., Liu, Z.: Biosensing platform based on fluorescence resonance energy transfer from upconverting nanocrystals to graphene oxide. Angew. Chemie. Int. Ed. **50**, 6851–6854 (2011). https://doi.org/10.1002/anie.201100769
144. Luoshan, M., Li, M., Liu, X., Guo, K., Bai, L., Zhu, Y., Sun, B., Zhao, X.: Performance optimization in dye-sensitized solar cells with β-$NaYF_4$: Er^{3+}/Yb^{3+} and graphene multifunctional layer hybrid composite photoanodes. J. Power Sources **287**, 231–236 (2015). https://doi.org/10.1016/j.jpowsour.2015.04.068
145. Liu, Y., Xu, Y., Geng, X., Huo, Y., Chen, D., Sun, K., Zhou, G., Chen, B., Tao, K.: Synergistic targeting and efficient photodynamic therapy based on graphene oxide quantum dot-upconversion nanocrystal hybrid nanoparticles. Small **14**, 1800293 (2018). https://doi.org/10.1002/smll.201800293
146. Bera, D., Qian, L., Tseng, T.-K., Holloway, P.H.: Quantum dots and their multimodal applications: a review. Materials (Basel) **3**, 2260–2345 (2010). https://doi.org/10.3390/ma3042260
147. Mattsson, L., Wegner, K.D., Hildebrandt, N., Soukka, T.: Upconverting nanoparticle to quantum dot FRET for homogeneous double-nano biosensors. RSC Adv. **5**, 13270–13277 (2015). https://doi.org/10.1039/C5RA00397K
148. Bednarkiewicz, A., Nyk, M., Samoc, M., Strek, W.: Up-conversion FRET from Er^{3+} /Yb^{3+}: $NaYF_4$ nanophosphor to CdSe quantum dots. J. Phys. Chem. C **114**, 17535–17541 (2010). https://doi.org/10.1021/jp106120d
149. Chang, J., Liu, Y., Li, J., Wu, S., Niu, W., Zhang, S.: Strong red and NIR emission in $NaYF_4$: Yb^{3+}, Tm^{3+}/QDs nanoheterostructures. J. Mater. Chem. C **1**, 1168–1173 (2013). https://doi.org/10.1039/C2TC00184E

150. Antoniak, M.A., Wawrzyńczyk, D., Zaręba, J.K., Samoć, M., Nyk, M.: Spectrally resolved two-photon absorption properties and switching of the multi-modal luminescence of $NaYF_4$: Yb, Er/CdSe hybrid nanostructures. J. Mater. Chem. C **6**, 5949–5956 (2018). https://doi.org/10.1039/C8TC00969D
151. Bi, X., He, G., Di, W., Qin, W.: Enhanced near-infrared upconversion luminescence of $NaYF_4$: Yb^{3+}, Tm^{3+}/CdSe nanoheterostructures. Mater. Lett. **173**, 187–190 (2016). https://doi.org/10.1016/j.matlet.2016.02.158
152. Cui, S., Xu, S., Song, H., Xu, W., Chen, X., Zhou, D., Yin, Z., Han, W.: Highly sensitive and selective detection of mercury ions based on up-conversion FRET from $NaYF_4$: Yb^{3+}/Er^{3+} nanophosphors to CdTe quantum dots. RSC Adv. **5**, 99099–99106 (2015). https://doi.org/10.1039/C5RA16200A
153. Feng, P., Pan, Y., Ye, H.: Core–shell structured $NaYF_4$: Yb, Tm@CdS composite for enhanced photocatalytic properties. RSC Adv. **8**, 35306–35313 (2018). https://doi.org/10.1039/C8RA06800C
154. Yan, C., Dadvand, A., Rosei, F., Perepichka, D.F.: Near-IR photoresponse in new up-converting CdSe/$NaYF_4$: Yb, Er nanoheterostructures. J. Am. Chem. Soc. **132**, 8868–8869 (2010). https://doi.org/10.1021/ja103743t
155. Song, D., Chi, S., Li, X., Wang, C., Li, Z., Liu, Z.: Upconversion system with quantum dots as sensitizer: improved photoluminescence and PDT efficiency. ACS Appl. Mater. Interfaces **11**, 41100–41108 (2019). https://doi.org/10.1021/acsami.9b16237
156. Ambroz, F., Macdonald, T.J., Martis, V., Parkin, I.P.: Evaluation of the BET theory for the characterization of meso and microporous MOFs. Small Methods **2**, 1800173 (2018). https://doi.org/10.1002/smtd.201800173
157. Osterrieth, J.W.M., Fairen-Jimenez, D.: Metal-Organic Framework composites for theragnostics and drug delivery applications. Biotechnol. J. **2000005**, 2000005 (2020). https://doi.org/10.1002/biot.202000005
158. Li, Y., Tang, J., He, L., Liu, Y., Liu, Y., Chen, C., Tang, Z.: Core-shell upconversion nanoparticle@metal-organic framework nanoprobes for luminescent/magnetic dual-mode targeted imaging. Adv. Mater. **27**, 4075–4080 (2015). https://doi.org/10.1002/adma.201501779
159. Deng, K., Hou, Z., Li, X., Li, C., Zhang, Y., Deng, X., Cheng, Z., Lin, J.: Aptamer-mediated up-conversion core/MOF shell nanocomposites for targeted drug delivery and cell imaging. Sci. Rep. **5**, 7851 (2015). https://doi.org/10.1038/srep07851
160. Yuan, Z., Zhang, L., Li, S., Zhang, W., Lu, M., Pan, Y., Xie, X., Huang, L., Huang, W.: Paving metal-organic frameworks with upconversion nanoparticles via self-assembly. J. Am. Chem. Soc. **140**, 15507–15515 (2018). https://doi.org/10.1021/jacs.8b10122
161. Wang, D., Zhao, C., Gao, G., Xu, L., Wang, G., Zhu, P.: Multifunctional $NaLnF_4$@MOF-Ln nanocomposites with dual-mode luminescence for drug delivery and cell imaging. Nanomaterials **9**, 1274 (2019). https://doi.org/10.3390/nano9091274
162. Cong, H.-L., Jia, F.-F., Wang, S., Yu, M.-T., Shen, Y.-Q., Yu, B.: Core-shell upconversion nanoparticle@metal-organic framework nanoprobes for targeting and drug delivery. Integr. Ferroelectr. **206**, 66–78 (2020). https://doi.org/10.1080/10584587.2020.1728627
163. Li, Z., Qiao, X., He, G., Sun, X., Feng, D., Hu, L., Xu, H., Xu, H.-B., Ma, S., Tian, J.: Core-satellite metal-organic framework@upconversion nanoparticle superstructures via electrostatic self-assembly for efficient photodynamic theranostics. Nano Res. **13**, 3377–3386 (2020). https://doi.org/10.1007/s12274-020-3025-0
164. Li, M., Wang, J., Zheng, Y., Zheng, Z., Li, C., Li, Z.: Anchoring $NaYF_4$: Yb, Tm upconversion nanocrystals on concave MIL-53(Fe) octahedra for NIR-light enhanced photocatalysis. Inorg. Chem. Front. **4**, 1757–1764 (2017). https://doi.org/10.1039/C7QI00366H
165. Li, M., Zheng, Z., Zheng, Y., Cui, C., Li, C., Li, Z.: Controlled growth of metal-organic framework on upconversion nanocrystals for NIR-enhanced photocatalysis. ACS Appl. Mater. Interfaces **9**, 2899–2905 (2017). https://doi.org/10.1021/acsami.6b15792
166. Liu, Y., Zhang, C., Liu, H., Li, Y., Xu, Z., Li, L., Whittaker, A.: Controllable synthesis of up-conversion nanoparticles UCNPs@MIL-PEG for pH-responsive drug delivery and potential

up-conversion luminescence/magnetic resonance dual-mode imaging. J. Alloys Compd. **749**, 939–947 (2018). https://doi.org/10.1016/j.jallcom.2018.03.355
167. Mukherjee, P., Kumar, A., Bhamidipati, K., Puvvada, N., Sahu, S.K.: Facile strategy to synthesize magnetic upconversion nanoscale metal-organic framework composites for theranostics application. ACS Appl. Bio. Mater. **3**, 869–880 (2020). https://doi.org/10.1021/acsabm.9b00949
168. Dong, B., Song, H., Yu, H., Zhang, H., Qin, R., Bai, X., Pan, G., Lu, S., Wang, F., Fan, L., Dai, Q.: Upconversion properties of Ln^{3+} doped $NaYF_4$/polymer composite fibers prepared by electrospinning. J. Phys. Chem. C **112**, 1435–1440 (2008). https://doi.org/10.1021/jp076958z
169. Yan, B., Boyer, J.-C., Habault, D., Branda, N.R., Zhao, Y.: Near infrared light triggered release of biomacromolecules from hydrogels loaded with upconversion nanoparticles. J. Am. Chem. Soc. **134**, 16558–16561 (2012). https://doi.org/10.1021/ja308876j
170. Wang, J., Hu, J., Tang, D., Liu, X., Zhen, Z.: Oleic acid (OA)-modified LaF_3: Er, Yb nanocrystals and their polymer hybrid materials for potential optical-amplification applications. J. Mater. Chem. **17**, 1597–1601 (2007). https://doi.org/10.1039/B617754A
171. Boyer, J.C., Johnson, N.J.J., van Veggel, F.C.J.M.: Upconverting lanthanide-doped $NaYF_4$-PMMA polymer composites prepared by *in situ* polymerization. Chem. Mater. **21**, 2010–2012 (2009). https://doi.org/10.1021/cm900756h
172. Kim, S.Y., Won, Y.-H., Jang, H.S.: A Strategy to enhance Eu^{3+} emission from $LiYF_4$: Eu nanophosphors and green-to-orange multicolor tunable, transparent nanophosphor-polymer composites. Sci. Rep. **5**, 7866 (2015). https://doi.org/10.1038/srep07866
173. Hu, F., Liu, X., Chen, R., Liu, Y., Mai, Y., Maalej, R., Yang, Y.: Judd-Ofelt parameters of the up-conversion phosphors: Er^{3+} doped $BaGd_2ZnO_5$/PMMA and $NaYF_4$/PMMA. J. Rare Earths. **35**, 964–969 (2017). https://doi.org/10.1016/S1002-0721(17)61000-7
174. Li, J., Zhao, Q., Shi, F., Liu, C., Tang, Y.: NIR-mediated nanohybrids of upconversion nanophosphors and fluorescent conjugated polymers for high-efficiency antibacterial performance based on fluorescence resonance energy transfer. Adv. Healthc. Mater. **5**, 2967–2971 (2016). https://doi.org/10.1002/adhm.201600868
175. Dai, Y., Ma, P., Cheng, Z., Kang, X., Zhang, X., Hou, Z., Li, C., Yang, D., Zhai, X., Lin, J.: Up-conversion cell imaging and pH-induced thermally controlled drug release from $NaYF_4$: Yb^{3+}/Er^{3+}@hydrogel core-shell hybrid microspheres. ACS Nano **6**, 3327–3338 (2012). https://doi.org/10.1021/nn300303q
176. Darwish, A.M., Sagapolutele, M.T., Sarkisov, S., Patel, D., Hui, D., Koplitz, B.: Double beam pulsed laser deposition of composite films of poly(methyl methacrylate) and rare earth fluoride upconversion phosphors. Compos. Part B Eng. **55**, 139–146 (2013). https://doi.org/10.1016/j.compositesb.2013.06.013
177. Darwish, A.M., Moore, S., Mohammad, A., Alexander, D., Bastian, T., Dorlus, W., Sarkisov, S., Patel, D., Mele, P., Koplitz, B., Hui, D.: Polymer nano-composite films with inorganic upconversion phosphor and electro-optic additives made by concurrent triple-beam matrix assisted and direct pulsed laser deposition. Compos. Part B Eng. **109**, 82–90 (2017). https://doi.org/10.1016/j.compositesb.2016.10.053
178. Tan, H., Xie, S., Li, N., Tong, C., Xu, L., Xu, J., Zhang, C.: Synthesis and characterization of $NaYF_4$: Yb, Er up-conversion phosphors/poly(vinyl alcohol) composite fluorescent films. Mater. Express **8**, 141–148 (2018). https://doi.org/10.1166/mex.2018.1420
179. Niu, W., Chen, H., Chen, R., Huang, J., Sun, H., Tok, A.I.Y.: $NaYF_4$: Yb, Er-MoS_2:from synthesis and surface ligand stripping to negative infrared photoresponse. Chem. Commun. **51**, 9030–9033 (2015). https://doi.org/10.1039/C4CC10399H
180. Zhou, N., Xu, B., Gan, L., Zhang, J., Han, J., Zhai, T.: Narrowband spectrally selective near-infrared photodetector based on up-conversion nanoparticles used in a 2D hybrid device. J. Mater. Chem. C **5**, 1591–1595 (2017). https://doi.org/10.1039/C6TC05113H

181. Chatti, M., Adusumalli, V.N.K.B., Ganguli, S., Mahalingam, V.: Near-infrared light triggered superior photocatalytic activity from MoS_2-$NaYF_4$: Yb^{3+}/Er^{3+} nanocomposites. Dalt. Trans. **45**, 12384–12392 (2016). https://doi.org/10.1039/C6DT02548J
182. Qiao, Y., Zhou, X., Geng, H., Sun, L., Zhen, D., Cai, Q.: β-$NaYF_4$: Yb, Er, Gd nanorods@1T/2H-MoS_2 for 980 nm NIR-triggered photocatalytic bactericidal properties. New. J. Chem. **44**, 12201–12207 (2020). https://doi.org/10.1039/D0NJ00908C